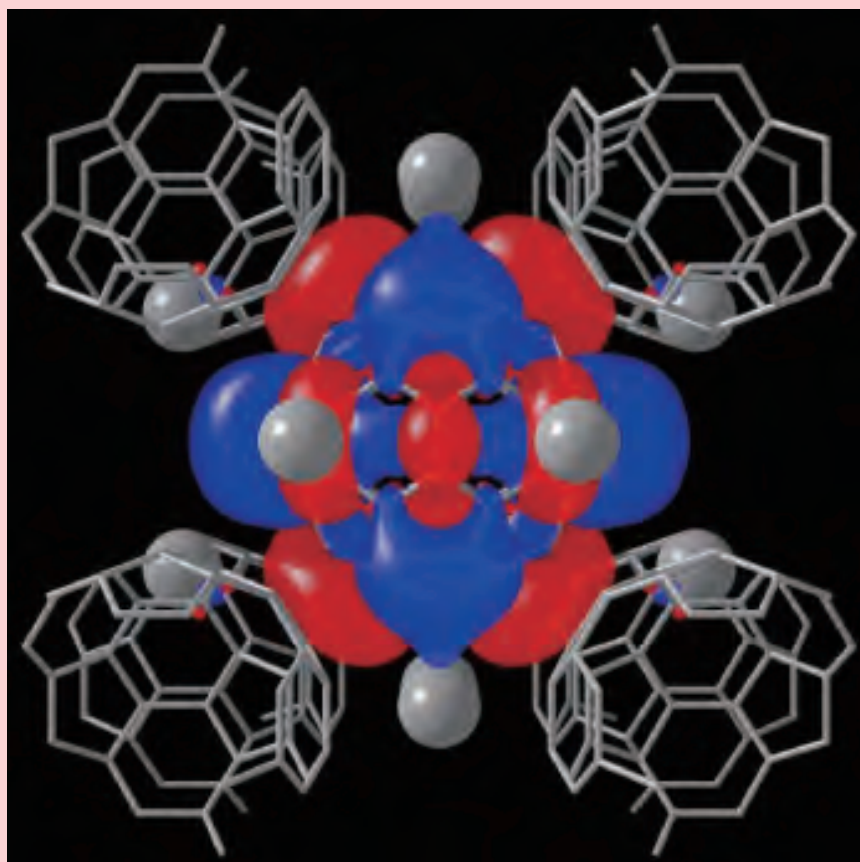




MATERIALS DESIGN AND  
CHARACTERIZATION LABORATORY  
SUPERCOMPUTER CENTER

# ACTIVITY REPORT 2014



INSTITUTE FOR SOLID STATE PHYSICS  
THE UNIVERSITY OF TOKYO

## **Materials Design and Characterization Laboratory (MDCL)**

The MDCL was established as the third research facility of the Institute for Solid State Physics (ISSP) when the latter was reorganized in May 1996. Its aim is to promote material science with an emphasis on the “DSC cycle”, where DSC stands for design, synthesis and characterization, three processes for developing new materials.

The MDCL consists of two sections, Materials Design (MD) section and Materials Synthesis and Characterization (MSC) section. The Supercomputer Center of the ISSP (SCC-ISSP) is placed in the MD section, while in the MSC section there are six laboratories for joint use; Materials Synthesis Laboratory, Chemical Analysis Laboratory, X-ray Diffraction Laboratory, Electron Microscope Laboratory, Electromagnetic Measurement Laboratory, and Spectroscopy Laboratory.

Almost all the facilities of the MDCL are open to scientists in Japan through the User Programs conducted by two steering committees of the MDCL. One is the steering committee of the SCC-ISSP, under which the Supercomputer Project Advisory Committee is placed for reviewing proposals. The other is the steering committee of the MSC facilities. More than half of the members of these committees are from the outside of ISSP.

## PREFACE

The Supercomputer Center (SCC) is a part of the Materials Design and Characterization Laboratory (MDCL) of ISSP. Its mission is to serve the whole community of computational condensed-matter physics of Japan providing it with high performance computing environment. In particular, the SCC selectively promotes and supports large-scale computations. For this purpose, the SCC invites proposals for supercomputer-aided research projects and hosts the Steering Committee, as mentioned below, that evaluates the proposals.

The ISSP supercomputer system consists of three subsystems: System A, which is intended for a parallel computation with relatively smaller number of nodes connected tightly, and System B, which is intended for more nodes with relatively loose connections. In July, 2010, the SCC replaced the two supercomputer subsystems. The current system B is SGI Altix ICE 8400EX, which consists of 30 racks or 15360 cores whereas the system A is NEC SX-9, which consists of 4 nodes or 64 cpus. They have totally 200 TFlops. System C - FUJITSU PRIMEHPC FX10 was installed in April, 2013. It is highly compatible with K computer, the largest supercomputer in Japan. System C consists of 384 nodes, and each node has 1 SPARC64TM IXfx CPU (16 cores) and 32 GB of memory. The total system achieves 90.8 TFlops theoretical peak performance.

The hardware administration is not the only function of the SCC. The ISSP started hosting Computational Materials Science Initiative (CMSI), a new activity of promoting materials science study with next-generation parallel supercomputing. This activity is financially supported by the MEXT HPCI strategic program, and in CMSI, a number of major Japanese research institutes in various branches of materials science are involved. The SCC supports the activities of CMSI as its major mission.

All staff members of university faculties or public research institutes in Japan are invited to propose research projects. The proposals are evaluated by the Steering Committee of SCC. Pre-reviewing is done by the Supercomputer Project Advisory Committee. In school year 2014 totally 247 projects were approved for ISSP joint research projects and 16 for CMSI projects.

The ISSP joint research projects are roughly classified into the following three (the number of projects approved):

- First-Principles Calculation of Materials Properties (119)
- Strongly Correlated Quantum Systems (38)
- Cooperative Phenomena in Complex, Macroscopic Systems (90)

All the three involve both methodology of computation and its applications. The results of the projects are reported in the present volume of 'Activity Report 2014' of the SCC. Every year 3-4 projects are selected for "invited papers" and published at the beginning of the volume. This year's invited papers are the following three:

"All-Electron First-Principles GW+Bethe-Salpeter Program: Development & Applications",

Yoshifumi NOGUCHI

"First-Principles Study on Superconductivity in Alkali-Doped Fullerenes",

Ryotaro ARITA

"Development of Simulation Methods for Membrane Protein Structure Predictions and

Replica-Exchange Methods",

Ryo URANO and Yuko OKAMOTO

June 2, 2015

Hiroshi Noguchi  
(Chairman of the steering committee, SCC, ISSP)



# CONTENTS

## PREFACE

<b>1 OUTLINE</b>	<b>1</b>
1.1 Supercomputer System	1
1.2 Project Proposals	1
1.3 Committees	3
1.4 Staff	6
<b>2 STATISTICS OF FISCAL YEAR 2014</b>	<b>7</b>
2.1 System Statistics	7
2.2 Queue, Job, and User Statistics	7
<b>3 RESEARCH REPORTS</b>	<b>14</b>
3.1 Invited Articles	14
3.2 First-Principles Calculation of Material Properties	39
3.3 Strongly Correlated Quantum Systems	144
3.4 Cooperative Phenomena in Complex Macroscopic Systems	183
3.5 CMSI projects	267
<b>4 PUBLICATION LIST</b>	<b>286</b>
ISSP Joint Research Projects	287
CMSI Projects	320
Doctor Theses	325
Master Theses	326

# 1 Outline

## 1.1 Supercomputer System

In SY 2014, the ISSP supercomputer center provided users with three supercomputing systems: NEC-SX9 (System A), SGI Altix ICE 8400EX (System B), and FUJITSU PRIMEHPC FX10 (System C) (Fig. 1). Systems A and B began service on July 1, 2010, and their operation has terminated on April 1, 2015. FUJITSU PRIMEHPC FX10 (System C) entered service at the beginning of SY 2013. All the systems were all installed in the main building of ISSP.

System A - NEC SX9 is a vector computer with 4 nodes (64 CPUs). Vectorization and parallelization between CPUs can automatically be done by the C/Fortran compilers. One node contains 1 TB of shared memory, and the total system achieves 6.5 TFlops theoretical peak performance. All the nodes are connected to a 13 TB storage system with high throughput.

System B - SGI Altix ICE 8400EX is a massively-parallel supercomputer with 1,920 nodes (3,840 CPUs / 15,360 cores) achieving 180.0 TFlops theoretical peak performance. Each node has 24 GB of memory (46 TB in total) and two Intel Xeon X5570 CPUs running at 2.93 GHz connected by dual QPI links ( $2 \times 25.6$  GB/sec). Up to 128 nodes are connected by enhanced hypercube 4×QDR InfiniBand networks with 40 GB/s bisection bandwidth. A 110 TB Lustre file system is connected to the entire system also with InfiniBand, realizing I/O throughput on the order of GB/sec.

System C - FUJITSU PRIMEHPC FX10 is highly compatible with K computer, the largest supercomputer in Japan. System C consists of 384 nodes, and each node has 1 SPARC64TM IXfx CPU (16 cores) and 32 GB of memory. The total system achieves 90.8 TFlops theoretical peak performance.

For further details, please contact ISSP Supercomputer Center (SCC-ISSP).

[Correspondence: center@issp.u-tokyo.ac.jp]

## 1.2 Project Proposals

The ISSP supercomputer system provides computation resources for scientists working on condensed matter sciences in Japan. All scientific staff members (including post-docs) at universities or public research institutes in Japan can submit proposals for projects related to research activities on materials and condensed matter sciences. These proposals are peer-reviewed by the Advisory Committee members (see Sec. 1.3), and then the computation resources are allocated based on the review reports. The leader of an approved project can set up user accounts for collaborators. Other types of scientists, including graduate students, may also be added. Proposal submissions, peer-review processes, and user registration are all managed via a web system.

The computation resources are distributed in a unit called “point”, determined as a function of available CPU utilization time and consumed disk resources. There

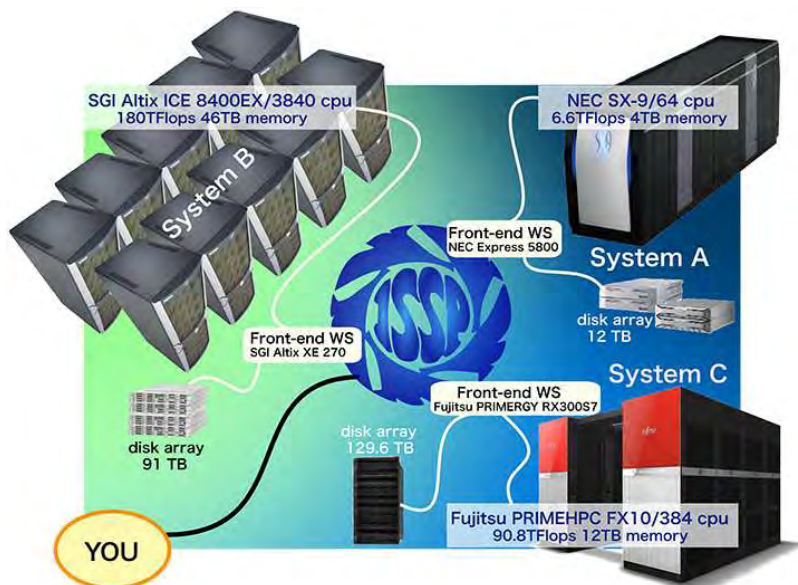


Figure 1: Supercomputer System at the SCC-ISSP

were six classes of research projects in SY 2014. The number of projects and the total number of points that were applied for and approved in this school year are listed in Table 1.

In addition, from SY 2010, ISSP Supercomputer is providing 20% of its computational resources for Computational Materials Science Initiative (CMSI), which aims at advancing parallel computations in condensed matter, molecular, and materials sciences on the 10-PFlops K Computer. The points for projects run by CMSI are distributed in accord with this policy. Computer time has also been allotted to Computational Materials Design (CMD) workshops run by CMSI.

- Proposals for projects in Classes B (small), C (mid-size), E (large-scale), and S (exceptional) can be submitted twice a year. Approved projects in Classes A, B, C, E, and S continue to the end of the school year.
- In Class D, projects can be proposed on rapidly-developing studies that need to perform urgent and relatively large calculations. An approved project continues for 6 months from its approval.
- Class S is for projects that are considered extremely important for the field of condensed matter physics and requires extremely large-scale computation. The project may be carried out either by one research group or cooperatively by several investigators at different institutions. A project of this class should be applied with at least 10,000 points; there is no maximum. We require group leaders applying for Class S to give a presentation on the proposal to the Steering Committee of the SCC-ISSP.
- Project leaders can apply for points so that the points for each system do not exceed the maximum point shown in this table.

Table 1: Classes of research projects in SY 2014

Class	Max. Point			Application
	Sys-A	Sys-B	Sys-C	
A	100	100	100	any time
B	2k	1k	500	twice a year
C	20k	10k	2.5k	twice a year
D	20k	10k	2.5k	any time
E	–	30k	2.5k	twice a year
S	(Sys-A+B)>10k		–	twice a year

Class	# of Proj.	Total points					
		Applied			Approved		
		Sys-A	Sys-B	Sys-C	Sys-A	Sys-B	Sys-C
A	9	500	600	400	500	600	400
B	53	40.8k	44.8k	6.3k	33.8k	29.4k	5.7k
C	151	637.0k	1210.2k	141.2k	429.0k	360.5k	111.4k
D	10	12.0k	71.7 k	0	12.0k	57.6k	0
E	23	–	621.0k	42.0k	–	270.0k	37.4k
S	1	0	60.0k	0	0	25.0k	0
CMSI	18	–	–	–	–	–	140.0k

### 1.3 Committees

In order to fairly manage the projects and to smoothly determine the system operation policies, the Materials Design and Characterization Laboratory (MDCL) of the ISSP has organized the Steering Committee of the MDCL and the Steering Committee of the SCC-ISSP, under which the Supercomputer Project Advisory Committee (SPAC) is formed to review proposals. The members of the committees in SY 2014 were as follows:

#### Steering Committee of the MDCL

HIROI, Zenji	ISSP (Chair person)
KATO, Takeo	ISSP
KAWASHIMA, Naoki	ISSP
MORI, Hatsumi	ISSP
NAKATSUJI, Satoru	ISSP
NOGUCHI, Hiroshi	ISSP
SUGINO, Osamu	ISSP
SUEMOTO, Toru	ISSP
TSUNEYUKI, Shinji	Univ. of Tokyo
KIMURA, Kaoru	Univ. of Tokyo
MIYASAKA, Hitoshi	Tohoku Univ.

HASEGAWA, Tadashi	Nagoya Univ.
OKAMOTO, Yuko	Nagoya Univ.
OTSUKI, Tomi	Sophia Univ.
OGUCHI, Tamio	Osaka Univ.
NOHARA, Minoru	Okayama Univ.

#### Steering Committee of the SCC-ISSP

NOGUCHI, Hiroshi	ISSP (Chair person)
KAWASHIMA, Naoki	ISSP
SUGINO, Osamu	ISSP
TAKADA, Yasutami	ISSP
HARADA, Yoshihisa	ISSP
TSUNETSUGU, Hirokazu	ISSP
SHIBA, Hayato	ISSP
WATANABE, Hiroshi	ISSP
KASAMATSU, Shusuke	ISSP
MORITA, Satoshi	ISSP
HATANO, Naomichi	Univ. of Tokyo
IMADA, Masatoshi	Univ. of Tokyo
NAKAJIMA, Kengo	Univ. of Tokyo
TSUNEYUKI, Shinji	Univ. of Tokyo
MOHRI, Tetsuo	Tohoku Univ.
OTSUKI, Tomi	Sophia Univ.
ODA, Tatsuki	Kanazawa Univ.
OKAMOTO, Yuko	Nagoya Univ.
MORIKAWA, Yoshitada	Osaka Univ.
SUZUKI, Takafumi	Univ. of Hyogo
YOSHIMOTO, Yoshihide	Tottori Univ.
YATA, Hiroyuki	ISSP
FUKUDA, Takaki	ISSP

#### Supercomputer Project Advisory Committee

NOGUCHI, Hiroshi	ISSP (Chair person)
KAWASHIMA, Naoki	ISSP
SUGINO, Osamu	ISSP
TAKADA, Yasutami	ISSP
HARADA, Yoshihisa	ISSP
TSUNETSUGU, Hirokazu	ISSP
SHIBA, Hayato	ISSP
WATANABE, Hiroshi	ISSP
KASAMATSU, Shusuke	ISSP
MORITA, Satoshi	ISSP
AOKI, Hideo	Univ. of Tokyo

HATANO, Naomichi	Univ. of Tokyo
HUKUSHIMA, Koji	Univ. of Tokyo
IKUHARA, Yuichi	Univ. of Tokyo
IMADA, Masatoshi	Univ. of Tokyo
IWATA, Jun-Ichi	Univ. of Tokyo
MIYASHITA, Seiji	Univ. of Tokyo
MOTOME, Yukitoshi	Univ. of Tokyo
NAKAJIMA, Kengo	Univ. of Tokyo
OGATA, Masao	Univ. of Tokyo
OSHIYAMA, Atsushi	Univ. of Tokyo
TSUNEYUKI, Shinji	Univ. of Tokyo
WATANABE, Satoshi	Univ. of Tokyo
NEMOTO, Koji	Hokkaido Univ.
YAKUBO, Kosuke	Hokkaido Univ.
AKAGI, Kazuto	Tohoku Univ.
KAWAKATSU, Toshihiro	Tohoku Univ.
KURAMOTO, Yoshio	Tohoku Univ.
MOHRI, Tetsuo	Tohoku Univ.
SHIBATA, Naokazu	Tohoku Univ.
YANASE, Yoichi	Niigata Univ.
ARITA, Ryotaro	RIKEN
ISHIBASHI, Shoji	AIST
MIYAMOTO, Yoshiyuki	AIST
OTANI, Minoru	AIST
KOBAYASHI, Kazuaki	NIMS
TATEYAMA, Yoshitaka	NIMS
HATSUGAI, Yasuhiro	Univ. of Tsukuba
KOBAYASHI, Nobuhiko	Univ. of Tsukuba
OKADA, Susumu	Univ. of Tsukuba
YABANA, Kazuhiro	Univ. of Tsukuba
HIDA, Kazuo	Saitama Univ.
TOMITA, Yusuke	Shibaura Inst. Tech.
NAKAYAMA, Takashi	Chiba Univ.
FURUKAWA, Nobuo	Aoyama Gakuin Univ.
MATSUKAWA, Hiroshi	Aoyama Gakuin Univ.
TAKANO, Hiroshi	Keio Univ.
YAMAUCHI, Jun	Keio Univ.
YASUOKA, Kenji	Keio Univ.
OTSUKI, Tomi	Sophia Univ.
OBATA, Shuji	Tokyo Denki Univ.
ANDO, Tsuneya	Tokyo Inst. Technology
HOTTA, Takashi	Tokyo Metropolitan Univ.
OKABE, Yutaka	Tokyo Metropolitan Univ.
TOHYAMA, Takami	Tokyo Univ. of Sci.
WATANABE, Kazuyuki	Tokyo Univ. of Sci.

HAGITA, Katsumi	National Defense Academy
INOUE, Junichiro	Nagoya Univ.
KONTANI, Hiroshi	Nagoya Univ.
OKAMOTO, Yuko	Nagoya Univ.
SHIRAISHI, Kenji	Nagoya Univ.
TANAKA, Yukio	Nagoya Univ.
ODA, Tatsuki	Kanazawa Univ.
SAITO, Mineo	Kanazawa Univ.
ARAKI, Takeaki	Kyoto Univ.
KAWAKAMI, Norio	Kyoto Univ.
MASUBUCHI, Yuichi	Kyoto Univ.
YAMAMOTO, Ryoichi	Kyoto Univ.
KASAI, Hideaki	Osaka Univ.
KAWAMURA, Hikaru	Osaka Univ.
KUROKI, Kazuhiko	Osaka Univ.
KUSAKABE, Koichi	Osaka Univ.
MORIKAWA, Yoshitada	Osaka Univ.
OGUCHI, Tamio	Osaka Univ.
SHIRAI, Koun	Osaka Univ.
YOSHIDA, Hiroshi	Osaka Univ.
YUKAWA, Satoshi	Osaka Univ.
HARIMA, Hisatomo	Kobe Univ.
SUGA, Seiichiro	Univ. of Hyogo
SUZUKI, Takafumi	Univ. of Hyogo
TATENO, Masaru	Univ. of Hyogo
SAKAI, Toru	Japan Atomic Energy Agency
HOSHINO, Kozo	Hiroshima Univ.
HOSHI, Takeo	Tottori Univ.
YOSHIMOTO, Yoshihide	Tottori Univ.
YASUDA, Chitoshi	Univ. of the Ryukyus
OZAKI, Taisuke	ISSP
KATO, Takeo	ISSP
TADA, Tomofumi	Tokyo Inst. Technology
TODO, Synge	Univ. of Tokyo

## 1.4 Staff

The following staff members of the SCC-ISSP usually administrate the ISSP Supercomputer.

NOGUCHI, Hiroshi	Associate Professor (Chair person)
KAWASHIMA, Naoki	Professor
SUGINO, Osamu	Associate Professor
WATANABE, Hiroshi	Research Associate
KASAMATSU, Shusuke	Research Associate



NOGUCHI, Yoshifumi	Research Associate
SHIBA, Hayato	Research Associate
MORITA, Satoshi	Research Associate
YATA, Hiroyuki	Technical Associate
FUKUDA, Takaki	Technical Associate
ARAKI, Shigeyuki	Technical Associate

## 2 Statistics (School Year 2014)

### 2.1 System and User Statistics

In the following, we present statistics for operation time taken in the period from April 2014 to March 2015 (SY 2014). In Table 2, we show general statistics of the supercomputer system in SY 2014. The total number of CPUs in System A, B, and C is 64, 3840, and 384 respectively. Consumed disk points amount to about 4%, 5%, and 1% of the total consumed points in System A, B, and C respectively.

In the left column of Fig. 2, availabilities, utilization rates, and consumed points in each system are plotted for each month. Throughout the school year, the utilization rates were high enough. Especially in System B, they were exceeding 90% throughout most of the year. In System C, roughly half of the total utilized resources were used by CMSI projects. This amounts to about 20% of the total usage of the computational resources in this school year. The user statistics are shown in the right column of Fig. 2. The horizontal axis shows the rank of the user/group arranged in the descending order of the execution time (hour $\times$ CPU). The execution time of the user/group of the first rank is the longest. The vertical axis shows the sum of the execution time up to the rank. From the saturation points of the graphs, the number of “active” users of each system is around 50, 250, and 70 for System A, B, and C respectively. The maximum ranks in the graphs correspond to the number of the users/groups that submitted at least one job.

### 2.2 Queue and Job Statistics

Queue structures of System A, B, and C in SY 2014 are shown in Table 3. In each system, the queues are classified by the number of CPUs the user can use and the maximum duration of each submitted job. In System A, in addition to the usual P class jobs, there is a queue “D1” for debugging, and “L1” for jobs which require only one CPU but quite a long time. Parallel jobs are executed with “P4” and “P16”, 16 CPUs being available at maximum with one job using “P16”.

In System B, a highly detailed classification is adopted. The biggest portion (20 racks out of 30 in total) of the resources is allotted for “F256”, which mainly uses 128 or 256 CPUs at once. “F16”, “F32”, and “F64” are for smaller-scale jobs using 16, 32, and 64 CPUs respectively. The elapsed-time limit of the above queues is 24 hours for one job, while it is set smaller for smaller-scale queues (“F4”



Table 2: Overall statistics of SY 2014

	System-A	System-B	System-C
total service time (k hour $\times$ CPU)	544.0	32441.1	3264.4
number of executed jobs	24884	148290	25020
total consumed points (k point)	139.2	499.7	105.4
CPU points (k point)	134.9	471.1	99.9
disk points (k point)	4.3	28.6	5.5
points consumed by CMSI (k point)	—	—	62.4
total exec. time (k hour $\times$ CPU)	444.27	29096.3	2323.8
availability	97.2%	96.4%	96.8%
utilization rate	81.7%	89.5%	71.2%

and “F8”) to speed up their rotation. For time-demanding jobs, L-type queues are also introduced, whose time limit is set longer than F-type queues. “P64” queue is set up to accept jobs which require any number of CPUs more than 1 and not exceeding 64. “i32” is a queue for debugging, which corresponds to interactive mode in the previous system. In “i32”, users can execute their jobs using up to 16 nodes at once from the command line, as if they were logging into the calculation node.

In System C, the “F” and “L” queues are set up similarly to System B. In addition, a debug queue is set up for short debugging jobs utilizing 1 to 4 CPUs, and an interactive queue that can use 1 to 4 CPUs is also available.

The CPU points are set smaller for larger-scale queues for System B as shown in Table 3, while it is more uniform in System A. To prevent overuse of the storage, points are charged also for usage of disk quota in the three systems, as shown in Table 4. Disk points are revised often for optimal usage of the resources by examining usage tendencies each year.

Although we do not mention here in detail, to promote utilization of the massively parallel supercomputer, background queues (“B16”, “B32”, “B64”, and “B256”), which charge no CPU points for the jobs, have also been open in System B.

The ISSP Supercomputer also supports large-scale jobs, which use tens of thousands of cores at once by exclusively using the necessary number of CPUs. In-advance application is necessary to execute this type of job. Large-scale jobs can be executed in queues “P512”, “P1024”, “P2048”, and “P3840” just after the scheduled monthly maintenance. However, since such large-scale jobs are now covered by the K Computer, no jobs were executed in these queues since SY2013.

The number of jobs, average waiting time, and total execution time in each queue are shown in Table 5. In System A, the average waiting times of P4 and P16 are a bit long compared with the elapsed-time limit (24 hours). This is because a few active users tend to submit many jobs at once. Because fair-share scheduling is adopted, the waiting time is considered to be appropriate for fair distribution

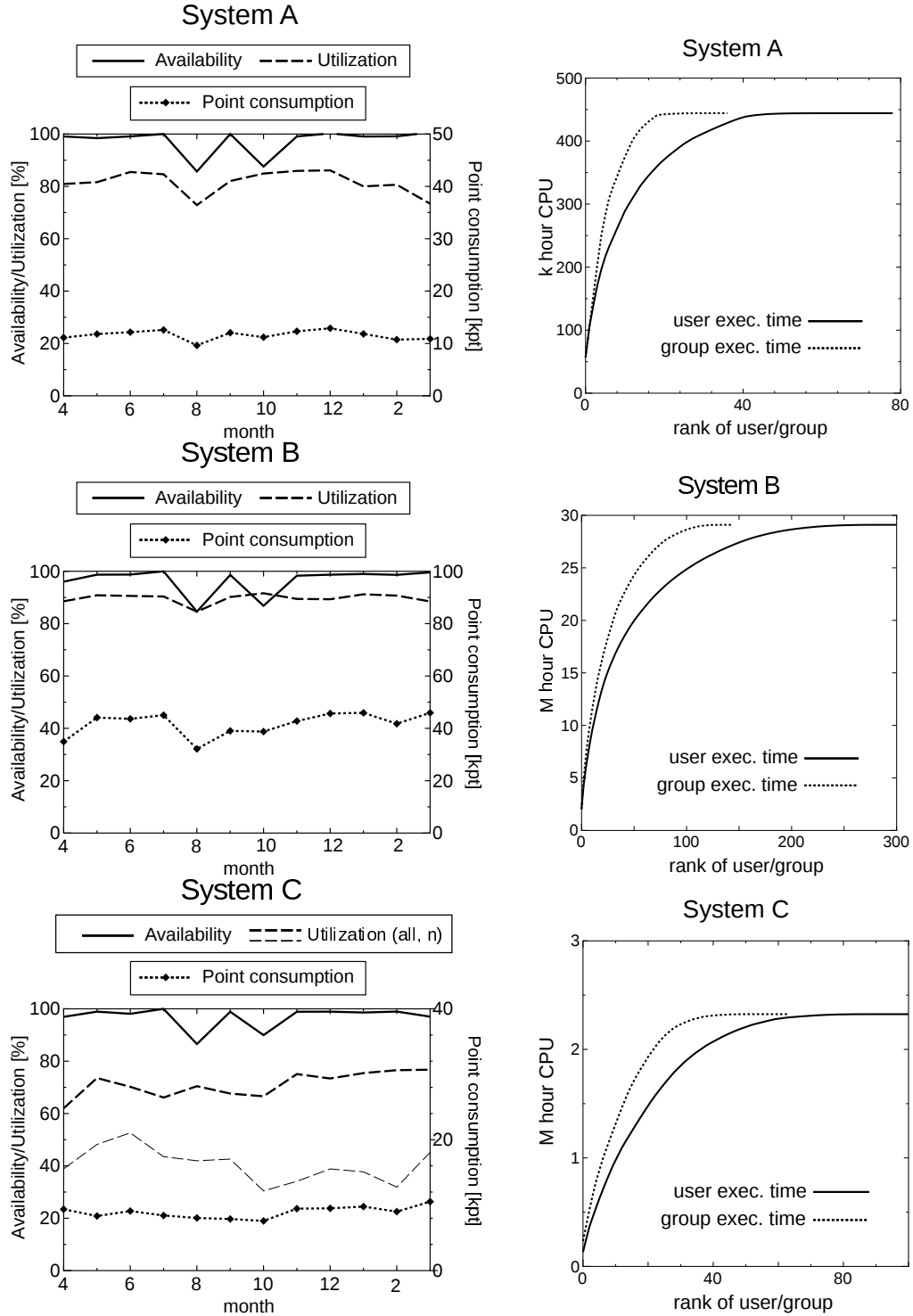


Figure 2: Left: Availabilities, utilization rates and point consumptions of each month during SY 2014. For System C, the utilization by CMSI projects (denoted by “n”) is plotted in addition to the total utilization. Right: User statistics. The horizontal axis shows the rank of the user/group arranged in the descending order of the execution time (hour×CPU). The vertical axis shows the sum of the execution time up to the rank.

Table 3: Queue structures in SY 2014

System-A					
queue name	Elapsed time limit (min)	# of CPU /Job ( $n$ )	# of CPU /queue ( $p$ )	memory size	CPU points / (CPU·day)
D1	15	1	2	60GB	7.776
L1	7200	1	4	60GB	7.776
P1	1440	1	10-30	60GB	7.776
P4	1440	4	16-32	240GB	7.776
P16	1440	16	16	960GB	6.048

System-B				
queue name	Elapsed time limit (min)	# of CPU /Job ( $n$ )	# of CPU /queue ( $p$ )	CPU points / (CPU·day)
P1	720	1	32	0.690
P64	720	2-64	64	0.518
F4	720	4	96	0.518
F8	720	8	96	0.518
F16	1440	16	1024	0.518
F32	1440	32	1024	0.518
F64	1440	64	1024	0.518
L16	7200	16	64	0.518
L32	7200	32	64	0.518
L64	7200	64	64	0.518
i32	20	1-32	64	0.518
F256	1440	65-256	2560	0.358
L256	7200	65-256	512	0.358
P512	—	128-512	512 or 1024	0.358
P1024	7200	384-1024	3072	0.358
P2048	—	128-2048	2048	0.358
P3840	1440	1024-3840	3840	0.358

\* The available memory size is limited to 21 GB per one node.

\* P queues require in-advance application (see main text). The elapsed-time limit for P512 and P2048 queues is determined on a per-application basis.

System-C				
queue name	Elapsed time limit (min)	# of CPU /Job ( $n$ )	# of CPU /queue ( $p$ )	CPU points /(CPU·day)
debug	30	1-4	24	1
interactive	30	1-4	24	1
F12	1440	2-12	60	1
F96	1440	2-12	288	1
L12	7200	24-96	24	1
L96	7200	24-96	192	1

\* The available memory size is limited to 28 GB per one CPU.

Table 4: Disk points of System A, B, and C

			point/day
System A	/home	$0.0125 \times \theta(q - 10)$	
	/work	$0.005 \times \theta(q - 50)$	
System B	/home	$0.05 \times \theta(q - 10)$	
	/work	$0.005 \times \theta(q - 100)$	
System C	/home	$0.05 \times \theta(q - 10)$	
	/work	$0.005 \times \theta(q - 100)$	

\*  $q$  is denoted in unit of GB.

\*  $\theta(x)$  is equal to the Heaviside step function  $H(x)$  multiplied by  $x$ , i.e.,  $xH(x)$ .

of computational resources. We will continue to look for more appropriate queue settings also in the next school year to meet the user's tendency of resource usage.

In System B, a large portion of jobs have been executed in queues “F16”, “F32”, “F64”, and “F256”. As we intended, most of the execution time has been consumed in “F256” and “L256”. In all of these queues, the queue settings meet the user's tendencies in that the waiting times are on the order of the elapsed-time limit.

In System C, the waiting times for the “F” queue jobs are less than twelve hours. The “L96” queue has a waiting time of nearly five days, owing to the large amount of resources the jobs occupy when run in this queue.

## Acknowledgments

The staffs would like to thank Prof. Takafumi Suzuki (now at University of Hyogo) for developing WWW-based system (SCM: SuperComputer Management System) for management of project proposals, peer-review reports by the SPAC committee, and user accounts. We also thank Ms. Reiko Iwafune for creating and maintaining a new WWW page of the ISSP Supercomputer Center.

Table 5: Number of jobs, average waiting time, total execution time, and average number of used CPU's per job in each queue.

System-A				
queue	# of Jobs	Waiting Time (hour)	Exec. Time (k CPU $\times$ hour)	# of CPU
D1	3886	0.01	0.20	1.00
P1	15337	14.70	122.08	1.00
L1	399	27.84	11.69	1.00
P4	4401	40.74	187.35	3.83
P16	830	108.63	122.92	15.25

System-B				
queue	# of Jobs	Waiting Time (hour)	Exec. Time (k CPU $\times$ hour)	# of CPU
P1	31395	23.88	126.39	1.0
P64	22491	25.51	325.88	3.3
F4	18724	20.31	289.28	4.0
F8	9508	9.62	355.97	8.0
F16	28654	15.88	2929.68	16.0
F32	8317	16.13	1927.59	32.0
F64	4076	39.53	2503.65	64.0
L16	457	45.15	189.65	16.0
L32	46	115.47	37.48	32.0
L64	26	258.68	96.05	64.0
i32	8216	0.02	20.32	16.8
F256	8029	21.54	17437.37	193.3
L256	178	16.07	1464.29	159.0
P512	0	0	0.00	0
P1024	0	0	0.00	0
P2048	0	0	0.00	0
P3840	0	0	0.00	0

System-C				
queue	# of Jobs	Waiting Time (hour)	Exec. Time (k CPU $\times$ hour)	# of CPU
F12	11890	9.27	385.52	5.2
L12	127	27.60	6.65	1.9
F96	4929	26.46	1904.18	36.2
L96	9	63.51	19.96	64.8
debug	5725	0.11	1.37	1.8
interactive	1942	0.00	0.29	1.1

## Erratum

In the previous Activity Report 2013, on page 8, there is an error in the bottom right part of Fig. 2 (User statistics for System C), which should be replaced by the Fig. 3 shown below. The number of active users was about 80 in SY 2013 for System C.

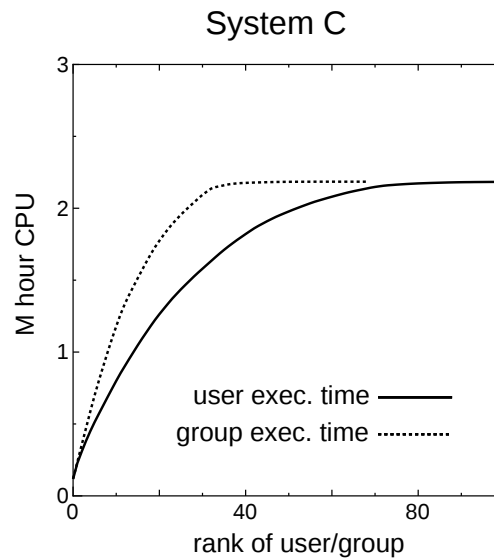


Figure 3: User statistics in SY2013 for System C.

## 3 RESEARCH REPORTS

### 3.1 Invited Articles

All-Electron First-Principles GW+Bethe-Salpeter Program:  
Development & Applications 15

Yoshifumi NOGUCHI

First-Principles Study on Superconductivity  
in Alkali-Doped Fullerides 23

Ryotaro ARITA

Development of Simulation Methods for Membrane Protein  
Structure Predictions and Replica-Exchange Methods 31

Ryo URANO and Yuko OKAMOTO

# All-Electron First-Principles $GW$ +Bethe-Salpeter Program: Development & Applications

Yoshifumi NOGUCHI

*Institute for Solid State Physics, The University of Tokyo  
Kashiwa-no-ha, Kashiwa, Chiba 277-8581*

## Abstract

We have developed our original first-principles  $GW$ +Bethe-Salpeter program code employing an all-electron mixed basis approach, aiming to achieve highly accurate and reliable first-principles simulations of excited state spectra. To extend the treatable system size in this method, we redesigned and rewrote our program code as a hybrid parallel version employing both Message Passing Interface (MPI) and OpenMP. We report  $GW$ +Bethe-Salpeter calculations targeting 110-atoms systems in this report. In addition, in the first attempt world-wide, we applied the *fully* first-principles  $GW$ +Bethe-Salpeter method to x-ray absorption spectra (XAS) and successfully simulated the oxygen 1s XAS for acetone and acetic acid. The calculated XAS are directly compared with the available experimental data without any artificial shifting.

## 1 Introduction

The first-principles Green's function method based on many-body perturbation theory beyond the framework of density functional theory (DFT) is a powerful tool in reliably simulating the excited energy spectra of a wide range of materials. One example is the  $GW$  approximation (GWA), in which  $GW$  quasiparticle energies corresponding to the poles of the one-particle Green's function directly yield the one-particle excitation energy spectra, involving the informa-

tion related with the experimental (inverse) photoemission spectra. Similarly, the two-particle excitation processes can be described by an electron-hole two-particle Green's function, and the energy spectra are directly obtained from the poles of the two-particle Green's function. A standard method of determining the poles of the electron-hole two-particle Green's function from first-principles is known as the  $GW$ +Bethe-Salpeter method, in which the Bethe-Salpeter equation (BSE) is solved within the GWA. Both the  $GW$  and  $GW$ +Bethe-Salpeter methods enable us to accurately simulate excited energy spectra.

Despite great successes, these methods still have a much higher computational cost than the conventional DFT-method, scales as  $O(n^3)$ . The treatable system size of  $GW$ +Bethe-Salpeter is quite small. Hence, the development of a program code (or algorithm) capable in extending the treatable system size is strongly desired. For this purpose, we redesign and rewrite our program as a hybrid parallel version employing both OpenMP and Message Passing Interface (MPI) and tackle this problem.

Another topic in this report is a first-principles description of the core-electron excitations. Although information obtained from x-ray absorption spectra (XAS) is useful in understanding the properties of real materials, it is still challenging to simulate realistic XAS from first-principles without any empirical parameters, reference values from experiments,



or prior practice calculations to increase accuracy, even when the modern first-principles techniques are used rather than old-fashioned techniques based on the total-energy-difference method. The reason is that the simulation of XAS involves two difficult issues: (1) the use of an all-electron basis set capable of describing all of the electronic states from the core electron states with cusp conditions to the free electron states above vacuum level, and (2) the description on the strong electron-hole interaction, including many-body effect (so-called excitonic effect). Therefore, in contrast to the case of UV-vis absorption spectra, in which a valence electron is excited to the empty state, there are a few *fully* first-principles calculations for XAS to date. Our method, which combines an all-electron mixed basis approach and the first-principles  $GW$ +Bethe-Salpeter method, can overcome these two problems simultaneously and potentially simulates realistic XAS, which can be directly compared with those obtained experimentally.

In this report, we first introduce our method and the benchmark tests of our program, focusing on accuracy and performance, and then review recent applications.

## 2 Methodology

### 2.1 DFT

In the present method, the DFT calculation can be regarded as the starting point for subsequent calculations and adds a negligible computational cost to the entire  $GW$ +Bethe-Salpeter calculation. Therefore, we always place a priority on the developing the  $GW$  and Bethe-Salpeter components rather than the DFT component. Consequently, DFT component of our program has very limited features compared to other first-principles program packages, which are freely available online. The exchange-correlation function available in our program is only the local density approximation (LDA), and some algorithms

related with the LDA that accelerate or stabilize the convergence in the self-consistent-field (SCF) loop are available. For example, band-by-band steepest decent, conjugate gradient, or block Davidson methods are available as iterative method for diagonalizing LDA Hamiltonian. To perform the iterative procedures more efficiently, we implemented recursive blocking Gram-Schmidt method of orthonormalizing wave functions and MRRR method of subspace diagonalization which is the most computationally expensive in these iterative procedures and scales as  $O(n^3)$ . Further, as an electron-charge-mixing method, we implemented the simple or optimal linear charge mixing method and the Kerker+RMM-DIIS charge-mixing method. To stabilize the convergence for some systems with narrow band gaps, we also implemented Gaussian smearing. These algorithms allow us to perform stabilized, efficient DFT-calculations for various types of systems. The accuracy and performance of the LDA are examined in Sec. 3.

### 2.2 $GW$ approximation

The  $GW$  quasiparticle energies ( $E_\nu^{GW}$ ) are simply given by replacing the LDA exchange-correlation potential ( $\mu_{xc}^{LDA}$ ) with the  $GW$  self-energy operator ( $\Sigma^{GW}$ ), as follow:

$$E_\nu^{GW} = E_\nu^{LDA} + Z_\nu < \nu | \Sigma^{GW} - \mu_{xc}^{LDA} | \nu >, \quad (1)$$

$$\Sigma^{GW} = iG_0W_0 = iG_0v + iG_0(W_0 - v), \quad (2)$$

where  $G_0$  is a one-particle Green's function,  $v$  is a bare Coulomb interaction, and  $W_0$  is a dynamically screened Coulomb within a random phase approximation (RPA). The first term on the right hand side of Eq. (2) is the Fock-exchange term ( $\Sigma^{ex}$ ) and the second term is the  $GW$  correlation term ( $\Sigma^c$ ). The variables here,  $\Sigma^{GW}$ ,  $W_0$ , and  $G_0$ , are all functions of  $\omega$ ; therefore,  $\omega$ -integral is necessary in evaluating Eq. (2). We analytically perform this  $\omega$ -integral using the Hybertsen-Louie-type generalized plasmon-pole (HL-GPP) model for the inverse of the dielectric function.

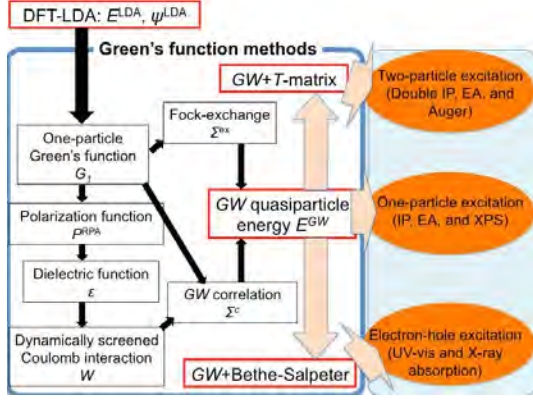


Figure 1: Flowchart of  $GW$ +Bethe-Salpeter and  $GW$ + $T$ -matrix calculations.

### 2.3 Bethe-Salpeter equation

The description on the excitonic effect is significant in simulating photoabsorption spectra. To explicitly consider the excitonic effect in the present calculation, we construct the BSE and solve an  $\omega$ -independent eigenvalue problem,

$$H_{o,o';e,e'}^{\text{BSE}} A_{o,e}^i = \Omega_i A_{o,e}^i, \quad (3)$$

$$H_{o,o';e,e'}^{\text{BSE}} \equiv (E_e^{\text{GW}} - E_o^{\text{GW}}) \delta_{o,o'} \delta_{e,e'} + \Xi_{o,o';e,e'}^{\text{GW}}, \quad (4)$$

where  $\Xi_{o,o';e,e'}^{\text{GW}}$  is a matrix element of an electron-hole interaction kernel within the GWA,

$$\Xi^{\text{GW}} = \frac{\partial}{\partial G_0} (\Sigma^H + \Sigma^{\text{GW}}). \quad (5)$$

The resulting eigenvalues ( $\Omega$ ) and eigenvectors ( $A$ ) in Eq. 3 give the excitation energy spectra and corresponding transition probabilities. We again use the HL-GPP model and analytically perform  $\omega$ -integral in the BSE to take into account the dynamical excitonic effect. The details of our method are given in Ref. [1]

### 2.4 All-electron mixed basis program

Our program has unique features; not only does the basis set use both plane waves (PWs) and numerical atomic orbitals (AOs) but also some Green's function methods beyond the

framework of DFT for simulating the excited energy spectra of the real materials are available (note that DFT-purpose calculations are outside of our scope in developing our program code because we can find a number of DFT programs online). Figure 1 shows a flowchart of the Green's function methods. Depending on the excited energy spectra of interest, our program provides three main options; the  $GW$  (or second-order Møller-Plesset perturbation, called MP2) calculation for single-particle excited energy spectra such as first-ionization potential (IP), electron affinity (EA), and band gap, the  $GW$ +Bethe-Salpeter calculation for photoabsorption spectra, and the  $GW$ + $T$ -matrix calculation for two-particle excited energy spectra such as double IP and double EA, and Auger spectra (note that MP2 and the  $GW$ + $T$ -matrix are outside of the scope of this review).

## 3 Accuracy & Performance

### 3.1 Benchmark test I: LDA

First, we compare our LDA results (using all-electron mixed basis) with those of the QUANTUM ESPRESSO suite [2] with three different pseudopotentials (norm conserving, ultrasoft, and PAW) to check the accuracy and convergence. Figure 2 shows (a) the LDA Kohn-Sham orbital energies at the highest occupied molecular orbital (HOMO) and the lowest unoccupied molecular orbital (LUMO), and (b) the HOMO-LUMO gap of Benzene molecule (note that because both programs, the mixed basis and ESPRESSO, can determine the vacuum level using the Coulomb cutoff technique, we can directly compare the absolute values of these orbital energies). In figure 2 (a), the Kohn-Sham orbital energies converge at same values, and we cannot see a difference among these four calculations in this energy range (horizontal axis). In figure 2 (b), a remarkable difference is found rather among the results of ESPRESSO, where the norm conserving pe-

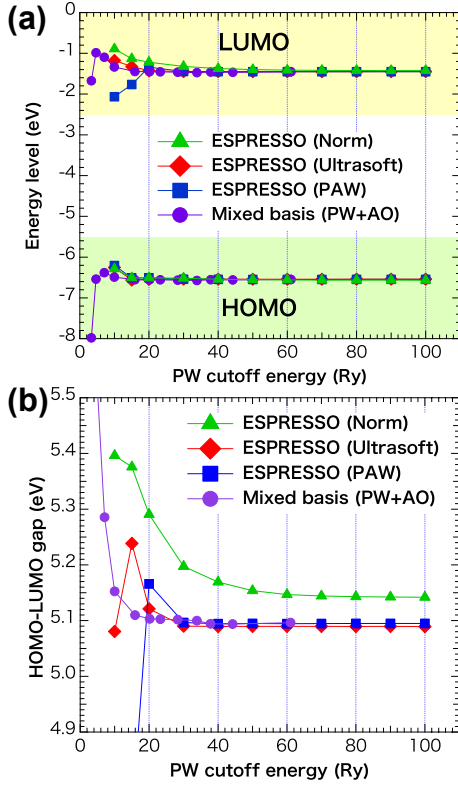


Figure 2: (a) LDA Kohn-Sham orbital energies at HOMO and LUMO levels in absolute values and (b) HOMO-LUMO gaps calculated for Benzene molecule by the present program (purple circle) and ESPRESSO with three different pseudopotentials (green triangle: norm conserving, red diamond: ultrasoft, and blue square: PAW).

dopotential conserves quite slowly against the PW cutoff energy and reaches points that differ slightly (by about 0.05 eV) from those of the other methods. In contrast, the mixed basis converges at almost same value as the ultrasoft and PAW pseudopotentials, and the required PW cutoff energy is about 15 Ry, which is almost half that given by ESPRESSO with the ultrasoft and PAW pseudopotentials (=30 Ry). These comparisons confirm the efficiency and accuracy of mixed basis method.

Table 1: Computational cost required for simulating the photoabsorption spectra of warped nanographene ( $C_{80}H_{30}$ ) on Fujitsu FX10. Here “CPU time” is defined as “# of CPUs”  $\times$  “Elapse time”.

	LDA	GWA	BSE
# of CPUs	6	24	24
Elapse time (hour)	2.0	11.8	66.2
CPU time (hour)	11.9	283.2	1588.8

Table 2: Theoretical and experimental optical gaps (eV) of warped nanographene. For experimentally assigned peaks are listed here [3]. The values in “error” is discrepancies between “BSE” and “Expt.”.

label	BSE	error	Expt.
$S_1$	2.70	0.17	2.53
$S_4$	2.94	0.20	2.74
$S_7$	3.15	0.18	2.97
$S_{30}$	4.00	0.16	3.84

### 3.2 Benchmark test II: $GW$ +Bethe-Salpeter

Next, we check the  $GW$ +Bethe-Salpeter calculation in terms of its performance and agreement with the experiments; we choose a grossly warped nanographene ( $C_{80}H_{30}$ ) as a benchmark test system. The computational costs required for LDA, GWA, and BSE calculations for  $C_{80}H_{30}$  are listed in table 1. Although the GWA and BSE calculations require much longer CPU time than the LDA (see table 1), our hybrid parallel program with OpenMP and MPI can complete the  $GW$ +Bethe-Salepeter calculation for  $C_{80}H_{30}$  with 24 CPUs on a Fujitsu FX10 supercomputer.

As our inviolability policy for developing program code, we do not employ any algorithms that might potentially reduce the accuracy and reliability in the slightest degree, even if they can dramatically accelerate the calculation speed or reduce the computational



Figure 3: Atomic geometries of acetone and acetic acid optimized by B3LYP/cc-pVTZ.

cost. Hence, the errors found in our calculations are originated from purely theoretical considerations (note that this is an important point when we consider the development of a more accurate method beyond the present theory). We compare the BSE and experimental optical gaps for the four experimentally assigned peaks at 2.53 eV, 2.74 eV, 2.97 eV, and 3.84 eV [3]. The corresponding BSE gaps are  $S_1$  (=2.70 eV),  $S_4$  (=2.94 eV),  $S_7$  (=3.15 eV), and  $S_{30}$  (=4.00 eV), respectively, and the remaining errors compared with the experimental values are less than 0.2 eV. Our method can handle a 110-atoms system without loss of accuracy.

## 4 Applications

We have applied our method to a simulation of two-particle excitation [4], simulations of UV-vis absorption spectra for systems such as sodium clusters [5], CdSe clusters [6],  $M^+@C_{60}$  (where  $M = H, Li, Na, \text{ and } K$ ) [7], firefly luciferin [8], and defective nanographenes [9], and oxygen 1s XAS simulations [10]. We review the most recent two examples [9, 10] in following sections.

### 4.1 Oxygen 1s XAS of acetone and acetic acid

In this study, we applied our method to acetone and acetic acid and simulated the oxygen 1s XAS. As shown in Fig. 3, acetone has one oxygen atom chemically bonded with a carbon

Table 3: Excitation energies from oxygen 1s to LUMO (eV). Experimental values are from Refs. [11, 12].

Acetone	BSE	TD-LDA	Expt.
O <sub>O=C</sub>	533.76	504.76	531.4
Acetic acid	BSE	TD-LDA	Expt.
O <sub>O=C</sub>	534.74	505.34	532.13
O <sub>O-H</sub>	540.34	506.64	535.44

atom (O=C), and acetic acid has two oxygen atoms chemically bonded with a carbon atom (O=C), one of which is also bonded with a hydrogen atom (O-H). Acetone and acetic acid have the same number of electrons, and only the region in the blue rectangle in Fig. 3 is different. We see how accurately our method can simulate the absolute values of the excitation energies from oxygen 1s compared with the experimental values and whether our method can distinguish the effect of chemical bonding environment, i.e., O=C and O-H.

The calculated excitation energies corresponding to the excitation from oxygen 1s to the LUMO are listed in table 3 together with the results of time-dependent LDA (TD-LDA) calculations and the available experimental values [11, 12] for comparison. Here TD-LDA values are calculated using the Gaussian09 package [13] and the aug-cc-pVTZ basis set. Although it is well-known that the TD-LDA can determine reasonable excitation energies around UV-vis photon energy range of less than about 10 eV especially for small molecules such as acetone and acetic acid, it is obviously inaccurate for the core electron excitations. The discrepancies between the TD-LDA and experimental values are about 26.6 eV for acetone (O<sub>O=C</sub>), 26.8 eV for acetic acid (O<sub>O=C</sub>), and 28.8 eV for acetic acid (O<sub>O-H</sub>). This means that the static and local excitonic effect considered in TD-LDA is insufficient to describe the strong interaction between oxygen 1s core hole and excited electron. In addition,

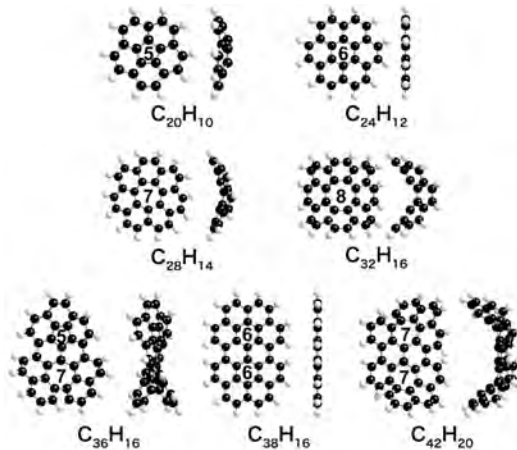


Figure 4: Atomic geometries of single and double defect molecules optimized by B3LYP/cc-pVTZ.

because the Gaussian-type-orbital (GTO) fails to describe the cusp condition of oxygen  $1s$ , the effect might not be negligibly small. On the other hand, the BSE, which considers a more realistic, i.e., dynamical and non-local, excitonic effect yields dramatically improved excitation energies. The remaining errors compared with the experiment are only 2.4-5.0 eV for all the cases.

Although the present results are not perfect agreement and removing these errors is not easy task, this is the first attempt worldwide to apply a *fully* first-principles  $GW$ +Bethe-Salepter method to XAS simulation. To determine the origin of the errors, we need more experience with applying this method to other systems.

## 4.2 Optical properties of defective nanographenes

Since Kawasumi *et al.*, successfully synthesized a grossly warped nanographene ( $C_{80}H_{30}$ ) in 2013, it has become more important to understand the role of defects in determining the structural and electronic properties, not only because of scientific interest but also because of potential industrial applications in the future.

In this study, we applied the  $GW$ +Bethe-Salepter method to defective and defectless nanographenes and systematically investigated the defect dependence of their properties, focusing on the optical properties such as the HOMO-LUMO gaps, optical gaps, and UV-vis absorption spectra. In particular, to see the effect of various types of the defects, such as pentagonal, heptagonal, and octagonal defect, and the effect of interaction between defects, we simulated the optical properties of the single- and double-defect molecules and the defectless counterparts, as shown in Fig. 4.

Table 4 shows the simulated optical gaps. The minimal gaps ( $S_1$ ) of the single-defect molecules are all forbidden transition (dark exciton) owing to the symmetries of the corresponding wave functions, and the first dipole allowed transition (bright exciton) occurs at higher transitions, ( $S_n$ ,  $n \geq 2$ ). Although the atomic geometries of single-defect molecules:  $C_{20}H_{10}$ ,  $C_{28}H_{14}$ , and  $C_{32}H_{16}$ , are slightly distorted from that of defectless molecule,  $C_{24}H_{12}$ , the high-symmetries are still retained (see Fig. 4). Actually,  $\pi$ -like wave functions are observed for both these single defect molecules and the defectless molecule.

As the defect changes from pentagonal to octagonal, the molecular size increases and the minimal gaps ( $S_1$ ) become smaller. This tendency can be regarded as the molecular size dependence rather than a defect dependence. We cannot discuss the defect dependence for these molecules, because a strong molecular size dependence appears and hide the effect of defects.

We next discuss the interaction between defects for the double-defect molecules. Because the presence of two defects significantly distorts the atomic geometries (see Fig. 4) and also the symmetries of the corresponding wave functions, the situation differs from that of the single-defect molecules. That is, the minimal gaps,  $S_1$ , are the first dipole-allowed transition for  $C_{36}H_{16}$  with pentagonal and heptagonal de-

Table 4: First dipole forbidden (dark) and allowed (bright) excitons calculated for single- and double defect-molecules and defectless molecules.

		Exciton type bright or dark	BSE gap (eV)
C <sub>20</sub> H <sub>10</sub> :	S <sub>1</sub>	dark	3.43
	S <sub>12</sub>	bright	4.46
C <sub>24</sub> H <sub>12</sub> :	S <sub>1</sub>	dark	2.52
	S <sub>2</sub>	bright	2.92
C <sub>28</sub> H <sub>14</sub> :	S <sub>1</sub>	dark	2.63
	S <sub>27</sub>	bright	4.40
C <sub>32</sub> H <sub>16</sub> :	S <sub>1</sub>	dark	2.03
	S <sub>3</sub>	bright	3.10
C <sub>36</sub> H <sub>16</sub> :	S <sub>1</sub>	bright	2.28
C <sub>38</sub> H <sub>16</sub> :	S <sub>1</sub>	dark	1.92
	S <sub>2</sub>	bright	2.42
C <sub>42</sub> H <sub>20</sub> :	S <sub>1</sub>	bright	2.24

fects, and C<sub>42</sub>H<sub>20</sub> with two heptagons; for the defectless counter molecule, C<sub>38</sub>H<sub>16</sub>, S<sub>1</sub> is forbidden transition, and S<sub>2</sub> is the first dipole-allowed transition. The bright excitons of the defective molecules are commonly about 0.1-0.2 eV smaller values than that of the defectless molecule. This is because the excitonic effect becomes stronger for smaller atomic geometries of the defective molecules, in addition to the fact that S<sub>1</sub> is dipole-allowed transition.

## 5 Summary

We have developed a first-principles *GW*+Bethe-Salpeter program employing all-electron mixed basis approach, aiming specifically at massively parallel calculations with OpenMP and MPI and XAS simulations. Using 24 CPUs on Fujitsu FX10 supercomputer, we successfully simulated first-principles *GW*+Bethe-Salpeter calculations for 110-atoms systems without reducing accuracy and theoretical validation. Using our program, we investigated the optical

properties of sodium clusters, CdSe clusters, M<sup>+</sup>@C<sub>60</sub>, firefly luciferin, and defective nanographenes. Furthermore, our method combining an all-electron mixed basis approach and the *GW*+Bethe-Salpeter method can simulate XAS as well as UV-vis absorption spectra within the same program code and same theoretical framework. The calculated oxygen 1s XAS of acetone and acetic acid show 2.4-5.0 eV errors compared with the experimental values; these errors are quite small compared with those of the TD-LDA.

## References

- [1] M. Rohlfing and S. G. Louie, Phys. Rev. B, **62**, 4927 (2000).
- [2] P. Giannozzi *et al.*, J. Phys.: Condens. Matter **21** 395502 (2009)
- [3] K. Kawasumi, Q. Zhang, Y. Segawa, L. T. Scott, and K. Itami, Nat. Chem., **5**, 739 (2013).
- [4] Y. Noguchi, K. Ohno, I. V. Solov'yev, and T. Sasaki, Phys. Rev. B, **81**, 165411 (2010).
- [5] Y. Noguchi and K. Ohno, Phys. Rev. A, **81**, 045201 (2010).
- [6] Y. Noguchi, O. Sugino, M. Nagaoka, S. Ishii, and K. Ohno, J. Chem. Phys., **137**, 024306 (2012).
- [7] Y. Noguchi, O. Sugino, H. Okada, and Y. Matsuo, J. Phys. Chem. C, **117**, 15362 (2013).
- [8] Y. Noguchi, M. Hiyama, H. Akiyama, and N. Koga, J. Chem. Phys., **141**, 044309 (2014).
- [9] Y. Noguchi and O. Sugino, J. Chem. Phys., **142**, 064313 (2015).
- [10] Y. Noguchi, M. Hiyama, H. Akiyama, Y. Harada, and N. Koga, J. Chem. Theor. Compt., **11**, 1668 (2015).

- [11] T. Tamenori, O. Takahashi, K. Yamashita, T. Yamaguchi, K. Okada, K. Tabayashi, T. Gejo, and K. Honma, J. Chem. Phys., **131**, 174311 (2009).
- [12] K. Tabayashi, K. Yamamoto, T. Maruyama, H. Yoshida, K. Okada, Y. Tamenori, I. H. Suzuki, T. Gejo, and K. Honma, J. Electron Spectrosc. Relat. Phenom., **184**, 134 (2011).
- [13] M. J. Frisch *et al.*, *Gaussian 09* Revision **C.1**, Gaussian Inc. Wallingford CT 2010.

# First-principles study on superconductivity in alkali-doped fullerenes

Ryotaro ARITA

*RIKEN Center for Emergent Matter Science*

*Wako, Hirosawa, Saitama 351-0198*

*Isobe Degenerate  $\pi$ -Integration Project, JST, ERATO*

*Aoba-ku, Sendai 980-8577*

## Abstract

Superconductivity in alkali-doped fullerenes ( $A_3C_{60}$ ) is of great interest in particular due to its high transition temperature ( $T_c$ ) that is the highest among molecular solids. In the phase diagram, the superconducting phase resides next to a Mott-insulating phase. While this situation is similar to that of cuprates, superconductivity in  $A_3C_{60}$  is more non-trivial and interesting, since the gap function has an on-site s-wave symmetry for which one usually expects that local electron correlations causing the Mott-Hubbard transition severely suppress its  $T_c$ . To clarify the pairing mechanism of  $A_3C_{60}$ , we recently performed first-principles studies based on superconducting density functional theory (SCDFT) and multi-scale *ab initio* scheme for correlated electron systems (MACE). Our results establish that the multi-orbital electronic correlations and phonons cooperate to reach high  $T_c$  s-wave superconductivity in  $A_3C_{60}$ .

## 1 Introduction

Superconductivity in alkali-doped fullerenes ( $A_3C_{60}$ ) was discovered in 1991[1]. At that time, the transition temperature ( $T_c \sim 40K$ ) was the second highest which was only surpassed by the cuprates. Since then, the pairing mechanism of the high  $T_c$  superconductivity has been attracting broad interest. In Ref.[2], Yildirim *et al.* made a famous plot for  $T_c$  as a function of the lattice constant  $a$  of the system, which clearly shows that  $T_c$  and  $a$  (or the vol-

ume per  $C_{60}^{-3}$ ) has a positive correlation. This result can be understood in terms of the standard BCS theory, in which  $T_c$  is given by the following equation:

$$T_c = \omega_{ph} \exp\left(\frac{-1}{N_F V_{eff}}\right),$$

where  $\omega_{ph}$ ,  $N_F$  and  $V_{eff}$  represent the averaged phonon frequency, the density of states at the Fermi level and the attractive pairing interaction, respectively. Since the band width becomes narrower for larger  $a$ , we expect larger  $N_F$  and higher  $T_c$ . Namely,  $a$  and  $T_c$  should have a positive correlation.

Recently, a new experimental method to synthesize highly crystalline Cs-doped fullerenes has been established, and the phase diagram is extended to the region for larger  $a$ [3, 4, 5]. There, it has been shown that the superconducting phase has a dome-like shape, and resides next to a Mott insulating phase.

Motivated by these experimental observations, we recently performed first-principles calculations to investigate the pairing mechanism of  $A_3C_{60}$ . One is a study based on the density functional theory for superconductors (SCDFT)[6, 7, 8, 9], and the other is based on the multi-scale *ab initio* scheme for correlated electron systems (MACE)[10].

In the former, we calculated  $T_c$ s for  $K_3C_{60}$ ,  $Rb_3C_{60}$  and  $Cs_3C_{60}$  to examine the validity of the Migdal-Eliashberg theory[11]. We found that the theoretical values of  $T_c$  are systematically lower than half of the experimental values. This result strongly suggests that we have to go beyond the Migdal-Eliashberg theory to



understand the high  $T_c$  superconductivity in  $A_3C_{60}$ .

In the latter, we formulated a new scheme to derive electron-phonon coupled models from first principles[12], and applied it to  $A_3C_{60}$ . After we determined all the relevant parameters in the effective Hamiltonian, we solve it by means of the extended dynamical mean field theory (EDMFT)[13]. The experimental values of  $T_c$  and the phase boundary of the Mott-Hubbard transition was successfully reproduced at a quantitative level[14].

## 2 Validity of the Migdal Eliashberg theory

Let us first examine whether the high  $T_c$  superconductivity in  $A_3C_{60}$  can be understood in terms of the conventional Migdal Eliashberg theory. To this end, we performed a calculation based on SCDF. SCDF is an extension of DFT for normal states to superconducting states. In the standard DFT, we start with the Hohenberg-Kohn theorem[15] which guarantees the one-to-one correspondence between the charge density of the ground state ( $\rho$ ) and the external potential  $v$ . In SCDF, we introduce the anomalous density  $\rho_s$  on top of the normal density  $\rho$ , and the Hohenberg-Kohn theorem is extended to a one-to-one correspondence between two kinds of potential ( $v, \Delta$ ) and two kinds of density ( $\rho, \rho_s$ ). Then the Kohn-Sham equation[16] is extended to the Kohn-Sham Bogoliubov-de Gennes equation from which we can derive the linearized gap equation,

$$\Delta = -\frac{1}{2} \sum_j \mathcal{K}_{ij} \frac{\tanh[\beta \xi_j / 2]}{\xi_j} \Delta_j, \quad (1)$$

where  $\xi$  and  $\beta$  are the Kohn-Sham energy and inverse temperature, respectively. The kernel of the gap equation,  $\mathcal{K}_{ij}$ , is obtained by taking the second functional derivative of the exchange correlation functional[6, 7, 8, 9].

Here, it should be noted that  $\mathcal{K}$  is a universal functional. Therefore, one can calculate  $T_c$  from first principles for any materials once he obtains the exact form of  $\mathcal{K}$ . In fact, recently,

$\mathcal{K}$  for conventional phonon-mediated superconductors has been proposed[8, 9], and has been successfully employed in the calculations for a variety of systems. In Fig.1, we show a benchmark result for Al and Nb. Here, we plot the gap function  $\Delta$  at the Fermi level as a function of temperature  $T$ .  $\Delta$  vanishes at  $T = T_c$ , and we see that the agreement between the theoretical and experimental  $T_c$ s is remarkably good. Thus the kernel  $\mathcal{K}_{ij}$  proposed in Ref.[8, 9] successfully takes account of the physics of the Migdal-Eliashberg theory, i.e., the retardation effect and the mass enhancement effect due to the electron-phonon coupling.

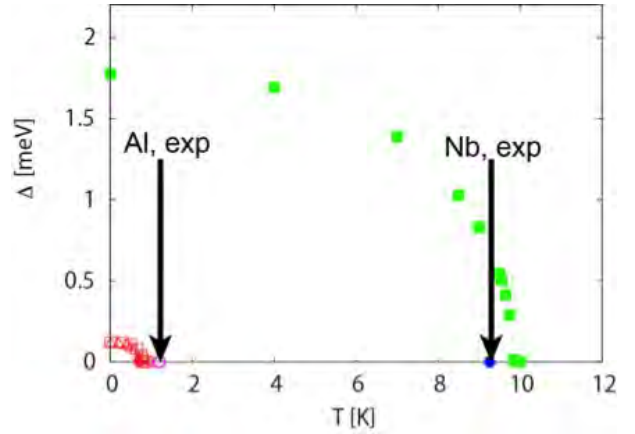


Figure 1: Temperature dependence of the gap function in SCDF calculated for Al and Nb. Experimental  $T_c$ s are indicated by arrows.

We then studied whether SCDF with the same kernel  $\mathcal{K}_{ij}$  reproduces the experimental  $T_c$  for  $A_3C_{60}$ . In Fig.2, we see that the theoretical  $T_c$ s are systematically lower than the experimental values. This trend is very different from the situation in many conventional superconductors, which raises a question on the validity of the Migdal-Eliashberg theory for doped fullerenes.

## 3 Analysis based on Multi-scale *ab initio* scheme

### 3.1 Low-energy Hamiltonian

Let us here move on to another approach based on MACE[10]. In this approach, we first derive

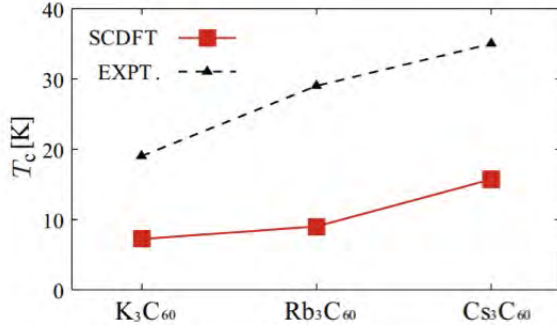


Figure 2: Superconducting transition temperature ( $T_c$ ) calculated for  $K_3C_{60}$ ,  $Cs_3C_{60}$  and  $Rb_3C_{60}$ .

an effective low energy model from first principles and then solve it by modern many-body theory.

In Fig.3, we show the band structure of  $K_3C_{60}$  obtained by the standard density functional theory[17]. There are three  $t_{1u}$  bands around the Fermi level, which are well isolated from other high-energy bands. In the present study, we are going to construct an effective low energy model for the  $t_{1u}$  model.

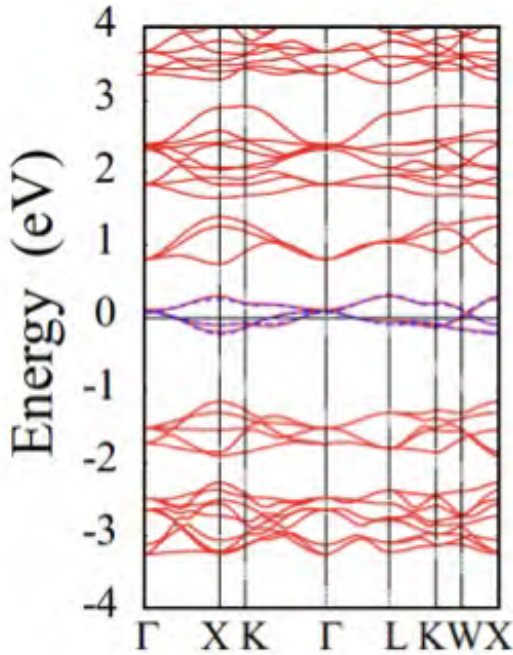


Figure 3: Band structure of  $K_3C_{60}$ . Wannier-interpolated  $t_{1u}$  bands are indicated by blue dotted lines.

The Hamiltonian is given by

$$\begin{aligned} \mathcal{H} = & \sum_{\mathbf{k}} \sum_{ij} [H_0(\mathbf{k})]_{ij} c_{i\sigma}^\dagger(\mathbf{k}) c_{j\sigma}(\mathbf{k} + \mathbf{q}) \\ & + \sum_{\mathbf{q}} \sum_{\mathbf{k}, \mathbf{k}'} \sum_{i, i', j, j'} U_{i, j, i', j'}(\mathbf{q}) \\ & c_{i\sigma}^\dagger(\mathbf{k} + \mathbf{q}) c_{i'\sigma'}^\dagger(\mathbf{k}') c_{j'\sigma'}(\mathbf{k}' + \mathbf{q}) c_{j\sigma}(\mathbf{k}) \\ & + \sum_{\mathbf{q}\nu} \sum_{\mathbf{k}} \sum_{i, j} \sum_{\sigma} g_{ij\nu}(\mathbf{k}, \mathbf{q}) \\ & c_{i\sigma}^\dagger(\mathbf{k} + \mathbf{q}) c_{j\sigma}(\mathbf{k}) (b_\nu(\mathbf{q}) + b_\nu^\dagger(-\mathbf{q})) \\ & + \sum_{\mathbf{q}\nu} \omega_\nu(\mathbf{q}) b_\nu^\dagger(\mathbf{q}) b_\nu(\mathbf{q}), \end{aligned}$$

where  $c_{i\sigma}^\dagger(\mathbf{k})$  ( $c_{i\sigma}(\mathbf{k})$ ) is a creation (annihilation) operator for the  $i$ -th orbital electron having spin  $\sigma$  and momentum  $\mathbf{k}$ .  $b_\nu^\dagger(\mathbf{q})$  ( $b_\nu(\mathbf{q})$ ) is a creation (annihilation) operator for a phonon having momentum  $\mathbf{q}$  in the  $\nu$ -th branch.

The first term in the Hamiltonian (2) is the one-body term of electrons. To derive this term, following the procedure formulated in Ref.[18], we constructed three maximally localized Wannier functions from the  $t_{1u}$  band (one of which is shown in in Fig.4). As we can see in Fig.3, the Wannier interpolated band reproduces the original band dispersion in the DFT calculation.

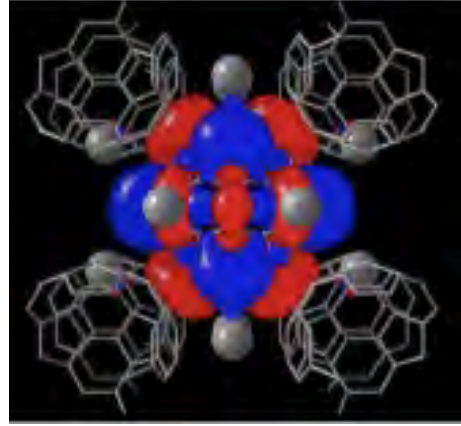


Figure 4: One of the three maximally localized Wannier functions constructed from the  $t_{1u}$  bands. Sign of the wave function is indicated in blue and red.

### 3.2 Electron-correlation terms

The second term in eq.(2) represents electron correlations, which consists of density-density

interactions such as the Hubbard  $U$  and exchange interactions like the Hund's coupling  $J$ . When we evaluate these interaction parameters, we have to carefully treat the screening effect. Since screening by low-energy electrons are considered when we solve the effective model, we should exclude its contributions when we derive the model. To this end, we employed the constrained random phase approximation (cRPA)[19].

In RPA, the screened Coulomb interaction  $W$  is given by

$$W = (1 - v\chi)^{-1}v,$$

where  $v$  is the bare Coulomb interaction, and  $\chi$  is the polarizability,

$$\chi = \sum_i^{\text{occupied}} \sum_j^{\text{unoccupied}} \frac{\psi_i(\mathbf{r})\psi_j^*(\mathbf{r})\psi_i^*(\mathbf{r}')\psi_j(\mathbf{r}')}{\omega - \epsilon_j + \epsilon_i}.$$

Here,  $\psi_i$  is the  $i$ -th Bloch wave function having an eigenenergy of  $\epsilon_i$ . Let us call  $\psi_i$  "occupied state" ("virtual state") when  $\epsilon_i$  is lower (higher) than those of the  $t_{1u}$  bands. In  $\chi$ , there are four types of processes: Transitions from occupied states to the  $t_{1u}$  states, those from the  $t_{1u}$  states to virtual states, those from occupied states to virtual states, and transitions between the  $t_{1u}$  states. In cRPA, we calculate "partially" screened Coulomb interaction without the contribution of the last transition processes.

In Fig.5, we show the correlation strength  $(\bar{U} - \bar{V})/W$  for fcc  $A_3C_{60}$  ( $A=K, Rb$  and  $Cs$ ), where  $\bar{U}$  is the averaged onsite Hubbard interaction,  $\bar{V}$  is the offsite Coulomb interaction between neighboring sites, and  $W$  is the band width of the  $t_{1u}$  band, respectively[20]. For  $A=Cs$ , we performed calculations for three volumes, i.e., where  $T_c$  takes its maximum ( $V_{SC}^{\text{opt.P}}$ ), where the metal-insulator transition occurs ( $V_{MIT}$ ) and where the system is an antiferromagnetic insulator ( $V_{AFI}$ ). We see that the electron correlation is stronger than the band width in all the five cases. Here, it is interesting to note that  $Cs_3C_{60}$  having higher  $T_c$  has stronger electronic correlations than  $K_3C_{60}$ . This trend cannot be understood in terms of the standard BCS theory, where the Coulomb interaction always suppresses superconductivity.

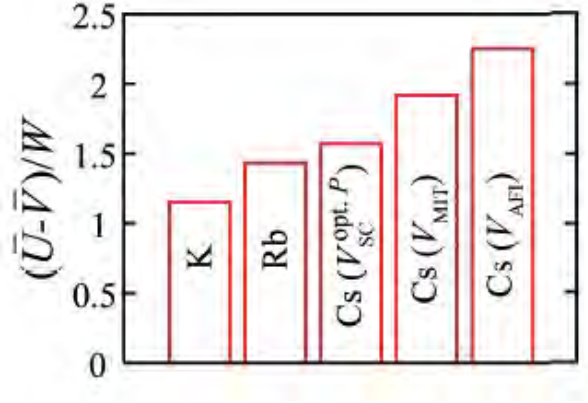


Figure 5: Correlation strength  $(\bar{U} - \bar{V})/W$  calculated by cRPA for  $A_3C_{60}$  ( $A=Cs, K$  and  $Rb$ ).

In Fig.6, we plot the values of the Hund's coupling  $J$  for  $A_3C_{60}$ . We see that the size of  $J$  is as large as 0.03eV. Since  $U$  is  $\sim 1$ eV, the ratio  $J/U$  is less than 5 %, which is much smaller than a typical value for transition metal compounds[21], 10 ~ 20%. This is because the spreads of Wannier functions are huge for molecular systems. In fact, as we will see below, the energy scale of the antiferromagnetic exchange coupling  $J_{ph}$  due to the dynamical Jahn-Teller effect is as large as that of  $J$ . The competition between  $J_{ph}$  and  $J$  is of great interest, since unconventional superconductivity can emerge when the former dominates over the latter[22, 23].

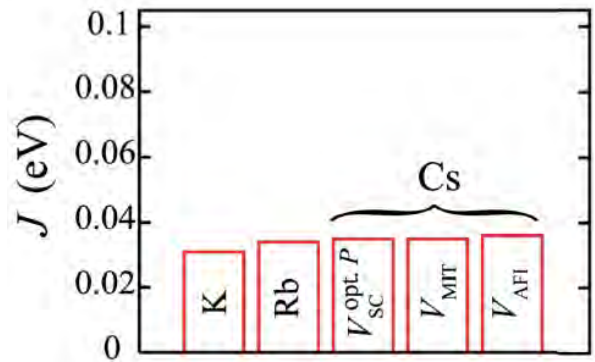


Figure 6: Hund's coupling  $J$  calculated by cRPA for  $A_3C_{60}$  ( $A=Cs, K$  and  $Rb$ ).

### 3.3 Phonon terms

Let us now look into the detail of the competition between  $J$  and  $J_{\text{ph}}$ . To calculate the value of  $J_{\text{ph}}$  from first principles, we evaluated the electron-phonon coupling  $g_{ij\nu}(\mathbf{k}, \mathbf{q})$  and the phonon frequency  $\omega_\nu(\mathbf{q})$  in the third and fourth term in the Hamiltonian (2). Here, as in the case of cRPA, we should take account only of screening by high energy electrons. To this end, we recently formulated a new scheme, which we call constrained density functional perturbation theory (cDFPT)[12].

In the standard DFPT, the electron-phonon coupling is estimated by calculating the matrix element of

$$\langle \psi_{i\mathbf{k}+\mathbf{q}} | \frac{\partial v}{\partial u} | \psi_{j\mathbf{k}} \rangle,$$

where  $v$  is the atomic potential and  $u$  is the displacement of nuclei. On the other hand, the phonon frequency is obtained by taking the second derivative of the total energy  $E$  with respect to  $u$ . Since all the physical quantities in DFT are represented in terms of the electron density  $\rho$ , if we know the response of  $\rho$  against  $u$ , we can evaluate  $g_{ij\nu}(\mathbf{k}, \mathbf{q})$  and  $\omega_\nu(\mathbf{q})$  through the chain rule,  $\partial/\partial u = \partial\rho/\partial u \partial/\partial\rho$ . The response of the charge density  $\Delta\rho$  can be calculated by the perturbation theory[24],

$$\begin{aligned} \Delta\rho &= 2 \sum_i \psi_i^* \Delta\psi_i, \\ \psi_i &= \sum_{j \neq i} \psi_j \frac{\langle \psi_j | \Delta V | \psi_i \rangle}{\varepsilon_i - \varepsilon_j}. \end{aligned}$$

In cDFPT, we introduce a constraint in the sum over  $j$ , and exclude the contribution of the  $t_{1u}$  states. Then we obtain partially screened  $g_{ij\nu}(\mathbf{k}, \mathbf{q})$  and  $\omega_\nu(\mathbf{q})$ .

The phonon-mediated exchange coupling  $J_{\text{ph}}$  is given by

$$J_{\text{ph}} = - \sum_{\mathbf{q}\nu} g_{ij\nu}(\mathbf{k}, \mathbf{q}) \frac{2\omega_\nu(\mathbf{q})}{\Omega_n^2 + \omega_\nu^2(\mathbf{q})} g_{ji\nu}(\mathbf{k}, \mathbf{q}),$$

where  $\Omega_n$  is the bosonic Matsubara frequency (see the Feynman diagram in Fig. 7). We estimated  $J_{\text{ph}}$  for  $A_3\text{C}_{60}$  ( $A=\text{K}, \text{Rb}, \text{and Cs}$ ) and found that  $J_{\text{ph}}$  is negative and favors low-spin configurations. While the absolute value of  $J$  is  $0.03 \sim 0.035$  eV and does not show significant frequency dependence, that of  $J_{\text{ph}}$  is  $\sim 0.05$  eV

for small  $\Omega_n$  and decays quickly within the energy scale of the Debye frequency. Thus for low-energy electrons,  $J_{\text{ph}}$  dominates over  $J$ .

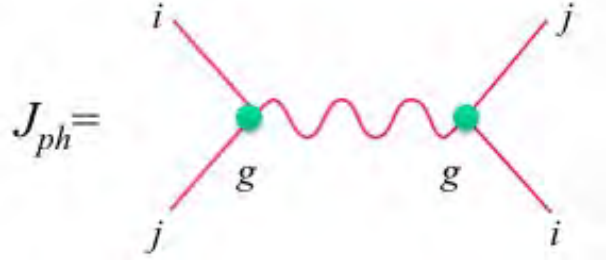


Figure 7: Diagram for the phonon-mediated exchange coupling  $J_{\text{ph}}$ . The wavy line denotes the Green's function of phonons.

In Ref.[22, 23], Capone *et al.* proposed an interesting unconventional pairing mechanism for strongly correlated multi-orbital systems with inverted Hund's rule coupling. When the electron correlations become stronger, the effective mass of the quasiparticle becomes heavier and the energy scale of the kinetic energy becomes smaller as  $W \rightarrow ZW$ , where  $Z$  is the quasiparticle weight. While the heavy quasiparticle experiences reduced repulsion  $ZU$  in the charge channel, the interaction in the spin channel  $J_{\text{eff}} = J + J_{\text{ph}}$  is not renormalized. Namely, the spin degrees of freedom is still active even when the charge fluctuations are frozen. Thus, when  $Z$  is extremely small in the vicinity of the Mott insulating phase, the quasiparticles feel attractive interactions which induce unconventional  $s$ -wave superconductivity. Although the symmetry of the gap function is on-site  $s$ -wave, this superconducting phase is sometimes separated from the conventional BCS superconducting phase in the phase diagram.

### 3.4 Extended dynamical mean field theory

To investigate the possibility of high  $T_c$   $s$ -wave superconductivity in the vicinity of the Mott insulating phase, we then solve the effective low-energy model derived in the previous subsection by means of EDMFT[13]. In DMFT, we map the original lattice many-body prob-



lem onto a single-site impurity problem and solve it self-consistently. DMFT has been applied to various problems in strongly correlated electron systems, and has succeeded in describing physics of local electron correlations[25].

In EDMFT, we can take account of the effect of off-site long-range Coulomb interaction. There, the momentum dependence of the Coulomb interaction in the original lattice model is represented by the frequency dependent Hubbard  $U_V(\omega)$  in the impurity model. The effect of electron-phonon coupling can also be represented by the frequency dependent Hubbard  $U_{ph}(\omega)$ [26, 27].

In Fig.8, we show the Matsubara-frequency dependence of the effective intra- and inter-orbital interactions ( $U_{\text{eff}}(i\Omega_n)$  and  $U'_{\text{eff}}(i\Omega_n)$ , respectively) in the impurity model. Due to screening by the off-site Coulomb interaction, the Hubbard  $U$  and  $U'$  in the original lattice model is reduced to be  $U + U_V = U - V$  and  $U' + U'_V = U' - V'$  at  $\Omega_n \rightarrow 0$ . As for the relation between  $U$  and  $U'$ ,  $U = U' + 2J$  holds in the original lattice model. Since the Hund's coupling  $J$  is positive and favors high-spin states,  $U > U'$ . In Fig.8, we can see that the same inequality is also satisfied for  $U + U_V$  and  $U' + U'_V$ .

However, the situation changes if we consider the contribution of  $U_{ph}$  and  $U'_{ph}$ . As we have seen in the previous subsection,  $J_{ph}$  dominates over  $J$ , so that  $U + U_V + U_{ph} < U' + U'_V + U'_{ph}$  for small  $\Omega_n$ . Therefore, in the impurity model, electrons tend to occupy the same orbital, rather than different orbitals (the so-called (2,1,0)-configurations shown in Fig.9). On top of that, there are pair-hopping processes between various (2,1,0)-configurations governed by the negative  $J_{\text{eff}} = J + J_{ph}$ ,

Let us now turn to the phase diagram. We solved the effective impurity model by means of continuous time quantum Monte Carlo method based on the strong coupling expansion[28], considering explicitly the anomalous Green's function. We calculated  $T_c$  by looking at the temperature dependence of the anomalous self energy. We also determined the phase boundary between the metallic (superconducting) state and the Mott insulating phase ( $T_c^{\text{MIT}}$ ). We calculate  $T_c$  and  $T_c^{\text{MIT}}$  as a

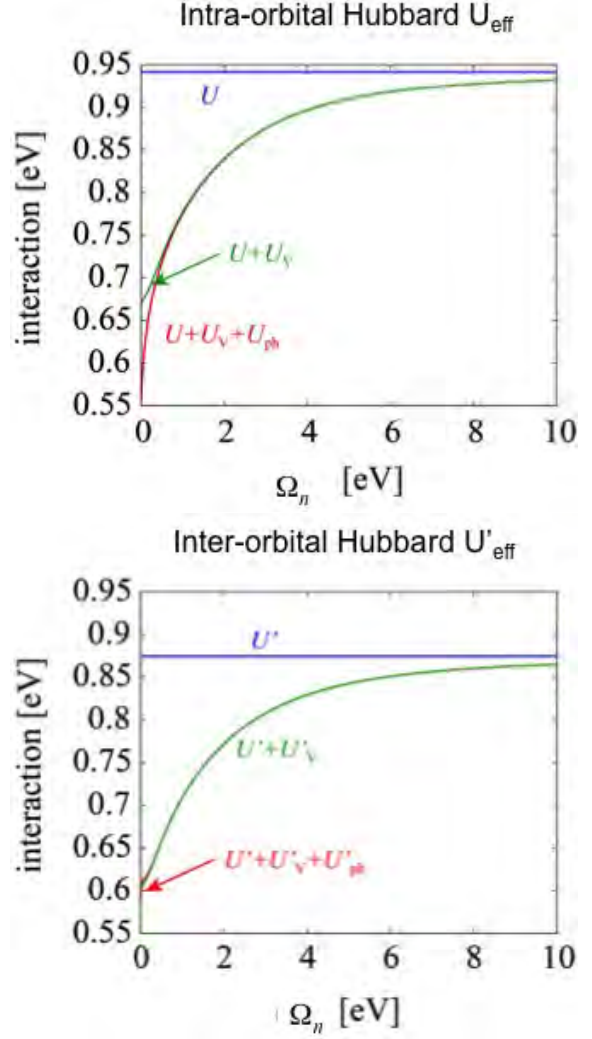


Figure 8: Matsubara frequency dependence of the intra-(inter-)orbital Hubbard  $U_{\text{eff}}$  ( $U'_{\text{eff}}$ ) parameters in the effective impurity model in EDMFT.

function of the volume of the unit cell ( $V_{\text{C}_{60}^{-3}}$ ). As we can see in Fig.10,  $T_c = 20 \sim 30\text{K}$  for  $V_{\text{C}_{60}^{-3}} = 720 \sim 780\text{\AA}^3$ , which is in quantitatively good agreement with the experimental phase diagram[29]. As for the Mott-Hubbard transition,  $T_c^{\text{MIT}}$  has a negative slope and becomes zero at  $V_{\text{C}_{60}^{-3}} \sim 780\text{\AA}^3$ , which also agrees well with the experiment[29].

To pin down the origin of the high  $T_c$  superconductivity, we have performed some additional calculations. First, we switched off the pair hopping term, keeping the values of the other interaction terms. We then found

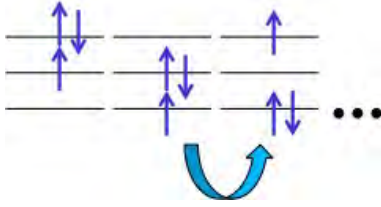


Figure 9: Schematic picture for the (2,1,0) configuration.

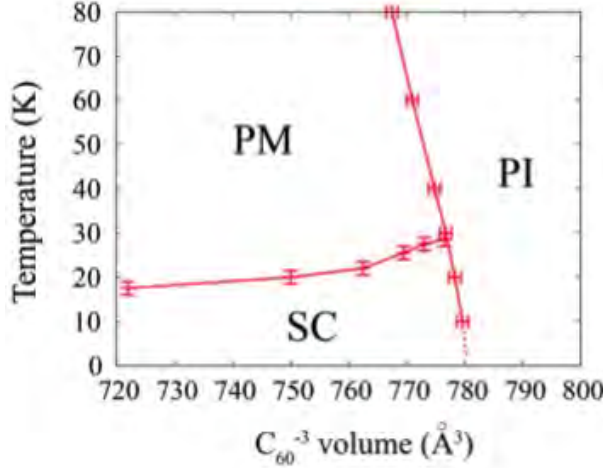


Figure 10: Phase diagram obtained by EDMFT calculation.

that there is no superconducting solution. On the other hand, if we switched off the spin flip term, the superconducting solution survives and is even enhanced. These results suggest that the pair hopping (spin flip) term is crucial (irrelevant) for superconductivity. Here, it should be noted that, although the energy scale of the pair hopping term is very small ( $J_{\text{eff}} = J + J_{\text{ph}}$ ), the effective band width is also small due to the strong electron correlations ( $U$  and  $U'$ ).

We have also performed a calculation with increasing the attractive phonon-mediated inter-orbital interaction and set  $U'_{\text{ph}} = U_{\text{ph}}$ . Here, while  $U'_{\text{eff}}$  is less repulsive, the inequality  $U_{\text{eff}} > U'_{\text{eff}}$  holds for all Matsubara frequencies. In this case, there is no superconducting solution. Therefore, the condition  $U_{\text{eff}} < U'_{\text{eff}}$  at small frequencies is also important for the superconductivity in this system.

## 4 Summary

In this article, we have reviewed our recent first-principles studies on superconductivity in alkali-doped fullerenes,  $A_3C_{60}$ . To study the validity of the standard Migdal-Eliashberg theory, We performed calculations based on SCDFT and compared the theoretical and experimental values of  $T_c$ . We found that SCDFT systematically underestimate  $T_c$ , which suggests that the high  $T_c$  superconductivity in doped fullerenes can not be understood in terms of the standard conventional mechanism.

In the approach based on MACE, we formulated a new scheme, cDFPT, to derive electron-phonon coupled effective models from first principles. We then solve the effective model within the framework of EDMFT, and succeeded in reproducing the experimental phase diagram quantitatively, including the superconducting phase and Mott insulating phase. We clarified that the negative Hund's coupling and the condition  $U_{\text{eff}} < U'_{\text{eff}}$  are crucial for the high  $T_c$  superconductivity in  $A_3C_{60}$ . These results establish that doped fullerenes are unique multi-orbital systems where electronic correlations and phonons cooperate to realize high  $T_c$  s-wave superconductivity.

## Acknowledgement

This work was done in collaboration with Y. Nomura, R. Akashi, S. Sakai, K. Nakamura and M. Capone.

## References

- [1] O. Gunnarsson: Rev. Mod. Phys., **69** 575 (1997).
- [2] T., Yildirim *et al.*: Solid State Commun. **93**, 269 (1995).
- [3] A. Y. Ganin *et al.*: Nat. Mater. **7**, 367 (2008).
- [4] Y. Takabayashi *et al.*: Science **323**, 1585 (2009)

- [5] A. Y. Ganin *et al.*: Nature **466**, 221 (2010).
- [6] L. N. Oliveira *et al.*: Phys. Rev. Lett. **60**, 2430 (1988).
- [7] T. Kreiblich and E.K.U. Gross: Phys. Rev. Lett. **86**, 2984 (2001).
- [8] M. Lüders *et al.*, Phys. Rev. B **72**, 024545 (2005).
- [9] M. Marques *et al.*, Phys. Rev. B **72**, 024546 (2005).
- [10] M. Imada and T. Miyake: J. Phys. Soc. Jpn, **79** 112001 (2010).
- [11] R. Akashi and R. Arita, Phys. Rev. B **88** 054510 (2013).
- [12] Y. Nomura, K. Nakamura, and R. Arita: Phys. Rev. Lett. **112** 027002 (2014).
- [13] G. Kotliar *et al.*: Rev. Mod. Phys. **78** 865 (2006)
- [14] Y. Nomura, S. Sakai, M. Capone, and R. Arita: submitted.
- [15] P. Hohenberg and W. Kohn: Phys. Rev. **136**, B864-B871 (1964).
- [16] W. Kohn and L.J. Sham: Phys. Rev. **140**, A1133-1138 (1965).
- [17] In the present study, we used the package of QUANTUM ESPRESSO, P. Giannozzi *et al.*, J.Phys.:Condens.Matter, **21**, 395502 (2009)
- [18] N. Marzari and D. Vanderbilt: Phys. Rev. B **56**, 12847 (1997).
- [19] F. Aryasetiawan *et al.*: Phys. Rev. B **70** 195104 (2004).
- [20] Y. Nomura, K. Nakamura, and R. Arita: Phys. Rev. B **85** 155452 (2012).
- [21] T. Miyake, K. Nakamura, R. Arita, and M. Imada: J. Phys. Soc. Jpn. **79** 044705 (2010)
- [22] M. Capone *et al.*: Science **296**, 2364 (2002).
- [23] M. Capone *et al.*: Rev. Mod. Phys. **81**, 943 (2009).
- [24] S. Baroni *et al.*, Rev. Mod. Phys. **73**, 515 (2001).
- [25] A. Georges *et al.*: Rev. Mod. Phys. **68**, 13 (1996)
- [26] I.G. Lang and Y. A. Firsov: Zh. Eksp. Teor. Fiz. 43, 1843 (1962).
- [27] P. Werner and A. J. Millis, Phys. Rev. Lett. **104**, 146401 (2010).
- [28] E. Gull *et al.*: Rev. Mod. Phys. **83**, 349 (2011).
- [29] R. H. Zadik *et al.*, to appear in Science Advances (2015).

# Development of Simulation Methods for Membrane Protein Structure Predictions and Replica-Exchange Methods

Ryo URANO<sup>1,\*</sup> and Yuko OKAMOTO<sup>1,2,3,4</sup>

<sup>1</sup>*Department of Physics, Graduate School of Science,  
Nagoya University, Nagoya, Aichi 464-8602, Japan*

<sup>2</sup>*Structural Biology Research Center, Graduate School of Science,  
Nagoya University, Nagoya, Aichi 464-8602, Japan*

<sup>3</sup>*Center for Computational Science, Graduate School of Engineering,  
Nagoya University, Nagoya, Aichi 464-8603, Japan*

<sup>4</sup>*Information Technology Center, Nagoya University, Nagoya, Aichi 464-8601, Japan*

## Abstract

We developed several simulation methods from two approaches. At first, we extended the previous method for membrane protein structure prediction to treat the flexibility of transmembrane backbone structures, which is often related to functions of proteins. With the new method, we reproduced the native structure of bacteriorhodopsin (BR) which includes distorted transmembrane structures. This method enables us to reduce the system size and computational resource. Secondly, we developed two methods in replica-exchange method (REM). One method is the deterministic replica-exchange method (DETREM), which introduces internal states evolved by an ordinary differential equation which controls replica exchange without pseudo random numbers. This method can resolve some problems of less efficiency in parallel computing caused by pseudo random numbers. The other is the designed walk replica-exchange method (DEWREM), which determines trajectory of replicas in temperature space without a random walk. We applied these new methods and reproduced the results of conventional REM in 2-dimensional Ising system.

## 1 Introduction

Computers have been developing for decades. However, system of interest has also been larger than before. Thus, efficient algorithm for computer simulation is always important to perform the simulation of current interest. For the purpose, there are two fundamental approaches: decrease of the number of molecule in system and enhancement of sampling. A former example is to adopt an implicit solvent model for solvent in a biomolecule system. In good models, this method can achieve the purpose of simulations although the implicit model abolishes atomistic resolution of solvent molecule

by a replacement of solvent molecule to a mean field function. A latter example is to employ replica-exchange method which enhances sampling of conformations. This method typically accelerates the crossing of free energy barriers using temperature change of replicas.

We developed new methods in each approach, and we show the results of simulations. At first, we proposed a membrane protein structure prediction method with flexible treatment of transmembrane backbone structures and the corresponding extension of the previous implicit membrane model. Using the method, we performed the structure prediction of bacteriorhodopsin and reproduced the native structure. We next proposed two new replica-exchange methods to increase efficiency of REM. One is the method that performs replica exchange with a differential equation without pseudo random numbers. The other is the method that specifies the order of replica exchange and, thus, the trajectory in temperature space among replicas. In 2-dimensional Ising model, we compared results of these new methods and their combination to results of the conventional Metropolis replica-exchange method.

This paper is organized as follows. In the first part, we will introduce the methods and results of membrane structure prediction for bacteriorhodopsin. In the second part, we will show the methods and results of new replica-exchange method in 2D-Ising model. Finally, we will give summary and future prospect of this paper.

## 2 Methods

We added the following four elementary harmonic constraints as a simple implicit membrane model to the original potential energy function in order to mimic the restrained membrane environment. The constraint energy function is given by

$$E_{\text{constr}} = E_{c1} + E_{c2} + E_{c3} + E_{c4}, \quad (1)$$

where each term is defined as follows:

$$E_{c1} = \sum_{i=1}^{N_H-1} k_1 \theta(r_{i,i+1} - d_{i,i+1}) [r_{i,i+1} - d_{i,i+1}]^2, \quad (2)$$

---

\* Present address: Chemistry Department, Boston University, 590 Commonwealth Avenue, Boston, MA 02215 USA



$$E_{c2} = \sum_{i=1}^{N_H} \left\{ k_2 \theta(|z_i^L - z_{0,i}^L| - d^L) [|z_i^L - z_{0,i}^L| - d^L]^2 + k_2 \theta(|z_i^U - z_{0,i}^U| - d^U) [|z_i^U - z_{0,i}^U| - d^U]^2 \right\}, \quad (3)$$

$$E_{c3} = \sum_{C_\alpha} k_3 \theta(r_{C_\alpha} - d_{C_\alpha}) [r_{C_\alpha} - d_{C_\alpha}]^2, \quad (4)$$

$$E_{c4} = \sum_{j=1}^{N_{BD}} k_4 \theta(|\phi_j - \phi_0| - \alpha_j^\phi) [|\phi_j - \phi_0| - \alpha_j^\phi]^2 + \sum_{j=1}^{N_{BD}} k_5 \theta(|\psi_j - \psi_0| - \alpha_j^\psi) [|\psi_j - \psi_0| - \alpha_j^\psi]^2. \quad (5)$$

$E_{c1}$  is the energy that constrains pairs of adjacent helices along the amino-acid chain not to be apart from each other too much (loop constraints), where  $r_{i,i+1}$  is the distance between the C atom of the C-terminus of the  $i$ -th helix and the  $C^\alpha$  atom of the N-terminus of the  $(i+1)$ -th helix, and  $k_1$  and  $d_{i,i+1}$  are the force constant and the central value constant of the harmonic constraints, respectively. Each  $d_{i,i+1}$  is proportional to the loop length connected between helices.  $\theta(x)$  is the step function, which has 1 when  $x$  is larger than or equal to 0, otherwise zero.  $N_H$  is the total number of transmembrane helices in the protein.

$E_{c2}$  is the energy that constrains helix N-terminus and C-terminus to be located near membrane boundary planes. Here, the  $z$ -axis is defined to be the direction perpendicular to the membrane boundary planes.  $k_2$  is the force constant of the harmonic constraints.  $z_{0,i}^L$  and  $z_{0,i}^U$  are the  $z$ -coordinate values of the  $C^\alpha$  atom of the N-terminus or C-terminus of the  $i$ -th helix near the fixed lower membrane boundary and the upper membrane boundary, respectively.  $z_{0,i}^L$  and  $z_{0,i}^U$  are the fixed lower boundary  $z$ -coordinate value and the upper boundary  $z$ -coordinate value of the membrane planes, respectively, and here they depend on each helix atoms due to the known data from OPM[1] although constant membrane plane region is also possible like a previous research condition.  $d^L$  and  $d^U$  are the corresponding central value constants of the harmonic constraints. This term has a non-zero value only when the  $C^\alpha$  atoms of the N-terminus or C-terminus of the  $i$ -th helix are apart more than  $d_i^L$  (or  $d_i^U$ ). This constraint energy was introduced so that the helix ends are not too much apart from the membrane boundary planes.

$E_{c3}$  is the energy that constrains all  $C^\alpha$  atoms within the sphere (centered at the origin) of radius  $d_{C^\alpha}$ .  $r_{C^\alpha}$  is the distance of  $C^\alpha$  atoms from the origin, and  $k_3$  and  $d_{C^\alpha}$  are the force constant and the central value constant of the harmonic constraints, respectively.

$E_{c4}$  is the energy that constrains dihedral angles of main chain within bending or kinked helix structures from ideal helix structures preventing them from forming random-coil structures.  $\phi_j$  and  $\psi_j$  are the backbone dihedral angle of the  $j$ -th residue.  $\phi_0$  and  $\psi_0$  are the reference value of the harmonic constraint to keep the helix structures without forming random coil structure, and  $\alpha_j^\phi, \alpha_j^\psi$  are the ranges of the harmonic constraints.  $N_{BD}$  is the total number of  $(\phi, \psi)$  angles in helix backbones.

We set  $k_1 = 5.0$ ,  $d_{i,i+1} = (46, 53, 34, 19, 95, 30)$  where  $i=1, 2, \dots, 6$ ,  $k_2 = 5.0$ ,  $z_{0,i}^L = (-14, -16, -20, -15, -19, -24, -18)$  where  $i=1, 2, \dots, 7$ ,  $z_{0,i}^U = (12, 14, 15, 15, 14, 11, 12)$  where  $i=1, 2, \dots, 7$ ,  $d^U = d^L = 2.0$ ,  $k_3 = 0.5$ ,  $d_{C^\alpha} = 80$ ,  $k_4 = 30.0$ ,  $k_5 = 30.0$ ,  $\phi_0 = -62$ ,  $\psi_0 = -40$ ,  $\alpha_j^\phi = 16$ , and  $\alpha_j^\psi = 13$ . Only the transmembrane helices were used in our simulations, and loop regions of the membrane proteins as well as lipid and water molecules were neglected. The membrane environment for this protein for the membrane thickness and the region of transmembrane region of the helices was taken from Orientation of Proteins in Membrane (OPM) [1]. The amino-acid sequences of the helices are EWIWLALGTALMGLGLTYFLVKG, KFYAITTLVPAIAFTMYLSMLL, IYWARYADWLFTTPLLDDLALL, QGTILALVGADGIMIGTGLVGAL, RFVWWAISTAAMLYILYVLFFGF, TFKVLRNVTVVLWSAYPVVWLIGSE, and LNIETLLFMVLDVSAKVGFGLLILL. The N-terminus and the C-terminus of each helix were blocked with the acetyl group and the N-methyl group, respectively. The initial structure for each helix was an ideal helix structure and they were placed in the membrane region randomly. We then perform REM simulations of these transmembrane helices. The MC program is based on CHARMM macro-molecular mechanics program[2, 3], and replica-exchange Monte Carlo method was implemented in it.

Replica-exchange method is explained in next Methods2 section. We here give the simulation conditions of REM. We used 40 replicas and the following temperatures: 400, 415, 435, 455, 485, 518, 552, 589, 629, 671, 716, 764, 815, 870, 928, 990, 1056, 1127, 1202, 1283, 1369, 1460, 1558, 1662, 1774, 1892, 2019, 2154, 2298, 2452, 2616, 2791, 2978, 3177, 3390, 3616, 3808, 4050, 4250, and 4500 K. We used rather high temperature values compared to experimental conditions. This is because our implicit membrane model guarantees the helix stability and enhances conformational sampling. Replica exchange was attempted at every 50 MC steps. We performed four independent simulations in total of 1,055,950,000 MC steps.

We used the CHARMM19 parameter set (polar hydrogen model) for the potential energy of the system[4, 5]. No cutoff was introduced to the non-bonded terms. Each helix structure was first minimized subjected to harmonic restraint on all the heavy atoms. In order to prepare random initial conformations, we first performed regular

constant MC simulations of all the replicas for 3,000,000 MC steps. We then performed equilibrium MC simulation for 3,000,000 MC steps at the above 40 temperatures, and the last conformation for each replica was the initial structure for the REM simulations. We repeated this process four times for four independent REM simulations. In those simulations, dielectric constant was set to  $\epsilon = 1.0$  as in the previous works[6–10]. In MC move, we updated conformations with a rigid translation and rotation of each  $\alpha$ -helix, a rotation of torsion angles of backbones by directional manipulation and concerted rotation[11–13], and torsion rotations of side-chains. There are  $2N_H + N_{SD} + N_{BD} + N_{CR}$  kinds of MC moves, where  $N_{SD}$  is the total number of dihedral angles in the side-chains of  $N_H$  helices and  $N_{CR}$  is the total number of the combination of seven successive backbone torsion angles by the concerted rotation in the helix backbone. One MC step in this article is defined to be an update of one of these degrees of freedom, which is accepted or rejected according to the Metropolis criterion.

We analyzed the simulation data by the principal component analysis[14–19]. At first, 42,238 conformational data were chosen at each temperature from the REM simulations. The structures were chosen from the trajectories at a fixed interval of 25,000 steps. The structures were superimposed on an arbitrary reference structure, for example, the native structures of PDB code:1PY6. Images were rendered by VMD[20]. The variance-covariance matrix is defined by

$$C_{ij} = \langle (q_i - \langle q_i \rangle)(q_j - \langle q_j \rangle) \rangle, \quad (6)$$

where  $\vec{q} = (q_1, q_2, q_3, \dots, q_{3n-1}, q_{3n}) = (x_1, y_1, z_1, \dots, x_n, y_n, z_n)$  and  $\langle \vec{q} \rangle = \sum_{k=1}^n \vec{q}(k)/n$ .  $x_i, y_i, z_i$  are Cartesian coordinates of the  $i$ -th atom, and  $n$  is the total number of atoms.

This calculation was performed by R program package[21], and the clustering was performed by k-means clustering method[22]. The first superposition was done to remove large eigenvalues from the translations and rotations of the system because we want to analyze the internal differences of structures. The eigenvalues were ordered in the decreasing order of magnitude.

### 3 Results1

We first identified the free energy minimum state in our simulations classified by principal component analysis. Fig. 1 shows the representative structure in each cluster from the highest density region. The root-mean-square-deviation (RMSD) value of each representative structure with respect to the  $C^\alpha$  atoms was 3.6 Å, 8.8 Å, 15.8 Å, 15.9 Å, and 16.6 Å for Cluster 1, Cluster 2, Cluster 3, Cluster 4, and Cluster 5, respectively. From these RMSD values, we found that the native-like structure is the second-lowest free energy state (Cluster 1) and that

the global-minimum free energy state (Cluster 2) is the second closest to the native structure. In the structure of Cluster 2, the space where the retinal molecule occupies in the native structure is filled with a helix, and this increases the contact between helices and seems to stabilize this structure more than the native-like structure of Cluster 1 with the empty space for the retinal molecule. Moreover, the result that a helix occupies the retinal space is consistent with previous works[6, 10] which did not include the flexibility of helix structures. However, the previous works were not able to obtain the native-like structure such as Cluster 1. Hence, the extension of including the freedom of helix structure distortion has improved the accuracy of prediction for membrane protein structure determination by simulation. Our results suggest that in the simulations without a retinal molecule the structures can interchange between the structures of Cluster 1 and Cluster 2. After an insertion of a retinal, it then stabilizes the native-like structure as shown in Fig.2. It is important that the association of helices enabled them to make a room for an insertion of a retinal molecule. This is consistent with the experimental results of bacteriorhodopsin, which observed the spontaneous insertion of a retinal molecule by a helix association[23].

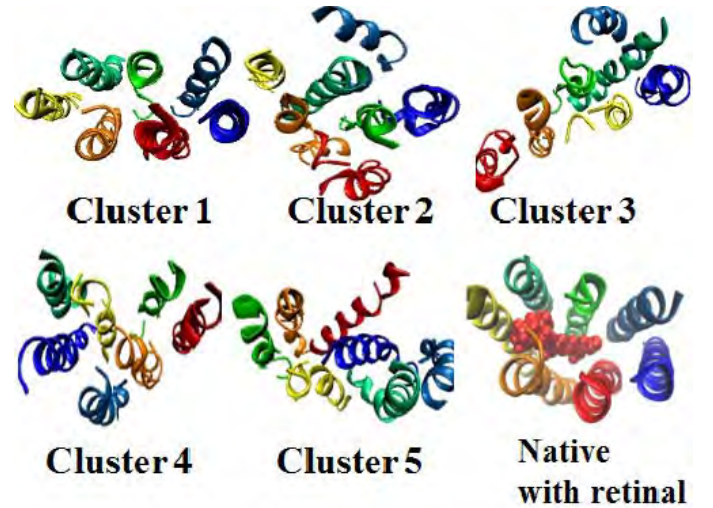


FIG. 1. Typical structures in each cluster selected in the highest density region. The RMSD from the native conformation with respect to all  $C^\alpha$  atoms is 3.6 Å, 8.8 Å, 15.8 Å, 15.9 Å, and 16.6 Å for Cluster 1, Cluster 2, Cluster 3, Cluster 4, and Cluster 5, respectively. Helices are colored from the N-terminus to the C-terminus: blue (Helix A), lightblue (Helix B), green (Helix C), deepgreen (Helix D), yellow (Helix E), orange (Helix F), and red (Helix G).

### 4 Methods2

We now give the details of our new replica-exchange methods. We prepare  $M$  non-interacting replicas at  $M$  different temperatures. Let the label  $i$  ( $=1, \dots, M$ ) stand

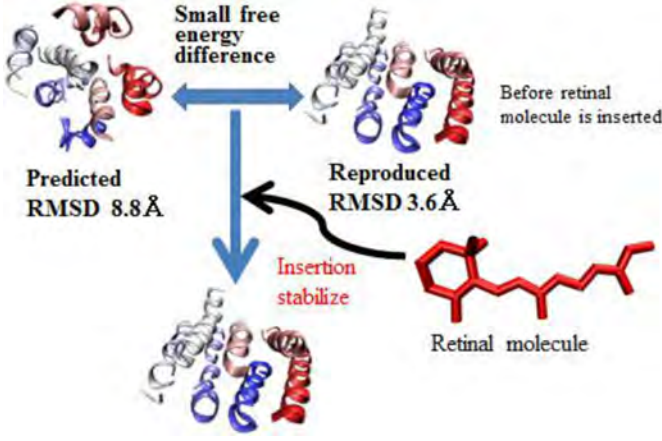


FIG. 2. Hypothesis about the relation between the global-minimum free energy state and the second-minimum. The effect of an insertion of a retinal molecule causes the stabilization of the native-like structure.

for the replica index and label  $m$  ( $=1, \dots, M$ ) for the temperature index. We represent the state of the entire system of  $M$  replicas by  $X = \{x_{m(1)}^{[1]}, \dots, x_{m(M)}^{[M]}\}$ , where  $x_m^{[i]} = \{q^{[i]}, p^{[i]}\}_m$  are the set of coordinates  $q^{[i]}$  and momenta  $p^{[i]}$  of particles in replica  $i$  (at temperature  $T_m$ ). The probability weight factor for state  $X$  is given by a product of Boltzmann factors:

$$W_{\text{REM}}(X) = \prod_{i=1}^M \exp[-\beta_{m(i)} H(q^{[i]}, p^{[i]})], \quad (7)$$

where  $\beta_m (= 1/k_B T_m)$  is the inverse temperature and  $H(q, p)$  is the Hamiltonian of the system. We consider exchanging a pair of replicas  $i$  and  $j$  corresponding to temperatures  $T_m$  and  $T_n$ , respectively:

$$X = \{\dots, x_m^{[i]}, \dots, x_n^{[j]}, \dots\} \rightarrow X' = \{\dots, x_m^{[j]}, \dots, x_n^{[i]}, \dots\}, \quad (8)$$

where  $x_n^{[i]'} \equiv \{q^{[i]}, p^{[i]'}\}_n$ ,  $x_m^{[j]'} \equiv \{q^{[j]}, p^{[j]'}\}_m$ , and  $p^{[j]'} = \sqrt{\frac{T_m}{T_n}} p^{[j]}$ ,  $p^{[i]'} = \sqrt{\frac{T_n}{T_m}} p^{[i]}$  [24].

Here, the transition probability  $\omega(X \rightarrow X')$  of Metropolis criterion for replica exchange is given by

$$\begin{aligned} \omega(X \rightarrow X') &= \min\left(1, \frac{W_{\text{REM}}(X')}{W_{\text{REM}}(X)}\right) \\ &= \min(1, \exp(-\Delta)), \end{aligned} \quad (9)$$

where

$$\Delta = \Delta_{m,n} = (\beta_n - \beta_m)(E(q^{[i]}) - E(q^{[j]})). \quad (10)$$

Because each replica visits various temperatures followed by the transition probability of Metropolis algorithm, REM performs a random walk in temperature space.

We now review two REMs, which are based on random walks in temperature space. Without loss of generality, we can assume that  $M$  is an even integer and that

$T_1 < T_2 < \dots < T_M$ . The conventional REM[24–27] is performed by repeating the following two steps:

1. We perform a conventional MD or MC simulation of replica  $i$  ( $= 1, \dots, M$ ) at temperature  $T_m$  ( $m = 1, \dots, M$ ) simultaneously and independently for short steps.
2. Pairs of exchange attempts are selected in replica pairs with neighboring temperatures, for example, for the odd pairs  $(T_1, T_2)$ ,  $(T_3, T_4)$ ,  $\dots$ ,  $(T_{M-1}, T_M)$  or even pairs  $(T_2, T_3)$ ,  $(T_4, T_5)$ ,  $\dots$ ,  $(T_{M-2}, T_{M-1})$ .

All the replica pairs thus selected are attempted to be exchanged according to the Metropolis transition probability in Eqs. (9) and (10) with  $n = m + 1$ .

We repeat Steps 1 and 2 until the end of the simulation. The canonical ensemble at any temperature is reconstructed by reweighting techniques[28–30].

We next present the deterministic replica-exchange method (DETREM)[31]. Only Step 2 is different from the conventional REM. At first, we introduce an internal state  $y_{m,n}$  as an index of a pair of replicas  $i$  and  $j$  at temperatures  $T_m$  and  $T_n$ , and consider the following differential equation:

$$\frac{dy_{m,m+1}}{dt} = \sigma_m \frac{1}{1 + \exp(\Delta_{m,m+1})}, \quad (11)$$

where  $t$  is a virtual time,  $\Delta_{m,m+1}$  is the same as in Eq. (10) with  $n = m + 1$ , and the signature  $\sigma_m$  of the pair of  $(T_m, T_{m+1})$  changes to 1 or  $-1$  to control the signature of the change of  $y_m$  which monotonically increases or decreases. In Step 2, instead of applying the Metropolis criterion in Eqs. (9) and (10), we solve the differential equation in Eq. (11) for the internal states  $y_{m,m+1} \in \{-1, 1\}$  for  $(T_m, T_{m+1})$ , where the total number of internal states is  $M-1$  with the following pairs: (1,2), (2,3),  $\dots$ ,  $(M-1, M)$  for the random-walk DETREM and the pairs: (1,2), (3,4),  $\dots$ ,  $(M-1, M)$  and (2,3), (4,5),  $\dots$ ,  $(M-2, M-1)$  for designed-walk REM. The replica exchange is done as follows[31]:

if updated  $y_{m,m+1} \geq \pm 1$ , then  $(T_m, T_{m+1}) \rightarrow (T_{m+1}, T_m)$ ,  
 $y_{m,m+1} \leftarrow y_{m,m+1} \mp 1$ , and  $\sigma_m \leftarrow \mp 1$ .

For the random-walk DETREM, if  $y_{m,m+1}$  performs exchanges,  $y_{m+1,m+2}$  is not time evolved and  $y_{m+2,m+3}$  is evolved to avoid the leap exchange of temperature such as from  $T_m$  to  $T_{m+2}$ .

Finally, the temperature walk can be implemented to both conventional REM and DETREM (and other REMs) as follows. Namely, the designed-walk replica-exchange method (DEWREM)[32] is performed by repeating the following steps.

1. We perform a conventional MD or MC simulation of replica  $i$  ( $= 1, \dots, M$ ) at temperature  $T_m$  ( $m =$

$1, \dots, M$ ) simultaneously and independently for short steps.

2. Replica exchange is attempted for all the odd pairs  $(T_1, T_2), (T_3, T_4), \dots, (T_{M-1}, T_M)$ .

3. Repeat Steps 1 and 2 until all odd pairs perform replica exchange exactly once. Namely, once a pair is exchanged, the exchanged pair stops exchange attempts and keep performing the simulation in Step 1 with the new temperatures. Replica exchange attempt in Step 2 is repeated until all the other odd pairs finish exchanges.

4-6. Repeat Steps 1-3 where the odd pairs in Steps 2 and 3 are now replaced by the even pairs  $(T_2, T_3), (T_4, T_5), \dots, (T_{M-2}, T_{M-1})$ .

7. The cycle of Steps 1 to 6 is repeated until the number of cycles is  $M$ , which is equal to the tunneling count and all replicas have the initial temperatures.

8. Begin the above cycle of Steps 1-7 with Steps 1 to 3 and Steps 4 to 6 interchanged. These eight steps are repeated until the end of the simulation.

The schematic picture of this procedure is shown in Fig. 3. We remark that Step 8, namely, reversing the cycle of Steps 1-3 and 4-6, is necessary for the detailed balance condition, because the entering states are the same as leaving states. For example, the state  $(x_1^{[1]}, x_2^{[2]}, x_3^{[3]}, x_4^{[4]}, x_5^{[5]}, x_6^{[6]})$  is reached from only two states  $(x_2^{[1]}, x_1^{[2]}, x_4^{[3]}, x_3^{[4]}, x_6^{[5]}, x_5^{[6]})$ ,  $(x_1^{[1]}, x_3^{[2]}, x_2^{[3]}, x_5^{[4]}, x_4^{[5]}, x_6^{[6]})$  only and makes transition to the two states, as shown in Fig. 3, where  $x_m^{[i]}$  is the state of replica  $i$  at temperature  $T_m$ . This exchange procedure satisfies the detailed balance condition for replica and temperature pair because the trial of exchange pair

$$\begin{aligned} & \gamma(i(m) \rightarrow i(m+1)) \times \\ & \omega((x_m^{i(m)}, x_{m+1}^{i(m+1)}) \rightarrow (x_{m+1}^{i(m)}, x_m^{i(m+1)})) \\ & = \gamma(i(m+1) \rightarrow i(m)) \times \\ & \omega((x_{m+1}^{i(m)}, x_m^{i(m+1)}) \rightarrow (x_m^{i(m)}, x_{m+1}^{i(m+1)})) \end{aligned} \quad (12)$$

is equal in the route as is shown in Fig. 3, where  $\gamma(i(m) \rightarrow i(m+1))$  is the selected probability of the exchange attempt.

This sequential exchange achieves one tunneling count when  $M$  cycles for each replica are finished. In theory, the estimated ratio of tunneling count between the odd-even sequential exchange and the conventional random walk is given by

$$\frac{TC_{\text{sequential}}}{TC_{\text{random walk}}} = \frac{N_{\text{trial}} \times P_{\text{correction}}^{\text{DEW}}}{\sqrt{N_{\text{trial}}} \times P_{\text{correction}}^{\text{RW}}} \propto \sqrt{N_{\text{trial}}}, \quad (13)$$

where  $N_{\text{trial}}$  is the number of exchange attempts,  $P_{\text{correction}}^{\text{DEW}}$  is the correction for waiting for all the replica

exchanges in Steps 3 and 6, and  $P_{\text{correction}}^{\text{RW}}$  is the correction for the deviation of random-walk probability from the value 1/2.

In order to test the effectiveness of the present methods, we performed simulations with conventional REM, DETREM and DEWREM for a 2-dimensional Ising model. The lattice size in a square lattice was 128 (hence, the number of spins was  $N = 128^2 = 16384$ ). We have performed conventional random-walk simulation and designed-walk simulation of both Metropolis REM and DETREM. We have also performed a mixed random-walk and designed-walk simulation of DETREM, where we repeated the two walks alternately. The total number of replicas  $M$  was 40 and the temperatures were 1.50, 1.55, 1.60, 1.65, 1.70, 1.75, 1.80, 1.85, 1.90, 1.94, 1.98, 2.01, 2.04, 2.07, 2.10, 2.13, 2.16, 2.19, 2.22, 2.25, 2.28, 2.31, 2.34, 2.358, 2.368, 2.38, 2.40, 2.42, 2.44, 2.47, 2.51, 2.57, 2.63, 2.69, 2.75, 2.82, 2.90, 3.00, 3.10, and 3.15. Boltzmann constant  $k_B$  and coupling constant  $J$  were set to 1. Thus,  $\beta = 1/k_B T = 1/T = \beta^*$ , and the potential energy is given by  $E(\mathbf{s}) = -\sum_{\langle i,j \rangle} s_i s_j$ , where  $s_i = \pm 1$ , and the summation is taken over all the nearest-neighbor pairs in the square lattice.

For the conventional random-walk REM and DETREM, replica-exchange attempt was made every 1 MC step. One MC step here consists of one Metropolis update of spins. The total number of MC steps for all the simulations was 100,000,000. To integrate Eq. (11), we used the fourth-order Runge-Kutta method with virtual time step  $dt = 1$ . For DEWREM, replica-exchange attempt was made every 20, 50, 100, 150, 200 MC steps in the conventional REM simulations and every 20, 50, 100, 150, 200, and 250 MC steps in the DETREM simulations (see Table I). The mixed-walk simulation was performed in which after  $4M (= 160)$  even-odd or odd-even cycles of designed-walk simulations (replica-exchange attempt was made at every 20 MC steps) were performed, 200,000 MC steps (which roughly corresponds to  $2M$  cycles) of random-walk simulations (replica-exchange attempt was made at every 1 MC step) were performed, and then this procedure was repeated. For reweighting analyses ([28-30, 33]), the total of 10,000 spin state data were taken with a fixed interval of 1,000 MC steps at each temperature from the REM simulations.

## 5 Results2

Table I lists the mean tunneling counts per replica for each method, which is the number of times where the replicas visit from the lowest temperature through the highest temperature and back to the lowest during the simulation. The mean tunneling counts per replica of the designed-walk simulations at every 10 MC attempts were about twice larger. These large tunneling counts imply that in designed-walk method all replicas traversed

more efficiently in temperature space, and our design to maximize the tunneling counts for all replicas without random walks was successful. For the mixed-walk simulation, the maximum tunneling count was about twice larger than that of random-walk DETREM. The mean tunneling count was almost the same as that of designed-walk DETREM.

We next examine physical quantities obtained from the designed-walk simulations with various replica-exchange attempt frequencies and mixed walk simulations and compare them to those from the conventional random-walk simulations. Fig. 4(a) and Fig. 4(b) show the specific heat  $C$  as a function of  $T$  during the conventional REM simulations and the DETREM simulations, respectively. They were obtained by the reweighting techniques[28–30, 33]. This shows that designed-simulation with shorter replica-exchange interval such as every 10 and 20 MC steps underestimated the heat capacity near the critical temperature although the transition point is sufficiently similar to the exact critical temperature at  $T_c = 2.269$ . As the intervals of replica-exchange attempts are longer, the accuracy of heat capacity is higher. Moreover, the combination of the random-walk and designed walk also increased the accuracy. This suggests that the designed-walk replica-exchange attempts caused correlation between replicas. The correlation seems to be very strong near the critical temperature. As a result, the heat capacity is underestimated slightly. Fig. 5(a) and Fig. 5(b) show susceptibility  $\chi$  as a function of temperature obtained from the random-walk and designed-walk simulations of Metropolis REM and DETREM, for DETREM including the mixed-walk simulation. This figure shows that by extending intervals of replica-exchange attempts DEWREM simulation can reproduce the results of random-walk REM in both conventional REM and DETREM. However, we observe slower relaxation of susceptibility in different replica exchange intervals to the conventional results than that of heat capacity. Moreover, these physical quantities show that repeating a random walk and designed walk simulation in mixed-walk simulation is an efficient way to increase the accuracy of results and the number of tunneling counts at the same time.

However, these physical quantities show that mixed-walk simulation can increase the accuracy of results and the number of tunneling counts and DEWREM simulation is suited for simulations with longer time intervals between replica-exchange attempts.

## 6 Summary and future prospect

The first part of this article gave the results of protein structure prediction for bacteriorhodopsin with the flexible treatment of transmembrane helix backbone structure and our recently extended implicit membrane model.

We obtained not only the native-like structure but also the associated structure with an empty space for retinal molecule insertion. These structures are also consistent with previous experimental results.

In the next part, we compared the deterministic replica-exchange method and designed walk replica-exchange method to the conventional REM in 2-dimensional Ising model. DETREM exactly reproduced the results of conventional REM including phase transition. On the other hand, DEWREM needs longer interval between replica-exchange trials because of correlation caused by the introduction of designed walk, which may break the Markov process in short interval resulting in the deviation from the exact value near the critical temperature. To avoid this correlation, mixing random walk is a better way to remove the correlation.

Finally, we will give some perspectives for future work. We will first apply our structure prediction method to unknown membrane proteins which obtained the low resolution structure.. Secondly, DETREM can introduce the methods for faster convergence in machine learning because this method has the same mathematical formulation of Boltzmann machine. Thirdly, the way for fast reduction of correlation among replicas in shorter interval is useful in the application of spin systems in DEWREM while another system such as a peptide usually employs longer time interval in REM.

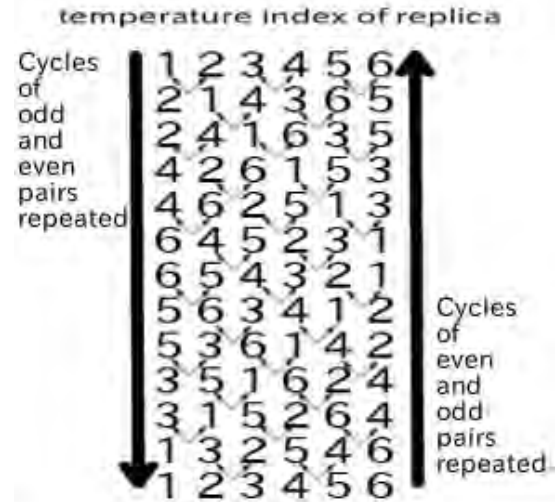


FIG. 3. An schematic picture of time series of temperature indices in DEWREM with 6 replicas. The left cycle begins with the temperature exchange of odd index pairs ( $T_1, T_2$ ), ( $T_3, T_4$ ), and ( $T_5, T_6$ ), then tries with even pairs ( $T_2, T_3$ ) and ( $T_4, T_5$ ). The right cycle begins with even pairs and next tries odd pairs. They are the reverse cycles of each other and their combination satisfies the detailed balance condition of replica exchange.

## Acknowledgments



TABLE I. The mean number of tunneling counts per replica.

TC	Random walk		Designed walk								Mixed walk
	Met	DETREM	Met				DETREM				DETREM
Interval	1	1	20	50	100	150	20	100	150	200	1 & 20
Mean	173	178	292	197	131	99	231	93	69	55	293
$\pm$ SD	9.5	8.8	56	41	27	21	48	20	15	11	6

TC, Interval, SD, Met stand for tunneling counts, the number of MC steps between replica-exchange attempts, standard deviation, and REM based on Metropolis criterion, respectively. The frequency (1 & 20) of Mixed walk means that it was 1 MC step for random walk REM and 20 MC steps for designed-walk REM.

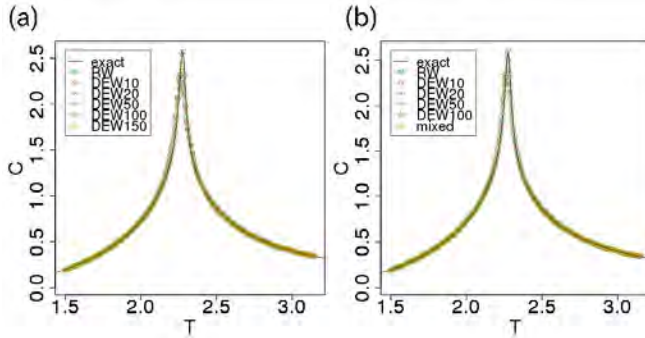


FIG. 4. Specific heat  $C$  as a function of  $T$  from the (a) REM, (b) DETREM simulations including the mixed-walk simulation. The error bars are smaller than the symbols. In the inset, the labels are as follows. exact: exact solution, RW: random walk, DEW $n$ : DEWREM with the interval of  $n$  MC steps, and mixed: mixed walk (see Table 1). The exact results for the lattice size  $L=128$  (black curves) were obtained by Berg's program [34] based on Ref. [35].

Some of the computations were performed on the supercomputers at the Institute for Solid State Physics, University of Tokyo. This work was supported, in part, Grants-in-Aid for Scientific Research (A) (No. 25247071), for Scientific Research on Innovative Areas ("Dynamical Ordering & Integrated Functions"), Program for Leading Graduate Schools "Integrative Graduate Education and Research in Green Natural Sciences", and for the Computational Materials Science Initiative, and for High Performance Computing Infrastructure from the Ministry of Education, Culture, Sports, Science and Technology (MEXT), Japan.

- [1] M. Lomize, A. Lomize, I. Pogozheva, and H. Mosberg, *Bioinformatics* **22**, 623 (2006).
- [2] B. R. Brooks, R. E. Bruccoleri, B. D. Olafson, D. J. States, S. Swaminathan, and M. Karplus, *J. Comput. Chem.* **4**, 187 (1983).

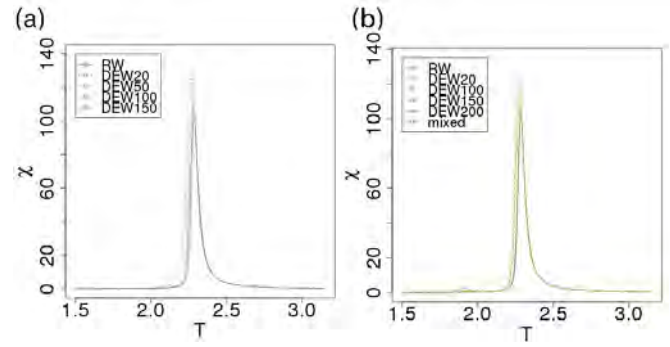


FIG. 5. Susceptibility  $\chi$  as a function of  $T$  from the (a) REM, (b) DETREM simulations including the mixed-walk simulation. The error bars are smaller than the symbols. Also see the caption of Fig. 4.

- [3] J. Hu, A. Ma, and A. R. Dinner, *J. Comput. Chem.* **27**, 203 (2006).
- [4] W. Reiher, *Theoretical studies of hydrogen bonding*, Ph.D. thesis, Harvard University (1985).
- [5] E. Neria, S. Fischer, and M. Karplus, *J. Chem. Phys.* **105**, 1902 (1996).
- [6] H. Kokubo and Y. Okamoto, *Biophys. J.* **96**, 765 (2009).
- [7] H. Kokubo and Y. Okamoto, *Chem. Phys. Lett.* **383**, 397 (2004).
- [8] H. Kokubo and Y. Okamoto, *J. Chem. Phys.* **120**, 10837 (2004).
- [9] H. Kokubo and Y. Okamoto, *J. Phys. Soc. Jpn.* **73**, 2571 (2004).
- [10] H. Kokubo and Y. Okamoto, *Chem. Phys. Lett.* **392**, 168 (2004).
- [11] A. R. Dinner, *J. Comput. Chem.* **21**, 1132 (2000).
- [12] N. Gō and H. A. Scheraga, *Macromolecules* **3**, 178 (1970).
- [13] L. Dodd, T. Boone, and D. Theodorou, *Mol. Phys.* **78**, 961 (1993).
- [14] M. Teeter and D. Case, *J. Phys. Chem.* **94**, 8091 (1990).
- [15] A. Kitao, F. Hirata, and N. Gō, *Chem. Phys.* **158**, 447 (1991).
- [16] A. Garcia, *Phys. Rev. Lett.* **68**, 2696 (1992).
- [17] R. Abagyan and P. Argos, *J. Mol. Biol.* **225**, 519 (1992).
- [18] A. Amadei, A. Linssen, and H. Berendsen, *Proteins* **17**, 412 (1993).
- [19] A. Kitao and N. Gō, *Curr. Opin. Struct. Biol.* **9**, 164 (1999).
- [20] W. Humphrey, A. Dalke, and K. Schulten, *J. Mol. Graphics* **14**, 33 (1996).
- [21] R. Ihaka and R. Gentleman, *J. Comput. Graph. Stat.* **5**, 299 (1996).
- [22] J. MacQueen, in *Fifth Berkeley Symposium on Mathematical Statistics and Probability*, eds Le Cam LM, Neyman J (Univ of California Press, Berkeley, CA) (1967) pp. 281–297.
- [23] J. L. Popot, S. E. Gerchman, and D. M. Engelman, *J. Mol. Biol.* **198**, 655 (1987).
- [24] Y. Sugita and Y. Okamoto, *Chem. Phys. Lett.* **314**, 141 (1999).
- [25] K. Hukushima and K. Nemoto, *J. Phys. Soc. Jpn.* **65**, 1604 (1996).
- [26] R. H. Swendsen and J.-S. Wang, *Phys. Rev. Lett.* **57**, 2607 (1986).

- [27] C. J. Geyer, Comput. Sci. Stat.: Proc. 23rd Symp. Interface, Interface Foundation, Fairfax Station, VA , 156 (1991).
- [28] A. M. Ferrenberg and R. H. Swendsen, Phys. Rev. Lett. **63**, 1195 (1989).
- [29] S. Kumar, J. M. Rosenberg, D. Bouzida, R. H. Swendsen, and P. A. Kollman, J. Comput. Chem. **13**, 1011 (1992).
- [30] A. Mitsutake, Y. Sugita, and Y. Okamoto, J. Chem. Phys. **118**, 6664 (2003).
- [31] R. Urano and Y. Okamoto, e-print: arXiv:1412.6959 (2014).
- [32] R. Urano and Y. Okamoto, e-print: arXiv:1501.00772 (2015).
- [33] M. R. Shirts and J. D. Chodera, J. Chem. Phys. **129**, 124105 (2008).
- [34] B. A. Berg, *Markov Chain Monte Carlo Simulations and Their Statistical Analysis* (World Scientific, Singapore, 2004).
- [35] A. E. Ferdinand and M. E. Fisher, Phys. Rev. **185**, 832 (1969).

## **3.2 First-Principles Calculation of Material Properties**



# Atomic Structures and Electronic Properties of Hard- and Soft-Nanomaterials

Atsushi Oshiyama

*Department of Applied Physics, The University of Tokyo  
Hongo, Tokyo 113-8656*

Main purpose of this project is to develop the density-functional approach which enables us to perform more accurate and larger scale static and dynamical calculations on massively parallel architecture computers, to clarify underlying physics and chemistry in phenomena in nano-materials and structures, and to predict new phenomena in nano-world. The following is two examples which we have achieved in 2014 fiscal year.

## 1. Magnetic Ordering without Magnetic Elements on SiC Nanofacet

Nanometer-scale structures are now accessible. Common expectation that such nanostructures break through limitations of current technology may rely on a fact that nano-scale shapes affect wave-functions of relevant electron states. However, a way of designing nano-shapes which decisively affect the electron states and therefore are intriguing in science and useful in technology is lacking. Our calculations based on the density-functional theory (DFT) developed by the real-space scheme (RSDFT code) [Iwata et al., PRB 77, 115208 (2008); J. Comp. Phys. 229, 2339 (2010); Hasegawa et al., Int. J. HPC Appl. 28, 335 (2014)] show that peculiar electron states which are localized near but extended along step edges of the nano-facets of SiC exhibit either ferromagnetic (FM) or anti-ferromagnetic (AFM) spin polarization. Considering that SiC is an emerging material in the power electronics and that spin current is the new non-dissipative carrier for the information in future, this finding based on our RSDFT scheme has great impact.

Figure 1 shows the most stable nano-facet structure on SiC (0001) surface which we have found in our RSDFT calculations. We have found that the nano-facet structure is a bunched single bi-layer atomic steps and that the balance between the step-step repulsive energy and the surface-energy gain on the terrace causes the appearance of a particular shape of nano-facet: The facet angle  $\varphi$  which is the angle between (0001) and the experimentally

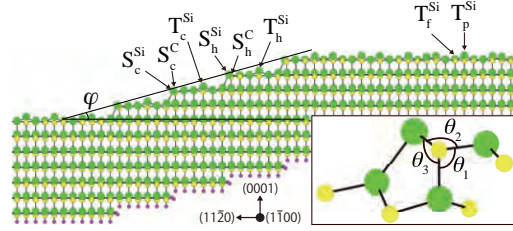


Figure 1: A side views of the  $(11\bar{2}n)$  ( $n = 12$ ) nanofacet with the facet angle  $\varphi = 15.3^\circ$  on the 4H-SiC(0001) vicinal surface. Green, yellow and purple balls indicate the Si, C and H atoms, respectively. The labels such as  $T_p^{\text{Si}}$  denote several particular sites which may be passivated by hydrogen.

observed  $(11\bar{2}n)$  is almost common (magic angle,  $\varphi = 12^\circ - 16^\circ$ ) and the height of the nanofacet along the (0001) direction is a integer or a half-integer of the unit-cell height [1].

We have found that step-edge localized states (Fig. 2) appear below Fermi level ( $E_F$ ) which show flat dispersion along the step edges. As is clear from Fig. 2, this flat-band states have a chemical character of dangling bonds of the edge C atoms. The dangling bonds of Si edge atoms constitute other states near  $E_F$  due to the lower electron affinity of Si.

Hydrogen adsorption is a common process to fabricate semiconductor devices. We have found that atomic sites on the terrace and the step edges shown in Fig. 1 exhibit different hydrogen-philicity: The step edge C atoms and then some edge Si atoms exhibit less adsorption energy of hydrogen atoms. Hence, it is likely that the terrace Si atoms and other edge Si atoms are H-terminated. In this situation, the flat-bands come up at  $E_F$  and show spin polarization.

Our RSDFT calculations actually show that the ground state is either ferromagnetic or anti-ferromagnetic and the spin density is distributed

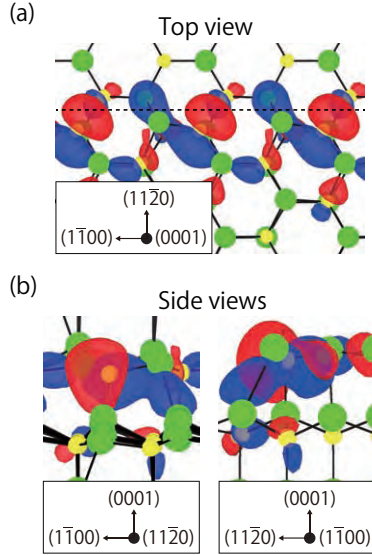


Figure 2: Expanded views of the Kohn-Sham orbital of the flat-band edge states localized near C atoms at the edges. The top and side views are displayed in (a) and (b), respectively. The red and blue colors depict positive and negative values, respectively, of the Kohn-Sham orbitals. The dashed line in (a) shows the step edge position.

solely along the step edges of the nanofacets. We predict that control of H-adsorption controls the filling of the flat-band states and then the distribution of the spin density in the magnetic states.

## 2. Stability and Gap Modulation through Atomic Protrusion in Bilayer Silicene

Bilayer graphene provides new aspects of graphene physics such as the band gap opening and moiré-pattern-induced electron localization. The interlayer interaction is obviously weaker than the intralayer interaction but decisive to modulate the electron states due to its symmetry breaking. Similar intriguing behavior with the extension related to the spin-degrees of freedom is expected for layered Si (silicene), which has been grown experimentally with forms of monolayer and of a few layers mainly on Ag substrates. One of the most important characteristics which discriminate silicene from graphene is the buckling of two sublattices caused by the preference of Si for  $sp^3$  hybridization. In fact, first-principles calculations within the local density approximation have clarified that a planar Si monolayer is unstable to the buckling, and that the resultant freestanding monolayer silicene with the buckling of 0.44 Å have the Dirac cone at the Fermi level,  $E_F$ . This buckling brings about a com-

plex but rich variation in structure and electronic properties in bilayer silicene.

We have performed systematic first-principles total-energy and phonon calculations for freestanding bilayer silicene with various lateral periodicities and atomic densities [3]. By extensive geometry optimization followed by the phonon calculations, we have unequivocally identified ten dynamically stable structures with distinct atomic configurations, symmetries, and periodicities. We have clarified that the ten structures include all the six structures reported in the past. Other four structures are newly found and more stable than the previously reported ones. We have found that the more stable structures have a single prominent structural characteristics, i.e. the protrusion of Si atom. We have also found that there is an energetically optimum lateral periodicity for the protruded structure, i.e.,  $\sqrt{3} \times \sqrt{3}$  or  $2 \times 2$ , depending on the stacking of the two Si layers. We have further clarified that the stable freestanding bilayer silicene is a semiconductor in which the energy gap is sensitive to the detailed protruded structure.

The calculated total energies of freestanding bilayer silicene with various stackings and periodicities [3] show that the hex-OR- $2 \times 2$  structure newly found here has the lowest energy, and the slide- $2 \times 2$  follows with the total-energy increase of 6 meV/atom. The OR- $\sqrt{3} \times \sqrt{3}$  and rect-OR- $2 \times 2$  structures are also close in energy (+9 and +10 meV/atom from the lowest energy, respectively). The AA- $\sqrt{3} \times \sqrt{3}$  and AA- $2 \times 2$  are in the second lowest energy group (+31 and +41 meV/atom, respectively). The OR-, AA-, slide-, AB- $1 \times 1$  structures have relatively high energy (+60, +78, +112 and +131 meV/atom, respectively) compared to the  $\sqrt{3} \times \sqrt{3}$  and  $2 \times 2$  structures.

## Related Publications

1. K. Sawada, J.-I. Iwata and A. Oshiyama, "Magic Angle and Height Quantization in Nanofacets on SiC(0001) Surfaces" Appl. Phys. Lett. **104**, 051605 (2014).
2. K. Sawada, J.-I. Iwata and A. Oshiyama, "Spontaneous Appearance of Low-dimensional Magnetic Electron System on Semiconductor Nanostructures" arXiv:1504.06934.
3. Y. Sakai and A. Oshiyama, "Structural Stability and Energy-Gap Modulation through Atomic Protrusion in Freestanding Bilayer Silicene" Phys. Rev. B (R) (2015) in press.

## Hydration effects on ligand binding to NylB enzyme

Yasuteru SHIGETA

*Center for Computational Sciences,*

*University of Tsukuba, 1-1-1 Tennodai, Tsukuba, Ibaraki 305-8577*

*Arthrobacter* sp. KI72, which is a bacterium found in the waste of a nylon factory, utilizes nylon oligomers as sole carbon and nitrogen sources for their growth [1]. Nylon hydrolases, NylB, have been extensively performed to enhance the hydrolysis activity both by experimental and theoretical works. According to the X-ray crystallographic analyses, NylB has two different forms, i.e. the substrate-free form (open form) and the substrate-bound form (closed form). To form the later structure, a loop-segment drastically moves towards the substrate showing the induced-fit mechanism. However there is no quantitative information about how much the substrate-enzyme complex is stabilized due to both the amino acid residues participating the induced-fit and the surrounding water molecules.

In this project, fragment molecular orbital (FMO) calculations have been successfully applied to NylB in order to investigate hydration effects on an enzyme-substrate binding structure.

(Statistically corrected) Inter-fragment interaction energy analyses on this system quantitatively characterise the interaction between an aminohexanate dimer (ALD) and amino acid residues such as Asp181, Ser112, and Ile 345, in NylB, which is considered important residues for constructing enzyme-substrate complex. Furthermore, we show that the direct interaction between ALD and NylB weakens by hydration because water molecules cause charge translation or polarization to ALD or each amino acid residue, but including interaction energy between ALD and water molecules, this complex are stabilized largely. This result indicates the hydration effects are of great importance in forming the enzyme-substrate complex [2].

### References

- [1] S. Kinoshita *et al.*, Agric. Biol. Chem **39** 1219-1223 (1975).
- [2] H. Ando, Y. Shigeta, T. Baba, C. Watanabe, Y. Okiyama, Y. Mochizuki, M. Nakano, *Mol. Phys.* **113**, 319-326 (2015).

# First-principles simulations of atomic geometries, electronic properties and chemical reactions at interfaces

Fahdzi MUTTAQIEN, Yuji HAMAMOTO, Kouji INAGAKI, Hidetoshi Kizaki, and  
Yoshitada MORIKAWA

*Department of Precision Science and Technology,  
Osaka University, Yamada-oka, Suita, Osaka 565-0871*

Adsorption and reaction of CO<sub>2</sub> on metal surfaces are fundamentally important in surface chemistry and other related fields [1,2]. Previous studies of CO<sub>2</sub> adsorption on single-crystal Cu surfaces have shown that on flat copper surfaces, CO<sub>2</sub> is weakly adsorbed molecularly and needs high activation energy to dissociate: 0.69 eV for Cu(110)[3]. On the Cu(311) surfaces, Fu and Somorjai found that CO<sub>2</sub> is adsorbed and dissociates to CO and O with a 4 L dose at 150 K using temperature

programmed desorption (TPD) experiment [4]. Boenicke *et al.* showed by means of thermal desorption spectroscopy (TDS) experiment that CO<sub>2</sub> is chemisorbed and dissociates at 95 K over the Cu(332) surface[5]. Recently, Koitaya and co-workers showed that CO<sub>2</sub> dissociation takes place on the stepped Cu(997) surface rather than on flat Cu(111) surface at 83 K by using infrared reflection absorption spectroscopy (IRAS) [6]. Meanwhile, it is not clear whether CO<sub>2</sub> dissociation takes place on

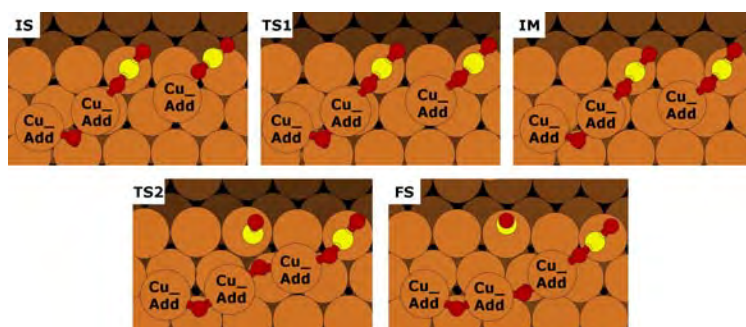


**Fig. 1.** Schematic of CO<sub>2</sub> dissociation followed by Cu-O-Cu chain formation on Cu(221) surface. IS, TS, FS, and IM represent initial, transition, final, and intermediate states, respectively.

Cu surfaces at low temperature theoretically. Thus, we studied the dissociative adsorption of CO<sub>2</sub> on the Cu(111), Cu(221), Cu(211), and Cu(11 5 9) surfaces by using state-of-the-art density functional theory (DFT) [7]. We obtained that the barrier energy for CO<sub>2</sub> dissociation on the flat Cu(111) surface is 1.33 eV. While, the barrier energies on stepped and kinked surfaces are 1.06 eV, 0.67 eV, and 1.02 eV for the Cu(221), Cu(211), and Cu(11 5 9) surfaces, respectively. Even though the activation energy is 0.66 eV lower on the

stepped Cu(211) surface than on the flat Cu(111) surface, we concluded that CO<sub>2</sub> does not dissociate on ideal flat, stepped or kinked Cu surfaces at low temperature.

We also studied the effect of Cu adatoms and water molecule in the CO<sub>2</sub> dissociation. We propose that the CO<sub>2</sub> dissociation is followed by the Cu-O-Cu chain formation (Fig. 1) with 0.46 eV barrier energy. By introducing water molecule impurity, CO<sub>2</sub> dissociation takes place via hydrocarboxyl (COOH) intermediate with 0.48 eV barrier energy. According to these results, additional factors on the Cu surface such as adatoms and/or gas phase impurity, which can be found in “real” experiment condition, are important to enhance CO<sub>2</sub> dissociation.

## References

- [1] H.-J. Freund and M.W. Roberts, *Surf. Sci. Rep.*, **25**, 225 (1996).
- [2] U. Burghaus, *Prog. Surf. Sci.*, **89**, 161 (2014).
- [3] J. Nakamura, J.A. Rodriguez, and C.T. Campbell, *J. Phys.: Condens. Matter* **1**, 149 (1989).
- [4] S. Fu and G.A. Somorjai, *Surf. Sci.* **262**, 68 (1992).
- [5] I.A. Boenicke, W. Kirstein, and F. Thieme, *Surf. Sci.* **307**, 177 (1994).
- [6] T. Koitaya, Y. Shiozawa, K. Mukai, S. Yoshimoto, and J. Yoshinobu, “14<sup>th</sup> International Conference on Vibrations at Surfaces in Kobe”, (2012), and personal communication.
- [7] F. Muttaqien, Y. Hamamoto, K. Inagaki, and Y. Morikawa, *J. Chem. Phys.* **141**, 034702 (2014).

# Theoretical study on the cohesive properties of organic solids with the van der Waals density functional

Susumu YANAGISAWA

*Department of Physics and Earth Sciences, Faculty of Science, University of the Ryukyus,  
Senbaru 1, Nishihara, Okinawa 903-0213*

Organic semiconductors have attracted a lot of attention as a component of the organic (opt)electronics, owing to their advantages, such as low-cost fabrication processes, flexibility, and low-power consumption. Their relevant electronic properties, such as charge transport, are determined not only by the electronic structures of constituent molecules, but also by their conformation and configuration. The theoretical treatment of organic semiconductors remains challenging, as the semilocal density functional theory fails to describe the dispersion forces accurately.

Here, we study the cohesive properties of organic semiconductor crystals using the van der Waals (vdW) density functional (vdW-DF), which describes the vdW interaction in molecular complexes or solids correctly at a reasonable computational cost [1,2]. We use a revised vdW-DF recently proposed (rev-vdWDF2) [3]. The calculations are done with the Vienna Ab-initio Simulation Package (VASP) [4] on the supercomputer system B in ISSP. We use 64-256 cores (Job class: F16-F64) depending on the unit cell size.

We examine the stable  $\alpha$ - and  $\beta$ - polymorphs of Zinc-Phthalocyanine (ZnPc) crystal. The lattice constants of  $\beta$ -ZnPc optimized with rev-vdW-DF2 are found to agree with experiments within 1 %. For  $\alpha$ -ZnPc, we optimize the geometry by using the experimental value of  $\alpha$ -CuPc as an initial guess.

The bandwidth of the highest-occupied

molecular orbital (HOMO)-derived band is estimated to be 64 meV. It is in fair agreement with the recent high-resolution angle-resolved photoelectron spectroscopy (ARPES) measurement (92 meV) [5].

To clarify the origin of the slight band dispersion, the HOMO bandwidth ( $W$ ) is calculated when (a) the intermolecular distance  $b$  between the two molecules in the unit cell is changed, or (b) the angle  $\theta_{\text{mol}}$  between the crystal axis and the normal of the molecular plane is changed.  $W$  is found to be sensitive to the intermolecular distance and the molecular orientation angle. Furthermore, by examining the Maximally-Localized Wannier Function (MLWF) [6] and estimating the transfer integral, we find that the HOMO dispersion is dominated by both the nearest- and second nearest-neighbor transfer integrals. The molecular configuration becomes most stable when the HOMO band energy is minimized, as a result of the balance between the antibonding and bonding interactions. The study demonstrates the roles of the inter-molecular distance and the molecular tilt angle in the formation of the band structure, and the importance of the accurate description of the crystal structure [7].

## References

- [1] M. Dion et al., Phys. Rev. Lett. 92, 246401 (2004).

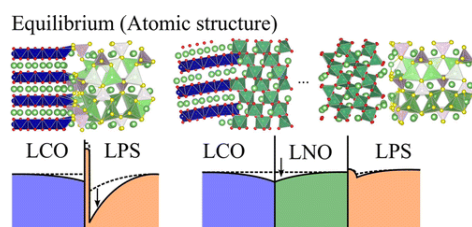
- [2] G. Román-Pérez and J. M. Soler, Phys. Rev. Lett. **103**, 096102 (2009).
- [3] I. Hamada, Phys. Rev. B **89**, 121103(R) (2014).
- [4] G. Kresse and J. Furthmüller, Phys. Rev. B **54**, 11169 (1996).
- [5] H. Yamane and N. Kosugi, Phys. Rev. Lett. **111**, 086602 (2013).
- [6] N. Marzari and D. Vanderbilt, Phys. Rev. B **56**, 12847 (1997).
- [7] S. Yanagisawa, K. Yamauchi, T. Inaoka, T. Oguchi, and I. Hamada, Phys. Rev. B **90**, 245141 (2014).

# DFT free energy analysis of redox reaction mechanisms at interfaces in batteries and catalysts

Yoshitaka TATEYAMA

*International Center for Materials Nanoarchitectonics (MANA), National Institute for Materials Science (NIMS), 1-1 Namiki, Tsukuba 305-0044, Elements Strategy Initiative for Catalysts & Batteries (ESICB), Kyoto University, Goryo-Ohara, Nishikyo-ku 615-8245. PRESTO, Japan Science and Technology Agency, 4-1-8 Honcho, Kawaguchi 333-0012.*

Our focus is on (1) development and/or establishment of theories and computational methods for problems in electro and interfacial chemistry based on the "density functional theory (DFT), and (2) understanding reaction mechanisms at interfaces in (photo)catalysts, photovoltaic cells, and batteries for universal interface science.



Initial Stage of Charging (Li ion concentration)  
Fig. 1. Schematic picture of space-charge layer mechanism at interface between the oxide cathode and sulfide electrolyte, and the buffer layer effect.

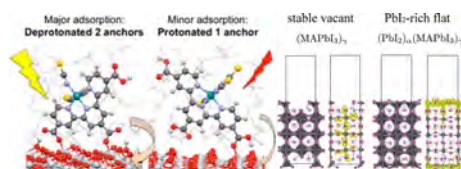


Fig. 2. Interfacial states of (left) dye-sensitized solar cell and (right) perovskite solar cell elucidated in our works.

In this year, we have elucidated several novel reaction mechanisms in Lithium-

ion batteries (Fig. 1) [1,2], dye-sensitized solar cells & perovskite solar cells (Fig. 2) [3,4,5], CeO<sub>2</sub> & diamond catalysts [6,7] as well as developed a new method for donor-acceptor electron transfer based on Marcus theory and DFT [8].

## References

- [1] \*K. Sodeyama, \*Y. Tateyama *et al.*, *J. Phys. Chem. C* **118**, 14091 (2014).
- [2] J. Haruyama, \*Y. Tateyama *et al.*, *Chem. Mater.* **26**, 4248 (2014).
- [3] \*Y. Tateyama *et al.*, *J. Phys. Chem. C* **118**, 16863 (2014).
- [4] J. Haruyama, \*Y. Tateyama *et al.*, *J. Phys. Chem. Lett.* **5**, 2903 (2014).
- [5] Y. Ootani, \*Y. Tateyama *et al.*, *J. Phys. Chem. C*, **119**, 234-241 (2015).
- [6] Z. Futera, \*Y. Tateyama *et al.*, *J. Phys. Chem. C* **118**, 22040 (2014).
- [7] L. Szabova, Y. Tateyama *et al.*, *J. Phys. Chem. C* **119**, 2537-2544 (2015).
- [8] Z. Futera, \*Y. Tateyama *et al.*, *Phys. Chem. Chem. Phys.* **16**, 19530 (2014).



# First-principles meta-dynamics analysis in Catalytic Referred Etching method

## Reaction barrier in etching of GaN, SiC and SiO<sub>2</sub>

Kouji INAGAKI

*Precision Science and Technology & Applied Physics, Graduate School of Engineering,  
Osaka University, Yamada-oka 2-1, Suita, Osaka 565-0871*

We investigated chemical etching reaction processes in Catalyst Referred Etching (CARE) surface finishing method by which step-and-terrace shaped smooth surfaces can be formed by wiping the surface by a catalyst plate in an etching solution [1]. It has been reported by experimentalist that crystalline SiO<sub>2</sub> can be smoothened by using water etchant with Pt catalyst. In this project, we analyzed this etching process and the role of Pt catalyst in an atomic scale by using first-principles reaction barrier calculations with STATE code [2]. Figure 1 shows applied  $\alpha$ -quartz SiO<sub>2</sub> step-surface model with OH terminated and with and without Pt (111) slab.

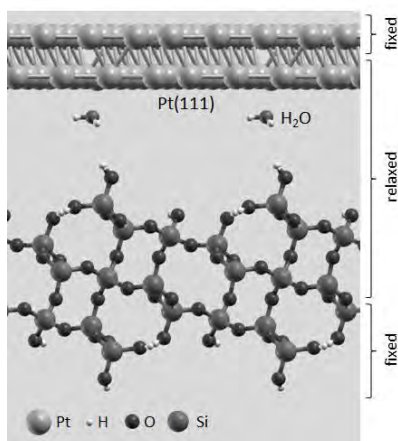


Fig. 1: Calculation model .

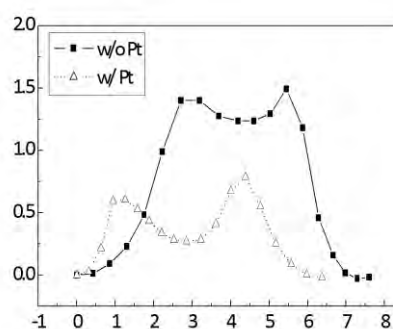


Fig. 2: Energy profile in dissociative adsorption.

We calculated the reaction process of dissociative adsorption of H<sub>2</sub>O at SiO<sub>2</sub> surface initially placed on SiO<sub>2</sub> surface as the initial stage of etching reaction process by using NEB method. NEB calculation is performed by using multi-replica MPI calculation. The energy profile (Fig. 2) indicates that the reaction barrier height is reduced in the model with Pt slab. The analyzed barrier height reduction mechanism will be published elsewhere.

## References

- [1] H.Hara, et al., J.Electron.Mater. 35 (2006) L11.
- [2] Y. Morikawa, Phys. Rev. B 63 (2001) 033405.

## Exploratory study on electric field effect of the magnetic anisotropy in the spintronics material with the oxide layer

Tatsuki ODA<sup>1,2</sup>, Daiki YOSHIKAWA<sup>2</sup>

*Institute of Science and Engineering, Kanazawa University, Kanazawa, Ishikawa 920-1192*

*Graduate School of Natural Science and Technology, Kanazawa University, Kanazawa, Ishikawa, 920-1192*

We investigated the structural, electronic, and magnetic properties in the slab of interface Fe/SrTiO<sub>3</sub>(001). It was found that such interface has a large electric field effect on magnetic anisotropy. This may come from the property of a large dielectric constant in SrTiO<sub>3</sub>. We obtained a negative slope in the EF variation of magnetic anisotropy energy (MAE). This showed a contrast with the system measured in the previous experiments, in which the latter had a positive slope in Fe/MgO systems.

The development of the memory which utilizes magnetic resistivity, magnetic random access memory (MRAM), has been carried out very actively in spintronic applications. The heat energy dissipation remains as a critical problem in the process of magnetization reversal. To solve such problem, reduction on the energy barrier by external electric field (EF) is considered to be a promising solution. Thus, the system having a large EF effect on MAE has been desired. In one of such approaches, the high-K material of a large dielectric constant, such as SrTiO<sub>3</sub> (STO), can be useful to the insulating separator in the magnetic memory cell.

For the slab of Fe(3ML)/TiO<sub>2</sub>/SrO/TiO<sub>2</sub>, in which the interface Fe atom was placed to the next of O atom, we carried out first-principles

calculation which employs the density functional theory (DFT) and fully relativistic ultrasoft pseudopotentials. Energy cutoffs for electron density and wavefunction are 300Ry and 30Ry respectively. We used the (32, 32, 1) mesh of k space sampling. The generalized gradient approximation was adopted for exchange correlation energy. The structural optimization was performed by using atomic forces except the in-plane lattice constant. For the lattice constant, we fixed the value extracted from the bulk STO, which is slightly smaller than those of Fe and MgO. The ESM method with zero external EF condition was used to avoid artificial built-in EF in the repeated slab model; vacuum/Fe STO/vacuum/ESM. For both vacuum layers, the width of 5.29Å was taken. We used the house-made program code which was parallelized in sampling k-point, applying it to System B in ISSP.

We estimated MAEs for the external EF. Due to the Fe-O bonds at the interface, the system showed a large perpendicular magnetic anisotropy (about 1.2 mJ/m<sup>2</sup> of MAE). The MAE increased when applying an EF of electron accumulation condition at the interface. The rate was obtained to be 7.3 fJ/Vm with respect to the external EF. The system Fe/STO was found to be a good candidate of both perpendicular magnetic anisotropy and large EF effect.

## Analyses on atomic structure, magnetism, and electronic structure in spintronics materials

Tatsuki ODA<sup>1,2</sup>, Daiki YOSHIKAWA<sup>2</sup>, Hiroto NAKANO<sup>2</sup>, Naohiro KITAGAWA<sup>2</sup>, Masao OBATA<sup>2</sup>

*Institute of Science and Engineering, Kanazawa University, Kanazawa, Ishikawa 920-1192*

*Graduate School of Natural Science and Technology, Kanazawa University, Kanazawa, Ishikawa, 920-1192*

We performed the first-principles density functional calculation of the slab systems, MgO(5ML)/Fe(5ML), Fe(5ML)/MgO(5ML)/Fe(5ML), and MgO(3ML)/Fe(3ML)/MgO(1 or 7 ML). We investigated structural and electronic properties in the Fe/MgO interfaces. The slab of a tunnel junction Fe/MgO/Fe exceptionally has a short Fe-O distance and a large Mg displacement from the O layer. In the junction with a small in-plane lattice constant, the interface resonance state tends to shift to a low energy, resulting in a partially electron-occupied state.

For the slab models, we used the generalized gradient approximation for the density functional theory (DFT), and the ultra-soft pseudopotentials. Energy cutoffs for electron density and wavefunction are 300Ry and 30Ry respectively. We used the 24x24x1 mesh of k space sampling. We optimized electronic wavefunctions and atomic positions by minimizing the total energy functional. The structural optimization was performed by using atomic forces except the in-plane lattice constant. For each slab system, the two lattice constants extracted from Fe and MgO bulks were employed. We used the house-made program code which was parallelized in sampling k-point, applying it to Systems B and C in ISSP.

We estimated the layer distances in the

Fe/MgO interface and in the Fe layer, and calculated the partial density of states (PDOS) projected on the Fe at the interface. We usually obtained the rigid Fe-O bond, the Mg displacement, and the interface resonance state (IRS) just above EF. The Fe/MgO/Fe slab exceptionally showed the differences in the layer distances around the interface between the slabs with MgO and Fe lattice constants and tended to have the partial occupied IRS.

The PDOS of  $d(x^2-y^2)$  largely depended on the slab. This PDOS forms a peak around EF, however the peak is smaller than those of  $d(xy)$  and  $d(yz+zx)$ . This is because the  $d(x^2-y^2)$  orbital extends to the neighboring Fe atoms within the Fe plane, while the orbitals of  $d(xy)$  and  $d(yz+zx)$  to the directions that have no covalent bond in the interface. We also observe small minority-spin states in  $d(yz+zx)$  and  $d(x^2-y^2)$  at just below (-0.2 eV) and above (0.25 eV) the Fermi level, respectively, in the MgO/Fe/MgO slab, but these states smear out in the Fe/MgO/Fe and MgO/Fe slabs. As well as the IRS, the variation in location of  $d(x^2-y^2)$  could be a key to control of electronic and magnetic properties in the interface.

The properties obtained in this calculation will be available to a fine control in a fabrication process of the interface and an improved design in the magnetic material for an EF-driven device.

## Analyses on atomic structure, magnetism, and electronic structure in spintronics materials and molecular magnets

Tatsuki ODA<sup>1,2</sup>, Daiki YOSHIKAWA<sup>2</sup>, Masao OBATA<sup>2</sup>, Naohiro KITAGAWA<sup>2</sup>, Hiroto NAKANO<sup>2</sup>,

*Institute of Science and Engineering, Kanazawa University, Kanazawa, Ishikawa 920-1192*

*Graduate School of Natural Science and Technology, Kanazawa University, Kanazawa, Ishikawa, 920-1192*

We investigated the electric field (EF) effect on the interface magnetic anisotropy of a thin MgO/Fe/MgO layer using density functional theory (DFT). The perpendicular magnetic anisotropy energy (MAE) increased not only under electron depletion but also under some electron accumulation conditions, showing a strong correlation with the number of electrons on the interface Fe atom. The reverse variation in the MAE under the EF was ascribed to novel features on the charged interface, such as electron leakage. We discussed the origin in terms of the electronic structures [1].

In magnetic tunnel junctions, duplication of a single junction has been introduced to improve performance. Similarly, in a magnetic device intended to exploit the EF-driven change in the magnetic anisotropy, a proposed double interface structure has shown a large enhancement in the EF-induced effect on the MAE. In the experiment, the researchers found unusual nonlinear behavior of the EF dependence of the MAE. For both electron depletion and electron accumulation conditions at the interface of the magnetic metallic layer, the MAE changes to favor stability in the magnetic direction perpendicular to the interface plane. The origin of this preference in such a double interface structure was not yet clear. The establishment of nonlinear behavior in the MAE variation may extend the range of

applications of EF-driven magnetic devices. A theoretical understanding of the behavior will accelerate development. In the present calculation, we successfully obtained this behavior using a realistic model with a double interface, while MAE variation had been investigated theoretically only at single interfaces.

We used a slab system, vacuum (0.79 nm)/MgO [4 atomic monolayers (ML)]/Fe (3ML)/MgO (7 ML)/vacuum (0.79 nm). We carried out a first-principles density functional calculation that used fully relativistic ultrasoft pseudopotentials and a planewave basis by using the generalized gradient approximation. The MAE was estimated from the total energy difference between the [100] (x-axis) and [001] (z-axis) magnetization directions, that is,  $\text{MAE} = E[100] - E[001]$ . We used a  $32 \times 32 \times 1$  mesh in k point sampling, and the in-plane lattice constant was fixed at the value for the MgO layer extracted from the bulk. We used the house-made program code which was parallelized in sampling k-point, applying it to Systems B and C in ISSP.

The MAE data calculated and variation rate with respect to the EF were in good agreement with the experimental data. The important results were summarized to two points: obtaining the non-linear dependence of MAE and a good agreement with the experimental

result on the EF variation rate of MAE. Property of the non-linear dependence was found to correlate with the number of electrons on the Fe atom at the interface which the EF was imposed on. We investigated the partial density of states (PDOS) projected to the 3d orbitals on the Fe atom at the interface. We obtained the localized electronic states of Fe 3d orbitals just above the Fermi level. They were found to extend to the directions where the covalent bond was not formed at the interface, and also found to correspond well to the interface resonance state (IRS) observed in experiment.

In our model system, the negative slope of the MAE variation at a finite negative EF was understood to represent electron leakage from the interface to the MgO(R) layer, particularly to the surface adjacent to the vacuum layer. In the real system, the existence of charging spots (places where electrons are trapped) in the MgO(R) layer may be needed to explain the observed negative bias voltage. There could be an impurity site or a defect site in such systems.

The existence of charging spots was consistent with the fact that the variation in the number of electrons was reduced on the interface at EFs below  $E_c$  where the MAE had the minimum value. The number of negative charges at the charging spots increased as the external EF decreases, reducing the effective EF imposed on the Fe/MgO(R) interface. In addition, another candidate for charging spots is an IRS at another MgO/Fe interface. This IRS should be assumed not to contribute to electron conduction along the perpendicular direction. In the previous experiment, there was an Fe-alloy/MgO/Fe junction, in which the IRS at MgO/Fe may act as a charging spot when negative voltages are applied, supposing that the IRS forms a set of localized states (nonconducting states). The theoretical base obtained highly encourages experimental

research.

Other than the calculation of EF variation of MAE, we calculated the following topics; electronic structures in Ti/Si(111) and Ti/Si(110), structural properties in the pair of Fe phthalocyanine (FePc) molecules, and stress calculation of the van der Waals density functional method.

The rest of this report is devoted to the results on van der Waals density functional (vdW-DF) method [2]. In this method, the options of atomic forces and cell stresses were introduced. Concerned with magnetic systems, we obtained systematically good results in the calculations of the solid oxygen. The new functional for vdW spin-polarized density functional method, which was developed and investigated for magnetic materials in the last year, was applied to solid oxygen. The crystal structural data of solid oxygen at ambient pressure was examined. The results of LDA and GGA differed largely from the respective experimental data, however, the vdW-DFs much improve the structural data, particularly, the equilibrium volume agrees well with the experimental data. The magnetic energy, defined by the total energy difference between the antiferro- and ferro-magnetic states, was found to be comparable to the energy gain from vdW interaction in the equilibrium crystal structure. It is important as a next step that the extension to spin-polarized materials of vdW-DF is applied to both the study of solid oxygen under high pressure and the application of magnetic systems other than oxygen system in order to verify the effectiveness of vdW-DF.

## References

- [1] D. Yoshikawa, M. Obata, Y. Taguchi, S. Haraguchi, and T. Oda, *Appl. Phys. Express* **7**, 113005(2014).
- [2] M. Obata, M. Nakamura, I. Hamada, and T. Oda, *J. Phys. Soc. Jpn.* **84**, 024715 (2015).

# Atomic structures, structural stabilities, and electronic properties of impurity-doped carbon-based materials

Yoshitaka FUJIMOTO

*Department of Physics, Tokyo Institute of Technology  
Oh-okayama, Meguro, Tokyo 152-8551*

Since its discovery, graphene, a monolayer sheet of graphite, has received a lot of attention from nanoscience and nanotechnology. The few-layered sheets of graphene have also attracted great attention since they exhibit different electronic structures from monolayer of graphene.

One of the effective ways to tune the electronic properties of carbon-based nanomaterials is to dope them with foreign atoms. There have been several studies on doping with boron (B) and nitrogen (N) into monolayer graphene. Actually, the chemical doping with B and N atoms can modify the electronic properties of graphene, and therefore chemically doped carbon nanomaterials are applied to developments of nanoelectronics, sensors, storages, etc. However, our knowledge as to B and N doping into bilayer graphene is still limited at present.

Here, we report energetics of B-doped and N-doped bilayer graphenes with *AA* and *AB*-stacking patterns using first-principles electronic-structure calculations within the density-functional theory. It is found that B and N-doped bilayer graphenes stacked with *AA* pattern are energetically favorable than those stacked with *AB* pattern. It is also found that the formation energies for N-doped *AB* stacking bilayer graphene depend on dopant sites, whereas those for B-doped ones show almost the same.

To discuss the energetics of B- and N-doped bilayer graphenes, the formation energy is defined by

$$E_f = E_{\text{tot}} - m_C \mu_C - \mu_{\text{BorN}}, \quad (1)$$

where  $E_{\text{tot}}$  is the total energy of the B- or

N-doped bilayer graphene with *AA*, *AB1* and *AB2* stacking patterns,  $m_C$  is the number of C atoms in a supercell, and  $\mu_C$ ,  $\mu_B$  and  $\mu_N$  are the chemical potentials of pristine bilayer graphene with corresponding *AA* or *AB* stacking pattern,  $\alpha$ -boron crystal, and  $\text{N}_2$  molecule, respectively. Here, *AB1* stacking is that the C atom on top of the C atom of the adjacent graphene layer is replaced with a dopant, and *AB2* stacking is that the C atom on top of the center of a hexagon of the adjacent graphene layer is replaced with a dopant.

The formation energy of substitutional B doping into *AA*-stacked bilayer graphene is 1.36 eV, which is found to be the smallest among doping sites into three kinds of stacking patterns *AA*, *AB1*, and *AB2*. In the case of the substitutional N doping, the formation energy is the smallest value of 0.24 eV for the *AA* stacking. In addition, our calculated formation energies of monolayer graphene doped with B and N atoms are found to be 1.42 eV and 0.32 eV, respectively [1]. The B- and N-doping into *AA*-stacked bilayer graphene are found to be energetically favorable compared with those into monolayer graphene [2].

In the case of B doping into *AB*-stacked bilayer graphene, the formation energies for *AB1* doping site is similar to that for *AB2* site by only 6 meV difference. On the other hand, in the case of the N-doped graphene, *AB1*-stacked graphene has the considerably larger formation energy (by 28 meV) compared with *AB2* stacking, indicating that the substitution with N atom on top of the center of a hexagon becomes energetically favorable rather than that on top of C atom. Thus, the formation

energy for the substitution with N atom depends on the substitution site, whereas that for B atom does not depend on it.

In summary, we have studied energetics of B-doped and N-doped bilayer graphenes with *AA* and *AB*-stacking patterns using first-principles density-functional calculations. The formation energy results suggest that the B and N dopings into *AA*-stacked bilayer graphene become energetically the most favorable among three types of stacking patterns *AA*, *AB1*, and *AB2*. It is found that the formation energies for N-doped *AB* stacking bilayer graphene depending on N-doped sites, whereas those for B-doped ones show almost the same values.

## References

- [1] Y. Fujimoto and S. Saito, Phys. Rev. B **84**, 245446 (2011).
- [2] Y. Fujimoto and S. Saito, Surf. Sci., in press.

# First-principles calculation of interactions between extreme pulse light and matter

Kazuhiro YABANA

*Center for Computational Sciences,*

*University of Tsukuba, Tsukuba, 351-8577*

In recent optical sciences, measurements in time domain using extremely short laser pulses have been developing. Nonlinear phenomena utilizing extremely intense laser pulses have also been attracting interests. We have been developing a first-principles computational method to describe interactions between pulsed light and solids based on real-time time-dependent density functional theory. We solve the time-dependent Kohn-Sham equation in real time and real space for electrons in a unit cell of crystalline solids where the electric field of pulsed light is treated as spatially-uniform, time-dependent vector potential.

We have applied our method to analyze several experimental measurements employing extreme light pulses. One is the analysis of ultrafast electric current produced at a surface of transparent materials irradiated by a strong and ultrashort laser pulses. We have analyzed electric current produced in the surface of crystalline  $\text{SiO}_2$  and found that measured features such as critical intensity and dependence on carrier envelope phase are well reproduced by our calculations [1].

We also applied our method to experiments exploring ultrafast changes of band gap of silicon under irradiation of a strong, a few cycle optical field. Our calculations show that the carrier generation by the pulsed light is caused by tunneling mechanism, and provide time evolution of orbital wave functions which may be used as an input for the analysis of attosecond transient absorption [2].

Electron dynamics calculations employing uniform spatial grids are robust but time consuming. We have investigated a possible basis expansion method which may provide accurate description with much less computational resources. We have confirmed that the basis expansion method works if we employ occupied orbitals of nearby k-points as well as those of the original k-point [3].

## References

- [1] G. Wachter et.al, Phys. Rev. Lett. **113**, 087401 (2014).
- [2] M. Schultze et.al, Science **346**, 1348 (2014).
- [3] S.A. Sato and K. Yabana, Phys. Rev. B **89**, 224305 (2014).



# Ab Initio Study of Excited Electronic States and Nonadiabatic Processes of Nanostructures under External Fields

Kazuyuki WATANABE, Chunping HU, Satoshi HAGIWARA,  
Taishi HIGUCHI, and Noriaki YAMAMOTO  
*Department of Physics, Tokyo University of Science*  
*1-3 Kagurazaka, Shinjuku-ku, Tokyo 162-8601*

In the project we investigated the following five topics this year. 1) Laser-assisted field emission from silicene nanoribbons by time-dependent density functional theory (TDDFT), 2) low-energy electron wavepacket scattering with graphene flakes (GFs) by TDDFT, 3) nanoplasmon dynamics and field enhancement of GFs by TDDFT, 4) positron states at a lithium-adsorbed Al(100) surface by two-component DFT (TC-DFT), and 5) nonadiabatic couplings by TDDFT and charge-transfer excitation energies by a perturbative approach.

1) *Laser-assisted field emission from silicene nanoribbons by TDDFT*[1]: We investigate laser-assisted field emission (LAFE) from a silicene nanoribbon (SiNR) using TDDFT simulation. The emission mechanism in the present study is considered to be over-barrier photoemission and is found to be governed by electronic dipole transitions, the characteristics of the excited states, and the energy levels of the excited states relative to the potential hump. The qualitative features of emission from the SiNR are similar to those from graphene nanoribbons (GNRs). The emission currents from SiNR, however, are found to be much larger than those from GNR for the same laser parameters in spite of a larger work function for SiNR. We reveal the emission currents in real time and space on an atomic scale, and observed current being driven back and forth in the early stage of emission. We further elucidate the dynamical correlation among the laser pulse, the Kohn-Sham potential and emission currents wiggling under the ponderomo-

tive force. We further explored the electron-emission dynamics under lasers of lower energies and higher powers than those of the simulations above and found a signature of carrier-envelope phase effect and phenomena of multi-step photo absorption by Kohn-Sham decomposition technique. These are still under investigation. Large-scale TDDFT calculations have been performed using System A.

2) *Low-energy electron wavepacket scattering with GFs by TDDFT*[2]: Low-energy electron scattering with GFs is investigated using a TDDFT simulation in real time and real space. By representing the incident electron as a finite-sized wave packet, we obtain diffraction patterns that show not only the regular features of conventional low-energy electron diffraction (LEED) for periodic structures but also special features resulting from the local atomic inhomogeneity. We have also observed  $\pi$  plasmon excitation upon electron impact on a GF. These results have been reported in Ref. 2. We further investigated the detailed properties of electron scattering from GFs and recently found a signature of secondary electron emission (SEE). We continue the simulations to elucidate the mechanism of SEE. Large-scale TDDFT calculations have been performed using System B.

3) *Nanoplasmon dynamics and field enhancement of graphene flakes by TDDFT*[3]: We investigate nanoplasmon dynamics in GF monomers and dimers using real time and space time-dependent density functional theory. By showing the characteristic features of dynamical polarizability, we verified that

the two distinct peaks in the optical absorption spectra can be attributed to  $\pi$  and  $\pi + \sigma$  plasmons. We clearly show a significant difference between on- and off-resonance responses of the  $\pi$  plasmon by demonstrating the spatial distribution of induced charge and the electric field. We thus reveal the mechanism of plasmon-induced field enhancement near GF edges, which shows great importance of first-principles study on molecular nanoplasmonics.

4) *Positron states at a lithium-adsorbed Al(100) surface by TC-DFT*[4]: The positron surface state and the energetics for positron reemission are investigated using two-component density functional theory (TC-DFT) in the projector augmented-wave framework. Trapping of positrons by the surface image potential and the effect of the positron band-shift energy in the surface region are appropriately described by the corrugated mirror model and the ramp potential, respectively, without empirical parameters. The results obtained for various physical quantities of positron states on a clean Al(100) surface, *i.e.*, the affinity, work function, life-time, binding energy, and activation energy, are in good agreement with the experimental results. The positron states on Li-adsorbed Al(100) surfaces are highly dependent on the Li coverage. In particular, the work function of positronium negative ions ( $\text{Ps}^-$ ) becomes negative at low Li coverage, which indicates the possible emission of  $\text{Ps}^-$  from the adsorbed surface. The present study not only elucidates the key energetics that are responsible for positron reemission from the surface, but also emphasizes the excellent performance of TC-DFT for prediction of the positron state on real surfaces.

5) *Nonadiabatic couplings by TDDFT and charge-transfer excitation energies by a perturbative approach*: Nonadiabatic couplings (NACs) between excited states were calculated using the frequency-domain TDDFT. The many-body wave functions of the excited states were constructed from the TDDFT expression of matrix elements between ground and excited states, using the Casida ansatz. In particular, the known problems in the application of the Casida ansatz in the litera-

ture were removed by considering the difference of the operators and adopting a method to avoid the accuracy problem due to the non-local pseudopotentials. We performed evaluation of both the first-order and second-order NACs in  $\text{H}_3$  near the conical intersection between the first and second doublet excited states. For the first-order NACs, the integral of angular NACs over a circular contour was shown to give a value quite close to the geometric phase of  $\pi$ . For the second-order NACs, the Cartesian components were shown to become large when approaching the intersection point and cannot cancel each other out in the sum. To calculate charge-transfer excitation energies which are severely underestimated by TDDFT within LDA or GGA, we implemented a perturbative approach based on DFT, which does not need the self-consistent calculation as required in  $\Delta\text{SCF}$  and thus can avoid the variation collapse in  $\Delta\text{SCF}$  due to charge sloshing. Benchmark calculations confirmed the usefulness of our implementation in the planewave pseudopotential framework when the molecular systems become large. Parallelized computing has been performed on System B.

## References

- [1] T. Higuchi, C. Hu, and K. Watanabe, *e-J. Surf. Sci. Nanotech.* **13**, 115 (2015).
- [2] K. Tsubonoya, C. Hu, and K. Watanabe, *Phys. Rev. B* **90**, 035416 (2014).
- [3] N. Yamamoto, C. Hu, S. Hagiwara, and K. Watanabe, *Appl. Phys. Express* **8**, 045103 (2015).
- [4] S. Hagiwara, C. Hu, and K. Watanabe, *Phys. Rev. B* **91**, 115409 (2015).

# Parallelized ultra-large-scale electronic-structure theory based on first principle calculation and novel numerical method

Takeo Hoshi

(1) *Department of Applied Mathematics and Physics, Tottori University,*

*4-101 Koyama-Minami, Tottori 680-8550, Japan;*

(2) *Japan Science and Technology Agency, Core Research for Evolutional Science and*

*Technology (JST-CREST), 5, Sanbancho, Chiyoda-ku, Tokyo 102-0075, Japan*

The program code 'ELSES' (<http://www.elses.jp>) were developed for order- $N$  massively parallel electronic structure theory on the ISSP supercomputer System B. A mathematical foundation is novel solver algorithms with Krylov subspace theory for the generalized shifted linear equations, in the form of  $(zS-H)\mathbf{x} = \mathbf{b}$ . Practical calculations were carried out with modelled (tight-binding-form) Hamiltonians. Several mathematical studies were also carried out as related methodologies.

A recent paper [1] gives a benchmark of amorphous-like conjugated polymers with upto one-hundred million atoms on the K computer. The K computer was used with upto the full-core calculations. The MPI/OMP hybrid parallelism is used.

As mathematical studies, we studied the convergence behavior of the block-Jacobi based massively parallel eigenvalue solver we developed last year both theoretically and experimentally [2]. We also developed basic

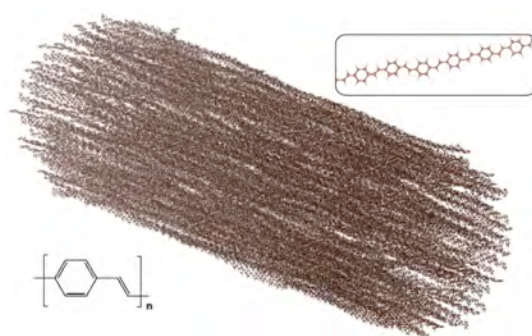


Fig. 1: A preliminary calculation of a bundled conjugated polymer (polyphenylene vinylene, PPV) with  $N = 117,962$  atoms. The length of a polymer is approximately 40 nm.

techniques to extend our algorithm to deal with the singular value decomposition and made some preliminary performance evaluation [3][4].

As applications, organic materials were calculated preliminary, such as bundled conjugated polymer (Fig.1) [5]. Moreover, optimally hybrid numerical solvers were constructed for massively parallel generalized eigenvalue computations [5], in which a routine is chosen for each subprocedure from the three

parallel solver libraries of ScaLAPACK, ELPA[6] and EigenExa [7]. The strong scaling benchmark was carried out on the K computer for electronic structure calculation problems in the matrix sizes of  $M = 10^4$ - $10^6$ . As results, the two newer libraries, ELPA and EigenExa and their hybrid give better benchmark results than the conventional ScaLAPACK library. The benchmark with the ISSP supercomputer system B was carried out with smaller matrix sizes of  $M < 10^5$ , because the benchmark was carried out by regular job class in which the largest number of nodes is 256.

The present project was carried out in collaboration, mainly, with Susumu Yamamoto (Tokyo University of Technology), Tomohiro Sogabe, Takafumi Miyata, Shao-Liang Zhang (Nagoya University), Yusaku Yamamoto (University of Electro-Communications), Hiroto Imachi (Tottori University).

## References

- [1] T. Hoshi, T. Sogabe, T. Miyata, D. Lee, S.-L. Zhang, H. Imachi, Y. Kawai, Y. Akiyama, K. Yamazaki, S. Yokoyama, ‘Novel linear algebraic theory and one-hundred-million-atom quantum material simulations on the K computer’, PoS 202, 065, 13.pp (2014).
- [2] Y. Yamamoto, L. Zhang and S. Kudo, ‘Convergence analysis of the parallel classical block Jacobi method for the symmetric eigenvalue problem’, JSIAM Letters, Vol. 6, pp. 57-60 (2014).
- [3] T. Yamashita, K. Kimura and Y. Yamamoto, ‘A new subtraction-free formula for lower bounds of the minimal singular value of an upper bidiagonal matrix’, Numerical Algorithms, to appear. ( DOI : 10.1007/s11075-014-9931-z )
- [4] S. Araki, K. Kimura, Y. Yamamoto and Y. Nakamura, ‘Implementation details of an extended oqds algorithm for singular values’, JSIAM Letters, Vol. 7, pp. 9-12 (2015).
- [5] (invited talk) T. Hoshi and H. Imachi, ‘Krylov subspace theories and one-hundred-million-atom electronic structure calculations on the K computer’, International Symposium on Computics Quantum Simulation and Design (ISC-QSD-2014), 1-3, Dec., 2014, Koshiba Hall, University of Tokyo.
- [6] A. Marek, et al., ‘The ELPA Library - Scalable Parallel Eigenvalue Solutions for Electronic Structure Theory and Computational Science’, J. Physics, Condensed Matter 26, 213201, (2014); <http://elpa.rzg.mpg.de/>
- [7] T. Imamura, ‘The EigenExa Library - High Performance & Scalable Direct Eigensolver for Large-Scale Computational Science’, ISC 2014, Leipzig, Germany(2014); [http://www.aics.riken.jp/labs/lpnctr/index\\_e.html](http://www.aics.riken.jp/labs/lpnctr/index_e.html)

# Nudged elastic band method with constant bias potential

Minoru OTANI

*National Institute of Advanced Industrial Science and Technology (AIST),  
1-1-1 Umezono, Tsukuba, Ibaraki 305-8568*

An electrochemical reaction at the electrode-electrolyte interface is one of the most important issues on performance and durability of energy harvesting devices such as a fuel cell, a secondary battery, a photovoltaic cell and a photoelectrochemical cell. We have been trying to understand the electrochemical reaction by developing a method called effective screening medium (ESM) method [1].

Recently, we have successfully developed an extension for the ESM method [2], in which we can control the bias potential applied to the interface. In contrast to the convectional method, we need to discuss the following grand potential instead of the total energy:

$$\Omega = E_{\text{tot}} - \mu n_{\text{FCP}},$$

We demonstrated the constant bias method combined with the nudged elastic band method [3]. We calculated a hydrogen atom diffusion of Al(001) surface. As shown in the figure 1, the energy profile of the diffusion and the amount of charge depends on the applied potential.

This constant bias method allows us to simulate bias dependent atom diffusion in electrochemical system.

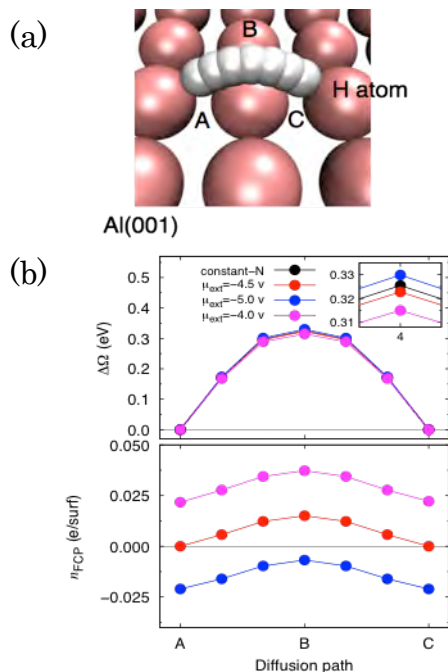


Fig.1 (a) H atom diffusion on Al(001) surface. (b) The energy profile and the variation of the excess charge of the surface along the path with constant- $\mu$  calculation.

## References

- [1] M. Otani and O. Sugino, Phys. Rev. B **73**, 115407 (2006).
- [2] N. Bonnet, T. Morishita, O. Sugino, and M. Otani, Phys. Rev. Lett. **109**, 266101 (2012).
- [3] G. Henkelman and H. Jónsson, J. Chem. Phys. **113**, 9901 (2000).

# Adsorption and Clustering of Metal Atoms on Organic Molecular Semiconductors

Takashi NAKAYAMA

*Department of Physics, Chiba University*

*1-33 Yayoi, Inage, Chiba 263-8522*

Organic molecular semiconductors are key materials for future optical and electronic devices because of their unique characteristics such as softness and light mass. During the device fabrication, a variety of impurity metal atoms are often incorporated into semiconductor layers and they are believed to deteriorate semiconducting properties. However, there have been no systematic studies on how these impurities are located in semiconductors and what electronic properties are produced by these impurities. The purpose of this project is to answer these questions, by using the first-principles calculation based on the density functional theory. In this report, we show some of the results.

We first consider what interaction is produced between impurity metal atoms when they are adsorbed on a molecule. This is because such interaction is essentially important to understand the preference of metal-atom clustering. Figure 1(a) shows the calculated interaction energy between two metal atoms (Al or Au) adsorbed on a pentacene molecule as a function of the metal-atom distance. It is seen that the energy is negative independent of the distance, which indicates that metal atoms prefer to adsorb on the same molecule and the inter-atom interaction is basically attractive. This result is quite different from the cases of Al atoms on a polyacetylene and graphene reported in the last year, where Al atoms are ionized and the inter-atom interaction becomes repulsive. Such difference of interaction character originates from the dimensionality of a molecule. Since a polyacetylene molecule and a graphene sheet are one and two-dimensional systems, respectively, they have various dispersive bands around the band gap.

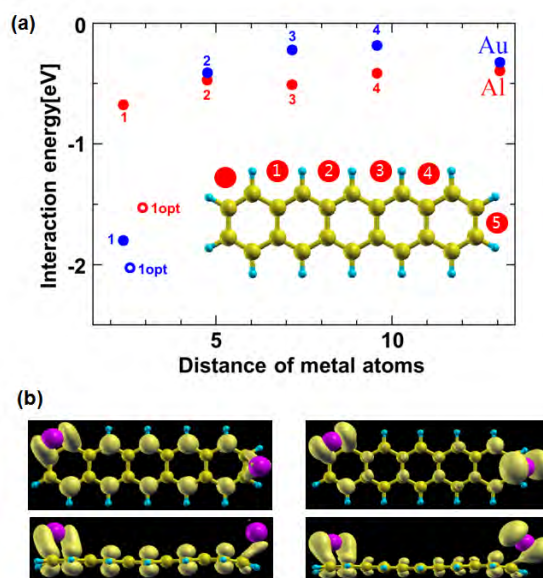


Fig.1. (a) Interaction energy between two metal atoms adsorbed on a pentacene molecule as a function of the inter-atom distance. (b) Density of electron occupied bonding state (left) and unoccupied anti-bonding state (right).

Therefore, by using various freedoms of electronic states in molecules, the adsorbed metal atoms produce the independent bonds to the molecules. On the other hand, because a pentacene molecule is zero-dimensional system, respective energy band is located separately. As a result, adsorbed metal atoms produce the bonds by the strong hybridization with a single electronic state of the molecule. In fact, when two Al atoms are adsorbed on a pentacene molecule, as shown in Fig.1(b), there appear the bonding and anti-bonding orbitals between two Al atoms with the help of the electronic state of a pentacene. In this way, the interaction between adsorbed metal atoms basically changes depending on the electronic structures of molecules, i.e., especially the dimensionality of



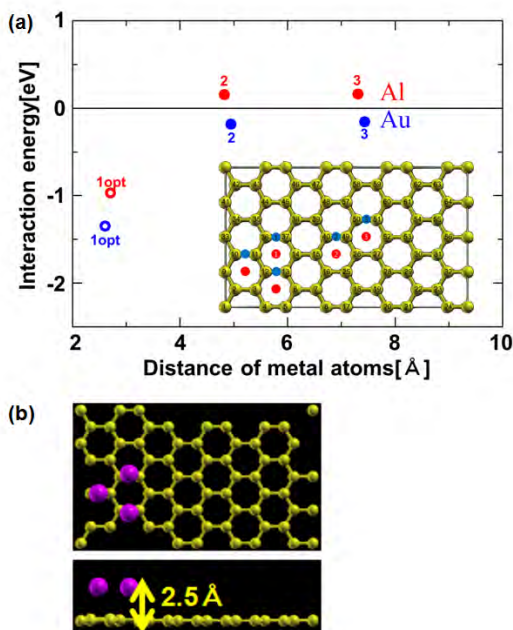


Fig.2. (a) Calculated interaction energy between a single metal atom and two metal atoms adsorbed on graphene sheet as a function of the inter-atom distance. (b) Schematic picture of the most stable atom configuration.

molecules as a medium.

As seen in Fig.1(a), the interaction energy gain becomes the largest as the metal atoms are located nearby, which indicates that metal atoms prefer to produce a cluster. To confirm this feature, for example, we set three metal atoms on graphene sheet and study the interaction between two and one atoms, the result being shown in Fig.2(a). It is clearly seen that metal atoms prefer to combine as a single cluster. However, it is interesting to note that stable atom position changes from the center of hexagonal carbon ring in case of two atoms (Fig.2(a) inset) to the top of the ring in case of three atoms (Fig.2(b)). This occurs because the metallic bonding is first produced when more than three Al atoms are located nearby.

Finally, we consider how these metal-atom impurity changes the transport property of carriers. We adopt the Born approximation for the scattering of carriers by the impurity and calculate the hole carrier mobility based on the first-principles

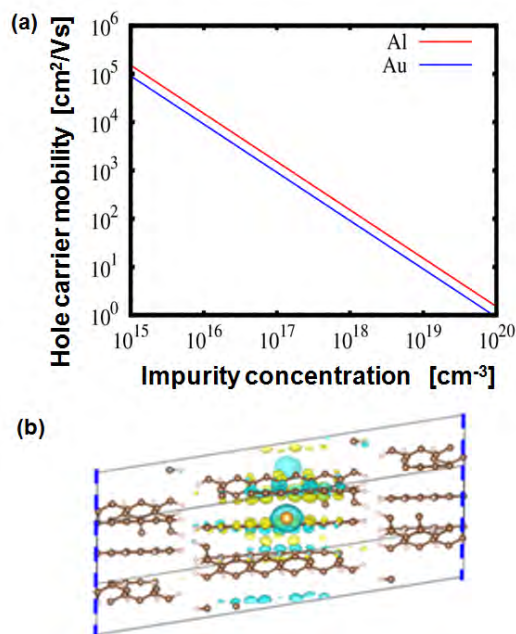


Fig.3. (a) Calculated hole mobility of a pentacene solid as a function of impurity concentration in cases of Al and Au impurities. (b) Schematic picture of Al induced scattering potential in pentacene solid.

method, where the local potential difference (Fig.3(b)) is used as a perturbation. Figure 3(a) shows the hole mobility of pentacene thin film as a function of the impurity concentration, for cases of neutral Au and Al impurities. From this result, one can theoretically estimate the mobility of organic system by the first principles calculations for the first time.

These calculations were obtained using the TAPP and xTAPP codes developed by our consortium. In order to realize the calculations for organic systems, because the system is often made of a large number of atoms (more than 200 atoms), a large inter-molecule space, and a variety of molecular geometries, the advanced computing facility having higher-speed CPU more than 100G Flops, larger-size memory around 100GB, larger-size storage more than 1.0TB, and particularly a multi-task operation is indispensable. These conditions are never prepared in personal research laboratory. Only the present super-computing system of the ISSP can realize these calculations.

# Theoretical analysis on the hydrogen-bonded conductor

Yusuke KANEMATSU and Masanori TACHIKAWA

*Quantum Chemistry Division,*

*Yokohama City University, Seto 22-2, Kanazawa-ku, Yokohama 236-0027, Japan*

We have performed the computational analysis on the conductance of the novel hydrogen-bonded material, catechol-fused ethylenedithio-tetrathiafulvalene ( $\text{H}_2\text{Cat-EDT-TTF}$ ). This material has been reported to show the significant conductivity compared with the other non H-bonding conductors [1]. Whereas the important contribution of the hydrogen nuclear quantum fluctuation in hydrogen bond has been expected, the detailed molecular mechanism of electronic conduction is still unclear. The understanding of such mechanism would be useful for the further development of the conducting material.

In order to elucidate the role of the hydrogen fluctuation in H-bond on the conductance, we calculated the dependency of the energy and the electrostatic properties on the position of the hydrogen atom in H-bond with some hydrogen bonded cluster models that were quarried out from the X-ray crystal structure. We found the significant change of the charge population upon the migration of the

hydrogen atom, which expand to the neighbor molecular unit through the  $\pi$ - $\pi$  stacking. According to the computational results, the significant intermolecular charge transfer coupled with the proton transfer was suggested [2].

We have a plan to perform the path integral molecular dynamics (PIMD) simulation to pursue how the thermal effect and nuclear quantum fluctuation of the hydrogen nuclei in H-bond will affect on the conductivity. The H/D isotope effect with PIMD simulation will be also carried out.

## References

- [1] T. Isono, H. Kamo, A. Ueda, K. Takahashi, A. Nakao, R. Kumai, H. Nakao, K. Kobayashi, Y. Murakami, H. Mori: Nat. Commun. **4** (2013) 1344.
- [2] K. Yamamoto, Y. Kanematsu, and M. Tachikawa, Theoretical analysis of hydrogen bonds in a purely organic single-component conductor, in preparation (2015).



## Design of nanoscale carbon materials: Nearly free electron states of graphene nanoribbon under an electric field

Susumu OKADA

*Graduate School of Pure and Applied Sciences,*

*University of Tsukuba, Tennodai, Tsukuba, Ibarakai 305-8571*

Recently, we have demonstrated that nearly free electron (NFE) states, which is inherent in the layered materials, are tunable by applying an external electric field normal to the atomic layers of these layered materials [1,2,3]. The NFE states of few-layered graphite shift downward under an external electric field and cross the Fermi level at a certain critical electric field that strongly depends on the thickness of the graphite thin films. Similar downward shifts have been also observed in h-BN thin films and transition metal dichalcogenide thin films, which exhibit electric field dependence similar to graphite thin films. In these cases, electrons are injected into NFE states under the critical electric field, which depends on both the thickness of the thin films and the constituent atom species of these materials. These downward shifts of the NFE state by the perpendicular electric field are ascribed to the potential gradient outside the films by the electric field that effectively leads to an attractive potential for the electronic states. In the present project, we aim to investigate the possibility of NFE state tuning by an electric field lateral to the graphene nanoribbons using

the first principles total energy calculation based on density functional theory with effective screening medium method.

We found that the NFE state appears not only in the vacuum region above the atomic layer of graphene, but also in the vacuum region outside the leftmost or rightmost atomic sites [4,5]. Furthermore, the NFE state substantially shifts downward with the application of a lateral electric field, and it eventually crosses the Fermi level, at which the nearly free electron carriers are injected outside the graphene nanoribbons. We also demonstrated that the critical electric field for injecting electrons into the NFE state strongly depends on the width of the graphene nanoribbon. The present findings indicate the possibility of an unusual one-dimensional electron system outside and along the edge atomic site of graphene in a lateral electric field. Furthermore, the accumulated electrons may decrease the contact resistance between graphene and metal electrodes.

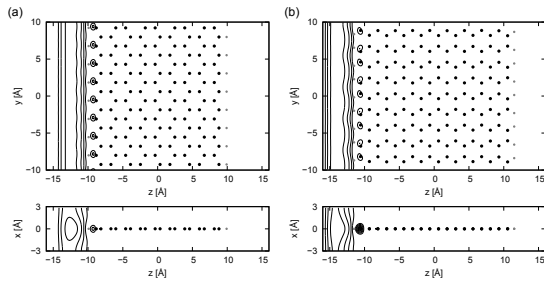


Fig. 1 NFE states appeared in the alongside of the graphene nanoribbons

## References

[1] M. Otani and S. Okada, J. Phys. Soc. Japan,

**79**, 073701 (2010).

[2] S. Konabe and S. Okada, J. Phys. Soc. Japan, **81**, 113702 (2012).

[3] M. Otani and S. Okada, Phys. Rev. B **83**, 73405 (2011).

[4] A. Yamanaka, S. Okada: Jpn. J. Appl. Phys. **53**, 06JD05 (2014).

[5] A. Yamanaka, S. Okada: Appl. Phys. Express **7**, 125103 (2014).

# Development of first-principles electronic-structure and transport calculation method based on real-space finite-difference approach

Tomoya ONO

*Center for Computational Sciences, University of Tsukuba  
Tennodai 1-1-1, Tsukuba, Ibaraki 305-8577*

Silicon carbide (SiC) is attracted much attention due to its excellent physical properties, such as a high thermal conductivity, high breakdown strength, and large band gap. However, unlike Si MOSFETs, SiC MOSFETs suffer from unacceptably low carrier mobility. One of the origins for the low carrier mobility is the generation of large amount of interface defects at SiC/SiO<sub>2</sub> interface during dry oxidation process. The understanding and precise control of the atomic structure of SiC/SiO<sub>2</sub> interface is necessary to increase the carrier mobility of SiC MOSFETs. In this project, density functional theory (DFT) calculations for the oxidation process of 4H-SiC(0001) surfaces and 4H-SiC(0001)/SiO<sub>2</sub> interfaces for examining the initial and middle stage of oxidations, respectively, are conducted.

The DFT calculations are performed using the real-space finite-difference approach[1]. The details of calculation are introduced in Ref. 2. We first calculate the oxidation energies of the surface assuming the initial stage of the oxidation. The oxidation energies are computed by sequentially inserting O atoms between Si-C bonds around a particular C atom at 4H-SiC(0001) surfaces since the Si-O-C bonds are the most preferable structure except the drastic rearrangement of the bonding network at the interface. The typical computational models for the oxidation of 4H-SiC(0001) surface are illustrated in Fig. 1. The oxidation energy for inserting an O atom be-

tween Si-C bonds at the surface,  $E_n^{ox}$ , is determined by  $E_n^{ox} = E_{(n-1)O} + \mu_O - E_{nO}$ , where  $n$  is the number of inserted O atoms,  $E_{nO}$  is the total energy of the system with  $nO$  atoms, and  $\mu_O$  is chemical potential of an O atom calculated by the total energy of O<sub>2</sub> molecule. We show in Fig. 2 the oxidation energy of the SiC surface with respect to  $n$  by white bars. For investigation of the C removal mechanism, C atom is taken from each model as a form of CO or CO<sub>2</sub> molecule. The possible sets of C and O atoms are removed from the oxidized surface and the most stable configuration are obtained. The energy gain of the emission from the system with  $nO$  atoms,  $E_n^{(CO_x)}$ , is determined by  $E_n^{CO_x} = E_{nO}^{w/C} - E_{(n-x)O}^{w/oC} + E_{CO_x}^{total}$ , where  $E_{nO}^{w/C}$ ,  $E_{(n-x)O}^{w/oC}$ , and  $E_{CO_x}^{total}$  are the total energies of the system with  $nO$  atoms, that with  $(n-x)O$  atoms without one C atom, and the total energy of the CO<sub>x</sub> molecule, respectively. The calculated energies of the CO and CO<sub>2</sub> emissions with respect to  $n$  are shown in Fig. 2(a) by gray and black bars, respectively. CO<sub>2</sub> molecules are found to be the most preferable species at the initial stage of the oxidation.

We then examine the oxidation of a 4H-SiC(0001)/SiO<sub>2</sub> interface as a middle stage of the oxidation. Figures 1(d), 1(e) and 1(f) show the typical interface atomic structures during the oxidation. Figure 3 shows the calculated oxidation energies of the SiC/SiO<sub>2</sub> interfaces defined by the same procedure of the initial

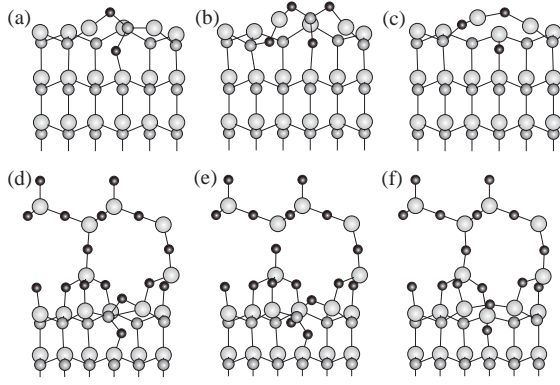


Figure 1: 4H-SiC(0001) surface models of (a)  $n=2$ , (b)  $n=4$ , (c)  $n=4$  after  $\text{CO}_2$  emission. 4H-SiC(0001)/ $\beta$ -tridymite  $\text{SiO}_2$  interface model. (d)  $n=2$ , (e)  $n=3$ , and (f)  $n=3$  after CO emission. Large dark gray, small dark gray, and light gray balls are C, O, and Si atoms, respectively. Reprinted from Ref. 2.

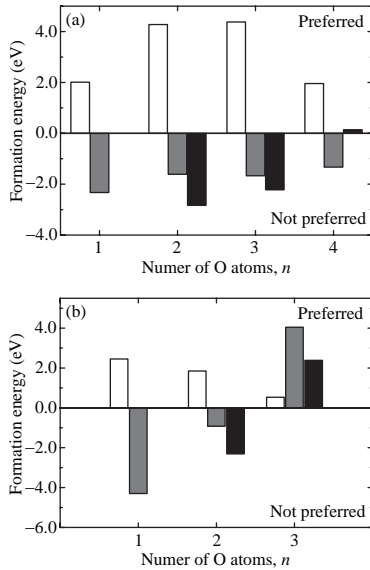


Figure 2: Oxidation energies (white bars) and formation energies of CO emission (gray bars) and  $\text{CO}_2$  emission (black bars) at (a) SiC surface and (b) SiC/ $\text{SiO}_2$  interface for different numbers of inserted O atoms,  $n$ . Reprinted from Ref. 2.

oxidation. Then the C emission from the interface is investigated. The energy gains due to the CO and  $\text{CO}_2$  emissions are shown in Fig. 2(b). CO emission is preferred at  $n=3$  because of the absence of the Si dangling bonds and Si-O-C bonds after the emission (see Fig. 1(f)). On the other hand,  $\text{CO}_2$  emission is not the most preferable. This is because the inserted O atoms are preferentially consumed to form  $\text{SiO}_2$  unit than  $\text{CO}_2$  molecule. It is intuitive that the insertion of oxygen atoms increases volume. The CO emission at  $n=3$  and the  $\text{CO}_2$  emission at  $n=4$  generate perfect  $\text{SiO}_2$  networks containing neither dangling bonds nor Si-O-C bonds. In the case of the surface, the increase of volume due to the insertion of O atoms can be released in the direction perpendicular to the surface owing to the absence of  $\text{SiO}_2$ , which results in the negative energy gain of the CO emission. On the other hand, the presence of  $\text{SiO}_2$  prevents the increase of volume in the case of the interface. Therefore, CO molecules are emitted so as to reduce the volume of SiC substrate at  $n=3$ . Our results indicate that the formation of the interfaces is affected by the interface stress due to the lattice constant mismatch between 4H-SiC(0001) and  $\text{SiO}_2$ . It is known that the electronic structure of the interface fabricated by the thermal oxidation shows different characteristics from that formed by the oxide deposition. The interface stress causes this difference in the electronic structure during the thermal oxidation.

## References

- [1] K. Hirose, T. Ono, Y. Fujimoto, and S. Tsukamoto, First Principles Calculations in Real-Space Formalism, (Imperial College, London, 2005).
- [2] T. Ono and S. Saito: Appl. Phys. Lett. **106** (2015) 081601.

## First-Principles Molecular-Dynamics Study of Structural and Electronic Properties of Covalent Liquids under Pressure

Fuyuki SHIMOJO, Akihide KOURA, Arifin RIZAL, Kenta IDEUE, Tomoya HAKAMATA

*Department of Physics, Kumamoto University, Kumamoto 860-8555*

To clarify the microscopic mechanism of changes in the structural and dynamic properties of amorphous or liquid covalent materials under pressure, we have carried out first-principles molecular-dynamics simulations [1-3]. To investigate the pressure dependence of the static structure, we obtain the structure factors, the pair distribution functions, and the distribution of the coordination numbers as a function of pressure. The bond-overlap populations and the Mulliken charges as well as the electronic density of states show the change in the covalent character in the materials due to compression.

From the simulations for amorphous silica, we found that a qualitative change occurs between 10 and 15 GPa in the pressure dependence of the static structure factor at ambient temperature. Up to 10 GPa, each Si atom is connected to four O atoms, and each O atom to two Si atoms. Reflecting the fact that the density becomes larger, the peaks in the bond-angle distributions shift to smaller angles. When the pressure reaches 15 GPa, Si atoms five-fold coordinated to O atoms appear, and also O atoms three-fold coordinated to Si atoms emerge. The bond-angle distributions spread to

lower angles to form high asymmetry profiles. Si atoms six-fold coordinated to O atoms appear at 20 GPa, while four-fold coordinated O atoms exist at higher pressures over 40 GPa. Most of Si atoms have six-fold coordination, and the bond-angle distributions have new peaks at 40 GPa. We will study the pressure and temperature dependence of the transition to the permanent high-density structure by decreasing the pressure to ambient.

The local structure of amorphous and liquid germanium telluride mixtures has been also investigated. The calculated static structure factors are in good agreement with the experimental results. We confirmed that the shorter and longer bonds exist in amorphous GeTe as in the crystalline phase. It is known that crystalline GeTe has a rhombohedral A7 structure, distorted from rocksalt, where Ge and Te atoms are threefold-coordinated to Te and Ge atoms, respectively. However, a large fluctuation of atomic configurations was found, i.e., bond exchange between shorter and longer bonds occurs in amorphous GeTe. In the liquid phase, Ge atoms diffuse faster than Te atoms, and the Ge-Ge homo-polar bonds play crucial role for the larger diffusion coefficient.

# First-principles study of quantum transport in nanostructures

NOBUHIKO KOBAYASHI

*Institute of Applied Physics, University of Tsukuba*

*1-1-1 tennodai Tsukuba Ibaraki 305-8573*

## 1 Introduction

The aim of this project is to reveal charge and heat transport in materials using atomistic theory. Quantum nature is essential in nanoscale systems, and atomistic analysis based on detailed electronic states calculations are indispensable to discuss the transport property. In order to analyze transport properties, we have developed the nonequilibrium Green's function (NEGF) method, and the time dependent wave-packet diffusion (TD-WPD) method. Using these methods, we have investigated charge and heat transport properties of atomic wires, organic molecules and so on.

## 2 Charge Transport

We have developed an efficient numerical calculation code for the ab-initio electron transport based on the DFT and NEGF formalism using Fortran and Message Passing Interface(MPI). The parallel computation technique with MPI is employed for efficient computations of density matrix via the the Green's functions, which depend on the energy and two-dimensional wave vectors. Since each matrix element of the Green's functions depends only on the single energy and two-dimensional wave vector point, it is possible to divide the calculations in the energy and wave vectors, which are carried out separately in each process. As a demonstration of the efficiency of the present code, the numerical calculations of electron transport properties of Al(100)-Si(100)-Al(100) heterostructures are shown in Fig.1. The computational efficiency is seen to

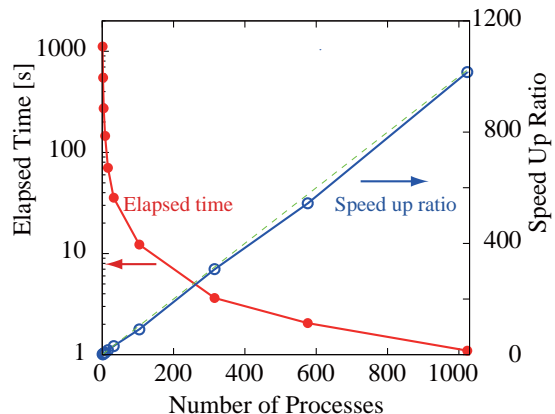


Figure 1: Speed-up ratio of total elapsed time by the parallelization of MPI in the ab-initio electron transport calculations in System B.

improve as the total number of processes becomes larger with the latency by the communication between whole process negligible. For an application, electron transport properties such as transmission spectra and total density of states are investigated for the systems with different thicknesses of Si layers. [1]

## 3 Heat Transport

Atomistic calculations of phonon transport properties have been performed using ab initio calculations and the nonequilibrium Green's function method. The dynamical matrix is calculated on the basis of the density functional theory, and the transmission function is obtained using the Green's function, which is useful for the analysis of atomic-scale structures and the inclusion of quantum effects. Furthermore, phonon lifetime due to the phonon-

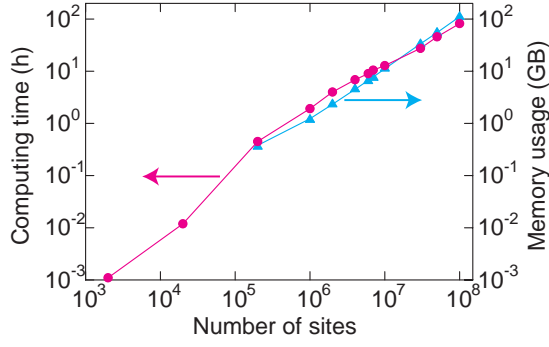


Figure 2: Computing time (red circles) and memory usage (blue triangles) per one initial wave packet as a function of site number of the lattice.

phonon scatterings by the anharmonic terms of interatomic forces is elucidated from atomistic levels. [2]

## 4 O(N) Method

We have also developed the O(N) TD-WPD method for the quantum transport calculation of huge systems of up to 100 million atoms. We calculated the conductance and the mobility of the system with micron-order lengths at room temperature based on the Kubo-Greenwood formula. Using this method we can study the transport properties from diffusive to ballistic regimes including the effect of realistic electron-phonon scattering, and determine the mean free path and relaxation time from an atomistic viewpoint. We performed DFT calculations of electronic structures and interactions between molecules of pentacene and rubrene single-crystal organic semiconductors including the effect of the van der Waals interaction, and applied the TD-WPD method to the analysis of transport properties of the organic semiconductors.

Based on the TD-WPD method, we have developed a methodology to evaluate the Hall effects of large-scale systems. We first apply the present method to the two-dimensional square lattice with the Anderson-type static disorder and confirm appropriate magnetic-field dependence of conductivities from the classical (weak magnetic field) to quantum (strong magnetic

(a) Rubrene

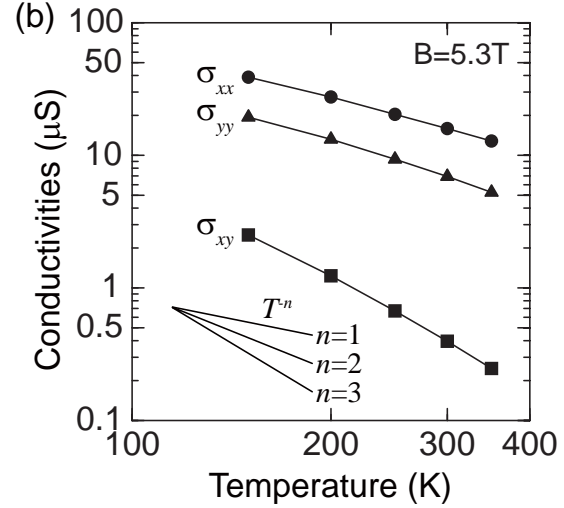
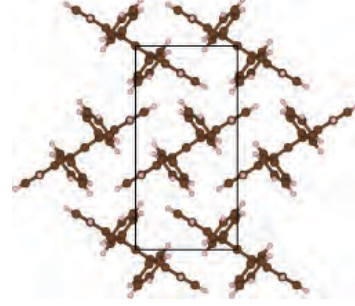


Figure 3: (a) Molecular packing structure of rubrene organic semiconductor single crystal. (b) Temperature dependence of conductivities  $\sigma_{xx}$ ,  $\sigma_{yy}$ , and  $\sigma_{xy}$ .

field) Hall effect regimes. Furthermore, we extend the method to take the microscopic molecular vibration effects into account and evaluate the influence of dynamical disorder on the Hall effects of organic semiconductors. [3]

## References

- [1] H. Takaki, N. Kobayashi, K. Hirose, J. Nanomaterials, 2014 (2014) 172169 (1-5).
- [2] N. Kobayashi, K. Yamamoto, H. Ishii, K. Hirose, e-J. Surf. Sci. Nanotechnol. 12 (2014) 154-156.
- [3] H. Ishii, H. Tamura, M. Tsukada, N. Kobayashi, K. Hirose, Phys. Rev. B 90 (2014) 155458 (1-5).

# Analysis of hydrogen and oxygen reactions on solid surface/interface

Hideaki KASAI

*Department of Applied Physics, Osaka University*

*Center for Atomic and Molecular Technologies, Osaka University*

*Center for Continuing Professional Development, Osaka University*

*2-1, Yamadaoka, Suita, Osaka 565-0871*

Understanding reactions on surfaces and interfaces is important for developing advanced materials and technologies. Various interesting physical and chemical phenomena are discovered at surfaces and interfaces, ranging from fundamental phenomena like tunneling effects to applications like catalytic reactions and migration of oxygen. This fiscal year, we have conducted various kinds of studies related to surfaces and interfaces [1], in different research areas. Highlights from our recent works include clean energy related issues, such as in photocatalysis [2] and several types of fuel cells, e.g., solid oxide fuel cell (SOFC), polymer electrolyte fuel cell (PEFC), or direct borohydride fuel cell (DBFC) [3, 4, 5, 6]. For diesel engine exhaust catalyst, we have widely investigated platinum based nanoparticles with different host/core materials using 3d-transition metals, wherein the activation of NO oxidation is determined [7, 8]. Due to the availability of the powerful and useful ISSP computational facilities, it has been possible for us to investigate various interesting and complex problems which can be difficult to deal with experimentally. In this report, we focus on the particular subject, i.e., surface of alloy materials, for instance Cu<sub>3</sub>Au. The composition ratio of these kind of materials at the surface layer usually differs from the bulk. This phenomena is called surface segregation. Surface segregation varies depending on the surface en-

vironment, e.g., oxygen pressure. To clarify these phenomena, we investigated the surface energies of different surface compositions with the aid of first principles calculations [9, 10]. In the clean surfaces, Au atoms tend to deposit on the first layer. The amount of Au atoms is highest in the (110) facet, 50 %-Au in (100) and (111) facets, and 75 %-Au in (110) facet. The (110) surface has the highest Au concentration among three facets because (110) surface is an open surface and has enough space for Au atoms which is relatively large atomic radius compared to Cu atoms. For an alloy surface in an oxygen environment, the oxygen atoms are adsorbed on the hollow site on the (100) and (111) facets, and at the long-bridge site on (110) facet. With increasing oxygen coverage, Cu atom concentration at the first layer becomes higher and reaches 100 % at 0.50 ML of oxygen for all facets considered. These results are well agreeing with experiments. We further investigated oxygen atom penetration into the subsurface. We found that the activation barrier is quite higher on the segregated surface in comparison with pure Cu surfaces for all cases. This indicates that alloying of Cu with Au prevent oxidation of the material through surface segregation. The knowledge obtained in this study will help problems related to degradation of materials encountered in industry.



## References

- [1] <http://www.dyn.ap.eng.osaka-u.ac.jp>
- [2] N.H. Linh, H. Kasai, in press
- [3] H. Kasai, W.A. Diño, K. Kojima, and Y. Kawahito, e-J. Surf. Sci. Nanotech., 12 (2014) 203.
- [4] A.A.B. Padama and H. Kasai, J. Phys. Chem., 140 (2014) 144707.
- [5] B. Chantaramolee, A.A.B. Padama, and H. Kasai, J. Membr. Sci. 474 (2014) 57.
- [6] M.C.S. Escaño, R.L. Arevalo, E. Gyenge, and H. Kasai, J. Phys.: Condens. Matter, 26 (2014) 353001.
- [7] F. Oemry, H. Nakanishi, H. Kasai, H. Maekawa, K. Osumi, and K. Sato, J. Vac. Soc. Jpn, 57 (2014) 277.
- [8] R.L. Arevalo, K. Oka, H. Nakanishi, H. Kasai, H. Maekawa, K. Osumi, and N. Shimazaki, Catal. Sci. Technol., 5 (2015) 882.
- [9] Y. Tsuda, K. Oka, T. Makino, M. Okada, W.A. Diño, M. Hashinokuchi, A. Yoshigoe, Y. Teraoka, and H. Kasai, Phys. Chem. Chem. Phys., 16 (2014) 3815.
- [10] K. Oka, Y. Tsuda, T. Makino, M. Okada, M. Hashinokuchi, A. Yoshigoe, Y. Teraoka, and H. Kasai, Phys. Chem. Chem. Phys. 16 (2014) 19702.

# First principles calculations on electronic structures and magnetism in transition-metal films and organic metal complexes

Kohji NAKAMURA

*Department of Physics Engineering, Mie University*

*Tsu, Mie 514-8507*

*Giant perpendicular magnetocrystalline anisotropy* [1] — Much interest in 3d transition-metal thin films with a perpendicular magnetic easy axis (PMCA) for the MgO-based magnetic tunnel junction has increased in nonvolatile spin-electronics. We here proposed a giant PMCA, up to 3 meV of  $E_{\text{MCA}}$ , in a 7-layer Fe-Ni film/MgO(001), where an Fe<sub>2</sub>/Ni/Fe/Ni/Fe<sub>2</sub> atomic-layer alignment with a bcc-like-layer stacking and the Fe/MgO interfaces lead to the large PMCA. The PMCA was importantly found to overcome enough over the magnetic dipole-dipole anisotropy that favors the in-plane magnetization even when the film thickness increases.

*Electric-field-induced modification in Curie temperature* [2] — The Electric-field ( $E$ -field) induced magnetism in 3d transition-metal thin films has shown promise as a potential approach offering a new pathway to control magnetism at the nano-scale with ultralow-energy power consumption. We here demonstrate an  $E$ -field-induced Curie temperature ( $T_{\text{C}}$ ) modification of a freestanding Fe monolayer and a Co monolayer on Pt(111). An applied  $E$ -field is found to modify the magnon energy; the change arises from the  $E$ -field-induced screen-

ing charge density in the spin-spiral states due to  $p$ - $d$  hybridizations. The Heisenberg exchange parameters obtained by the magnon energy suggest an  $E$ -field-induced modification of the  $T_{\text{C}}$ , which is demonstrated via Monte Carlo simulations.

*Electronic configurations and magnetism in organic-metal complexes* [3] — In organometallic molecules, the electronic configuration of  $d$  electrons is an essential aspect in magnetic properties but it is often difficult to analyze it. Here, based on the constraint density functional theory, we systematically investigated for prototypical molecules of metallocenes, MCp<sub>2</sub>. The results predict that the ground states for M=Cr, Mn, Fe, Co, and Ni are the  $^3E_{2g}$ ,  $^2E_{2g}$ ,  $^1A_{1g}$ ,  $^2E_{1g}$ , and  $^3A_{2g}$  states, respectively, and the magnetizations of the CoCp<sub>2</sub> and NiCp<sub>2</sub> energetically favor highly orienting along the perpendicular and parallel directions to the cyclopentadienyl plane.

## 参考文献

- [1] Nakamura et.al., JAP**117**, (2015) 17C31.
- [2] Oba et.al., PRL**114**, (2015) 107202.
- [3] Nawa et.al., JAP**117**, (2015) 17E131.

# Theoretical Analyses on Electronic and Ionic Transport Properties of Nanostructures

Satoshi WATANABE

*Department of Materials Engineering, the University of Tokyo  
7-3-1 Hongo, Bunkyo-ku, Tokyo, 113-8656*

## 1 Introduction

Although the electrical properties of nanostructures have been extensively investigated in the last few decades, our understanding on them is still insufficient to design and control novel nanoscale electronic devices. In particular, further studies on complicated situations and phenomena, such as time-varying electronic transport and the interplay among electronic and ionic transport at nanoscale, are strongly desired.

Keeping the above in minds, we have been investigating these topics using theoretical analyses based on atomic/electronic level simulations. In the followings, some of our results in the fiscal year 2014 are described.

## 2 AC transport in nanostructures

Clarifying responses of nanostructures to AC signals is crucial for the realization of next-generation ultrafast devices. So we have been studying AC transport properties of metallic carbon nanotubes (m-CNTs). Recently, we have examined the AC transport properties of m-CNTs with randomly distributed impurities using the nonequilibrium Green's function method [1]. In doing so, we focus on the dependence of the transport behaviors on the impurity potential's range and amplitude and the impurity concentration.

We have found that the short-range impurity scattering causes a decrease in the emittance as well as the DC conductance. This behavior can

be attributed to electron scattering [2]. On the other hand, we found that the long-range impurity scattering causes the emittance increase when the potential amplitude and/or impurity concentration increase. Considering the fact that the variation of this scattering does not alter the DC conductance, the above behavior is interesting. We have shown that the behavior can be understood from the change in the dwell time of electrons and their multiple scattering: The multiple scattering increases the dwell time, which in turn increases the kinetic inductance and thus also the emittance. Our results show that the electron scattering is important to understand the inductive response as well as the capacitive one.

## 3 Interface structures in tantalum-oxide-based resistance switches

Resistance switching devices based on amorphous tantalum oxide (a-TaO<sub>x</sub>) have attracted attention as promising candidates of future memory devices. Aiming at the microscopic understanding on their switching behaviors, we had examined atomic structures of conductive filaments (CFs) in the oxide using the density functional theory (DFT) [3, 4]. Recently, we have examined the structures of the interfaces between the oxide and metal electrodes to get an insight into the initial process of the CF formation [5].

Models of a-TaO<sub>x</sub> were obtained using melt-quenching process via first-principles molec-

ular dynamics. Then structure optimization and subsequent melt-quenching were performed for the heterostructures consisting of an a-TaO<sub>x</sub> layer sandwiched between fixed Cu and Pt layers. Finally, the obtained Cu/a-TaO<sub>x</sub>/Pt heterostructures were further equilibrated at room temperature and then optimized with the relaxation of all atoms. To examine the effect of interface O concentration, we adopted three models, Cu<sub>108</sub>Ta<sub>32</sub>O<sub>80</sub>Pt<sub>84</sub>, Cu<sub>108</sub>Ta<sub>32</sub>O<sub>88</sub>Pt<sub>84</sub> and Cu<sub>108</sub>Ta<sub>32</sub>O<sub>96</sub>Pt<sub>84</sub>.

We have found that the O-rich Cu/TaO<sub>x</sub> interface is stable within a wide range of O chemical potentials. At this interface, a considerable number of interface Cu atoms tend to migrate to the a-TaO<sub>x</sub> layer, which causes the formation of the Cu<sub>2</sub>O layer. The interface Cu atoms become more ionized with an increase in the interface O concentration and/or temperature. These ionized Cu<sup>+</sup> ions could work as a main source for the formation of CFs in the Cu/a-TaO<sub>x</sub>/Pt resistance switch. On the other hand, the Pt electrode is not ionized, irrespective of the interface O concentration and temperature.

#### 4 Capacitance of charged bilayer graphene

Bilayer graphene (BLG) is promising as a channel material in the field effect transistor (FET) owing to the controllability of band gap by electric field. Recently, quantum capacitance of BLG was measured to get a clue for improving the performance of BLG-based FET [6], because the quantum capacitance is closely related to the density of states. However, it is difficult in experiments to distinguish the capacitance change due to the band structure change by the doping and/or applied field from the quantum capacitance. So we have calculated the dielectric properties, especially capacitance, of BLG using the DFT.

First, the electronic states of BLG have been calculated with applying an electric field but without doped charges. Local relative permit-

tivity of BLG has been estimated from the calculated changes in electrostatic potential and charge distribution due to the applied field. The local relative permittivity is larger than two even in the middle of the two graphene layers, which suggests that the simple picture behind the capacitance consideration, two metallic electrodes, is not relevant in this case, and the BLG should be regarded as a single dielectric material.

Next, the electronic structures of BLG with doped charges under an applied electric field have been calculated by the effective screening medium method within the DFT. The results suggest that the energy required to modify the band structure of BLG is in the order of 10 meV, and thus the effect of the band structure change on the quantum capacitance measurement of BLG is negligible. In addition, we find that the band gap is weakly dependent on the amount of doping, besides being dependent on the applied electric field.

#### References

- [1] D. Hirai, T. Yamamoto and S. Watanabe: Appl. Phys. Lett. **105** (2014) 173106.
- [2] D. Hirai, T. Yamamoto and S. Watanabe: J. Appl. Phys. **115** (2014) 174312.
- [3] B. Xiao, T. Gu, T. Tada and S. Watanabe: J. Appl. Phys. **115** (2014) 034503.
- [4] B. Xiao and S. Watanabe: Nanoscale **6** (2014) 10169.
- [5] B. Xiao and S. Watanabe: ACS Appl. Mater. Interfaces **7** (2015) 519.
- [6] K. Nagashio, K. Kanayama, T. Nishimura and A. Toriumi: Electron Devices Meeting (IEDM), 2013 IEEE International, 19.5.1 (2013).

# Ab initio study of thermoelectric properties of molecules between magnetic electrodes

Tatsuhiko OHTO

*Graduate School of Engineering Science,*

*Osaka University, 1-3 Machikaneyama, Toyonaka, Osaka 560-8531*

The molecular junction is a promising system to achieve maximum thermoelectric efficiency due to the quantum confinement of the molecular orbital (MO) into the nanoscale gap [1]. We propose to use molecular junctions with ferromagnetic electrodes as it can induce the spin polarization of MOs and then tune the Seebeck coefficient. We investigate the transport properties of Ni-benzenedithiol (BDT) - Ni molecular junction with the nonequilibrium Green's function method based on density functional theory. Result revealed that one of the spin split highest occupied MO of BDT appears just above the Fermi level, indicating an increase in the magnitude of  $S$  (compared to when Au electrode was used) and a change in the sign as well. We obtained negative and large  $S$  for Ni-BDT-Ni junctions. We further investigated the effect of spin configuration of electrodes and surface roughness on  $S$  [2].

We also performed a computational research to confirm the possibility of a molecular resistive switch obtained via sliding multiple anchoring points. Our calculation revealed that the change in the effective wire length of the oligo-thiophene between Au electrodes explains the three conductance values obtained in the experiment.

The structural optimization performed with the SIESTA program [3] on System B was very helpful to advance our research works.

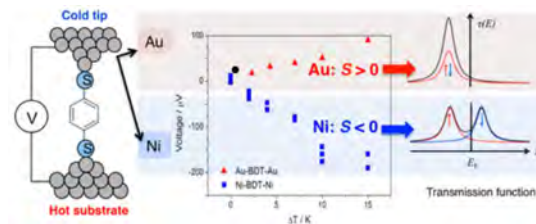


Figure 1: Sign change of the Seebeck coefficient due to the spin-splitting at the Ni-BDT-Ni junction.

## References

- [1] H. Park, Nat. Mater. **6** (2007) 330.
- [2] S. K. Lee, T. Ohto et al., Nano Lett. **14** (2014) 5276.
- [3] M. Kiguchi, T. Ohto et al., JACS. **136** (2014) 7327.
- [4] J. M. Soler et al., J. Phys.: Condens. Matter **14** (2002) 2745.

# First-principles molecular dynamics simulation of the water/surfactant interfaces

Tatsuhiko OHTO

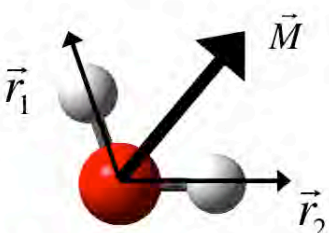
*Graduate School of Engineering Science,*

*Osaka University, 1-3 Machikaneyama, Toyonaka, Osaka 560-8531*

The sum-frequency generation (SFG) spectroscopy is a powerful tool to study the structure and dynamics of interfacial molecule, because molecules in a few nm regions at surfaces or interfaces give SFG signals. Since the SFG signals are often complex reflecting the inhomogeneous environment of interfaces, all-atom simulations are useful for the interpretation. The classical molecular dynamics (MD) simulation based on the force field model is usually used to simulate the SFG signal. However, delocalized electronics states of the solid surfaces are difficult to be described by force-field models.

Ab initio MD (AIMD) is a powerful tool to describe heterogeneous systems such as the water/solid interface. Although AIMD is computationally too expensive to calculate the SFG signal. We developed a surface-specific velocity-velocity autocorrelation function, relating to the SFG spectroscopy. By using this function, converged SFG signals can be obtained from ~100 ps trajectory, which is an order of magnitude shorter than the conventional dipole-polarizability time

correlation function. First of all, the SFG spectrum of the water/air interface calculated from AIMD trajectory should be checked. We accumulated 160 ps trajectories by using the CP2K code [1] and revealed that the SFG signal reproduces the most of the features found in experiments [2].



$$R_{abc}^{\text{SFG}}(\omega) \propto \int_0^\infty dt e^{-i\omega t} \left\langle \dot{M}_c(0) A_{ab}(t) \right\rangle$$

Response function      Dipole moment • Polarizability correlation

$$= \mu^i(\omega) \alpha^j(\omega) \int_0^\infty dt e^{-i\omega t} \sum_i \left\langle \dot{r}_{ci}(0) r_i^{\text{proj}}(t) \right\rangle$$

Transition Components      Velocity-velocity correlation

Fig. 1: SFG response function of water OH stretch mode represented by velocity-velocity autocorrelation function.

## References

- [1] The CP2K developers group, <http://cp2k.berlios.de/>
- [2] T. Ohto *et al.* to be submitted.

# Ab-initio study of organic semiconductor thin film growth

Kazume NISHIDATE and Masayuki HASEGAWA

*Faculty of Engineering, Iwate University*

*Ueda 4-3-5, Morioka, Iwate 020-8551*

Organic semiconductors have attracted considerable interest because of their favorable electrical properties for development of organic electronic devices. Among them, Pentacene (Pen) is an important organic-semiconductor material because of its high carrier mobility characteristic when it applies to the thin-film transistors. It is well known that the matching of the work function of the electrode layer with the energy level of organic semiconductors is crucial to inject carriers effectively. However, conventional electrode such as Al has poor electrical conduct with Pen due to their mismatching. Recently, graphene has attracted much attention in the application for transistors, light-emitting diodes, and solar cells.[1, 2] In addition, it is particularly suited for implementing transplant electrode in organic devices. Acceleration of the carrier mobility has also been tried by forming Pen layers on a graphene electrode. Because both the frameworks of Pen and graphene consist of carbon atoms, the best energy matching between the electrode and the organic molecule can be expected. Surprisingly, electronic property at the interface between the graphene electrode and the organic semiconductors is not well known. In this work, we performed large scale van der Waals density functional electronic structure calculations (vdW-DFT) to investigate the detailed electronic structure at the interface. The results are compared to those of the Grimme's D2 calculation (DFT-D2) where the vdW interaction force is empirically implemented in

the DFT. The standard DFT calculations with the local density approximation (LDA) and with the generalized gradient approximation (GGA/PW91) are also performed for verification.

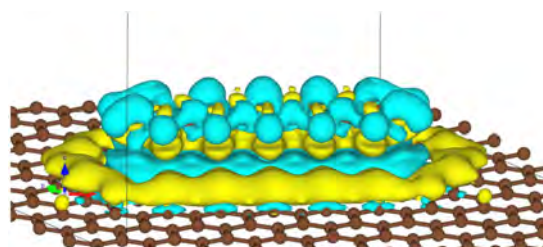


Figure 1: Pentacene on graphene. Bright (yellow) part is the increased charge density region as a result of the adhesion.

## References

- [1] Sang Wan Cho et al.: *Synthetic Materials* **161**, 2488 (2011).
- [2] Gunho Jo et al.: *Nanotechnology* **23**, 112001 (2012).

# Computer Simulations of the Barkhausen Effects

Shuji OBATA

*School of Science & Engineering, Tokyo Denki University  
Ishizaka, Hatoyama, Hiki, Saitama 350-0394, Japan*

Relating with the last year investigations of the nano-materials magnetizations, the Barkhausen effects caused by the magnetic dipole moment interactions in Fe metal are cleared in this work. Using the ISSP system A (shii), the Fortran programs of the nano-Fe magnetizations are executed by about 500 line programing compiled with sxf90. The used times are about 18 hours par job using p4-system for drawing the domain structures, the magnetization curves and the Barkhausen effects.

The magnetic systems of spins are generally calculated using the Hamiltonian

$$\hat{H} = \sum_{i \leq j} J_{ij} \hat{\mu}_i \cdot \hat{\mu}_j + \sum_{i \leq j} W_{ij} + \sum_j \mu_j \cdot \mathbf{H}, \quad (1)$$

where the first term is the electronic binding energy with spin-spin interactions, the second term is the dipole moment interactions of spins and the third term is magnetization energy in the external field  $\mathbf{H}$ . The electronic binding energies of 3d electrons in Fe are induced from the tight binding interactions of the directed magnetic moments bounded by the Hunts rule. These 3d and 4s electrons construct the eigenstates in the external field environments. In this situation, the quantum states take the same reversible states at the same external field  $\mathbf{H}$ . These states trace only the one line magnetization curve without irreversible hysteresis curves. Thus, many-many investigations using the Hamiltonian without the second term cannot explain the Fe hysteresis curves. The realistic magnetization curves are produced by the Hamiltonian (1) including the three terms.

In this paper, only the Hamiltonian composed of the second and the third terms are calculated for only clearing the hysteresis characteristics. Setting distance vector  $\mathbf{d}_{ij} = \mathbf{e}_{ij} d_{ij}$  between dipole moments at  $i$  and  $j$ , the interaction energies are equated as

$$W_{ij} = \frac{1}{4\pi\mu_0 d_{ij}^3} \{ (\boldsymbol{\mu}_i \cdot \boldsymbol{\mu}_j) - 3(\boldsymbol{\mu}_i \cdot \mathbf{e}_{ij})(\boldsymbol{\mu}_j \cdot \mathbf{e}_{ij}) \}. \quad (2)$$

In simulations of Fig.2 and Fig. 3, the magnetic moments are set to have freedoms of

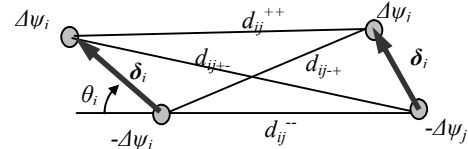


Fig. 1. Two magnetic moment interactions. The dipole moments are equated as  $\boldsymbol{\mu}_i = n_b \boldsymbol{\mu}_B^0 = \delta_i \Delta\psi$

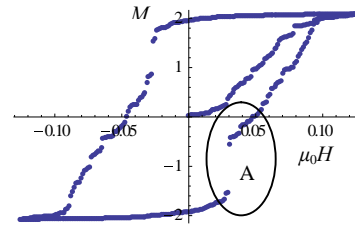


Fig. 2 Magnetization curve ( $B_m = n_b$ ) in a  $N_x N_y N_z = 20 \times 4 \times 40$  lattice point system. The aria A is precisely calculated and drawn in Fig. 3 to show the B effects.

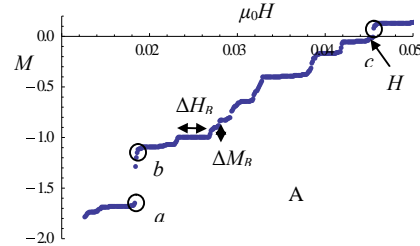


Fig. 3 The terraces  $\Delta H_B$  and the jumps  $\Delta M_B$  of the B effects in the precise magnetization curve at the aria A in Fig.2. The coercivity becomes  $\mu_0 H_c = 0.0456$  T, which coincide with the experimental data.

26 directions.<sup>[1][2]</sup> The precise structures at the jump points of a circle in Fig. 2 are drawn in Fig. 3. Crystal Fe takes the BCC structure with the lattice constant  $a = 2.86 \times 10^{-10}$  [m] up to 911 °C and have the dipole moments of  $2n_b \mu_0 \mu_B$  per a lattice. The constants are  $n_b = 2.22$ , permeability  $\mu_0$  and the Bohr magneton  $\mu_B$  respectively. Through these results, the processes of the Barkhausen effects are clarified as the transitions of the dipole-moment arrangements in the magnetic domains.

[1] S. Obata : IEEE Trans. FM. **133** (2013) 489-499.

[2] S. Obata : Materials Transactions. **55** (2014) 1591-8.



# Coadsorbed-Induced Energy Shifts of Ferrocene Derivatives Adsorbed on Au(111) Electrode

Ken-ichi FUKUI

*Department of Materials Engineering Science, Graduate School of Engineering Science,  
Osaka University, Machikaneyama, Toyonaka, Osaka 560-8531*

A microscopic understanding of electrochemical properties is of fundamental importance for future electrochemistry. The assessment of the energy cost to remove an electron from molecules adsorbed on metal electrodes is essential for many applications. Using ferrocene terminated monolayers (Fc SAMs) on Au(111) electrodes, we have recently revealed a linear relation with a slope of  $\sim 0.7$  between the highest occupied molecular orbital (HOMO) and the electrochemical formal potential [1], but its microscopic origin is not clear at this stage. In this study, we calculated electronic properties of the Fc SAMs and compared to experimental formal potentials.

Structural optimization and electronic property calculations were performed using the program "STATE". Fig. 1 shows our Fc SAM systems. A Fc-terminated molecule was coadsorbed with three 1-butanethiol (Fc\_Me) or 4-mercapto-1-butanol (Fc\_OH). Their work function and energy of Fc backbone were calculated by usual methods.

The obtained values are summarized in Table 1. Work functions of the systems were consistent with the direction of dipole moment

of the coadsorbed molecules. HOMO energies were found to be shifted deeper with the decrease of the work functions. This indicated that the Fc backbone of the Fc\_OH system is more difficult to transfer an electron to the electrode Fermi level compared to that of the Fc\_Me system, in contrast to the expectation from the experimental formal potentials [2]. These results indicate the importance of solvation energy, which is our next target.

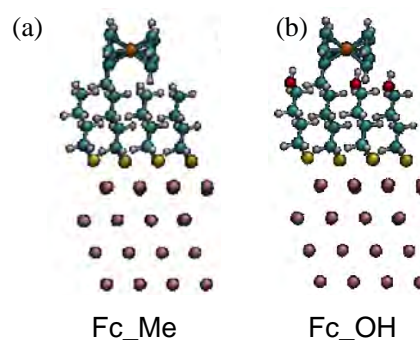


**Fig. 1:** Optimized structures of Fc SAMs.

**Table 1:** Electronic properties of two systems.

	Fc_Me	Fc_OH
Work function (eV)	3.81	3.41
HOMO energy (eV vs $E_F$ )	-0.53	-0.80
Formal potential (V) <sup>Expl.</sup>	+0.40	+0.27

## References

- [1] Y. Yokota et al., J. Phys. Chem. C, **118**, 10936 (2014).
- [2] S. E. Creager, G. K. Rowe, J. Electroanal. Chem., **420**, 291 (1997).

# Study on physical and structural properties of defects, surfaces, and interfaces for 2D semiconductors

Hiroyuki KAGESHIMA

*Interdisciplinary Graduate School of Science and Engineering, Shimane University  
Nishi-Kawatsucho, Matsue, Shimane 690-8504*

Two dimensional (2D) semiconductors such as graphene, h-BN, and transition metal dichalcogenide show very unique physical properties. In our project, we focus on the physical and structural properties of defects, surfaces and interfaces of them.

h-BN is expected as a high-quality supporting substrate for graphene. h-BN substrate rarely produces electron-hole puddles in graphene. h-BN is also expected as a high-quality gate insulator because of its wide band gap and atomic thickness. In both cases, h-BN must be uniform and free from any defects. However, the experiments based on TEM observe large holes in h-BN [1]. These holes are thought to be generated by the charging effect due to the electron beam injected by the TEM. Okada approached this phenomena theoretically based on the first-principles calculation [2]. We have extended his theoretical study and investigated larger holes such as  $V_{B6N3}$  and  $V_{B3N6}$  (Fig. 1). We use the first-principles calculation program PHASE [3] on System B for the purpose.

The obtained formation energies show that the larger holes are stabilized in the higher electronic chemical potential condition (Fig. 1). This suggests that accumulation of negative charge can induce larger holes in h-BN sheets. Further studies in detail of the electronic and structural properties of the h-BN holes are now in progress.

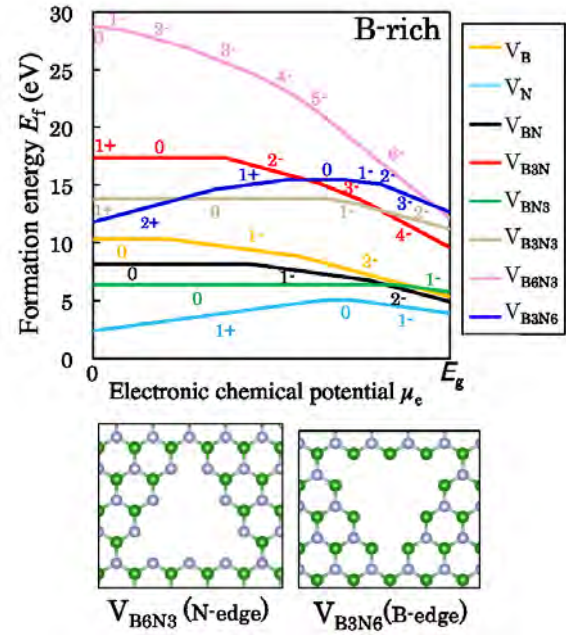


Figure 1: Formation energies of various holes as the function of the electronic chemical potential in the B-rich condition. Atomic structures of the holes  $V_{B6N3}$  and  $V_{B3N6}$  are also shown in the bottom.

## References

- [1] C. Jin et al, Phys. Rev. Lett. **102**, 195505 (2009).
- [2] S. Okada, Phys. Rev. B **80**, 161404(R) (2009).
- [3] <https://azuma.nims.go.jp/cms1>

# Development of *ab initio* GW plus cumulant code

Kazuma NAKAMURA

*Quantum Physics Section, Kyushu Institute of Technology  
1-1 Sensui-cho, Tobata, Kitakyushu, Fukuoka, 804-8550*

Using *ab initio* GW and its cumulant expansion method, we study quantitative accuracy of plasmaron states of various materials. The plasmaron state is a coupled state of free electron and plasmon, and can be observed in a metallic system, especially having isolated low-energy bands near the Fermi level. In the isolated-band materials, the plasma excitation can occur in this band, and then its energy scale is usually smaller than the bandwidth. In this case, the plasmon excitation can renormalize the bare band structure via the self-energy effect and generate a coupled state of free electron and plasmon.

In this report, we present a study for the low-energy plasmaron state of transition-metal oxide  $\text{SrVO}_3$  which is a typical isolated low-energy band system. This is widely known as a correlated material, but in this study, we investigate another point of view of the plasmon excitation. In fact, for this material, the low-energy plasmon excitation is experimentally observed in reflectance and electron energy loss spectroscopy (1.4 eV). The bandwidth estimated by density-functional calculations is 2.7 eV, and thus, the plasmon-excitation energy are smaller than the bandwidth. Therefore, it will be interesting to calculate the self-energy effect due to the plasmon excitation with the GW calculations. As is well appreciated, the GW calculation gives a good estimate for the quasi-particle energies, while it is less accurate for the satellite feature concerned with the plasmaron state of electronic structure.

To this end, we have extend our developed GW code to its cumulant-expansion one, which

is based on the plane wave basis set with the pseudopotential approximation. With these codes, we calculate the spectral function to see the formation of the plasmaron state, and compare the GW and the cumulant-expansion results. The code is massively parallelized, capable to treat huge systems such as organic compounds. All calculations were done at Supercomputer center at Institute for Solid State Physics, University of Tokyo.

Figure 1(a) is our calculated reflectance (curve) as a function of frequency of  $\text{SrVO}_3$ . The drop from 1 to 0 specifies the plasma frequency and the value is 1.8 eV. We found that our spectra well reproduce the experimental one such as a 1.4-eV drop (dots).

Figure 2 is the GW spectral function of  $\text{SrVO}_3$ , in which we display the region including oxygen-*p* band, as well as vanadium *t<sub>2g</sub>* band. The density-functional bands are drawn by solid curve. The bright regions around 11 eV at the *R* point and 5 eV at the  $\Gamma$  point indicate the formation of the plasmaron states. Figure 3 is the GW plus cumulant-expansion result. We see that the weights due to the plasmaron states become somewhat large and lower toward the Fermi level.

Finally, we compare the photoemission results among GW plus cumulant (thick curve), GW (dashed curve), density-functional theory (thin curve), and experiments (dots) of  $\text{SrVO}_3$ . Within the displayed energy range, the GW and GW plus cumulant results are similar and are in a reasonable agreement with the experimental results.

In summary, we have studied low-energy

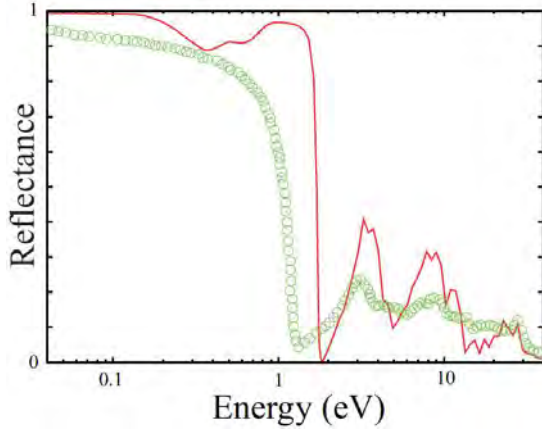


Figure 1: Comparison of reflectance between theory (curve) and experiments (dots) of  $\text{SrVO}_3$ .

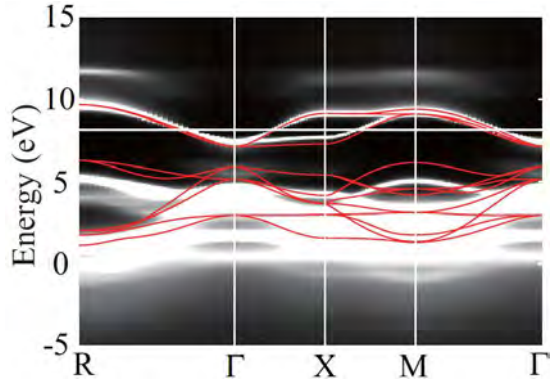


Figure 2: Calculated GW spectral function  $A(\mathbf{k}, \omega)$ . Red curves are the density-functional results and the Fermi level is 8.15 eV.

plasmon excitations of transition-metal oxide  $\text{SrVO}_3$ . To investigate the quantum accuracy of the plasmaron state, we have developed the GW plus cumulant-expansion method, and compared its electronic structure with the usual GW result and experiments.

## References

- [1] K. Nakamura, S. Sakai, R. Arita, and K. Kuroki, Phys. Rev. B **88**, 125128 (2013).

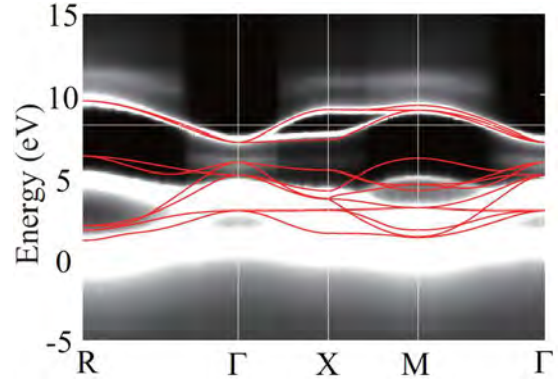


Figure 3: Calculated GW plus cumulant-expansion spectral function  $A(\mathbf{k}, \omega)$ .

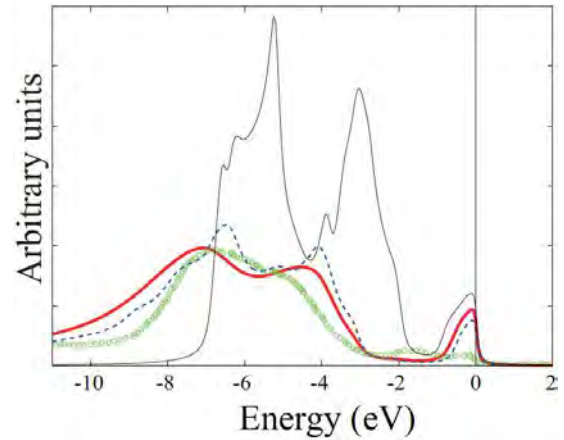


Figure 4: Comparison of photoemission spectra among GW plus cumulant (thick curve), GW (dashed curve), density-functional theory (thin curve), and experiments (dots) of  $\text{SrVO}_3$ .

# Ab-initio study of thermoelectric effect in ferroelectric BaTiO<sub>3</sub>

Kunihiko Yamauchi

*ISIR-SANKEN, Osaka University, Ibaraki, Osaka 567-0047*

By means of density-functional calculation and Wannier function method, Seebeck coefficients are calculated for *n*-type BaTiO<sub>3</sub> at the first time. It turns out that the polar structural distortion of Ti and O ions leads to the peculiar band dispersion of the lowest conduction Ti-*t*<sub>2g</sub> band, which enhances the Seebeck coefficients along the polar axis.

Since the finding of large Seebeck coefficients for Na<sub>x</sub>CoO<sub>2</sub>, transition-metal oxides have emerged as one category of thermoelectrics. Electron-doped SrTiO<sub>3</sub> and KTaO<sub>3</sub> have been found to have the large Seebeck coefficients *S*, which are comparable to that of Bi<sub>2</sub>Te<sub>3</sub>, while also having the metallic conductivity  $\sigma$ . Several density functional theory (DFT) calculations have been performed on such thermoelectric transition-metal oxides, which have mostly concluded that narrow *t*<sub>2g</sub> bands with the anisotropic mass  $m^*$  are responsible for the large Seebeck coefficients.[1]

In this study, we make use of the ferroelectric distortion in BaTiO<sub>3</sub> in order to enhance the anisotropy of the  $m^*$  of Ti-*t*<sub>2g</sub> electrons, which leads to the increase in the Seebeck coefficients. We performed DFT calculations using the VASP code with GGA-PBE potential. To calculate the band velocity, the Wannier function approach implemented in the BoltzWann code was employed. System B cluster system was mainly used for the computation. Our results show that the calculated Seebeck coefficients in BaTiO<sub>3</sub> is anisotropic as having low  $S_{xx}$  and high  $S_{zz}$ , the latter is superior than the *S* in SrTiO<sub>3</sub>. The increase in  $S_{zz}$  origi-

nates from a single-band contribution from the Ti-*d*<sub>xy</sub> band, which shows an isoenergy surface elongated along the *k*<sub>z</sub> direction. The polar structural distortion lifts the three-fold degeneracy in Ti-*t*<sub>2g</sub> bands, which in turn causes the strong anisotropy in the electron velocity. In this peculiar situation, the Seebeck coefficients are highly increased. Using the unique property, it might be possible to control the thermoelectric performance by using the piezoelectric effect. When uniaxial strain is applied on BaTiO<sub>3</sub> crystal, both the polar axis and the thermoelectrically favored direction could be manipulated as wished. This effect requires to be confirmed by future theoretical and experimental studies. More detail results and discussions can be found in a reference.[2]

## References

- [1] K. Shirai and K. Yamanaka, J. Appl. Phys. **113**, 053705 (2013).
- [2] H. Saijo, K. Yamauchi, K. Shirai, and T. Oguchi, J. Phys. Soc. Jpn. **84**, 054701 (2015).

# First-Principles Calculation of Transition-Metal Compounds

Tamio OGUCHI, Keisuke ISOYAMA, Hiromichi HIRANO

*Institute of Scientific and Industrial Research, Osaka University, Ibaraki 567-0047*

A first-principles density-functional-theory method has been applied to various condensed matter and surface systems for the last few decades. In this project, we study the electronic properties of several transition-metal compounds, especially oxide systems, and explore their chemical trends and effects associated with crystal structure and symmetry. In addition, continuing developments of numerical methods related to the first-principles calculations are also pursued. In FY2014, we focused on first-principles study of the electronic structure of *A*-site ordered perovskite-type transition-metal oxides.

Among the known *A*-site ordered perovskite oxides, we have investigated the electronic structure and magnetism of  $\text{CaCu}_3\text{Fe}_4\text{O}_{12}$  (CCFO) [1] and  $\text{CaCu}_3\text{B}_4\text{O}_{12}$  ( $\text{B}=\text{Ti, Ge, Zr, and Sn}$ ) [2] in the previous projects. Related to these oxides, the electronic structure of  $\text{LaCu}_3\text{Fe}_4\text{O}_{12}$  (LCFO) is investigated by means of first-principles calculations [3]. LCFO reveals metal-to-insulator and paramagnetic-to-antiferromagnetic transitions with a volume expansion by 1.3% at 393K as temperature decreases. This is believed to be associated with a charge transfer as  $3\text{Cu}^{2+} + 4\text{Fe}^{3.75+} \rightarrow 3\text{Cu}^{3+} + 4\text{Fe}^{3+}$ , according to a bond distance analysis. This is remarkably contrastive to the charge disproportionation as  $4\text{Fe}^{4+} \rightarrow 2\text{Fe}^{3+} + 2\text{Fe}^{5+}$  seen in CCFO. In LCFO the electronic structure changes from insulating to metallic as the Cu valence shifts from nonmagnetic  $\text{Cu}^{3+}$  to spin-polarized  $\text{Cu}^{2+}$  at the transition. This type of transition may occur by pressure as shown in Fig. 1, being consistent with experiments. The stability of the high-pressure phase is actually realized by the valence change of  $\text{Cu}^{3+}$  to  $\text{Cu}^{2+}$  and accordingly, a ferrimagnetic (FiM) phase is stabilized because of dominant anti-

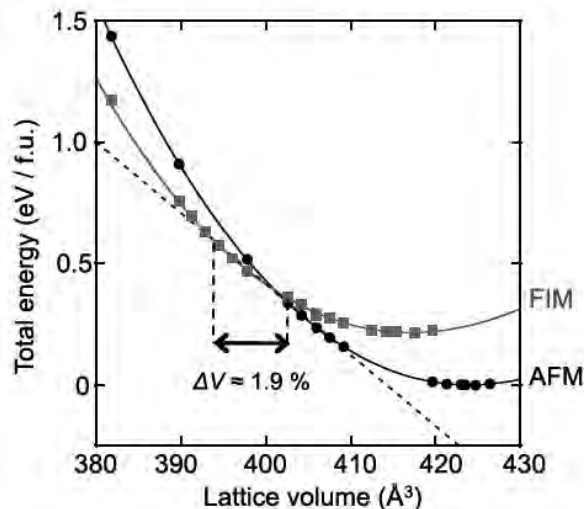


Figure 1: Calculated total energies of  $\text{LaCu}_3\text{Fe}_4\text{O}_{12}$  as a function of unitcell volume in antiferromagnetic (AFM) and ferrimagnetic (FiM) phases shown by dots and solid squares, respectively.

parallel magnetic couplings between Cu and Fe ions. Therefore, it is natural to consider the observed high-temperature phase is a paramagnetic phase associated with the FiM phase. We found that the volume change at the transitions is a key for understanding the changes in the electronic structure and magnetism.

## References

- [1] T. Ueda, M. Koder, K. Yamauchi, and T. Oguchi: J. Phys. Soc. Jpn. **82** (2013) 094718.
- [2] M. Toyoda, K. Yamauchi, and T. Oguchi: Phys. Rev. B **87** (2013) 224430.
- [3] K. Isoyama, M. Toyoda, K. Yamauchi, and T. Oguchi: J. Phys. Soc. Jpn. **84** (2015)

034709.

# Density functional theory study of stability and dynamics of metal nanoclusters on a silicon surface

Ikutaro HAMADA

*National Institute for Materials Science*

*Tsukuba 305-0044, Japan*

Small atomic clusters have attracted much attention, owing to their intriguing physical properties, and to the great potential as components of future microelectronics devices, high density storage devices, and catalysts. Recent progress in scanning probe microscopy enable one to manipulate atoms and molecules one by one, and it is becoming possible to fabricate well defined small atomic clusters on surfaces. Although the precise control of the number of constituent atoms in the cluster is possible, it is difficult to determine the atomic structures only from the experiment, and the atomistic simulation plays an important role to understand the atomic as well as electronic structures of clusters. In this work, I perform density functional theory calculations of  $\text{Pb}_3$  on  $\text{Si}(111)(7\times 7)$ , to clarify the atomic structures of the  $\text{Pb}_n$  clusters, and the mechanism of the atomic switching realized by the scanning tunneling microscopy (STM).

All the calculations were performed using the STATE[1] code. We used a plane-wave basis set to expand the wave functions and ultrasoft pseudo potentials to describe electron-ion interactions. The surface was modeled by a slab composed of eight atomic layers, and a thick enough vacuum was inserted between the neighboring slabs. The effective screening medium method[2] was used to eliminate spurious electrostatic interactions with the image slabs.

I have examined several configurations of  $\text{Pb}_3$  on  $\text{Si}(111)(7\times 7)$  and found that none

of them can reproduce the polarity dependent STM topography. This motivated me to consider the structures including Pb substitutions, because experimentally a single Pb atom replaces a substrate Si adatom at a few 100 °C and the contrast pattern strongly depends on the bias. By examining several cluster models with Pb substitutions, I have arrived at a structure, which nicely reproduces the observed filled and empty state STM images. Thus, the  $\text{Pb}_3$  is no longer a single-element cluster, but a binary cluster composed of Pb and Si atoms. Furthermore, it is proposed that the atomic switching induced by STM is caused by the formation of a single electron/hole, which strongly couples to the atomic motion. However, switching involves the complicated reaction pathway of the concerted atomic process, and further effort is required to understand its detailed mechanism.

## References

- [1] Y. Morikawa, H. Ishii, and K. Seki, *Phys. Rev. B* **69** (2004) 041403(R).
- [2] M. Otani and O. Sugino, *Phys. Rev. B* **73**, (2006) 115407.
- [3] I. Hamada, M. Otani, O. Sugino, and Y. Morikawa, *Phys. Rev. B* **80**, 165411 (2009).
- [4] E. Inami, I. Hamada, K. Ueda, M. Abe, S. Morita, Y. Sugimoto: *Nat. Commun.* **6**, 6231 (2015)



## Hybrid *ab initio* QM/MM calculations of biological macromolecules

Masaru TATENO

*Graduate School of Life Science, University of Hyogo*

To theoretically investigate functional mechanisms of biological macromolecular systems, we employed *ab initio* quantum mechanics (QM) calculations, coupling to molecular mechanics (MM) calculations for the systems involving the entire structures. In the hybrid QM/MM calculations, we used our interface program, which connects highly-parallelized engines for the QM and MM calculations. In this study, we analyzed the interactions between the catalytic center of an enzyme and the ligands, to elucidate mechanisms involving the molecular recognition in the biological system based on the electronic structures of the reaction center.

Cytochrome c oxidase (CcO), which is the terminal enzyme of the electron transfer system from a biological point of views, reduces an oxygen molecule ( $O_2$ ) to two water molecules (i.e.,  $O_2 + 4H^+ + 4e^- \rightarrow 2H_2O$ ). The catalytic reaction produces the free energy, which is utilized for the proton pump activity of CcO, generating the gradient of the proton concentrations between mitochondrial membranes.

The catalytic reaction center of CcO is composed of so called the  $Cu_B$  site and heme  $a_3$ , including transition metals, i.e., Cu and Fe ions, respectively (**Fig. 1**). Thus, the reaction center is referred to as the binuclear center (BNC). The binding of oxygen to the BNC is a trigger of the

catalysis. However, from an experimental point of views, various ligands, such as CO, NO, and CN, have been employed to investigate the three-dimensional (3D) structures of the ligand-bound forms of CcO (this is because it is impossible to obtain a stable structure in the complex with the reactive molecule).

Thus, our aim is to investigate the interaction mechanisms between the ligand oxygen molecule and the BNC, thereby approaching to the catalytic mechanisms of CcO. Still, it is not always so easy even to definitely identify the correct configurations of the (inactive) ligands that are bound to the transition metals in the BNC. Thus, the interaction modes between the BNC and the (inactive) ligands are still left to be clarified.

To identify the optimal configurations of CO and the BNC, we calculated the interaction energy values between the ligand and the  $Cu_B$  site of bovine CcO, by putting the ligand molecule to various positions (500 configurations for each case) in the vicinity of the BNC. Here, we employed the UB3LYP functional and the TZVP basis set for the transition atoms and the coordinated atoms. Also, we examined advanced functionals, such as M06X, for the comparison.

Our systematic energy mapping analysis revealed that the appropriate CO configurations are dispersed as a spheroid in the vicinity of the

Cu ion. In fact, this is consistent with the electron density that was observed in the crystallographic data. Furthermore, we found that at least the two “distinct” configurations exhibited a “small” energy difference ( $< 2$  kcal/mol). In fact, the atomic distances between O atom of CO and Fe of heme  $a_3$  are different, by as large as  $\sim 1\text{\AA}$ , with respect to the two distinct types of the configurations.

To further examine the characteristic features in the ligand configurations, we calculated the IR spectrums, and found that the corresponding peaks fit well to the experimental values. Note here that the two configurations of CO are corresponding to the distinct IR peaks, thus indicating again that these configurations were involved in the (semi)stable interactions of the  $\text{Cu}_B$  and CO.

Moreover, we found that the Val243 side chain contacted the CO where the distance of O

atom and the Fe of heme  $a_3$  is closer, thereby producing the configuration that is distinct from another one. We further found that a previous biochemical mutagenesis study in terms of this Val residue also supported our data.

Note here that the above-mentioned modulation of the ligand configuration through the Val243 side chain led to the presence/absence of hybridization between a  $p$ -orbital of the CO and a  $d$ -orbital of Fe in heme  $a_3$ , thereby resulting in the two distinct vibrational modes of the CO stretching, which were corresponding to the previous spectroscopic data. Thus, we concluded that Val243 is a determinant for the configuration of CO interacting with the  $\text{Cu}_B$  site.

## References

[1] Kang, J., Matsuoka, T., and Tatenno, M., *submitted*.

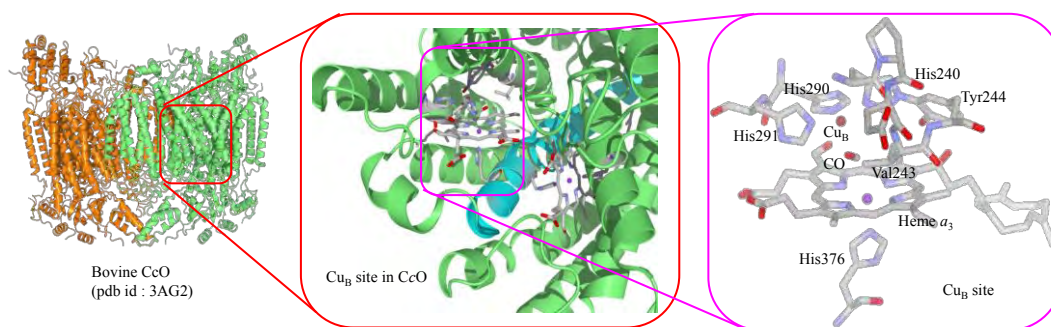


**Fig. 1.** The catalytic reaction center of bovine cytochrome c oxidase (CcO) is depicted. The reaction site involves heme  $a_3$  and the  $\text{Cu}_B$  site, thus referred to as the binuclear center (BNC). The  $\text{Cu}_B$  site and heme  $a_3$  include Cu and Fe ions, respectively. In the  $\text{Cu}_B$  site,

the three histidine (His) residues coordinate to  $\text{Cu}_B$  ion (for one His residue, Tyr244 is covalently-bonded), and a His residue coordinates to Fe ion from an axial direction in heme  $a_3$ . In the right panel, Val243 (see text) is depicted.

# First-Principles Study on Charge-Discharge Reaction Mechanism in Cathode Materials of Secondary Batteries

Hiroyoshi MOMIDA<sup>1</sup> and Tomoki YAMASHITA<sup>2</sup>

<sup>1</sup>*Institute of Scientific and Industrial Research, Osaka University  
8-1 Mihogaoka, Ibaraki, Osaka 567-0047*

<sup>2</sup>*Elements Strategy Initiative for Catalysts and Batteries, Kyoto University  
1-30 Goryo-ohara Nishikyo-ku, Kyoto 615-8245*

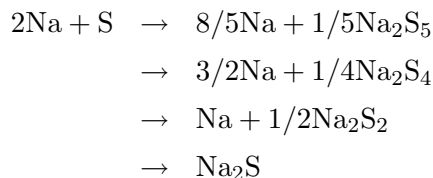
We have mainly used the supercomputer systems to investigate battery reaction mechanisms in cathode materials of Na-ion secondary batteries in the fiscal year 2014. In this project, first-principles calculations were done by using the HiLAPW code which is based on the density functional theory with the all-electron full-potential linearized augmented plane wave method. We have mainly studied microscopic reaction mechanisms in a solid Na/S battery system [1] and in the  $\text{Na}_x\text{C}_6\text{O}_6$  organic cathode material [2]. This research was done in collaboration with Tamio Oguchi. We also contribute partly to clarify electronic properties of a perovskite oxide system [3].

## Structural and electronic properties of $\alpha$ -S and Na-S crystals [1]

To understand microscopic mechanisms of charge and discharge reactions in low-temperature Na/S batteries, there has been increasing needs to study fundamental atomic and electronic structures of elemental S as well as that of Na-S phases. The most stable form of S is known to be an orthorhombic  $\alpha$ -S crystal at ambient temperature and pressure, and  $\alpha$ -S consists of puckered  $\text{S}_8$  rings which crystallize in space group  $Fddd$ .

In this study, the crystal structure of  $\alpha$ -S is examined by using first-principles calculations with and without the van der Waals interaction

corrections of Grimme's method, and results clearly show that the van der Waals interactions between the  $\text{S}_8$  rings have crucial roles on cohesion of  $\alpha$ -S. We also study structure stabilities of  $\text{Na}_2\text{S}$ ,  $\text{Na}_2\text{S}_2$ ,  $\text{Na}_2\text{S}_4$ , and  $\text{Na}_2\text{S}_5$  phases with reported crystal structures. Using calculated total energies of the crystal structure models, we estimate discharge voltages as shown in Figure 1 assuming the four-step discharge reaction equations as



estimated from the energy stability analyses. Calculated voltage-capacity characteristics in solid Na/S battery systems are discussed by comparing with recently reported experimental results.

## Electronic and atomic structures of $\text{Na}_x\text{C}_6\text{O}_6$ organic cathode material [2]

Na-ion batteries have been explored as a promising alternative to Li-ion batteries owing to a significant advantage of a natural abundance of Na. Recently, it has been reported that disodium rhodizonate,  $\text{Na}_2\text{C}_6\text{O}_6$  (Figure 2), exhibit good electrochemical properties and cycle performance as a minor-metal free

organic cathode for Na-ion batteries. However, its crystal structures during discharge/charge cycle still remain unclear.

In this work, we theoretically propose feasible crystal structures of  $\text{Na}_{2+x}\text{C}_6\text{O}_6$  depending on Na concentrations  $x$  using first-principles calculations. Structural phase transitions have been found:  $\text{Na}_4\text{C}_6\text{O}_6$  has a different  $\text{C}_6\text{O}_6$  packing arrangement from  $\text{Na}_2\text{C}_6\text{O}_6$ . Voltage values and electronic structures of  $\text{Na}_{2+x}\text{C}_6\text{O}_6$  as a function of  $x$  are clarified and discussed comparing with the experimental results. Our theoretical findings could contribute to understand the microscopic discharge/charge reaction mechanisms of  $\text{Na}_2\text{C}_6\text{O}_6$ .

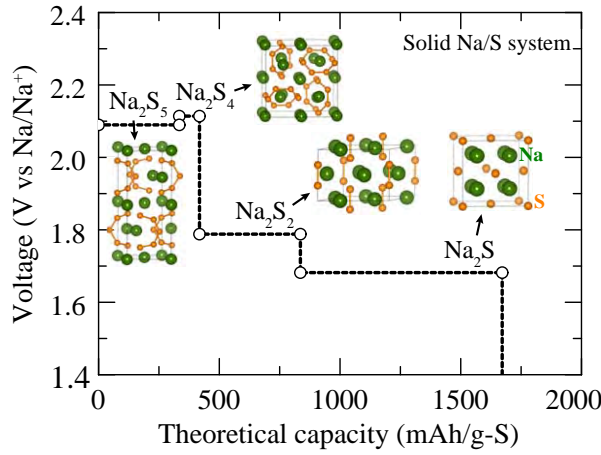


Figure 1: Calculated capacity-voltage curve of solid Na/S battery under the assumption of four-step discharge reaction equation.

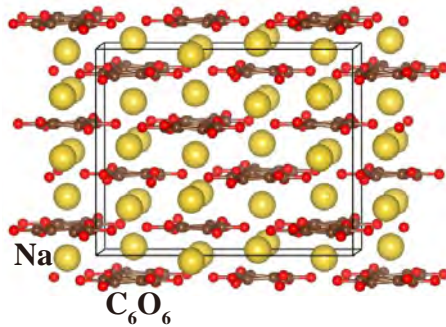


Figure 2: Crystal structure of disodium rhodizone  $\text{Na}_2\text{C}_6\text{O}_6$ .

## References

- [1] H. Momida, T. Yamashita, and T. Oguchi: J. Phys. Soc. Jpn. **83** (2014) 124713.
- [2] T. Yamashita, H. Momida, and T. Oguchi: submitted.
- [3] H. Fujii, M. Toyoda, H. Momida, M. Mizumaki, S. Kimura, and T. Oguchi: Phys. Rev. B **90** (2014) 014430.

# First-Principles Calculation of Transition Metal Oxides Interfaces

Fumiyuki ISHII

*Faculty of Mathematics and Physics, Institute of Science and Engineering,  
Kanazawa University, Kanazawa, 920-1192, Japan*

Recently, the two-dimensional electron gas (2DEG) formed at the transition metal oxides interface has attracted much attention for applications in the next generation device. The perovskite heterostructure composed dielectric materials  $\text{LaAlO}_3/\text{SrTiO}_3$  is one of such systems extensively studied. The polar interface induces large built-in electric field. Therefore, the electric-field induced spin-orbit interaction (SOI) in the perovskite heterostructure is quite important in understanding the electronic structures. In this research, by using large-scale first-principles calculations based on the density functional theory implemented OpenMX[1], we revealed specific electronic states and properties formed at the interface of the transition metal oxides modeled by superlattice. We focused on how spins can be controlled by electric field (electric polarizations and charge carriers). In additions to the 2DEG in the oxides heterostructure, we also revealed that the effect of SOI in strained ZnO film, The applications of 2DEG at the oxide interface, we proposed anomalous Seebeck effect.

We have performed first-principles calculations of  $(\text{LaAlO}_3)_n/(\text{SrTiO}_3)_n$  ( $n=2-8$ ). We evaluated the spin-orbit coupling constant, the Rashba parameter, for the interface states. In addition, we investigated the spin textures, i.e., momentum vector dependent magnetic field in the Brillouin zone. We found electron doping in the  $\text{TiO}_2$  layer at  $\text{LaO}$  interface and hole doping in the  $\text{AlO}_2$  layer at  $\text{SrO}$  interface. Due to the built-in electric field at the interface, the interface states show spin splitting and vortex-like spin textures in momentum space, i.e. Rashba effect. Calculated

Rashba coefficient is of the same order as that of the experimental value and theoretical value for  $n=2$ [2].

We also have perform first-principle calculations of wurtzite ZnO and thin-film surface system. We have performed large scale computation up to 120 ZnO bilayer and the period of unitcell is about 20 nm. We evaluated the spin texture whose energy is slightly higher than that of the conduction band bottom in the surface bands in nonpolar surface. We find that in-plane electric polarization induces the quasi-one dimensional orientations of the spin textures. The atomic relaxation drastically changes surface states. The atomic relaxation also changes the electric field at the surface. Therefore the spin textures and spin-orbit coupling constant of the surface states is strongly affected by the atomic relaxations. We find that the values of the spin-orbit strength and the wavelength of the spin-helix are comparable with those observed for various zinc-blende quantum well structures.

## References

- [1] T. Ozaki et al., [http:// www.openmx-square.org/](http://www.openmx-square.org/)
- [2] M. Nishida, F. Ishii, H. Kotaka, and M. Saito, Mol. Simul., *published online* DOI:10.1080/08927022.2014.987986.

# First-Principles Calculation of Oxide Topological Insulators

Fumiyuki ISHII

*Faculty of Mathematics and Physics, Institute of Science and Engineering,  
Kanazawa University, Kanazawa, 920-1192, Japan*

Pyrochlore iridates  $A_2\text{Ir}_2\text{O}_7$ , ( $A=\text{Pr}$ ,  $\text{Nd}$ ,  $\text{Sm}$ ,  $\text{Eu}$ , ..., and  $\text{Y}$ ) have attracted great interest for experimental observations of a chiral spin liquid state below 1.4 K and of possible underscreened Kondo effects around 20 K for  $A=\text{Pr}$  and insulator-semimetal transitions for  $A=\text{Nd}$ ,  $\text{Sm}$ ,  $\text{Eu}$ , ..., and  $\text{Y}$ . They are candidate materials for hosting nontrivial topological electronic structures with and without the electron correlation, because of the strong spin-orbit interaction of Ir  $5d$  electrons compared to the bandwidth and the Coulomb interaction. Ad hoc tight-binding and Hubbard model calculations for these materials have suggested a possibility of realizing novel states of matter; (i) a non-Fermi-liquid semimetal with the Fermi surface shrinking into the Gamma point at which two Kramers degenerate quadratic bands meet from below and above, (ii)  $Z_2$  topological insulators with and without a broken cubic symmetry, (iii) a Weyl semimetal and an axion insulator in the presence of the all-in, all-out antiferromagnetic (AF) order. There is a report of the first-principles calculations, based on the linear muffin-tin orbital method, on the pyrochlore iridates. However, it yields an antiferromagnetic order even for  $\text{Pr}_2\text{Ir}_2\text{O}_7$ , in sharp contrast to experiments. Therefore, more careful calculations from the first principles are called for to achieve a coherent understanding.

We revisit this issue through extensive fully relativistic LSDA and LSDA+ $U$  electronic structure calculations on  $\text{Y}_2\text{Ir}_2\text{O}_7$  and  $\text{Pr}_2\text{Ir}_2\text{O}_7$  (with  $\text{Pr}$  being replaced with  $\text{La}$ ) by using OpenMX code[1]. With increasing  $U$ , a transition from a paramagnetic semimetal to an all-in, all-out topologically non-trivial

AF semimetal, and to all-in, all-out topologically trivial Mott insulator occurs. A choice of  $U=1.3\text{eV}$  explains experiments on a narrow-gap AF insulator for  $\text{Y}_2\text{Ir}_2\text{O}_7$  and a paramagnetic semimetal close to an onset of the AF order for  $\text{Pr}_2\text{Ir}_2\text{O}_7$ . In the case of  $U=0$  for  $\text{Pr}_2\text{Ir}_2\text{O}_7$ , we demonstrate that decreasing the trigonal compression of  $\text{IrO}_6$  octahedra, as basically achieved by changing  $A$ -site elements, drives successive transitions to the Fermi-point semimetal of an electron and a hole quadratic bands, and then to a cubic  $Z_2$  topological band insulator which we confirmed by  $Z_2$  indexes derived from parity eigenvalues.

## References

- [1] T. Ozaki et al., [http:// www.openmx-square.org/](http://www.openmx-square.org/)

# Interface magnetic anisotropy of Nd-Fe-B magnets

Yoshihiro GOHDA

*Department of Materials Science and Engineering, Tokyo Institute of Technology  
J1-3, Nagatsuta-cho 4259, Midori-ku, Yokohama 226-8502, Japan*

As the most powerful class of permanent magnets, Nd-Fe-B sintered magnets have been used in many applications. However, the origin of their high coercivity is still open for discussion. Since the inside of the crystalline main phase, i.e.  $\text{Nd}_2\text{Fe}_{14}\text{B}$ , cannot pin the domain-wall motion, microstructural interfaces between the main phase and a sub-phase will play an important role in exhibiting the coercivity of the magnets. The magnetic anisotropy of a Nd atom is dominated by the anisotropy of the electrostatic potential felt by the  $4f$  electrons of the Nd atom. Thus, it is very important to clarify the electronic structure of interfaces, which determines the electrostatic potential. Since the triple-point phase, one of the sub-phases, is the source of the stray field, i.e. the origin of demagnetization field, we focused the triple-point phase, in particular Nd oxides. We aimed to determine a stable atomic structure and electronic states of interfaces.

In our calculations, the interface consists of  $\text{Nd}_2\text{Fe}_{14}\text{B}-(\sqrt{5} \times \sqrt{5})$  and  $\text{Nd}_4\text{O}(001)-(\sqrt{2} \times \sqrt{2})$ , where oxygen atoms are located at tetrahedral sites of Nd atoms as shown in Fig. 1 (a). From our results, we find that a disturbance from the bulk structure of  $\text{Nd}_4\text{O}$  near the interface is relaxed, as the distance from the interface becomes longer. This choice is motivated by experiments, where the triple-point phase directly in touch with the main phase is identified as Nd oxides with the fcc Nd sublattice ( $\text{NdO}_x$ ) [1, 2]. We identified that O atoms at the interface prefer to present with Nd compared with Fe. We have also found that the electronic structure inside the main phase is hardly perturbed by the presence of the interface as shown in Fig. 1 (b). Examining the anisotropy constants of Nd at the

interface and inside the main phase, we derived an effective spin Hamiltonian, with which we performed atomistic micromagnetics simulations. The single-ion anisotropy constants due to localized  $4f$  electrons in Nd were calculated by the crystal-field analysis. As for the site-decomposed anisotropy induced by itinerant  $3d$  electrons of Fe, we employed our computationally efficient method [3], where the sum rule is satisfied by including indirect off-site contributions in the second-order perturbation. Considering the anisotropy of Fe sublattice [3], approximately 10% of estimated coercivity is attributed to the effect of Fe sublattice.

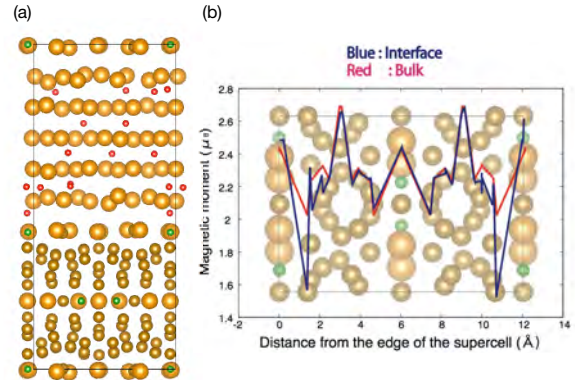


Figure 1: (a) The atomic structure of a  $\text{Nd}_2\text{Fe}_{14}\text{B}$ - $\text{NdO}_x$  interface and (b) depth profile of the magnetic moment within the main phase.

- [1] H. Sepehri-Amin, T. Ohkubo, T. Shima, and K. Hono, *Acta Mater.* **60**, 819 (2012).
- [2] T. Fukagawa, T. Ohkubo, S. Hirose, and K. Hono, *J. Magn. Magn. Mater.* **322**, 3346 (2010).
- [3] Z. Torbatian, T. Ozaki, S. Tsuneyuki, and Y. Gohda, *Appl. Phys. Lett.* **104**, 242403 (2014).

# Large scale ab initio calculations on the fundamental processes of energy convergence devices and on their optimization for high conversion efficiency

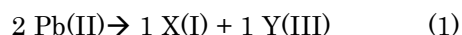
Koichi YAMASHITA

*Department of Chemical System Engineering,*

*The University of Tokyo, Hongo, Bunkyo-ku, Tokyo 113-8656*

## **1. Structural, Electronic, and Optical Properties of mixed organic-inorganic halide perovskites. Chemical solutions for working and environmental issues.**

We have investigated during the last year several properties of mixed organic-inorganic halide perovskites. In particular we have focused in the possibility of reducing the reported hysteresis in the J-V curve measurements of the perovskite solar cells. We have thus focused on the calculation of systems where the most common organic cation present in these mixed perovskites is replaced by other with a reduced dipole moment. We similarly have investigated the possibility of replacing lead atom in such perovskites with other less environmentally risky metals, according to the aliovalent replacement:



We have performed quantomechanic calculations by means of the DFT as implemented in several computational packages. Optimizations and electronic structure calculations have been performed mainly using

the Atomic Orbital based Siesta code and the Plane wave based PWscf one.

Our calculations predict the thermodynamic stability of intermediate alloys using molecular organic cations different from methylammonium (mainly guanidinium and formamidinium) that can find applicability in Photovoltaics. Similarly, systems using couples of metallic cations different from Pb(II), that respect the stoichiometry of the initial systems (Eq. 1), are found to have possible applicability in Photovoltaics since the calculated similarities with the parental species MAPbI<sub>3</sub>.

## **2. Atomic scale interface of RuO<sub>2</sub>/water under electrochemical conditions**

Oxygen reduction reaction (ORR) and oxygen evolution reaction (OER) are the key reactions in both the cathode reaction of polymer electrolyte fuel cells (PEFCs) and the photoelectrocatalytic water-splitting reaction. Toward the higher energy efficiency, electrochemical reaction and interface in atomic scale is fundamental and has the possible benefits for designing the materials.



For this purpose, the reaction mechanism of ORR on Ta<sub>3</sub>N<sub>5</sub> (100) surfaces was examined first and then the interfacial structure of RuO<sub>2</sub>/water under given pH and potential was examined. DFT calculations including the effect of pH and electrode potential are performed using GPAW software. The GGA/RPBE functional and PAW method are used for all calculations. As a result, surface Pourbaix diagram of RuO<sub>2</sub>/water was obtained with corresponding structure. The results indicate the pH dependent interfacial structure. The reason for such behavior is originated to the stable hydrogen network and electric field effect at the interface. Focusing on the OER potential region, pH condition causes the different Ru formal valence and composition of first water layer because the higher pH condition stabilizes the interfacial structure with lower work function. Such structural difference possibly results in the pH-dependent behavior of OER either through the mechanisms or the probability of starting reactions.

### **3. Ab-initio investigations on tantalum oxynitrides : novel materials for photocatalysis**

Perovskite tantalum oxynitrides ATaO<sub>2</sub>N (A = Ba, Sr, Ca) are promising candidates for water-splitting photocatalyst due to their ability to produce hydrogen under visible light irradiation. However, oxygen production has

not reported yet, and accordingly further optimization of the band edge positions is mandatory. Previous studies suggest possible modifications of the properties of such materials by changing geometrical structures such as perovskite octahedral-tilting [1] and oxynitride anion ordering [2]. Here, to demonstrate the effects of them in tantalum oxynitride perovskites, we have investigated the structural and electronic properties of CaTaO<sub>2</sub>N and MgTaO<sub>2</sub>N with various anion ordering, by means of DFT based calculations.

All the calculations were done on VASP with GGA/PBE functional. On-site coulomb interaction  $U = 5.0$  eV was adopted on tantalum d-orbitals.

Among the models with different anion orderings, bandgaps differ up to 1.3 eV in MgTaO<sub>2</sub>N and up to 0.6 eV in CaTaO<sub>2</sub>N, despite exactly the same chemical compositions, with the former class (MgTaO<sub>2</sub>N) characterized by bandgaps larger than the latter (CaTaO<sub>2</sub>N). The band structures showed that the octahedral-tilting mainly impacts on the conduction band structure and anion ordering impacts on the valence band structure, through the difference in the mixing of tantalum d-orbitals and anion p-orbitals.

## **References**

- [1] H. W. Eng, P. W. Barnes, B. M. Auer, P. M. Woodward: *J. Solid State Chem.* **175** (2003) 94
- [2] A. Fuertes: *J. Mater. Chem.* **22** (2012) 3293

# Development and application of first-principles simulator for dynamics in electron transport

Yoshiyuki EGAMI

*Division of Applied Physics, Faculty of Engineering, Hokkaido University  
Kita 13, Nishi 8, Kita-ku, Sapporo, Hokkaido 060-8628*

Recently, in the research and development of new electronic devices comprising nanoscale materials, theoretical investigations have attracted much interest. So far, a lot of first-principles studies on the electron-transport properties of nanoscale materials were performed and many remarkable results have been reported. However, most of these studies discuss the static characteristics in the steady state, and there remains a lot of uncertainty on the dynamic behavior of electrons flowing across the materials.

In order to examine the dynamic transport properties of the nanoscale materials sandwiched between semi-infinite crystalline electrodes, we improved the impulse response (IR) method [1] which is the dynamic electron-transport calculation method based on the real-space finite-difference approach [2] within the framework of the time-dependent density functional theory. In the conventional IR method, a system connected to semi-infinite jellium electrodes is considered and an impulse wave localized with respect to the transporting direction is prepared as an incident wave. Here, the impulse wave is treated as the linear combination of plane waves with various incident energies, which are the generalized Bloch states in the jellium electrode. After several time steps, the scattering wave function for the incident electron with certain incident energy can be obtained by means of the Fourier analysis of time-evolved wave functions. In this subject, we developed a new al-

gorithm to deal with the initial impulse wave consisting of superposition of the generalized Bloch states in the crystalline electrode. Moreover, we adopted the improved IR method to demonstrate the electron transport in the BN-dimer embedded graphene connected to semi-infinite graphene electrodes, where the calculations were performed with a few hundred cores on FUJITSU PREMEHPC FX10 (System C).

As the results, we observed the electrons incident from one crystalline electrode were propagating toward another one and being scattered by the impurity potential of BN dimer. However, it is found that there are some logical errors in the algorithm of calculating the conductance spectrum and the efficiency of the parallel computing is terribly low. Challenges to resolve these problems are in progress.

## References

- [1] Y. Egami and K. Hirose: JPS Conf. Proc. **1**, 016012 (2014).
- [2] K. Hirose *et al.*: *First-Principles Calculations in Real-Space Formalism*, (Imperial College Press, London, 2005).

# First principles calculation of van der Waals interaction in Pt clusters on graphene

Yuji HAMAMOTO

*Department of Precision Science and Technology, Osaka University*

*1-7 Yamadaoka, Suita, Osaka 565-0871*

Since the discovery of graphene, a two-dimensional material composed of a hexagonal lattice of carbon atoms, a great deal of effort has been made to apply its peculiar electronic properties to industries. One of the most important examples is application to automotive catalysts, where graphene is expected to influence the catalytic activity of metallic nanoclusters deposited on it. Indeed, it has experimentally demonstrated that Pt nanoclusters supported on graphene shows higher catalytic activity than on other carbon allotropes such as HOPG surfaces and carbon nanotubes [1]. Towards the development of further efficient catalyst materials, there is a compelling need for the microscopic elucidation of the characteristic support effect of graphene on metallic nanoclusters.

The first step to the theoretically understanding of such systems is determination of the structure of metallic nanoclusters, since the catalytic activity is highly dependent on the surface structure. So far the structure of Pt nanoclusters has been extensively investigated with first principles calculation based on the generalized gradient approximation (GGA) [3, 4, 5]. As the size of Pt nanoclusters is increased, however, it becomes more important to consider the influence of non-local van der

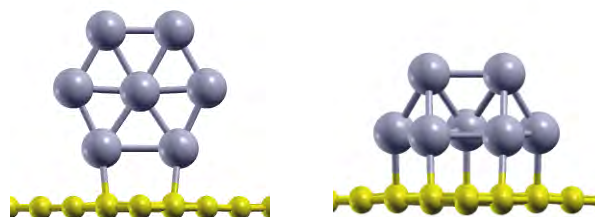


Fig. 1: Flat (left) and 3D (right) Pt<sub>7</sub> nanocluster supported on graphene

Waals (vdW) interaction, which is not taken account of in GGA.

Here we report an investigation of the influence of vdW interaction on the stability of Pt<sub>7</sub> nanoclusters supported on pristine graphene, among which two characteristic relaxed structures are shown in Fig. 1. The first principles calculation was performed using STATE codes and vdW correction was included semi-empirically via the DFT-D2 method [2]. We adopted a rhombic  $4 \times 4$  unit cell for a graphene sheet, and  $3 \times 3 \times 1$   $k$  points are sampled uniformly. We first confirmed that vertical adsorption of the flat Pt<sub>7</sub> nanocluster shown in Fig. 1 gives the largest adsorption energy, defined by  $E_{\text{int}} \equiv E_{\text{Pt}_7/\text{gra}} - E_{\text{Pt}_7} - E_{\text{gra}}$ , in good agreement with Ref. [4]. When the vdW correction is taken into account, on the other hand, we found that the three-dimensional (3D) Pt<sub>7</sub> nanocluster (see Fig. 1) becomes

more stable than the flat one by 0.63 eV. This means that adsorption of the 3D nanocluster is stabilized by vdW interaction between graphene and Pt atoms directly connected to graphene. Although it has been widely believed that vdW interaction plays a dominant role mainly in weak physisorption in sparse materials, our findings suggest that vdW interaction is also important for metallic nanoclusters on graphene. To investigate the influence of vdW interaction more precisely, we need to adopt more sophisticated treatment such as vdW-DF [6].

## 参考文献

- [1] E.-J. Yoo, T. Okata, T. Akita and M. Kohyama, J. Nakamura and I. Honma, Nano Lett. **9**, 2255 (2009).
- [2] S. Grimme, J. Comput. Chem. **27**, 1781 (2006).
- [3] Y. Okamoto, Chem. Phys. Lett. **420**, 382 (2006).
- [4] K. Okazaki-Maeda, Y. Morikawa, S. Tanaka and M. Kohyama, Surf. Sci. **604**, 144 (2010).
- [5] T.-u. Park, Y. Tomita and T. Nakayama, Surf. Sci. **621**, 7 (2014).
- [6] M. Dion, H. Rydberg, E. Schröder D. C. Langreth and B. I. Lundqvist, Phys. Rev. Lett. **92**, 246401 (2004)

# First principles calculation of point defects in electrodes of solid oxide fuel cells

Akihide KUWABARA

*Nanostructures Research Laboratory*

*Japan Fine Ceramics Center, Atsuta-ku, Nagoya, Aichi 456-8587*

Acceptor-doped BaZrO<sub>3</sub> shows high proton conductivity under a wet condition and is a promising material used for a proton conductive electrolyte. A problem for realization of BaZrO<sub>3</sub> as the electrolyte is a proton-trapping phenomenon. In the acceptor-doped BaZrO<sub>3</sub> systems, it has been reported that a part of the protons are captured around the dopants. This is because there are attractive coulomb interactions between protons and acceptors those have opposite charge states. Such trapping results in reduction of number of charge carriers. In this study, our main purpose is to clarify the proton-trapping phenomena in the acceptor-doped BaZrO<sub>3</sub> by calculations based on density functional theory.

Total energy calculations were performed using the VASP code. Electron-ion interactions were represented by the projector augmented wave method, and the generalized gradient approximation was chosen for the exchange-correlation functional. Plane waves up to an energy cut-off of 400 eV were used as the basis set for wave functions. Supercells of BaZrO<sub>3</sub>

containing 625 atoms,  $5 \times 5 \times 5$  unit cells, was constructed for the calculations of defective systems. Only the  $\Gamma$  point was adopted in the k-point sampling for the supercells. All atomic positions in defective systems were fully relaxed until all residual forces were less than 0.02 eV/Å.

Figure 1 is plots of calculated association energies of dopants (Sc and Y) and proton to distances between the point defects. According to approaching of the proton to the dopant, association of proton-dopant becomes more stable. A proton is the most stable at the nearest neighbor site from Sc. In case of Y-doped system, the second nearest neighbor site energetically prefer to the nearest neighbor one.

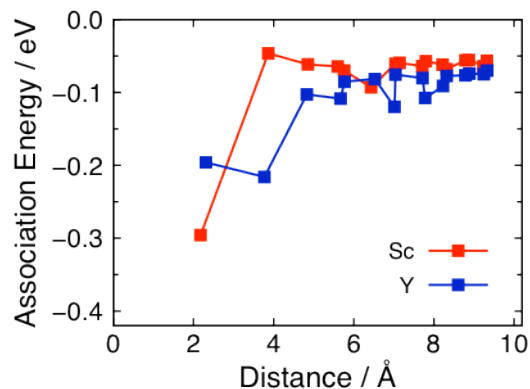


Fig. 1. Dependence of association energies of dopant-proton pairs on distances between defects.

# First principles calculations of point defects nearby grain boundaries of alpha $\text{Al}_2\text{O}_3$

Akihide KUWABARA

*Nanostructures Research Laboratory*

*Japan Fine Ceramics Center, Atsuta-ku, Nagoya, Aichi 456-8587*

Growth of alumina scales on aluminum-containing alloys in thermal barrier coatings (TBCs) is dominated by inward oxygen and outward aluminum diffusion at grain boundaries (GBs) across the scale. Recent oxygen permeation experiments of  $\alpha\text{-Al}_2\text{O}_3$  wafers at high temperatures of 1750–1950 K, to elucidate the mass transfer behavior in the GBs, have shown that the diffusing species switches between aluminum and oxygen vacancies depending on the applied oxygen partial pressure. In this study, we investigate the influence of dopant segregation nearby grain boundaries on mass transport in  $\alpha\text{-Al}_2\text{O}_3$ .

Total energy calculations were performed using the VASP code. Electron-ion interactions were represented by the projector augmented wave method, and the generalized gradient approximation was chosen for the exchange-correlation functional. Plane waves up to an energy cut-off of 500 eV were used as the basis set for wave functions. Atomic configurations of the  $\Sigma 31$  grain boundary are shown in Fig. 1. In the present study, we focus on  $\text{Y}^{3+}$  ion as a dopant, which is known to suppress oxide ion transport nearby grain boundaries. We introduce oxide ion vacancies ( $V_{\text{O}}^{\cdot\cdot}$ ) at a bulk-like region and on the grain boundary of the Y-doped  $\Sigma 31$  grain boundary model. Formation energies of  $V_{\text{O}}^{\cdot\cdot}$  are evaluated for the each case. Formation energies of  $V_{\text{O}}^{\cdot\cdot}$  near the grain boundary are about 1.7 eV lower than those in the bulk-like region.  $V_{\text{O}}^{\cdot\cdot}$  will accumulate near the grain boundary. In addition,  $V_{\text{O}}^{\cdot\cdot}$  become

more stable at neighboring sites to  $\text{Y}^{3+}$  ions at the  $\Sigma 31$  grain boundary. This result indicates that the segregated  $\text{Y}^{3+}$  ions act as trapping sites to  $V_{\text{O}}^{\cdot\cdot}$ . Our calculations clarify the mechanism of mass transport suppression by Y doping in  $\alpha\text{-Al}_2\text{O}_3$ .

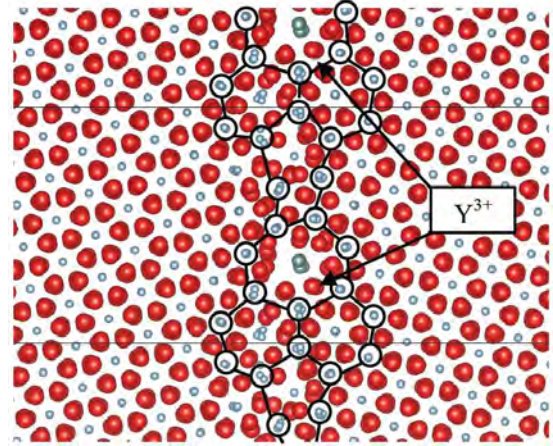


Figure 1: Atomistic structures of Y-doped  $\Sigma 31$   $\text{Al}_2\text{O}_3$  grain boundary.

# Simulation of Electronic Properties in Materials for Spintronics

Mineo SAITO

*Institute of Science and Technology, Kanazawa University  
Kakuma, Kanazawa, 920-1192 Japan*

Graphene is considered to be one of the candidates for spintronics materials. For the device application of the graphene, we need to consider the effect of substrate. In this study, we perform first-principles calculations on graphenes on ferromagnetic Ni substrate.

We first spin polarized density functional calculations on few layer graphenes on Ni and find that the electronic structure of the first layer which touches the Ni (111) substrate is greatly affected by the Ni substrate. On the other hand, the partial density of states of the other layers are close to that of the free standing graphene. By analyzing the partial density of states, we find that the electrons are somewhat transferred to these layers.

Then, we focus on the single layer graphene on the Ni substrate. First, we consider the case that the direction of the magnetization of Ni is perpendicular to the surface ([111]) and find that the spin structure of the graphene is close to the antiferromagnetic structure. This result is consistent with those of our previous study [1].

Next we consider the case that the direction of the magnetization is parallel to the surface. We first carry out calculations without including

the spin-orbit interaction (SOI) and next do calculation with the SOI. By analyzing the results of the two calculations, we estimate the Rashba effect. The split due to the Rashba effect is estimated to be 10 meV. There are two experimental results which support large split due to the Rashba effect (225 meV)[2] and small split (less than 45 meV.) Our result supports the latter result [3]. In any case, we find that the Ni substrate has a substantial SOI effect on the mono-layer graphene.

## References

- [1] K. Sawada, F. Ishii, and M. Saito, Phys. Rev. B 82, 245426 (2010).
- [2] Yu. S. Dedkov, M. Fonin, U. Rüdiger, and C. Laubschat, Phys. Rev. Lett. 100, 107602 (2008).
- [3] O. A. O. Rader, A. Varykhalov, and J. Sanchez-Barriga, D. Marchenko, A. Rybkin, and A. M. Shikin, Phys. Rev. Lett. 102, 057602 (2009)

# First principles study on lattice thermal conductivity reduction in multinary zinc-blende-type semiconductors

Kenji YASUOKA

*Department of Mechanical Engineering, Keio University  
Kohoku, Yokohama, Kanagawa 223-8522*

By introducing different cation species to Zn sites, a zinc-blende-type semiconductor can be converted from a binary to multinary compound. This system has been drawing much attention since one can create various semiconductors having different properties through this modulation. In this respect, recently  $\text{Cu}_2\text{ZnSnS}_4$  is considered as a candidate for a thermoelectric material.[1] While its good performance is characterized by the low thermal conductivity which is an order of magnitude lower than ZnS, the lowering mechanism is still an open question. In this study, we dealt with this problem by calculating and comparing the lattice thermal conductivity of three zinc-blende-type materials, namely, ZnS,  $\text{CuGaS}_2$  and  $\text{Cu}_2\text{ZnGeS}_4$  as presented in Figure 1. To simplify the problem, we kept the averaged mass of the cations. The detailed results will be reported elsewhere. To obtain thermal conductivity, we evaluated the cubic interatomic force constants by finite-displacement methods. It amounts to more than 5000 density functional theory (DFT) calculations of a 64-atom supercell with atoms displaced in different directions. This large-scale calculation was carried out on F16 and L16 queue in System B. The DFT calculations were done using the

VASP code[2] with a 450 eV plane-wave cut-off and a  $\Gamma$ -centred  $2 \times 2 \times 2$  k-point mesh for ternary and quaternary cases. The Phonopy package was used for structure generation and post-processing.[3]

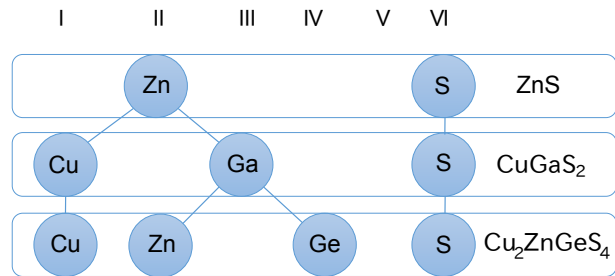


Figure 1: Schematic view of our approach.

## References

- [1] M. L. Liu, F. Q. Huang, L. D. Chen and I. W. Chen: Appl. Phys. Lett. **94** (2009) 202103.
- [2] G. Kresse and J. Hafner: Phys. Rev. B **47** (1993) 558.
- [3] A. Togo, F. Oba and I. Tanaka: Phys. Rev. B **78** (2008) 134106.



## **Study on the capacitance of bilayer graphene by density functional simulation under electric fields**

Yasunobu ANDO, Yutaro Mori, Emi Minamitani, and Satoshi Watanabe

*Department of Materials Engineering,*

*The University of Tokyo, 7-3-1 Hongo, Bunkyo-ku, Tokyo, 113-8656*

Atomic-layer materials such as graphene, MoS<sub>2</sub>, and h-BN have attracted great attention because of their potential as electronic devices. Especially, bilayer graphene (BLG) is a promising candidate for a channel material in field-effect transistors because of its high mobility and capability of band gap control by electric fields. In order to develop high-performance devices with the atomic-layer materials, it is necessary to understand the behavior of capacitance at nanoscale in the atomic-layer devices, which is crucial for the circuit operation but have not been understood enough yet and difficult to estimate theoretically.

It has been studied how to improve the on/off ratio of field-effect transistors made of BLG in experiments. They thought that the information of interface states seen in the density of states (DOS) must give them a clue for this, and observed the quantum capacitance of BLG, which is closely related to its DOS, under electric fields. However, their results are difficult to understand: nanoscale information

of electronic states, which is difficult to obtain from experiments, seems crucial to understand this. Our objective of this research is to facilitate the interpretation of their experiments using theoretical simulation in nanoscale.

We carried out the simulation of the electronic states under external electric fields on the basis of the density functional theory. An isolated BLG in vacuum is considered.

From the response of electrostatic potential to the electric field, the relative permittivity of the BLG is determined for several field strengths. Interestingly, the relative permittivity is not diverged on graphene sheets, which indicates that the graphene sheets are no longer metallic. As a result of incomplete screening of the graphene sheets, even between the sheets, the relative permittivity is larger than one. Therefore, we conclude that the BLG should be regarded as not a pair of the metallic sheets but a single dielectric material. The modeling from this perspective is necessary when analyzing the BLG system.

# Atomic and Electronic Structure of Diamond/Cubic Boron Nitride Interface

Zhongchang WANG, Chunlin CHEN, Yuichi IKUHARA

*Advanced Institute for Materials Research, Tohoku University, Sendai 980-8577*

*Institute of Engineering Innovation, The University of Tokyo, Tokyo 113-8656*

Diamond and cubic boron nitride (c-BN) are two materials having the highest hardness on this planet due to their extremely strong covalent bonding between atoms with a  $sp^3$  configuration. For this reason, fabricating diamond and c-BN of a high quality and discovering their novel properties and applications have attracted extensive interest. However, the issues, how diamond and c-BN can actually join at the heterojunction are still unclear. Understanding of these issues will greatly promote the study of combining these two materials for enhanced properties.

Figure 1a shows a high-angle annular-dark-field (HAADF) STEM image of the coherent area viewed from  $[1\bar{1}0]$  direction. One can note that the interface is epitaxial and atomically abrupt. Since the intensity of an atomic column in the HAADF imaging mode is directly proportional to  $Z^{1.7}$  ( $Z$ : atomic number), the image contrast is brighter for heavier atoms. By interpreting the image contrast, we find that C is bonded directly to B at the interface. Figure 1b shows a HAADF STEM image of a stacking fault area, from which the atomically abrupt junction (indicated by red arrows) and the direct B-C bonding can be confirmed. The stacking fault is found to locate on the c-BN side, which is attributed to the fact that the c-BN has a lower hardness and stacking fault energy than the diamond.

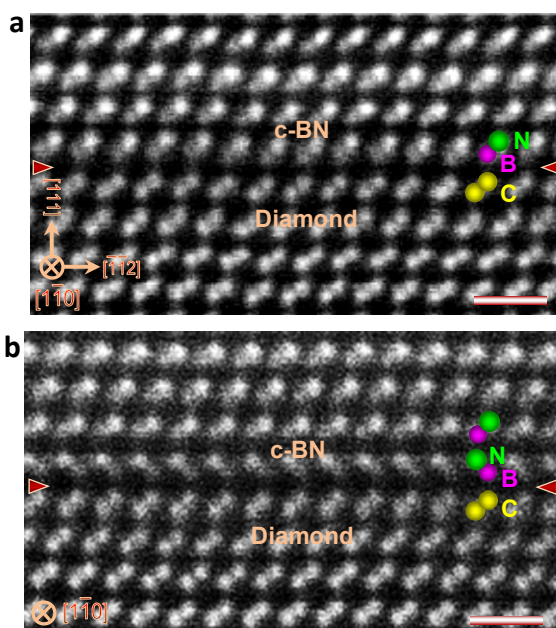


Fig. 1: HAADF STEM images taken along  $[1\bar{1}0]$  zone axis in (a) the directly bonded coherent area and (b) the stacking fault area.

To gain insights into electronic structure of the interface and offer a deeper understanding of the images, we performed density functional theory (DFT) calculations, taking into account both the B and N terminations for the BN. Adhesion energy calculations reveal that the B-terminated interface (Fig. 2a) has a much stronger adhesion than the N-terminated one ( $5.577 \text{ Jm}^{-2}$  for the B termination and  $2.906 \text{ Jm}^{-2}$  for the N termination), consistent with the HAADF observations (Fig. 1a).

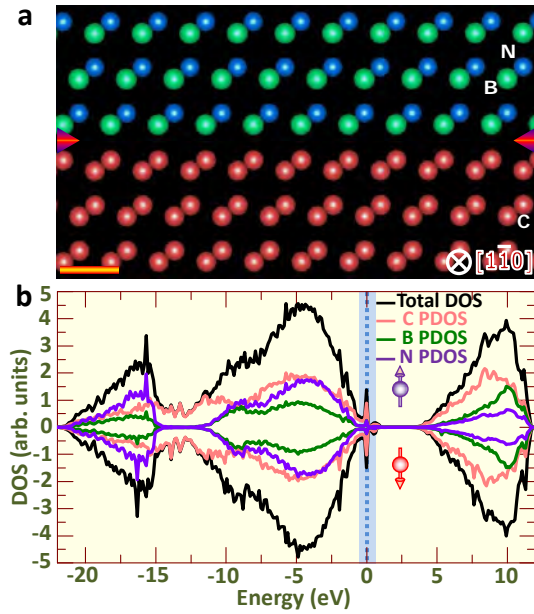


Fig. 2: (a) Relaxed atomic model for the interface between B-terminated BN and diamond. (b) Total DOS and PDOS of the C, B, and N atom contributions for the relaxed interface.

Calculations of electronic structure predict that there emerge electronic states at Fermi level ( $E_F$ ) for both spins, indicating that the interface shows a full metallic character (Fig. 2b). Unexpectedly, the  $E_F$  lies precisely at a peak position of a band of electronic states, implying that the interface may be superconducting. The electronic states at  $E_F$  come mainly from the interfacial C sp orbitals and are confined to the interface, forming two-dimensional (2D) electron gas (2DEG) [1]. The 2DEG may be ascribed to the polar discontinuity across interface and may be formed on other orientations. Figure 3a,b shows spatial distribution in electronic wavefunction along  $[1\bar{1}0]$  and  $[11\bar{2}]$  projection [2]. One can note that electrons are spatially separated along  $[1\bar{1}0]$  direction, yet connected along  $[11\bar{2}]$  direction *via* the hybridization of C sp orbitals, implying that this interface shows a quasi-1D

nature in electrical conductivity [3]. Further analysis of the charge density and density difference along  $(1\bar{1}0)$  plane reveals that most of charges are localized on C and N atoms, and the charge distribution on each atom is severely distorted toward their neighbors, indicating that the interfacial bonds have a strong covalent character. Moreover, a large number of charges are accumulated along the interfacial B-C bonds and these charges are somewhat more than those along the C-C and B-N bonds in the respective bulks, offering an explanation to the strengthening of the interface.

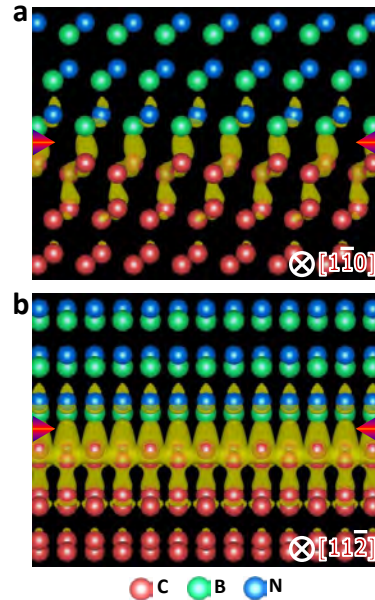


Fig. 3: Electron density at  $E_F$  viewed from (a)  $[1\bar{1}0]$  and (b)  $[11\bar{2}]$  direction. Charges are found to be confined at the interface.

## References

- [1] Z. C. Wang, M. Okude, M. Saito, S. Tsukimoto, A. Ohotomo, M. Tsukada, M. Kawasaki, Y. Ikuhara: Nature Communications **1**, (2010) 106.
- [2] C. L. Chen, Z. C. Wang, T. Kato, N. Shibata, T. Taniguchi, Y. Ikuhara: Nature Communications **6**, (2015) 6327.
- [3] Z. C. Wang, L. Gu, M. Saito, S. Tsukimoto, M. Tsukada, F. Lichtenberg, Y. Ikuhara, J. G. Bednorz: Adv. Mater. **25** (2013) 218.

## First Principles Based Analysis of Electronic Structures and Reactions on Surfaces/Interfaces

Yuji KUNISADA

*Center for Advanced Research of Energy and Materials, Faculty of Engineering,  
Hokkaido University, Sapporo, Hokkaido 060-8628*

We investigated the electronic structures and reactions on surfaces/interfaces, with the aid of the first principles calculation based on the density functional theory (DFT). In addition, we adopted the quantum dynamics calculation code for atomic nuclei to consider the quantum mechanics behaviors of the oxygen molecules. [1]

At first, we investigated the electronic structures of Pd/ZnO interfaces, which is formed with internal oxidation process. [2] The full-potential linearized augmented plane wave (FLAPW) calculation based on DFT was carried out through WIEN 2k [3] on F16 queue in system B. We installed parallelized WIEN 2K with Intel® MPI Library and Intel® Math Kernel Library. We calculated the O-K edge electron energy-loss spectra at Pd/ZnO interfaces with the corresponding supercell, using TELNES3 program which is implemented in WIEN 2k. We found that the sharp peak appears in the vicinity of 530 eV energy loss. This peak appears in the configuration with O atoms bonding on Pt atoms. This result shows the good agreement with our experimental O-K edge electron

energy-loss spectra.

We also investigated the quantum effects in the O<sub>2</sub> dissociative adsorption on Ag(111) surfaces. [4] We performed the two-dimensional quantum dynamics calculations with corresponding potential energy surfaces [5] on P1 queue in system B. We found that there are non-negligible tunneling effects in the dissociative adsorption and significant energy transfer and coupling from vibration to translational motion.

### References

- [1] Y. Miura, H. Kasai and W. A. Diño: J. Phys. Soc. Jpn. **68** (1999) 887.
- [2] N. Sakaguchi, K. Watanabe and Y. Kunisada: Microscopy **63** (2014) 463.
- [3] P. Blaha, K. Schwarz, G. Madsen, D. Kvasnicka, and J. Luitz, WIEN 2k, Augmented Plane Wave + Local Orbitals Program for Calculating Crystal Properties, Vienna, Austria, 2001.
- [4] Y. Kunisada and N. Sakaguchi: RSC Adv. **4** (2014) 63508.
- [5] Y. Kunisada, M. C. Escaño and H. Kasai: J. Phys.: Condens. Matter **23** (2011) 394207

# Oxide electrocatalysts

Osamu SUGINO

*Institute for Solid State Physics, University of Tokyo  
Kashiwa-no-ha, Kashiwa, Chiba 277-8581*

In the polymer electrolyte fuel cells (PEFCs), platinum-alloys are commonly used as the electrocatalyst because of their reasonably high activity and acid-durability. It is considered, however, that development of more active, durable, and cheap catalysts are necessary for the renewable energy society. In this context, the group 4 transition metal oxide, such as zirconia ( $\text{ZrO}_2$ ), tantalia ( $\text{Ta}_2\text{O}_5$ ), and titania ( $\text{TiO}_2$ ), has attracted attention. In particular, with the development of introducing oxygen vacancy and nitrogen impurity into the sample, the activity for the oxygen reduction reaction (ORR) is improving year by year. However, the structure of the active site and the reaction mechanism are remained unclear yet.

To provide a microscopic explanation, we studied the structure of the crystalline  $\text{Ta}_2\text{O}_5$  and the oxygen vacancy using the first-principles DFT-GGA (hybrid DFT) calculation and found that there are several crystalline structures of comparable total-energy and the vacancy structures, hampering thereby reliable calculation. This year, we have analyzed the structure in more detail and found that the lattice relaxation is exceptionally large and long ranged around the vacant site [1]. This fact, together with the coexisting structures, indicates that larger computational cells are required to perform reliable first-principles calculation.

Regarding  $\text{ZrO}_2$ , on the other hand, no such difficulty is found. We have performed a first-principles molecular dynamics simulation to investigate the ORR pathway. The re-

sult indicates that the oxygen vacancy plays an important role in the ORR mechanism but is concerned with the rate-limiting step such that the vacancy needs to be stabilized more to enhance the ORR activity. We then performed a total-energy calculation on the vacancy-stability, and found that the nitrogen impurity can change the charge state of the vacancy with a effect of stabilizing the vacancy. This result naturally explains the experimental result why the nitrogen can enhance the activity.

## References

- [1] Electronic structures of oxygen-deficient  $\text{Ta}_2\text{O}_5$ : Y. Yang, H.-H. Nahm, O. Sugino and T. Ohno, AIP Advances **3** (2013) 042101(1-8).
- [2] Possible magnetic behavior in oxygen-deficient  $\beta\text{-PtO}_2$ : Y. Yang, O. Sugino and T. Ohno, Phys. Rev. B **85** (2012) 035204(1-13).
- [3] Exceptionally long-ranged lattice relaxation in oxygen-deficient  $\text{Ta}_2\text{O}_5$ : Y. Yang, O. Sugino and Y. Kawazoe, Solid State Communications **195** (2014) 16.

# Theoretical material design of transition metal oxides hetero-structure based on the orbital distillation effect

Hirofumi SAKAKIBARA

*Computational Condensed Matter Physics Laboratory, RIKEN*

*Wako, Saitama 277-8581*

One of the ultimate goals of theoretical physics is designing the materials with novel properties ahead of experimental discoveries. Owing to the extension of computational resources and the development of calculation techniques, it is getting worth tackling this problem. To this end, hetero-structure superlattices are good target because we are able to “tune” their material property artificially.

We have studied the perovskite osmate  $\text{BaOsO}_3$  and its (001) super lattice  $[\text{BaOsO}_3]_1/[\text{BaTiO}_3]_1$  scheming to engineer its physical properties. Here  $\text{BaTiO}_3$  works as blocking layer.  $\text{BaOsO}_3$  has three-dimensional cubic symmetry (without rotation or tilting of octahedron) and shows metallic conductivity. By cooling this compound, magnetic susceptibility shows Curie-Weiss behavior without magnetic transition[1]. Previous theoretical study by first-principles calculation suggests the osmate locates in the vicinity of magnetic phase[2]. Theoretically, it can be speculate that the width of the band which intersects the Fermi level decrease by dimensional lowering. This is because that the band structure in the vicinity of the Fermi level is dominated by the  $J_{\text{eff}}=1/2$  states which is induced by the cooperation between strong spin-orbit coupling effect (SOC) and crystal fields splitting. This  $J_{\text{eff}}=1/2$  state consists three types of  $t_{2g}$  orbitals ( $d_{xy}$ ,  $d_{yz}$  and  $d_{zx}$ ) and two of them spread along  $z$  direction, therefore the prevention of perpendicular

hopping path degrades total band widths of  $J_{\text{eff}}=1/2$  states. To confirm this speculation, we have performed first-principles calculation for the both of  $\text{BaOsO}_3$  and  $[\text{BaOsO}_3]_1/[\text{BaTiO}_3]_1$  using WIEN2k package[3]. Fig.1 shows the band structure and the thick line shows the weight of  $J_{\text{eff}}=1/2$  states. From these results, the electron correlation effect should strengthen in the super lattice, and it is expected that the possibility of magnetic transition will go up.

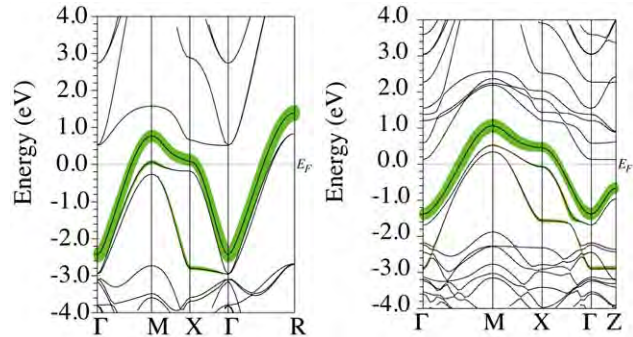


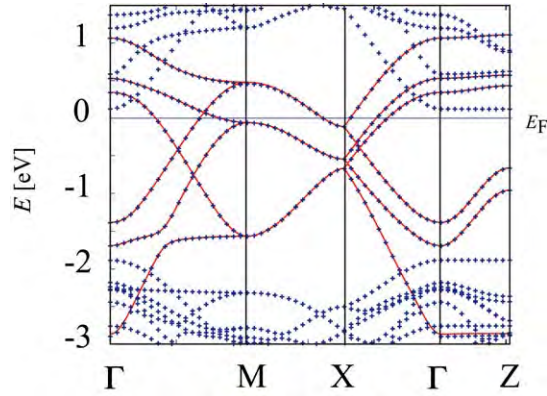
**Fig.1 Band structure of  $\text{BaOsO}_3$ (left) and  $[\text{BaOsO}_3]_1/[\text{BaTiO}_3]_1$ (right)**

To investigate what types order might be favorable, we have constructed the maximally localized Wannier function[4] to obtain tight-binding  $t_{2g}$  orbital model for the super lattice. Fig.2 depicts the band structure around the Fermi level comparing the result of first-principles and present model. In this



model, the spin-orbit coupling is taken into account in local hopping term among each Wannier orbitals. Based on this accurate model, we have constructed multi-orbital Hubbard model considering local interaction. Here we consider onsite intra-(inter-)orbital Coulomb repulsion  $U(U')$  and Hunds' coupling  $J$  and pair-hopping  $J'$ . By applying Hartree-Fock approximation to this model assuming  $U \sim 1.4\text{eV}$ ,  $J \sim 0.1U$ ,  $U' = U - 2J$  and  $J' = J$ , we have obtained antiferromagnetic insulating ground state. From this result, we prospect that the property of superlattice  $[\text{BaOsO}_3]_m/[\text{BaTiO}_3]_1$  ( $m=1,2,\dots$ ) might change depending on thickness  $m$  of the conducting layer.

This work was done in collaboration with Dr. T. Shirakawa and Dr. S. Yunoki.



## References

- [1] Y. Shi *et al.*, J. Am. Chem. Soc. **135**, 16507(2013).
- [2] M.-C. Jung *et al.*, Phys. Rev. B **90**, 045120(2014).
- [3] P. Blaha *et al.*, Comput. Phys. Commun. **59**, 399 (1990).
- [4] N. Marzari and D. Vanerbilt, Phys. Rev. B **56**, 12847(1997)

**Fig.2 Band structure of tight binding model(solid line) derived from maximally localized Wannier orbital in  $\text{BaOsO}_3/\text{BaTiO}_3$ . Dots show the original band structure obtained from LDA calculation.**

# Numerical simulation of metal oxides redox reaction on various supports

Fumihiko Kosaka, Junichiro Otomo

*Department of Environment Systems, Graduate School of Frontier Sciences,  
The University of Tokyo, 5-1-5, Kashiwa-no-ha, Kashiwa, Chiba 277-8563, Japan*

Redox reaction of metal oxides (MO) such as nickel oxide and iron oxide is one of candidates for energy conversion and storage systems [1,2]. Fuels such as hydrogen and methane reduce MO to metal (M), while oxygen and water oxidize M to MO. During the reduction process energy is stored as chemical energy in metal. On the other hand, thermal energy and chemical energy such as hydrogen are produced in oxidation process. The metal oxides have higher energy densities in comparison with the present lithium ion battery. Therefore, the systems using redox of the metal oxides have attracted much interest. Recently, we reported acceleration of redox reaction of metal oxides with oxide ion conducting supports. For further improvement of redox reaction rate, reaction mechanism of the redox reaction should be clarified. In this study, we focus on oxidation process of metal iron by water vapor. Dissociation of water molecule on Fe(100) surface, i.e., adsorption energies and dissociation barriers, was investigated using the density functional theory (DFT) and the nudged elastic band method (NEB). SIESTA code [3] was used for the DFT calculations. The

generalized gradient approximation (GGA) using the RPBE functional [4] was used as the exchange correlation function.  $p(2 \times 2)$  unit cell and vacuum layers of 10 Å was sampled with  $2 \times 2 \times 1$  k-point grid automatically generated using the Monkhorst-Pack method [5]. During relaxation, positions of atoms in bottom two layers were fixed. Climbing image nudged elastic band method (CI-NEB) was used for the calculation of transition state [6]. Crystal structures were visualized using VESTA software [7].

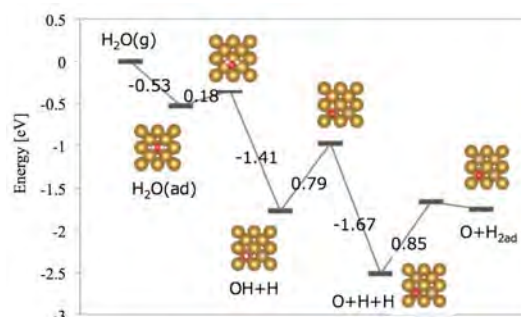


Fig. 1: calculated energy profile of water dissociation and top view of different adsorbed and transition states.

Fig. 1 shows the calculated energy profile of water dissociation on Fe(100) surface.  $\text{H}_2\text{O}$  adsorbed at the top of Fe atom, followed by the dissociation to adsorbed OH and H. Then, OH dissociated to O and H. Dissociation barrier of



OH and recombination of H to produce H<sub>2</sub> were almost the same and highest among the reaction barriers. It was found that acceleration of these reactions might lead to the improvement of oxidation reaction of iron in water vapor atmosphere. The present result can contribute to clarify the mechanism of hydrogen production process using oxidation of iron by water vapor.

## References

- [1] J. Adanez *et al.*, *Prog. Energy Combust. Sci.*, **38** (2012) 215.
- [2] N. Xu *et al.*, *Energy Env. Sci.*, **4** (2011) 4942.
- [3] J. M. Soler *et al.*, *J. Phys.: Condens. Matter.*, **14** (2002) 2745.
- [4] Y. Zhang *et al.*, *Phys. Rev. Lett.*, **80** (1998) 890.
- [5] H.J. Monkhorst *et al.*, *Phys. Rev. B*, **13** (1976) 5188.
- [6] G. Henkelman *et al.*, *J. Chem. Phys.*, **113** (2000) 9901.
- [7] K. Momma *et al.*, *J. Appl. Crystallogor.*, **44** (2011) 1272.

## Synthesis of proton conducting electrolyte and evaluation of ion conductivity of interfaces

Aki Iwanaga, Junichiro Otomo

*Department of Environment Systems, Graduate School of Frontier Sciences, The University of Tokyo, 5-1-5 Kashiwanoha, Kashiwa, Chiba 277-8563, Japan*

Proton conducting intermediate temperature fuel cells with proton-conducting solid electrolyte (p-ITFC) have been proposed, which is expected to have high material durability and power generation efficiency. In order to utilize it, it is needed to improve its efficiency. For this mission one of the bottleneck is proton conductivity of electrolyte. To improve proton conductivity, I focused on hetero interface between other kinds of electrolytes. There are some reports that oxide ion conductivity was promoted in hetero interface, so in this study I try to check if promotion of proton conductivity in hetero interface occur or not.

As electrolyte  $\text{SrTiO}_3$ (STO) was chosen. To think what happens in hetero structure, there are some phenomenon that affect to proton conductivity. One is segregation of dopant and one is shrinkage of lattice constant. It was proved by a experiment<sup>[1]</sup> that dopants segregate in hetero structure and it was said that lattice constant shrinkage has good affect on oxide conductivity.[2] In this study proton diffusion in STO was investigated using density functional theory (DFT) and nudged elastic band (NEB) method. DFT calculations were carried out with the SIESTA code<sup>[3]</sup>. The double- $\zeta$  split-valence basis set with polarization orbitals (DZP) was used in the calculations. The generalized gradient approximation (GGA) using the RPBE functional<sup>[4]</sup> was used as the exchange correlation function, and k-points were sampled with  $2 \times 2 \times 2$  grids using the Monk horst-Pack method<sup>[5]</sup>.

First, proton diffusion barrier was calculated in dopant

segregated and non-segregated system using nudged elastic band method. The picture of the both system and diffusion path of proton were shown in Fig.1. and the proton diffusion barrier is shown in Fig. 2.

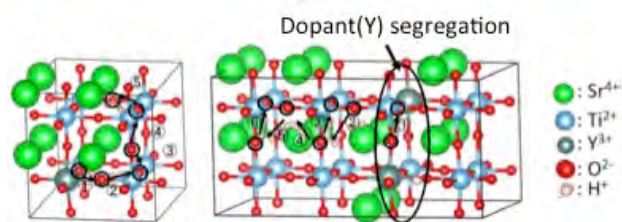


Fig.1 diffusion path of proton in (a): dopant segregated system and (b): non-segregated system

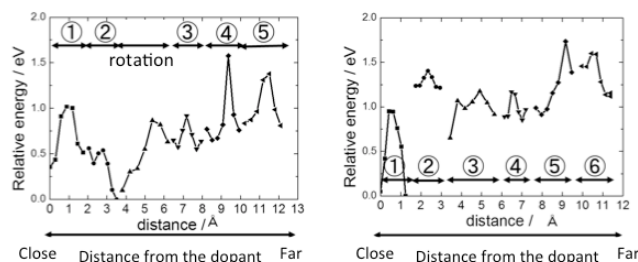


Fig.2 proton diffusion barrier in (a): dopant segregated system and (b): non-segregated system

Proton concentrate around most stable area and in both the system diffusion paths are ① and ②. The barriers are almost the same in the both system. Thus from this results it can be indicated that dopant segregation has no effect on proton conductivity.

Second, shrinkage of lattice constant was investigated. The diffusion path in the system with lattice constant shrinkage is the same with non-segregated system. In lattice constant shrinkage system, lattice constant is shorter by 5 % comparing to normal system. The proton diffusion barrier in shrinkage system is shown in Fig.3. Here, diffusive path is also ① and ②. The diffusive barrier in path ② is bigger than normal system. It might be because by shrinkage of lattice constant, the path with

low barrier has been lost. Comparing with normal system, diffusion barrier around ① and ② is high in lattice constant shrink system. Thus from this result, it can be suggested that the lattice constant shrinkage does not have good effect on proton diffusion.

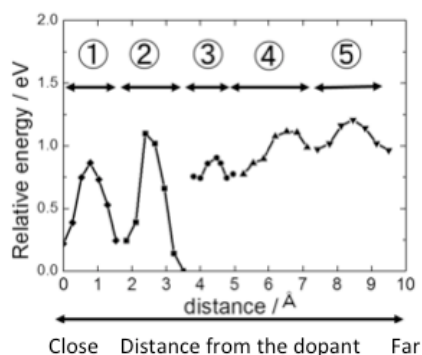


Fig.3 proton diffusion barrier in shrinkage system

In conclusion, lattice shrinkage and dopant segregation might not have positive effect on proton diffusion in  $\text{SrTiO}_3$ . There are not so much previous report on promotion of proton diffusion, thus this phenomenon might be difficult to occur. To confirm this, more experimental and theoretical investigation should be done.

## Reference

- [1] P.F. Yan et al.:Solid State Ionics 31-37 (2012) 222-223
- [2] C.Korte et al., *Phys. Chem. Chem. Phys.*, **10** (2008) 4623
- [3] J. M. Soler et al.: J. Phys.: Condens. Matter., 14, (2002) 2745-2779.
- [4] Y. Zhang, W. Yang: Phys. Rev. Lett., 80(4), (1998) 890.
- [5] H. J. Monkhorst and J. D. Pack: Phys. Rev. B, 13, (1976) 5188-5192.

# *Ab initio* molecular dynamics study of molecular dissociation by irradiation of X-FEL

Satoshi Ohmura

*Research Center for Condensed Matter Physics,*

*Hiroshima Institute of Technology, Miyake, Saeki-ku, Hiroshima 731-5193*

Recent developments in x-ray free electron laser (X-FEL) have opened up to access to the femtosecond-scale dynamics of molecules. When a molecule containing a heavy atom is irradiated by X-FEL in hard x-ray region, an inner-shell electron is emitted only in the heavy atom and many electrons are ejected from the molecule through the cascade of Auger decay process. The highly-charged molecule becomes quite unstable due to the large Coulomb repulsive force and dissociates quickly into many fragment ions. The fragment ions may convey information about the molecular structure. This technic is referred to as Coulomb explosion imaging. To improve this technic, it is needed to understand about the explosion process of the highly-charged molecule. Under these circumstance, we have investigated the dissociation mechanism of the highly-charged molecule after X-FEL radiation by using *ab initio* molecular dynamics simulations. In this study, we used iodouracil ( $\text{I-C}_4\text{H}_3\text{O}_2\text{N}_2$ ) as a target molecule. To take into account Auger cascade in the simulation, we gave charges to the system in sequence (charge build up).

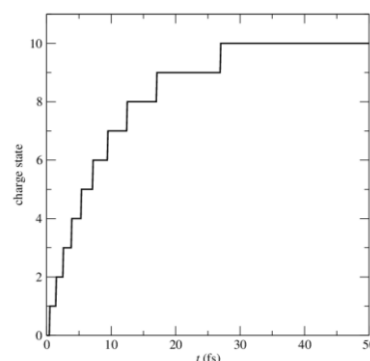


FIG. 1. Time evolution of the charge state of the iodouracil.

Figure 1 shows the time evolution of charge state of iodouracil. We calculated kinetic energies for ejected ions of the sequential charged molecule at the beginning, which is measurable physical quantity from experiments. The kinetic energies obtained from our simulation for hydrogen atoms ( $\text{H}^+$ ), and oxygen atoms ( $\text{O}^+$ ) and iodine atom ( $\text{I}^{2+}$ ) are about 28 eV, 14 eV and 5 eV, respectively. These values are consistent with experimental results. From these results, the sequential charge build up is thought to be effective. The simulation clarified the dissociation mechanism of iodouracil from a microscopic point of view.

# Ultrahigh-pressure structures of liquid oxygen and nitrogen

Satoshi Ohmura

*Research Center for Condensed Matter Physics,*

*Hiroshima Institute of Technology, Miyake, Saeki-ku, Hiroshima 731-5193*

Oxygen and nitrogen are infinitely familiar and famous elements because they are high abundant elements in the solar system and closely related to life on earth. Liquid states of these elements consist of diatomic ( $O_2$ ,  $N_2$ ) molecules. Under high pressure, breaking bond of these molecules on compression may lead to formation of extended structures. Recently, ultrahigh-pressure (multiterapascal pressure) research have been intensive studied with the recent progress in the experimental and computational methodologies. For the high pressure studies of liquid oxygen or nitrogen, however, structures of these liquid under multiterapascal pressures have not been investigated.

For these reasons, we have performed molecular dynamics (MD) simulations based on density-functional theory (DFT) to investigate the structural and electronic properties of liquids oxygen and nitrogen under multiterapascal pressure.

Figure 1 shows pair distribution functions  $g(r)$  of liquid oxygen at 154.1 GPa and 5017.7 GPa obtained by our simulation. At 154.1 GPa, the first peak at about 1.22 Å reflects the

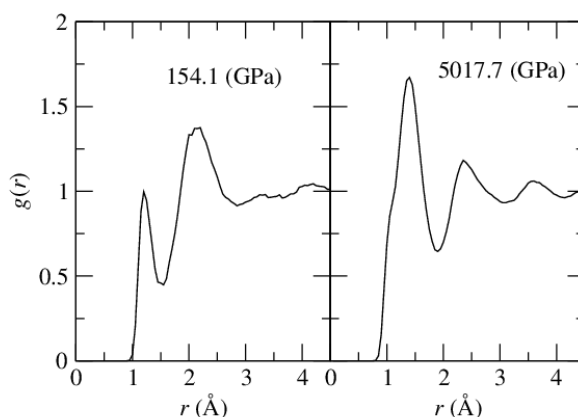


FIG. 1: pair distribution functions  $g(r)$  of liquid oxygen at 154.1 GPa and 5017.7 GPa.

covalent bond in  $O_2$  molecule. With increasing pressure, the second peak at about 2.3 Å, whose position shifts to smaller  $r$ . The first peak becomes incorporated into the second peak and changes to shoulder. On the other hand, for liquid nitrogen, the first peak of  $g(r)$ , which also reflects the covalent bond in  $N_2$  molecule, disappears completely at less than 100 GPa.

This study clarified multiterapascal -pressure structures of liquid oxygen and nitrogen. It also highlighted the difference between structures of these two liquids under high pressure.

# First-principles study on the defects in semiconductors

Jun YAMAUCHI

*Faculty of Science and Technology, Keio University*

*3-14-1 Hiyoshi, Kohoku-ku, Yokohama-shi, Kanagawa 223-8522*

As the size of devices on integrated circuits decreases, the behavior of dopant atoms make relatively larger effect on the device performance. Especially, it is very important to understand the unfavorable defects including the dopant atoms. The experimental observations on each defect is extremely difficult. One of the major difficulties for detecting dopant configurations is the very weak signals from the defects of very low concentration comparing to those from the matrix semiconductors. However, recently, as a solution for the above problem, it is suggested to use powerful synchrotron radiation facilities to measure the X-ray photoelectron spectroscopy (XPS) signals of defects. On the other hand, there have been few reliable first-principles core-level XPS calculations for impurity defects in semiconductors, because the local potential boundary condition of defect model systems has not yet been sufficiently evaluated. To obtain reliable shifts in the XPS binding energy, it is necessary to take a sufficiently large supercell for a defect.

To investigate the dependence of the substrate semiconductors on the XPS binding energies, we carried out a comprehensive study on the dopant core-level XPS binding energies for defects including B, Al, P, and As in crystalline 3C-SiC[2], and for defects including B, As, P in crystalline Si, using a first-principles calculation with careful evaluation of the lo-

cal potential boundary condition for the model system. The code used in this study is xTAPP, which is a hybrid paralleled density functional theory calculation program with plane-wave basis[1].

It is found that the relative range of XPS binding energy in SiC is about 4 eV, which is much larger than that of 1 eV in Si. This is because, while the Si is the elemental semiconductor, the SiC is the compound semiconductor and the deviation of the local potential is much larger than that in Si. On the other hand, the variation size of the relaxation energy, where the surrounding wave functions relax under the effect of the hole after the photoelectron emission, is roughly the same for the Si and SiC substrates.

The SiC has many polymorphs. We calculated some defects in 4H-SiC as well as 3C-SiC, and found that the dependence of the XPS binding energy on the polymorphs is not large.

## References

- [1] xTAPP (eXtended Tokyo Ab initio Program Package)  
(<http://xtapp.cp.is.s.u-tokyo.ac.jp>)
- [2] N. Matsushima, and J. Yamauchi: JPS Conf. Proc. **1** (2014) 012027.

## Geometric and electronic structures of honeycomb sheet consisting of atoms in 14th group

Noriaki TAKAGI<sup>1</sup>, Ryuichi ARAFUNE<sup>2</sup>, Mao KANNO<sup>1</sup>, and Emi MINAMITANI<sup>3</sup>

<sup>1</sup>*Department of Advanced Materials Science, University of Tokyo*

*Kashiwa-no-ha, Kashiwa, Chiba 277-8561,*

<sup>2</sup>*International Center for Materials Nanoarchitectonics, National Institute for Materials,*

*Science, 1-1 Namiki, Ibaraki 304-0044,*

<sup>3</sup>*Department of Materials Engineering, The University of Tokyo, 7-3-1 Hongo,*

*Bunkyo-ku, Tokyo 113-8656, Japan..*

The discovery of one-atom thick carbon honeycomb sheet, graphene, has triggered the competition to form exotic honeycomb materials and to uncover their hidden properties. Silicene, a two-dimensional (2D) honeycomb sheet consisting of Si atoms, has attracted lots of attention. It is theoretically predicted that a freestanding silicene hosts Dirac fermions [1] and that silicene is also a 2D topological insulator due to the sizable spin-orbit coupling of Si atom [2]. We carried out two projects: (1) exploring of new substrates to form exotic silicene and (2) determination of geometric structure of multilayer silicene.

(1) We investigated the stability of silicene on Ni(111) covered with a hexagonal boron nitride (h-BN) layer by using density functional theory (DFT) calculations. The DFT calculations were carried out by the plane-wave-based Vienna Ab initio Simulation Package (VASP) [3, 4] with the projected augmented wave method [5]. The silicene on h-BN/Ni(111) was modeled by using a

supercell which consists of a silicene layer lying on a h-BN layer on top of a 5-layer Ni slab with a vacuum of 15 Å thick along the surface normal. The positions of atoms in silicene, h-BN, and top four layers of Cu slab were optimized without any constraint until the forces on individual atoms were less than 0.01 eV/Å. In order to weak interface couplings, van der Waals correction was included. From the total energy calculations for various configurations of silicene lattice relative to the h-BN lattice, we found that the silicene is stable, and that Dirac fermion feature survives similarly to the freestanding silicene.

(2) The multilayer silicene is also attractive because the recent of photoemission experiment has presented a Dirac fermion feature [6]. Two structure models have been proposed for the multilayer silicene. One is a bilayer honeycomb structure in which two buckled honeycomb layers are stacked [7]. The other is very similar to the reconstructed structure formed by the

adsorption of Ag atoms on Si(111) [8]. There is a hot debate about the geometric structure. We calculated electronic structures of both models and tried to compare the energy spectrum of multilayer silicene measured by using metastable atom electron spectroscopy (MAES).

#### Reference

- [1] S. Cahangirov et al.: Phys. Rev. Lett. **102**, 236804 (2009).
- [2] M. Ezawa, Phys. Rev. Lett. **109**, 055502 (2012).
- [3] G. Kresse and J. Furthmüller: Phys. Rev. B **56** (1996) 11169.
- [4] G. Kresse and J. Furthmüller: Comput. Mater. Sci. **6** (1996) 15.
- [5] P. E. Blöchl: Phys. Rev. B **24** (1994) 17953.
- [6] P. De Padova et al.: Appl. Phys. Lett. **102**, 163106 (2013).
- [7] Z.-X. Guo, A. Oshiyama: Phys. Rev. B **89**, 155418 (2014).
- [8] T. Shirai et al.: Phys. Rev. B **89**, 241403(R) (2014).



## Geometric structure and magnetism of molecules connecting with metal electrode

Noriaki TAKAGI<sup>1</sup>, Ryouichi HIRAOKA<sup>1</sup> and Emi MINAMITANI<sup>2</sup>

<sup>1</sup>*Department of Advanced Materials Science, University of Tokyo  
Kashiwa-no-ha, Kashiwa, Chiba 277-8561*

<sup>2</sup>*Department of Materials Engineering, The University of Tokyo, 7-3-1 Hongo,  
Bunkyo-ku, Tokyo 113-8656, Japan.*

Molecule under scanning tunneling microscope (STM) junction provides a model of a single molecule quantum dot. The metal substrate and the tip of STM work as electrodes. This molecular dot can be used as a simulator to manipulate the quantum state of the dot by changing the tip-molecule distance to tune the coupling strengths of the molecule with the electrodes.

We tried to manipulate the Kondo resonance states of iron(II) phthalocyanine (denoted as FePc) on Au(111) [1,2] experimentally. When the tip was far away from the FePc molecule on Au(111), a Fano-Kondo (F-K) antiresonance was observed together with a broad FK resonance. As the tip approached to the central Fe ion of the molecule, the F-K antiresonance gradually became symmetric and a pair of conductance steps appeared in the dI/dV spectrum. The broad FK resonance also disappeared finally when the tip

touched with the molecule. The conductance step was split by applying an external magnetic field vertically to the molecular plane. This indicates that the origin of the step is spin excitation relevance of fine energy structure caused by the spin-orbit interaction (SOI). This spectral evolution was reversibly observed when the tip moved away from the molecule. These results indicate the crossover of Hamiltonian of the molecular quantum dot between the Kondo regime and the regime governed by SOI.

In order to understand the experimental results, we calculated in detail the geometric structure, electronic structure and spin state of FePc in the STM junction by the plane-wave-based Vienna Ab initio Simulation Package (VASP) [3, 4] with the projected augmented wave method [5]. The STM junction was modeled by using a supercell. The STM tip was modeled by a trigonal pyramid

consisting of Au atoms. The FePc molecule is located on a four-layer Au slab. To describe the Coulomb interaction at the Fe ion, we used local density approximation +U method. We calculated the geometric structure, density of states and spin state as a function of the position of the STM tip. Approaching the tip to the  $\text{Fe}^{2+}$  ion, the spin state and the electronic configuration were not drastically changed. In contrast, the position of the  $\text{Fe}^{2+}$  ion was significantly changed. When the tip was far away from the molecule, the ion was slightly shifted to the Au substrate because of the chemical interaction between them. When the tip was close to the ion, the ion was moved to the tip. We found the switching of the ion position takes place. Looking at the charge density distribution, the electron charges are accumulated at the interface between the ion and the substrate. When the tip was set close to the ion, the accumulation is reduced and instead the charges are accumulated in the region of tip-ion interface. The spectral evolution and the crossover is explained by changing the coupling of molecule and substrate.

#### Reference

- [1] N. Tsukahara *et al.*: Phys. Rev. Lett. **106** (2011) 187401.
- [2] E. Minamitani *et al.*: Phys. Rev. Lett. **109**, 086602 (2012).
- [3] G. Kresse and J. Furthmüller: Phys. Rev. B **56** (1996) 11169.
- [4] G. Kresse and J. Furthmüller: Comput. Mater. Sci. **6** (1996) 15.
- [5] P. E. Blöchl: Phys. Rev. B **24** (1994) 17953.

# First-principles study on magnetism and atomic structures of transition-metal oxides

Masayuki TOYODA

*Institute of Scientific and Industrial Research,  
Osaka University, 8-1, Mihogaoka, Ibaraki, Osaka 567-0047*

The magnetic spin structures of the A-site-ordered perovskite oxides  $\text{YMn}_3\text{Al}_4\text{O}_{12}$  and  $\text{LaMn}_3\text{V}_4\text{O}_{12}$ , and the isostructural phase transition in  $\text{LaCu}_3\text{Fe}_4\text{O}_{12}$  have been investigated by using first-principles calculations.

$\text{YMn}_3\text{Al}_4\text{O}_{12}$  and  $\text{LaMn}_3\text{V}_4\text{O}_{12}$  both crystallize in cubic  $Im\bar{3}$  structure and exhibit antiferromagnetic (AFM) spin ordering at low temperatures. However, the ground-state spin structure is collinear  $G$ -type AFM ( $G$ -AFM) in  $\text{YMn}_3\text{Al}_4\text{O}_{12}$  whereas non-collinear AFM with rhombohedral  $R\bar{3}$  symmetry in  $\text{LaMn}_3\text{V}_4\text{O}_{12}$ . In order to clarify the microscopic origin of those spin structures, the electronic structures were calculated based on the density-functional theory and the generalized gradient approximation. The calculations were performed on FUJITSU PRIMEHPC FX10 (System C) in the super-computer center of ISSP. The calculations revealed that the magnetic spin structures are determined by Mn-O-Mn super-exchange interaction, which changes the amplitude and sign depending on the Mn valence. In  $\text{YMn}_3\text{Al}_4\text{O}_{12}$ , the nearest neighbor (NN)  $\text{Mn}^{3+}$  ions are coupled antiferromagnetically to stabilize the  $G$ -AFM structure. In  $\text{LaMn}_3\text{V}_4\text{O}_{12}$ , on the other hand, 2nd NN pairs of  $\text{Mn}^{2+}$  ions are coupled antiferromagnetically, which stabilizes the noncollinear AFM spin structure [1].

The isostructural phase transition in  $\text{LaCu}_3\text{Fe}_4\text{O}_{12}$  occurs at  $T_c = 393$  K, accompanied by decrease in the crystal volume, magnetic transition from AFM to paramagnetism

(PM), and insulator-to-metal phase transition. Furthermore, a similar phase transition also occurs when pressure is applied. Our calculations revealed that the Cu valence is  $\text{Cu}^{3+}$  in the low-temperature (or larger-volume) insulating AFM phase but  $\text{Cu}^{2+}$  in the high-temperature (or smaller-volume) metallic PM phase. The change of Cu valence from  $\text{Cu}^{3+}$  to  $\text{Cu}^{2+}$  and corresponding charge transfer between Cu and Fe ions play a crucial role both in the temperature- and pressure-induced phase transitions.

## References

- [1] T. Saito, M. Toyoda, C. Ritter, S. Zhang, T. Oguchi, J. P. Attfield, and Y. Shimakawa, Phys. Rev. B **90**, 214405 (2014).
- [2] K. Isoyama, M. Toyoda, K. Yamauchi, and T. Oguchi, J. Phys. Soc. Jpn. **84**, 034709 (2015).

# Theoretical elucidation on the full reaction mechanism of threonine synthase

Mitsuo SHOJI

*Center of Computational Science, University of Tsukuba, 1-1-1 Tennodai,  
Tsukuba, Ibaraki, 305-8577 Japan*

Molecular mechanisms of the efficient chemical reactions and energy transformations in biological systems are crucially important to be solved not only for biology but also for various application fields including medicine, pharmacy, chemical industry, and material developments, and rapid returns to the society can be expected by the developments of researches. Especially, chemical reactions in enzymes are extremely efficient and highly selective, the detailed understandings for why such abilities are possessed are very important. For example, the reactions in photosynthesis are helpful for the developments of efficient artificial solar systems, and these research areas have attracted a lot of attentions in recent years. X-ray diffraction (XRD) analysis at the Spring-8, x-ray free-electron leaser (XFEL) at SACLA, high-sensitive EPR and time resolved spectroscopies are the typical cases. However, by these drastic experimental developments, the chemical reaction mechanisms and detections of the proton atoms are not easily performed experimentally. Therefore, whole reaction mechanisms at the atomic level are still unclear for many important

biological systems.

On the other hand for theoretical approaches, fine analyses on the stability, dynamics and geometrical structures can be performed in most all cases, and by using modern theoretical methodologies, physical properties which can directly compare to the experimental results can be calculated. For such computational simulations, huge amounts of computational resources are required, however, by utilizing supercomputers (SCs), it becomes easier to perform such heavy theoretical calculations.

We have been performed classical molecular dynamics (MD) and mixed quantum mechanics/molecular mechanics (QM/MM) calculations using large-scale theoretical models. We have investigated for the (1) oxygen evolving complex in photosystem II, light absorption in photosystem, circular dichroism of heme in myoglobin, reaction mechanism of nitrile hydratase. Their molecular details were successfully elucidated in good agreements with experimental results [1-8]. In this report, the results obtained for the threonine synthase is mainly described in the following sections [1].

Threonine synthase (ThrS) is a pyridoxal-5'-phosphate (PLP)-dependent enzyme which catalyzes the last step of the L-threonine biosynthesis. The reaction involves a stereospecific and regiospecific steps and is most complicated among the PLP enzymes. ThrS is characterized as a "product-assisted catalysis", which means that the product phosphate ion enhances the latter catalytic steps, and this mechanism is one of the critically important functions of native enzymes. Exhaustive theoretical search on the intermediate states and the reaction pathways were performed by using the QM/MM (quantum mechanics/molecular mechanics) method for the latter half reactions from PLP- $\alpha$ -aminocrotonate aldimine to the main product of L-threonine and to the side product of vinylglycine (Figure 1). A complete reaction mechanism has been revealed, and we found that (1) PLP-pyridine N1 is unprotonated, (2) phosphate ion is monoprotonated, and (3) the protonated amino group of Lys 61 functions as a general acid in the regiospecific protonation at C $\alpha$  of the PLP Schiff base. Phosphate ion maintains a hydrogen bond to the hydroxyl group of the substrate and that contributes to stabilize the main reaction pathway. We found that the hydrogen bond interaction is critically important for the product-assisted catalysis. These findings are very important not only for the understanding of the catalytic reactions of PLP enzymes, but also for all the chemical reactions to improve the reaction

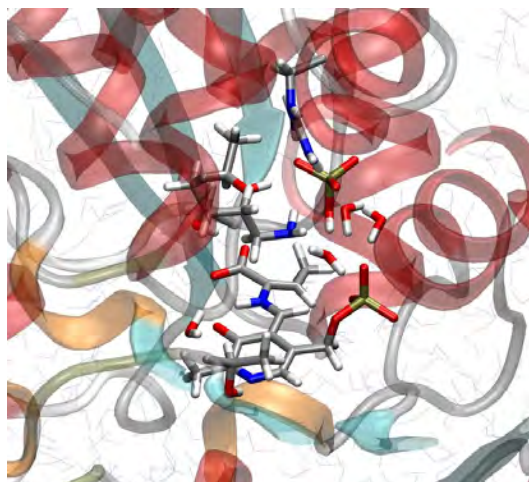


Fig 1. Active site of the threonine synthase. QM atoms are shown in the tube model.

efficiencies and selectivities.

## References

- [1] M. Shoji, et al: J.Am.Chem.Soc. **136** (2014) 4525-4533.
- [2] M. Shoji, et al: Chem.Phys.Lett. **608** (2014) 50-54.
- [3] K. Komatsu, et al: Mol.Phys, accepted 2014.
- [4] K. Komatsu, et al: Int.J.Astrobio., accepted 2014.
- [5] M. Nagai, et al: J.Phys.Chem. B **119** (2015) 1275-1287.
- [6] M. Kayanuma, et al: Chem.Phys.Lett. **623(2)** (2015) 8-13.
- [7] M.Shoji et al: Chem.Phys.Lett. **623(2)** (2015) 1-7.
- [8] M. Shoji et al: Chem.Phys.Lett. **627(1)** (2015) 44-52.

# Defect formation energies due to hydrogen and helium-dopants on interstitial sites in a pyrochlore-type $\text{Y}_2\text{Ti}_2\text{O}_7$ oxide

Bun Tsuchiya<sup>1</sup>, Kazuhito Ohsawa<sup>2</sup>

<sup>1</sup>*Faculty of Science and Technology,*

*Meijo University, 1-501, Shiogamaguchi, Tempaku-ku, Nagoya 468-8502*

<sup>2</sup>*Institute for applied Mechanics, Kyushu University,*

*Kasuga-koen 6-1, Kasuga-shi, Fukuoka 816-8580*

Nano-structured ferritic alloys (NFAs) containing a very high density of nanometer-sized pyrochlore-type Y-Ti-O oxide nanofeatures (NFs) are ones of candidate materials for advanced fission and fusion energy applications [1]. In the present study, in order to assess the relative stability of trapping H and He in  $\text{Y}_2\text{Ti}_2\text{O}_7$ , various point defect structures with H and He atoms doped into the tetrahedral and octahedral-interstitial sites and the associated energies, that is indicative of defect formation energies, have been investigated using ab initio density functional theory (DFT) calculations [2] and compared with those of H and He interstitials in iron (Fe) and Fe vacancy (substitutional).

The core-electron interactions are described by the projector augmented wave method (PAW) as implemented in VASP. Convergence tests show that a high energy cutoff of 650 eV and a  $5 \times 5 \times 5$  Monkhorst-Pack k-mesh for  $\text{Y}_2\text{Ti}_2\text{O}_7$  in its conventional cell, and 350 eV and  $7 \times 7 \times 7$  k-mesh for Fe in its  $4 \times 4 \times 4$  bcc supercells, are sufficient for both pure bulk and defect calculations.

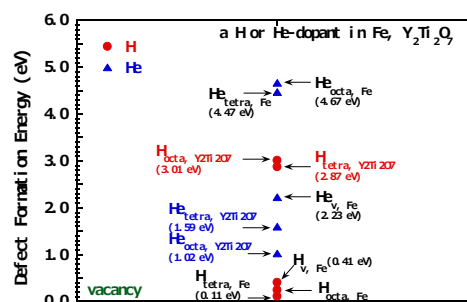


Fig. 1: Defect formation energies due to H and He doped into  $\text{Y}_2\text{Ti}_2\text{O}_7$ .

The extrinsic H and He atoms prefer to occupy individual tetrahedral and octahedral interstitial sites, respectively, in  $\text{Y}_2\text{Ti}_2\text{O}_7$ , with resulting defect formation energies of 2.87 eV and 1.02 eV, respectively, according to the DFT calculation. In addition, the occupancy of He atom of the octahedral-interstitial in  $\text{Y}_2\text{Ti}_2\text{O}_7$  is more favored than that of tetrahedral, octahedral interstitial or substitutional site (defect formation energies : 4.47, 4.67, and 2.23 eV, respectively) in Fe. On the other hand, the trapping of H at any of the interstitial and substitutional sites in Fe is more favored than those in  $\text{Y}_2\text{Ti}_2\text{O}_7$ .

## References

- [1] P. Erhart, J. Appl. Phys. **111** (2012) 113502.
- [2] <http://www.top500.org/lists/2010/11R>

# First-principles approach to magnetic properties and spin-orbit interaction

Takashi MIYAKE

*Nanomaterials Research Institute, AIST  
Umezono, Tsukuba, Ibaraki 305-8568*

## Rare-earth magnet compounds [1]

Large magnetization and high coercivity are required for high-performance permanent magnet. Recently, NdFe<sub>12</sub>N has been synthesized as a film on top of W underlayer on the MgO substrate [2]. The compound shows better intrinsic magnetic properties than Nd<sub>2</sub>Fe<sub>14</sub>B, the champion magnet compound, for wide temperature range between room temperature and the Curie temperature, although thermodynamic stability is a bottleneck for industrial applications.

We have investigated the magnetic properties of RFe<sub>12</sub>N and RFe<sub>11</sub>TiN ( $R=Y, Nd, Sm$ ) by the first-principles method using QMAS code. The calculation is based on the density functional theory with the generalized gradient approximation. The rare-earth 4f electrons are treated as open-core states. The magnetocrystalline anisotropy is evaluated from the crystal field theory. The crystal-electric-field (CEF) parameter  $A_l^m$  is computed from the Kohn-Sham potential as

$$\langle r^l \rangle A_l^m = F_l^m \int_0^{R_c} W_l^m(r) \phi^2(r) dr, \quad (1)$$

where  $F_l^m$  is a prefactor of the real spherical harmonics, and  $W_l^m$  is the radial part of the Kohn-Sham potential at the rare-earth site. The magnetic anisotropy constant is estimated from the lowest CEF parameter  $A_2^0$  as

$$K_1 = -3J(J - \frac{1}{2})\alpha_J \langle r^2 \rangle A_2^0 n_R, \quad (2)$$

where  $J$  is the total angular momentum,  $n_R$  is

the concentration of the rare-earth atoms, and  $\alpha_J = -7/1089$  (13/315) for Nd (Sm).

We found that the magnetization is enhanced by nitrogenation in all the compounds we have studied. The increment of the magnetic moment depends on  $R$ , but does not strongly depend on Ti substitution. The CEF parameter  $\langle r^2 \rangle A_2^0$  substantially increases by nitrogenation for  $R=Nd$  and Sm. This suggests that uniaxial (in-plane) anisotropy is induced in the Nd (Sm) compound.

## Trigonal Tellurium under pressure [3]

Trigonal tellurium has characteristic structure. Helical chains are arranged in a hexagonal array. The unit cell contains three atoms. The space group is  $P3_121$  or  $P3_221$ , and there is no inversion symmetry.

We have studied the electronic states of tellurium using first-principles calculation. The calculation is based on the fully relativistic density functional theory in the local density approximation, and the GW self-energy correction is added on top of it. The Hamiltonian is represented in the maximally localized Wannier basis, and interpolated for studying energy levels at arbitrary  $k$  point.

When the spin-orbit interaction is neglected, the material undergoes insulator-semimetal transition under pressure. As the pressure is increased further, a Dirac cone is formed at certain pressure in the metallic phase. When the spin-orbit interaction is included, the transition pressure decreases, and a Weyl

semi-metallic phase appears between the insulating phase and metallic phase.

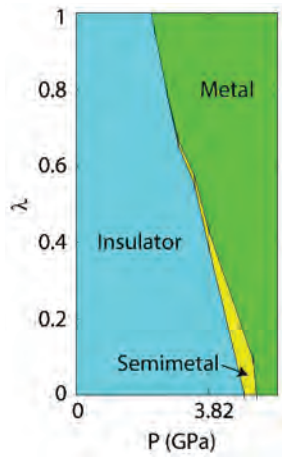


Figure 1: Phase diagram of trigonal tellurium under pressure. The vertical axis is the scale factor of the spin-orbit interaction.

## References

- [1] Yosuke Harashima, Kiyoyuki Terakura, Hiori Kino, Shoji Ishibashi and Takashi Miyake, JPS Conf. Proc. **5**, 011021 (2015).
- [2] Y. Hirayama, Y. K. Takahashi, S. Hiro-sawa, and K. Hono, Scr. Mater. **95**, 70 (2015).
- [3] Motoaki Hirayama, Ryo Okugawa, Shoji Ishibashi, Shuichi Murakami and T. Miyake, JPS Conf. Proc. **5**, 011024 (2015).



## Pt adsorption sites in rutile-TiO<sub>2</sub> (110) surface

Kazuaki Toyoura

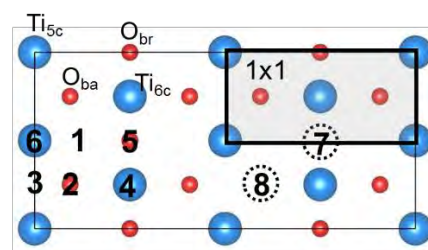
*Department of Materials Science and Engineering,  
Nagoya University, Furo, Chikusa, Nagoya 464-8603*

The (110) surface of rutile TiO<sub>2</sub> is often used as a model system for fundamental research in the fields of surface science and catalysis [1-3]. Therefore, adsorption of metal atoms and clusters on the surface and their catalytic functions have been well investigated by means of both experimental and theoretical approaches. In the present study, Pt adsorption on the surface was theoretically investigated from first principles.

All the calculations were performed on the basis of the first-principles projector augmented wave (PAW) method implemented in the VASP code [4]. The plane wave cutoff energy was set to be 500 eV. The 3d4s orbitals for Ti; 2s2p for O; and 5d6s for Pt were treated as valence states. The generalized gradient approximation (GGA) parametrized by Perdew, Burke, and Ernzerhof [5] was used for the exchange-correlation term with +U correction for Ti3d electrons ( $U = 5.8$  eV) [6]. A (2×4) surface slab with 7 cation layers and a 14 Å vacuum layer was used with a 2×2×1 grid for k-point sampling in the Brillouin zone.

Possible adsorption sites of a single Pt atom on the TiO<sub>2</sub> (110) surface and the calculated adsorption energies at the individual sites were

shown in Fig. 1. In the stoichiometric surface without oxygen vacancies (sites 1–6), the hollow1 site has the highest adsorption energy. On the other hand, a Pt atom tends to be adsorbed to oxygen vacancies in the reduced surface, whose adsorption energies are ~1 eV higher than those at the hollow1 site. This indicates that the surface off-stoichiometry should greatly influence on the Pt adsorption, possibly leading to change in the catalytic function.



- |                               |                                       |
|-------------------------------|---------------------------------------|
| 1 : hollow1 (2.72 eV)         | 5 : O <sub>br</sub> (1.47 eV)         |
| 2 : O <sub>ba</sub> (2.31 eV) | 6 : Ti5c (1.31 eV)                    |
| 3 : hollow2 (1.85 eV)         | 7 : O <sub>br</sub> vacancy (3.64 eV) |
| 4 : Ti6c (1.76 eV)            | 8 : O <sub>ba</sub> vacancy (3.82 eV) |

Fig. 1: Possible Pt adsorption sites on the rutile TiO<sub>2</sub> (110) surface. Two kinds of oxygen vacancy sites were considered in addition to the six sites on the stoichiometric surface. Energies in parentheses are the Pt adsorption energies at the individual sites.

### References

- [1] U. Diebold, *Surf. Sci. Rep.* **48**, 53 (2003).
- [2] M. V. Ganduglia-Pirovano, et al. *Surf. Sci. Rep.* **62**, 219 (2007).

- [3] C. L. Pang et al., *Chem. Rev.* **113**, 3887 (2013).
- [4] G. Kresse et al., *Phys. Rev. B* **59**, 1758 (1999).
- [5] J. P. Perdew et al., *Phys. Rev. Lett.* **77**, 3865 (1996).
- [6] K. Yang et al., *Phys. Rev. B* **81**, 033202 (2010).

# Search for new electronic properties of new nanoscale interfaces

Katsuyoshi KOBAYASHI

*Department of Physics, Ochanomizu University  
2-1-1 Otsuka, Bunkyo-ku, Tokyo 112-8610*

In 2014 we studied the electronic states of SnTe and PbTe(001) monolayers.

Recently topological crystalline insulators are extensively studied. Topological crystalline insulator (TCI) is a concept introduced by Fu [1]. Electronic states of insulators are classified according to topological numbers defined by point group symmetries of crystals. The first realistic materials of TCI are SnTe and its alloy with Pb. They were theoretically proposed and have been experimentally verified. They are three-dimensional materials. Recently two-dimensional (2D) materials of TCI are theoretically predicted, and their new applications were proposed [2]. However, they have not been materialized experimentally. We theoretically studied electronic states of 2D TCI thin films.

The proposal of 2D TCI is based on electronic-state calculations for free-standing thin films [2]. When we make some experiments or devices using 2D TCI, it would be necessary to place them on substrates or embed in materials. In contrast to the topological insulators whose topological character is protected by the time-reversal symmetry, the topological character of TCI is guaranteed by crystal symmetries of systems which is easily broken by the interaction with substrates and environments. Therefore it is important to study the effect of substrates and environments on electronic structures of 2D TCI. In this study we calculated electronic states of SnTe and PbTe monolayers with supports [3].

We calculate electronic states of isolated monolayers assuming planar structures by a density-functional method. We find that the PbTe monolayer has edge states that are char-

acteristics of TCI. However, geometrical optimization shows that the planar structure is unstable. Buckling occurs and the mirror symmetry is broken. In order to maintain the planar structure we consider structures of monolayers with supports. We choose alkali-halide surfaces as supports. Figure 1 shows a band structure of a SnTe monolayer wire sandwiched between two NaBr surfaces. Edge states are present in the band gap between the valence and conduction bands, which suggests that this system is a 2D TCI. Geometrical optimization shows that the planar structure is stable in this system.

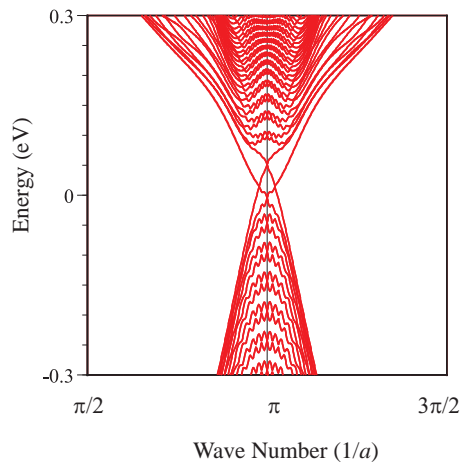


Figure 1: Band structure of a SnTe monolayer wire sandwiched between two NaBr surfaces.

## References

- [1] L. Fu: Phys. Rev. Lett. **106** (2011) 106802.
- [2] J. Liu *et al.*: Nature Mat. **13** (2014) 178.
- [3] K. Kobayashi: to be published in Surf.Sci.

# Electronic structure of $\beta$ -FeSi<sub>2</sub>(100) surface

Ken HATTORI

*Graduate School of Materials Science, Nara Institute of Science and Technology  
Takayama, Ikoma, Nara 630-0192*

Recently the authors' group found the formation of  $\beta$ -FeSi<sub>2</sub>(100) on Si(001) prepared in ultra-high vacuum, using scanning tunneling microscopy (STM) and low-energy electron diffraction (LEED) [1]. Using Simulation Tool for Atom TEchnology (STATE)-Senri [2] in SCC-ISSP system A, the author calculated total energies and STM images for  $\beta$ -FeSi<sub>2</sub>(100)1x1 with adatoms (20 models, 66 atoms/model) and without adatoms (1 model, 64 atoms), in order to survey the surface structure.

The details for the calculations are described in Ref. [1]. The calculated substrate structure consists of 1st-layer Si (8 atoms per  $\beta$ (100)1x1 unit-cell)/2nd-Fe (2 atoms)/3rd-Fe (2)/4th-Si (8)/5th-Fe (4)/6th-Si (8)/7th-Fe (2)/8th-Fe (2)/9th-Si (8)/10th-Fe (4)/11th-Si (8)/12th-H (8). The atomic positions were relaxed except those in the last three layers.

Two hollow-site models (named as H<sub>3</sub> and H<sub>4</sub>, and they were almost degenerated) were found to be stable for both Fe and Si adatom models, having  $p2$  symmetry. However, the experimental LEED results require  $p2gg$  symmetry, thus these models can be denied. Only the one candidate, WO model (without adatoms) with  $p2gg$  symmetry, was consistent with the STM and LEED results, moreover, indicated almost the same structure obtained by LEED I-V analysis [1]. Therefore, we can state *the WO model is the surface structure of  $\beta$ -FeSi<sub>2</sub>(100)*.

The author also calculated the  $k$ -resolved atomic orbital based local density-of-states ( $k$ -AO-LDOS) [3], to identify surface electronic states. A  $k$ -AO-LDOS,  $\rho(k, E, i, l)$ , is a function of a wave vector  $k$ , energy  $E$ , atom species  $i$  and orbital of the  $i$ -th atom  $l$ .  $k$ -AO-LDOS was averaged over the LDOS of atoms (number

of which is  $N$ ) within a layer (or a slab) and summed over the corresponding orbitals of the atoms,

$$\rho(k, E) = \frac{1}{N} \sum_i \sum_l \rho(k, E, i, l). \quad (1)$$

When  $i$  runs over all atoms in the slab, Eq. 1 shows  $\rho_{tot}(k, E)$  ( $N_{tot} = 64$ ) for the all atoms, while the topmost atoms only,  $\rho_{surf}(k, E)$  ( $N_{surf} = 8$ ) for the surface atoms. In order to enhance the  $k$ -AO-LDOS weight of the particular layer, *i.e.*, surface state components, the surface  $k$ -AO-LDOS was squared and normalized on the total  $k$ -AO-LDOS. This partial  $k$ -AO-LDOS was defined as,

$$\rho'(k, E) = \frac{N_{surf}}{N_{tot}} \frac{\rho_{surf}}{\rho_{tot}} \rho_{surf} = \eta \rho_{surf} \quad (2)$$

*The partial  $k$ -AO-LDOS  $\rho'(k, E)$  predicted some surface-states dispersions clearly even in the bulk projection [1]. One of them exists in the band gap crossing the Fermi level, which leads to metallic nature. Indeed, a previous angle-integrated photoemission measurements indicated the metallic behavior [4].*

The author thank Prof. Morikawa in Osaka University, Dr. Yanagisawa in Ryukyu University, and Dr. Hamada in NIMS for their great support in STATE-Senri calculations.

## References

- [1] O. Romanyuk, K. Hattori, M. Someta, and H. Daimon: Phys. Rev. B **90** (2014) 155305.
- [2] Y. Morikawa: Phys. Rev. B **63** (2001) 033405, and references therein.
- [3] K. Toyoda, I. Hamada, S. Yanagisawa, and Y. Morikawa: Appl. Phys. Express **3** (2010) 025701.
- [4] J. Chrost, J. Hinarejos, P. Segovia, E. Michel, and R. Miranda: Surf. Sci. **371** (1997) 297.

## Bonding states of organic molecules adsorbed at defects on metal surface

Ken-ichi SHUDO

*Faculty of Engineering/Science,*

*Yokohama National University, Hodogaya-ku, Yokohama 240-8501 JAPAN*

Organic molecules are of great interest as new material for semiconductor and functional devices. Aromatic molecules on metal and semiconductor surfaces are typical interfacial systems to be benchmarked. It is useful to elucidate the electronic states and structure of such heterostructure at the nanometer scale.

We take three-dimensional aromatic molecules, carboran and its derivative, on a stable metal surface for future functional applications. In the current project, we estimated the stable structure in adsorption, and bonding energy in terms of the bonding site by means of first principle electronic simulation partly executed on the Facility of Supercomputing Center at the Institute for Solid State Physics (SCC-ISSP).

We used Vienna Ab initio Simulation Package (VASP) code. Molecules of *p*-carboran-thiol and decamethyl carboran-thiol are adsorbed on Au(111) slab models (The former is shown in Figure 1.) The size of the slab was larger enough than the inter-molecular size of crystalline, so that this structure represents the isolated adsorption at the dilute coverage.

The *p*-carboran-thiol is preferably adsorbed at the three-fold hollow site slightly shifted from the center. The binding energy of this molecule is 1.66 eV (with H-dissociation canceled out). A sharp electronic state of Au-S bond lays at -1.8 eV from Fermi level.

The decamethyl derivative has much weaker adsorption energy. This instable adsorption to the flat terrace is due to steric effect of ten methyl groups on the surface. This suggests that the decamethyl derivative is hard to be adsorbed on the terrace at room temperature. This result is consistent with our observation with a scanning tunneling microscope (STM).

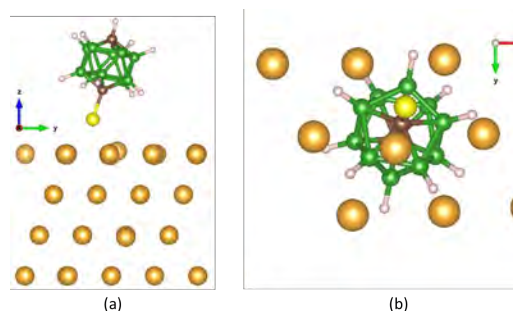


Figure. 1. Stabilized structure of *p*-carboran-thiol adsorbed on Au(111) surface. (a) top and (b) bottom views.

# First-Principles Molecular Dynamics Simulations on Water Dissociation in Water-Bi-Layer on Stepped Pt Surface

PHO VAN BUI, TAKUYA NISHITANI, HIDETOSHI KIZAKI, KOUJI INAGAKI, and  
YOSHITADA MORIKAWA

*Graduate School of Engineering,*

*Osaka University, 2-1, Yamada-oka, Suita, Osaka 565-0871*

Water interaction with Pt surface plays important roles in many catalytic surface reactions, corrosion processes, and electrochemistry. Recently, intact adsorption and dissociation of water on flat Pt have been extensively studied by both experiments and simulations [1, 2]. A recent study on adsorption and dissociation of water at the edge of Pt(211) surface showed that the dissociation energy is 0.2 eV for a dimer and nearly zero in the case of a trimer [3]. Moreover, water adsorption on a stepped Pt(111) surface, which is observed after deposition of Pt by X-ray diffraction [4] and commonly occurring in realistic situations, is not well understood.

In this study, we use first-principles simulation tool for atom technology program package (STATE) to elucidate the adsorption and dissociation of water on a stepped Pt(111) surface and between Pt/SiC interface during the etching of SiC in water before molecular dynamics simulations. The calculations are based on the density functional theory within a generalized gradient approximation of Perdew et al. Barrier height is evaluated by means of climbing image nudged elastic band method

[5]. A stepped Pt(111) surface composed of 3-layer slab, in which the two topmost layers are kept fixed to mimic the bulk. A step-and-terrace 3C-SiC (111) surface was used as a model for the simulation as shown in Fig. 1. The model is periodically repeated unit cells of four bi-layers. During the simulation, the two topmost atomic layers with terminated surface atoms were allowed to fully relax, while the remaining atoms were kept fixed to maintain the substrate structure.

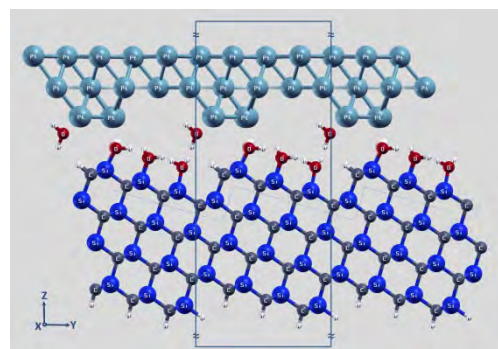


Fig. 1: 3C-SiC(111) and Pt(111) surfaces in the simulation model. The box showed a unit cell.

In this study, we focus on the reaction pathways and reaction barriers of the interaction between  $\text{H}_2\text{O}$  molecules and OH-terminated step edge Si with the present

of platinum (Pt) catalyst in the calculation model. The adsorption of water on a stepped Pt surface is preferentially at the step edge of Pt, stabilized by the effect of chemical bonds with Pt and hydrogen bonds. The results show that the barrier height of water dissociation on Pt affected by the distance of Pt and SiC surfaces. The shorter distance between Pt and SiC surfaces, the smaller the barrier height. The adsorption and dissociation of water at Pt/SiC interface play important roles in etching of SiC in water.

## References

- [1] A. Hodgson et al., Sur. Sci. Reports 64, (2009) 381-451.
- [2] J. L. Fajín, et al., J. Phys. Chem. A 118, (2014) 5832-5840.
- [3] D. Donadio et al., J. Am. Chem. Soc. 134, (2012) 19217-19222.
- [4] T. Aoltonen et al., Chem. Matter. 15, (2003) 1924.
- [5] Henkelman et al., J. Chem. Phys. 113 9901 (2000).

# Electronic Structure of Rare Earth Magnets

Hisazumi AKAI

*Institute for Solid State Physics, University of Tokyo*  
*Kashiwa-no-ha, Kashiwa, Chiba 277-8581*

The most important permanent magnet materials up to now is  $\text{Nd}_2\text{Fe}_{14}\text{B}$  for its high energy product. It, however, has a problem that Dy, which is a rare element, must be added to keep the good performance at operating temperature of around  $200 \sim 300^\circ\text{C}$ . Decreasing the content of Dy from  $\text{Nd}_2\text{Fe}_{14}\text{B}$  magnets is a big issue. Yet another candidate of high efficiency permanent magnet materials is  $\text{Sm}_2\text{Fe}_{17}\text{N}_3$ . It shows much larger magnetic anisotropy and higher Curie temperature than  $\text{Nd}_2\text{Fe}_{14}\text{B}$ , although its saturation magnetization is slightly smaller than that of  $\text{Nd}_2\text{Fe}_{14}\text{B}$ 's. Unfortunately,  $\text{Sm}_2\text{Fe}_{17}\text{N}_3$  is not chemically stable at high temperature, which prevent us to produce permanent magnets by sintering.

In order to design permanent magnet materials that meet the requirement for new generation permanent magnets, the mechanisms that govern the magnetization, Curie temperature, and magnetic anisotropy of existing permanent magnet materials must be revealed. This is not an easy task since those magnetic systems contains rare-earth metals as an ingredient. One of our main efforts concern with how to deal with f-states of rare-earths in the framework of the density functional theory (DFT). We have developed the method of self-interaction correction (SIC) and the optimised effective potential (OEP) method within exact-exchange (EXX) and static RPA (sRPA) schemes[1].

Figure 1 shows the structure of  $\text{Nd}_2\text{Fe}_{14}\text{B}$  and some of exchange coupling parameters calculated in the framework of SIC. The couplings between Nd and Fe are one order of magnitude smaller than those between Fe's. Although

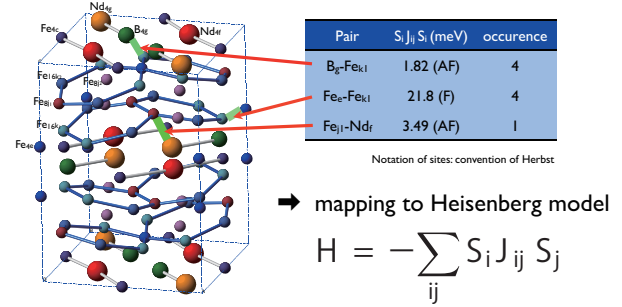


Figure 1: Some of calculated exchange coupling parameters of  $\text{Nd}_2\text{Fe}_{14}\text{B}$ .

these values are calculated in the framework of SIC-DFT, it is possible to map the degrees of freedom of local magnetic moments to the Heisenberg model. From this mapping the finite temperature behaviour of magnetization and magnetic anisotropy can be analysed. Thus, it is speculated that the exchange coupling between Nd and Fe should play an important role for the high-temperature behaviour of the magnetic anisotropy.

The magnetic anisotropy of  $\text{Sm}_2\text{Fe}_{17}\text{N}_3$  is also calculated using SIC-DFT. The role of N for the system to exhibit the uniaxial anisotropy are discussed in detail within the same framework.

The calculations are performed using system B of the ISSP supercomputer systems and KKR-Green's function code (AkaiKKR).

## References

- [1] T. Fukazawa and H. Akai, J. Phys. Condens. Matter 27 (2015) 115502.



# A First-principles study on exchange stiffness constants in magnetic films

Yoshio MIURA

*Electrical Engineering and Electronics,*

*Kyoto Institute of Technology, Matsugasaki, Sakyo-ku, Kyoto 606-8585*

Recently, fully epitaxial  $\text{Co}_2\text{Fe}_x\text{Mn}_{1-x}\text{Si}$  (CFMS)/Ag/ $\text{Co}_2\text{Fe}_x\text{Mn}_{1-x}\text{Si}$  multilayers for current perpendicular giant magnetoresistance (CPP-GMR) devices were fabricated by systematically changing the Fe/Mn composition ratio  $x$ , and the highest intrinsic GMR ratios, 184% at 30 K, were observed in the device with  $x=0.4$  and  $t_{\text{CFMS}}=3(\text{nm})$ [1]. However, a reduction of the GMR ratio of 58% was found at room temperature (RT). One possible reason of the large temperature dependence of the GMR ratio in CFMS/Ag/CFMS multilayer is thermal fluctuation of the interfacial magnetic moment providing the spin-flip scattering and reducing the spin polarization of the CFMS/Ag interfaces. In order to elucidate the mechanism of the spin-flip scattering at the interfaces, we theoretically investigate interfacial spin-flip scattering of magnetic films caused by the noncollinear magnetic structures as a result of thermal fluctuation of the local spin-moment.

To estimate the exchange stiffness of the interfacial spin-moments, we calculated the increase of the band energy  $E(\theta)$  relative to the collinear-spin system ( $\theta=0$ ) as a function of the angle of local moments  $\theta$  for interfacial layers of CMS/Ag(001) and CFS/Ag(001) junctions with Co, MnSi and FeSi terminations

using the quantum code ESPRESSO[2]. We constructed multilayer CMS/Ag and CFS/Ag structures containing seventeen atomic layers of CMS or CFS and nine atomic layers of Ag. Other parameters of the first principles calculations are shown in Ref. [3].

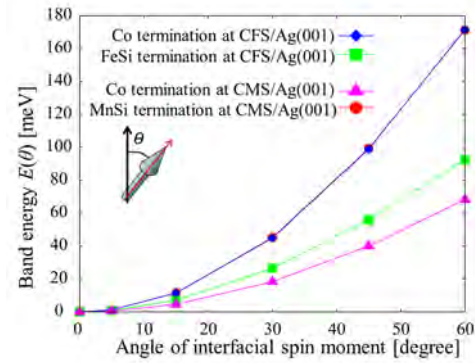


Fig. 1: Increase of band energy as a function of the angle of local spin moment at  $\text{Co}_2\text{XSi}/\text{Ag}(001)$  ( $\text{X}=\text{Fe}, \text{Mn}$ ) interface.

As can be seen in Fig.1, the Co termination of CMS/Ag interface and FeSi termination of CFS/Ag interface show a weak dependence of band energy with increasing  $\theta$ , indicating the relatively small exchange stiffness constant of these interfaces. The small exchange stiffness constant at interfaces will provide a thermal fluctuation of interfacial spin moment, leading to the reduction of GMR ratio at RT.

## References

- [1]Y. Sakuraba, *et al.*, APL 101,252408 (2012).
- [2]P.Giannozzi, *et al.*, JPCM 21,395502 (2009).
- [3]Y. Miura, *et al.*, PRB 83, 214411 (2011).

# First-Principles Modeling on Emerging Memory Devices

Masaaki Araidai

*Graduate School of Engineering, Nagoya University,  
Furo-cho, Chikusa-ku, Nagoya, 464-8603*

Superlattice phase change memory (superlattice PCM) consisting of  $(\text{GeTe})_2/\text{Sb}_2\text{Te}_3$  stacked structure is one of the most promising candidates for next-generation non-volatile memories and it has received considerable attention in recent years [1,2]. The memory operations are attributed to small structural change between two atomic configurations before and after switching. Therefore, the energy required for switching between higher and lower resistive states is much lower than that of conventional PCMs utilizing phase transition between crystal and amorphous phases [3]. However, the reaction pathway on the switching of superlattice PCM has not yet been clarified and the detailed analyses of the structural transition between high-resistive and low-resistive states are prerequisites for fully understanding the switching mechanism.

In this work, we investigated the switching process of superlattice  $(\text{GeTe})_2/\text{Sb}_2\text{Te}_3$  PCM using the first-principles electronic states calculations. The atomic structures and the electronic states were calculated by VASP code [4], which is based on density functional theory with plane-wave basis sets, PBE-type exchange-correlation functional and the projector augmented-wave method. For the calculations,  $k$  points of  $8 \times 8 \times 4$  Monkhorst-Pack grid were used and the cutoff energy was 500eV.

We found that atomic configurations of

high-resistive and low-resistive states are not stable but metastable [5]. Therefore, the superlattice  $(\text{GeTe})_2/\text{Sb}_2\text{Te}_3$  PCM can do cyclic operations due to the metastability. In addition, we clarified the structural transition process between high-resistive and low-resistive states. The transition process is shown in Fig. 1. First, the centered Ge and Te atoms in the low-resistive state move vertically, approaching to the transition state which consists of a honeycomb double layer (Fig. 1(a)  $\rightarrow$  (b)). Next, the honeycomb layers in the double layer slide in different directions and rotate by 60 degrees (Fig. 1(c)  $\rightarrow$  (d)). Finally, the Ge and Te atoms move vertically again, resulting in the high-resistive state (Fig. 1(e)  $\rightarrow$  (f)). The opposite process is the same. The validity of our proposal was shown from the detailed analyses of the potential energy surface and electron-density distribution.

## References

- [1] J. Tominaga, et al., Jpn. J. Appl. Phys. **48**, 03A053 (2009).
- [2] N. Takaura, et al., IEDM Tech. Dig., 29.2.1-29.2.4 (2014).
- [3] R. E. Simpson, et al., Nat. Nanotech. **6**, 501 (2011).
- [4] G. Kresse and J. Hafner, Phys. Rev. B **47**, 558 (1993).
- [5] R. Ohyanagi, et al., Appl. Phys. Lett. **104**, 252106 (2014).

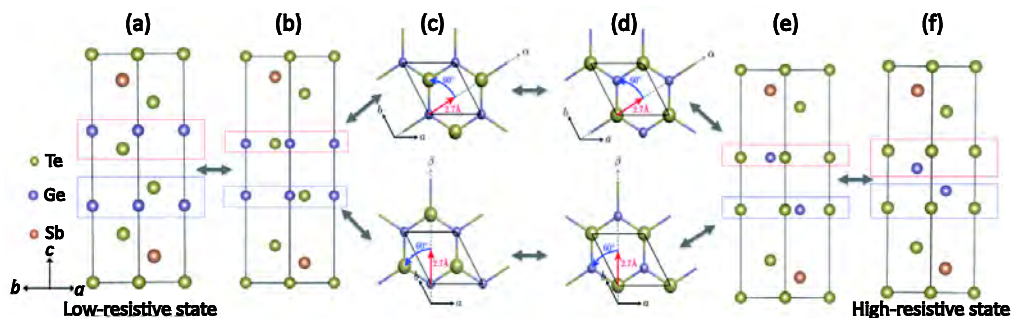


Figure 1: Structural transition process of superlattice  $(\text{GeTe})_2/\text{Sb}_2\text{Te}_3$  phase change memory between high-resistive and low-resistive states.

# Thermo-Chemical Wear Mechanism of Diamond Cutting Tool

Yutaka Uda, Shoichi Shimada

*Osaka Electro-Communication University, Hatsu-cho, Neyagawa, Osaka 572-8530*

*Sakuro Honda*

*Technology Research Institute of Osaka Prefecture, Ayumino, Izumi, Osaka 594-1157*

Demand has been increasing for highly durable molds of heat-resistant materials for complex and precise optical components with high aspect ratio. Diamond is the only ideal cutting tool material for high efficient ultraprecision cutting of complex three-dimensional metal works. However, it is well known that diamond cutting tool shows severe wear in cutting of heat-resistant materials such as ferrous metals and nickel.

On the other hand, in cutting of electroless nickel deposits (Ni-P), which is used as a material of precision molds, remarkably less tool wear is observed than in case of pure nickel [1,2]. Phosphorous addition should have an important role for tool wear suppression. However, the essential mechanism of wear suppression has not yet been understood well. To understand the wear mechanism of diamond cutting tool in machining of nickel and ferrous metals is very much meaningful to realize useful fabrication technique of the precise and durable molds with high accuracy and low cost.

Single grain cutting tests and erosion tests suggest that the wear occurs not by mechanical process but by thermo-chemical one [3-5]. Therefore, in order to reveal the mechanisms of the initial stages of wear process and wear suppression by phosphorous addition, ab initio molecular dynamics calculations of chemical

reaction on diamond surface in contact with Ni and Ni-P surfaces were carried out using double-grid method for real-space electronic-structure calculations proposed by Dr. T. Ono of Osaka University [6].

A  $C_{10}H_{14}$  cluster, shown in Figure 1, is used as a model of diamond (100) surface. The atom at the bottom of the model is the radical carbon interacting with metal surface. The dangling bonds of the other carbon atoms of diamond are terminated by hydrogen atoms. White and yellow figures express atomic and bond populations, respectively. The dimensions,  $x \times y \times z$ , of Ni (100) surface model is  $2a \times 2a \times a$ , where  $a$  is lattice constant of Ni. The model has periodic boundaries in  $x$  and  $y$  directions and aperiodic boundary in  $z$  direction. The atomic populations of all Ni atoms are almost 10.0.

Figure 2 shows the optimized atomic configuration of the diamond cluster interacting with Ni and Ni-12wt%P surfaces. By the

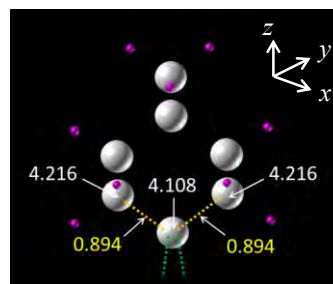


Fig.1 Model of diamond (100) surface

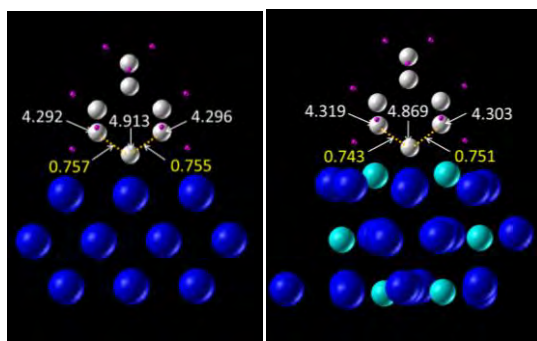


Fig.2. Effect of phosphorous addition to interaction with diamond

interaction with Ni, the atomic population of radical carbon increases to 4.91 from 4.11 and those of Ni decreases to 9.73. The result suggests that the strength of ionic bond between carbon and Ni increases. As the population of back bonds of radical carbon decrease to 0.76 from 0.89, the strength of covalent bond of back bonds decreases and the radical carbon has a chance to dissociate from the diamond surface when it has a large kinetic energy due to cutting temperature. On the other hand, in case of interacting with Ni-P, both of decrease of back bond population and increase of atomic population of radical carbon are remarkably suppressed. The result suggests that phosphorous addition reduces the dissociation of carbon atoms on diamond surface.

The dissociation energy of the radical carbon was estimated as shown in Figure 3. Diamond model was lifted up from the stable state interacting with work material leaving the radical carbon on work material surface to a position where the force acting to the radical carbon changes from upward to downward direction. The radical carbon is considered to be dissociated at the position. The dissociation energy can be estimated from the difference between the total energy of the system

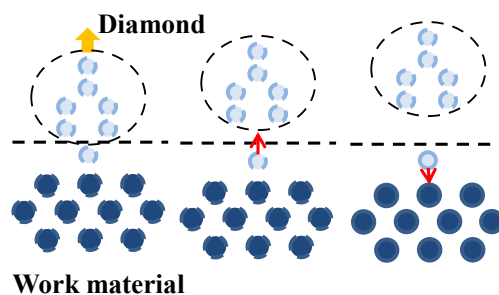


Fig.3 Estimation of dissociation energy of radical carbon atom

composed of diamond and work material at the stable state and that at the dissociating state. Although the atomic structure was not optimized in pulling up process, the dissociation energies of radical carbon by different work materials can be relatively compared. The dissociation energies estimated are 5.01 eV for diamond-Ni system and 5.70 eV for diamond-Ni-P system, respectively. The result suggests that the wear of diamond cutting tool in cutting of Ni-P is less than that in cutting pure Ni.

## References

- [1] C.K. Syn, J.S. Taylor, R.R. Donaldson: Proc. SPIE, **676** (1986) 128.
- [2] J.M. Oomen, L. Eisses: Precision Engineering, **14**, (1992) 206.
- [3] T. Tanaka, N. Ikawa: Bull. JSPE, **7** (1973) 97.
- [4] S. Shimada, H. Tanaka, M. Higuchi, T. Yamaguchi, S. Honda, K. Obata: Annals of the CIRP, **53**, (2004) 57.
- [5] N. Furushiro, H. Tanaka, M. Higuchi, T. Yamaguchi, S. Shimada: Annals of the CIRP, **59**, (2010) 105.
- [6] T. Ono, K. Hirose: Physical Review Letters, **82** (1999) 5016.

***Ab initio* Lattice Anharmonicity in Iron-bearing Bridgmanite at High Pressure**

Haruhiko DEKURA

*Geodynamics Research Center**Ehime University, 2-5 Bunkyo-cho, Matsuyama 790-8577, Japan*

Iron-bearing Bridgmanite ( $\text{Mg,Fe})\text{SiO}_3$  is believed to be the most constituent mineral in the earth's lower mantle. Determination of the phonon transport property, i.e., lattice thermal conductivity ( $\kappa$ ), of the material should be therefore a key to understanding the dynamics and evolution of the earth's deep interior. Lattice anharmonicity owing to the phonon-phonon interaction strongly relates the phonon transport. The primary purpose of this project in this period is to determine the anharmonic properties of the iron-bearing system at a deep mantle pressure of about 100 GPa.

We have performed density-functional theoretic calculations combined with the LDA+ $U$  method [1] and have extracted the large number of anharmonic force constants (AFC) by higher order derivatives of the adiabatic potential surface [2]. All of the calculations were performed using the QUANTUM-ESPRESSO package [3]. Figure 1 shows The simulation cell of  $(\text{Mg}_{0.9375}, \text{Fe}^{2+}_{0.0625})\text{SiO}_3$  that includes 160 atoms was adopted in this study. The ferrous iron was treated in the high spin state ( $S = 2$ ).

During this period, we have succeeded in the determination of about 40% of the total number of AFC ( $\sim 220,000$ ) to nearest neighbor

shell by the use of supercomputer (system B). Our preliminary results show that the amount of each AFC strongly varies from bond to bond. In addition, we have found that the average value of AFC is about 20% bigger than that of the iron free system, i.e.,  $\text{MgSiO}_3$  Bridgmanite, indicating a moderate decrease in  $\kappa$  accompanied with the iron incorporation. We will continue to promote this research in the next period.

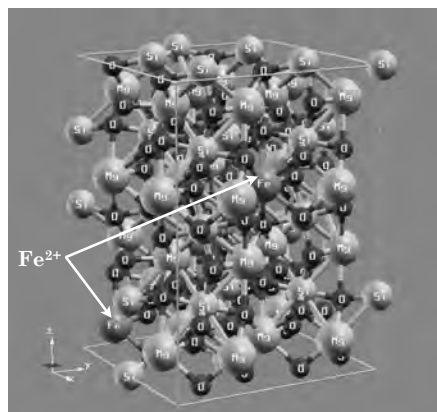


Fig. 1: Crystal structure of iron-bearing Bridgmanite  $(\text{Mg}_{0.9375}, \text{Fe}^{2+}_{0.0625})\text{SiO}_3$  optimized at 100 GPa.

**References**

- [1] T. Tsuchiya and X. Wang: J. Geophys. Res. **118** (2013) 83.
- [2] K. Esfarjani and H. T. Stokes: Phys. Rev. B **77** (2008) 144112.
- [3] <http://www.quantum-espresso.org/>

# Theory of magnetic and electronic structure for Mn-based ordered alloys with Cu<sub>3</sub>Au-type crystal structure

Takashi UCHIDA

*Hokkaido University of Science*

*4-1, 7-15, Maeda, Teine-ku, Sapporo 006-8585*

The Mn-based ordered alloys Mn<sub>3</sub>X (X=Pt, Rh, Ir), which all have Cu<sub>3</sub>Au-type crystal structure, are frustrated itinerant magnets with an octahedral configuration of Mn local magnetic moments. Neutron diffraction experiments [1] suggest that below the Néel temperatures  $T_N$ , Mn<sub>3</sub>Rh and Mn<sub>3</sub>Ir exhibit a single ordered phase: triangular magnetic structure with  $\Gamma_{4g}$  symmetry. On the other hand, Mn<sub>3</sub>Pt exhibits two ordered phases: triangular magnetic structure for  $T < 400$  K and collinear antiferromagnetic structure for  $400\text{K} < T < 475\text{K}$ , the latter phase accompanying tetragonal distortion with volume expansion.

To clarify the physical origin of the magnetic structures of these alloys from the theoretical point of view, we have investigated the temperature dependence of the magnetic and electronic structures by means of the first-principles molecular dynamics (MD) approach for itinerant magnets [2]. The theory is formulated by incorporating the first-principles TB-LMTO Hamiltonian into the MD approach for itinerant magnets on the basis of the functional integral method and the isothermal MD technique. The MD approach allows us to determine automatically the magnetic structure of a large system with several hundred atoms in a unit cell at finite temperatures.

In the present MD analysis, we solved the isothermal MD equations of motion by using site-dependent effective medium in order to treat the magnetic phase transition correctly. We used the recursion method to calculate the local electronic structure in determining the site-dependent effective medium and in calcu-

lating magnetic forces at each time step of the MD equations of motion. Because the time-consuming recursion process consists of parallelizable loop calculations, we utilized the MPI parallel calculation scheme in the recursion calculation. The MPI parallel process is found to be quite effective in saving computing time because more than 90 % of the CPU time concentrates on the recursion calculation.

We have calculated the electronic and magnetic structure for a system with  $4 \times 4 \times 4$  fcc lattice with fixing the crystal structure and lattice constant to their room-temperature values. At sufficiently low temperatures below  $T_N$ , Mn<sub>3</sub>X (X = Mn, Rh, Ir) all exhibit the triangular magnetic structure, being consistent with experiment. With increasing temperature from 25 K, Mn<sub>3</sub>Pt exhibits a second-order transition to another noncollinear ordered phase around 350 K, accompanying a development of Mn-Eg DOS at Fermi energy  $E_F$ . This is in contrast with the result of previous calculation using uniform effective medium which shows a first-order transition to a low-moment ordered phase. Mn<sub>3</sub>Rh and Mn<sub>3</sub>Ir, on the other hand, show no sign of a magnetic phase transition up to  $T_N$ . Further analysis on the magnetic structure of these alloys are now in progress.

## References

- [1] T. Ikeda and Y. Tsunoda, J. Phys. Soc. Jpn. **72** (2003) 2614.
- [2] T. Uchida and Y. Takehashi, J. Korean Phys. Soc. **62** (2013) 1748.



# First-principles calculation of atomic arrangement and electronic structure in ceramic grain boundaries

Yukio SATO

*Department of Materials Science and Engineering,*

*Kyushu University, 744 Motoooka, Fukuoka, Fukuoka, 819-0395*

Grain boundary (GB) is lattice defect in crystalline solid. Atomic arrangement at GB becomes different from that in crystal bulk, and various properties also become different. Some researchers have proposed that this point can be used for obtaining superior physical properties. An example can be found in Ref. 1. With this viewpoint, in the present study, I tried to modify the atomic arrangement and the electronic structure of a GB in  $\text{SrTiO}_3$  (STO), which is the prototypic perovskite material by means of first-principles density-functional theory (DFT) calculations.

We chose the  $[001]/(310)$  symmetric tilt GB of STO for this study. First, stable atomic arrangement and density of state (DOS) for the undoped GB (Fig. 1 (a)) was calculated. Next, ruthenium (Ru) doped GB (Fig. 1 (b)) was studied. DFT calculation was carried out using the VASP code. Here, generalized gradient approximation (GGA) potential was used. The GB supercells contained 100 atoms.

Figures 2 (a) and (b) show DOS for both of the GBs. In the case of undoped GB, there is a band gap of 1.1 eV. This is quite close to the value calculated for STO bulk crystal, and it is therefore considered that the GB electronic state is not significantly altered. Underestimation of the band gap value from the experimental one of  $\sim 3.3$  eV is due to error caused by GGA.

On the other hand, for the Ru-doped case (Fig. 2(b)), due to creation of extra electronic state in the band gap, there is no band gap. It is considered that electronic state of the GB is metallic. It is therefore suggested that if this kind of GB structure can be fabricated, metallic electrical conduction confined within GB plane may be observed.

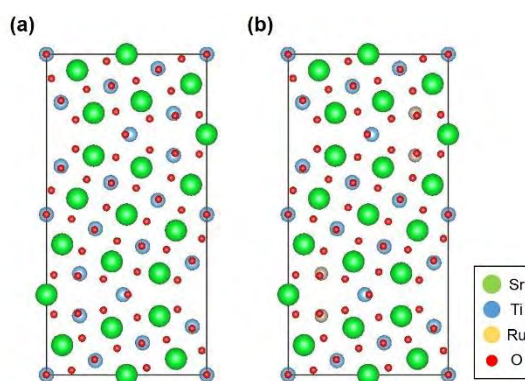


Fig. 1: Grain boundary supercell of  $\text{SrTiO}_3$   $\Sigma 5$   $[001]/(310)$  GBs used in this study. (a) The undoped and (b) the Ru-doped cases. Figure is drawn using VESTA [2].

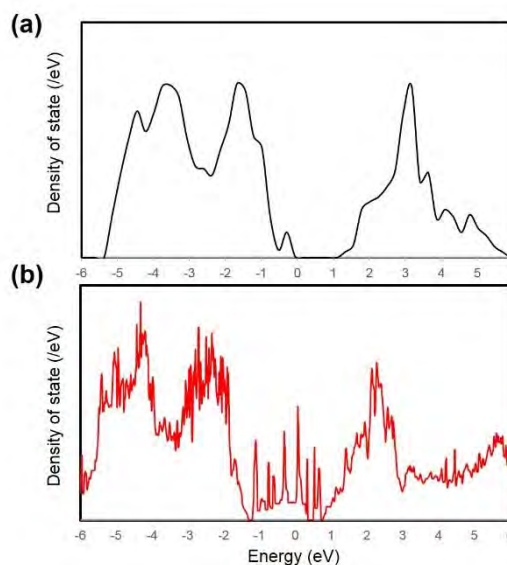


Fig. 2: Density of state of the GB supercells. (a) The undoped and (b) the Ru-doped cases.

## References

- [1] K. Koumoto *et al.*, J. Am. Ceram. Soc. **96** (2013) 1.
- [2] K. Momma and F. Izumi, J. Appl. Cryst. **44** (2011) 1272.

# Electronic State and Proximity Effects around Interface in Layered Superlattices

Kunitomo HIRAI

*Department of Physics, Nara Medical University  
Kashihara, Nara 634-8521*

The purpose of the present research is to elucidate characteristics of electronic state in superlattices with layered structures, in particular, to illustrate proximity effects of each layer on adjacent layers in the superlattices. This research of a first-principles electronic structure calculation is performed by means of the Korringa-Kohn-Rostoker (KKR) Green function method within the framework of the local spin density (LSD) functional formalism.

The calculation by means of the KKR method was so far carried out for superlattices of ferromagnetic layers with nonmagnetic spacer layers such as Fe/Cr, Fe/V, Fe/Cu, ... ones, with magnetizations of two successive Fe layers being aligned parallel or antiparallel. Oscillatory interlayer exchange coupling between ferromagnetic layers with respect to spacer thickness was investigated, and relation between bulk effects inherent in the spacer layer and the proximity effects due to the ferromagnetic layers was analyzed. In the calculation, every atom in a monolayer stacked in the superlattices is assumed to be equivalent, and there is one site in each monolayer. This assumption can be justified for the superlattices with ideal interfaces without structure, but not for those with realistic interfaces with structures like steps, islands, or such, and hence there are two or more sites in each monolayer for the superlattices with realistic interfaces.

A need of the calculation for superlattices with more sites in each monolayer arises also for layered superlattices of ordered alloys or

compounds, which now attract broad interests particularly in viewpoint of spintronics. We then start preparation of the calculation for superlattices with more sites in each monolayer, which results in increase of the number of atoms in a unit cell and involves vast increase of computation times. In the preparation of the calculation, installation of parallelization with use of the OpenMP into program codes of the KKR methods is intended, together with parallelization with use of the MPI which was already achieved, that is, installation of hybrid parallelization is intended.

The installation of the OpenMP is in progress and will be achieved in the next term, and then the proximity effects in the superlattices with realistic interfaces will be investigated to elucidate the roles of the interfaces in the superlattices. The calculation will be carried out for Fe superlattices with steps, and magnetic frustration caused by the steps is investigated, in particular reference to possible mechanism of increase of total magnetization of the Fe layers, where fcc(001) or fcc(111) superlattices are considered together with usual bcc(001) ones and difference between those superlattices is to be analyzed. In addition, the calculation will be carried out for layered superlattices of ordered alloys, such as fcc(001) superlattices consisting of Fe and FePt layers, in particular reference to ferromagnetic or antiferromagnetic coupling between layers and within a monolayer.



### 3.3 Strongly Correlated Quantum Systems

# Unified understanding of the non-monotonic $T_c$ variance of the 1111 iron pnictide superconductors

KAZUHIKO KUROKI

*Department of Physics, Osaka University*

*1-1 Machikaneyama, Toyonaka, Osaka, 560-0043, Japan*

Recently, non-monotonic variance of the  $T_c$  against chemical substitution is observed in some 1111 iron-based superconductors. We have theoretically investigated the origin of such variances taking into account the change in the band structure with chemical substitution.

## ARSENIC PHOSPHORUS ISOVALENT DOPING SYSTEMS

In isovalent doping system  $\text{LaFe(As,P)(O,F)}$ , recent experiments show that  $T_c$  is first suppressed as the phosphorus content is increased, but then it is re-enhanced and takes a local maximum at some P/As ratio.[1–3] As the phosphorus content is increased and the Pn-Fe-Pn bond angle increases, the  $d_{xy}$  hole Fermi surface is expected to be lost, and the top of the  $d_{xy}$  band moves away from the Fermi level. Therefore, the  $d_{xy}$  band contribution to the spin fluctuation decreases monotonically as the phosphorus content increases, especially after the  $d_{xy}$  Fermi surface disappears. The spin-fluctuation-mediated pairing is strongly degraded when the  $d_{xy}$  hole Fermi surfaces is absent, suggesting that the  $d_{xy}$  band plays an important role in the occurrence of high  $T_c$  superconductivity. Nonetheless, our recent calculation shows that  $T_c$  of the spin-fluctuation-mediated pairing shows a non-monotonic behavior even after the  $d_{xy}$  hole Fermi surface is lost; it exhibits a local maximum around a certain phosphorus content (i.e., certain Pn-Fe-Pn bond angle) greater than that at which the  $d_{xy}$  Fermi surface disappears, as shown in Fig.1(a)[4]. The origin of this non-monotonic variance is traced back to the fact that the disappearance of the  $d_{xy}$  hole Fermi surface leads to a better nesting within the  $d_{xz/yz}$  portion of the Fermi surface, thereby enhancing the low lying spin excitations. It is also found in our calculation that the Pn-Fe-Pn bond angle at which the  $T_c$  is locally maximized decreases when the electron doping rate is increased. These results are consistent with recent experimental observations [1–3]. This indicates that the  $d_{xz/yz}$  orbitals by themselves can play the main role in the occurrence of spin-fluctuation-mediated superconductivity, although the  $T_c$  in those cases is not very high.

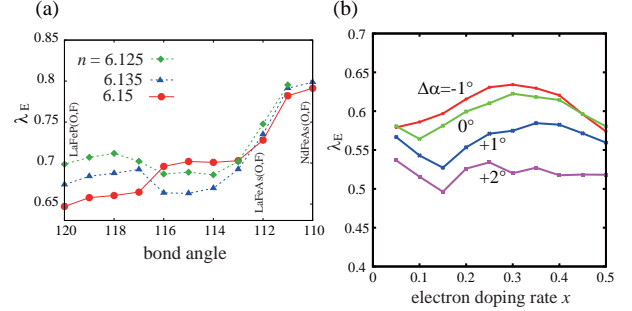


FIG. 1. (a) Eigenvalue of the linearized Eliashberg equation  $\lambda_E$  plotted against the hypothetically varied Pn-Fe-Pn bond angle for the model of  $\text{LnFe(As,P)(O,F)}$ .  $n$  is the electron density and  $n - 6$  corresponds to the electron doping rate (taken from [4]). (b)  $\lambda_E$  plotted against the electron doping rate for the model of  $\text{LnFe(As,P)(O,H)}$ .  $\Delta\alpha$  is the Pn-Fe-Pn bond angle deviation with respect to that of  $\text{LaFeAsO}$  (taken from [8]). In both (a) and (b),  $\lambda_E$  can be considered as a qualitative measure for  $T_c$ , and smaller bond angle corresponds to smaller P/As content ratio or replacing the rare earth as  $\text{La} \rightarrow \text{Nd}$  or  $\text{Sm}$ . for  $s\pm$ -wave pairing

## HYDROGEN DOPED SYSTEMS

In the hydrogen doped system  $\text{LaFeAsO}_{1-x}\text{H}_x$ , electron doping rate can exceed 50 percent, and the  $T_c$  phase diagram against the doping rate  $x$  exhibits a double dome structure, where the second dome with higher doping concentration has the higher  $T_c$ [5]. In a rigid band picture, such a large amount of electron doping would wipe out the hole Fermi surfaces, so that the Fermi surface nesting would no longer be good in the higher  $T_c$  second dome. However, first principles band calculation that takes into account the band structure variation with chemical substitution reveals that the band structure rapidly changes with doping, and the rigid band picture is not valid[6–8]. In momentum space, the  $d_{xz/yz}$  hole Fermi surfaces around (0,0) shrink monotonically and are eventually lost with sufficient electron doping, and in turn an electron Fermi surface appears. On the other hand, an interesting point is that the  $d_{xy}$  hole Fermi surface around  $(\pi, \pi)$  is barely changed with the doping rate  $x$ , which is clearly a non-rigid band feature. Surprisingly, this is due to a rapid decrease of  $t_1$

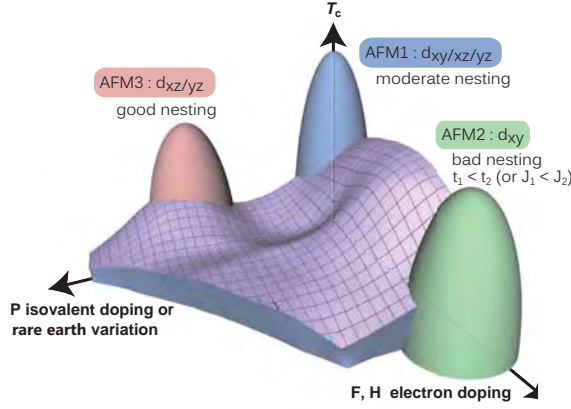


FIG. 2. A theoretical interpretation of the superconducting phase diagram of the 1111 family (taken from [4]).

within the  $d_{xy}$  orbital upon increasing  $x$ , which pushes up the  $d_{xy}$  band top at  $(\pi, \pi)$ , so that it follows the increase of the Fermi level.

As seen in the above, the  $d_{xy}$  hole Fermi surface remains even at large electron doping rate, while the  $d_{xz/yz}$  hole Fermi surfaces are lost, so that the importance of the  $d_{xy}$  orbital increases with doping. Interestingly, our fluctuation exchange study of these non-rigid band models show that the spin fluctuation and the  $s \pm$  pairing are both enhanced in this largely doped regime, exhibiting a double dome feature of the superconducting  $T_c$  as a function of doping. Moreover, the two domes are merged into a single dome when the Pn-Fe-Pn bond angle is reduced (a change that takes place when the rare earth is varied as  $\text{La} \rightarrow \text{Ce} \rightarrow \text{Sm} \rightarrow \text{Gd}$ ), as shown in Fig.1(b), in agreement with the experiment. Although the  $d_{xy}$  hole Fermi surface remains unchanged in the highly doped regime, the Fermi surface nesting (in its original sense of the term) is monotonically degraded because the volume of the electron Fermi surfaces increases, so the origin of the second dome in  $\text{LaFeAsO}_{1-x}\text{H}_x$  cannot be attributed to a good Fermi surface nesting. Here one should recall that  $s \pm$  pairing is a next nearest neighbor pairing, which is favored by the relation between nearest and next nearest neighbor antiferromagnetic interactions  $J_2 > J_1$ , corresponding to  $t_2 > t_1$ . In fact, as mentioned above,  $t_2$  dominating over  $t_1$  is what is happening in the second  $T_c$  dome regime. Hence, intuitively,  $t_2 > t_1$  can be considered as the origin of the  $T_c$  enhancement in the largely doped regime. To be precise, however, the fluctuation exchange approximation is a weak coupling method based on the itinerant spin model, so using the  $J_1 - J_2$  term of the localized spin model is not conceptually correct. In reality, the entire

$d_{xy}$  portion of the band structure is strongly modified in a manner that it favors the second nearest neighbor pairing.

An important point here is that the  $t_1$  reduction is largely due to the increase of the positive charge within the blocking layer by  $\text{O}(2-) \rightarrow \text{H}(1-)$  substitution, which in turn reduces the As 4p electronic level and leads to the suppression of the indirect component of  $t_1$  [8]. Interestingly, we have recently found that a similar situation can occur when pressure is applied to some of the iron-based superconductors. The study on this problem is now in progress.

## CONCLUSION

The hydrogen doped case shows that a good Fermi surface nesting is not necessary for the spin fluctuation mediated pairing even in the itinerant spin picture. On the other hand, in the isovalent doping system, the nesting of the  $d_{xz/yz}$  Fermi surface can enhance the pairing. In total, the nesting and  $s \pm$  superconductivity can in some cases be correlated with the Fermi surface nesting, while in other cases not. This also explains why the strength of the low energy spin fluctuation probed by NMR is in some cases correlated with  $T_c$ , while in other cases not, because the low energy spin fluctuation is largely governed by the Fermi surface nesting. We have summarized these theoretical interpretations in Fig.2.

- 
- [1] S. Miyasaka, A. Takemori, T. Kobayashi, S. Suzuki, S. Saijo, S. Tajima, J. Phys. Soc. Jpn. 82, 124706 (2013).
  - [2] K. T. Lai, A. Takemori, S. Miyasaka, F. Engetsu, H. Mukuda, S. Tajima, Phys. Rev. B 90, 064504 (2014).
  - [3] H. Mukuda, F. Engetsu, K. Yamamoto, K. T. Lai, M. Yashima, Y. Kitaoka, A. Takemori, S. Miyasaka, S. Tajima, Phys. Rev. B 89, 064511, (2014).
  - [4] H. Usui, K. Suzuki, and K. Kuroki, arXiv:1501.06303.
  - [5] S. Iimura, S. Matsuishi, H. Sato, T. Hanna, Y. Muraba, S.W. Kim, J. E. Kim, M. Takata and H. Hosono, Nat. Commun. 3, 943 (2012).
  - [6] S. Iimura, S. Matsuishi, M. Miyakawa, T. Taniguchi, K. Suzuki, H. Usui, K. Kuroki, R. Kajimoto, M. Nakamura, Y. Inamura, K. Ikeuchi, S. Ji, and H. Hosono, Phys. Rev. B, 060501(R) (2013).
  - [7] K. Suzuki, H. Usui, K. Kuroki, S. Iimura, Y. Sato, S. Matsuishi, and H. Hosono, J. Phys. Soc. Jpn. 82, 083702 (2013).
  - [8] K. Suzuki, H. Usui, S. Iimura, Y. Sato, S. Matsuishi, H. Hosono, and K. Kuroki Phys. Rev. Lett. 113, 027002 (2014)

# Numerical studies on novel realistic quantum phases induced by cooperative spin-orbit couplings and electron correlations

Masatoshi IMADA

*Department of Applied Physics, University of Tokyo,  
7-3-1, Hongo, Bunkyo-ku, Tokyo 113-8786, Japan*

Topological aspects in electronic structure of materials have been an intensively studied subject in recent research in condensed matter physics. In particular, interplay of spin-orbit interaction and electron correlations has revealed unprecedented and rich properties in a number of iridium oxides which is known as touchstone compounds of the interplay.

We have extended studies on an iridium oxide with the honeycomb structure,  $\text{Na}_2\text{IrO}_3$  based on first principles.  $\text{Na}_2\text{IrO}_3$  was proposed to show a novel Kitaev spin liquid [1], while experimental observation has established the zig-zag type magnetic order [2]. Our first principles study has reproduced the observed zig-zag type order [3]. In this project, we have further shown that the neutron scattering measurements, and thermodynamic properties are quantitatively consistent with the results calculated from the first principles study. The way to reach the Kitaev spin liquid has also been examined.

In this activity report, we summarize studies on another series of iridium oxides, with the pyrochlore lattice structure  $\text{A}_2\text{Ir}_2\text{O}_7$  with  $A$  being rare earth elements, where predictions on novel topological properties at the domain wall of their magnetically ordered phase have been made [4].

$\text{A}_2\text{Ir}_2\text{O}_7$  with  $A$  being rare earth elements was first predicted to have an all-in-all-out (AIAO) type antiferromagnetic order in case of  $A = \text{Y}$  [5] and experimentally confirmed for  $A = \text{Nd}$  and  $\text{Y}$  [6]. This AIAO order is expected to host Weyl fermions in the bulk. Although the Weyl fermion is fragile when the magnetic

order grows, magnetic domain walls offer topologically novel interfaces [4].

Namely, we have theoretically predicted that a class of magnetic domain walls induces unexpected interface metals accompanied by a net uniform magnetization around the domain wall, in the background of seemingly trivial bulk antiferromagnetic insulator, where uniform magnetization is cancelled each other in the bulk. The metallicity of the domain wall is substantiated by the formation of Fermi arcs at the domain walls, which have originally been formed by the Weyl electrons. The Fermi arc evolves into the Fermi surface when the Weyl fermions are eliminated. We have revealed that the magnetic domain walls of the AIAO phase are characterized by a zero-dimensional class A Chern number [4].

The electron correlation not only plays a crucial role in the formation of the AIAO order but also subsequent phase transitions emerging in the two-dimensional electrons at the domain wall. We have predicted that the metallic electrons have a helical nature at the Fermi surface with some similarity to the Rashba metals. We have shown by using an effective Hamiltonian, the helical nature induces an anomalous Hall conductivity, circular dichroism, and optical Hall conductivity under external magnetic fields. By increasing the electron correlation, the metallic domain wall states undergo the phase transitions from a degenerate helical metal to a spontaneously symmetry-broken helical metal, where the product of the inversion and time reversal symmetry is broken. With further increasing the interaction, it eventu-

ally becomes a topologically trivial antiferromagnetic insulator even at the domain wall.

This work has been done in collaboration with Youhei Yamaji.

## References

- [1] G. Jackeli and G. Khaliullin, Phys. Rev. Lett. **102** (2009) 017205; J. Chaloupka, G. Jackeli, and G. Khaliullin, Phys. Rev. Lett. **105** (2010) 027204.
- [2] S. K. Choi *et al.*, Phys. Rev. Lett. **108** (2012) 127204; F. Ye *et al.*, Phys. Rev. B **85** (2012) 180403.
- [3] Y. Yamaji, Y. Nomura, M. Kurita, R. Arita and M. Imada, Phys. Rev. Lett. **113** (2014) 107201.
- [4] Y. Yamaji and M. Imada, Phys. Rev. X **4** (2014) 021035.
- [5] X. Wan, A. M. Turner, A. Vishwanath, and S. Y. Savrasov, Phys. Rev. B **83** (2011) 205101.
- [6] K. Tomiyasu, *et al.*, J. Phys. Soc. Jpn. **81** (2012) 034709; H. Sagayama *et al.*, Phys. Rev. B **87** (2013) 100403.

# Intersite electron correlations in two-dimensional Hubbard Penrose Lattice

AKIHISA KOGA

*Department of Physics, Tokyo Institute of Technology  
Meguro, Tokyo 152-8551, Japan*

Quasiperiodic systems have attracted considerable interest since the discovery of quasicrystals. One of the specific features is the existence of a long-range order without translational symmetry. Recently, interesting low-temperature properties have been observed in the quasicrystal  $\text{Au}_{51}\text{Al}_{34}\text{Yb}_{15}$  and its approximant  $\text{Au}_{51}\text{Al}_{35}\text{Yb}_{14}$  [1]. In the former compound, the specific heat and susceptibility exhibit power-law behavior with a nontrivial exponent at low temperatures. In contrast, the approximant with the periodic structure shows conventional heavy fermion behavior. These findings suggest that electron correlations and quasiperiodic structure play a crucial role in stabilizing quantum critical behavior at low temperatures. Therefore, it is desirable to clarify how electron correlations affect low-temperature properties in quasiperiodic system.

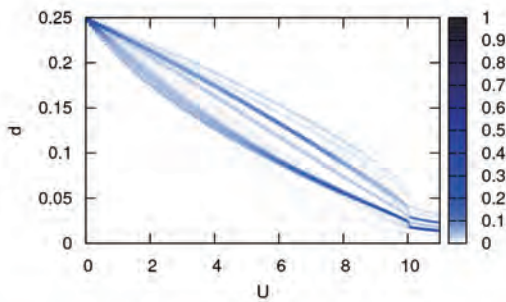


Figure 1: Density plot of double occupancy as a function of interaction strength  $U$  in the half-filled Penrose-Hubbard model with 4481 sites when  $T = 0.05$ .

Motivated by this, we have investigated the half-filled Hubbard model on the two-dimensional Penrose lattice, combining the Real-space DMFT[2] with the CTQMC method. Computing the double occupancy and renormalization factor at each site, we have discussed the Mott transition at finite temperatures. Furthermore, we have found that the quasiparticle weight strongly depends on the site and its geometry[3]. However, intersite correlations cannot be taken into account with RDMFT. In the present work, we developed Dual Fermion approach[4] where inter-site correlations in inhomogeneous system are taken into account. We will investigate how magnetic fluctuations develop in quasiperiodic system.

## References

- [1] K. Deguchi, S. Matsukawa, N. K. Sato, T. Hattori, K. Ishida, H. Takakura, and T. Ishimasa, *Nat. Mater.* **11**, 1013 (2012).
- [2] A. Georges, G. Kotliar, W. Krauth, and M. J. Rozenberg, *Rev. Mod. Phys.* **68**, 13 (1996).
- [3] N. Takemori, A. Koga, *J. Phys. Soc. Jpn.* **84**, 023701 1-5 (2015).
- [4] A. N. Rubtsov et al., *Phys. Rev. B* **77**, 033101 (2008).

# Stability of the superfluid state with internal degree of freedom

AKIHISA KOGA

*Department of Physics, Tokyo Institute of Technology  
Meguro, Tokyo 152-8551, Japan*

Superfluid state in ultracold atomic systems has attracted current interest. Recently, fermionic systems with internal degrees of freedom have experimentally been realized [1, 2, 3], which stimulates further theoretical investigation on the superfluid state in multi-component fermionic systems [4, 5]. Since the fermionic system with even number of components should be equivalent to the strongly correlated electron systems with degenerate orbitals, it is highly desired to discuss how the superfluid state is realized in these systems.

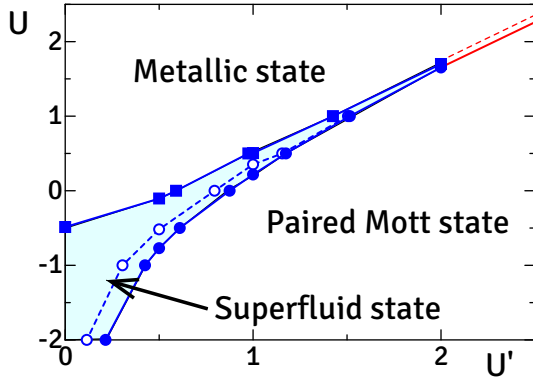


Figure 1: Phase diagram of the four-component Fermionic system equivalent to the degenerate orbital system with intraorbital (interorbital) Coulomb interaction  $U$  ( $U'$ ) at  $T = 0.01$ .

Motivated by this, we have studied low temperature properties of the degenerate Hubbard model with the intra- and inter-orbital Coulomb repulsions, which is equivalent to the four component fermionic sys-

tem. By combining dynamical mean-field theory with a continuous-time quantum Monte Carlo method, we have obtained the finite temperature phase diagram, as shown in Fig. 1. We have found that the  $s$ -wave superfluid state realized by the attractive interaction  $U$  is adiabatically connected to that in the repulsive interacting region [6]. It is expected that this superfluid state should capture the essence of the superconducting state in the fullerene-based solid  $A_3C_{60}$ . It is an interesting problem to clarify this point, which is now under consideration.

## References

- [1] T. B. Ottenstein et al., Phys. Rev. Lett. **101** 203202 (2008).
- [2] T. Fukuhara et al., Phys. Rev. Lett. **98**, 030401 (2007).
- [3] B. J. DeSalvo et al., Phys. Rev. Lett. **105**, 030402 (2010).
- [4] K. Inaba and S. Suga, Phys. Rev. Lett. **108**, 255301 (2012); K. Inaba and S. Suga, Mod. Phys. Lett B **27**, 1330008 (2013).
- [5] Y. Okanami, N. Takemori and A. Koga, Phys. Rev. A **89**, 053622 (2014).
- [6] A. Koga and P. Werner, Phys. Rev. B **91**, 085108 (2015).



# Unified description of the electronic properties of $\text{Sr}_2\text{RuO}_4$ in a paramagnetic phase

Naoya ARAKAWA

*Center for Emergent Matter Science, RIKEN  
Wako, Saitama 351-0198*

Correlated multiorbital systems show various electronic properties due to the combination of electron correlation and complex degrees of freedom such as charge, spin, and orbital. Examples are anisotropic superconductivity, giant magnetoresistance effect, and non-Fermi-liquid-like behaviors. Among several correlated multiorbital systems, ruthenates have rich electronic states, depending on the crystal structure or the chemical composition or both. For example,  $\text{Sr}_2\text{RuO}_4$  becomes a spin-triplet superconductivity at very low temperatures,  $\text{Ca}_2\text{RuO}_4$  becomes a Mott insulator, and  $\text{Sr}_2\text{Ru}_{0.075}\text{Ti}_{0.025}\text{O}_4$  becomes a nearly-antiferromagnetic metal. Since those electronic states are realized in other correlated multiorbital systems and the basic electronic structure of ruthenates is simpler, research on ruthenates is suitable to understand the roles of electron correlation and complex degrees of freedom in a correlated multiorbital system.

Despite extensive research, the electronic properties of  $\text{Sr}_2\text{RuO}_4$  even in a paramagnetic phase have not been correctly understood. It is experimentally established that  $\text{Sr}_2\text{RuO}_4$  is categorized into a quasi-two-dimensional  $t_{2g}$ -orbital system with moderately strong electron correlation. In addition, the temperature dependence of the physical quantities such as the spin susceptibility and the inplane resistivity are the same as those in Landau's Fermi liquid theory. However, there have been several remaining problems such as the origin of the larger mass enhancement of the  $d_{xy}$  orbital

than that of the  $d_{xz/yz}$  orbital.

In this project, I studied several electronic properties of  $\text{Sr}_2\text{RuO}_4$  using the fluctuation-exchange approximation with the current vertex corrections arising from the self-energy and Maki-Thompson four-point vertex function due to electron correlation for a  $t_{2g}$ -orbital Hubbard model on a square lattice and achieved the satisfactory unified description of the low-temperature electronic properties [1, 2], which are the larger mass enhancement of the  $d_{xy}$  orbital, the strongest enhancement of the spin fluctuation at  $\mathbf{q} \approx (\frac{2}{3}\pi, \frac{2}{3}\pi)$ , the crossover of the inplane resistivity from the  $T$  dependence to the  $T^2$  dependence at low temperature, and the nonmonotonic temperature dependence of the Hall coefficient including an appearance of a peak at low temperature; the agreement in the orbital dependence of the mass enhancement is better than that in case of the dynamical-mean-field theory. This study [1, 2] leads to taking an important step towards understanding the characteristic roles of electron correlation and complex degrees of freedom in ruthenates and the ubiquitous properties of correlated multiorbital systems.

## References

- [1] N. Arakawa: Phys. Rev. B **90** (2014) 245103.
- [2] N. Arakawa: arXiv:1503.06937; accepted for publication in Modern Physics Letters B as an invited brief review article.



# Microscopic theory on charge transports of a correlated multiorbital system

Naoya ARAKAWA

*Center for Emergent Matter Science, RIKEN  
Wako, Saitama 351-0198*

Many-body effects are important to discuss the electronic properties of correlated electron systems. For several correlated electron systems, Landau's Fermi liquid (FL) theory describes many-body effects in terms of quasiparticles. In this theory, the temperature dependence of the physical quantities are the same as those in noninteracting case and many-body effects are the changes of its coefficient due to the mass enhancement or the FL correction or both. However, for correlated electron systems near a magnetic quantum-critical point (QCP), many-body effects cause non-FL-like behaviors, the deviations from the temperature dependence expected in Landau's FL theory; for example, in  $\text{Sr}_2\text{Ru}_{0.075}\text{Ti}_{0.025}\text{O}_4$ , which is located near an antiferromagnetic (AF) QCP, the spin susceptibility shows the Curie-Weiss-like behavior and the resistivity shows the  $T$ -linear dependence. Thus, the emergence of such non-FL-like behaviors indicates the importance of discussing many-body effects beyond Landau's FL theory.

However, many-body effects in correlated multiorbital systems have been little understood compared with understanding many-body effects in correlated single-orbital systems. This is because of difficulty taking the enough numbers of the mesh of the Brillouin zone and the Matsubara frequency in the presence of orbital degrees of freedom for the numerical calculations including many-body effects; the enough numbers are necessary to obtain reasonable results of the electronic prop-

erties at low temperatures without the problematic numerical errors due to the finite size effects. This large numerical cost becomes severer for storing two-particle quantities such as the susceptibility in a spin sector than for storing single-particle quantities such as the self-energy since the two-particle quantity has four orbital indices, which is twice as large as the orbital indices of the single-particle quantity.

With the above background, I formulated the resistivity and the Hall coefficient in the weak-field limit for a multiorbital Hubbard model using the linear-response theory and the extended Éliashberg theory and adopted this method to the inplane charge transports of paramagnetic (PM) quasi-two-dimensional ruthenates away from and near the AF QCP in combination with the fluctuation-exchange (FLEX) approximation with the current vertex correction (CVC) arising from the self-energy and the Maki-Thompson (MT) four-point vertex function for the  $t_{2g}$ -orbital Hubbard model on a square lattice [1, 2]. To my knowledge, this [1] is the first research to study the transport properties of a correlated multiorbital system including the CVCs arising from the self-energy and four-point vertex function due to electron correlation. From a technical point of view, I resolved the numerical difficulty explained above by using the symmetry of the system and utilizing the arrays efficiently, resulting in the reductions of the memory of the arrays and the time of the numerical calculations.

There were several remaining issues in my previous studies [1, 2], although I succeeded in reproducing several experimental results of  $\text{Sr}_2\text{RuO}_4$  and  $\text{Sr}_2\text{Ru}_{0.075}\text{Ti}_{0.025}\text{O}_4$  satisfactorily and obtaining several characteristic aspects of a correlated multiorbital system. Among those remaining issues, it is highly desirable to clarify the main effects of the CVC arising from the Aslamasov-Larkin (AL) four-point vertex function on the inplane charge transports. In the previous studies [1, 2], I neglected the AL CVC since I assumed that the CVCs arising from the self-energy and the MT four-point vertex function are sufficient for qualitative discussions. This is because it is known in a single-orbital Hubbard model on a square lattice [3] that the AL CVC does not qualitatively change the transport properties near an AF QCP since the MT CVC is more important. However, it is unclear whether the AL CVC keeps the results obtained in the previous studies qualitatively unchanged since there has been no previous research to study its effects in a correlated multiorbital system. Thus, it is necessary to check the validity of the assumption used in the previous studies. Furthermore, the analysis of the effects of the AL CVC is important for a deeper understanding of the roles of the CVCs in a correlated multiorbital system since not only the MT but also the AL CVC is vital to hold conservation laws.

Due to the above importance to clarify the main effects of the AL CVC, I studied these effects by considering the main terms of the AL CVC in this project [4]. As a result, I showed that the results of the previous studies remain qualitatively unchanged even including the main terms of the AL CVC and obtained several important results. The most important result is finding the existence of two distinct regions of the temperature dependence of the transport properties near the AF QCP: in low temperature region, the CVCs arising from the self-energy and the MT four-point vertex function are sufficient even in a quantitative level;

in high temperature region, the CVC arising from the self-energy is sufficient since the effects of the MT and the AL CVC are nearly cancelled out. Although the existence of the former region was pointed out about 16 years ago by H. Kontani *et al.* [3] on the basis of the analytic discussion, it is important to show the existence of the two distinct region in the numerical calculations for a deeper understanding of the effects of the CVCs. In addition, this finding gives a useful guide to choose the simple theory that is sufficient to study the transport properties.

Since the developments of the computational resources are one of the vital factors to achieve the above important result, it is very important to continue providing the computational resources of the Supercomputer Center at the Institute for Solid State Physics in order to develop our understanding of many-body effects in a correlated electron system.

## References

- [1] N. Arakawa: Phys. Rev. B **90** (2014) 245103.
- [2] N. Arakawa: arXiv:1503.06937; accepted for publication in Modern Physics Letters B as an invited brief review article.
- [3] H. Kontani, K. Kanki, and K. Ueda: Phys. Rev. B **59** (1999) 14723.
- [4] N. Arakawa: in preparation.

# Quantum Phase Transition in the Hubbard Model on the $\text{CaV}_4\text{O}_9$ lattice

Yuki Yanagi

*Department of Physics, Faculty of Science and Technology, Tokyo University of Science  
Noda, Chiba 278-8510*

$\text{CaV}_4\text{O}_9$  is a well-known typical example of spin-gapped systems[1]. The minimal model for  $\text{CaV}_4\text{O}_9$ , the Heisenberg model on the 1/5-depleted square lattice shows two distinct spin gapped phases depending on values of  $J_1$  and  $J_2$ , where  $J_1$  and  $J_2$  are the intra-plaquette and intra-dimer couplings, respectively[2].

Inspired by the results of the Heisenberg model, we have investigated the nonmagnetic Mott transition in the itinerant model on the same lattice, the 1/5-depleted square lattice Hubbard model at half-filling[3]. In this project, we have revealed the nature of the Mott transition for  $t_1 < t_2$  by using the 8-site cellular dynamical mean field theory (CDMFT), where  $t_1$  and  $t_2$  are the intra-plaquette and intra-dimer hoppings, respectively (see Fig. 1). In the CDMFT, a lattice problem is mapped onto a cluster one with open boundary conditions embedded in a electronic bath which is self-consistently determined. We have employed the auxiliary field continuous-time quantum Monte Carlo method (CT-AUX) as the cluster solver[4]. This numerically exact method is based on a decoupling of the on-site Coulomb interaction term by auxiliary Ising spins and a weak coupling expansion of the partition function. Although the CT-AUX is suitable for the cluster solver with large cluster sizes, numerical calculations at low temperatures and for large Coulomb interactions  $U$  are rather time-consuming. Therefore, to reduce the computation time, we have performed the parallel cal-

culatation in system-B. We have calculated the double occupancy  $d$ , electron self-energy and one-particle Green's function. We have found that the Mott transition occurs without any discontinuous jumps in  $U$ - $d$  curves and clarified that the transition is nothing but a Lifshitz transition driven by the dimerization due to the non-local correlation effects.

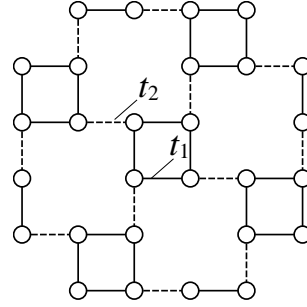


Figure 1: Schematic of the 1/5-depleted square lattice.

This work was done in collaboration with Prof. K. Ueda.

## References

- [1] S. Taniguchi *et al.*, J. Phys. Soc. Jpn. **64**, 2758 (1995).
- [2] K. Ueda *et al.*, Phys. Rev. Lett. **76**, 1932 (1996)
- [3] Y. Yanagi and K. Ueda, Phys. Rev. B **90**, 085113.
- [4] E. Gull *et al.*, Rev. Mod. Phys. **83**, 349.

# Multipolar excitations in pyrochlore systems

MASAFUMI UDAGAWA

*Department of Physics, Gakushuin University*

*1-5-1 Mejiro, Toshima-ku, Tokyo, 171-8588*

Recently, multipole ordering has been drawing considerable interest as a driving force of novel multiferroic response and anomalous transport phenomena. We have pursued the realization of multipole ordering in systems with frustrated pyrochlore structure and their variants, and found several ordering patterns, as well as the existence of non-trivial multipolar excitations.

Among many multipole orderings, here we focus on the toroidal excitation realized in the non-equilibrium process in pyrochlore spin ice system. Spin ice is a prototypical frustrated magnet, with a number of remarkable features, such as ground-state degeneracy, fractional monopole excitations, and quasi-long range correlation, which now serve as fundamental concepts to understand frustrated magnetism in general. Among these properties, dynamical character of spin ice has drawn a considerable attention. Indeed, in dipolar spin ice, drastic divergence of relaxation time has been observed at low temperatures, and it has been revealed theoretically that monopole excitations play a key role in the slow dynamics.

In a variant of spin ice model,  $J_1$ - $J_2$ - $J_3$  spin ice model, the monopole exceptions interact with each other via short-range forces. We analyzed the classical dynamics of this model with a waiting-time Monte Carlo method, and clarified the time evolution of monopole density and magnetization for all the range of  $J_2 = J_3 \equiv J$ . In particular, we found several quasi-stable macroscopic states survive as a steady state with macroscopically long relaxation

time, even though they have higher energy compared with ground state. Among them, we found a collective excitation which we term "monopole jellyfish" (1). This monopole jellyfish excitation possesses a toroidal spin structure, and can be regarded as a sort of multipole excitation. This excitation may give a crucial clue to the spontaneous Hall effect [1] observed in  $\text{Pr}_2\text{Ir}_2\text{O}_7$ , which is known as a metallic spin ice [2].

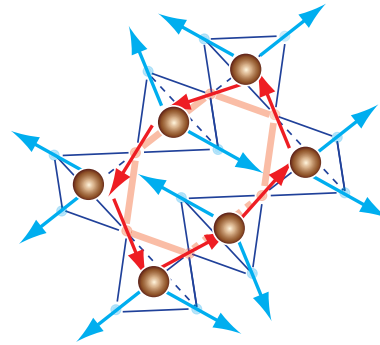


図 1: Schematic figure of monopole jellyfish.

## 参考文献

- [1] Y. Machida et al., *Nature* **463**, 210 (2010).
- [2] M. Udagawa, L. D. C. Jaubert, C. Castelnovo and R. Moessner, in preparation

# Research on Kondo effect in electron-phonon systems by numerical renormalization group method

Takashi HOTTA

*Department of Physics, Tokyo Metropolitan University  
1-1 Minami-Osawa, Hachioji, Tokyo 192-0397*

In this research, we discuss the Kondo effect in a spinless two-orbital conduction electron system coupled with anharmonic Jahn-Teller vibration by employing a numerical renormalization group technique [1]. When a temperature  $T$  is decreased, we encounter a plateau of  $\log 3$  entropy due to quasi-triple degeneracy of local low-energy states, composed of vibronic ground states and the first excited state with an excitation energy of  $\Delta E$ . Around at  $T \approx \Delta E$ , we observe an entropy change from  $\log 3$  to  $\log 2$ . This  $\log 2$  entropy originates from the rotational degree of freedom of the vibronic state and it is eventually released due to the screening by orbital moments of conduction electrons, leading to the Kondo effect of a Jahn-Teller ion.

The Hamiltonian for electrons coupled with anharmonic Jahn-Teller vibration is given by

$$H_0 = g(\tau_x Q_2 + \tau_z Q_3) + (P_2^2 + P_3^2)/(2M) \\ + A(Q_2^2 + Q_3^2) + B(Q_3^3 - 3Q_2^2 Q_3) \\ + C(Q_2^2 + Q_3^2)^2,$$

where  $g$  is the electron-vibration coupling constant,  $\tau_x = d_a^\dagger d_b + d_b^\dagger d_a$ ,  $\tau_z = d_a^\dagger d_z - d_b^\dagger d_b$ ,  $d_\tau$  is the annihilation operator of spinless fermion with orbital  $\tau$ ,  $a$  and  $b$  correspond to  $x^2 - y^2$  and  $3z^2 - r^2$  orbitals, respectively,  $M$  is the reduced mass of Jahn-Teller oscillator,  $Q_2$  and  $Q_3$  denote normal coordinates of  $(x^2 - y^2)$ - and  $(3z^2 - r^2)$ -type Jahn-Teller oscillation, respectively,  $P_2$  and  $P_3$  indicate corresponding canonical momenta,  $A$  indicates the quadratic term of the potential, and  $B$  and  $C$  are, respec-

tively, the coefficients for third- and fourth-order anharmonic terms. Note that we consider only the anharmonicity which maintains the cubic symmetry. Here we consider the case of  $A > 0$  and  $C > 0$ , while  $B$  takes both positive and negative values.

After some algebraic calculations, we obtain

$$H_0 = \sqrt{\alpha}\omega[(a_2 + a_2^\dagger)\tau_x + (a_3 + a_3^\dagger)\tau_z] \\ + \omega(a_2^\dagger a_2 + a_3^\dagger a_3 + 1) + \beta\omega[(a_3 + a_3^\dagger)^3 \\ - 3(a_2 + a_2^\dagger)^2(a_3 + a_3^\dagger)]/3 \\ + \gamma\omega[(a_2 + a_2^\dagger)^2 + (a_3 + a_3^\dagger)^2]/8,$$

where  $\omega$  is the vibration energy, given by  $\omega = \sqrt{2A/M}$ ,  $a_2$  and  $a_3$  are annihilation operators of phonons for Jahn-Teller oscillations,  $\alpha$  is the non-dimensional electron-phonon coupling constant, given by  $\alpha = g^2/(2M\omega^3)$ ,  $\beta$  and  $\gamma$  are non-dimensional anharmonicity parameters, defined by  $\beta = 3B/[(2M)^{3/2}\omega^{5/2}]$  and  $\gamma = 2C/(M^2\omega^3)$ , respectively.

Note that it is important to consider the parity for phonon vibration, when we determine the properties of phonon states more precisely. However, such a discussion is meaningful only in the high-temperature region, and so we do not mention it anymore in this report, since we are interested only in the low-temperature properties of Kondo phenomena. Here we remark the appearance of the peculiar chaotic properties of the anharmonic Jahn-Teller vibration in the high-temperature region [2].

Now we consider the conduction electron hybridized with localized electrons. Then, the

model is expressed as

$$H = \sum_{\mathbf{k}\tau} \varepsilon_{\mathbf{k}} c_{\mathbf{k}\tau}^\dagger c_{\mathbf{k}\tau} + \sum_{\mathbf{k}\tau} (V c_{\mathbf{k}\tau}^\dagger d_\tau + \text{h.c.}) + H_0,$$

where  $\varepsilon_{\mathbf{k}}$  is the dispersion of conduction electron,  $c_{\mathbf{k}\tau}$  is an annihilation operator of conduction electron with momentum  $\mathbf{k}$  and orbital  $\tau$ , and  $V$  is the hybridization between conduction and localized electrons. The energy unit is a half of the conduction bandwidth, which is set as unity in the following.

To investigate the electronic and phononic properties of  $H$  at low temperatures, we usually discuss the corresponding susceptibilities, entropy, and specific heat. For the evaluation of these quantities, here, we employ the numerical renormalization group (NRG) method, in which the momentum space is logarithmically discretized to efficiently include the conduction electrons near the Fermi energy.

In Fig. 1, we show the typical NRG result of entropy and specific heat. In a high-temperature region, entropy is rapidly decreased with decreasing temperature  $T$  and it forms a plateau of  $\log 3$  between  $10^{-5} < T < 10^{-2}$ . The origin of the  $\log 3$  entropy is the quasi-degeneracy of local low-energy states, originating from the position degree of freedom of oscillation in the strong anharmonic potential with three minima. As easily understood from the above explanation, the quasi-triple degeneracy should be lifted at approximately  $T = \Delta E$ , where  $\Delta E$  denotes the first excitation energy among local low-energy states. In fact, we observe a clear peak in the specific heat at  $T \approx \Delta E$ , since the entropy is changed from  $\log 3$  to  $\log 2$ . The  $\log 2$  entropy originates from the double degeneracy in the local vibronic states with double degeneracy, corresponding to clockwise and anticlockwise rotational directions. At a temperature where the rotational moment is screened by orbital moments of conduction electrons, the entropy of  $\log 2$  is eventually released and a peak is formed in the specific heat. This peak naturally defines a characteristic temperature,

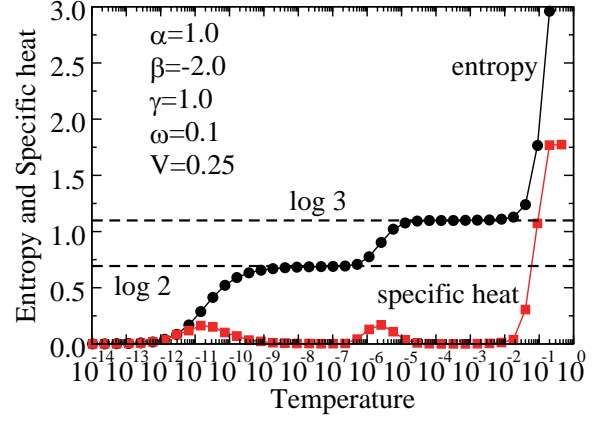


Figure 1: Entropy and specific heat for  $\omega=0.1$ ,  $\alpha=1$ ,  $\beta=-2$ , and  $\gamma=1$ .

which is called here the Kondo temperature  $T_K$ . Due to the lack of the space, we do not show further results in this report, but it has been confirmed that  $T_K$  is well explained by the effective  $s$ - $d$  model with anisotropic exchange interactions. As for details, readers should refer Ref. [1].

In summary, we have clarified the Kondo effect in the Jahn-Teller-Anderson model with cubic anharmonicity. We have found the  $\log 3$  plateau in the entropy due to quasi-triple degeneracy in the low-energy states including vibronic ground states. With further decrease in temperature, we have observed the region of the  $\log 2$  plateau due to the vibronic state with rotational degree of freedom. The rotational moment of the vibronic state has been found to be suppressed by the screening of orbital moments of conduction electrons, leading to the Kondo effect.

## References

- [1] T. Hotta, J. Phys. Soc. Jpn. **83**, 104706 (2014).
- [2] T. Hotta and A. Shudo, J. Phys. Soc. Jpn. **83**, 083705 (2014).

# Theoretical Analysis of Quantum Properties at Heterostructures and Superlattices of Strongly Correlated Systems

NORIO KAWAKAMI

*Department of Physics, Kyoto University, Kyoto 606-8502, Japan*

Starting with their experimental realization, multilayered heterostructures of strongly-correlated electron systems have attracted much attention among the primary topics in condensed matter physics. New aspects in this field have been revealed via recent work on  $(\text{LaVO}_3)_n/(\text{SrVO}_3)_m$  perovskite superlattices, consisting of the periodically aligned  $\text{LaVO}_3$  and  $\text{SrVO}_3$  layers. The bulk  $\text{LaVO}_3$  is a Mott insulating antiferromagnet, while  $\text{SrVO}_3$  is a strongly correlated paramagnetic metal with one conducting  $d$  electron per V ion, which is changed into an insulator in the 2D thin film. The experiments on the  $(\text{LaVO}_3)_n/(\text{SrVO}_3)_m$  superlattices have reported the following intriguing phenomena[1]. (i) The temperature dependence of the in-plane resistivity shows an anomalous peak structure around the characteristic temperature  $T^*$ . Particularly a Fermi liquid metallic behavior is observed sufficiently below  $T^*$ . In addition the magnitude of  $T^*$  is altered with inserting additional  $\text{SrVO}_3$  layers between  $\text{LaVO}_3$  layers. (ii) Other transport measurements detect occurrence of a MIT in  $(\text{LaVO}_3)_n/(\text{SrVO}_3)_1$  superlattices with varying the number of  $\text{LaVO}_3$  layers from one to three. Some theoretical attempts of understanding magnetic properties have already been made, but the nature of exotic transport properties are currently under discussion.

In this paper, we propose a microscopic mechanism resolving the issues of resistivity measurements on  $(\text{LaVO}_3)_n/(\text{SrVO}_3)_m$  superlattices[2]. For this purpose, we study the Mott physics in a simple Hubbard superlattice model consisting of the Mott-insulating layers and metal layers. The computed resistivity is shown in Fig.1. It is seen that the 3D

Fermi-liquid metallic state is realized for various choices of superlattice configuration with decreasing temperature. We find that electron correlation effects under the superlattice geometry are strongly influenced by the periodicity of the superlattice, and cause an even-odd oscillation in the quasi-particle weight depending on the number of metal layers. We further clarify that this dependence further induces the detectable difference in the electrical resistivity, which may be essential for understanding some key experiments. Our model provides a reasonable explanation for experiments on  $(\text{LaVO}_3)_n/(\text{SrVO}_3)_m$ , including a peak formation in the resistivity and also the occurrence of a metal-insulator transition.

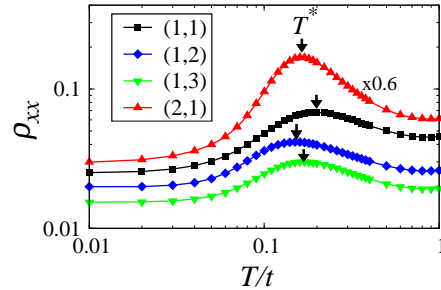


Figure 1: Temperature dependence of the in-plane resistivity  $\rho_{xx}$  for the  $(m,n)$  superlattices, where the unit cell consists of  $m$  Mott insulator layers and  $n$  metallic layers. The arrows show the peak position of the resistivity.

## References

- [1] A. David et al., Appl. Phys. Lett. **98**, 212106 (2011); U. Lueders et al., J Phys Chem Solids **75**, 1354 ((2014).
- [2] S. Ueda and N. Kawakami, submitted.

# Theoretical Studies of Correlation Effects for Quantum Phase Formation in Non-Homogeneous Systems

NORIO KAWAKAMI

*Department of Physics, Kyoto University, Kyoto 606-8502, Japan*

To reveal how interaction between particles influence physical properties has been a central issue in the past few decades. The influence caused by the spatial non-homogeneity has been also analyzed from 1958 when P. W. Anderson suggested the localization of electrons due to a random potential [1]. While it is expected that the competition or collaboration between these two effects might trigger novel physical phenomena, there are many open questions to this day.

Cold atoms in optical lattices have provided a great deal of control over system parameters. One can easily tune the strength of the interaction between particles by Feshbach resonance and also realize the systems with the spatial non-homogeneity by suitably combining different laser beams[2]. Therefore, the cold atomic systems provide an intriguing platform where one analyzes the competition(collaboration) between the interaction and the effects of the spatial non-uniformity.

One of the main issues in our research project is to study how the spatial non-uniformity affects the properties of the multi-component Fermi systems which are realized in cold atomic systems. We focus on the  $SU(N)$  attractive Fermi systems, where the interaction between the particles is independent of the components of particles. The  $SU(N)$  Fermi systems with the disordered potential in cold atoms are well-described by a  $SU(N)$  attractive Anderson-Hubbard model. It is known that the charge-density-wave (CDW) state and the  $s$ -wave superfluid (SF) state are degenerate in the  $SU(2)$  model without disorder at zero temperature and half-filling in a two-dimensional square lattice. Disorder lifts this

degeneracy and hence stabilizes the SF state as a ground state. By contrast, for  $N > 2$ , in the absence of disorder the CDW state is stabilized as a ground state. Therefore, what kind of state is stabilized as the ground state in the  $SU(N > 2)$  systems with disorder is an interesting open question.

To answer this question, we have first analyzed the  $SU(3)$  and  $SU(4)$  attractive Anderson-Hubbard model by using a real-space Bogoliubov-de Gennes(BdG) method. Within our method, the non-homogeneity of disordered systems is fully captured though we treat the effects of the attractive interaction as a mean-field. BdG equations are solved on a finite-size lattice and a disorder average of the physical quantities obtained by this method is taken. If the calculations are performed for smaller lattice sizes, we might overestimate the physical quantities corresponding to long-range orders, for example the superfluid order parameter, the charge structure factor, and so on. Also, a disorder average over only a small number of configurations might lead to erroneous conclusions owing to the sample dependence. For these reasons, the calculations are performed for lattice sizes up to  $32 \times 32$ , and the results are averaged over 12-40 different configurations in this study. To perform the large-scale numerical calculations, we have fully made use of the supercomputer resource at ISSP. Namely, we have performed large-scale parallel computing to diagonalize matrices with a large dimension.

The ground-state phase diagrams of the  $SU(3)$  and  $SU(4)$  cases have been obtained in this study [3]. The phase diagram for the  $SU(3)$  case is shown in Fig.1 and that for



SU(4) in Fig.2, respectively. From Fig.1, it is found that disorder triggers the CDW-SF transition at some disorder strength, and the SF-Anderson localized state(AL) transition occurs as the disorder strength further increases. Also, each critical disorder where the CDW-SF transition and the SF-AL transition occur increases as the strength of the attractive interaction increases. It is pointed out in this study that the CDW-SF transition and the SF-AL transition are of first order. The phase diagram for the SU(4) case indicates that the CDW state directly undergoes a transition to the AL. This result suggests that the SF state cannot be stabilized as a ground state in the SU(4) attractive Fermi systems with disorder at half-filling because the CDW state is rather stable and thus the energy gained by the SF order is not large enough to stabilize the superfluidity in between the CDW state and the AL.

However, the above conclusion has been drawn within the mean-field approximation. Hence it is important to evaluate the validity of this conclusion by using more accurate methods. For this purpose, we have performed additional calculations using quantum Monte Carlo simulations. The results obtained by these calculations will soon be reported elsewhere.

## References

- [1] P. W. Anderson, Phys. Rev. **109**, 1492 (1958).
- [2] J. E. Lye *et al.*, Phys. Rev. Lett. **95**, 070401 (2005).
- [3] M. Sakaida *et al.*, Phys. Rev. A. **90**, 013632 (2014).

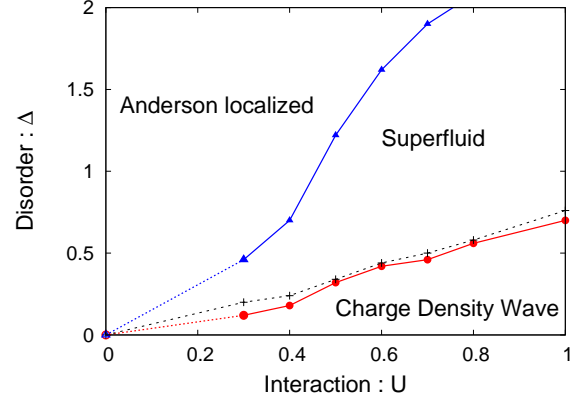


Figure 1: Ground-state phase diagram of the SU(3) attractive Anderson-Hubbard model. The red solid line with closed circles shows the CDW-SF transition points and the blue solid line with closed triangles the SF-AL transition points. The black dashed line denotes the points where the value of the free energy of the CDW state corresponds to that of the SF state.

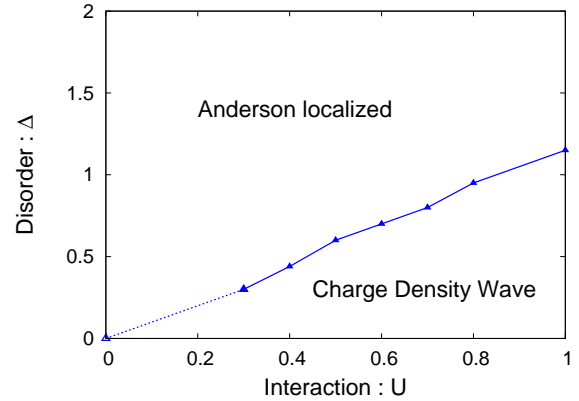


Figure 2: Ground-state phase diagram of the SU(4) attractive Anderson-Hubbard model. The CDW-AL transition points are denoted by the blue solid line with closed triangles.

# Numerical Studies on Localization and Fractionalization of Many-Body Electrons with Strong Spin-Orbit Couplings

Youhei YAMAJI

*Quantum-Phase Electronics Center, University of Tokyo  
Hongo, Bunkyo-ku, Tokyo 113-8656*

Theoretical prediction of emergent quantum phases in iridium oxides has stimulated both of experimental and further theoretical studies. Especially, a honeycomb lattice iridium oxide  $\text{Na}_2\text{IrO}_3$  has attracted much attention as a candidate of the Kitaev's spin liquid. Recent experiments, however, show that the ground state of  $\text{Na}_2\text{IrO}_3$  is a magnetically ordered insulator.

A remaining challenge is to realize the Kitaev's spin liquid by learning from  $\text{Na}_2\text{IrO}_3$ . First of all, we need to clarify what the effective hamiltonian of  $\text{Na}_2\text{IrO}_3$  is. Then, we may understand how to design spin liquid materials.

By employing an *ab initio* scheme to derive low-energy effective hamiltonians based on the density functional theory, we construct an effective spin hamiltonian of  $\text{Na}_2\text{IrO}_3$  given as a generalized Kitaev-Heisenberg model [1],

$$\hat{H} = \sum_{\Gamma=X,Y,Z} \sum_{\langle \ell, m \rangle \in \Gamma} \vec{S}_\ell^T J_\Gamma \vec{S}_m, \quad (1)$$

where the bond-dependent exchange couplings are defined as

$$J_X = \begin{bmatrix} K' & I_2'' & I_2' \\ I_2'' & J'' & I_1' \\ I_2' & I_1' & J' \end{bmatrix},$$

$$J_Y = \begin{bmatrix} J'' & I_2'' & I_1' \\ I_2'' & K' & I_2' \\ I_1' & I_2' & J' \end{bmatrix},$$

$$J_Z = \begin{bmatrix} J & I_1 & I_2 \\ I_1 & J & I_2 \\ I_2 & I_2 & K \end{bmatrix}. \quad (2)$$

Here we estimated these exchange couplings as  $K = -30.7$  meV,  $J = 4.4$  meV,  $I_1 = -0.4$  meV,  $I_2 = 1.1$  meV,  $K' = -23.9$  meV,  $J' = 2.0$  meV,  $J'' = 3.2$  meV,  $I_1' = 1.8$  meV,  $I_2' = -8.4$  meV, and  $I_2'' = -3.1$  meV.

Based on numerically simulated specific heat of the generalized Kitaev-Heisenberg model, we propose that half plateau structures of temperature-dependences of entropy are hallmarks of the Kitaev's spin liquids or quantum spin systems close to the Kitaev's spin liquids [1, 2].

We have examined the effective spin hamiltonian so far. However,  $\text{Na}_2\text{IrO}_3$  is expected to be close to metal-insulator transitions. To clarify effects of itinerancy of electrons, we have recently developed a variational Monte Carlo method applicable to *ab initio*  $t_{2g}$  hamiltonian with strong spin-orbit couplings [3].

## References

- [1] Y. Yamaji, Y. Nomura, M. Kurita, R. Arita, and M. Imada: Phys. Rev. Lett. **113** (2014) 107201.
- [2] Y. Yamaji: to appear in AIP Conference Proceedings.
- [3] M. Kurita, Y. Yamaji, S. Morita, and M. Imada: arXiv:1411.5198.

# Ab initio calculations for Mn analog of iron-based superconductors LaMnAsO and LaMnPO

Takahiro MISAWA

*Department of Applied Physics, University of Tokyo,  
7-3-1 Hongo, Bunkyo-ku, Tokyo 113-8656, Japan*

In iron-based superconductors, although it is believed that electron correlations play key roles in stabilizing the high-temperature superconductivity, its role is not fully understood yet. Because iron-based superconductors are multi-orbital system (typically five  $d$  orbitals exist around the Fermi level), it is also suggested the orbital degrees of freedom play key role. To clarify microscopic mechanism of superconductivity in iron-based superconductors, it is necessary to evaluate strength of interactions in an *ab initio* way and it is also necessary to seriously examine the effects of electronic correlations. To challenge these issues, we employ *ab initio* downfolding scheme [1]. In this scheme, we first calculate the global band structures for target materials. Then, we eliminate high-energy degrees of freedom by using the constrained random-phase-approximation method and obtain the low-energy effective model. To solve the *ab initio* low-energy effective models, we use many-variable variational Monte Carlo method, which properly takes into account both spatial and dynamical quantum fluctuations. We applied this method to the iron-based superconductors and we showed that the calculated magnetic order was shown to correctly reproduce the experimental material dependences [2, 3].

In this project, by extending these normal state studies, we study how the superconductivity emerges in the low-energy effective model of an electron-doped iron-based superconductor LaFeAsO [4]. To solve the low-energy effective model, we mainly use the system B with hybrid parallelization (typically 8 OPENMP threads  $\times$  256 MPI processes). As a result, we show that superconductivity

emerges in essential agreement with the experimental results. The pairing satisfies gapped  $s_{\pm}$  symmetry and the specific orbital ( $X^2 - Y^2$ ) is shown to play a key role in stabilizing the superconducting phase as well as the antiferromagnetic phase. Furthermore, we find a one-to-one correspondence between superconductivity and enhanced uniform charge fluctuations. We also perform the analysis for the Hubbard model and find that similar one-to-one correspondence also exists in the Hubbard model [5], which is one of the simplest models for cuprates. Despite many differences between iron-based superconductors and cuprates, our study suggests that the enhanced uniform charge fluctuations play a key role in stabilizing the superconductivity in both materials. Further theoretical exploration such as examining the stability of the superconductivity in hole-doped materials such as LaMnAsO and LaMnPO is intriguing issue but is left for future study.

## References

- [1] For a review, see T. Miyake and M. Imada: J. Phys. Soc. Jpn. **79** (2010) 112001.
- [2] T. Misawa, K. Nakamura, and M. Imada: J. Phys. Soc. Jpn. **80** (2011) 023704.
- [3] T. Misawa, K. Nakamura, and M. Imada: Phys. Rev. Lett. **108** (2012) 177007.
- [4] T. Misawa and M. Imada: Nat. Commun. **5** (2014) 5738.
- [5] T. Misawa and M. Imada: Phys. Rev. B **90** (2014) 1115137.

# Non-equilibrium phase transitions in superconductors and electron-phonon systems

Hideo AOKI

*Department of Physics, University of Tokyo  
Hongo, Tokyo 113-0033*

## Thermalization crossover in electron-phonon systems[1]

We study the relaxation of the Holstein model, a simplest possible electron-phonon system, after a sudden switch-on of the interaction with the nonequilibrium dynamical mean field theory (DMFT)[1]. We show that, on the weaker interaction side the phonon oscillations are damped more rapidly than the electron thermalization time scale, while converse is true in the stronger interaction regime. In equilibrium, we have shown that the phase diagram contains a supersolid phase accompanied by a quantum critical point.[2]

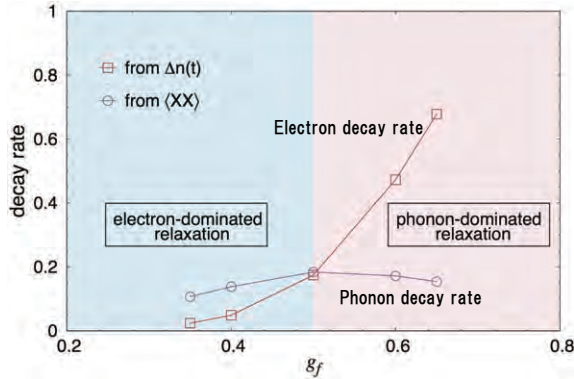


Figure 1: Thermalization crossover[1].

## Nonequilibrium dynamical mean-field theory and its cluster extension[3, 4]

Nonequilibrium DMFT is one of the most powerful approaches to deal with nonequilibrium correlated many-body systems, as we have reviewed in Ref.[3]. We have also pro-

posed the nonequilibrium dynamical cluster approximation (DCA) [4], in which the lattice model is mapped to a multi-site cluster. We have applied it to the one- and two-dimensional Hubbard models.

## Topological Mott insulator in cold atoms on an optical lattice[5]

We design for fermionic cold atoms in an optical lattice a spontaneous symmetry breaking induced by the inter-atom interaction into a topological Chern insulator in a continuous space. Such a state, sometimes called the topological Mott insulator (TMI), requires, in the tight-binding model, unusually large off-site interactions. Here we overcome the difficulty by introducing a spin-dependent potential, where a sizeable inter-site interaction is achieved by a shallow optical potential. We employ the density functional theory for cold-atoms, here extended to accommodate non-collinear spin structures emerging in the topological regime, to quantitatively demonstrate the phase transition to TMI.

## Light-induced collective pseudospin precession resonating with Higgs mode in a superconductor[6, 7]

We show that a strong light field can induce oscillations of the superconducting order parameter with twice the frequency  $\Omega =$  of the terahertz field. This is a collective pre-

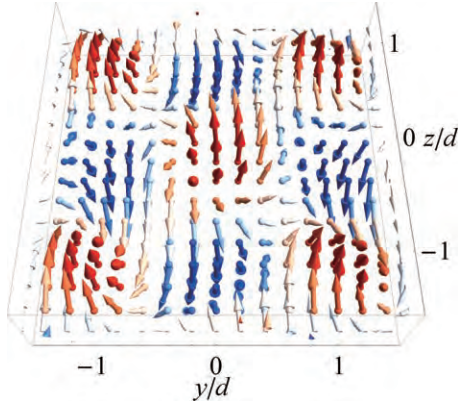


Figure 2: Spatial texture of the magnetization (arrows) for the designed topological Mott insulator[5].

cession of Anderson's pseudospins in ac driving fields through a nonlinear light-matter coupling, and experimentally detected in NbN. Furthermore, a resonance between the field and the Higgs amplitude mode of the superconductor is shown to occur at  $2\Omega =$  the superconducting gap. This produces a large third-harmonic generation, which is also experimentally verified. We have then examined this more accurately in the attractive Hubbard model with the nonequilibrium DMFT to endorse that the resonance for the third harmonic generation does remain.

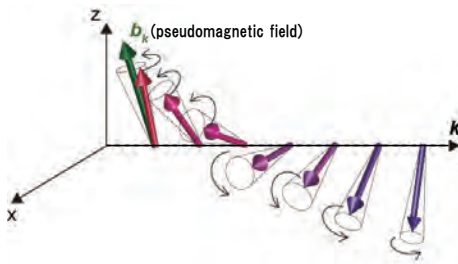


Figure 3: A schematic picture of the pseudospin precession in the Higgs mode in a superconductor.[6]

## References

- [1] Yuta Murakami, Philipp Werner, Naoto Tsuji and Hideo Aoki: Interaction quench in the Holstein model: Thermalization crossover from electron- to phonon-dominated relaxation, *Phys. Rev. B* **91**, 045128 (2015).
- [2] Yuta Murakami, Philipp Werner, Naoto Tsuji and Hideo Aoki: Supersolid phase accompanied by a quantum critical point in the intermediate coupling regime of the Holstein model, *Phys. Rev. Lett.* **113**, 266404 (2014).
- [3] Hideo Aoki, Naoto Tsuji, Martin Eckstein, Marcus Kollar, Takashi Oka and Philipp Werner: Nonequilibrium dynamical mean-field theory and its applications, *Rev. Mod. Phys.* **86**, 779 (2014).
- [4] Naoto Tsuji, Peter Barmettler, Hideo Aoki and Philipp Werner: Nonequilibrium dynamical cluster theory, *Phys. Rev. B* **90**, 075117 (2014).
- [5] S. Kitamura, N. Tsuji and H. Aoki: An interaction-driven topological insulator in fermionic cold atoms on an optical lattice: A design with a density functional formalism, arXiv:1411.3345.
- [6] Ryusuke Matsunaga, Naoto Tsuji, Hiroyuki Fujita, Arata Sugioka, Kazumasa Makise, Yoshinori Uzawa, Hirotaka Terai, Zhen Wang, Hideo Aoki, and Ryo Shimano: Light-induced collective pseudospin precession resonating with Higgs mode in a superconductor, *Science* **345**, 1145 (2014).
- [7] Naoto Tsuji and Hideo Aoki: Theory of Anderson pseudospin resonance with Higgs mode in a superconductor, arXiv:1404.2711.

# Insulating state of multi-orbital electronic system with strong spin-orbit coupling

Toshihiro SATO

*Computational Condensed Matter Physics Laboratory, RIKEN  
Wako, Saitama 351-0198, Japan*

Recently, many experimental studies have reported interesting behaviors of 5d transition-metal Ir oxides. These materials show a strong spin orbit coupling (SOC) with an electron correlation and the SOC splits the  $t_{2g}$  bands with the low-spin state in the crystal field into the effective local angular momentum  $J_{\text{eff}} = 1/2$  doublet and  $J_{\text{eff}} = 3/2$  quartet bands. The well-known material is  $\text{Sr}_2\text{IrO}_4$  with totally five electrons in the  $t_{2g}$  bands and  $J_{\text{eff}} = 1/2$  antiferromagnetic (AF) insulator, indication of the half-filled  $J_{\text{eff}} = 1/2$  and full-filled  $J_{\text{eff}} = 3/2$  bands, has been observed[1, 2, 3, 4]. However, the ground state of multi-orbital systems with the competition between the electron correlations and the SOC has not been well understood.

We study electronic structure of the three-orbital Hubbard model with the full Hund' rule coupling and the SOC terms at five electrons filling

$$\begin{aligned}
 H = & \sum_{\langle i,j \rangle, \gamma, \sigma} t^\gamma c_{i\sigma}^\dagger c_{j\sigma}^\gamma - \sum_{i, \gamma, \sigma} \mu^\gamma n_{i\sigma}^\gamma, \\
 & + U \sum_{i, \gamma} n_{i\uparrow}^\gamma n_{i\downarrow}^\gamma + \frac{U' - J}{2} \sum_{i, \gamma \neq \delta, \sigma} n_{i\sigma}^\gamma n_{i\sigma}^\delta \\
 & + \frac{U'}{2} \sum_{i, \gamma \neq \delta, \sigma} n_{i\sigma}^\gamma n_{i\sigma}^\delta - J \sum_{i, \gamma \neq \delta} c_{i\uparrow}^\dagger c_{i\downarrow}^\gamma c_{i\downarrow}^\delta c_{i\uparrow}^\dagger \\
 & + J' \sum_{i, \gamma \neq \delta} c_{i\uparrow}^\dagger c_{i\downarrow}^\gamma c_{i\downarrow}^\delta c_{i\uparrow}^\dagger \\
 & + \lambda \sum_{i, \gamma, \delta, \sigma, \sigma'} \langle \gamma | \mathbf{L}_i | \delta \rangle \cdot \langle \sigma | \mathbf{S}_i | \sigma' \rangle c_{i\sigma}^\dagger c_{i\sigma'}^\delta,
 \end{aligned}$$

where  $t^\gamma$  is the nearest-neighbor hopping amplitude with orbital  $\gamma = (yz, zx, xy)$  and  $\mu^\gamma$  is the chemical potential.  $U$  ( $U'$ ) is the intra-orbital (inter-orbital) Coulomb interaction and  $J$  ( $J'$ ) is the Hund' s (pair-hopping) coupling,

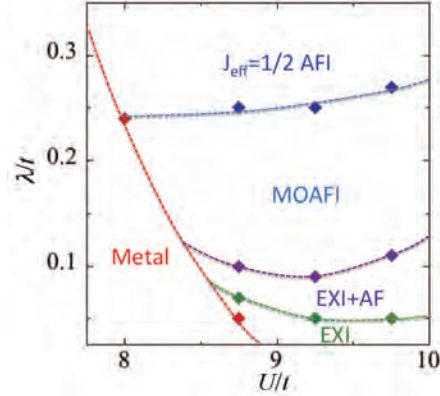


Figure 1:  $U$ - $\lambda$  phase diagram at  $T = 0.06t$ . (MO)AFI and EXI show antiferromagnetic insulating and excitonic insulating phases, respectively.

and we set  $U = U' + 2J$  and  $J = J' = 0.15U$ .  $\lambda$  is the SOC and  $\mathbf{L}_i$  ( $\mathbf{S}_i$ ) is the orbital (spin) angular momentum operator at site  $i$ .  $c_{i\sigma}^\dagger$  ( $c_{i\sigma}^\gamma$ ) is an electron creation (annihilation) operator with spin  $\sigma$  and orbital  $\gamma$  at site  $i$  and electron density operator is  $n_{i\sigma}^\gamma = c_{i\sigma}^\dagger c_{i\sigma}^\gamma$ . By using the dynamical mean field theory [5] employing a semielliptic bare density of states with the equal bandwidth ( $t^\gamma = t$ ) for  $t_{2g}$  bands and the continuous-time quantum Monte Carlo solver based on the strong coupling expansion [6], we investigated the phase diagram in the parameter space of  $\lambda$  and  $U$  at temperature  $T$  fixed. This numerical calculation was performed by the numerical computations using facilities at Supercomputer Center in ISSP, e.g., for  $\lambda = 0.1t$ ,  $U = 8t$ , and  $T = 0.06t$ , about  $10^8$  Monte Carlo sweeps and averaging over 64 samples, and the self-consistency loop of the DMFT converges about 100 hours.

Figure 1 presents the  $U$ - $\lambda$  phase diagram at

the lowest temperature  $T = 0.06t$ . Increasing  $\lambda$  at  $U = 8t$  fixed, we confirmed the transition from metallic to insulating state with a magnetic order. The insulator shows  $J_{\text{eff}} = 1/2$  AF insulator. Moreover, we found that excitonic insulator by the electron-hole paring between  $J_{\text{eff}} = 1/2$  and  $J_{\text{eff}} = 3/2$  bands is realized by  $\lambda$  at larger  $U$ , in addition to the  $J_{\text{eff}} = 1/2$  AF insulator [7].

This work was done in collaboration with Dr. T. Shirakawa and Dr. S. Yunoki.

## References

- [1] B. J. Kim *et al.*: Phys. Rev. Lett. **101** (2008) 076402.
- [2] B. J. Kim *et al.*: Science **323** (2009) 1329.
- [3] K. Ishii *et al.*: Phys. Rev. B **83** (2011) 115121.
- [4] H. Watanabe *et al.*: Phys. Rev. Lett. **105** (2010) 216410.
- [5] G. Kotliar *et al.*: Phys. Rev. Lett. **87** (2001) 186401.
- [6] P. Werner *et al.*: Phys. Rev. Lett. **97** (2006) 076405.
- [7] T. Sato *et al.*: Phys. Rev. B **91** (2015) 124122.



# Electric transport near the antiferromagnetic transition in a square-lattice Hubbard model

Toshihiro SATO

*Computational Condensed Matter Physics Laboratory, RIKEN  
Wako, Saitama 351-0198, Japan*

As for strongly correlated electronic systems, it is interesting to investigate how magnetic frustration influences the electronic transport. This is the main issue of our work and we study optical conductivity near the magnetic transition in strongly correlated electronic systems.

The model to study is the one-band Hubbard Hamiltonian on a square lattice at half filling

$$H = -t \sum_{\langle i,j \rangle, \sigma} c_{i\sigma}^\dagger c_{j\sigma} + U \sum_i n_{i\uparrow} n_{i\downarrow} - \mu \sum_{i,\sigma} n_{i\sigma},$$

where  $t$  is the nearest-neighbor hopping amplitude,  $U$  is the on-site Coulomb repulsion and  $\mu$  is the chemical potential.  $c_{i\sigma}^\dagger$  ( $c_{i\sigma}$ ) is the electron creation (annihilation) operator at site  $i$  with spin  $\sigma$  and  $n_{i\sigma} = c_{i\sigma}^\dagger c_{i\sigma}$ . We focused on the electric transport and computed optical conductivity, particularly near the magnetic transition based on the cluster dynamical mean field theory (CDMFT) [1] employing a four-site square cluster. The numerical solver is the continuous-time quantum Monte Carlo (CTQMC) method based on the strong coupling expansion[2]. Furthermore, in order to investigate the effect of magnetic fluctuation to electronic transport, we have proceeded the formation of optical conductivity including vertex corrections in CDMFT both magnetic and paramagnetic states based on the Ref. [3]. This is a big challenge in numerical computations and was performed by the large-scale numerical computations using facilities at Supercomputer Center in ISSP, e.g., for  $U = 6.5t$  at temperature  $T = 0.42t$  in the paramagnetic phase, about  $10^8$  Monte Carlo sweeps and averaging over 1024 samples, which take about 96 hours.

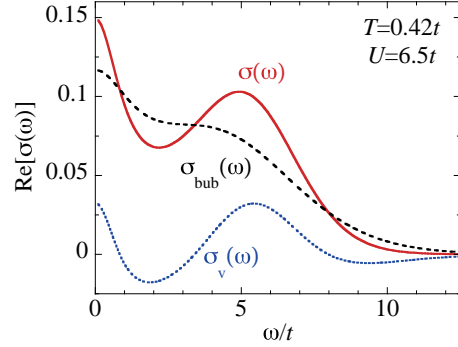


Figure 1: Contributions of vertex corrections on  $\sigma(\omega)$ .

We first examined  $T$ -dependence of electronic structure at  $U = 6.5t$  fixed, and then confirmed that a staggered magnetization is finite below  $T = 0.35t$ . We have calculated the optical conductivity  $\sigma(\omega)$  near  $T = 0.35t$  and have examined the contribution of vertex corrections in detail. Figure 1 presents the contributions of vertex corrections;  $\sigma(\omega)$  is the result with vertex corrections,  $\sigma_{\text{bub}}(\omega)$  is the result without vertex corrections, and the contribution of vertex corrections is  $\sigma_v(\omega) = \sigma(\omega) - \sigma_{\text{bub}}(\omega)$ . The data for  $T = 0.42t$  are typical result on the paramagnetic states. We found that the contribution of vertex corrections is important. Vertex corrections change two peaks near  $\omega \sim 0$  and  $\omega \sim Ut$  into a larger weight and a narrower width. We have also confirmed that the contribution of vertex corrections is important for  $T$ -dependence of dc-conductivity  $\sigma_0 = \sigma(0)$ . In the future, we will investigate optical conductivity including vertex corrections below  $T = 0.35t$  and will discuss the effect of magnetic fluctuation to electronic transport through detailed analysis of the contribution of vertex corrections.



This work was done in collaboration with  
Prof. H. Tsunetsugu.

## References

- [1] G. Kotliar *et al.*: Phys. Rev. Lett. **87**  
(2001) 186401.
- [2] P. Werner *et al.*: Phys. Rev. Lett. **97**  
(2006) 076405.
- [3] T. Sato *et al.*: Phys. Rev. B **86** (2012)  
235137.

# Theoretical study on the correlation between the spin fluctuation and $T_c$ in the isovalent-doped 1111 iron-based superconductors

Hayato Arai and Yuki Fuseya

*Dept. Engineering Science, University of Electro-Communications*

*1-5-1 Chofugaoka, Chofu, Tokyo 182-8585*

The mechanism of the iron-based superconductors has been studied since  $\text{LaFeAsO}_{1-x}\text{F}_x$  was found[1]. One of the possible mechanisms would be the spin-fluctuation mechanism[2]. But the low-energy spin fluctuation characterized by the relaxation rate ( $1/T_1$ ) of NMR study seems to have no relationship to the transition temperature ( $T_c$ )[3]. Therefore it is of prime importance to understand the relationship between  $T_c$  and the spin fluctuation measured by  $1/T_1$ .

The isovalent doping provides the rich electron system for the iron-pnictide. It has been found that  $\text{LnFeAsO}_{1-x}\text{F}_x$  with ( $\text{Ln}=\text{Gd}, \text{Sm}, \text{Ce}, \text{La}$ ) has high  $T_c$ . This lanthanoid-doping enable us to control the Fe-As-Fe bond angle. Large amount of electrons can be doped by substituting O with H in  $\text{LnFeAsO}$  ( $\text{Ln}=\text{Gd}, \text{Sm}, \text{Ce}, \text{La}$ ). Surprisingly, it has been shown that the superconductivity appears even up to 40% of electron doping. Particularly in  $\text{LaFeAs}(\text{O},\text{H})$ [4] and  $\text{SmFe}(\text{As},\text{P})(\text{O},\text{H})$ [5], the phase diagram exhibits a double-dome structure as a function of the electron doping. These experimental findings suggest that the change of electronic structure due to the Fe-As-Fe bond angle is responsible for  $T_c$ .

The conventional five-orbital model whose Fe-As-Fe bond angle is the controllable parameter are constructed based on the most localized Wannier functions. We study the electron structure, finite energy spin fluctuation, and  $T_c$  for this five-orbital model of isovalent-

doped 1111 iron-based superconductors on the basis of the fluctuation exchange approximation (FLEX). We also calculate the eigenvalue of the Eliashberg equation under the  $s^\pm$  projection ( $\lambda^\pm$ ). Their self-consistent calculations are too heavy to carry out by the workstation in our laboratory, so we need to calculate by using the ISSP system.

The obtained results reveal that the higher energy spin fluctuation is responsible for  $T_c$  and lower energy spin fluctuation is for  $1/T_1$ . It is also found that two orbitals ( $d_{xz/yz}$  and  $d_{xy}$ ) of isovalent-doped 1111 iron-based superconductors is very important for superconductivity. Finally, double-dome of  $T_c$  observed in 1111 iron-based superconductor can be explained within the spin fluctuation mechanism. This work was published in Physical Review B[6].

## References

- [1] Y. Kamihara, T. Watanabe, M. Hirano, H. Hosono: J. Am. Chem. Soc., **130**, 3296 (2008).
- [2] K. Kuroki, S. Onari, R. Arita, H. Usui, Y. Tanaka, H. Kontani, and H. Aoki, Phys. Rev. Lett. **101** (2008) 087004.
- [3] H. Mukuda, F. Engetsu, K. Yamamoto, K.T. Lai, M. Yashima, Y. Kitaoka, A. Takemori, S. Miyasaka, and S. Tajima, Phys. Rev. B **89**, 064511 (2014).

- [4] S. Iimura, S. Matsuishi, H. Sato, T. Hanna, Y. Muraba, S. W. Kim, J. E. Kim, M. Takata and H. Hosono, Nat. Commun. **3**, 943 (2012).
- [5] S. Matsuishi, T. Maruyama, S. Iimura, and H. Hosono, Phys. Rev. B **89**, 094510 (2014).
- [6] H. Arai, H. Usui, K. Suzuki, Y. Fuseya, K. Kuroki, Phys. Rev. B. **91**, 134511 (2015).

# Monte Carlo Approach to Chiral Helimagnets

Shintaro HOSHINO, Misako SHINOZAKI and Yusuke KATO

*Department of Basic Science, The University of Tokyo, Meguro, Tokyo 153-8902, Japan*

A chirality in magnetic materials causes antisymmetric Dzyaloshinskii-Moriya (DM) interaction in addition to the symmetric Heisenberg interaction. The competition between these two effects gives rise to a helical magnetic structure which is indeed realized in  $\text{Cr}_{1/3}\text{NbS}_2$  [1]. Under the external magnetic field perpendicular to the helical chain axis, an interesting spin texture called chiral soliton lattice is developed [2].

Recent theoretical studies have treated this system as a one-dimensional chain with continuum approximation, which is known as the chiral sine-Gordon model [2]. The temperature dependence of the spin moment has been discussed phenomenologically in these works, and is in good agreement with experiments. For more quantitative description of the magnetic phase transition at finite temperature, however, it is necessary to go beyond the one-dimensional system. To deal with this issue, we take classical chiral helimagnet on a three-dimensional simple cubic lattice, and numerically investigate the finite-temperature properties. The Hamiltonian reads

$$\mathcal{H} = - \sum_{\langle ij \rangle} J_{ij} \mathbf{S}_i \cdot \mathbf{S}_j - \sum_{\langle ij \rangle} \mathbf{D}_{ij} \cdot (\mathbf{S}_i \times \mathbf{S}_j)$$

where the summation is taken over the nearest neighbor sites. We consider the ferromagnetic interaction  $J_{ij} > 0$ , and take  $J_{ij} = J^\parallel$  ( $J^\perp$ ) for the  $z$ -axis ( $x, y$ -axis) bond. On the other hand, the DM interaction is given by  $\mathbf{D}_{ij} = (0, 0, D)$  for the  $z$ -axis bond, and is zero for  $x$ - and  $y$ -axis bonds. This model is simulated by the heat-bath method [3] using the facilities of the system B. In order to improve the accuracy, we additionally apply the exchange Monte Carlo method [4].

Figure 1 shows the transition temperature

$T_c$  obtained by the Monte Carlo method (circle symbols). Here we take  $D/J^\parallel = 0.16$  which is relevant to  $\text{Cr}_{1/3}\text{NbS}_2$ . For comparison, the mean-field result is shown by red line, which have the higher transition temperature. We have also analyzed the system by simulating the  $xy$ -plane using the Monte Carlo method and treating the interactions along  $z$ -axis by the mean-field approximation. As shown by square symbols in Fig. 1, much better results are obtained compared to the fully mean-field description.

In addition to  $T_c$ , we have also estimated the value of the critical field where the chiral soliton lattice turns into the forced ferromagnetic state at zero temperature. By comparing our numerical results with the experimental data, we have derived the energy scales of the interaction parameters in  $\text{Cr}_{1/3}\text{NbS}_2$ .

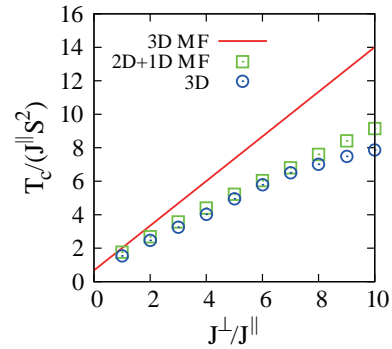


Figure 1:  $J^\perp$ -dependence of the transition temperatures in the chiral helimagnet.

## References

- [1] T. Moriya and T. Miyadai, Solid State Commun. **42**, 209 (1982).
- [2] J. Kishine, K. Inoue, and Y. Yoshida, Prog. Theor. Phys. Suppl. **159**, 82 (2005).
- [3] Y. Miyatake *et al.*, J. Phys. C: Solid State Phys. **19**, 2539, (1986).
- [4] K. Hukushima and K. Nemoto, J. Phys. Soc. Jpn. **65**, 1604 (1996).

# Quantum Monte Carlo simulation and electronic state calculations in correlated electron systems

Takashi YANAGISAWA

*Electronics and Photonics Research Institute*

*National Institute of Advanced Industrial Science and Technology (AIST)*

*AIST Central 2, 1-1-1 Umezono, Tsukuba 305-8568*

## Superconductivity and Strong Correlation

The mechanisms of superconductivity in cuprate high-temperature superconductors have been extensively studied by using two-dimensional models of electronic interactions. To clarify the electronic state of  $\text{CuO}_2$  plane in cuprates is important to resolve the mechanism of superconductivity. It is well known that the parent materials are a Mott insulator and the hole doping leads to superconductivity. In this report we present the results on the d-p model. To use computers more efficiently, we performed parallel computing with 64 or 128 cores.

The three-band model that explicitly includes Oxygen p orbitals contains the parameters  $U_d$ ,  $U_p$ ,  $t_{dp}$ ,  $t_{pp}$ ,  $\tilde{d}$  and  $\tilde{p}$ .  $U_d$  is the on-site Coulomb repulsion for d electrons and  $U_p$  is that for p electrons.  $t_{dp}$  is the transfer integral between adjacent Cu and O orbitals and  $t_{pp}$  is that between nearest p orbitals. The energy unit is given by  $t_{dp}$ .

The wave function is the Gutzwiller-type wave function given by the form  $\Psi_G = P_G \Psi_0$ , where  $P_G$  is the Gutzwiller projection operator given by  $P_G = \prod_i [1 - (1 - g)n_{di\uparrow}n_{di\downarrow}]$  with the variational parameter in the range from 0 to unity.  $P_G$  controls the on-site electron correlation on the copper site.  $\Psi_0$  is a one-particle wave function such as the Fermi sea or the Hartree-Fock state with spin density wave.  $\Psi_0$  contains the variational parameters  $\tilde{t}_{dp}$ ,  $\tilde{t}_{pp}$ ,  $\tilde{d}$  and  $\tilde{p}$ :  $\Psi_0 = \Psi_0(\tilde{t}_{dp}, \tilde{t}_{pp}, \tilde{d}, \tilde{p})$ . In the non-interacting case,  $\tilde{t}_{dp}$  and  $\tilde{t}_{pp}$  coincide with  $t_{dp}$  and  $t_{pp}$ , respectively.

The subject whether there is a super-

conducting instability induced by the on-site Coulomb repulsion is still controversial although there have been many works on the Hubbard model. In my opinion, high-temperature superconductivity can be expected in the strongly correlated region in the Hubbard model or the d-p model. In the two-dimensional Hubbard model, the ground state goes into a strongly correlated region when  $U/t$  is beyond 7, i.e.  $U_c/t = 7$ . The superconducting condensation energy  $E_{\text{cond}}$  increases rapidly near  $U/t = 7$  and has a maximum at  $U/t = 12$  as shown in Fig.1. Here,  $E_{\text{cond}}$  is defined as  $E_{\text{cond}} = E_{\text{normal}} - E_g(\Delta)$  where  $E_{\text{normal}}$  is the energy of the normal state and  $E_g(\Delta)$  is the minimum of the energy when we introduced the superconducting gap function  $\Delta$ .

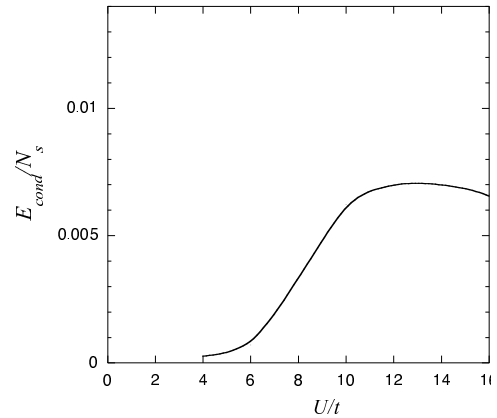


Figure 1: Superconducting condensation energy of the 2D Hubbard model as a function  $U$ . Parameters are  $t'/t = 0.2$  and the electron density is  $n_e = 0.84$ . The system size is  $10 \times 10$ . We assumed the  $d$ -wave pairing for the gap function.

Let us examine the two-dimensional d-p model where the subject is whether the strongly correlated region exists in the d-p model. We expect that the superconducting correlation function is enhanced in the strongly correlated region.

The Fig.2 exhibits the ground state energy per site  $E/N_d$  in the half-filled case as a function of  $\Delta_{dp}$  for the d-p model. Here we adopt the wave function given by

$$\Psi = \exp(\lambda K) \Psi_G, \quad (1)$$

where  $K$  is the kinetic part of the total Hamiltonian  $H_{dp}$  and  $\lambda$  is a variational parameter. We can find that the curvature of the energy, as a function of  $\Delta_{dp}$ , is changed near  $\Delta_{dp} \approx 2$ . The energy is well fitted by  $1/\Delta_{dp}$  shown by the dashed curve when  $\Delta_{dp}$  is large. This is because the most energy gain comes from the exchange interaction between nearest neighbor d and p electrons. This exchange interaction, denoted by  $J_K$ , is given by  $J_K = t_{dp}^2(1/\Delta_{dp} + 1/(U_d - \Delta_{dp}))$ . In the insulating state the energy gain is proportional to  $J_K$ ,

$$E = \frac{E}{N_d} \propto J_K. \quad (2)$$

The critical value of  $\Delta_{dp}$  is  $(\Delta_{dp})_c \simeq 3t_{dp}$ .

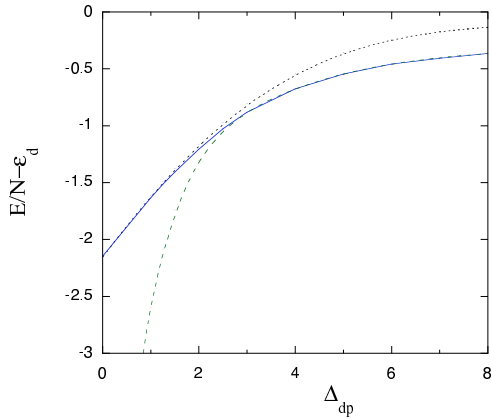


Figure 2: Ground-state energy of the 2D d-p model at half-filling as a function of  $\Delta_{dp}$  for  $t_{pp} = 0.0$  and  $U_d = 8$  in units of  $t_{dp}$ . The calculations were performed on  $6 \times 6$  lattice. The dotted curve is for the Gutzwiller function with  $\lambda = 0$ .

As shown in Fig.2, the region for  $\Delta_{dp}$  being larger than the critical value  $\Delta_{dp} \approx 3 \sim 4t_{dp}$

may be regarded as the strongly correlated region. We examine our question: whether the superconducting correlation is enhanced in the strongly correlated region in the d-p model as for the 2D Hubbard model. We found that the  $d$ -wave pairing state is indeed stabilized in the region with large  $\Delta_{dp}$ . The condensation energy  $E_{\text{cond}}$  shows a rapid increase as  $\Delta_{dp}$  is increased beyond the critical value  $\Delta_{dp,c}$ . The behaviour of  $E_{\text{cond}}$  is shown in Fig.3 as a function of the level difference  $\Delta_{dp}$ . This indicates a possibility of high-temperature superconductivity in the strongly correlated region of the d-p model.

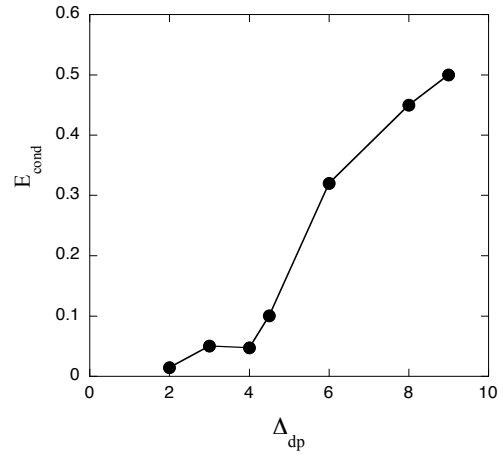


Figure 3: Superconducting condensation energy of the 2D d-p model as a function of  $\Delta_{dp}$  for  $t_{pp} = 0.4$  and  $U_d = 10$  in units of  $t_{dp}$ . The calculations were performed on  $6 \times 6$  lattice. The dotted curve is for the Gutzwiller function with  $\lambda = 0$ .

## References

- [1] T. Yanagisawa, Phys. Rev. B75, 224503 (2007) (arXiv: 0707.1929).
- [2] T. Yanagisawa, New J. Phys. 15, 033012 (2013).
- [3] T. Yanagisawa and M. Miyazaki, EPL 107, 27004 (2014).

# Multi-variable variational Monte Carlo study of the Holstein-Hubbard model

Takahiro OHGOE

*Department of Applied Physics, University of Tokyo*  
*7-3-1, Hongo, Bunkyo-ku, Tokyo, 113-0033*

Electron-phonon interaction plays important roles in various phenomena of conventional superconductor, charge density wave, and resistivity. Although its roles are well understood in those phenomena. They have not been fully understood in strongly-correlated systems such as high- $T_c$  cuprates. Even for the Holstein-Hubbard model, which is one of the simplest models of electron-phonon coupled systems, it is difficult to study its property in two or three dimensions because of limitations on methodologies. However, we have recently developed a multi-variable variational Monte Carlo method for electron-phonon coupled system [1]. In this study, we applied it to the Holstein-Hubbard model on a square lattice to reveal its zero-temperature phase diagrams. We first studied the half-filling case. In this case, we found not only spin-density wave (SDW) phase and charge-density wave (CDW) phase but also an intermediate metallic phase between them. Such an intermediate phase was also observed in the one-dimensional case [2]. To clarify whether the intermediate region includes a superconducting phase or not, we measured the superconducting correlation function, but we did not find evidence of superconductivity. In addition to the half-filling case, we next studied the system away from the half-filling. In this case, we observed the appearance of superconductivity. Moreover, we revealed the optimal filling where the superconducting order becomes largest. As a result, we could capture the overall behavior of

the phase diagram. In this study, we needed to perform simulations at various different parameter sets and up to large system sizes (linear dimension  $L = 16$  or  $18$ ). Therefore, we performed intensive independent simulations for different parameters. In each simulation, we utilized a MPI parallelization (# of process  $\sim 64$ ) to increase the number of samples. Most of these simulations were performed on System B.

## References

- [1] T. Ohgoe and M. Imada, Phys. Rev. B **89**, 195139 (2014).
- [2] Fehske et al., Eur. Phys. Lett. **84**, 57001 (2008).

# Study of novel quantum states in correlated electron systems with multi-degrees of freedom

Sumio ISHIHARA

*Department of Physics, Tohoku University  
Sendai 980-8578*

Multi-degrees of freedom of electron and lattice play essential roles in magnetic, dielectric, transport and optical properties in correlated electron systems, such as transition-metal oxides, and low dimensional organic salts. In the projects (H26-Ba-0022, H26Bb-0004), we have studied numerically the novel quantum phase and non-equilibrium states in correlated systems with multi degree of freedom. The following are the list of the obtained results.

1) Transient dynamics of hole carriers injected into a Mott insulator with antiferromagnetic long-range order are studied. The theoretical framework for the transient carrier dynamics is presented based on the two-dimensional  $t$ - $J$  model. The time dependencies of the optical conductivity spectra, as well as the one-particle excitation spectra, are calculated based on the Keldysh Green's function formalism at zero temperature combined with the self-consistent Born approximation. Time evolutions of the Green's functions are solved numerically. In the early stage after dynamical hole doping, the Drude component appears, and then incoherent components originating from hole-magnon scattering start to grow. Fast oscillatory behavior owing to coherent magnon and slow relaxation dynamics are confirmed in the spectra. The time profiles are interpreted as doped bare holes being dressed by magnon clouds and relaxed into spin polaron quasiparticle states. The characteristic relaxation times for Drude and incoherent peaks strongly depend on the momen-

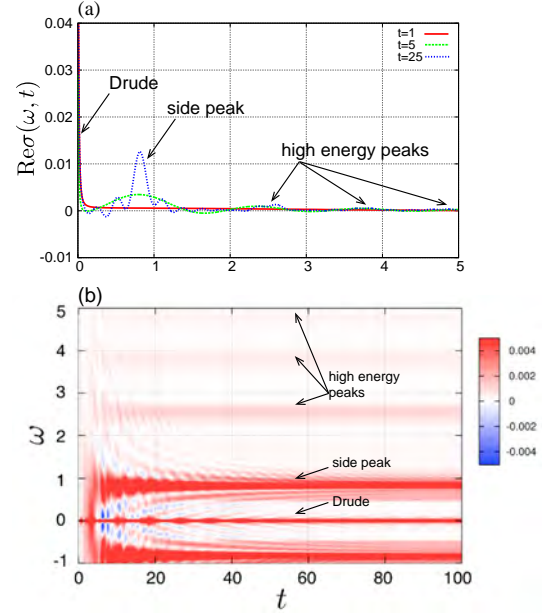


Figure 1: Transient optical conductivity spectra. (a) The spectra for several time after dynamical doping. (b) A contour map of the spectra as a function of frequency and time [1].

tum of the dynamically doped hole and the exchange constant [1].

2) Photo-excited charge dynamics of interacting charge-frustrated systems are studied using a spinless fermion model on an anisotropic triangular lattice. Real-time evolution of the system after irradiating a pump-photon pulse is analyzed by the exact diagonalization method based on the Lanczos algorithm. We focus on photo-excited states in the two canonical charge-ordered (CO) ground states, i.e., horizontal stripe-type and verti-



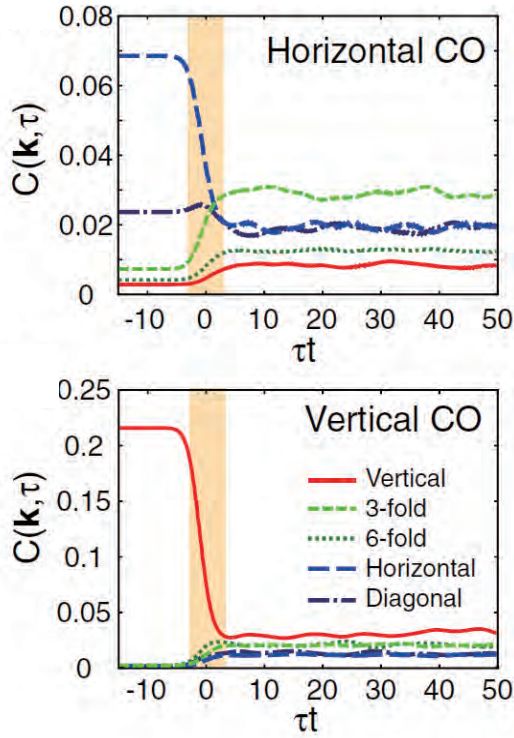


Figure 2: Time-dependences of the charge correlation functions in the horizontal-stripe and vertical-stripe CO phases [2].

cal stripe-type COs, which compete with each other owing to the charge frustration. We find that the photo-induced excited states from the two types of COs are distinct. From the horizontal stripe-type CO, a transition to another CO state called the three-fold CO phase occurs. In sharp contrast, the vertical stripe-type CO phase is only weakened by photo-irradiation. Our observations are attributable to the charge frustration effects occurring in the photo-excited states [2].

3) Short-range resonating valence-bond states in an orbitally degenerate magnet on a honeycomb lattice are studied. A quantum-dimer model is derived from the Hamiltonian which represents the superexchange interaction and the dynamical Jahn-Teller (JT) effect. We introduce two local units termed “spin-orbital singlet dimer,” where two spins in a nearest-neighbor bond form a singlet state as-

sociated with an orbital polarization along the bond, and “local JT singlet,” where an orbital polarization is quenched due to the dynamical JT effect. A derived quantum-dimer model consists of the hopping of the spin-orbital singlet dimers and the JT singlets, and the chemical potential of the JT singlets. We analyze the model by the mean-field approximation, and find that a characteristic phase, termed “JT liquid phase,” where both the spin-orbital singlet dimers and the JT singlets move quantum mechanically, is realized [3].

The present researches has been collaborated with E. Iyoda (University of Tokyo), J. Nasu (Tokyo Institute of Technology), M. Naka (Tohoku University), H. Hashimoto (Tohoku University), H. Matsueda (Sendai National College of Technology) and H. Seo (RIKEN, CEMS). Some parts of the computation in the present works has been done using the facilities of the Supercomputer Center, the Institute for Solid State Physics, the University of Tokyo.

## References

- [1] E. Iyoda and S. Ishihara, Phys. Rev. B **89**, 125126 (2014).
- [2] H. Hashimoto, H. Matsueda, H. Seo and S. Ishihara, J. Phys. Soc. Jpn. **83**, 123703 (2014).
- [3] J. Nasu and S. Ishihara, Phys. Rev. B **91**, 045117 (2015).

# Numerical study of flux quench in one-dimensional quantum systems

Yuya NAKAGAWA<sup>1</sup>, Grégoire MISGUICH<sup>2</sup>, Masaki OSHIKAWA<sup>1</sup>

<sup>1</sup> *Institute for Solid State Physics, University of Tokyo*

*Kashiwa-no-ha, Kashiwa, Chiba 277-8581*

<sup>2</sup> *Institut de Physique Théorique, CEA, IPhT,*

*CNRS, URA 2306, F-91191 Gif-sur-Yvette, France*

We study a *flux quench* problem in the spin-1/2 XXZ chain. The flux quench is a quantum quench where the flux  $\phi$  piercing the XXZ chain is turned off at  $t = 0$  suddenly. If we formulate the XXZ chain as a spinless fermion model, the flux  $\phi$  corresponds to a vector potential on each bond and this flux quench can be viewed as imposing a pulse (delta function) of electric field. Therefore some particle (or spin) current is generated in the system at  $t = 0$ . Recently this quench was studied to illustrate the breakdown of the generalized Gibbs ensemble in integrable systems [1].

Here, we focus on the time-evolution of the spin current after the quench and calculate it numerically by the infinite time-evolving block decimation (iTEBD) method [2]. We used the bond dimension  $\chi = 1000$  typically, and did numerical simulations for various parameters of the system (the anisotropy of the XXZ chain and the initial flux). We implemented  $U(1)$  symmetry (the conservation of magnetization) to the iTEBD algorithm so as to reduce the computational cost of singular value decomposition.

We find that the dynamics of the spin current depends strongly on the anisotropy parameter  $\Delta$  of the XXZ chain and the amount of flux initially inserted. The long-time limit ( $t \rightarrow \infty$ ) of the current matches with predictions of linear response theory as the initial flux decreases, but the deviation from linear

response theory is largely affected by the sign of interactions. Furthermore, in some parameter region the current oscillates in time (Fig. 1) and the frequency of the oscillation is proportional to  $|\Delta|$ . Remarkably, the dynamics of momentum distribution of the spinless fermions reveals that this oscillation of the current is governed by excitations deep inside the shifted Fermi sea (Fig. 2). This mechanism of oscillations cannot be captured by the effective Luttinger model corresponding to the microscopic XXZ chain, which is in contrast with the previous studies on different types of quench in the same model [3].

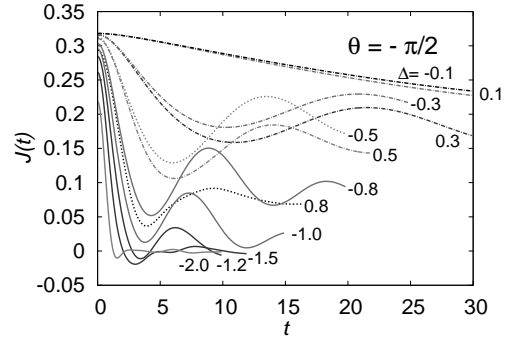


Figure 1: Dynamics of the spin current after the quench.  $\theta$  is initial flux per site. Anisotropy  $\Delta$  is defined as  $H_{\text{XXZ}} = -\sum_i (S_i^x S_{i+1}^x + S_i^y S_{i+1}^y + \Delta S_i^z S_{i+1}^z)$ .

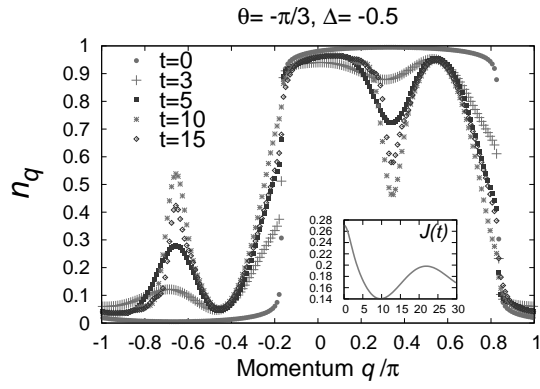


Figure 2: Momentum distribution of the spinless fermions. The dip (peak) structure deep inside the shifted Fermi sea is observed (the inset shows the time-evolution of the current).

## References

- [1] M. Mierzejewski, P. Prelovsek, and T. Prosen: Phys. Rev. Lett. **113** (2014) 020602.
- [2] G. Vidal: Phys. Rev. Lett. **98** (2007) 070201.
- [3] C. Karrasch *et al*: Phys. Rev. Lett. **109** (2012)126406., F. Pollmann, M. Haque, and B. Dóra: Phys. Rev. B **87** (2013) 041109(R).

# Investigation of unconventional superconductivities by extension of the dynamical mean-field theory

Junya OTSUKI

*Department of Physics, Tohoku University, Sendai 980-8578*

For theoretical descriptions of superconductivities in strongly correlated systems, we need a coherent treatment of local correlations and spatial fluctuations. For this purpose, we establish a practical scheme using the dual fermion approach, which provides a way to perform a diagrammatic expansion around the dynamical mean-field theory (DMFT) [1]. The computation process consists of two auxiliary problem as summarized in Fig. 1.

We first solve an effective single-impurity problem as in the DMFT. A difference to the DMFT is that we compute the vertex part  $\gamma_{\omega\omega',\nu}$  as well as the Green's function  $g_\omega$ . We used the continuous-time quantum Monte Carlo (QMC) method [2], and performed parallel computations using MPI.

The quantities  $g_\omega$  and  $\gamma_{\omega\omega',\nu}$  define a dual-lattice problem. We evaluate the dual self-energy  $\tilde{\Sigma}_{\omega\mathbf{k}}$  taking account of diagrams as in the fluctuation exchange approximation (FLEX). Thus, influence of long-range fluctuations are incorporated in addition to the local correlations in DMFT. We invented a way to carry out stable computations even near an antiferromagnetic quantum critical point, making possible to obtain solutions near a Mott insulator [3]. The calculation of  $\tilde{\Sigma}_{\omega\mathbf{k}}$  was parallelized as well.

After  $\tilde{\Sigma}_{\omega\mathbf{k}}$  is computed, we update the bath function  $\Delta_\omega$  and solve again the single-impurity problem. These calculations are repeated until convergence is reached. The Green's function in the original lattice,  $G_{\omega\mathbf{k}}$ , are finally obtained from  $\tilde{\Sigma}_{\omega\mathbf{k}}$ .

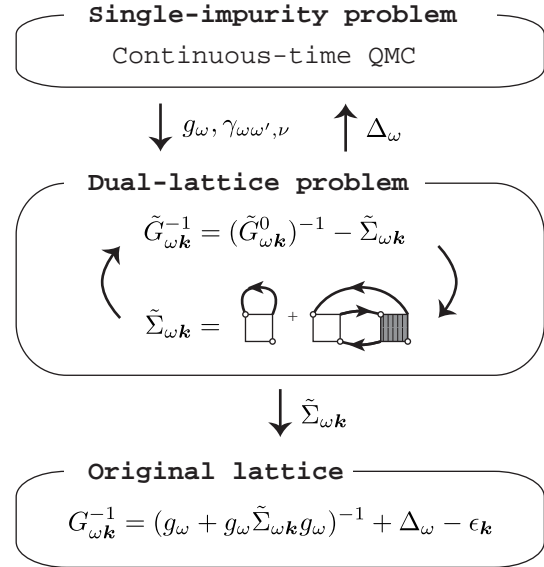


Figure 1: Computation scheme.

Applying the above scheme, we have investigated superconductivities in the two-dimensional Hubbard model. We observed  $d$ -wave superconductivity ( $d$ -SC) and phase separation (PS) near the Mott insulator [3]. It turned out that a pure  $d$ -SC emerges only in a limited doping regime because of the PS.

## References

- [1] A. N. Rubtsov *et al.*, Phys. Rev. B **79**, 045133 (2009).
- [2] E. Gull *et al.*, Rev. Mod. Phys. **83**, 349 (2011).
- [3] J. Otsuki, H. Hafermann, A. I. Lichtenstein, Phys. Rev. B **90**, 235132 (2014).

# Numerical simulation of $^4\text{He}$ adsorbed on substrates

Yuichi MOTOYAMA

*Institute for Solid State Physics, University of Tokyo*  
*Kashiwa-no-ha, Kashiwa, Chiba 277-8581*

$^4\text{He}$  adsorbed on a substrate such as graphite has been studied experimentally and numerically as an ideal two dimensional interacting bosonic system. Although the numerical simulations of the first layer of  $^4\text{He}$  on graphite almost agree with the experiments, for the second layer the latest first-principle numerical result [1] did not agree with the latest experimental result [2] even in quality. The authors of the former calculated the superfluid density and the structure factor of the number density, and concluded there are three phases; gas-liquid coexisting phase (GL), superfluid liquid phase (SF), and incommensurate solid phase (IC). The latter experiment gave anomalous behavior of the specific heat and the authors concluded that there are more phases; GL, SF, SF and commensurate solid (C) coexisting phase, C, C-IC coexisting, and IC. The specific heat is one of the important observables that can be obtained from experiments. The past simulations, however, did not show these data since it is difficult for numerical simulation to calculate energy and specific heat accurately.

Aiming to verify the past numerical simulation and fill the gap between experiments and simulations, I am developing a path-integral Monte Carlo simulation for interacting boson particles in continuous space introduced by ref [3]. In this algorithm, which was used in the past numerical paper [1], it takes time proportional to the number of particles to perform one Monte Carlo update, and so this enables us to simulate large size system. I performed simulation of two dimensional  $^4\text{He}$  system for several temperature and fixed number

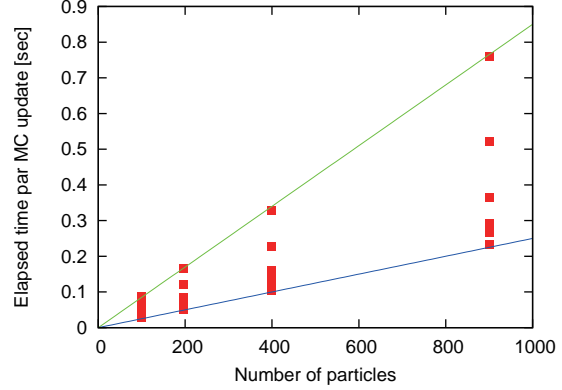


Figure 1: Elapsed time for one Monte Carlo update of two dimensional  $^4\text{He}$  simulation for several temperature ( $0.5\text{K} \leq T \leq 1\text{K}$ ). Computational cost is  $O(N)$  with particle number  $N$ . Two solid lines are for eye-guide.

density  $\rho = 0.0432\text{\AA}^{-2}$  on ISSP supercomputer system-B and examined the scaling of update time [4]. Figure 1 shows that the linear scaling of elapsed time is achieved.

## References

- [1] P. Corboz, M. Boninsegni, L. Pollet, and M. Troyer, Phys. Rev. B **78**, 245414 (2008).
- [2] S. Nakamura, K. Matsui, and H. Fukuyama, arXiv:1406.4388.
- [3] M. Boninsegni, N. V. Prokof'ev, and B. V. Svistunov, Phys. Rev. E **74**, 036701 (2006).
- [4] I use ALPS/parapack library [5] for embarrassingly parallelization and scheduling.
- [5] B. Bauer et al. (ALPS collaboration), J. Stat. Mech. P05001 (2011).

# Theoretical study for exciton condensation induced by interband interaction

Hiroshi WATANABE

*RIKEN CEMS*

*2-1, Hirosawa, Wako-shi, Saitama 351-0198*

In multiband electron systems, interband interaction induces various interesting phenomena. One of the notable examples is exciton condensation which has been proposed in 1960s. The exciton is a bound electron-hole pair mediated by interband Coulomb interaction and is expected to condense in low carrier density system like semimetal or semiconductor. Although there are several candidates of exciton condensation in real materials, none of them have been confirmed so far. Since most of the previous theoretical studies are based on simplified ideal models, they are not enough to discuss the exciton condensation in real materials. Furthermore, the Coulomb interaction is treated within the mean-field approximation and the many-body effect is not appropriately included.

To discuss the possibility of exciton condensation in real materials, we have constructed the realistic two-dimensional Hubbard model and studied the ground state property of the model [1, 2]. The variational Monte Carlo (VMC) method is used for the calculation of physical quantities. Our VMC code includes more than one hundred variational parameters and the many-body effect is much more properly included compared with mean-field approximation. The system size for calculation is from  $8 \times 8$  to  $28 \times 28$  and the size dependence is systematically studied.

We have found three phases in the ground state phase diagram of intra- ( $U/t$ ) and interband ( $U'/t$ ) Coulomb interactions in the

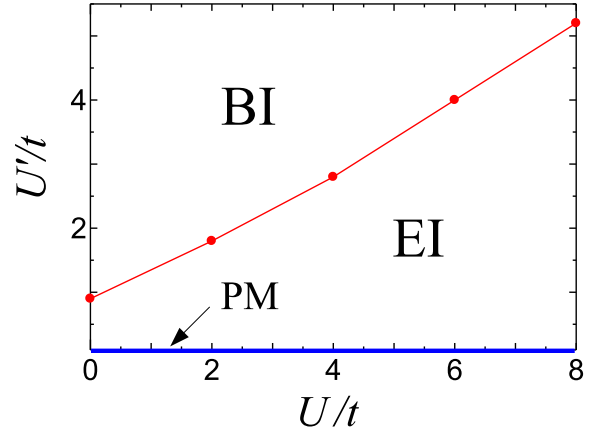


Figure 1: Ground state phase diagram for the Hubbard model in a square lattice with perfectly nested electron and hole Fermi surfaces [1].

unit of nearest-neighbor hopping integral  $t$  [1] (Fig. 1): paramagnetic metal (PM), excitonic insulator (EI) originated from exciton condensation, and band insulator (BI). The transition from PM to EI is induced by an infinitesimal interband Coulomb interaction, i.e.,  $U'_c = 0$  (Fig. 1), when the electron and hole Fermi surfaces are perfectly nested in a square lattice. As  $U'$  increases, the character of exciton changes from weak-coupling BCS-type to strong-coupling BEC-type pairing within EI, which is known as BCS-BEC crossover. As  $U'$  increases further, EI finally collapses and BI appears. On the other hand, EI is absent and direct transition from PM to BI is observed in

a triangular lattice [2]. It suggests that the stability of EI greatly depends on the nesting of the Fermi surface. In real materials, the nesting of the Fermi surface is not perfect and the realization of EI would be limited to a special case. Our result will contribute to the further understanding and realization of exciton condensation in real materials.

## References

- [1] H. Watanabe, K. Seki, and S. Yunoki: J. Phys.: Conf. Ser. **592** (2015) 012097.
- [2] H. Watanabe, K. Seki, and S. Yunoki: submitted to Phys. Rev. B.

## **3.4 Cooperative Phenomena in Complex Macroscopic Systems**



# Quantum spin-liquid behavior in the spin-1/2 random Heisenberg antiferromagnet on the kagome lattice

Hikaru Kawamura, Ken Watanabe and Tokuro Shimokawa

*Graduate School of Science, Osaka University, Toyonaka 560-0043*

The quantum spin-liquid (QSL) state possibly realized in certain  $S=1/2$  frustrated magnets has attracted interest of researchers. After a long experimental quest, several candidate materials were recently reported in certain geometrically frustrated magnets, including both the triangular-lattice and the kagome-lattice antiferromagnets (AFs).

Examples of the triangular-lattice AF might be  $S=1/2$  organic salts such as  $\kappa$ -(ET)<sub>2</sub>Cu<sub>2</sub>(CN)<sub>3</sub> [1] and EtMe<sub>3</sub>Sb[Pd(dmit)<sub>2</sub>]<sub>2</sub>, while an example of the kagome-lattice AF might be herbertsmithite CuZn<sub>3</sub>(OH)<sub>6</sub>Cl<sub>2</sub> [2]. Aiming at clarifying the origin of the QSL behavior observed in the organic triangular salts, we investigated in the last year's project the properties of the bond-random  $S=1/2$  AF Heisenberg model on the triangular lattice by means of an exact diagonalization method, and found that the model exhibited a randomness-induced gapless QSL behavior at low temperatures [3]. This "random singlet" state apparently explains many of the experimental features observed in the triangular organic salts. It was also argued that in these triangular organic salts the quenched bond-randomness was self-generated in the spin degrees of

freedom via the slowing-down of the dielectric degrees of freedom intrinsic to these organic salts consisting of molecular dimers.

Kagome herbertsmithite has also been known to possess the quenched bond-randomness, which is associated with the random substitution of nonmagnetic Zn<sup>2+</sup> on the triangular layer adjacent to the kagome layer by the magnetic Cu<sup>2+</sup> [2]. Inspired by this experimental observation, and by the success of the random-singlet picture of the triangular model in explaining the QSL behavior, we studied in this year's project the effect of the quenched bond randomness on the low-temperature properties of the  $S=1/2$  AF Heisenberg model on the *kagome* lattice [4].

We consider the AF bond-random  $S=1/2$  Heisenberg model on the kagome lattice whose Hamiltonian is given by  $\sum_{\langle ij \rangle} J_{ij} S_i S_j - H \sum_i S_{iz}$ , where  $S_i = (S_{ix}, S_{iy}, S_{iz})$  is a spin-1/2 operator at the  $i$ -th site on the lattice, and  $H$  is the magnetic-field intensity. For the exchange coupling  $J_{ij}$ , we assume for simplicity the random nearest-neighbor AF coupling obeying the bond-independent uniform distribution between  $[(1-\Delta)J, (1+\Delta)J]$  with the mean  $J$ . The parameter  $\Delta$  represents the extent of the

randomness:  $\Delta=0$  corresponds to the regular system, and  $\Delta=1$  to the maximally random system.

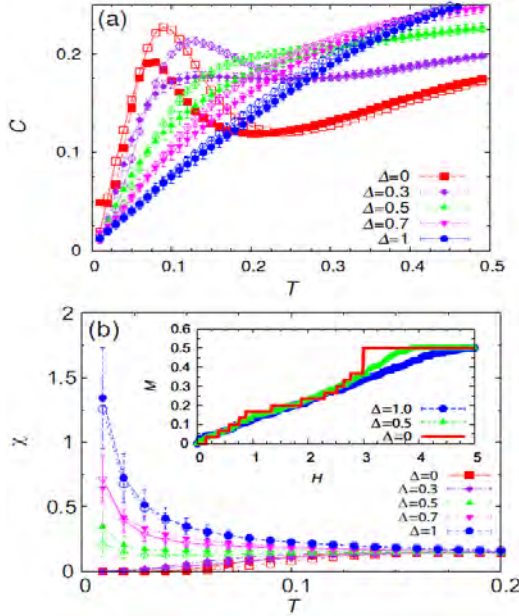


Fig. 1: The temperature dependence of (a) the specific heat per spin, and of (b) the uniform susceptibility per spin, for several randomness  $\Delta$  for  $N=12$  (open symbols) and 18 (solid symbols). The inset of (b) represents the  $T=0$  magnetization curve for  $N=30$ .

In Fig.1(a), we show the temperature dependence of the specific heat per spin (in units of Boltzmann constant) for several values of  $\Delta$ . As in the triangular case, the specific heat of the random model exhibits a  $T$ -linear behavior at lower temperatures. In Fig.1(b), we show the temperature dependence of the magnetic susceptibility per spin. While the susceptibility goes to zero in the  $T \rightarrow 0$  limit for weaker randomness  $\Delta < 0.5$ , it tends to a finite value at  $\Delta=0.5$ , and diverges obeying the Curie

law for stronger randomness  $\Delta > 0.7$ . The appearance of a Curie-like component suggests that a small fraction of free spins  $\sim 4\%$  are generated at low temperatures.

The state at  $\Delta > \Delta_c$  has properties similar to those of the random-singlet state identified in the corresponding triangular-lattice model [3], including the  $T$ -linear specific heat, the gapless susceptibility with a Curie-like component for the stronger randomness, and the near linear magnetization curve without plateau-like structures, suggesting that the gapless spin-liquid-like state realized at  $\Delta > \Delta_c$  is indeed the random-singlet state.

Further details, including the sublattice magnetization, the spin freezing parameter, the single/triplet ratio and the dynamical spin structure factor are given in Ref.[4].

## References

- [1] Y. Shimizu, K. Miyagawa, K. Kanoda, M. Maesato and G. Saito, Phys. Rev. Lett. **91**, 107001 (2003).
- [2] D.E. Freedman, T.H. Han, A. Prodi, P. Muller, Q.-Z. Huan, Y.-S. Chen, S.M. Webb, Y.S. Lee, T.M. McQueen, and D.G. Nocera, J. Am. Chem. Soc., **132**, 16185 (2010).
- [3] K. Watanabe, H. Kawamura, H. Nakano and T. Sakai, J. Phys. Soc. Jpn. **83**, 034714 (2014).
- [4] H. Kawamura, K. Watanabe, and T. Shimokawa, J. Phys. Soc. Jpn. **83**, 103704 (2014).

# Characteristic length scale in the one-dimensional Burridge-Knopoff model of earthquakes

Koji Yoshimura and Hikaru Kawamura

*Graduate School of Science, Osaka University, Toyonaka, Osaka 560-0043*

An earthquake is a stick-slip dynamical instability of a pre-existing fault driven by the motion of a tectonic plate. Numerical simulations of earthquakes based on a simplified statistical model, the so-called Burridge-Knopoff (BK) model, has been popular in statistical physics and provided much information about statistical properties of earthquakes. Some of the properties of the BK model was reviewed in Ref.[1].

One fundamental question about the nature of earthquakes has been whether it is “critical” or “characteristic”. In other words, do earthquakes possess their intrinsic length (or time, energy, etc) scale? If earthquakes are intrinsically critical, they should not possess any characteristic scale, while they are characteristic, they should possess some characteristic scales. The well-known Gutenberg-Richter law concerning the earthquake size (magnitude) distribution, if taken literally, means the critical nature of the earthquake energy. On the other hand, there also exist some observations suggestive of the more characteristic nature of earthquakes.

In this year’s project, aiming at clarifying the possible existence of a characteristic *length*

*scale* in the one-dimensional BK model under the rate-and-state friction (RSF) law, we newly computed the rupture-zone size distribution, and analyzed its properties.

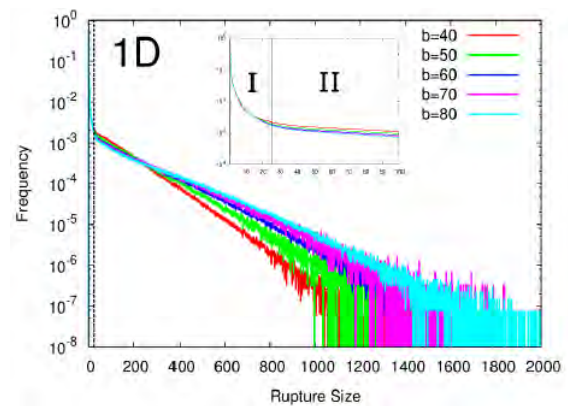


Fig.1 The rupture-zone size distribution on a semi-logarithmic plot for various values of the frictional weakening parameter  $b$  characterizing the RSF law.

As can be seen from Fig.1, the rupture-zone size  $L_r$  exhibits an exponential behavior  $L_r \sim \exp[-L_r/L_0]$  with a characteristic length scale  $L_0$ . This observation clearly demonstrates that earthquake events of the model possesses an intrinsic characteristic length scale.

## References

- [1] For review, see, H. Kawamura, T. Hatano, N. Kato, S. Biswas and B.K. Chakrabarti, Rev. Mod. Phys. 84, 839-884 (2012).

# Novel Quantum Phases and Phase Transitions in Bosonic System on Periodic Potentials \*

Naoki KAWASHIMA

*Institute for Solid State Physics,*

*The University of Tokyo, Kashiwa-no-ha, Kashiwa, Chiba 277-8581*

Since the success of the optical lattice Bosonic systems on lattice potentials acquire renewed interest. The effect of disorder on a large systems is among the list of subjects to be addressed in the optical lattice study. Experiments on more conventional counterparts, e.g., the He-4 atoms adsorbed on a surface of graphite, also present hints on non-conventional types of Bose-Einstein condensation including the possibility of the supersolid state of matter.

In the present project, we aim at developments of numerical techniques to attack the problems of Boson systems. For general optical lattice problems, the major technical obstacle has been the lack of parallelizable algorithm for quantum Monte Carlo simulation. The worm algorithm is the standard method for updating configurations in the quantum Monte Carlo simulation whereas it is well-known that it cannot be run on parallel computers as it stands. At the end of our preceding project in SY2013, we succeeded in developing a new scheme for parallelizing the worm algorithm. In SY2014, we developed the method further

elucidating the way for measuring the multi-body correlation function. [1] The most notable outcome is the new way of obtaining the "noise correlation" which is an important probe for experimentalists to detect superfluidity, and can be mapped to some four-point Green's function. In SY2014, we succeeded in a preliminary computation of the noise correlation function. [2]

As for the He-4 on graphite surface, it is vital to develop a computer program that can handle continuous space. In SY2014, we developed an original code based on the continuous-space worm algorithm. We tried the new code on the soft-core system in two dimensions, and have obtained results indicating the cluster super-fluid phase in which periodic structure spontaneously appears.[3]

-----  
[1] A. Masaki-Kato et al., Phys. Rev. Lett., **112**, 140603 (2014).

[2] A. Masaki-Kato et al., unpublished.

[3] Y. Motoyama et al., unpublished.

-----  
\* This work is done in collaboration with Akiko Masaki-Kato, Yuichi Motoyama, and Yoshihiko Hirano at ISSP.

# Topological phase transition in the frustrated magnets

Tsuyoshi OKUBO

*Institute for Solid State Physics, University of Tokyo  
Kashiwa-no-ha, Kashiwa, Chiba 277-8581*

Recently, frustrated magnets have attracted much interest because they often show novel ordering behaviors. In several two-dimensional frustrated Heisenberg spin systems, a topologically stable point defect, a  $Z_2$  vortex, plays an important role for ordering of the spins. About 30 years ago, a possible topological phase transition driven by binding-unbinding of the  $Z_2$  vortices was proposed [1]. The remarkable feature of the  $Z_2$ -vortex transition is that the spin correlation length keeps finite at the  $Z_2$ -vortex transition temperature  $T = T_v$ . It is a sharp contrast to the case of the Kosterlitz-Thouless transition in two dimensional  $XY$  spin systems, where the spin correlation length diverges below the transition temperature.

The nature of the possible  $Z_2$ -vortex transition has been studied mainly on the triangular-lattice Heisenberg antiferromagnet. Indeed, recent Monte Carlo simulation upto  $L = 1536$  suggested the occurrence of  $Z_2$ -vortex transition at a finite temperature [2]. However, the existence of “true” phase transition has not been resolved because the spin-correlation length at the estimated transition temperature was longer than the system size [2]. In order to clarify the true nature of the  $Z_2$ -vortex transition, we need larger systems beyond the spin-correlation length at the expected transition temperature.

In order to perform such larger scale Monte Carlo simulations, we consider an effective *non-frustrated* model of two-dimensional frustrated Heisenberg magnets. The Hamiltonian

of the model is give by

$$\mathcal{H} = -\frac{J}{4} \sum_{\langle i,j \rangle} \text{Tr} R_i R_j^t \quad (J > 0), \quad (1)$$

where  $R_i$  is a  $SO(3)$  rotation matrix on the site  $i$ , and  $\sum_{\langle i,j \rangle}$  means the sum over the nearest-neighbor pairs on the square lattice. This effective model does not have explicit frustrated interactions. However, it has topological  $Z_2$  vortices similar to the frustrated magnets, and therefore the  $Z_2$ -vortex binding-unbinding transition at a finite temperature is possible. One of the advantages of this unfrustrated model is that we can use cluster algorithm, which is not efficient for the frustrated interactions, in Monte Carlo simulations.

We have implemented MPI parallelized Wolff-Swendsen-Wang type cluster algorithm and investigated nature of possible  $Z_2$ -vortex transition by extensive Monte Carlo simulation of the model. The lattice is a  $L \times L$  square lattice with periodic boundary conditions. In this year project, we performed Monte Carlo simulation for  $L \leq 8192$ .

In fig. 1, we show the temperature dependence of the vorticity modulus  $v$ , defined through the free-energy cost against a vortex formation at  $L$ ,  $\Delta F(L)$ , as

$$v(L_1, L_2) \equiv \frac{\Delta F(L_1) - \Delta F(L_2)}{\log L_1/L_2}. \quad (2)$$

The vorticity modulus takes a finite value for  $T < T_v$ , while  $v = 0$  for  $T > T_v$ . We see that the vorticity modulus increases around  $T = 0.29J$ , indicating the finite temperature

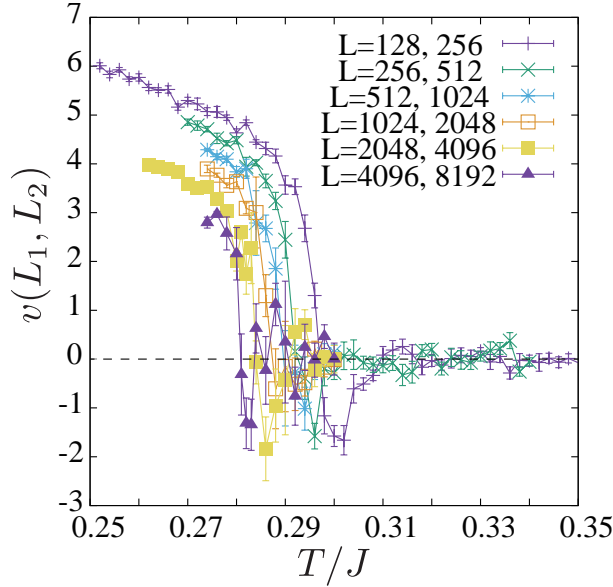


Figure 1: Vorticity modulus as a function of the temperature for various systems sizes  $128 \leq L \leq 8192$ .

phase transition. However, the characteristic temperatures where the vorticity modulus across  $v = 0$  shift to lower temperature as increasing the systems size. Thus, we need an extrapolation of the characteristic temperatures to the thermodynamic limit. A preliminary extrapolation leads the finite-temperature  $Z_2$ -vortex transition as  $T_v/J \simeq 0.275$ . At this temperature, the spin correlation length is estimated about from 5000 to 10000 lattice spacings. Because the present system is limited  $L \leq 8192$ , which is comparable with the correlation length at the estimated  $T_v$ , we need a careful analysis to conclude the existence of the finite-temperature topological phase transition.

## References

- [1] H. Kawamura and S. Miyashita: J. Phys. Soc. Jpn. **53** (1984) 4138.
- [2] H. Kawamura, A. Yamamoto, and T. Okubo: J. Phys. Soc. Jpn. **79** (2010) 023701.

# Novel ordering in frustrated spin systems

Tsuyoshi OKUBO

*Institute for Solid State Physics, University of Tokyo  
Kashiwa-no-ha, Kashiwa, Chiba 277-8581*

Ir-based transition metal oxides have attracted much recent interest due to their strong spin-orbit coupling (SOC).  $\text{Na}_2\text{IrO}_3$  and  $\text{Li}_2\text{IrO}_3$  are typical examples of such compounds. In these compound, it was suggested that the interaction between the effective spins induced by the strong SOC can be expressed so-called Kitaev-Heisenberg Hamiltonian which contains an isotropic Heisenberg interaction and an anisotropic Kitaev interaction [1, 2]. Recently, a theoretical study proposed an new effective model of  $\text{Na}_2\text{IrO}_3$  which included complex off-diagonal interactions and further neighbor interactions in addition to the nearest-neighbor Kitaev-Heisenberg terms [3].

In this year project, we have investigated the ground-state property of such a “generalized” Kitaev-Heisenberg model by the infinite Projected Entangled Pair State (iPEPS) tensor network method. In the iPEPS method, we represent the ground state wave-function as a two-dimensional network of tensor products. By optimizing each tensors so as to minimize the energy, we obtain a wave function close to the ground state. The optimization is done by the imaginary time evolution (ITE) with Suzuki-Trotter decomposition. Because the tensors obtained after multiplying the ITE-operator have lager bond dimensions than the original iPEPS, we perform the singular value decomposition (SVD) of the tensor to truncate the bond-dimensions. In order to treat the second and the third neighbor interactions in ITE optimization, we have implemented a successive SVD method. After obtaining optimized iPEPS, we calculate observables such as

the energy by using the corner transfer-matrix method.

Firstly, we have calculated the ground state at the *ab initio* parameter of the  $\text{Na}_2\text{IrO}_3$ . By iPEPS calculation upto the bond dimension  $D = 7$ , we concluded that the ground state is the magnetically ordered zigzag phase which is consistent with the experimental observations. We have also investigated the phase diagram varying the the trigonal distortion from the *ab initio* value. The phase diagram obtained by iPEPS is qualitatively similar to that of the 24-sites exact diagonalization [3]. However, we also observed several differences in details of the ordering patterns. Observed differences seem to be an advantage of iPEPS calculation which treat the thermodynamic limit directly.

## References

- [1] G. Jackeli, and G. Khaliullin, Phys. Rev. Lett. **102** (2009) 017205.
- [2] J. Chaloupka, G. Jackeli, and G. Khaliullin, Phys. Rev. Lett. **105** (2010) 027204.
- [3] Y. Yamaji, Y. Nomura, M. Kurita, R. Arita, and M. Imada, Phys. Rev. Lett. **113** (2014) 107201.

# Numerical Study on Novel Phases of the Spin Nanotubes

Tôru SAKAI<sup>1,2</sup>, Hiroki NAKANO<sup>2</sup>, Tokuro SHIMOKAWA<sup>3</sup>,  
and Makoto ISODA<sup>4</sup>

<sup>1</sup>*Quantum Beam Science Directorate, Japan Atomic Energy Agency  
SPring-8, Kouto, Sayo, Hyogo 679-5148, Japan*

<sup>2</sup>*Department of Material Science, University of Hyogo,  
Kouto, Kamigori, Hyogo 678-1297, Japan*

<sup>3</sup>*Osaka University, Toyonaka, Osaka 560-0043, Japan*

<sup>4</sup>*Faculty of Education, Kagawa University,  
Takamatsu, Kagawa 760-8522, Japan*

## 1 Introduction

Recently some quantum spin systems on tube lattices, to called spin nanotubes, have been synthesized. They are expected to be interesting low-dimensional systems like the carbon nanotubes. As the first step of theoretical study on the spin nanotube, we investigate the  $S=1/2$  three-leg spin tube, which is the simplest one, using the density matrix renormalization group (DMRG) and the numerical exact diagonalization (ED), combined with a precise finite-size scaling analysis named level spectroscopy[1]. The spin gap, which is one of the most interesting macroscopic quantum effects, was revealed to be open for sufficiently strong rung exchange couplings, in contrast to the three-leg spin ladder system which is gapless. The critical point of a quantum phase transition between the gapped and gapless phases was estimated. It is consistent with the previous effective Hamiltonian approach. We also found a new quantum phase transition caused by an asymmetric rung interaction. When one of the three rung coupling constants is changed, the spin gap would vanish. In addition we theoretically predicted some new field-induced quantum phase transitions.

A chirality-mediated novel superconductivity mechanism was also proposed[2, 3].

## 2 Ring Exchange Induced Novel Spin Gap Phase

The  $S=1/2$  three-leg spin nanotube with the ring exchange interaction at each plaquette is investigated using the numerical diagonalization of finite-size systems. The previous work suggested that the system without the ring exchange interaction has a spin excitation gap between the singlet ground state and the triplet excitation, because a spontaneous dimerization occurs in the ground state. The present study indicates that as the ring exchange increases, a quantum phase transition occurs at some critical value to another spin gap phase where the pattern of the dimerization is different from the initial one. The spin gap is revealed to vanish at the phase boundary[4].

These results were obtained by the numerical exact diagonalization of the  $S = 1/2$  spin tube with 30 spins, using the system A with 8 nodes.



## References

- [1] T. Sakai, M. Sato, K. Okunishi, Y. Otsuka, K. Okamoto and C. Itoi: Phys. Rev. B 78 (2008) 184415.
- [2] T. Sakai, M. Sato, K. Okamoto, K. Okunishi and C. Itoi: J. Phys.: Condens. Matter 22 (2010) 403201.
- [3] K. Okunishi, M. Sato, T. Sakai, K. Okamoto and C. Itoi: Phys. Rev. B 85 (2012) 054416.
- [4] T. Sakai, T. Kasahara, K. Hijii, H. Ohta, and H. Nakano: submitted to Synthetic Metals.

# Ground-State Phase Diagram of an $S=2$ Antiferromagnetic Chain with Bond-Alternation and On-Site Anisotropy

Takashi Tonegawa

*Professor Emeritus, Kobe Univ. and Visiting Professor, Osaka Prefecture Univ.*

The purpose of this report is to explore the ground-state phase diagram of an  $S=2$  antiferromagnetic chain with bond-alternation and on-site anisotropy by using mainly numerical methods. We express the Hamiltonian which governs this system as

$$\mathcal{H} = \sum_{\ell=1}^N \{1 + (-1)^\ell \alpha\} \vec{S}_\ell \cdot \vec{S}_{\ell+1} + D \sum_{\ell=1}^N (S_\ell^z)^2, \quad (1)$$

where  $\vec{S}_\ell$  and  $S_\ell^z$  are the  $S=2$  operator at the  $\ell$ th site and its  $z$ -component, respectively;  $\alpha$  ( $0.0 \leq \alpha \leq 1.0$ ) is the parameter representing the bond-alternation;  $D$  ( $-\infty < D < \infty$ ) is the on-site anisotropy constant;  $N$ , being assumed to be even, is the total number of spins in the system. Hereafter, we denote the  $z$ -component of the total magnetization by  $M$  ( $= \sum_{\ell=1}^N S_\ell^z$ ).

Several authors [1-3] have recently shown that, when  $D=0.0$ , two successive Gaussian phase transitions, one of which is the one from the Haldane to the dimer1 phase and the other is the one from the dimer1 to the dimer2 phase, take place with increasing the value of  $\alpha$ ; the transition points for the former and latter transitions are, respectively,  $\alpha=0.1866(7)$  and  $\alpha=0.5500(1)$  [3]. Furthermore, it has been shown [4,5] that, when  $\alpha=0.0$ , the Berezinskii-Kosterlitz-Thouless (BKT) transition [6] from the Haldane to the XY (Tomonaga-Luttinger-type spin liquid) phase and that from the XY to the large- $D$  phase successively occurs with increasing the value of  $D$  ( $\geq 0.0$ ); the transition points for the former and latter are, respectively,  $D \sim 0.043$  and  $D \sim 2.39$  [5]. The physical pictures of the Haldane, dimer1, dimer2, and large- $D$  phases are depicted in Fig. 1. As can be seen from this figure, in the case where we assume open boundary conditions, the appearance of an edge mode is expected in the dimer1 state, while it is not expected in all of the Haldane, dimer2, and large- $D$  states. Thus, only the dimer1 state is the symmetry-protected topological state [7,8] to which special attention has been devoted in very recent years.

Figure 2 shows our result for the ground-state phase diagram on the  $\alpha$  versus  $D$  plane for the

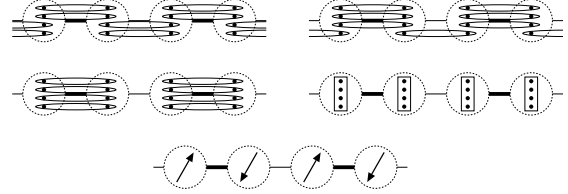


Figure 1: Physical pictures of the Haldane (top left), dimer1 (top right), dimer2 (central left), large- $D$  (central right), and Néel (bottom) phases. Large dotted circles denote  $S=2$  spins, and dots in these circles  $S=1/2$  spins. Thick and thin lines connecting nearest-neighboring  $S=2$  spins represent, respectively, the  $(1+\alpha)$  and  $(1-\alpha)$  bonds. Two  $S=1/2$  spins in each flat ellipse form singlet pairs, and four  $S=1/2$  spins in each rectangle are in the  $(S_{\text{tot}}, S_{\text{tot}}^z) = (2, 0)$  state.

present  $S=2$  chain. It consists of the above phases and the Néel phase which appears in the  $D < 0.0$  region. The physical picture of the Néel phase is also represented in Fig. 1. We emphasize that the dimer2 and large- $D$  states belong to the same phase, which we called the dimer2/large- $D$  phase; more details will be briefly discussed later.

In the following, we discuss how we have determined the phase boundary lines in the ground-state phase diagram. Let  $E_0^{(p)}(N, M)$  and  $E_1^{(p)}(N, M)$  be the lowest and second-lowest energy eigenvalues of the Hamiltonian  $\mathcal{H}$  under periodic conditions within the subspace characterized by  $N$  and  $M$ . It is noted that  $E_0^{(p)}(N, 0)$  gives the ground-state energy of the system for all values of  $\alpha$  and  $D$ . We also denote by  $E_0^{(t)}(N, M, P)$  the lowest energy eigenvalue of  $\mathcal{H}$  under twisted conditions within the subspace characterized by  $N$ ,  $M$ , and  $P$ , where  $P$  ( $= +1$  or  $-1$ ) is the eigenvalue of the space inversion operator with respect to the twisted bond. Then, according to the level spectroscopy theory [9,10], among the three energies,  $E_0^{(p)}(N, 2)$ ,  $E_0^{(t)}(N, 0, +1)$ , and  $E_0^{(t)}(N, 0, -1)$ , the first is lowest in the XY region, the second is lowest in the Haldane and dimer2/large- $D$  regions, and the third is lowest in the dimer1 region, in the thermody-

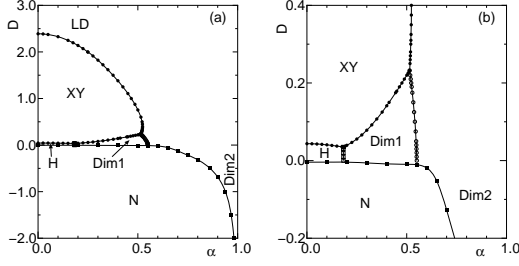


Figure 2: Ground-state phase diagram on the  $\alpha$  versus  $D$  plane determined in the present work; the region  $-0.2 \leq D \leq 0.4$  in (a) is enlarged in (b). Here, LD, H, Dim1, Dim2, and N stand, respectively, for large- $D$ , Haldane, dimer1, dimer2, and Néel.

namic ( $N \rightarrow \infty$ ) limit.

From the above arguments, we see that for a given value of  $D$ , the Gaussian transition point between the Haldane and dimer1 phases,  $\alpha_{\text{cr}}^{(\text{H,Dim1})}$ , and that between the dimer1 and dimer2 phases,  $\alpha_{\text{cr}}^{(\text{Dim1,Dim2})}$ , can be estimated by the  $N \rightarrow \infty$  extrapolations of  $\alpha_{\text{cr}}^{(\text{H,Dim1})}(N)$  and  $\alpha_{\text{cr}}^{(\text{Dim1,Dim2})}(N)$ , respectively, calculated numerically from the equation,

$$E_0^{(t)}(N, 0, +1) = E_0^{(t)}(N, 0, -1) < E_0^{(p)}(N, 2). \quad (2)$$

Practically, the calculated results for  $N=6, 8, 10$ , and 12 are extrapolated by assuming that their  $N$ -dependences are quadratic functions of  $N^{-2}$ . Plotting these extrapolated results as functions of  $D$ , we have finally determined the phase boundary lines for the above two transitions.

We have followed a similar procedure to obtain the phase boundary lines for both the BKT transition between the XY and Haldane phases and that between the XY and dimer2/large- $D$  phases; in these cases we have used the equation,

$$E_0^{(t)}(N, 0, +1) = E_0^{(p)}(N, 2) < E_0^{(t)}(N, 0, -1), \quad (3)$$

instead of eq.(2). Furthermore, in a similar way, we have obtained the phase boundary line for the the BKT transition between the XY and dimer1 phase by using the equation,

$$E_0^{(t)}(N, 0, -1) = E_0^{(p)}(N, 2) < E_0^{(t)}(N, 0, +1). \quad (4)$$

The phase transitions between the Néel and one of the Haldane, dimer1, and dimer2/large- $D$  phases are the two-dimensional Ising-type transition, because the  $Z_2$  symmetry is broken in the former phase, while it is not broken in the latter phases. In this case, the phenomenological renormalization group (PRG) method [11] is, at present, the most useful tool to determine the phase boundary line. We have numerically solved the PRG

equation given by

$$(N-2) \{E_1^{(p)}(N-2, 0) - E_0^{(p)}(N-2, 0)\} \\ = N \{E_1^{(p)}(N, 0) - E_0^{(p)}(N, 0)\} \quad (5)$$

to obtain the solution  $D_{\text{cr}}^{(N,X)}(N)$  ( $X=\text{H, Dim1, or Dim2}$ ) for a given value of  $\alpha$  or the solution  $\alpha_{\text{cr}}^{(N,\text{Dim2})}(N)$  for a given value of  $D$ . Then, we have extrapolated, to estimate the transition points, these results for  $N=8, 10$ , and 12 by assuming that their  $N$ -dependences are quadratic functions of  $(N-1)^{-2}$ .

The fact that the crossover between the dimer2 and large- $D$  states occurs, that is, both states belong to the same phase is very reasonable because of the following reasons: (1) Both states take the same value of  $P(=+1)$  and (2) There exists no edge state in both states when open boundary conditions are assumed. Very similar phenomena has been found so far in other several one-dimensional systems [12-16].

This work has been done in collaboration with K. Okamoto and T. Sakai. Performing the numerical calculations, we have used the Lanczos fortran program package KOBEPACK, which is very well vectorized for the NEC SX-9 system.

- [1] S. Yamamoto: J. Phys. Soc. Jpn. **63** (1994) 4327; Phys. Rev. B **51** (1995) 16128.
- [2] A. Kitazawa and K. Nomura: J. Phys. Soc. Jpn. **66** (1997) 3379.
- [3] M. Nakaura and S. Todo: Phys. Rev. Lett. **89** (2002) 077204.
- [4] U. Schollwöck and Th. Jolicœur: Europhys. Lett. **30** (1995) 493.
- [5] K. Nomura and A. Kitazawa: J. Phys. A: Math. Gen. **31** (1998) 7341.
- [6] Z. L. Berezinskii: Sov. Phys.-JETP **34** (1971) 610; J. M. Kosterlitz and D. J. Thouless: J. Phys. C: Solid State Phys. **6** (1973) 1181.
- [7] Z.-C. Gu and X.-G. Wen: Phys. Rev. B **80** (2009) 155131.
- [8] F. Pollmann et al.: Phys. Rev. B **85** (2012) 075125.
- [9] A. Kitazawa: J. Phys. A **30** (1997) L285.
- [10] K. Nomura and A. Kitazawa: J. Phys. A **31** (1998) 7341.
- [11] M. P. Nightingale: Physica A **83** 561 (1976).
- [12] T. Tonegawa et al.: J. Phys. Soc. Jpn. **65** (1996) 3317.
- [13] S. Todo et al.: Phys. Rev. B **64** (2001) 224412.
- [14] T. Tonegawa et al.: J. Phys. Soc. Jpn. **80** (2011) 043001.
- [15] K. Okamoto et al: JPS Conf. Proc. **3** (2014) 014022.
- [16] J. A. Kjäl et al: Phys. Rev. B **87** (2013) 235106.

# Precise estimation of dynamic correlation lengths in highly supercooled liquids

Hayato SHIBA

*Institute for Solid State Physics, University of Tokyo  
Kashiwa-no-ha, Kashiwa, Chiba 277-8581*

Takeshi KAWASAKI

*Department of Physics, Nagoya University  
Furo-cho, Chikusa-ku, Nagoya, Aichi 464-8602 Japan*

Kang KIM

*Department of Physics, Niigata University  
8050 Ikarashi, Nishi-ku, Niigata, 950-2181, Japan*

The physical understanding of glass transition remains a major challenge. 20 years has already passed since dynamical heterogeneity (DH) of supercooled liquids was found in various glass-forming systems by molecular simulations.

Four-point function has widely been employed for characterization of spatiotemporal scales of DH. However, bond-breaking events also be used to characterize heterogeneous motion taking place in a supercooled state. To see whether the correlation functions for these two quantities characterize different physics or not, we have previously simulated a large two-dimensional (2D) system (with up to 256,000 particles) to investigate cooperative motion using repulsive 12th-core systems[1]. Because large-wavelength vibration modes becomes prevailing, these two are found to provide different dynamic length scales with strong finite-size effects in the length characterized by the four-point function.

Long-wavelength vibration modes should be weaker in three-dimension (3D). To confirm whether the finite size effects remain or not, we have simulated systems up to 10,240,000 par-

ticles, using Kob-Andersen model and other models. In the parameter range we investigated, the structure factors of four-point and bond-breakage correlation functions converge at small wavenumber regions. Therefore, our system size is large enough for precise estimation of dynamic correlation lengths. Our result certifies the uniqueness of the dynamic correlation length in 3D, in contrast to 2D case[2].

## References

- [1] H. Shiba, T. Kawasaki, and A. Onuki, *Phys. Rev. E* **86** (2012), 041504.
- [2] H. Shiba, T. Kawasaki, and K. Kim, in preparation.

# Study of nonequilibrium phase transitions in low-Re non-Brownian colloidal dispersions

Hayato SHIBA

*Institute for Solid State Physics, University of Tokyo  
Kashiwa-no-ha, Kashiwa, Chiba 277-8581*

Kotaro OTOMURA and Masaki SANO

*Department of Physics, University of Tokyo  
Hongo, Bunkyo-ku, Tokyo 113-0033*

The objective of this project is to study nonequilibrium transitions taking place at high density. To study the dispersion rheology, we have adopted KAPSEL simulator, in which particles immersed in a fluid is solved using the Smoothed Profile method (SPM)[1]. In the simulation code, shear flow has been implemented, on a primitive level, in which calculation of full information of rheology is not established. In this project, we have extended SPM to achieve AC shear flow with large amplitude, under the constraint of the Lees-Edwards boundary conditions.

We started with a reformulation of the SPM, so that Lees-Edwards boundary condition becomes available, under DC or AC shear flow. By this reformulation, direct calculation of local and total shear stresses can be realized. Three rheological simulations are performed for a spherical particle, a rod of beads under flow, and collision of two spherical particles. Quantitative validity of these simulation method is established by comparing the viscosity with that obtained from theory and Stokesian Dynamics simulation.[2]

Our simulation is further extended to colloidal suspension with higher densities. It is known that a non-Brownian suspension with a high volume fraction undergoes the reversible-irreversible phase transition. In this transition,

the imaginary part of the complex viscosity,  $\eta''$ , assumes non-zero value only when the system is the irreversible state[3]. Applying our reformulated method to the non-Brownian suspension, we could reproduce the one-to-one correspondence between the irreversibility and the elasticity.

We found crystallization at extremely high volume fractions. By application of several periods of oscillatory shear flow on random configuration of the particles, the colloidal particles become rearranged to get well-ordered. The elastic modulus is also found to decrease as the particle configuration get ordered.

## References

- [1] Y. Nakayama, K. Kim, and R. Yamamoto, Eur. Phys. J. E **26**, 361-368 (2008).
- [2] J. J. Molina, K. Otomura, H. Shiba, H. Kobayashi, M. Sano, and R. Yamamoto, submitted.
- [3] L. Corte, P. Chaikin, J. Gollub and D. J. Pine, Nature Phys. **4**, 420-424 .

# Multiscale Simulation of Polymer Melts with Element Deformation

Takahiro MURASHIMA

*Department of Physics, Tohoku University*

*Aramaki-Aza-Aoba, Aoba-Word, Sendai, Miyagi 980-8578*

Soft matters, e.g. polymer melt, surfactant solution, liquid crystal, colloid dispersion, etc., are important for our daily life. Their processability and formability of soft matter fluid yield a variety of manufactures. To increase the processability and formability, it is important for investigating the fluid dynamics of soft matters.

Fluids in general are described with Euler equations; equations of mass density conservation, momentum conservation, and energy density conservation. When we focus on an isothermal and incompressible fluid, the dynamics of fluid is described with the following Cauchy momentum equation.

$$\rho \frac{dv_\alpha}{dt} = \nabla_\beta \sigma_{\beta\alpha} + f_\alpha, \quad (1)$$

where  $\rho$  is the density of mass,  $v_\alpha$  is the velocity,  $\nabla_\beta$  is the vector differential operator,  $\sigma_{\beta\alpha}$  is the stress tensor, and  $f_\alpha$  is the external force. Each subscript represents the components of vector or tensor. Here (and hereafter) we use Einstein summation convention. The stress tensor  $\sigma_{\alpha\beta}$  is originated in an isotropic pressure, time-independent viscous stress and time-dependent stress.

$$\sigma_{\alpha\beta} = -p\delta_{\alpha\beta} + \eta(\nabla_\alpha v_\beta + \nabla_\beta v_\alpha) + \sigma_{\alpha\beta}^t, \quad (2)$$

where  $\eta$  is a viscous coefficient. From the incompressible condition,

$$\nabla_\alpha v_\alpha = 0, \quad (3)$$

the Cauchy momentum equation (1) trans-

forms to

$$\rho \frac{dv_\alpha}{dt} = -\nabla_\alpha p + \eta \nabla^2 v_\alpha + \nabla_\beta \sigma_{\beta\alpha}^t + f_\alpha, \quad (4)$$

If we know the time-dependent stress  $\sigma_{\alpha\beta}^t$ , we can solve eq. (4) with using computational fluid dynamics techniques.

The time-dependent stress  $\sigma_{\alpha\beta}^t$  depends on the microscopic structure of molecules in the fluid element. The structural change of molecules in the bulk system is investigated with using non-equilibrium molecular dynamics simulation. In the computational fluid dynamics simulation, each fluid element is the local thermodynamic equilibrium and the molecules in the fluid element is regarded as to be in the bulk system. We can use the molecular dynamics simulation to obtain the time-dependent stress  $\sigma_{\alpha\beta}^t$  at each fluid element. We set periodic boundary condition to the molecular dynamics simulation at each fluid element. The transportation of molecules between fluid elements exists but the effect of the transportation is negligibly small in the homogeneous fluids. Then, the molecules at each fluid element are regarded as to be independent of the molecules at the other fluid elements. This assumption simplifies our multiscale approach bridging the macroscopic fluid dynamics and microscopic molecular dynamics and the coarse-grained parallel computing is available. The macroscopic fluid system is divided into  $N_e$  fluid elements and each fluid element has  $N_s$  simulators. The total number of the microscopic simulators in this system is

$N_t = N_e \times N_s$ . When the number of CPUs is equal to  $N_t$  or the integral multiple of  $N_t$ , the multiscale simulation is most efficient. On System B (SGI Altix ICE 8400EX) with 1024 cores, the weak scaling parallel efficiency of our multiscale simulation is almost 100 because the microscopic simulators are independent of the others during a time-interval of a fluid dynamic simulation and the time of communication is negligibly small in a total computation time[4].

The multiscale simulation technique bridging the macroscopic fluid dynamics and microscopic (mesoscopic) molecular dynamics to simulate a fluid dynamic behavior of polymer melts reveals the spacial nonhomogeneity of number of entanglements, chain stretch, orientation [1, 2, 3]. These field data are intuitively difficult to imagine the molecular states at each position. We need a more intuitive visualization technique.

Polymers in equilibrium state have an isotropic structure, but in non-equilibrium state an anisotropic structure. The mean conformation of polymers can be represented with a sphere or an ellipsoid by a statistical way. To visualize the local deformation of polymer chains, we develop the conversion method from the conformation of polymers in a fluid element to a triaxial ellipsoid. The process is as follows.

1. Obtain the inertia tensor.
2. Compute the eigen vectors of the inertia tensor.
3. Obtain mean projection lengths onto the eigen vectors.

The eigen vector represents the principal axis of ellipsoid and the mean projection length onto the eigen vector represents the length of semi-axis of ellipsoid. We have checked the above procedure using COGNAC and PASTA[5]. As shown in fig. 1, we have succeeded in obtaining a sphere in equilibrium state and a triaxial ellipsoid in non-equilibrium state. Moreover, we have found a relationship

between the shape of ellipsoid and the transient behavior of stress. Using the ellipsoid in our multiscale simulation, we can grasp the local strain field and polymer states at a glance.

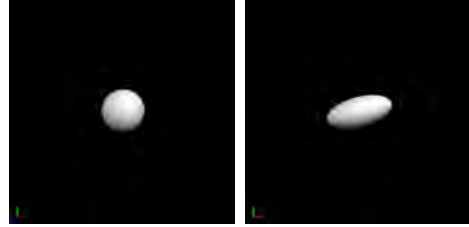


Figure 1: Polymers in equilibrium state has an isotropic conformation which is represented with a sphere (left). Polymers under shear flow has an anisotropic conformation which is characterized with a triaxial ellipsoid (right).

## References

- [1] T. Murashima, T. Taniguchi, EPL, 96 (2011) 18002.
- [2] T. Murashima, T. Taniguchi, JPSJ, 81 (2012) SA013.
- [3] T. Murashima, S. Yasuda, T. Taniguchi, R. Yamamoto, JPSJ, 82 (2013) 012001.
- [4] T. Murashima, ISSP Activity Report (2013) 222.
- [5] COGNAC and PASTA are developed in OCTA system found in <http://octa.jp>.

# Numerical study of bulk-edge correspondence

Y. Hatsugai

*Division of Physics*

*Faculty of Pure and Applied Sciences, University of Tsukuba*

*1-1-1 Tennodai, Tsukuba 305-8571, Ibaraki, Japan*

Topological phases are characterized by absence of relevant symmetry breaking to specifies their ground states. One may have some symmetry breaking such as superconductor/superfluidity, it is not fundamental to distinguish the states, say, from the ABM to the BW phases by a symmetry point of view. In this example, we know that the energy gap of the bulk quasiparticle is vanishing in one of the phases, which clearly stable characterization since the gap node in three dimensions is topologically stable. This is a three dimensional analogue of the graphene where symmetry requirement reduces the effective degree of freedom. In these example, there are characteristic boundary physics reflecting non trivial bulk. This is an example of the bulk-edge correspondence stating that existence of non trivial edge states is directly governed by the bulk as is also discussed in the quantum (spin) Hall effects. Topological quantities such as the Chern number and the Berry (Zak) phases of the bulk predict the existence of the edge states with various boundaries. By substantial numerical calculations, we have established this bulk-edge correspondence for electronic systems with filling factor  $1/4$  [6], layered systems[5] and also for quantum spin systems[1]. Further basic concepts of the bulk-edge correspondence are discussed and clarified from various aspects ( quantum entanglement [1,2,4] and generalized chiral symmetry[3]) supplementing analytical/numerical methods[2-5].

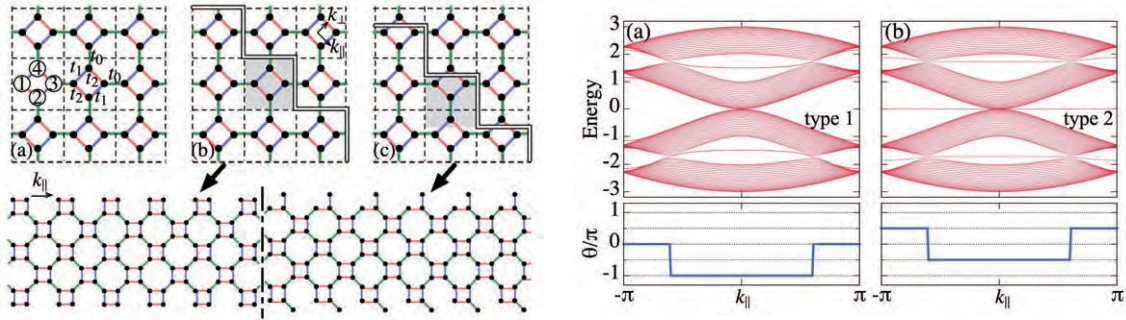


Figure 1: Left: Examples of various boundaries by cutting a periodic system in various ways. Right: Corresponding energy spectrum and the Berry (Zak) phases (See details.[6])

## References

- [1] T. Kariyado and Y. Hatsugai, arXiv:1412.7901
- [2] T. Fukui and Y. Hatsugai, Journal of the Physical Society of Japan, 84, 043703 (2015).
- [3] Y. Hatsugai, T. Kawarabayashi and Hideo, Aoki, Phys. Rev. B **91** 085112 (2015).
- [4] T. Fukui and Y. Hatsugai, Journal of the Physical Society of Japan, 83, 113705 (2014).
- [5] Y. Yoshimura, K.-I. Imura, T. Fukui and Y. Hatsugai, Phys. Rev. B **90**, 155443 (2014).
- [6] T. Kariyado and Y. Hatsugai, Phys. Rev. B **90**, 085132 (2014).



# Equations of State for Lennard-Jones Related Crystalline States

Kazuhiro Fuchizaki, Yuta Asano, Kazuma Okamoto, and Seishiro Doi  
*Department of Physics, Ehime University, Matsuyama 790-8577*

The equations of state (EOSs) for two crystalline systems, whose constituent particles are interacted with one another via the Lennard-Jones (LJ) related potential functions, were established. The supercomputers were utilized to generate well-equilibrated isothermal–isobaric ensembles for the systems to compile  $p$ – $v$ – $T$  ( $p$ : pressure,  $v$ : specific volume,  $T$ : temperature) data to construct the EOSs.

The first system is a model molecular crystal  $\text{GeI}_4$ . The molecule was modeled as a rigid regular tetrahedron with four interaction-sites at its vertices. Neglecting the detailed electronic distribution in the molecule, iodine atoms take a closed electronic shell. Thus, the interaction between the electronically neutralized intermolecular iodine atoms is approximated by the van der Waals interaction, which is well described by the LJ potential function. The model parameters were carefully determined as  $\epsilon/k_B = 280.5$  K and  $\sigma = 3.7185$  Å [1] ( $k_B$ : Boltzmann’s constant) to ensure the nominal lattice constant and the melting point at ambient pressure. Comparison of model’s melting curve with the actual one allows us to determine the upper bound of pressure below which the model is applicable to examine the liquid structure [1]. The melting curve itself was rationalized from the thermodynamic quantities of the solid phase [1]. To derive those quantities, the EOS was established. However, the derivation of the EOS in Ref. [1] is far from complete even referring to Supplemental Material attached. Information excluded from Ref. [1] is presented here.

The second crystalline system whose EOS is presented is the modified LJ (mLJ) system. The success of explaining the melting curve [1] prompted us to investigate a simpler system

with the same prescription to establish a firm basis in treating the melting-curve equation from the one-phase approach. It then needed to construct the EOS, from which the thermodynamic quantities required for solving the melting-curve equation should be extracted. This trial ended in success [2]. The derivation of the EOS is presented here but only briefly. It is worth publishing the derivation in standardizing the mLJ system [3], and the full details will be presented elsewhere.

Supplement to Appendix A of Ref. [1]

We chose  $T_0 = 300$  K as a reference temperature, at which the EOS was assumed to be derived purely energetically. As a candidate for the EOS at  $T_0$ , the first-order Murnaghan (1st-M), the Birch–Murnaghan (BM), the constrained Parsafar–Mason (cPM), and the Vinet (V) EOSs were examined. Although the fitted values for the parameters involved in these EOSs were listed, the aspect of fitting was not shown. The experimental compression profile is shown in Fig. 1 together with the curves representing the fitted EOSs.

Among these EOSs, we chose, without any special reason, the BM EOS as the EOS at  $T_0$ , to which thermal pressure contribution was added to obtain the EOS valid at elevated temperatures. The latter contribution was evaluated from integrating two thermodynamic identities successively. Integrating the first identity required the boundary condition for  $\alpha K|_{v=1} = (\partial p/\partial T)_{v=1}$  ( $\alpha$ : thermal expansion coefficient,  $K$ : bulk modulus), whose value,  $1.13583 \times 10^{-3}$  GPa K<sup>−1</sup>, was estimated from the unconstrained Parsafar–Mason (uPM) EOS. To make the integration of the second identity easy, we could invoke Anderson’s ansatz of constant  $(\partial K/\partial T)_v$  to ob-

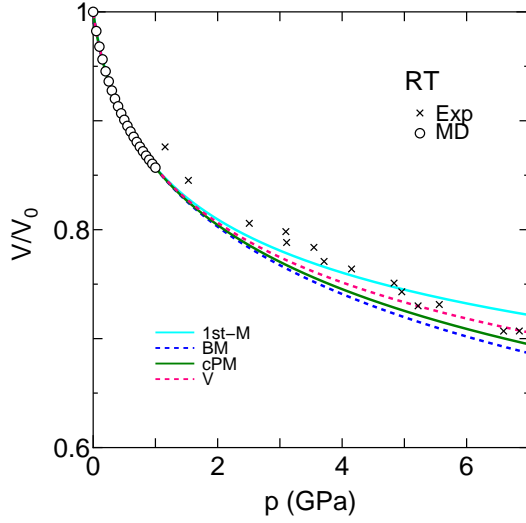


Figure 1: The compression feature of the model crystal at  $T_0$  (circles) is fitted to the various EOSs mentioned in the text. The fitted curves coincide with one another within the fitting region. The compression behavior of the real substance is also shown (crosses) for reference.

tain the Birch–Murnaghan–Anderson (BMA) EOS. Instead, we fitted the compression data at elevated temperatures to the BMA EOS (as shown in Fig. 2), treating  $(\partial K/\partial T)_v$  as merely a fitting parameter. Its linear dependence on  $T$  (shown in the inset) was described by Eq. (A5) of Ref. [1] to complete the BMA EOS.

#### EOS for the crystalline mLJ system

We employed a system consisting of 6912 mLJ particles to reduce unfavorable finite-size effects as much as possible. The cell list method facilitated not only treating a large number of particles but also parallelization of the code. More than 350 equilibrium states were generated for a set of  $T \in [0.20, 1.65]$  and  $p \in [10^{-4}, 10]$ . (Here,  $p$  and  $T$  are suitably reduced using the mLJ parameters.)

We followed exactly the same route as the one adopted in Ref. [1] to construct the EOS. The lowest temperature was chosen to be defined as the reference temperature  $T_0 = 0.20$ , and the BM EOS was settled at  $T_0$  as  $p_{\text{BM}}(v, T_0) = \frac{3}{2}K_0(v^{-7/3} - v^{-5/3})(1 - \zeta(v^{-2/3} - 1))$  with  $K_0 = 46.03(30)$  and  $\zeta = \frac{3}{4}(4 - K'_0) = -5.511(77)$ . The quantity with a subscript “0” means that it is evaluated at ambient pressure, and a prime for  $K$  stands for a pressure deriva-

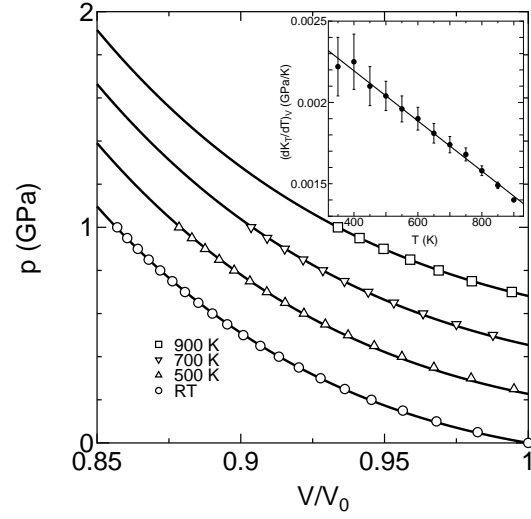


Figure 2: Only the data along the selected isotherms are shown to avoid unnecessary complexity.  $(\partial K/\partial T)_v$  decreases linearly with  $T$  (inset).

tive. The number in brackets indicates the accuracy of the last digits.

The next task was to obtain the uPM EOS,  $p_{\text{uPM}} = A_0(T)v^{-2} + A_1(T)v^{-3} + A_2(T)v^{-4}$ , where the temperature-dependent coefficients were found as  $A_0(T) = 61.015(59) + 8.989(144)T + 0.434(76)T^2$ ,  $A_1(T) = -175.73(4) + 4.74(9)T - 1.30(5)T^2$ , and  $A_2(T) = 113.02(6) - 5.22(15)T + 0.60(8)T^2$ . Although the uPM EOS itself is a closed equation applicable for  $T \geq T_0$ , it can be used to evaluate  $\alpha K|_{v=1} = 8.1153(139)$ .

Finally, again treating  $(\partial K/\partial T)_v$  as a fitting parameter, we arrived at the BMA EOS,  $p_{\text{BMA}}(v, T) = p_{\text{BM}}(v, T_0) + \alpha K|_{v=1}(T - T_0) - [(B + CT_1 + DT_1^2)(T - T_0)\theta(T_1 - T) + \{(B + CT_1 + DT_1^2)(T_1 - T_0) + B(T - T_1) + \frac{C}{2}(T^2 - T_1^2) + \frac{D}{3}(T^3 - T_1^3)\}\theta(T - T_1)] \ln T$ , where  $B = 21.69(65)$ ,  $C = -16.17 \pm 1.22$ , and  $D = 4.70(54)$ .  $T_1 = 0.75$  is a newly introduced characteristic temperature, and  $\theta$  stands for the step function.

#### References

- [1] K. Fuchizaki and Y. Asano: J. Phys. Soc. Jpn. **84** (2015) in press.
- [2] K. Okamoto *et al.*: Mem. Fac. Sci. Ehime Univ. **20** (2015) in press.
- [3] K. Fuchizaki: presented at CCMS 4th Symposium, Nov. 12–14, 2014, ISSP.

# Simulation studies of the hydrodynamic effects in model colloidal suspensions

Akira Furukawa

*Institute of Industrial Science, University of Tokyo  
Komaba 4-6-1, Meguro-ku, Tokyo 153-8505*

Using a fluid-particle dynamics (FPD) method [1], which is a hybrid simulation method for the dynamics of complex colloidal suspensions, we numerically studied the effects of hydrodynamic interactions on the collective dynamics in model colloidal suspensions. Hydrodynamic simulations of the following issues (i) and (ii) were partially performed at the ISSP Supercomputer Center. The programs are parallelized with a combination of OpenMP and MPI techniques.

(i) Colloidal gels are out-of-equilibrium structures, made up of a rarefied network of colloidal particles. With simulations which properly include hydrodynamics, we confirmed that hydrodynamic interactions suppress the formation of larger local equilibrium structures of closed shapes, and instead leads to the formation of highly anisotropic threads, which is crucial for making up the open gel network. Based on the three-point correlation function, we proposed a scale-resolved quantitative measure for the anisotropy of the gel structure. We found a strong discrepancy for distances just under twice the particle diameter between systems with and without hydrodynamics, quantifying the role of hydrodynamics from a structural point of view [2].

(ii) In recent experiments on *E. coli* in the presence of attractive forces (created via a depletion potential due to polymer additives) it

was shown experimentally and by simulation that activity produces a significant shift of the phase boundary compared to that of a passivated system with the same attractions [3]. However, in general, the configurations favored by such an attraction do not coincide with those stabilized by the activity-induced hydrodynamic interactions, and thus, there may arise significantly different steady states with and without hydrodynamics. Using a recently proposed model of motile bacteria [4], we are currently addressing this problem by simulation [5].

## References

- [1] H. Tanaka and T. Araki, Phys. Rev. Lett. **85**, 1338 (2000).
- [2] C. P. Royall, J. Eggers, A. Furukawa, and H. Tanaka, accepted for publication in Phys. Rev. Lett.
- [3] J. Schwarz-Linek, C. Valeriani, A. Cacciuto, M.E. Cates, D. Marenduzzo, A.N. Morozov, and W.C.K. Poon, PNAS **109**, 4052 (2012).
- [4] A. Furukawa, D. Marenduzzo, and M.E. Cates, Phys. Rev. E, **90**, 022303 (2014).
- [5] in preparation

# A possible replica-symmetry-breaking in finite-dimensional statistical-mechanics models

Koji HUKUSHIMA

*Department of Basic Science, University of Tokyo*

*3-8-1 Komaba, Meguro-ku, Tokyo 153-8902*

Some mean-field spin-glass models with the one-step replica-symmetry breaking (RSB) have attracted much attention of many researchers in recent years. For instance,  $p$ -state Potts glass with  $p \geq 3$  belongs to this class. These models are regarded as a prototype of a phenomenological picture of structural glass transition, called random first-order transition (RFOT), which is characterized by the existence of two different transitions, a dynamical transition at  $T_d$  and a static glass transition at  $T_c < T_d$ . The advisability of the RSB picture in finite dimensional spin glass models comes to an issue in the context of the structural glass transition. In particular, the dynamical transition is considered to be smeared out in finite dimensions because of thermal activation process.

While the existence of the spin-glass transition of the Potts glass in three dimensions is clarified for  $p \leq 6$ [1,2], no feature predicted by RFOT based on the one-step RSB is found in numerical simulations. Recently, we have found that a 7-state Potts glass model in three dimensions with third neighbor couplings is a candidate for the model system exhibiting RFOT in finite dimensions[3], where a thermodynamic spin-glass transition occurs with discontinuous order-parameter emergence and no latent heat at  $T_c$ . In this project, we studied further static and dynamic properties of the model by using Monte Carlo simulations in order to strengthen our previous results.

First, we study phase diagram of the coupled replica system of the model. When the original system exhibits RFOT at finite temperature, the existence of a real first-order transition is predicted in the coupled system. In fact, we obtained the first-order transition line in temperature-coupling parameter space and

the critical end point.

Next, Franz-Parisi glass potential has been investigated for our model, which is obtained as a function of the order parameter near  $T_c$  by a biased sampling Monte Carlo method. It is found that a minima of the potential at a certain finite value of order parameter emerges above  $T_c$ , indicating the discontinuous jump of the order parameter at  $T_c$ . These findings are completely consistent with the RFOT picture.

On the other hand, dynamical properties we have studied are very far from those in the mean-field spin glasses with 1RSB. In particular, no indication of the dynamical transition is found above  $T_c$  in our model. Here, we carefully study dynamical susceptibility, called  $\chi_4$ , which is often investigated in model systems of structural glass transition. In the long time limit, the  $\chi_4$  susceptibility corresponds to the static spin-glass susceptibility which must diverges at  $T_c$ . Our large-scale dynamical simulations show that the  $\chi_4$  susceptibility has a clear peak at finite time scale before the long time limit depending on temperature. The peak height, as well as the time scale, increases with decreasing temperature. Finite-size scaling of  $\chi_4$  suggests that it diverges at finite temperature very close to  $T_c$  and the exponent is significantly larger than that of the spin-glass susceptibility. This strongly indicates that the dynamical transition, if any, occurs at  $T_c$  but the dynamical singularity is separated from the static one. This might be a possible scenario in finite dimensions based on RFOT, which must be studied in a further research.

The present work has been done in collaboration with Takashi Takahashi.

[1] L. W. Lee, et al: Phys. Rev. B **74** (2007) 0104416.

[2] A. Cruz, et al: Phys. Rev. B **79** (2009) 184408.

[3] T. Takahashi and KH: Phys. Rev. E **91** (2015) 020102(R).

# Quantum Monte Carlo Study for Kitaev Spin Liquids

Yukitoshi Motome

*Department of Applied Physics, University of Tokyo  
Hongo 7-3-1, Bunkyo, Tokyo 113-8656*

The Kitaev model is a spin-1/2 model on a 2D honeycomb lattice, which has attracted much attention from broad areas of physics, such as quantum magnets, statistical physics, and quantum information. The model has highly-anisotropic interactions of Ising type, whose spin component depends on the bond directions, as shown in Fig. 1(a). These peculiar interactions are strongly frustrated, and prevent the system from developing a long-range order. Indeed, the ground state is exactly shown to be a quantum spin liquid. Although the model is solved in the ground state, the finite-temperature properties have not been fully clarified thus far. In particular, it was unclear how the quantum spin liquid evolves from the high-temperature paramagnet.

In the present study, we investigate the thermodynamic properties of the Kitaev model and its extensions. Since the conventional quantum Monte Carlo simulation on the basis of the world-line technique suffers from the negative sign problem due the frustration in the model, we have developed a new quantum Monte Carlo method by using the Majorana fermion representation, which is free from the negative sign problem. We have carried out the parallelization by using MPI hybridized with openMP for diagonalization of the Majorana fermion system, and also the replica exchange technique for enhancing the efficiency of Monte Carlo sampling at low temperatures. We have applied this method to a 3D extension of the Kitaev model shown in Fig. 1(b) as well as the original 2D one. In both cases, we observed the well-separated two-stage entropy release

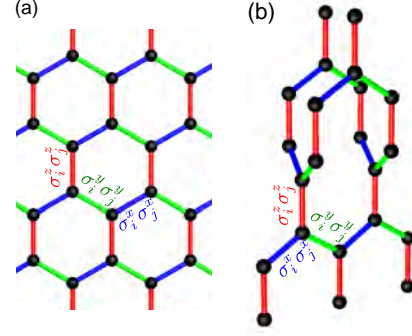


Figure 1: Kitaev models on (a) a honeycomb lattice and (b) a hyperhoneycomb lattice.

while changing temperature, indicating that an  $S = 1/2$  quantum spin is thermally fractionalized into two different types of Majorana fermions. In the 2D case, these two are both crossovers [1]. In contrast, we found that the 3D model exhibits a finite-temperature transition at the lower temperature between the quantum spin liquid and paramagnet [2–4]. This transition is characterized by the topological nature of the excited states.

## References

- [1] J. Nasu, M. Udagawa, and Y. Motome, arXiv:1504.01259.
- [2] J. Nasu, T. Kaji, K. Matsuura, M. Udagawa, and Y. Motome, Phys. Rev. B **89** (2014) 115125.
- [3] J. Nasu, M. Udagawa, and Y. Motome, Phys. Rev. Lett. **113** (2014) 197205.
- [4] J. Nasu, M. Udagawa, and Y. Motome, J. Phys.: Conf. Ser. **592** (2015) 012115.

# Explore in new aspects of phase transitions

Seiji MIYASHITA

*Department of Physics, University of Tokyo*  
 7-3-1 Hongo, Bunkyo-ku, Tokyo 113-0033, Tokyo

We have studied cooperative phenomena in both quantum and classical system, and also in static and dynamical field.

## 1 Quantum dynamics under driving fields

We studied quantum dynamics under time dependence field in the following systems. We study the distribution of the states under driving force with a dissipative mechanism by quantum master equation method. We found that under some conditions, distribution of state in the stationary state of a system driven by periodic external field is given by a canonical distribution with respect to the Floquet quasi-eigenstates.[1] We also found that there exists a metastable long-lived state in the relaxation process of a system with driving force.[2]

We also studied quantum dynamics of reverse process of magnetization under sweeping field (from parallel to antiparallel) in a uniaxial magnetic systems. It is known that in corresponding classical system a kind of spinodal transition takes place which is known as Stoner-Wohlfarth (SW) transition. In quantum system this type of process has been studied for the spin dynamics of single molecular magnets, where the dynamics is characterized by successive Landau-Zener transitions among energy levels. The classical spinodal type criticality was found expressed by singular change of gaps at avoided-level crossings. The adiabatic motion in the classical system until the SW point is realized when we sweep the field very slowly. This process corresponds to the perfect non-adiabatic transition at each level crossings in quantum system. As an interest-

ing quantum phenomenon, we found a beating of the spin-amplitude after the SW point. Dependence of the period of this beating on the system parameters is clarified.[3]

We made detailed study of ESR data of  $V_{15}$ [4], and also proposed a new scheme of the numerical method for ESR by making use of the Wiener-Khinchin relation.[5] We pointed out the method of thermal typical state  $e^{-\beta\mathcal{H}}|\text{random state}\rangle$  gives a kind of converged distribution of the expectation value of spectrum density of driven spins which expectation value is zero.

## 2 Cooperative Phenomena and Phase Transitions

We also studied phase transitions in the following systems.

We studied static and dynamical aspects of phase transition of an Ising model on the small-world network. The system exhibits a phase transition of the mean-field universality class. We confirmed this property and obtained dependence of the critical temperature on the density of small-world short cuts. We found that the system does not show metastability in contrast to the case of the infinite-range (Husimi-Temperley) model which has the mean-field type static phase transition and also exhibits the spinodal transition as a dynamical phase transition.[6]

Phase transitions in systems with bistable local electric states, such as the spin-crossover, Jahn-Teller system, and martensite systems has been important topic in our group.[7] In the last year, we studied phase transitions in a system with frustrated short-range interactions: ANNNI model, which seems realized in a material:  $[\text{FeH}_2\text{L}^{2-\text{Me}}](\text{ClO}_4)_2$ [8], and anti-

ferromagnet on the triangular lattice with next nearest neighbor interaction (Mekata model) changed by the elastic interaction.[9] We studied fundamental properties of statistical mechanism for the long-range interacting model.[10]

We formulated a finite temperature LLG (Landau-Lifshitz-Gilbert) equation, and we studied the stability of the metastable magnetic structure at finite temperatures.[11], and investigated mechanisms of coercive force of real magnets.

We also studied quantum phase transition of an itinerant ferromagnetism, in which the system exhibits both the Mott singlet and Nagaoka ferromagnetic state under a continuous control of the electron density profile.[12]

### 3 Stochastic process

Dync process is a diffusion process in which the thermal kernel is replaced by the so-called Dynck operator. One of the Dynck processes is a Brownian motion of particles interacting with the Coulomb force. We have studied dynamics of the distribution of the particles from a view point of the intertwining operator. Asymptotic dependence on the system parameter  $\beta$  and its relation from a given initial state to the stationary state.[13]

### References

- [1] T. Shirai, T. Mori, S. Miyashita, Condition for emergence of the Floquet-Gibbs state in periodically driven open systems, *Phys. Rev. E*, **91**, 030101(R) (2015).
- [2] T. Mori, Floquet resonant states and validity of the Floquet-Magnus expansion in the periodically driven Friedrichs models, *Phys. Rev. A* **91**, 020101 (R) (2015).
- [3] T. Hatomura, B. Barbara and S. Miyashita, Quantum Stoner-Wohlfarth model, arXiv:1503.06658.
- [4] M. Marthens, J. Tol. van, NS Dalal, S. Bertaina, B. Barbara, B. Tsukerblat, A. Muller, S. Garai, S. Miyashita, I. Chiorescu, Anisotropy of the molecular magnet V-15 spin Hamiltonian detected by high-field electron spin resonance, *Phys. Rev. B*, **89** 195439 (2014).
- [5] H. Ikeuch, S. Bertaina and S. Miyashita, Numerical study on ESR by making use of Wiener-Khinchin relation in time domain, arXiv:1503.06111.
- [6] F. Futami, Static and dynamical properties of magnetic order in small world networks, Master thesis (2014) The University of Tokyo.
- [7] C. Enachescu, M. Nishino, S. Miyashita, K. Boukheddaden, F. Varret, P.A. Rikvold, Shape effects on the cluster spreading process of spin-crossover compounds analyzed within an elastic model with Eden and Kawasaki dynamics, *Phys. Rev. B* **91**, 104102 (2015).
- [8] H. Watanabe, S. Miyashita, K. Tanaka, N. Bréfuel, J.-F. Letard, H. Cailleau, M. Nishino, and E. Collet, Local versus long-range ordering of high and low spin state described by ANNNI model, unpublished.
- [9] M. Nishino and S. Miyashita, Effect of elastic interactions on the Kosterlitz-Thouless phase of spin-crossover systems in triangular lattices with short-range frustrated interactions, unpublished.
- [10] T. Mori, Natural correlation between a system and a thermal reservoir, *Phys. Rev. A* **89**, 040101(R) (2014).
- [11] M. Nishino and S. Miyashita, Realization of the thermal equilibrium in inhomogeneous magnetic systems by the Landau-Lifshitz-Gilbert equation with stochastic noise, and its dynamical aspects, *Phys. Rev. B* **91**, 134411 (2015).
- [12] H. Onishi, S. Miyashita, Doping control of realization of an extended Nagaoka ferromagnetic state from the Mott state, *Phys. Rev. B*, **90**, 224426 (2014).
- [13] S. Andraus, M. Katori, S. Miyashita, Two limiting regimes of interacting Bessel processes, *J. Phys. A: Math. Theor.* **47** 235201, (2014).

# Morphological changes of amphiphilic molecular assemblies induced by chemical reaction

Koh M. NAKAGAWA and Hiroshi NOGUCHI

*Institute for Solid State Physics, University of Tokyo*

*Kashiwa-no-ha, Kashiwa, Chiba 277-8581*

In soft matter systems, chemical reaction often induces interesting shape changes (*e.g.*, self-beating gel [1] and self-reproducing vesicle [2]). We studied shape transformations of amphiphilic molecular assemblies induced by chemical reaction as an example of such shape changes [3]. Coarse-grained molecular simulation technique is used. A binding reaction between hydrophilic and hydrophobic molecules is considered.

Figure 1 shows an example of shape development of the molecular assembly. As an initial condition, a droplet of the hydrophobic particles is centered in water and the hydrophilic particles are dispersed in water. No amphiphilic molecules initially exist. It is found that the reaction induces transformation of an oil droplet to a tubular vesicle via bicelles and vesicles with discoidal arms. The discoidal arms close into vesicles, which are subsequently fused into the tubular vesicle. Similar extension of discoidal arms from the vesicles are observed in the experiments [2].

Under the chemical reaction, the bicelle-to-vesicle transition occurs at smaller sizes than in the absence of the hydrophobic molecules. We investigated the origin of this enhancement by calculating the bending rigidity, Gaussian curvature modulus and edge line tension. (SGI Altix ICE 8400 and FUJITSU PRIMEHPC FX10 are used for the calculation of the Gaussian curvature modulus.) As the result, it is revealed that the enhancement of this transition is due to embedded hydrophobic particles

that reduce the membrane bending rigidity [3]. Due to this enhancement effect, multiple vesicle formations appear in this system.

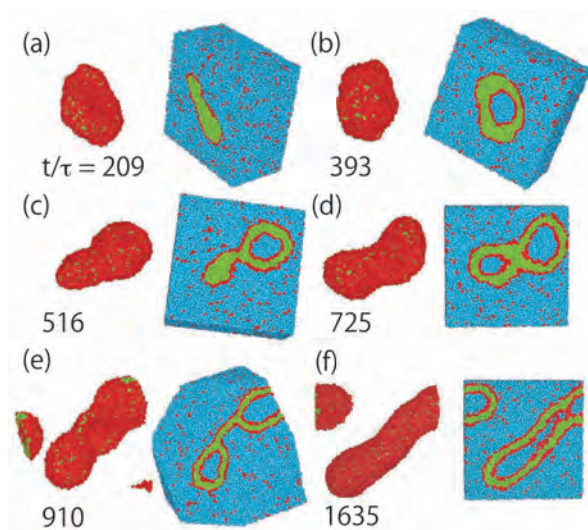


Figure 1: Sequential snapshots of an amphiphilic molecular assembly under the binding reaction. The number represent the simulation time  $t/\tau$ . Sliced snapshots with water (blue) particles are shown on the right panels.

## References

- [1] R. Yoshida and Y. Uesasaki, *Biomacromolecules* **6**, 2923–2926 (2005).
- [2] K. Takakura, *et al.*, *J. Am. Chem. Soc.* **125**, 8134–8140 (2003).
- [3] K. M. Nakagawa and H. Noguchi, *Soft Matter* **11**, 1403–1411 (2015).



# Self-Assembly of Banana-Shaped Rods on Biomembranes

Hiroshi Noguchi

*Institute for Solid State Physics, University of Tokyo  
Kashiwa-no-ha, Kashiwa, Chiba 277-8581*

Various proteins are associated with membrane shape deformations in protein transport, endo/exocytosis, cell motility, and cell division. Many of these proteins have a binding module called BAR (Bin-Amphiphysin-Rvs) domain, which consists of a banana-shaped dimer [1]. The BAR domain absorbs on biomembranes and changes their local curvature. The extension of membrane tubes from a giant unilamellar liposome have been experimentally observed.

We have studied the effects of anisotropic spontaneous curvature of the banana-shaped rods using an implicit-solvent meshless membrane simulations [2, 3]. Replica exchange molecular dynamics with 128 replicas were performed using System B in order to obtain the thermal equilibrium states. The proteins are modeled as banana-shaped rods strongly adhered to the membrane. No direct attractive interaction is considered between the rods to investigate the membrane-curvature-mediated interactions.

On a membrane tube, the rods with zero spontaneous curvature are randomly distributed and its orientation is along the axial direction. With an increase in the rod curvature, the rods rotate into the azimuthal direction. With a further increase, the rods assemble along the azimuthal direction and the membrane tube deforms into an ellipse. With an even further increase, the rods also assemble along axial direction. Thus, the rods assemble via two continuous directional phase separations unlike a conventional two-dimensional phase separation [2]. In the longer tubes, the phase separation in the axial direction occurs at lower value of the rod curvature.

In the vesicle, in the addition to these two assembly processes, further increase in the rod curvature induces tubular scaffold formation (see Fig. 1) [2]. As the rod curvature increases, the vesicle becomes oblate and then forms a cockscomb-like bump and a tubule. Thus, the anisotropy of the rod spontaneous curvature induces the step-wise rod assembly coupled with membrane deformation.

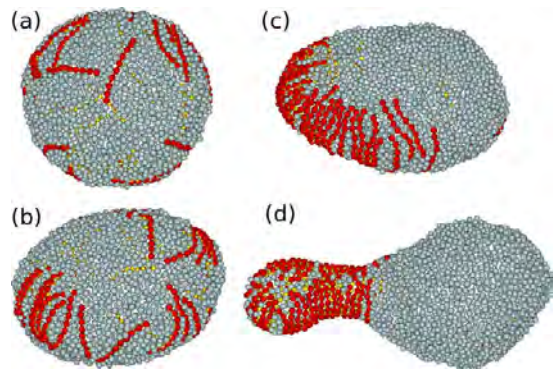


Figure 1: Snapshots of a vesicle with banana-shaped rods. (a) randomly distributed state. (b) Rod assembly on the equator of oblate vesicle. (c) Rod assembly in both direction. (d) Tube formation.

## References

- [1] T. Itoh and P. D. Camilli: *Biochim. Biophys. Acta* **1761** (2006) 897.
- [2] H. Noguchi: *EPL* **108** (2014) 48001.
- [3] H. Noguchi: *arXiv:1503.00973*.

# Study on Quantum Information Science Based on Statistical Physics

Shu TANAKA

*Waseda Institute for Advanced Study, Waseda University  
1-6-1 Nishi Waseda, Shinjuku-ku, Tokyo 169-8050*

Quantum information processing has been expected as a next-generation information technology toward advanced information society and big-data society. In this project, we studied three topics related to quantum information science from a viewpoint of statistical physics [1, 2, 3, 4].

## **(A) Entanglement properties of exactly solvable quantum systems [1, 2]**

We studied entanglement properties of the ground state of a quantum hard-core lattice gas model on square and triangle ladders. We constructed the model so that the ground state can be obtained exactly. We divided total system into two subsystems  $A$  and  $B$  across the mirror symmetric axis. The reduced density matrix was calculated as  $\rho_A = \text{Tr}_B \rho$ , where  $\rho$  represents the density matrix of total system. Using  $\rho_A$ , we calculated the entanglement entropy, the entanglement spectrum, and the nested entanglement entropy as a function of fugacity of quantum particle  $z$ . By analyzing the reduced density matrix, the characteristic value of  $z_c$  can be determined.  $z_c$  is the critical point of the corresponding classical model. At  $z = z_c$ , the entanglement properties show critical phenomena. In the case of square ladder, the entanglement properties correspond to the universality class of two-dimensional Ising model whereas the entanglement properties in the case of triangle ladder correspond to the universality class of two-dimensional three-state Potts model. In this study, we performed large-scaled exact di-

agonalizations to consider entanglement properties of the ground state and power method to obtain the ground state of large-scaled quantum systems. This work has been done in collaboration with Ryo Tamura (NIMS) and Hosho Katsura (The Univ. of Tokyo).

## **(B) Control of phase transition behavior toward quantum annealing [3]**

Quantum annealing is a new type of quantum information processing. A bottleneck of quantum annealing is the energy-gap problem which appears at the phase transition point. Thus, to control of phase transition behavior is an important task for quantum annealing. We demonstrated how to control phase transition behavior in the Potts model. By adding the invisible states, the order of phase transition in the Potts model is varied without changing the ground state properties. Though the result does not immediately solve the energy-gap problem in quantum annealing, we now consider a related model which directly relates to quantum annealing. In this study, we performed large-scaled Monte Carlo simulations using parallelization technique. This work was done in collaboration with Ryo Tamura (NIMS).

## **(C) Topological phase transition in a generalized cluster-Ising model [4]**

One of the simplest models which show topological phase transitions is the cluster-Ising model. We considered a generalized cluster-Ising model by adding the cluster interaction

into the original cluster-Ising model. The ground-state phase diagram of the model is determined by correlation functions and entanglement spectrum. We also considered dynamic properties of this model under sweeping interaction parameter across the critical point. As the sweep speed decreased, we observed characteristic spatial structures in entanglement entropy and string correlation function. In this study, we performed time-evolving block decimation for infinite systems (iTEBD) and large-scaled exact diagonalizations. This work was done in collaboration with Takumi Ohta (YITP), Ippei Danshita (YITP), and Keisuke Totsuka (YITP).

## References

- [1] S. Tanaka, R. Tamura, and H. Katsura, “Physics, Mathematics, And All That Quantum Jazz” *Kinki University Series on Quantum Computing - Vol. 9* (World Scientific) pp. 71-88 (2014).
- [2] S. Tanaka, R. Tamura, and H. Katsura, *in preparation*.
- [3] R. Tamura and S. Tanaka, “Physics, Mathematics, And All That Quantum Jazz” *Kinki University Series on Quantum Computing - Vol. 9* (World Scientific) pp. 135-161 (2014).
- [4] T. Ohta, S. Tanaka, I. Danshita, and K. Totsuka, arXiv:1503.03204 *to appear in J. Phys. Soc. Jpn.*

# Study on Phase Transition in Frustrated Spin Systems

Shu TANAKA

*Waseda Institute for Advanced Study, Waseda University  
1-6-1 Nishi Waseda, Shinjuku-ku, Tokyo 169-8050*

Frustrated spin systems often show new types of phase transitions due to characteristic density of states. To investigate new functional properties and exotic phase transitions in frustrated systems, we focus on two topics [1, 2].

## (A) Phase transition in a generalized Potts model with invisible states [1]

We proposed a toy model called the Potts model with invisible states to explain a new type of phase transition in two-dimensional frustrated spin systems. The phase transition is the first-order phase transition with three-fold symmetry breaking, which is not appeared in a usual Potts model. We generalized the Potts model with invisible states by adding the interaction between invisible states. By the mean-field analysis and numerical calculations, we found that the transition temperature decreases and the latent heat increases as the interaction between invisible states increases. In this study, we performed large-scaled Monte Carlo simulations including the Wang-Landau method. The result will be reported somewhere soon. This work has been done in collaboration with Ryo Tamura (NIMS).

## (B) Magnetic refrigeration [2]

Magnetic refrigeration is a next-generation cooling technology and needs theoretical studies from a viewpoint of statistical physics. As the preliminary stages toward studies of magnetic refrigeration using frustrated spin systems, we considered the magnetic refrigera-

tion efficiency of the ferromagnetic, A-type, C-type, and G-type antiferromagnetic Ising models. We proposed a scheme to obtain the maximum cooling performance according to the obtained magnetic entropy. In principle, our scheme can be used not only for the ferromagnetic, A-type, C-type, and G-type antiferromagnetic Ising models but also for geometrically frustrated Ising models and random Ising models. We now study the magnetic refrigeration efficiency using geometrically frustrated Ising models and random Ising models. In this study, we performed large-scaled Monte Carlo simulations including the Wang-Landau method. This work has been done in collaboration with Ryo Tamura (NIMS), Takahisa Ohno (NIMS), and Hideaki Kitazawa (NIMS).

## References

- [1] S. Tanaka and R. Tamura, *in preparation*.
- [2] R. Tamura, S. Tanaka, T. Ohno, and H. Kitazawa, J. Appl. Phys. **116**, pp. 053908-1-12 (2014).

# Numerical study of non-magnetic phase in quantum spin systems

Kenji HARADA

Graduate School of Informatics, Kyoto University, Kyoto 606-8501, Japan

Valence bond solid (VBS) order has been discussed in a non-magnetic phase of quantum spin systems. They are confirmed not only in exact solvable cases as AKLT models[1], but also in general quantum spin models. In particular, we are recently interested in the quantum phase transition between the VBS phase and the other phase[2]. For example, in the terms of deconfined quantum criticality[3, 4], the quantum criticality between VBS and different symmetry breaking phases has been much studied[5–7].

In this project, we studied the quantum criticality between VBS and the symmetry protected topological phases in a one-dimensional  $SO(N)$  bilinear-biquadratic model and the finite-temperature phase transition to the VBS phase in two-dimensional  $SU(N)$  JQ models.

In the former case, using a special mapping based on a generalized Jordan-Wigner transformation, we obtain a new sign-free model as the  $N$ -color bosonic model. We studied the quantum continuous phase transition between dimer and  $Z_4$  magnetic ordered phases on the new bosonic model by quantum Monte Carlo simulations on the ISSSP super computer system B. We found the correct CFT of the quantum criticality from the finite-size scaling analysis.

In the latter case, we have done comprehensive quantum Monte Carlo calculations for the finite-temperature phase transition to the VBS phase[8]. In the case of square lattice, we confirmed the two-dimensional Ising weak universality class for the finite-temperature phase transition. On the other hand, in the case of honeycomb lattice, we confirmed the two-dimensional three-state Potts universality class. In both cases, we have not found the crossover behavior of the first-order transition down to very low temperatures (See FIG. 1(b)).

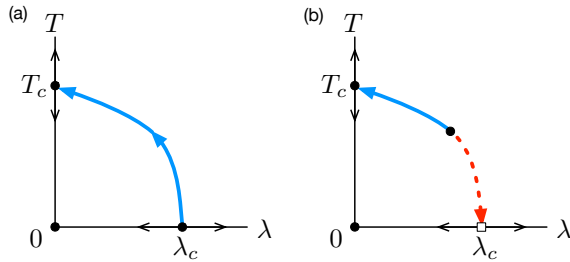


FIG. 1. Schematic phase diagram and renormalization flow of the JQ model. The thick solid (dashed) curves correspond to the second (first)-order transition. The horizontal axis is the coupling ratio of the Heisenberg term  $J$  and the multibody interaction term  $Q_m$ . The open square represents a discontinuous transition. Each solid circle denotes a fixed point, such as the two-dimensional Ising, three-state Potts, and multicritical fixed points. The coordination origin corresponds to the low-temperature fixed point. All arrows indicate renormalization flows. (a) Deconfined critical phenomena scenario. (b) First-order transition scenario.

- 
- [1] I. Affleck, T. Kennedy, E. Lieb, and H. Tasaki, *Physical Review Letters* **59**, 799 (1987).
  - [2] M. Matsumoto, C. Yasuda, S. Todo, and H. Takayama, *Physical Review B* **65**, 014407 (2001).
  - [3] T. Senthil, L. Balents, A. Vishwanath, and S. Sachdev, *Science* **303**, 1490 (2004).
  - [4] T. Senthil, L. Balents, S. Sachdev, and A. Vishwanath, *Physical Review B* **70**, 144407 (2004).
  - [5] K. Chen, Y. Huang, Y. Deng, A. B. Kuklov, N. V. Prokof'ev, and B. V. Svistunov, *Phys. Rev. Lett.* **110**, 185701 (2013).
  - [6] M. S. Block, R. G. Melko, and R. K. Kaul, *Physical Review Letters* **111**, 137202 (2013).
  - [7] K. Harada, T. Suzuki, T. Okubo, H. Matsuo, J. Lou, H. Watanabe, S. Todo, and N. Kawashima, *Physical Review B* **88**, 220408(R) (2013).
  - [8] T. Suzuki, K. Harada, H. Matsuo, S. Todo, and N. Kawashima, *Physical Review B* **91**, 094414 (2015).

# Magnetic structure dependence of adiabatic temperature change under magnetic field

Ryo TAMURA

*Computational Materials Science Unit, National Institute for Materials Science,  
1-1 Namiki, Tsukuba, Ibaraki, 305-0044*

Magnetic refrigeration [1,2] is a next generation cooling technology using magnetic materials. In adiabatic process, the rise and fall of the temperature of magnetic materials are induced by changing magnetic field. This change of temperature of magnetic materials is called adiabatic temperature change. In active magnetic regenerator (AMR) cycle which is one of the thermal cycles used in magnetic refrigeration, the adiabatic temperature change is directly used for cooling process. Then, it is important to synthesize magnetic materials having large adiabatic temperature change for practical realization of magnetic refrigeration.

We studied the magnetic structure dependence of the adiabatic temperature change by numerical simulations. By Monte Carlo simulations based on the Wang-Landau method [3], we obtained the temperature dependence of magnetic entropy of the Ising model on a cubic lattice. In ferromagnets, when the magnetic field is decreased, the temperature of magnetic materials always decreases (Fig. 1 (a)). In this process, the refrigerant is cooled by the decrease of temperature of magnetic materials. On the other hand, in antiferromagnets, there is the case that the temperature of magnetic materials increases when the magnetic field is decreased (Fig. 1 (b)). In this process, the refrigerant is heated. Then, the behavior of the adiabatic temperature change of ferromagnets differs from that of antiferromagnets. From these facts, we proposed a new method which can produce the maximum adiabatic temper-

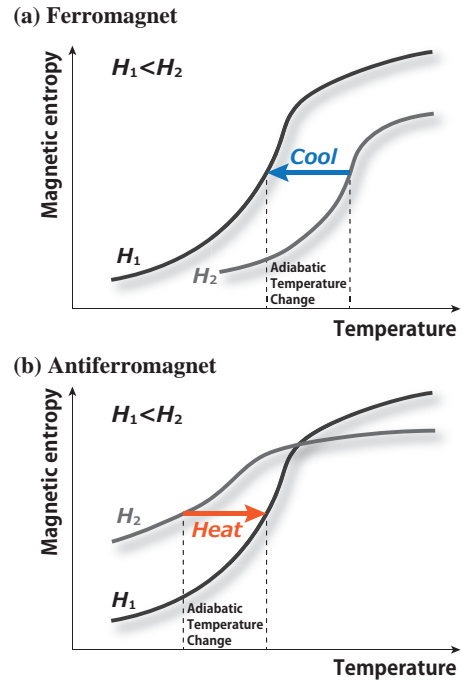


Figure 1: Schematics of the adiabatic temperature change in (a) ferromagnet and (b) antiferromagnet.

ature change of antiferromagnets [4]. When we use this method, the refrigerant is always cooled. Thus, the AMR cycle with our proposed method will exhibit high refrigeration efficiency. Furthermore, this method is the same as the method to obtain maximum isothermal magnetic entropy change [5].

This work was done in collaboration with Shu Tanaka (Waseda University), Takahisa Ohno (NIMS), and Hideaki Kitazawa (NIMS).

## References

- [1] A. M. Tishin and Y. I. Spichkin: *The Magnetocaloric Effect and its Applications* (Taylor & Francis, London, 2003).
- [2] S. Toyoizumi, H. Kitazawa, Y. Kawamura, H. Mamiya, N. Terada, R. Tamura, A. Dönni, K. Morita, and A. Tamaki: J. Appl. Phys. **117** (2015) 17D101.
- [3] F. Wang and D. P. Landau: Phys. Rev. Lett. **86** (2001) 2050.
- [4] R. Tamura, S. Tanaka, T. Ohno, and H. Kitazawa: J. Appl. Phys. **116** (2014) 053908.
- [5] R. Tamura, T. Ohno, and H. Kitazawa: Appl. Phys. Lett. **104** (2014) 052415.  
**[This topic was reported in Press Release in NIMS (March 10, 2014), MyNavi News (March 12, 2014), The Chemical Daily (March 19, 2014), The Science News (March 28, 2014).]**

# A new measure to calculate cooling capacity in magnetic refrigeration

Ryo TAMURA

*Computational Materials Science Unit, National Institute for Materials Science,  
1-1 Namiki, Tsukuba, Ibaraki, 305-0044*

In magnetic refrigeration [1,2], it is important to use magnetic materials having huge cooling capacity. The cooling capacity  $q$ , which is the amount of transferred heat from low temperature reservoir ( $T_l$ ) to high temperature reservoir ( $T_h$ ), is given by

$$q = \int_{T_l}^{T_h} \Delta S_M(T, H_2 \rightarrow H_1) dT, \quad (1)$$

where  $\Delta S_M(T, H_2 \rightarrow H_1)$  is the isothermal magnetic entropy change when the magnetic field is changed from  $H_2$  to  $H_1$ . Furthermore, the relative cooling power (RCP) is generally used in experiments to understand the cooling capacity of each magnetic material [3]. The RCP is defined as

$$\begin{aligned} \text{RCP}(H_2 \rightarrow H_1) \\ = \Delta S_{M \text{ max}}(H_2 \rightarrow H_1) \times \Delta T_{1/2}(H_2 \rightarrow H_1), \end{aligned} \quad (2)$$

where  $\Delta S_{M \text{ max}}(H_2 \rightarrow H_1)$  and  $\Delta T_{1/2}(H_2 \rightarrow H_1)$  are the maximum value and the half width of  $\Delta S_M(T, H_2 \rightarrow H_1)$ , respectively. It is well known that the RCP approximately characterizes the cooling capacity  $q$ .

We studied the performance of the magnetic refrigeration depending on the magnetic structures. By performing numerical simulations on the super computer, we calculated the isothermal magnetic entropy change of ferromagnets and antiferromagnets. In ferromagnets, we confirmed that the RCP value is nearly 4/3 times the cooling capacity. On the other hand, in antiferromagnets, the temperature depen-

dence of  $\Delta S_M$  has more than single peak under our proposed protocol which produces the maximum isothermal magnetic entropy change [4]. Thus, the RCP is not well-defined when our proposed protocol is used. To consider the efficiency of the magnetic refrigeration under the proposed protocol more appropriately, we introduced a new measure, the total cooling power (TCP) [5]. The TCP is defined as

$$\begin{aligned} \text{TCP} = \int_0^\infty \Delta S_M(T, H_2 \rightarrow H_1) \\ \times \Theta(\Delta S_M(T, H_2 \rightarrow H_1)) dT, \end{aligned} \quad (3)$$

$$\Theta(x) = \begin{cases} 0 & (x < 0) \\ 1 & (x \geq 0) \end{cases}. \quad (4)$$

The TCP characterizes the whole potential of the cooling capacity of the target material. We confirmed that the TCP value is almost 3/2 times the RCP value in the ferromagnet. For the antiferromagnets, we found that the TCP of the proposed protocol is greater than that of the protocol which is conventionally used in experiments. Thus, by using the TCP, we can understand true cooling capacity of any magnetic material.

This work was done in collaboration with Shu Tanaka (Waseda University), Takahisa Ohno (NIMS), and Hideaki Kitazawa (NIMS).

## References

- [1] A. M. Tishin and Y. I. Spichkin: *The Magnetocaloric Effect and its Applications*



(Taylor & Francis, London, 2003).

- [2] S. Toyozumi, H. Kitazawa, Y. Kawamura, H. Mamiya, N. Terada, R. Tamura, A. Dönni, K. Morita, and A. Tamaki: J. Appl. Phys. **117** (2015) 17D101.
- [3] K. A. Gschneidner and V. K. Pecharsky: Annu. Rev. Mater. Sci. **30** (2000) 387.
- [4] R. Tamura, T. Ohno, and H. Kitazawa: Appl. Phys. Lett. **104** (2014) 052415.  
**[This topic was reported in Press Release in NIMS (March 10, 2014), MyNavi News (March 12, 2014), The Chemical Daily (March 19, 2014), The Science News (March 28, 2014).]**
- [5] R. Tamura, S. Tanaka, T. Ohno, and H. Kitazawa: J. Appl. Phys. **116** (2014) 053908.

# Heat Transfer Characteristics of Condensate Film Flow along Vertical Plates with Microscopic Grooves

Takahiro ADACHI

*Department of Mechanical Engineering, Akita University  
Tegata-Gakuen 1-1, Akita, Akita 010-8502*

The characteristics of thin, falling liquid films due to condensation along a vertical plate have been of interest to engineers, for example, in plate-type absorber, plate-type condenser and so on. In order to enhance the heat transfer, fluted parts along the streamwise direction have been established on the plate. This is because the liquid film spreads as thinly as possible over the plate surface since strong surface tension aids in the removal of film from the top to bottom of the fluted parts, thereby producing a very thin liquid film. This is called a drainage effect[1].

On the other hand, little research was done on the film flow along a plate with a grooved part setting perpendicular to the streamwise direction due to some mathematical difficulties. Therefore, our objective in this study is to clarify how the grooved part affects the flow patterns and heat transfer.

We consider a liquid film flow along a plate with a rectangular groove setting perpendicular to the stream-wise direction on its surface. Figure 1 shows a geometry of the problem and the coordinate system. The  $x$ -axis is taken to be parallel to the vertical direction and the  $y$ -axis to be perpendicular to it. Nondimensional parameters to characterize the plate configuration, height  $h$  of the groove, width of the groove  $w_b$ , inlet length  $w_i$  and outlet length  $w_o$  are, using  $\delta_0^*$  at the inlet as a characteristic length, defined as

$$h = \frac{h^*}{\delta_0^*}, \quad w_b = \frac{w_b^*}{\delta_0^*}, \quad w_i = \frac{w_i^*}{\delta_0^*}, \quad w_o = \frac{w_o^*}{\delta_0^*} \quad (1)$$

where we represent physical quantities with their dimensions by attaching a superscript  $*$  to them, and the total plate length is  $L =$

$w_i + w_b + w_o$ . The characteristic length  $\delta_0^*$  can be derived from Nusselt's film theory such as

$$\delta_0^* = \left( \frac{3\nu_l^* Q^*}{g^*} \right)^{1/3}, \quad (2)$$

where  $\nu_l^*$ ,  $g^*$  and  $Q^*$  are dynamic viscosity of the fluid, gravitational acceleration and flow rate, respectively.

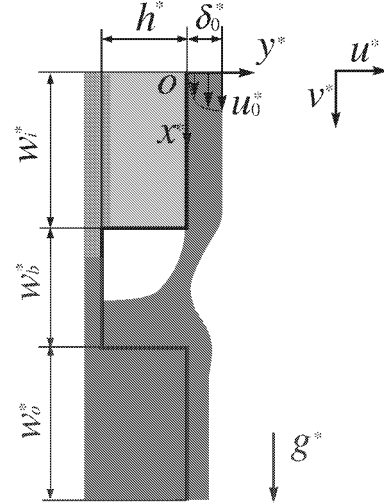


Fig.1 Geometry and coordinates.

We assume that the flow is two-dimensional because the film flow is thin and the depth in the spanwise direction of plate is large enough. Moreover, the fluid is assumed to be incompressible and the shear stress from the gas phase side can be negligible. Then we make non-dimensional the following quantities, by using characteristic length  $\delta_0^*$  and surface velocity at the reference point as  $u_0^* = \rho_l^* g^* \delta_0^{*2} / (2\mu_l^*)$  which is also derive from Nusselt's film theory, as

$$\mathbf{x} = \frac{\mathbf{x}^*}{\delta_0^*}, \quad \mathbf{u} = \frac{\mathbf{u}^*}{u_0^*}, \quad t = \frac{t^* u_0^*}{\delta_0^*}, \quad p = \frac{p^*}{\rho_l^* u_0^{*2}},$$

$$\rho = \frac{\rho^*}{\rho_l^*}, \quad \mu = \frac{\mu^*}{\mu_l^*}. \quad (3)$$

This time, we proceed our calculations not only for liquid phase but also for gas phase. Then, the governing equations for the velocities and pressure are written in non-dimensional forms as

$$\nabla \cdot \mathbf{u} = 0, \quad (4)$$

$$\rho \left\{ \frac{\partial \mathbf{u}}{\partial t} + (\mathbf{u} \cdot \nabla) \mathbf{u} \right\} = \rho Fr \mathbf{e}_x - \nabla p - \frac{Fr}{Bo} \kappa \nabla H + \frac{1}{Re} \nabla \left[ \mu \{ \nabla \cdot \mathbf{u} + (\nabla \cdot \mathbf{u})^T \} \right], \quad (5)$$

Nondimensional parameters in the equations are the Reynolds number, Flude number and Bond number respectively defined as

$$Re = \frac{u_0^* \delta_0^*}{\nu^*}, \quad Fr = \frac{\delta_0^* g^*}{u_0^{*2}}, \quad Bo = \frac{\delta_0^{*2} \rho^* g^*}{\sigma^*}. \quad (6)$$

First, we solve the governing equations Eq. (4) and (5) for velocity and pressure fields numerically by Highly Simplified Marker and Cell (HSMAC) method using staggered grid system. In addition to HSMAC method for the velocity and pressure fields, we have used a Coupled Level-Set and Volume Of Fluid (CLSVOF) method[2,3] to determine the free surface between gas and liquid phases, wehre we have been dealing with a new approach to impose surface tension effect and discontinuous changes of physical quantities between liquid and gas phases. Namely, Ghost Fluid Method(GFM)[4] are examined as well as CLSVOF Mmethod in our program.

Before, we used CSF(Continuum Surface Force) model proposed by Brackbill et al.[5] in order to express the surface tension effect.

In such model, a continuous Heaviside function was used. However in this study, we have used a discontinuous Heaviside function in the Ghost Fluid method defined as

$$H(\phi) = 1, \quad \text{if } \phi \geq 0, \\ = 0, \quad \text{if } \phi \leq 0. \quad (7)$$

Therefore, we can express the discontinuous changes of density and viscosity between the liquid and gas phased as

$$\rho = \frac{\rho_g^*}{\rho_l^*} (1 - H(\phi)) + H(\phi), \quad (8)$$

$$\mu = \frac{\mu_g^*}{\mu_l^*} (1 - H(\phi)) + H(\phi). \quad (9)$$

This leads to the more realistic calculation results in our study.

However, the treatment of condensation is very difficult. In addition, iteration process in HSMAC spends much time of about 80% to total time in our code. So we are now trying to parallelize the part by using MPI.

## References

- [1] R. Gregorig, Z. Angew. Math. Phys., Vol. 5, (1954) 36.
- [2] M. Sussman, E. G. Puckett. J. Comput. Phys., Vol. 162, (2000) 301.
- [3] G. Son, and N. Hur. Numer. Heat Transf., Part B, Vol. 42, (2002) 523.
- [4] G. Son, and V. K. Dhir. Numer. Heat Transf., PArt B, Vol. 52, (2007) 153.
- [5] U. J. Brackbill, D. B. Kothe, and C. Zemach. J. Comput. Phys., Vol. 100, (1992) 335.

# Numerical study of Nonequilibrium Many-body physics

Takashi OKA

*Department of Applied Physics,*

*The University of Tokyo, Bunkyo-ku, Tokyo 113-8656*

Recently, nonequilibrium properties of many-body systems are being intensively studied. The long term goal of this project is to develop an efficient numerical method which we can use to study strongly correlated electron systems far away from equilibrium.

We have tried and extended an approach, which was studied in the high-energy community namely the stochastic quantization and tested it in a simple model of scalar boson [1]. This method is based on a quantization of fields using the complex Langevin dynamics, and we calculate the propagator and make a comparison with analytical results. This is a first step toward general applications, and we focus only on the vacuum properties of the theory. While we can control stability of the numerical simulation for any coupling strength, our results turn out to flow into an unphysical

fixed-point, which is qualitatively understood from the corresponding Fokker-Planck equation. We propose a simple truncation scheme, "restricted phase-space approximation," to avoid the unphysical fixed-point. With this method, we obtain stable results at reasonably good accuracy. Finally we give a short discussion on the closed-time path formalism and demonstrate the direct computation of the vacuum expectation value not with the  $i$ -epsilon prescription but from an explicit construction of the Feynman kernel.

## References

- [1] Ryoji Anzaki, Kenji Fukushima, Yoshimasa Hidaka, Takashi Oka, *Annals of Phys.* 353, 107-208(2015).

# Successive phase transitions and magnetic orders in rare-earth metals

Takafumi SUZUKI

*Department of Engineering, University of Hyogo  
Shosha, Himeji, Hyogo 670-2280*

In this project, we studied successive phase transitions and magnetic orders in rare-earth metals and the thermal criticality of generalized SU(N) Heisenberg models on two-dimensional lattices. In this report, we introduce the later result.

In this decay, one of the most discussed topics is the possibility of deconfined critical phenomena (DCP) [1, 2] in quantum spin systems. The DCP are expected to be observed at a quantum phase transition (QPT) between the valence-bond-solid (VBS) phase and the magnetic ordered phase in two dimension (2D). The most famous model family in which such phase transition takes place is the SU(N)  $JQ_m$  model on 2D lattices [3]. We discussed the quantum criticality of the  $JQ_2$  model on the square lattice and the  $JQ_3$  model on the honeycomb lattice in the SU(3) and SU(4) cases [4]. In this project, we studied the criticality of thermal transition to the VBS phases [5].

The Hamiltonians for the SU(N)  $JQ_2$  model on the square lattice and  $JQ_3$  model on the honeycomb lattice are expressed by singlet projection operator  $P_{ij}$ . The singlet projection operator is defined as  $P_{ij} = -\frac{1}{N} \sum_{\alpha=1}^N \sum_{\beta=1}^N S_i^{\alpha\beta} \bar{S}_j^{\beta\alpha}$ , where  $S_i^{\alpha\beta}$  is the generators of the SU(N) algebra and  $\bar{S}_j^{\beta\alpha}$  is the conjugate operator. This singlet projection operator can give a simplified form for the Hamiltonian. The Hamiltonian can be written as

$$\mathcal{H} = -J \sum_{(ij)} P_{ij} - Q_2 \sum_{(ij)(kl)} P_{ij} P_{kl}, \quad (1)$$

in the square lattice case and

$$\mathcal{H} = -J \sum_{(ij)} P_{ij} - Q_3 \sum_{(ij)(kl)(mn)} P_{ij} P_{kl} P_{mn}, \quad (2)$$

in the honeycomb lattice case.  $(ij)$  is the nearest-neighbor sites and the summation for the  $Q_m$  terms runs over all pairs without breaking the rotational symmetry of lattice.

For the Hamiltonian (1) and (2), we performed the QMC computations up to  $L=192$  for the square lattice case and  $L=96$  for the honeycomb lattice case, changing the coupling ratio  $\lambda$  with the fixed energy scale,  $J+Q_m=1$ . The computations were executed by using the massively parallelized Loop algorithm code [6] provided in ALPS project [7]. To discuss the thermal transition to the VBS phase, we introduced the complex-VBS magnetization defined as  $\Psi_r \equiv \sum_{\mu=1}^z \exp[\frac{2\pi i}{z} \mu] \hat{P}_{r,r_\mu}$ , where  $\hat{P}_{r,r_\mu}$  is the diagonal component of projection operator,  $z$  is the coordination number of a lattice, and  $r_\mu$  represents the neighboring site of  $r$  along the  $\mu$  direction, respectively.

As the coupling ratio  $J/Q_m$  increases, the ground state of the above models changes from the VBS state to the Néel state. Here we introduce the coupling ratio defined as  $\lambda = J/(J+Q_m)$ . The values of the QPT points between the Néel phase and the VBS phase were already evaluated in ref. [4], and summarized as  $(N, \lambda_c) = (3, 0.665)$  and  $(N, \lambda_c) = (4, 0.918)$  for the square lattice case, and  $(N, \lambda_c) = (3, 0.797)$  and  $(N, \lambda_c) = (4, 0.985)$  for the honeycomb lattice case.

In figure 1, we show the  $\lambda$  dependence of

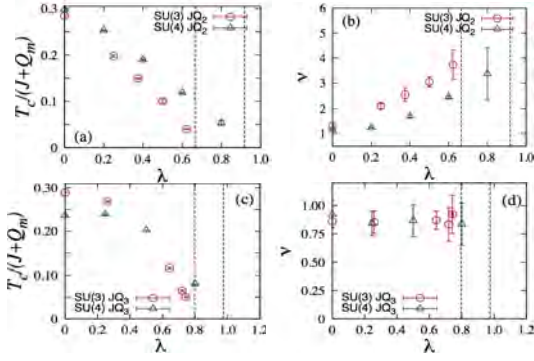


Figure 1:  $\lambda$  dependence of  $T_c$  and  $\nu$ . Vertical dotted lines corresponds to the quantum critical point between the Nèel phase and the VBS phase.

the critical temperature  $T_c$  and critical exponent  $\nu$ . The results were obtained by performing the Bayesian finite-scaling analysis [8] for the Binder ratio, creation length, and static structure factor of the VBS magnetization. In the honeycomb lattice case, the value of  $\nu$  stays at  $\nu \sim 5/6$  independently of  $\lambda$ . The VBS pattern of the honeycomb lattice case is characterized by the  $\pi/3$ -rotational symmetry breaking. Therefore, the universality class is the same as that of the 2D three-state Potts model as expected. In contrast to the honeycomb lattice case,  $\nu$  in the square lattice case monotonically increases in the square lattice case. In the square lattice case, the VBS pattern can be characterized by the  $\pi/4$ -rotational symmetry breaking. Thus it is expected that the universality class is the same as that of the 2D XY+ $Z_4$  model. In order to check the universality class, we evaluated the ratio  $B_R \equiv \langle \Psi^4 \rangle / \langle \Psi^2 \rangle^2$ . In figure 2, we show  $B_R(L/\xi)$  for the SU(N)  $JQ_2$  model and the 2D XY+ $Z_4$  model. The results for the 2D XY+ $Z_4$  model were obtained from the Monte Carlo calculations for  $\mathcal{H} = J \sum_{\langle ij \rangle} \cos(\theta_i - \theta_j) - h_4 \sum_i \theta_i$ . We find that  $B_R(L/\xi)$  shows the quite small system-size dependence while  $B_R(L/\xi)$  depends on  $\lambda$  and  $\alpha = h_4/(J + h_4)$ . The important point is that the trend of  $B_R(L/\xi)$  is same in both quantum

and classical models; the behavior of  $B_R(L/\xi)$  closes to that of the 2D Ising model, when  $\lambda \rightarrow 0$  and  $\alpha \rightarrow 1$ . This is reasonable because the  $Q$  term favors the columnar dimer configuration along the  $x$  or  $y$ -axis. In the classical model case, the similar behavior is also observed when  $\alpha \rightarrow 1$ , where the system can be expressed by the double Ising model exactly. Consequently we concluded that the universality class of the SU(N)  $JQ_2$  model possesses the same feature of the classical XY +  $Z_4$  model and this is independent of SU(N) spins.

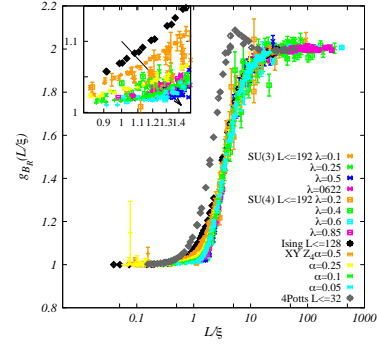


Figure 2:  $B_R(L/\xi)$  for the quantum  $JQ_2$  model and the related classical models. When  $h_4$  decreases or the system closes to the quantum critical point,  $B_R$  gradually moves as the arrow.

## References

- [1] T. Senthil, et al., Phys. Rev. B **70**, 144407 (2004).
- [2] T. Senthil, et al., Science **303**, 1490 (2004).
- [3] A. Sandvik, Phys. Rev. Lett. **98**, 227202 (2007).
- [4] K. Harada, et al., Phys. Rev. B **88**, 220408(R) (2013).
- [5] T. Suzuki, et al., Phys. Rev. B **91**, 094414 (2015); J. Phys.: Conf. Ser. **592**, 012114 (2015).
- [6] S. Todo, H. Matsuo, and H. Shitara, unpublished.
- [7] B. Bauer, et al., J. Stat. Mech. P05001 (2011).
- [8] K. Harada, Phys. Rev. E **84**, 056704 (2011).

# Dynamical properties of effective models for $\text{Na}_2\text{IrO}_3$

Takafumi SUZUKI

*Department of engineering,*

*University of Hyogo, Shosha, Himeji, Hyogo 670-2280*

In this project, we studied dynamical properties of effective models for  $\text{Na}_2\text{IrO}_3$ . Recently, this compound has been much attracted because it is expected that a strong spin orbit coupling causes interesting magnetic properties; the Kitaev-type anisotropic interactions [1] among  $\text{Ir}^{4+}$  ions in addition to the conventional Heisenberg interactions exist owing to the edge-sharing structure of  $\text{IrO}_6$  octahedrons [2]. Thus the effective model of  $\text{Na}_2\text{IrO}_3$  can be described by the Kitaev-Heisenberg (KH) model on the honeycomb lattice, where the spin-liquid ground state may be realized. Experimentally, it was observed that this compound exhibits the magnetic phase transition at a finite temperature and a zigzag order is stabilized in the lower temperature region. However, the zigzag order does not exist in the ground state phase diagram of the simplest KH model, where the only nearest neighbor interaction is considered. To explain the origin of zigzag order, the coupling parameters were estimated in pioneering works [3-7] and discussed the key interactions. Several parameter sets were proposed via ab-initio calculations or spin-wave analysis, but there are quite large discrepancy each other.

From the above background, we calculated dynamical structure factors (DSFs) for proposed effective models by using numerical diagonalization method up to the system size  $N=32$ . To accelerate computations, we prepared parallelization code for the Lanczos method. In figure 1, we show the DSFs for the parameter set in ref. [6]. In order to discuss the low-energy excitation, we also performed spin-wave analysis and compared them with the DSF results. From obtained results, properties of the low-energy excitations were discussed and

compared with the INS results for powder samples [3]. We found that the model proposed in references [3] and [6] are almost consistent with experimental observations.

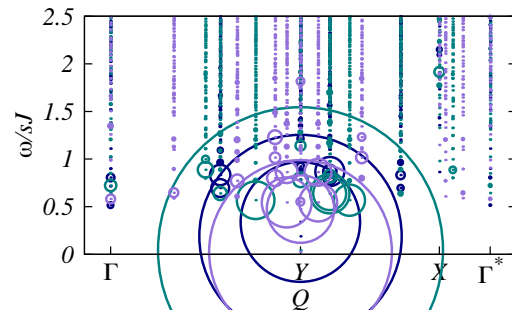


Figure1: Dynamical structure factors for  $N=24$  with different lattice geometry [8]. The result was obtained by using the parameter set in Ref. [6].

## References

- [1] A. Kitaev, Ann. Phys. **321**, 2-111 (2006).
- [2] G. Jackeli and G. Khaliullin, Phys. Rev. Lett. **102**, 017205 (2009).
- [3] S. K. Choi, et al., Phys. Rev. Lett. **108**, 127204 (2012).
- [4] J. Chaoupka, G. Jackeli, and G. Khaliullin, Phys. Rev. Lett. **110**, 097204 (2013).
- [5] Y. Singh, et al., Phys. Rev. Lett. **108**, 127203 (2012).
- [6] Y. Yamaji, et al., Phys. Rev. Lett. **113**, 107201 (2014).
- [7] Y. Sizyuk, et al., Phys. Rev. B **90**, 155126 (2014).
- [8] T. Yamada, T. Suzuki, and S. Suga, in preparation.

## Efficient sampling simulation of the soft modes significantly contribute to protein properties

Akio KITAO

*Institute of Molecular and Cellular Biosciences, University of Tokyo*

Transient receptor potential channel subfamily V member 4 (TRPV4) is a relatively non-selective cation channel. The channel is activated by various stimuli such as moderate heat, cell swelling, shear stress, and chemical ligands. TRPV4 is suggested to play a key role in the central nervous system, nociception and bone formation [1]. Mutations in TRPV4 cause neuropathies and skeletal dysplasias such as Charcot-Marie-Tooth disease type 2C [1, 2].

The X-ray crystallographic structure of the ankyrin repeat domain (ARD) of TRPV4 with inositol-1,4,5-trisphosphate (IP3) shows that ARD interacts with the phosphatidylinositol-4,5-bisphosphate (PI(4,5)P<sub>2</sub>) lipid membrane through the IP3 head groups of the PI(4,5)P<sub>2</sub> lipid [3]. Our docking studies support the binding site found in the crystal structure. We generated two models of ARD which interacts with the PI(4,5)P<sub>2</sub> lipid membrane. One model is based on the first ranked structure of our docking study (Fig.1a) that is close to the X-ray crystallographic structure. The other is the second ranked structure from the docking in which the interaction surface is different from that in the first ranked model (Fig.1b). We conducted 100-ns molecular dynamics (MD) simulations of both ARD models. MD simulation results showed that both ARD models were stably bound to the membrane, which supports the interaction of ARD with the PI(4,5)P<sub>2</sub> lipid membrane. It also may

suggest that ARD has multiple PI(4,5)P<sub>2</sub> binding sites of which one is found by the X-ray crystallographic study [3].

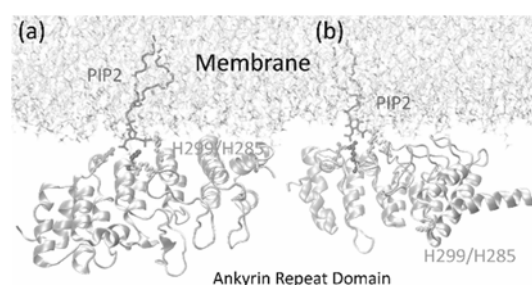


Fig.1 Models of ARD interacted with PI(4,5)P<sub>2</sub> lipid based on (a) X-ray crystallography (b) Second ranked structure obtained from docking study.

PI(4,5)P<sub>2</sub> is known to regulate the activity of TRPV4. Our investigation suggest that the interaction of ARD with PI(4,5)P<sub>2</sub> may control the activity of TRPV4. However, from recent studies of the entire TRPV1, ARDs of TRPV1 appear too distant from the membrane to interact with PI(4,5)P<sub>2</sub> in the membrane (Fig.2).

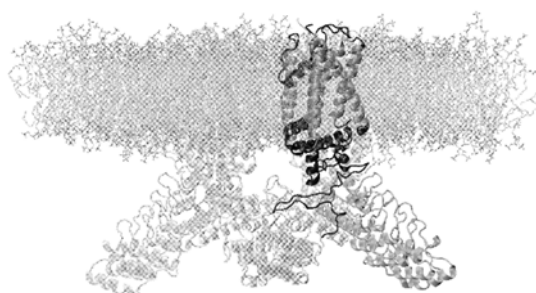


Fig.2 Model of TRPV1 tetramer in the membrane.



To elucidate how ARD interacts with PIP(4,5)P<sub>2</sub>, we conducted MD simulations of the TRPV1 tetramer in the membrane (Fig.2). We observed large flexible motions in one of the TRPV1 monomers in tetramer. The center of mass distance along bilayer normal ( $D_z$ , Fig.3) decreased by more than 10 Å and the angle defined using transmembrane (TM) domain, linker, and ARD decreased by 20 degrees.

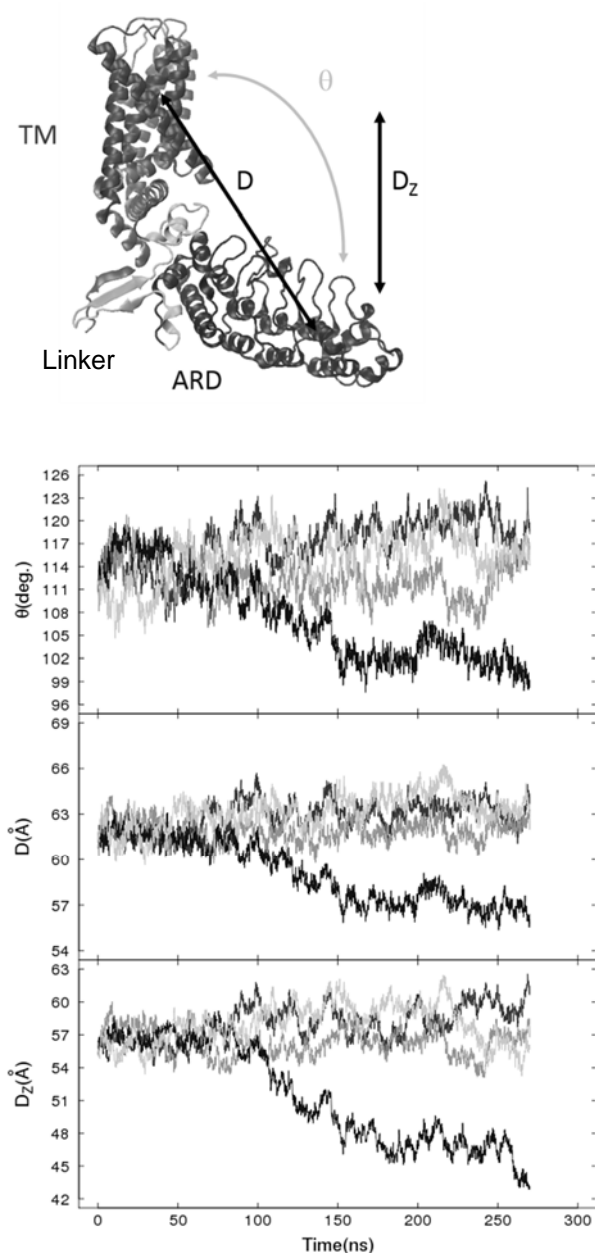


Fig.3 Definition and time evolution of the geometries of TRPV1.

The large flexible motions observed enhance the interaction with PIP(4,5)P<sub>2</sub>. We observed a snapshot in which 11 amino acids of ARD are in contact with PIP(4,5)P<sub>2</sub>. These amino acids are mainly positively charged residues (LYS or ARG) thus the motion above is most probably driven by electrostatic interactions. From the observations above we concluded that TRPV1 is flexible enough so that ARD can interact with PIP(4,5)P<sub>2</sub> in the membrane. These finding about TRPV1 support the suggested TRPV4 activity regulatory mechanism.

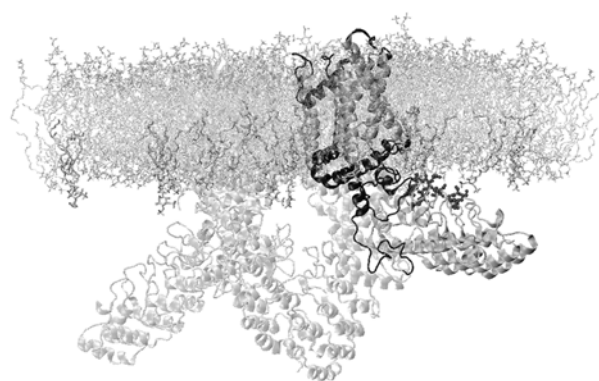


Fig.4 Snapshot of TRPV1 tetramer with the membrane.

## References

- [1] B. Nilius and T. Voets, EMBO Rep. **14**, 152 (2013).
- [2] W. Everaerts, B. Nilius, and G. Owisianik, Prog. Biophys. Mol. Biol. **103**, 2 (2010).
- [3] Nobuaki Takahashi et. al, Nat. Commun, **5**, 4994 (2014).
- [4] M. Liao, E. Cao, D. Julius, and Y. Cheng, Nature **504**, 107 (2013).
- [5] E. Cao, M. Liao, Y. Cheng, and D. Julius, Nature **504**, 113 (2013).

# Phase diagram and critical properties of disordered topological insulators

TOMI OHTSUKI<sup>1</sup>  
TOHRU KAWARABAYASHI<sup>2</sup>  
KEITH SLEVIN<sup>3</sup>  
KOJI KOBAYASHI<sup>1</sup>

1) Dept. Phys., Sophia University, Chiyoda-ku, Tokyo 102-8554, Japan

2) Dept. Phys., Toho University, Miyama 2-2-1, Funabashi 274-8510, Japan

3) Dept. Phys., Osaka University, Toyonaka, Osaka 560-0043, Japan

Recent discoveries of two-dimensional quantum spin Hall states and three-dimensional topological insulators (TIs) have inspired extensive research for these novel materials. In the impurity free systems where the translational invariance exists, the topological insulator is characterized by the non-zero topological numbers, which are defined via integral over Brillouin zone. This definition is no longer valid once the translational invariance is broken due to disorder. In this case, we usually use edge/surface states to characterize TIs.

Here we study the bulk properties of the disordered three-dimensional topological insulators numerically, and show how to distinguish TI from ordinary insulators by investigating the transport properties of bulk states. We first calculate bulk conductance via transfer matrix method, from which we draw the phase diagram for disordered TI [1]. Along the phase boundary between different TI phases, we show that the Dirac semimetal emerges even in the presence of disorder. With increase of disorder, the Dirac semimetal undergoes semimetal to metal transition. We propose that the density of states exhibits novel single parameter scaling behavior near the Dirac semimetal to metal transition. Scaling relations of vanishing density of states, diverging diffusion constant, vanishing conductivity as well as vanishing Dirac electron velocity are derived [2]. The multifractal behavior of wave function at the transition is verified numerically for  $60 \times 60 \times 60$  sites system

via MKL/feast, which is included in intel fortran MLK for sparse matrix diagonalization [3]. The effect of surface disorder is also discussed [4]. Additionally, we have developed a general framework for the massive and tilted Dirac electrons in two dimensions in which the robustness of the split  $n=0$  Landau levels is discussed [5].

## References

1. K. Kobayashi, T. Ohtsuki, K.-I. Imura: PRL **110**, 236803 (2013)
2. K. Kobayashi, T. Ohtsuki, K.-I. Imura, I. Herbut: PRL **112**, 016402 (2014)
3. T. Ohtsuki *et al.*: APS March meeting, 2015, Bulletin of the American Physical Society 60
4. V. Sacksteder, T. Ohtsuki, K. Kobayashi: arXiv:1410.7621
5. Y. Hatsugai, T. Kawarabayashi, and H. Aoki,

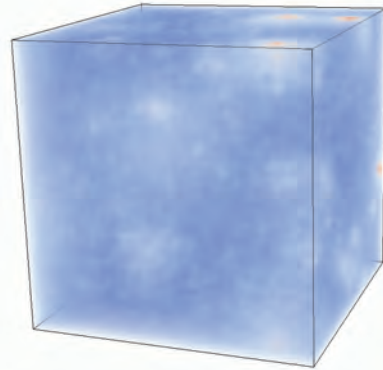


Figure 1: Multifractal wave function at the semimetal to metal transition.

# Numerical study on low-energy states of quantum spin systems

Hiroki NAKANO

*Graduate School of Material Science, University of Hyogo  
3-2-1 Kouto, Kamigori-cho, Ako-gun, Hyogo 678-1297, Japan*

Numerical approaches in condensed matter physics become more important because it is often difficult to estimate precisely physical quantities in systems of many-body problems. Computational studies, particularly, have contributed much to our deeper understanding of various quantum spin systems. Among such systems, however, are still difficult ones to be studied when the systems in spatial dimensions larger than one include frustrations. The reason for this difficulty is that such systems cannot be treated by the quantum Monte Carlo simulations and the density matrix renormalization group (DMRG) calculations. The numerical diagonalization method based on the Lanczos algorithm is an almost unique way as a valid method for such frustrated quantum spin systems in dimensions larger than one. However, this method has a weak point that only very small system sizes can be treated. Then, we successfully developed a hybrid-type parallelized code of Lanczos diagonalization to overcome this disadvantage[1]. We investigate several quantum spin systems using this Lanczos-diagonalization code we developed as a primary approach. We also employ other numerical methods as supplementary ones. Some quantum spin systems are examined from various points of view.

The primary study of this year in the present project examines the magnetization jumps in the magnetization processes in some  $S = 1/2$  Heisenberg antiferromagnets on various lattices. This phenomenon was originally observed in the case of the square-kagome lattice[2]. This phenomenon arises from the abrupt changes in spin directions between the states of  $m = 1/3$  and  $m > 1/3$ , where  $m$

is defined as the magnetization normalized by the saturation. We find additionally that the same behaviors is observed in the Heisenberg antiferromagnets on the Cairo-pentagon-lattice[3, 4], the  $\sqrt{3} \times \sqrt{3}$ -distorted kagome lattice[5, 6], and the *Shurien*-bonded honeycomb lattice[5]. The changes in spin directions are shared with the spin flop phenomenon observed in spin-anisotropic systems; it is remarkable that the changes appear even in the present systems are isotropic in spin space.

Properties of other frustrated Heisenberg antiferromagnet were studied by numerical-diagonalization method [7, 8, 9, 10]. Particularly, Ref. 8 clarifies the phase transition point has been estimated precisely between the gapless and the gapped phases in the three-leg spin nanotube. Our studies of quantum spin systems by several numerical approaches including parallelized calculations of Lanczos diagonalization contribute to our understandings of these systems.

## References

- [1] H. Nakano and A. Terai: J. Phys. Soc. Jpn. **78** (2009) 014003.
- [2] H. Nakano and T. Sakai: J. Phys. Soc. Jpn. **82** (2013) 083709.
- [3] H. Nakano, M. Isoda, and T. Sakai: J. Phys. Soc. Jpn. **83** (2014) 053702.
- [4] M. Isoda, H. Nakano, and T. Sakai: J. Phys. Soc. Jpn. **83** (2014) 084710.
- [5] H. Nakano, Y. Hasegawa, and T. Sakai: J. Phys. Soc. Jpn. **83** (2014) 084709.

- [6] H. Nakano and T. Sakai: J. Phys. Soc. Jpn. **83** (2014) 104710.
- [7] H. Nakano and T. Sakai: JPS Conf. Proc. **3** (2014) 014003.
- [8] T. Sakai, H. Nakano, and K. Okunishi: J. Low. Phys. **568** (2014) 042024.
- [9] T. Sakai and H. Nakano: J. Low. Phys. **568** (2014) 042025.
- [10] H. Nakano and T. Sakai: Jpn. J. App. Phys. **54** (2015) 00305.

# Quantum Monte Carlo Study of the Four-Point Correlation of Hardcore Bosons

Akiko MASAKI-KATO

*Institute for Solid State Physics,*

*The University of Tokyo, Kashiwa-no-ha, Kashiwa, Chiba 277-8581*

The time of flight imaging method in experiments of cold atoms is used to observe the momentum distribution of the atoms. Recently, the remarkable technique of observing the noise correlation, which is observed as the density-density correlation of the expanding atoms, is introduced in experiments of cold atoms [1]. Theoretically it is defined as the Fourier transformation of four-point correlation as following;

$$\Delta_{kk'} = \bar{n}_{kk'} - \bar{n}_k \bar{n}_{k'}, \quad (1)$$

$$\bar{n}_{kk'} = \sum_{ijklm} e^{i\{\mathbf{R}_{ij}k + \mathbf{R}_{lm}k'\}} \langle b_i^\dagger b_j b_l^\dagger b_m \rangle, \quad (2)$$

$$\bar{n}_k = \sum_{ij} e^{i(\mathbf{R}_i - \mathbf{R}_j)k} \langle b_i^\dagger b_j \rangle,$$

where  $b_i$  ( $b_i^\dagger$ ) is the annihilation (creation) operator at site  $i$ .  $\mathbf{R}_{ij}$  is distance between the sites  $i$  and  $j$ . Especially in Mott phase, the noise correlation is useful to study its physical properties rather than the time flight image.

In previous study, we proposed a nontrivial parallelization algorithm with nonlocal-update for the quantum Monte Carlo (QMC) algorithm, in particular the worldline algorithm based on Feynman's path-integral, by introducing many discontinuities of worldlines, called "worms"

[2]. In this study, we developed methods of calculating the physical quantities, e.g. winding number, transverse magnetization and arbitrary multi-point correlation function, especially the noise correlation (1), in the off-diagonal configuration space of our algorithm. For the benchmark calculation, we demonstrate the quartic scaling law of the correlation (2) at zero-momentum,  $\bar{n}_{00}$ , in the deep superfluid phase in two-dimension. Moreover we have prepared to open our source code using Github,

<https://github.com/qmc/dsqss/wiki>.

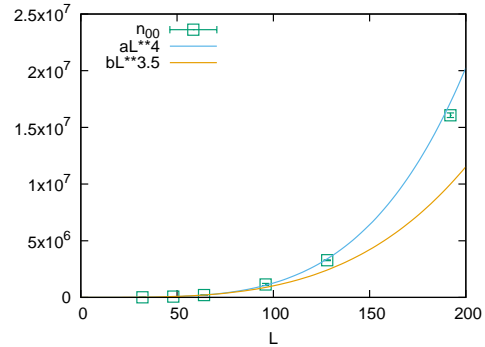


Fig. 1: the four-point correlation (2) at zero-momentum.

## References

- [1] S. Fölling et al., Nature, 434, 481 (2005).
- [2] A. Masaki-Kato et al., Phys. Rev. Lett., **112**, 140603 (2014).

# Magnetization Plateaux in a Frustrated Two-Leg Spin Ladder

Takami TOHYAMA

*Department of Applied Physics, Tokyo University of Science, Tokyo 125-8585*

A copper oxide compound  $\text{BiCu}_2\text{PO}_6$  (BCPO) contains a frustrated two-leg spin-1/2 ladder coming from  $\text{Cu}^{2+}$  ions. Both one dimensionality and frustration in the compound suppress magnetic long-ranged order. Experimental study on the magnetization process in BCPO has discovered sequential phase transitions induced by magnetic field without structural change. These transitions should be understood by the effective spin model of  $\text{BiCu}_2\text{PO}_6$ . Therefore, it is important to study a model of frustrated two-leg spin-1/2 ladder and clarify the effect of magnetic field on spin states.

We consider a model of frustrated two-leg spin-1/2 ladder characterized by a nearest-neighbor and next nearest-neighbor antiferromagnetic coupling,  $J_1$  and  $J_2$ , respectively, and a nearest-neighbor antiferromagnetic coupling on a rung bond  $J_\perp$ . In the limit of weak rung-coupling,  $J_\perp \ll J_1$ , this model approaches two frustrated spin chains, while a non-frustrated spin ladder is obtained in another limit of weak frustration,  $J_2 \ll J_1$ . Consequently this model bridges between frustrated spin chain and non-frustrated spin ladder through the change of  $J_\perp$  and  $J_2$ . In our previous publication, the effect of frustration on magnetic excitations in the model has been examined by using dynamical density-matrix renormalization group

(DMRG) method [1].

We calculate the magnetization curves in both the weak and the strong rung-coupling limits by using DMRG with an open boundary condition. The convergence of energy is achieved with truncation number  $m \leq 500$  for a 72-rung system [2]. With strong rung coupling, three magnetization plateaux are found at  $1/3$ ,  $1/2$ , and  $2/3$  due to frustration. These can be understood in terms of the concept of quasi-spinon reconstructed from the singlet and the triplets of spins on a rung. The plateau at  $1/2$  corresponds to the valence bond solid of the quasi-spinons, while the plateaux at  $1/3$  and  $2/3$  can be associated with the array of quasi spinons similar to soliton lattice. This is different from a usual Bose-Einstein-condensation picture of triplons. Our results will be useful to understand the magnetization process in BCPO.

## 参考文献

- [1] T. Sugimoto, M. Mori, T. Tohyama, and S. Maekawa: Phys. Rev. B **87** 155143 (2013).
- [2] T. Sugimoto, M. Mori, T. Tohyama, and S. Maekawa: to be submitted.

# Study of quantum correlations and topological order in quantum spin systems

Syngé Todo

*Department of Physics, University of Tokyo, Tokyo 113-0033, Japan*

Quantum phase transitions are phase transitions between two different ground states that are triggered by quantum fluctuations at absolute zero temperature. We develop various novel and powerful techniques to tackle various exotic quantum critical phenomena observed in quantum spin systems and performed large-scale and high-precision simulations on the ISSP supercomputer system.

## QMC measurement of local $Z_N$ Berry phase

We developed a loop cluster algorithm quantum Monte Carlo (QMC) method for calculating the local  $Z_N$  Berry phase of the quantum spin models. The Berry connection, which is given as the inner product of two ground states with different local twist angles, is expressed as a MC average on the worldlines with fixed spin configurations at the imaginary-time boundaries. We extend the technique to  $SU(N)$  spin models, where  $N$  topologically different phases can be distinguished successfully by the local  $Z_N$  Berry phase.

## QMC level spectroscopy

We have formulated a convergent sequence for the energy gap estimation in the worldline QMC method. Our estimation will be unbiased in the low-temperature limit and also the error bar is correctly estimated in general. The level spectroscopy from QMC data is developed as an application of the unbiased gap estimation. From the spectral analysis, we precisely determine the Kosterlitz-Thouless quantum phase-transition point of the spin-Peierls model.

## QMC simulation with dynamic control of anisotropy

In systems with strong spatial anisotropy, it is often difficult to carry out the conventional finite-size-scaling analysis due to large corrections to scaling. To overcome this difficulty, we develop a stochastic approximation algorithm where the aspect ratio of the system is optimized dynamically during the MC update so that the isotropy is recovered virtually. We extend out the scheme to the quantum critical point of the Bose-Hubbard model with the dynamical exponent  $z > 1$ .

## Critical phenomena of long-range interacting spin model

By using the order- $N$  cluster MC algorithm, we studied the critical exponents and critical amplitudes of the long-range interacting ( $J \sim r^{-\sigma}$ ) Ising model with on the square lattice. Especially, we have introduced a generic method to remove the leading correction term in the Binder cumulant, and precisely determined the critical amplitude, by which we successfully established the non-trivial dependence of the critical exponents on the exponent of interaction  $\sigma$ .

The programs used in the present research projects have been developed based on the open-source libraries: ALPS [1], ALPS/looper [2], BCL [3], worms [4], etc.

## References

- [1] <http://alps.comp-phys.org/>.
- [2] <http://wistaria.comp-phys.org/alps-looper/>.
- [3] <http://github.com/cmsi/bcl>.
- [4] <http://github.com/wistaria/worms>.

# Improvement of dynamical scaling by the use of kernel method and its applications to nonequilibrium relaxation analyses

Y. Ozeki and Y. Echinaka

*Graduate School of Informatics and Engineering, The University of Electro-Communications*

We investigate an improvement of dynamical scaling analysis in the nonequilibrium relaxation (NER) method [1] for the Kosterlitz-Thouless (KT) transition by the use of the Bayesian inference and the kernel method. We have already applied the method proposed for the finite size scaling analysis in second order transition cases [2,3]. In the present study, we will modify the improved dynamical scaling by considering corrections to scaling, and obtain more accurate estimations of the transition temperature and so on.

In the NER analysis of KT transition, it has been a efficient tool due to the finite-time scaling,

$$m(t, T) = t^{-\lambda} \Psi(t/\tau), \quad (1)$$

where  $m(t, T)$  is the relaxation of magnetization from the all aligned state.  $\tau(T)$  is the relaxation time, which is expected to diverge as

$$\tau(T) \sim \exp(c/\sqrt{T - T_{KT}}) \quad (2)$$

in  $T > T_{KT}$ . To estimate  $T_{KT}$ , one may calculate  $m(t, T)$  for several values of  $T$ , and fit the data to the above formula. Since the equilibration step is not necessary and the treatment is systematic irrespective of the detail of interactions, it has been used successfully to study various problems including frustrated and/or random systems. [1] In the improved method, one can fit data on a scaling function without using any parametric model function. The result does not depend on the way of scaling, and is much reliable and reproducible.

Recently, the corrections to scaling are included to the kernel method in the static case. [4] We apply this idea to the dynamical scaling analysis of NER data. The scaling form

$$m(t, T) = t^{-\lambda} \Psi(t/\tau, t^{-c}),$$

is applied instead of eq.(1). Here we demonstrate the method for the 2D Ising model in which usual second order transition take place instead of the KT transition, since the exact transition tempera-

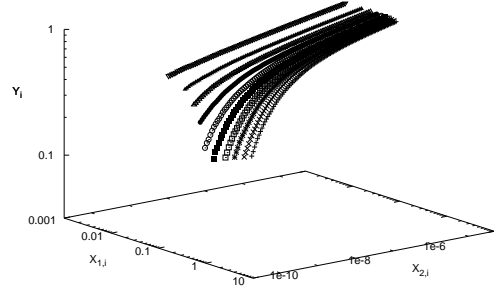


Figure 1: Scaling plot. Each axis is denoted by  $X_{1,i} \equiv t_i/\tau_i$ ,  $X_{2,i} \equiv t_i^{-c}$ , and  $Y_i = t_i^\lambda m(t_i, T_i)$ .

ture can be compared with that estimated numerically. In this case, the form

$$\tau(T) \sim |T - T_c|^{-z\nu}$$

is used for the relaxation time instead of eq.(2).

Calculations are carried out on the square lattice with  $1501 \times 1500$  up to 10000 MCS for 1024 samples in the temperature  $2.27 \leq T \leq 2.279$ . The resulting scaled data are plotted in Fig.1. with axes In the case without corrections, we have a estimation  $T_c = 2.2692301$ , while, in the present study, we obtained  $T_c = 2.2691851$ , which shows more accurate by comparing the exact value  $T_c = 2.2691853 \dots$ . Further investigations would be necessary to confirm the validity and efficiency of the method.

## References

- [1] Y. Ozeki, K. Ogawa and N. Ito, Phys. Rev. E **67** 026702 (2003), Y. Ozeki and N. Ito, J. Phys. A: Math. Theor. **40** R149 (2007);
- [2] K. Harada, Phys. Rev. E **84** 056704 (2011).
- [3] Y. Ozeki and Y. Echinaka, Activity Report 2012 (Supercomputer Center, ISSP, 2013)
- [4] K. Harada, cond-mat, stat-mech, arxiv: 1410.3622 (2014)



# Kinetic term of Ostwald ripening in bubble nucleation

Hiroshi Watanabe

*Institute for Solid State Physics, University of Tokyo  
Kashiwa-no-ha, Kashiwa, Chiba 277-8581*

If there are bubbles in liquid, larger bubbles grow at the expense of the smaller ones. This behavior is called Ostwald ripening. The time evolution of the distribution function of bubbles  $f(v, t)$ , describing a number of bubbles having volume  $v$  at time  $t$ , is given by

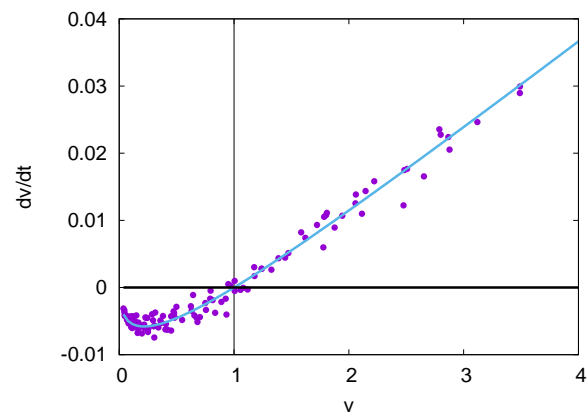
$$\frac{\partial f}{\partial t} = -\frac{\partial}{\partial v}(\dot{v}f), \quad (1)$$

where  $\dot{v}(v, t)$ , often called the kinetic term, denotes volume changes of bubbles. In the Ostwald ripening, there exists the critical volume  $v_c(t)$ . Bubbles larger than the critical size grow while bubbles smaller than it shrink, *i.e.*,  $\dot{v}(v, t) > 0$  when  $v > v_c(t)$  and  $\dot{v}(v, t) < 0$  when  $v < v_c(t)$ . While the dynamics of Ostwald ripening is governed by the kinetic term, it was quite difficult to observe explicit function form of the kinetic term. In order to observe the volume-dependence of the kinetic term directly, we performed huge-scale molecular dynamics simulations involving 680 million Lennard-Jones atoms [1]. The system was first maintained in liquid and the pressure decreased suddenly. Then many bubbles appeared and Ostwald ripening behavior followed. By following the volume of bubbles, we observed the kinetic term for the first time. We calculate the volume change ratio of bubbles in the following manner. First, we identify the same bubble between successive frames. We define that the two bubbles in different frames are the same one when the two spatially overlapped. Then we can observe the time evolution of volume of each bubble. At low temper-

ature, the kinetic term should have the form

$$\dot{v} \propto v^{1/3} \left[ \left( \frac{v}{v_c} \right)^{1/3} - 1 \right], \quad (2)$$

according to the classical theory. We confirmed that the function form of the kinetic term was well described by the theory. By fitting Eq. 2, we obtained the volume of the critical bubble precisely. We also confirmed that the time evolution of the critical volume obeys the classical theory. This is the first observation of the kinetic term in multiple-bubble nucleation.



## References

- [1] H. Watanabe, M. Suzuki, H. Inaoka, and N. Ito; *J. Chem. Phys.* **141**, 234703 (2014).
- [2] I. Lifshitz and V. Slyozov. *J. Phys. Chem. Solids*, 19:35–50, 1961.
- [3] C. Wagner. *Z. Elektrochem.*, 65:581–591, 1961.

# Multiscale Simulation for non-isothermal flows of complex fluids

Shugo YASUDA

*Graduate School of Simulation studies,*

*University of Hyogo, 7-1-28 Minatojima-minamimachi, Kobe 650-0047*

Predicting the transport phenomena of complex fluids such as colloids, polymers, and liquid crystals using computer simulations is challenging from both a scientific and an engineering point of view. Molecular-dynamics simulations are often used to investigate the intrinsic properties of a material based on a tiny sample of the material. However, applying a full molecular dynamics simulation to macroscopic behavior of actual systems is not relevant since significant computational resources are required to solve the dynamics of all of the molecules.

We have recently developed a new multi-scale simulation scheme, termed synchronized molecular dynamics (SMD), which enables us to treat the overall problem. In the SMD method, the molecular dynamics simulations are assigned to small fluid elements to calculate the local stresses and temperatures, but are synchronized at a certain time interval to satisfy the macroscopic heat and momentum transfer. The SMD method can drastically reduce the computational requirements compared with the full molecular dynamics simulation.

The SMD method is applied to polymer

lubrications with viscous heating. After applying different shear stresses, the simulation results reveal an interesting behavior of the conformation of polymer chains: the reentrant transition occurs in the linear stress-optical relation for large shear stresses due to the coupling of heat and momentum transfer.

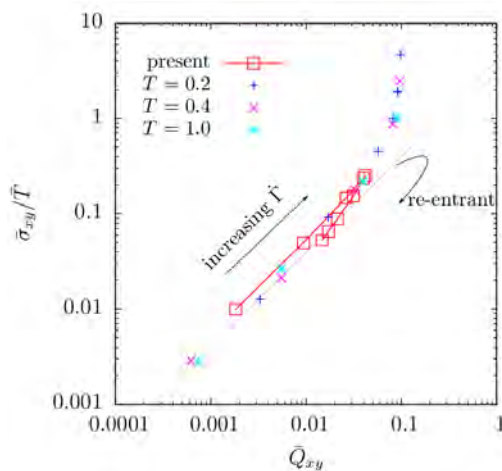


Fig. 1: (Reprinted from Ref. [1]) The stress-optical relation. The open squares indicate the present results, and the symbols +, x, and \* indicate the results obtained by the usual NEMD simulations.

## References

- [1] S. Yasuda and R. Yamamoto, Phys. Rev. X **4** (2014) 041011.

# Numerical study of the novel magnetic phenomenon on the honeycomb magnetism

Tokuro SHIMOKAWA and Hikaru KAWAMURA

*Faculty of Science, Osaka University  
Machikane-yama, Toyonaka Osaka 560-0043*

Triangular lattice antiferromagnet has attracted long and ongoing attention in the field of condensed matter physics because of their leading to a variety of nontrivial states owing to the geometrical frustration effect. Recent theoretical studies reported the realization of multiple- $q$  states in the classical antiferromagnetic (AF) Heisenberg model on the triangular lattice whose state is originated from the trigonal symmetry[1]. The  $S = 1/2$  random AF Heisenberg model on the triangular lattice with a moderately strong randomness provides a quantum spin-liquid state without no trivial long-range nor spin glass orders[2]. Motivated by these theoretical studies of triangular lattice, we here investigate the possibility of realization of the multiple- $q$  and randomness-relevant spin liquid state on the honeycomb lattice which also has the trigonal symmetry.

## 1 $J_1$ - $J_2$ classical Heisenberg model on the honeycomb lattice under the magnetic field

We have investigated the phase diagram of the  $J_1$ - $J_2$  classical Heisenberg model on the honeycomb model under the magnetic field whose Hamiltonian is given by,

$$\begin{aligned} \mathcal{H} = & J_1 \sum_{\langle i,j \rangle} \mathbf{S}_i \cdot \mathbf{S}_j + J_2 \sum_{\langle\langle i,j \rangle\rangle} \mathbf{S}_i \cdot \mathbf{S}_j \\ & - H \sum_i S_i^z, \end{aligned} \quad (1)$$

where  $\sum_{\langle i,j \rangle}$  and  $\sum_{\langle\langle i,j \rangle\rangle}$  mean the sum over the nearest-neighbor and the second-neighbor pairs, respectively.  $H$  is the magnetic field intensity. By using monte carlo method based on the heat-bath method combined with the over-relaxation and replica exchange methods, we have revealed the realization of several multiple- $q$  orders on the honeycomb lattice under the magnetic field. The phase diagram in the case of  $J_2/J_1=0.3$  is shown in Fig. 1. The phase structure is considerably difference from that in the triangular lattice. More interestingly, triple- $q$  state spin configuration of this honeycomb model forms “meron-like” structure in contrast to the “skyrmion lattice” structure in the triple- $q$  state of the triangular model[1]. These results were obtained by using system B.

## 2 $S=1/2$ random AF Heisenberg model on the honeycomb lattice

We consider the AF bond-random  $S=1/2$  quantum Heisenberg model on the honeycomb lattice whose Hamiltonian is given by,

$$\mathcal{H} = \sum_{i,j} J_{i,j} \mathbf{S}_i \cdot \mathbf{S}_j, \quad (2)$$

where  $\mathbf{S}_i=(S_i^x, S_i^y, S_i^z)$  is a spin-1/2 operator at the  $i$ -th site on the honeycomb lattice. Here,  $J_{ij} > 0$  is the random nearest-neighbor AF coupling obeying the bond-independence uniform distribution between  $[(1-\Delta)J, (1+\Delta)J]$ ,

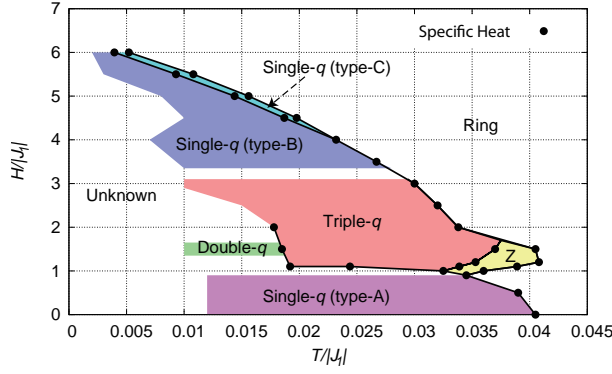


Figure 1: Phase diagram of the  $J_1$ - $J_2$  antiferromagnetic Heisenberg model on the honeycomb lattice with  $J_2/J_1 = 0.3$  obtained by monte carlo simulation. Black circle means the peak position of the specific heat. Each multiple- $q$  phase is determined by the static spin structures (not shown here).

with the mean  $J$ . The parameter  $\Delta$  means the extent of the randomness:  $\Delta = 0$  corresponds to regular (non-randomness) system and  $\Delta = 1$  to the maximally random system.

We have found that the Néel antiferromagnetic long-range order of this unfrustrated model survives even in the maximal randomness ( $\Delta = 1$ ) case not as in the case of triangular lattice[2] by using an exact diagonalization method and a quantum monte carlo method. Fig. 2 shows the system size dependence of the sublattice magnetization in each  $\Delta$ . One can see clearly confirm the sublattice magnetization survives in the thermodynamic limit from regular  $\Delta = 0$  case to maximal randomness  $\Delta = 1$  case. After considering the robustness of the Néel order against bond-randomness in the square lattice case[2], the realization of a randomness-relevant quantum spin liquid state needs both quantum fluctuation and frustration effects. These results were obtained by using system A and system B.

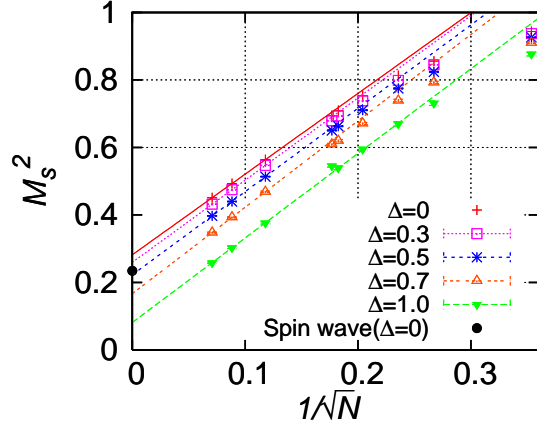


Figure 2: The size dependence of the squared sublattice magnetization for various values of the randomness  $\Delta$ .  $N$  means total number of spins.

## References

- [1] T. Okubo, S. Chung, and H. Kawamura : Phys. Rev. Lett. **108** (2012) 017206.
- [2] K. Watanabe, H. Kawamura, H. Nakano, and T. Sakai : J. Phys. Soc. Jpn. **83** (2014) 034714.

# Dynamical properties of Coulomb Glass

Takamichi TERAO

*Department of Electrical, Electronic and Computer Engineering,*

*Gifu University, Yanagido 1-1, Gifu 501-1193*

Electronic states in Coulomb glass, in which the disorder and many-body electron-electron interaction are incorporated, have been extensively studied during the last few decades. The properties of compensated doped semiconductors, ultrathin films, and granular metals are well described by these Coulomb-glass models. Most of the past numerical studies have been devoted to examining the properties of Coulomb glasses in equilibrium, and they have shown the existence of a Coulomb gap at the Fermi level. Recent experiments have demonstrated the non-equilibrium nature of Coulomb glasses, such as logarithmic relation, aging, and memory effects below some critical temperature. The two-time autocorrelation function  $C(t, t_w)$  has been also investigated to clarify the non-equilibrium nature of interacting electrons in disordered thin films.

In this study, kinetic Monte Carlo simulations of interacting electrons in disordered thin films with finite thickness have been performed, where strongly interacting electrons hopping between randomly distributed sites that correspond to the localization centers of the single-electron wave functions. The Hamiltonian of the system is given by

$$H = \sum_i \varphi_i n_i + \sum_{i < j} (n_i - K)(n_j - K) \frac{e^2}{|\mathbf{r}_i - \mathbf{r}_j|}, \quad (1)$$

where  $\mathbf{r}_i$  and  $\varphi_i$  denote the coordinates of the localization center of the  $i$ -th single-particle localized electronic state and the energy of an electron on the  $i$ -th state, respectively. The variable  $n_i$  with the values 0 or 1 describes the

occupation number of site  $i$ . The localization centers are distributed randomly and uniformly inside a slab with system size  $L \times L \times L_z$  ( $L \gg L_z$ ). We use periodic boundary conditions along the  $x$ - and  $y$ -directions and an open boundary condition along the  $z$ -direction. In addition, a charge of  $+Ke$  ( $-e$  is the charge of the electron) is placed on each site to guarantee charge neutrality ( $0 < K < 1$ ). In this study, we investigate such electronic systems assuming that the site energy to be  $\varphi_i = 0$  for all sites  $i$ , and the background charge density is given by  $K = 0.5$ .

To clarify the glassy behavior of the system, the mean square displacement (MSD) of electrons  $\langle r^2(t) \rangle$  and non-Gaussian parameter  $\alpha(t)$  (Figure 1) have been clarified. It was clarified that the MSD shows diffusive behavior at higher temperatures and becomes subdiffusive at lower temperatures. It was also shown that the non-Gaussian parameter  $\alpha(t)$  remains nonzero at lower temperatures.

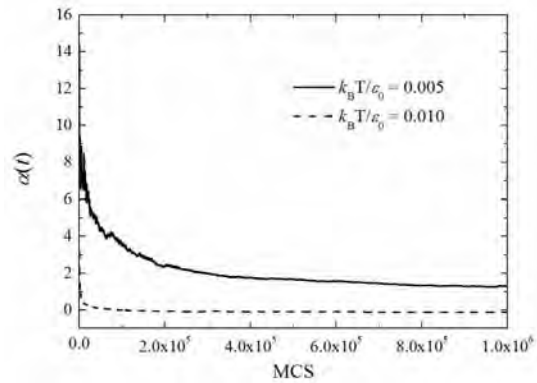


Fig. 1: Non-Gaussian parameter  $\alpha(t)$  of the system.

# Derivation of an $n$ -beam Takagi equation with a term of second-order differentiation

Kouhei OKITSU

*Institute of Engineering Innovation, University of Tokyo*

*2-11-16 Yayoi, Bunkyo-ku, Tokyo 113-8656*

Takagi equation is a widely known X-ray dynamical theory that can deal with an X-ray wave-field in a crystal with lattice distortion. The present author extended the equation to  $n$ -beam cases ( $n \in \{3, 4, 5, 6, 8, 12\}$ ) for the first time [1] in 41 years after it was derived by Takagi in 1962. Further, the present author developed a computer algorithm [2,3] to solve the equation. An excellent agreement was found between images calculated by solving the equation and six-beam pinhole topographs for a silicon crystal experimentally obtained by using beamline BL09XU of the SPring-8. In 2006, he published a paper [3] in which an excellent agreement between six-beam pinhole topographs experimentally obtained by using synchrotron X-rays whose polarization state was arbitrarily controlled with a ‘rotating four-quadrant phase retarder system’ (that was also developed by him [4,5]) and computer-simulated images. In 2011, he reported a method to solve the equation for a crystal with an arbitrary shape [6,7] by showing six-beam pinhole topographs for a channel-cut silicon crystal that almost perfectly coincide with computer-simulated images. However, the two- and  $n$ -beam Ewald-Laue theory can be solved only for a perfect parallel-sided crystal. In 2012, he derived the  $n$ -beam Takagi equation by Fourier-transforming the  $n$ -beam Ewald-Laue dynamical theory [8]. In this paper, three, four, five, six, eight and twelve-beam pinhole topographs experimentally obtained and computer-simulated that

almost completely coincide with each other, which verified the theory and the algorithm to solve it. An importance of development of an  $n$ -beam equation applicable for an arbitrary number of  $n$  was also pointed out in this paper to deal with the phase problem in protein crystal structure analysis.

On the other hand, the Ewald-Laue (two-beam) dynamical theory that can describe an X-ray wave field in a parallel-sided perfect crystal was extended to a three-beam case by Hildebrandt in 1967, Ewald and Héno in 1968 and Héno and Ewald in 1968 for the first time. A numerical method to solve the  $n$ -beam Ewald-Laue dynamical theory was given by Colella [9] in 1974. He demonstrated to solve the phase problem for a germanium crystal by comparing experimental results and numerical solutions for three-beam cases.

The fundamental equation of X-ray dynamical theory is described as follows,

$$\frac{k_i^2 - K^2}{k_i^2} \mathcal{D}_i = \sum_j [\mathcal{D}_j]_{\perp \mathbf{k}_i}. \quad (1)$$

Here,  $k_i$  is wavenumber of  $i$ th numbered Bloch wave whose wave vector is  $\mathbf{k}_0 + \mathbf{h}_i$  where  $\mathbf{k}_0$  is the wave vector of the forward-diffracted wave in the crystal,  $K (= 1/\lambda)$  is the wavenumber of X-rays in vacuum,  $\mathcal{D}_i$  and  $\mathcal{D}_j$  are complex amplitude vectors of  $i$ th and  $j$ th numbered Bloch waves,  $\sum_j$  is an infinite summation for  $j$ ,  $\chi_{h_i-h_j}$  is Fourier coefficient of electric susceptibility and  $[\mathcal{D}_j]_{\perp \mathbf{k}_i}$  is component vector of  $\mathcal{D}_j$  perpendicular to  $\mathbf{k}_i$ .

By applying an approximation that  $k_i + K \approx 2k_i$  to (1), the following equation is obtained,

$$\xi_i \mathcal{D}_i = \frac{K}{2} \sum_j \chi_{h_i - h_j} [\mathcal{D}_j]_{\perp \mathbf{k}_i}, \quad (2)$$

where  $\xi_i = k_i - K$ .

The above equation can be represented as a linear eigenvalue/eigenvector problem. The present author derived the  $n$ -beam Takagi equation by Fourier-transforming (2). However, Colella solved (1) directly as a second-order eigenvalue/eigenvector problem with a complex method without using the approximation,  $k_i + K \approx 2k_i$ .

The present author have Fourier-transformed Colella's equation to derive the following equation,

$$\begin{aligned} \frac{\partial}{\partial s_i} D_i^{(l)}(\mathbf{r}) + \frac{i}{4\pi K} \nabla^2 D_i^{(l)}(\mathbf{r}) \\ = -i\pi K \sum_{j=0}^{n-1} \sum_{m=0}^1 C_{i,j}^{(l,m)} \chi_{h_i - h_j} D_j^{(m)}(\mathbf{r}), \end{aligned} \quad (3)$$

where  $i, j \in \{0, 1, \dots, n-1\}$ ,

$n \in \{3, 4, 5, 6, 8, 12\}$ ,

$l, m \in \{0, 1\}$ .

When dealing with a lattice displacement field  $\mathbf{u}(\mathbf{r})$ ,  $\chi_{h_i - h_j}$  can be replaced with  $\chi_{h_i - h_j} \exp[i2\pi(\mathbf{h}_i - \mathbf{h}_j) \cdot \mathbf{u}(\mathbf{r})]$ . The second term of the left side of (3) does not exist in the  $n$ -beam Takagi equation the present author derived and even in the Takagi (two-beam) equation originally derived by Takagi in 1962.

By using this term of  $\nabla^2 D_i^{(l)}(\mathbf{r})$ , the  $n$ -beam (and also two-beam) Takagi equation can probably be integrated more rapidly compared with the conventional Takagi equation without this term. The present author is now coding a computer program to solve (3).

## References

- [1] K. Okitsu: Acta Cryst A **59** (2003) 235-244.
- [2] K. Okitsu, Y. Imai, Y. Ueji and Y. Yoda: Acta Cryst A **59** (2003) 311-316.
- [3] K. Okitsu, Y. Yoda, Y. Imai, Y. Ueji, Y. Urano and X.-W. Zhang: Acta Cryst A **62** (2006) 237-247.
- [4] K. Okitsu, Y. Ueji, K. Sato and Y. Amemiya: Acta Cryst A **58** (2002) 146-154.
- [5] K. Okitsu, Y. Yoda, Y. Imai and Y. Ueji: Acta Cryst A **67** (2011) 557-558.
- [6] K. Okitsu: Acta Cryst A **67** (2011) 550-556.
- [7] K. Okitsu: Acta Cryst A **67** (2011) 559-560.
- [8] K. Okitsu, Y. Imai and Y. Yoda: In-Tech *Recent Advances in Crystallography* (2012) 67-86 [Invited].
- [9] R. Colella: Acta Cryst. A **30** (1974) 413-423.

# Impurity Scattering in Junctionless transistor

Akiko Ueda

*Faculty of Pure and Applied Sciences, University of Tsukuba  
1-1-1 Tennodai, Tsukuba, 305-8573*

Junctionless transistor (JLT) is one of the alternative devices to overcome the scaling limit of the conventional transistors [1]. In JLTs, the homogenous atoms are doped uniformly in the contact and channel regions. The current of the JLTs flows the center of the cross section of the nanowire since the current is turned on in the condition of the flat band. The impurity scattering is dominant scattering mechanism due to the high doping concentration in the channel region. We investigate the effect of impurity scattering to the transport properties of JLT.

The schematic picture of the n-type circular gate all around nanowire JLT is shown in Fig. 1. The all regions in Si nanowire have the doping concentration of  $4 \times 10^{19} \text{ cm}^{-3}$  or  $8 \times 10^{19} \text{ cm}^{-3}$ . The electronic structure of the nanowire is calculated with  $sp^3d^5s^*$  tight binding model. The current is calculated by the nonequilibrium Green function (NEGF) method. The electrostatic potential and electron concentration are determined by solving the NEGF method and the Poisson equation self-consistently [2]. In a small nanowire structure with approximately 10000 atoms, the total size of the Green's function is about

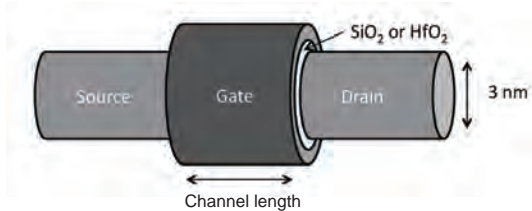


Figure 1: Schematic picture of JLT

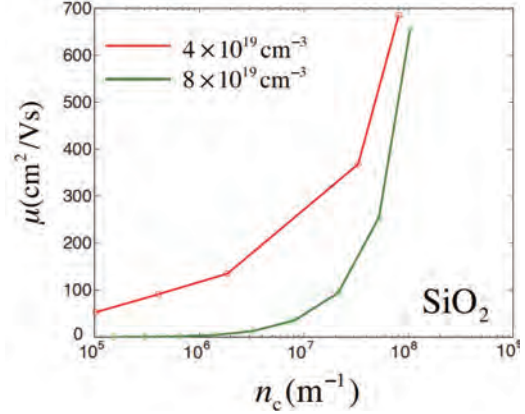


Figure 2: Mobility as a function of the number of electron per channel length.

$N_A \times t_B = 100000$ . We use 256 CPUs by adopting MPI in the code to solve the Green function.

In Fig. 2, we plot the mobility as a function of the number of electrons per wire length. The mobility is enhanced with increase of the electron concentration even for the high doping concentration thanks to the screening by the transporting electrons. Furthermore, we find that the mobility of the doping concentration of  $8 \times 10^{19} \text{ cm}^{-3}$  becomes higher than the one of  $4 \times 10^{19} \text{ cm}^{-3}$  with electron-phonon interaction.

## References

- [1] J.-P. Colinge et al., Nat. Nanotechnol., **5** (2010) 255
- [2] M. Luisier and G. Klimeck., Phys. Rev. B **80**, 155430 (2009) .



# Molecular Dynamics Simulation Study of Mechanism of Ice Nucleation Promotion by Calcium Oxalate Monohydrate

Hiroki NADA

*National Institute of Advanced Industrial Science and Technology (AIST)  
Onogawa16-1, Tsukuba, Ibaraki 305-8569*

Ice nucleation agents have been studied for many years in physics, chemistry, biology, mineralogy, earth science and engineering in connection with such issues as the formation of artificial snow and food processing [1]. Recently, our research group has found that calcium oxalate monohydrate (COM) crystals, which exist in abundance in nature, are potent ice nucleation agents. Our experimental studies have suggested that the (110) plane of COM crystals functions to promote ice nucleation. However, why and how the COM (110) plane promotes ice nucleation still remain unclear.

In the  $\langle 110 \rangle$  direction of a COM crystal, a positively-charged plane consisting of  $\text{Ca}^{2+}$  and  $\text{C}_2\text{O}_4$  (Ox1 plane) and a negatively-charged plane consisting of  $\text{C}_2\text{O}_4$  and  $\text{H}_2\text{O}$  (Ox2 plane) are piled up by turns. It is expected that either Ox1 or Ox2 planes (or both of those planes) functions as an ice nucleation promotor. Investigating the mechanism of ice nucleation on each of the planes at the molecular level is needed to elucidate it.

In this project, the mechanism of ice nucleation promotion by the COM (110) plane was investigated by means of a molecular dynamics (MD) simulation. The simulation was performed for a system in which a film of super-cooled water was sandwiched between the Ox1 and Ox2 planes of a COM crystal. The six-site model was used for estimation of the interaction between a pair of water molecules [2]. The interaction for calcium oxalate was estimated

using a model proposed by Tommaso et al. [3]. Temperature was set to 268 K. DL\_POLY version 2.20 was used for the simulation [4].

In the simulation, the formation of polar cubic ice was observed. The formation occurred preferentially on the Ox2 plane rather than on the Ox1 plane. Therefore, it is expected that the Ox2 plane functions to induce the nucleation of polar cubic ice. However, in real systems, the formation of ordinal non-polar hexagonal ice occurs even if COM crystals are present. Therefore, it is speculated that the structure of polar cubic ice, which is formed first on the Ox2 plane, finally transits to that of non-polar hexagonal ice. More extensive studies are needed to confirm it.

## References

- [1] R.E. Lee, Jr. et al. Biological Ice Nucleation and Its Applications, APS Press, St. Paul, 1997.
- [2] H. Nada and J.P.J.M. van der Eerden: J. Chem. Phys. **118**, (2003) 7401.
- [3] D. Tommaso et al.: RCS Advances. **2** (2012) 4664.
- [4] W. Smith: Mol Simul. **32** (2006) 933.

# Reconstruction of protein folding energy landscape based on a Multicanonical sampling method

Katsuyoshi Matsushita

*Cybermedia Center, Osaka University*

*Machikaneyamacho 1-32, Toyonaka, Osaka 560-0043*

The elucidation of the folding mechanism of proteins is a long-standing issue in biology and physics. The key to elucidating the folding is to clarify the energy landscape in the protein-structure space. A lot of effort are devoted to this clarification so far. However the method to clarify the energy landscape is not effective until now. The difficulty in the development of the method originates from the large dimension of the protein-structure space. Thus a reduction of the structure space is necessary for the development of an efficient method.

As a reduction method of the structure space, we proposed a Markov state model on the energy space[1]. To construct the Markov state model, we develop a multicanonical monte carlo method based on a structure-base coarse grain model of a protein. We applied the method to the G-related albumin-binding module (GA-module) and successfully obtain the Markov state model as a energy landscape as shown in Fig. 1.

The model consists of the nodes and the directional edges. A node indicate a state with a certain energy and the number at the node indicates the energy value of the node. A directional edge between two nodes indicates a large transition probability. The directions of the edges form a monotonic flow from the highest

energy state to the lowest energy state. Since the lowest energy state corresponds to a native structure of the GA module, the monotonic flow shows the fact that the GA-module easily folds to the native structure by the effect of the energy landscape.

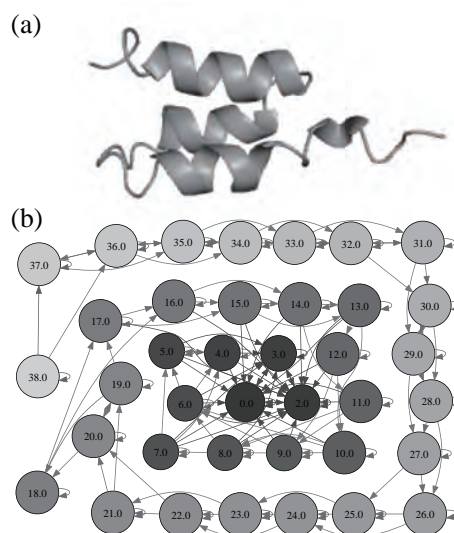


図 1: Markov state model as a folding energy landscape.

## 参考文献

- [1] K. Matsushita *et al.*, Proc. 19th Traffic flow Symposium, 61 (2013).

## Characterization of thermal transport at the solid-liquid interface

Junichiro SHIOMI

*Department of Mechanical Engineering,*

*The University of Tokyo, 7-3-1, Hongo, Bunkyo-ku, Tokyo, 113-8656*

Thermal transport across interfaces is highly important for cooling. Boiling has long been used as an effective method to induce this cooling, since the phase-change process coupled with mass transport is a highly effective method of removing energy from a surface. If boiling can be induced at a lower temperature, then the surface can be maintained at this lower temperature, hence there has been recent significant interest in achieving “sub-cooled” boiling [1,2].

The phase-change can be observed macroscopically in the form of air bubbles, however the initial nucleation begins on the nano-scale within the cavities of the surface. Experimental observation of the relation between this very initial stage of bubble formation and the surface structure is very challenging, and therefore molecular simulation has come to play an important role in elucidating these nano-scale dynamics [3].

In this work, we have elucidated the role of nano-scale structuring on the very initial moments of boiling, by conducting molecular dynamics simulations of surface-lift-off of water from a heated surface under various roughness and hydrophilicity conditions. Furthermore, we have considered the role of gas in the lift-off dynamics.

Figure 1 (left) shows a schematic outline of the boiling system. The system initially starts in equilibrium with both the surface and water at the same temperature. The surface is then suddenly heated to high temperature, which causes the water above to heat up, and within a few nanoseconds the water lifts off from the surface. The temperature of the water at the time of lift-off, along with the time it takes for the lift-off to occur, depends strongly on the surface characteristics (Fig. 1, right).

Analysis shows that increased nano-scale roughness leads to a decrease in the lift-off temperature, and that this can be explained to a large extent by the change in effective solid-liquid interaction strength, in the same way that simply changing the hydrophilicity of an atomically smooth surface changes the solid-liquid

interaction strength. Furthermore, by adding gas (nitrogen) into the system, our results demonstrate that the presence of gas helps to reduce the lift-off temperature by getting between the solid and liquid with a consequent reduction in solid-liquid interaction.

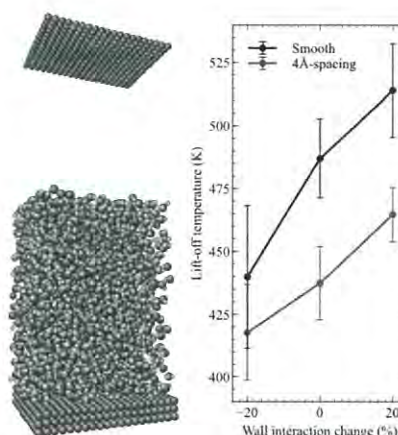


Fig. 1 Left: Snapshot of the simulation system. Right: Effect on the lift-off temperature of making the water-wall interaction weaker and stronger for a smooth surface and one with nano-scale roughness. A combination of roughness and weaker water-surface interaction is seen to lead to minimum lift-off temperature.

Similar to boiling phenomena, thermal transport at the solid-solid interface determines heat exchange, dissipation, thermoelectric efficiency, etc. Here the important physical quantity is the phonon transmission function at the interface, which describes how phonons can be transmitted at the interface. As a test, we have calculated the phonon transmission function and thermal boundary conductance at a lead telluride and lead sulfur (PbTe/PbS) interface by using non-equilibrium molecular dynamics simulation with interatomic force constants [4]. In the calculations, we found that inelastic phonon scattering at the interface contributes to 10% of overall thermal boundary conductance and cannot



be negligible; a fact which has not been identified by conventional transmission calculations[5]. Besides this, by applying our method to a silicon-germanium interface system, we found that interfacial phonon properties do not always determine thermal resistance and are strongly coupled to bulk phonon properties (T. Murakami, et al. 2014 [6]).

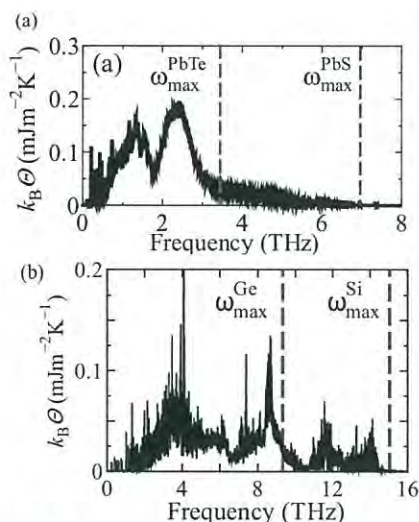


Fig. 2 Phonon transmission function at (a) PbTe/PbS and (b) Si/Ge interfaces. The dashed lines are the maximum frequencies of the bulk materials. The  $\Theta$  and  $k_B$  denote phonon transmission function and the Boltzmann constant.

Once phonon transport properties in bulk and at the interface are obtained, one can evaluate heat conduction in nanostructured materials by performing phonon Monte Carlo simulation [7]. In this work, we have calculate thermal conductivity of polycrystalline nanocrystal illustrated in Fig. 3(a). Polycrystalline nanocrystal can be made experimentally and has so far been demonstrated to be an effective form of structuring for large reduction of thermal conductivity. In fact, molecular dynamics simulation has been undertaken to calculate thermal conductivity of polycrystalline nanocrystal, however, mesoscopic effects such as grain size distribution and geometrical shape of nanograins have not been sufficiently considered. Therefore we have performed phonon Monte Carlo ray-tracing-based simulation to calculate thermal conductivities of nanocrystals with different geometrical conditions (Fig.3(b)).

Using molecular dynamics, lattice dynamics, and Monte Carlo techniques, we have investigated thermal transport at solid-solid and solid-liquid interfaces. Although further investigations are

required, the knowledge obtained thus far suggests that nanostructured-interface can enhance interfacial thermal transport and/or reduce overall thermal conductivity of thermoelectric materials. The simulation tools developed here have been also useful to interpret various experimental results of nanoscale heat conduction [9-11].

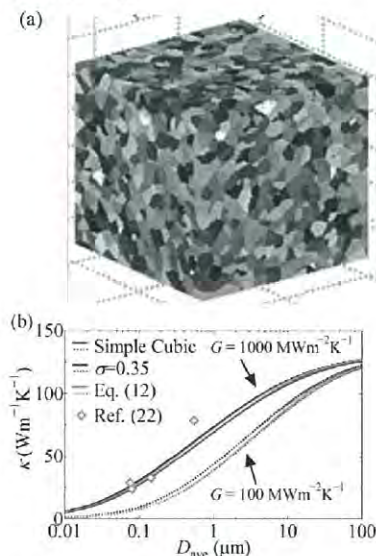


Fig. 3 (a) Polycrystalline nanocrystal obtained by Voronoi tessellation technique. (b) Thermal conductivity of polycrystalline nanocrystal silicon at room temperature as a function of mean grain size ( $D_{ave}$ ). Thermal boundary conductance  $G$  between grains here is set to 100  $\text{MWm}^{-2}\text{K}^{-1}$  and 1,000  $\text{MWm}^{-2}\text{K}^{-1}$ . Here  $\sigma$  denotes the amount of variation from  $D_{ave}$ .

#### References

- [1] Y. Takata, S. Hidaka and M. Kohno, Int. J. of Air-conditioning, **20**, 1 (2012).
- [2] X. Wang, S. Zhao, H. Wang, T. Pan, Appl. Therm. Eng., **35**, pp112-119 (2012).
- [3] T. Yamamoto, M. Matsumoto, J. Therm. Sci. Tech., **7**, pp 334-349 (2012).
- [4] T. Murakami, T. Shiga, T. Hori, K. Esfarjani, and J. Shiomi, EPL, **102**, 46002 (2013).
- [5] Z. Tian, K. Esfarjani, and G. Chen, Phys. Rev. B **84**, 104302 (2012).
- [6] T. Murakami, T. Hori, T. Shiga, and J. Shiomi, Appl. Phys. Express, **7**, 121801 (2014).
- [7] T. Hori, G. Chen, and J. Shiomi, Appl. Phys. Lett. **104**, 021915 (2014).
- [8] T. Hori, J. Shiomi, and C. Dames, Appl. Phys. Lett. **106**, 171901 (2015).
- [9] M. Sakata, T. Hori, T. Oyake, J. Maire, M. Nomura, J. Shiomi, Nano energy, Rapid communication, **13**, 601 (2015).
- [10] M. Nomura, Y. Kage, J. Nakagawa, T. Hori, J. Maire, J. Shiomi, D. Moser, O. Paul, Phys. Rev. B (in press)
- [11] Y. Nakamura, M. Isogawa, T. Ueda, S. Yamasaka, H. Matsui, J. Kikkawa, S. Ikeuchi, T. Oyake, T. Hori, J. Shiomi, A. Sakai, Nano Energy, Rapid communication (2014).

# Bound states in unconventional superconductors

Yuki NAGAI

*CCSE, Japan Atomic Energy Agency*

*Wakashiba, Kashiwa, Chiba 277-0871*

We addressed inhomogeneous superconducting states in multiple degree of freedom systems, focusing on the noncentrosymmetric system and the bilayer Rashba system. We employed quasiclassical Green's function method, which is appropriate for parallel computations. We can utilize the parallel computing for the wavenumber integral over the Fermi surface (FS), since the equation of motions of quasiclassical Green's function is independently determined at the Fermi wavenumber. In actual calculations, we used the MPI and usually submitted a job with 12 processes in system B.

We calculated the local density of states (LDOS) around a vortex core in the presence of non-magnetic impurities in noncentrosymmetric systems. We found that the zero-energy vortex bound states split off with increasing the impurity scattering rate for both  $s$ -wave and  $s + p$ -wave pairing state in the bare Born approximation [1]. We also showed that the impurity effect in the vicinity of a vortex core is independent of the spin-orbit coupling (SOC) for an  $s$ -wave pairing in the bare Born approximation [2], which is the same feature as that in the bulk. This result means that the Eilenberger equation is separated into the two equations defined on the each split FS. This is the case with the impurity scattering effect in the self-consistent Born approximation. On the other hand, in an  $s + p$ -wave pairing, we

found that the impurity effect can depend on the SOC in the bare and self-consistent Born approximations [2]. This means that the Eilenberger equation is not separated into the two equations, since the interband impurity scattering occurs around a vortex core for the  $s + p$ -wave pairing.

We have numerically investigated the electronic structure of a vortex core in bilayer Rashba superconductors by means of the self-consistent quasiclassical calculation. We found that the LDOS structure in the pair-density wave (PDW) state is quite different from that in the BCS state. The zero energy vortex bound state exists in the PDW state, whereas it is absent in the BCS state due to the Zeeman effect. This prominent difference stems from (i) whether or not there is particle-hole symmetry in the mirror sector of the block-diagonalized Bogoliubov-de Gennes Hamiltonian and (ii) the change of the internal structure of the Cooper pair due to the SOC. Another feature of the PDW state is that the core size is small compared with that in the BCS state in the vicinity of the BCS-PDW phase transition. The characteristic vortex core structure in the PDW state can be observed by scanning tunneling microscopy/spectroscopy at low temperature. The exotic superconducting phase under a magnetic field may be identified by investigating these features.

## References

- [1] Y. Higashi, Y. Nagai and N. Hayashi: JPS Conf. Proc. **3**, 015003 (2014).
- [2] Y. Higashi: Doctral thesis (Osaka Prefecture University, 2015).
- [3] Y. Higashi, Y. Nagai, T. Yoshida and Y. Yanase: J. Phys.: Conf. Ser. **568**, 022018 (2014).
- [4] Y. Higashi, Y. Nagai, T. Yoshida, Y. Masaki and Y. Yanase: submitted to Phys. Rev. B.

# Physical properties of low-dimensional electron systems created at solid surfaces and their control

Takeshi INAOKA

*Department of Physics and Earth Sciences, Faculty of Science,  
University of the Ryukyus, 1 Senbaru, Nishihara, Okinawa 903-0213*

Semiconductor band gaps are directly related to photoabsorption and luminescence, and we need to control them to improve performance of electronic devices. Strain engineering is a new approach to this higher performance through modification of electronic structure. By means of a hybrid density-functional method, we analyzed the strain effect on the band structure of bulk Si and Ge. This analysis forms a fundamental basis to understand the strain effect on subbands created at surfaces or interfaces.

We used the program package ‘Vienna ab initio Simulation Package’ (VASP) [1,2] mainly on the system B.

## (1) Tensile-strain effect of inducing the indirect-to-direct band-gap transition and reducing the band-gap energy of Ge [3]

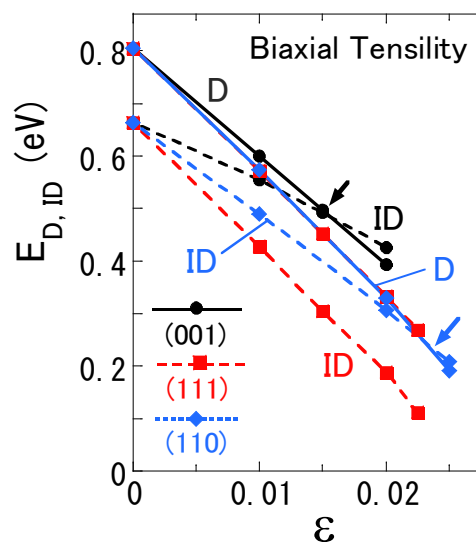
Application of tensile strain to Ge is expected to induce the indirect-to-direct band-gap transition and to reduce the band-gap energy. Under the condition of no normal stress, we take account of normal compression and internal strain, namely, relative displacement of two atoms in the primitive unit cell. Our analysis have shown that either normal compression or internal strain operates unfavorably to induce the gap transition, which increases the critical strain coefficient for the transition or even blocks the transition, and that cooperation of strain orientation and band anisotropy has a remarkable influence on the gap transition and the gap energy.

Figure 1 exhibits the strain-coefficient ( $\varepsilon$ ) dependence of the direct and indirect band gaps,  $E_D$  and  $E_{ID}$ , for three types of biaxial tensility under the condition of no normal stress. The circles, squares, and diamonds correspond to biaxial tensility in the (001), (111), and (110) planes,

respectively. The full and broken lines connecting these symbols display  $E_D$  at the  $\Gamma$  point and  $E_{ID}$  between the  $\Gamma$  point and the L point in the [111] direction, respectively. This L point is degenerate with some other L points according to band and strain symmetry. The  $E_D$  lines for (111) and (110) tensility overlap each other. The upper and lower arrows indicate the band-gap transition at  $\varepsilon=0.015$  and  $0.023$  for (001) and (110) tensility, respectively. No transition occurs for (111) tensility.

The conduction-band energy at the  $\Gamma$  point for (001) biaxial tensility is larger than that for (111) or (110) tensility, because larger normal compression in the former tensility operates to raise the energy more effectively. This explains the slower decrease in  $E_D$  for (001) tensility.

The behavior in  $E_{ID}$  is closely related to anisotropic conduction-band dispersion around the L points. Constant-energy surfaces around the L point form spheroids elongated conspicuously in the diagonal directions. With increasing  $\varepsilon$ , the L-point



**Fig. 1**  $\varepsilon$  dependence of the direct and indirect band gaps,  $E_D$  and  $E_{ID}$ , for (001), (111), and (110) biaxial tensility



energy falls most quickly in (111) tensility, because the (111) tensile-strain plane is exactly parallel to the short axes of the spheroids around the  $[111]$  or  $[\bar{1}\bar{1}\bar{1}]$  L point.

By relatively small tensility, we can lower the band gap, and consequently the photoabsorption edge down to a mid-wavelength infrared region.

## (2) Strain effect on the band gap of Si [4]

Strain application to Si is also expected to change band gaps significantly. Using a hybrid density-functional method, we have started investigating the strain effect on band gaps of Si, considering both normal and internal strain under the condition of no normal stress. This academic year, we analyzed the effect of  $[001]$  uniaxial compression and tensility on the band structure. Our analysis indicates that synergistic operation of strain orientation and band anisotropy has a great effect on the band gap.

When  $[001]$  uniaxial strain is applied, six conduction-band minima split into two groups, namely, two minima in the  $[001]$  and  $[00\bar{1}]$  directions and the others. We let CML and CMT denote the former and latter groups, respectively.

Figure 2 shows the indirect band gaps  $E_{ID}$  for no strain ( $\varepsilon=0$ ) and for 2% uniaxial compression ( $\varepsilon=-0.02$ ) and tensility ( $\varepsilon=0.02$ ) in the  $[001]$  direction. The circles and squares correspond to the  $E_{ID}$  values for the CML and CMT, respectively. The full and dotted lines connecting these symbols represent the results with normal (N) strain under the condition of no normal stress and those without normal strain, respectively. The  $[001]$  compression (tensility) operates to raise (lower) the CMT energy significantly, because the strain direction is parallel to the short-axis directions of the constant-energy spheroids around the CMT minima. A substantial increase (decrease) in both the valence-band maximum (VM) and CMT energy due to compression (tensility) leads to a relatively small change in  $E_{ID}$ . The  $E_{ID}$  value for the CMT in compression (tensility) is somewhat smaller than that

under no strain, since the increase (decrease) in the VM energy is somewhat larger (smaller) than that in the CMT energy. On the other hand, the  $[001]$  strain produces only a small change in the CML energy, because the strain direction is parallel to the long-axis directions of the CML spheroids. The  $E_{ID}$  value for the CML in compression is significantly smaller than that under no strain, since the change in  $E_{ID}$  is dominated by a great rise in the VM energy. Biaxial normal compression involved in 2% tensility operates to decrease the  $E_{ID}$  value for the CMT considerably. This can be ascribed to a substantial rise in the VM energy and only a small increase in the CMT energy. The latter small increase arises from the fact that the compression plane is parallel to the long-axis directions of the CMT spheroids.

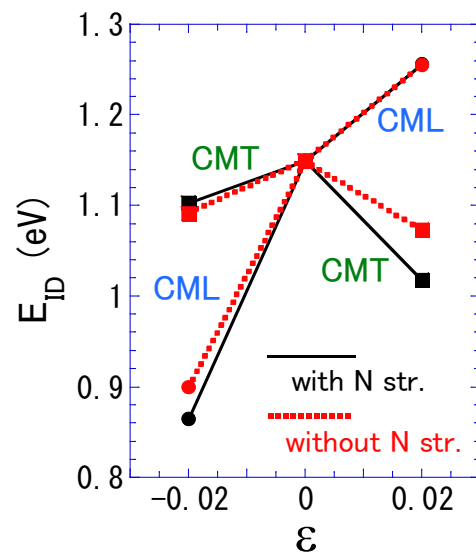


**Fig. 2** Indirect band gaps  $E_{ID}$  for no Strain and for 2% uniaxial compression and tensility in the  $[001]$  direction

## References

- [1] G. Kresse and J. Hafner. Phys. Rev. B **47** (1993) 558–561.
- [2] G. Kresse and J. Furthmüller. Comput. Mat. Sci. **6**: (1996) 15–50.
- [3] T. Inaoka, T. Furukawa, R. Toma, and S. Yanagisawa: submitted to J. Appl. Phys.
- [4] T. Inaoka, S. Yasuda, and S. Yanagisawa: unpublished.



# Self-propelled motion of a Janus particle in periodically phase-separating binary mixtures

Takeaki ARAKI and Shintaro FUKAI

*Department of Physics, Kyoto University Sakyo-ku, Kyoto 606-8504*

Self-propelled motions of micro- and nanoparticles have attracted much interest from a wide range of viewpoints. They will provide us with important applications, such as nanomachines and drug delivery. Recently, focus has been on their collective dynamics because they are very fascinating in a growing field of non-equilibrium physics, *i.e.*, active matter. Self-propelled particles use some energy or nutrients to generate the self-propulsion force. For example, biological molecules, such as ATPase and myosin, convert chemical energy to mechanical motion through chemomechanical coupling. In non-biological systems, Marangoni effect can induce spontaneous motions of liquid droplets.

Recent developments of science and technology enabled us to produce high performance particles such as Janus particles. Janus particles are a kind of colloidal particles whose surface is divided into two hemispheres having different chemical and physical properties. The asymmetry of the Janus particles causes a variety of phenomena which do not appear in normal colloidal systems. For example, strange properties are observed in their aggregated structures and electrical field responses.

The Janus particles are often employed as artificial self-propelled systems. Even when Janus particles are in symmetrical environments, they make asymmetry in their neighboring environment to move by themselves. An example is nano-particles partially coated with platinum. The catalytic decomposition of hydrogen peroxide, which occurs selectively on

the Pt-surface, drives the nanoparticles.

In this study, we numerically investigated the self-propelled motion of a single particle in binary mixtures where the temperature is changed repeatedly between above and below the phase transition temperature. The temporal change in the temperature leads to periodic phase separation and mixing. In the simulations, we used fluid particle dynamics method. In this scheme, we treat a colloidal particle as a fluid particle of high viscosity to deal with hydrodynamic interactions efficiently.

The simulation results indicate spontaneous motions of the Janus particle toward its head. The more wettable phase is selectively adsorbed to the particle tail during the demixing period. Growths of the adsorbed domains induce the hydrodynamic flow in the vicinity of the particle tail, and this asymmetric pumping flow drives the particle directionally. In the mixing periods, the particle motion almost ceases because the mixing occurs via diffusion and the resulting hydrodynamic flow is negligibly small. Repeating this cycle of phase separation and mixing, the Janus particle moves unboundedly. The particle speed and the directionality depend on the volume fraction and the duration of the periodic phase separation.

## References

- [1] T. Araki and S. Fukai, *Soft Matter* (in press, DOI: 10.1039/c4sm02357a).
- [2] T. Uchida, T. Araki and A. Onuki, *Soft Matter* **11** (2015) 2874.

# The ground state properties of Boltzmann liquid and its crystallization

Tomoki MINOGUCHI

*Institute of Physics, Faculty of Arts and Sciences,*

*The University of Tokyo, Komaba, Meguro-ku, Tokyo 153-8902*

The role of quantum statistics (QS), especially Bose statistics in a quantum liquid on the verge of crystallization is revisited recently in the context of quantum jamming, glass and crystallization[1,2]. In the solid phase, since the exchange between particles is less frequent, the free energy is mostly insensitive to the QS. The free energy of liquid, on the other hand, is affected by QS. The melting curve in the phase diagram is hence modified from the original one.

The purpose of this research is two-fold; First, there is a practical need to clarify to what extent the QS is included in quantum Monte Carlo simulations (QMC) for the so-called 4/7 phase of Helium-4 film on a graphite surface. The 4/7 phase, which is a bilayer of atomic films with density ratio 7:4, is quite important to explore quantum solidity. Specific heat measurements found this system to be a stable crystal bilayer[3]. In a QMC study for this system, however, it is quite difficult to include full QS: the results are in fact sharply dependent on the modeling of QS. On a first approximation, neglecting QS indeed leads to a description of the system compatible with a

bilayer solid phase[4]; the stability however is not guaranteed if QS is partially introduced[5].

The second topic of interest, with which our research is mostly concerned, is more general and regards the phase diagram of bulk He-4 without QS (Boltzmann liquid). By observing the melting density of the system at different temperatures, Boninsegni et. al[1] speculated that the melting pressure is strongly reduced and even negative if Bose statistics are removed from He-4 (See Fig.1). They remark that the melting curve must come up to the original melting pressure of true He-4 at zero temperature because the ground state of Boltzmann liquid is the same as Bose liquid. Therefore, the melting curve shapes "U".

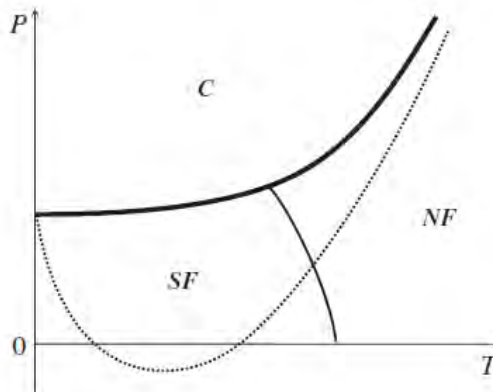


Fig.1 A rough sketch of phase diagram of

He-4 (solid lines) with a melting curve speculated for Boltzmann liquid (dotted line). The symbols C, SF and NF are crystal, superfluid and normal fluid phases respectively. This figure is extracted from [1].

We think, however, that the upcoming curve between zero temperature and the temperature at the bottom of "U" is strange, because the negative slope of the melting curve means that the entropy of the liquid is smaller than that of solid even in absence of superfluidity. In other words, the liquid phase is more ordered than the solid even if Bose statistics is removed!

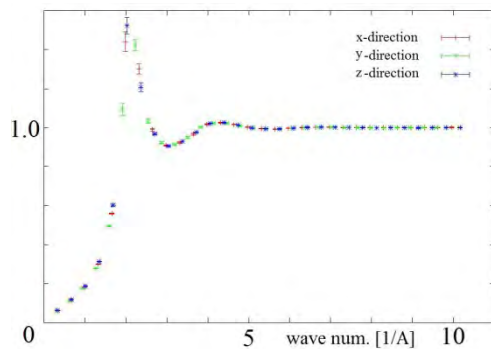


Fig.2 Static structure factor at the density  $0.0247 \text{ \AA}^{-3}$  and at 1 K.

To explore the melting pressure near zero temperature, we plan to study a system of Helium particles, with and without QS, at temperatures ranging from 1K to 0.2K. The method we use is the Path Integral Monte Carlo[6] (PIMC), a well established methodology for the study of quantum systems at finite temperature based on the Path Integral representation of the thermal density matrix. Our parallel implementation of PIMC has

already been successfully applied to a Boltzmann liquid[2] following a procedure used to simulate a metastable state[1] and is ready as is for the planned simulations.

Unfortunately, with the preliminary CPU time meant for testing we had to invest an unexpectedly large amount of time to import into the ISSP cluster the simulation program developed in the group at Milano University and we could use only a limited amount of CPU time. Nevertheless, we have obtained the static structure factor at the density  $0.0247 \text{ \AA}^{-3}$  and at 1 K as in Fig.2. It shows signals of a liquid phase or a liquid-solid coexistence, the determination of which needs further computation. We are now, however, ready to implement computation study straightforwardly.

I would like to thank Dr. Nava for the fruitful collaboration.

## References

- [1] M. Boninsegni, et. al: Phys. Rev. Lett. **109** (2012) 025302
- [2] T. Minoguchi, M. Nava, F. Tramonto, and D.E. Galli: J. Low Temp. Phys. **171** (2013) 259
- [3] S. Nakamura et. al: J. Phys. Conf. Series **400** (2012) 032061
- [4] T. Takagi: J. Phys. Conf. Series **150** (2009) 032102
- [5] Corboz et. al: Phys. Rev. B **78** (2008) 245414
- [6] D. M. Cerperley: Rev. Mod. Phys. **67** (1995) 279

# Theoretical design of graphene quantum devices

Koichi KUSAKABE

Graduate School of Engineering Science, Osaka University  
1-3 Machikaneyama, Toyonaka, Osaka 560-8531

## 1. Introduction

The topological zero mode is known to appear at a tri-hydrogenated vacancy of graphene,  $V_{111}$ . In a recent study, Ziatdinov *et al.* have succeeded in fabrication of  $V_{111}$ . [1, 2] Since the mode is given as an eigen state of the effective one-body Hamiltonian, we have no hybridization between the zero mode and Dirac modes of graphene, suggesting zero anti-ferromagnetic exchange by the conventional mechanism. We have estimated another spin-scattering channel, by which the Coulomb interaction causes various unrevealed low-energy phenomena.

## 2. Estimation of on-site correlation energy of the zero mode

Applying our method of the multi-reference density functional theory (MR-DFT), [3, 4] we have estimated on-site correlation energy  $U_0$  on the zero mode, where the screening effect appears as the scattering processes among quasi-particle excitations in the complementary space of the representation space. The estimated value of  $U_0 \simeq 1\text{eV}$  certifies existence of the localized spin at the zero mode, when the charge neutrality condition is kept.

## 3. Estimation of exchange scattering by the zero mode

A second order exchange path of the low-energy Dirac electron accompanied by the spin exchange is also determined by MR-DFT. We derived an effective anti-ferromagnetic interaction mechanism, which becomes dominant when the system size is enough large.

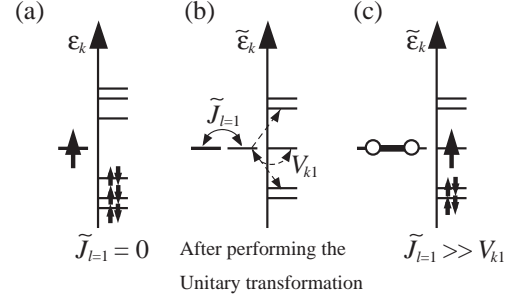


Figure 1: Scattering-driven Kondo screening.

## 4. The Kondo effect and device design

The amplitude of  $J_0$  as a sum of the higher order paths becomes as large as  $0.1\text{eV}$ , because the paths contribute additively to the integral. The anti-ferromagnetic Kondo screening becomes dominant in the dilute limit of the vacancies, where the Kondo temperature is estimated to be more than a few tens Kelvin.

The scheme of Fig. 1 suggests interesting quantum dynamics, where local excitation of a quantum spin at the zero mode by circular photon irradiation may cause a transfer of quantum information as a spin transfer from the zero mode to the Dirac mode by the exchange. The detection method will be presented elsewhere.

- [1] M. Ziatodinov, *et al.*: Phys. Rev. B **89** (2014) 155405. [2] S. Fujii, *et al.*: Faraday Discuss., **173** (2014) 10. [3] K. Kusakabe, *et al.*: J. Phys. Condens. Matter **19** (2007) 445009. [4] K. Kusakabe and I. Maruyam: J. Phys. A: Math. Theor. **44** (2011) 135305. [5] N. Morishita: arXiv:1412.8589.

# Excitation dynamics of frustrated quantum spin chain

Hiroaki ONISHI

*Advanced Science Research Center, Japan Atomic Energy Agency,  
Tokai, Ibaraki 319-1195*

Recently, a spin- $\frac{1}{2}$  ferromagnetic frustrated chain system in an applied magnetic field has attracted great interest as a prototypical model exhibiting a spin nematic state. Theoretically, it has been shown that the spin nematic state exists near the saturation, while a vector chiral state occurs with lowering the field [1]. As for the effect of the exchange anisotropy, the spin nematic state is destabilized by the easy-plane anisotropy [2].

In the present work, to clarify the properties of the spin nematic state from the viewpoint of the spin dynamics, we study the dynamical spin structure factor of  $J_1$ - $J_2$  XXZ chains with ferromagnetic  $J_1$  and antiferromagnetic  $J_2$  [3], by exploiting a dynamical DMRG method [4]. Note that the spectral weight at a point  $(q, \omega)$  is calculated by one DMRG run with fixed  $q$  and  $\omega$ , so that numerous runs are required to obtain the spectrum in the wide range of the  $q$ - $\omega$  space. The computations are accelerated by parallel simulations.

Figure 1 presents typical results of  $S^-(q, \omega)$  in the field-induced spin nematic regime. The overall spectral shape is similar even when we consider the exchange anisotropy. The energy of a lowest-energy peak in the XY-like case is decreased, compared with the Heisenberg case, indicating that the gap for the transverse spin excitation is suppressed. Detailed results have been reported in Ref. [3].

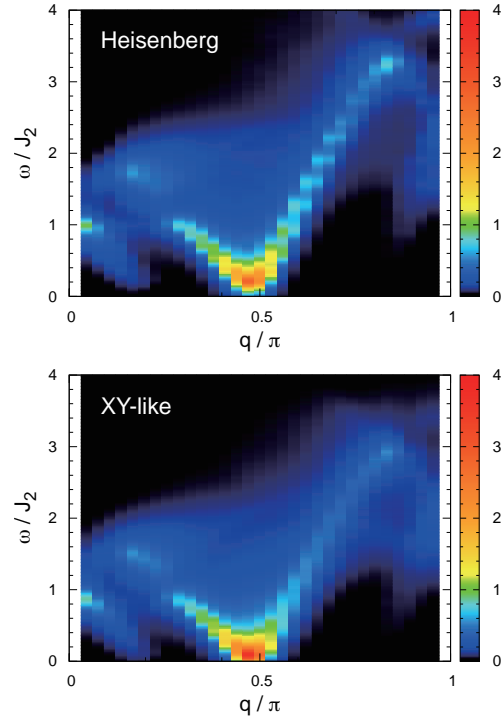


Fig. 1:  $S^-(q, \omega)$  in the Heisenberg case and the XY-like case.

## References

- [1] T. Hikihara, L. Kecke, T. Momoi, and A. Furusaki, Phys. Rev. B **78**, 144404 (2008).
- [2] F. Heidrich-Meisner, I. P. McCulloch, and A. K. Kolezhuk, Phys. Rev. B **80**, 144417 (2009).
- [3] H. Onishi, J. Phys.: Conf. Ser. **592**, 012109 (2015).
- [4] E. Jeckelmann, Phys. Rev. B **66**, 045114 (2002).

# Phonon Effects and Frustration in Quantum Spin Systems

Chitoshi YASUDA

*Department of Physics and Earth Sciences, Faculty of Science,  
University of the Ryukyus, Nishihara, Okinawa 903-0213, Japan*

In quantum spin systems with spin-phonon interactions (phonon systems), novel spin states are often formed due to strong quantum effects and have attracted considerable attention. We can derive effective Hamiltonians of the phonon systems by performing a unitary transformation. The effective Hamiltonians describe frustrated quantum spin systems with competing interactions (frustration systems). In our previous works, we investigated one-dimensional quantum Heisenberg-like models with spin-spin and spin-phonon interactions with a parameter to control a change of a geometric structure and found that the spin-phonon interaction causes the novel phase transition to the spin-liquid phase for some geometric structures [1, 2]. In the present research project, we take into account the next-nearest-neighbor spin-phonon interaction in addition to the nearest-neighbor interaction. The similar model with adiabatic phonons has been investigated in relation to  $\text{LiV}_2\text{O}_5$  and the ground state is suggested to be ‘a new tetramerized phase with three different bond lengths’ [3]. We expect that the new phase realizes also in our system. In order to perform a unitary transformation for the phonon systems with the next-nearest-neighbor spin-phonon interaction, we use the computational software program ‘Mathematica’. The effective Hamiltonian we obtained is expanded by the strength of the spin interaction  $J$  and those of the nearest- and next-nearest neighbor spin-phonon interactions  $g_1$  and  $g_2$ . In the present work, we derived the

effective Hamiltonian of fourth order in  $J$ ,  $g_1$  and  $g_2$ . The Hamiltonian consists of spin interactions up to sixth-nearest-neighbor and four-body interactions. First of all, we neglect long-range interactions and concentrate the nearest- and next-nearest-neighbor interactions. When we put the exchange integrals of the nearest- and next-nearest-neighbor interactions  $J_1$  and  $J_2$ , respectively, we found that the values of  $J_1$  and  $J_2$  become both positive and negative depending on values of  $g_1$  and  $g_2$ . Furthermore, we made the ground-state phase diagram parametrized by  $g_1$  and  $g_2$  by using information of the  $J_1$ - $J_2$  model. As results, various phases appear in the phase diagram, for example, the ferromagnetic, spin-liquid, dimer phases. In particular, for small  $g_1$  and  $g_2$  the range of the spin-liquid phase expands as the value of  $J$  is increased from zero. Currently, in order to investigate properties of the states, we are performing the exact diagonalization of the full effective Hamiltonian and calculating the generalized dimer susceptibility. This work is done in collaboration with Satoru Akiyama (National Institute of Technology, Wakayama College).

## References

- [1] S. Akiyama and C. Yasuda: J. Phys. Soc. Jpn. **80** (2011) 104709.
- [2] C. Yasuda and S. Akiyama: J. Phys. Soc. Jpn. **84** (2015) 014705.
- [3] F. Becca *et al.*: Phys. Rev. Lett. **91** (2003) 067202.

# Efficient Monte Carlo Spectral Analysis and Application to Quantum Spin Systems

Hidemaro Suwa

*Department of Physics, The University of Tokyo  
7-3-1 Hongo, Bunkyo, Tokyo 113-0033*

The energy spectrum of quantum systems reflects rich physics of its excitation and quantum phases. In topologically non-trivial systems, e.g., the toric code, the ground state do not have a classical order, but the system bears the characteristic gap and the fractional excitation that can be detected by experiments. In not only gapful phases but also critical phases, the energy gap of finite-size systems carries abundant physical information about the criticality. As important quantities to understand the thermodynamic phase with conformal invariance, the velocity and the scaling dimensions are efficiently attainable from the spectrum/gap analysis. Moreover, the precise gap calculation at different quantum numbers provides the effective analysis of phase transitions, which has been demonstrated as the level spectroscopy.

The gap calculation of a large-size system is not trivial. The energy gaps of a small-size system can be calculated by the full diagonalization or the Lanczos method. However, the reachable system size is strongly limited by the explosion of the needed memory and CPU cost. In the meanwhile, the worldline quantum Monte Carlo method has been successfully applied to many kinds of quantum systems. Nevertheless, the precise gap calculation by the Monte Carlo method has been a big challenge. It is because the spectrum calculation is nothing but the notorious Inverse Laplace transformation that is known as a numerically ill-posed problem. In the previous approaches, the gap has been obtained by the fitting method of the imaginary-time correlation to the asymptotic

form. This approach, however, has many tricky problems: unknown appropriate fitting region, ignored data correlation, and the trade-off between the systematic and the statistical error.

We have developed a new convergent sequence of the gap estimators using the Fourier transformed correlation functions at several Matsubara frequencies. It has been analytically shown that the estimator converges to the exact gap for discrete spectrum and also for continuum spectrum. Moreover, we have devised the quantum Monte Carlo level spectroscopy that allows for the effective analysis of quantum phase transitions by the accurate and precise gap calculation for larger-size systems than can ever be done. This novel analysis was applied to the  $S = 1/2$  spin-Peierls model, and the non-trivial Kosterlitz-Thouless transition between the Tomonaga-Luttinger liquid phase and the dimer phase was elucidated. We established that the quantum phonon effect is *relevant* to the spin-phonon interaction, or equivalently the (spinless) fermion-phonon interaction, and the universal quantum phase transition described by the  $SU(2)$   $k = 1$  Wess-Zumino-Witten model occurs from the antiadiabatic limit to the vicinity of the adiabatic limit.

We used up the allocated 1,500 points as the class C in the system B (project ID:H26-Cb-0056). Independent Monte Carlo simulations were efficiently run by the MPI parallelization.

## References

- [1] H. Suwa and S. Todo, arXiv:1402.0847.

# Numerical Study of One Dimensional Frustrated Quantum Spin Systems

Kazuo HIDA

*Division of Material Science, Graduate School of Science and Engineering  
Saitama, Saitama 338-8570*

Ground-state phase diagram of the spin-1/2 frustrated ladder

$$\mathcal{H} = \sum_{i=1}^{N/2} \left[ \sum_{\alpha=1}^2 J_L \mathbf{S}_{i,\alpha} \mathbf{S}_{i+1,\alpha} + J_R \mathbf{S}_{i,1} \mathbf{S}_{i,2} + J_D \{ (1 + \delta) \mathbf{S}_{i,1} \mathbf{S}_{i+1,2} + (1 - \delta) \mathbf{S}_{i+1,1} \mathbf{S}_{i,2} \} \right]$$

is investigated. We consider the case of  $J_L < 0$ ,  $J_R < 0$ , and  $J_D > 0$ . This model tends to the ferro(antiferro)magnetic spin-1 chain for  $J_L + J_D < 0(> 0)$  in the limit of  $J_R \rightarrow -\infty$ . We take the unit  $J_D = 1$ .

For  $\delta = 1$ , a series of topologically distinct spin-gap phases are found(Fig. 1(a))[1]. We confirmed that they are characterized by the degeneracy of the entanglement spectrum (ES) by the iDMRG method as shown in Fig. 1(b).

For  $\delta = 0$ [2], the columnar dimer (CD) and nematic (N) phases appear between the Haldane phase, and ferromagnetic or rung-dimer phase. The CD-N phase boundary is determined from the level crossing of the  $S = 0$  (CD) and the  $S = 2$  (N) excited state by the numerical diagonalization up to the size  $N = 32$ . In contrast to the case of spin-1 bilinear-biquadratic chain, the nematic phase has a finite width as shown in Fig. 2(b). Also, different spin gap phases are characterized by the degeneracy of ES as shown in Fig. 2(c). In the CD phase, ES oscillates with the iDMRG steps reflecting the spontaneously dimerized structure.

Even for small  $\delta = 0.1$ , the Haldane phase substantially expands to the region of large negative  $J_L$ , while the nematic phase is stable.

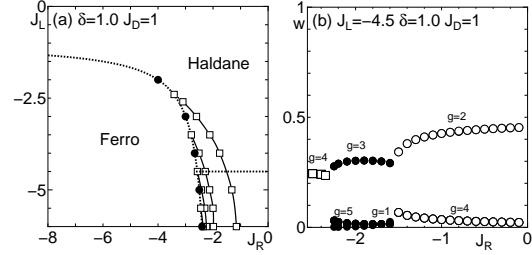


Figure 1: (a) Phase diagram for  $\delta = 1$ . (b) Several largest eigenvalues  $w$  of reduced density matrix and their degeneracy  $g$  along the dotted line of (a).

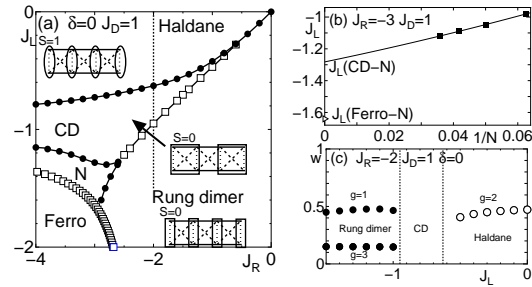


Figure 2: (a) Phase diagram for  $\delta = 0$ . (b) System-size dependence of the N-CD phase boundary for  $J_R = -3$ . (c) Several largest eigenvalues  $w$  of reduced density matrix and their degeneracy  $g$  along the dotted line of (a).

This work is supported by KAKENHI (C) (No. 25400389) from JSPS. The numerical diagonalization program is based on TITPACK ver.2 coded by H. Nishimori.

## References

- [1] K. Hida, K. Takano and H. Suzuki : J. Phys. Soc. Jpn. **82** 064703 (2013).
- [2] T. Hikihara and O. A. Starykh: Phys. Rev. B **81** 064432 (2010).



# High precision computation of Feigenbaum constant, 2nd.

Masanori SHIRO

*HIRI, National Institute of Advanced Industrial Science and Technology*

*Umezono 1-1-1 Central 2, Tsukuba, Ibaraki 305-8568*

A purposes of our project is calculating the second Feigenbaum constant with high precision. The constant correlates with many type of phase transitions strongly. Properties of critical exponents accompanied by the transitions are not necessarily revealed, although the transitions are found in many solid-state materials. We think that phase transitions are able to treat as chaotic transitions. Feigenbaum constant is an universal value between simple chaotic models and fractals. A series expansion for the constant is not known yet. It is just found in almost two hundreds digits in Briggs' thesis.

Basically, the constant is calculated by using an universal function  $g(x)$  which has following properties,

1.  $g(x)$  is an even function.
2.  $g(\alpha x)/\alpha = g(g(x))$
3.  $\alpha = 1/g(1)$
4.  $g(0) = 1$

We tried to find the function using C++ with Eigen and mpreal libraries. However the libraries cannot be installed in the ISSP system. Hence in this year, we wrote an alternative method without use of Eigen. The method is based on piecewise linear function and BOBYQA optimizer. We report our new method in submission, and some of our results

are reported in the annual meetings of JPS. We also found that a realistic digits by our new method is able to retrieve using general computers.

## References

- M. J. Feigenbaum, J. Statistical Physics 21 pp.669-706(1979).
- K. Briggs, Doctoral thesis, University of Melbourne (1997).
- K. Briggs, Math. Comp. 57, pp.435-439 (1991).
- S. H. Strogatz, Nonlinear Dynamics and Chaos, Westview Press (2014).
- M. Campanino, Topology 21 pp.125-129 (1982).
- K. Karamanos and I.S. Kotsireas, J. Franklin Institute (2005).
- M. Shiro, JPS abstracts in 2014 spring: 29pAD11 (2014).
- M. Shiro, JPS abstracts in 2014 autumn: 9aAN-12 (2014).
- <http://ab-initio.mit.edu/wiki/index.php/NLopt>.
- M. J. D. Powell, Report of Department of Applied Mathematics and Theoretical Physics, Cambridge University DAMTP (2009).

# Universality class of thermally equilibrium states for cold atoms with internal degrees of freedom

Michikazu KOBAYASHI

*Department of Physics and Astronomy, Graduate School of Science, Kyoto University  
Oiwakecho, Sakyo-ku, Kyoto 606-8502*

Ultracold atomic systems with internal degrees of freedom such as atomic spins show their ground states with various broken symmetries. Some of them are closely related to other condensed-matter systems and others are quite new ones. Compared to studies about ground states, there are less numbers of studies about properties at finite temperatures, especially, universality class of phase transitions.

In this study, we have concentrated on the properties of phase transitions in two-dimensional spinor Bose systems with  $S = 1$  spins. Compared to spinless Bose systems with quantized vortices with topological charge classified as  $\mathbb{Z}$ , various kinds of quantized vortices can be possible to exist for their ground states. For two-dimensional systems with broken continuous symmetry at the zero temperature, they show so-called Kosterlitz-Thouless (KT) transition at finite temperature. Because quantized vortices play key roles for the KT transition, we can expect various kinds of KT transition being related to properties and topological charges of quantized vortices.

Hamiltonian  $H$  of  $S = 1$  spinor Bose system can be written as follows

$$\begin{aligned} H &= H_0 + \int d^2x \left( \frac{g_0}{2} \rho + \frac{g_1}{2} \mathbf{S}^2 \right), \\ h_0 &= \int d^2x \sum_s (|\nabla \psi_s|^2 + q s^2 |\psi_s|^2), \\ \rho &= \sum_s |\psi_s|^2, \quad \mathbf{S} = \sum_{s_1, s_2} \psi_{s_1}^* \hat{\mathbf{S}}_{s_1, s_2} \psi_{s_2}, \end{aligned} \quad (1)$$

where  $\psi_s$  ( $s = -1, 0, 1$ ) is the field operator of  $S = 1$  bosons,  $q$  is the coefficient of

quadratic Zeeman field,  $\rho$  is the density,  $\mathbf{S}$  is the spin density, and  $g_0$  and  $g_1$  are the spin-independent and spin-dependent coupling constants. Because we are interested in the properties of the KT transition at finite temperatures, we here ignore the commutation relation  $[\psi_{s_1}^*(\mathbf{x}_1), \psi_{s_2}(\mathbf{x}_1)] = \delta_{s_1, s_2} \delta(\mathbf{x}_1 - \mathbf{x}_2)$  which are effective only near the zero temperature. Depending on  $q$  and  $g_{0,1}$  there are 8 characteristic ground state phases in this system (see Fig. 1).

By using the replica-exchange Monte Carlo method, we obtain the equilibrium values with the probability density  $P \propto e^{-H/T}$  with the temperature  $T$ . Here, we are interested in the order parameters for the global phase  $M_\phi$  and the spin  $M_S$ , and the helicity modulus for the global phase twisting  $\Upsilon_\phi$  and the spin twisting  $\Upsilon_S$ . In the following, we report our numerical results for all of 8 phases shown in Fig. 1.

Phase (i) : Ferromagnetic phase without quadratic Zeeman field. The order-parameter manifold is  $G/H \simeq SO(3)$  (same as Heisenberg antiferromagnet in the triangular lattice) and the topological charge of vortices is classified as  $\pi_1(G/H) \simeq \mathbb{Z}_2$ . In this phase, the mass current and the spin current are equivalent, and two order parameters  $M_\phi$  and  $M_S$  and helicity moduli  $\Upsilon_\phi$  and  $\Upsilon_S$  take same values. Our result shows that KT transition seems not to occur, i.e.,  $M_\phi$ ,  $M_S$ ,  $\Upsilon_\phi$ , and  $\Upsilon_S$  vanish at all temperatures except for  $T = 0$ .

Phase (ii) : Ferromagnetic phase with negative quadratic Zeeman field. The order-parameter manifold is  $G/H \simeq \mathbb{Z}_2 \times U(1)$ ,

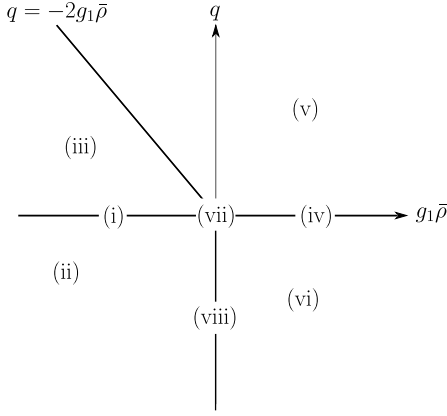


Figure 1: Ground-state phase diagram of the  $S = 1$  spinor Bose system.  $\bar{\rho} = \langle \rho \rangle$  is the mean density.

where  $\mathbb{Z}_2$  and  $U(1)$  come from the phase and spin parts respectively. Besides vortices for  $\pi_1(G/H) \simeq \mathbb{Z}$ , there exist domain walls classified as  $\pi_0(G/H) \simeq \mathbb{Z}_2$  (same as domain walls in the Ising ferromagnet) due to the discrete symmetry  $\mathbb{Z}_2$ . This discrete symmetry makes the thermodynamic phase transition possible for the spin part  $M_S > 0$  at  $T > T_c$ . At the same temperature  $T_c$ , KT transition occurs  $\Upsilon_\phi > 0$  for the phase part. Topological jump at the critical temperature  $\Delta\Upsilon_\phi = \Upsilon(T = T_c - 0) - \Upsilon_\phi(T = T_c + 0)$  is about 2 times larger than the topological jump  $\Delta\Upsilon_0$  for the spinless Bose system, meaning that the circulation of vortices contributing the KT transition is the half of that for vortices in the spinless Bose system. Circulations of vortices in the bulk and the domain walls are the same and the half respectively, and vortices in the domain walls play important roles for the KT transition.

Phase (iii) : Broken-axisymmetric phase. The order-parameter manifold  $G/H \simeq U(1) \times U(1)$  giving  $\pi_1(G/H) \simeq \mathbb{Z} \times \mathbb{Z}$ . Here, the phase and spin parts are completely separable, and KT transition of each parts for  $\Upsilon_\phi > 0$  and  $\Upsilon_S > 0$  occur at the different temperatures. Topological jumps become  $\Delta\Upsilon_\phi = \Delta\Upsilon_S = \Delta\Upsilon_0$ .

Phase (iv) : Antiferromagnetic phase with negative quadratic Zeeman field. The order-parameter manifold  $G/H \simeq \{U(1) \times U(1)\}/\mathbb{Z}_2$  giving  $\pi_1(G/H) \simeq \mathbb{Z} \times \mathbb{Z}$ . Being different from phase (iii), phase and spin parts are not separable, and both KT transitions for  $\Upsilon_\phi > 0$  and  $\Upsilon_S > 0$  occur at the same temperatures. Topological jumps become  $\Delta\Upsilon_\phi = \Delta\Upsilon_S = 2\Delta\Upsilon_0$  due to  $\mathbb{Z}_2$  symmetry of  $G/H$ .

Phase (v) : Antiferromagnetic phase with positive quadratic Zeeman field. The order-parameter manifold  $G/H \simeq U(1)$  for  $G/H$  comes from the phase part and the spin part is vanished in this phase, giving the same properties for the system of spinless bosons. KT transition, therefore, occurs only for the phase part:  $\Upsilon_\phi > 0$  and  $\Upsilon_S = 0$ . Topological jumps become  $\Delta\Upsilon_\phi = \Delta\Upsilon_0$ .

Phase (vi) : Antiferromagnetic phase without quadratic Zeeman field. The order-parameter manifold  $G/H \simeq \{U(1) \times S^2\}/\mathbb{Z}_2$  giving  $\pi_1(G/H) \simeq \mathbb{Z} \times \mathbb{Z}_2$ . The phase and spin parts for  $G/H$  are  $U(1)/\mathbb{Z}_2$  and  $S^2/\mathbb{Z}_2 \simeq \mathbb{R}P^2$  respectively, and corresponding topological charge are  $\mathbb{Z}$  and  $\mathbb{Z}_2$ . Similar to phase (v), KT transition occurs only for the phase part  $\Upsilon_\phi > 0$  and  $\Upsilon_S = 0$ . Topological jumps become  $\Delta\Upsilon_\phi = 2\Delta\Upsilon_0$  due to  $\mathbb{Z}_2$  symmetry of  $G/H$ .

Phase (vii) : Nonmagnetic phase without quadratic Zeeman field. The order-parameter manifold  $G/H \simeq S^5$  giving  $\pi_1(G/H) \simeq 1$ . There is no vortex in this phase and KT transition does not occur.

Phase (viii) : Nonmagnetic phase with negative quadratic Zeeman field. The order-parameter manifold  $G/H \simeq SU(2)$  giving  $\pi_1(G/H) \simeq 1$ . There is no vortex in this phase and KT transition does not occur.

# Search of close packing states of multicomponent hard-sphere systems by the parallelized Wang-Landau sampling

Tomoaki NOGAWA

*Faculty of Medicine, Toho University*

*5-21-16, Omori-Nishi, Ota-ku, Tokyo 143-8540*

To understand the particle configuration of glass materials, we investigate the densest packing of hard spheres. One of our interest is what kind of mixing of particle species, which is distinguished by particle size, makes disordered solid state stable. This may provide a strategy to find good composition of metal elements for a metallic glass material. To make the problem simple, we consider the state with minimal parameters, i.e., at infinite pressure.

As is known, the glassy disordered solid is a nonequilibrium state in principle, and the equilibrium ground state at infinite pressure is a segregated crystal in the thermodynamic limit. To treat disordered configurations, we use finite size amorphous drops. We apply the Wang-Landau sampling method [1,2] to an off-lattice system: monodisperse and bidisperse hard-spheres trapped by the harmonic potential. The goal is to obtain the densest packing state, which is represented by the lowest potential energy, efficiently. This is a hard optimization problem, particularly in the glassy bidisperse system, where diverging number of metastable states exist. When the system is trapped in a metastable state, the speed of updating the state in the simulation is crucially slowed down in ordinary Markov-Chain Monte-Carlo simulations.

The Wang-Landau sampling is usually used to calculate physical quantities in thermal equilibrium via learning the density of states of the system. In the final regime of this learning,

the system moves in the corresponding reduced state space freely like a random-walk. This means the time evolution is free from trapping in a local minimum. We can utilize this property to solve optimization problem.

In the present numerical simulation, we learn the density of state with three arguments: the number of particles of type I, the number of particles type II, and potential energy. In this case, we have to treat a three-dimensional state space, which is too large to explore. To improve the efficiency, we perform parallel computing by using replica exchange method customized for the Wang-Landau sampling [3].

We faced to a difficulty that the criterion of the finishing of the learning of the density state has not been never satisfied even for a small-size systems. This seems due to some property of off-lattice systems. To avoid this problem, we extrapolate the density of state of higher density region to estimate the the densest point. This works well for monodisperse systems and we continue to explore bidisperse systems.

## References

- [1] F. Wang and D. P. Landau, Phys. Rev. Lett. **86** (2001) 2050.
- [2] D. P. Landau, S.-H. Tsai, and M. Exler, Am. J. Phys. **72** (2004) 1294.
- [3] T. Nogawa, H. Watanabe and N. Ito, Phys. Rev. E, **84** (2011) 061107.

# Topological quantum-number projection in variational Monte Carlo method

Satoshi MORITA

*Institute for Solid State Physics, The University of Tokyo  
Kashiwa-no-ha, Kashiwa, Chiba 277-8581*

Calculation of the ground and excited states of quantum many-body systems is one of the main topics in computational physics. There are several high-precision numerical methods of obtaining the low-energy eigenstates of strongly correlated electron systems. Among others, the variational Monte Carlo (VMC) method based on the variational principle and the Monte Carlo sampling is a powerful tool without the negative-sign problem. Accuracy of this method is determined by a choice of variational wave functions. To reduce biases of the variational wave functions, Tahara and Imada proposed the many-variable variational Monte Carlo (mVMC) method combining with the quantum-number projection techniques [1] and we are developing it. This method uses a generalized one-body part of the variational wave functions so that they can compare competing states on equal footing. The quantum-number projections for the total spin and momentum not only enable higher accuracy but also allow us to calculate the energy gaps and excitation spectra directly.

We developed a generalized VMC method applicable in the presence of relativistic spin-orbit interactions [4]. The generalized wave function can describe a wide class of quantum states including topologically non-trivial states. In addition, we newly introduced quantum number projections which imposed the conservation of Wilson loops in the Kitaev

model. Our wave function with these quantum number projections reproduced the Kitaev spin liquid and its topological degeneracy of the ground states with high accuracy.

As an application of the mVMC method, we also investigated a spin  $1/2$   $J_1$ - $J_2$  Heisenberg model on the triangular and square lattices [2, 3]. This model is one of the simplest models proposed for the quantum spin liquid, which does not have any long range order even at zero temperature because of strong geometrical frustration and quantum fluctuation. The wave function of mVMC is able to describe the exact ground state of the  $4 \times 4$  system on the square lattice and provides higher accuracy than the conventional VMC method. Direct calculation of the triplet spin gap enables us to clarify the natures of the quantum spin liquid phase.

## References

- [1] D. Tahara, M. Imada: J. Phys. Soc. Jpn., **77** 114701, (2008).
- [2] R. Kaneko, S. Morita, and M. Imada: J. Phys. Soc. Jpn. **83**, 093707 (2014).
- [3] S. Morita, R. Kaneko, and M. Imada: J. Phys. Soc. Jpn. **84**, 024720 (2015).
- [4] M. Kurita, Y. Yamaji, S. Morita, and M. Imada: arXiv:1411.5198.

# Numerical Study of Long-Range Magnetic Correlations Based on the Nonlocal Dynamical CPA

Yoshiro KAKEHASHI and Sumal CHANDRA

*Department of Physics and Earth Sciences, Faculty of Science, University of the Ryukyus,  
1 Senbaru, Nishihara, Okinawa, 903-0213, Japan*

Recent study of the first-principles dynamical CPA has clarified that the single-site theory overestimates the Curie temperatures ( $T_C$ ) of Fe and Co by a factor of 1.8 [1]. One has to take into account the long-range inter-site correlations being characteristic of the metallic magnetism, in order to obtain quantitative value of  $T_C$ . Towards quantitative calculations of finite-temperature magnetism we have developed the dynamical cluster CPA which describes the long-range nonlocal correlations making use of the off-diagonal effective medium and the incremental cluster expansion.

In the dynamical cluster CPA, we transform the two-body interaction into a time-dependent dynamical potential in random charge and exchange fields, and introduce the off-diagonal effective medium  $\Sigma_{ij}(i\omega_l)$ . The free energy is given by an effective potential  $E_{\text{eff}}(\xi)$  projected onto the static exchange field  $\{\xi_i\}$ . The latter is obtained by the incremental cluster expansion. The medium is obtained from the stationary condition for the free energy; the self-energy is given by the average  $\mathcal{T}$  matrix for multiple scattering,  $\langle\mathcal{T}\rangle$ . The latter is again calculated by using the incremental cluster expansion, so that we obtain a self-consistent loop as shown in Fig. 1. The average  $\mathcal{T}^{(c)}$  matrices for clusters are calculated by making use of the isothermal molecular dynamics method.

Figure 2 shows a numerical example of magnetization vs temperature curve for the single-band Hubbard model on the fcc lattice in the high-temperature approximation. Calculated  $T_C$  is reduced by 14% due to the long-range non-local static correlations. The dynamical

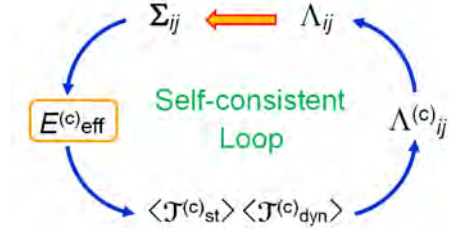


Figure 1: Self-consistent loop in the non-local dynamical CPA.

cal correlations are expected to reduce further  $T_C$ . The calculations including the dynamical terms are in progress.

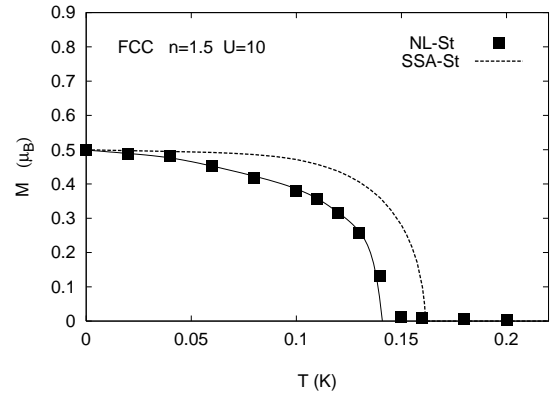


Figure 2: Calculated magnetization vs. temperature curves for the single-site static CPA (dashed-line) and the nonlocal dynamical CPA in high-temperature approximation (closed squares with thin line).

## References

- [1] Y. Kakehashi: 'Modern Theory of Magnetism in Metals and Alloys' (Springer, Heidelberg, 2013).

# Molecular dynamics simulation of ferroelectrics using shell models

T. Hashimoto

*Nanosystem Research Institute (NRI),*

*National Institute of Advanced Industrial Science and Technology (AIST),*

*Tsukuba Central 2, 1-1-1 Umezono, Tsukuba, Ibaraki 305-8568, Japan*

KNbO<sub>3</sub> is an ABO<sub>3</sub> type perovskite whose solid solution with other A site atoms could be a potential candidate for Pb free ferroelectric and piezoelectric materials. Just like BaTiO<sub>3</sub>, KNbO<sub>3</sub> undergoes phase transitions between cubic (C), tetragonal (T), orthorhombic (O), and rhombohedral (R) phases as the temperature is decreased, and it shows temperature as well as direction dependent susceptibilities.

We used the smooth particle mesh Ewald method for computing the Coulomb interactions. The Nosé-Hoover chain method and the Parrinello-Rahman method were used for generating constant temperature and constant pressure (NPT) ensembles. The externally applied pressure was set to 0 Pa.

In the MD simulation by Sepiarsky *et al.*[1], the susceptibility is calculated for only in one direction by applying an electric field. In this study, we calculated the susceptibility tensor of KNbO<sub>3</sub> by using a fluctuation formula, because applying an electric field in the direction that is not parallel to the macroscopic polarization often makes the system unstable.

The anisotropies and the overall temperature dependence of the experimental susceptibilities were reproduced in this study. Compared to the susceptibility of BaTiO<sub>3</sub> by using a shell model in which they are seriously underestimated[2], the present results are in better agreement with experiments. In this paper, the density of probability (DOP) of the local polarization is compared to previous results

for BaTiO<sub>3</sub>[2, 3, 4]. It is shown that the DOP's are more widely distributed around their average values compared to those for the shell model result of BaTiO<sub>3</sub>. This leads to larger fluctuations of the total dipole moments of the MD cell and to larger susceptibilities.

## References

- [1] M. Sepiarsky, S. R. Phillpot, D. Wolf, M. G. Stachiotti, and R. L. Migoni, *Appl. Phys. Lett.* **76** (2000) 3986.
- [2] T. Hashimoto and H. Moriwake, *Molecular Simulation*, in press.
- [3] G. Geneste, *Phys. Rev. B* **79** (2009) 144104.
- [4] G. Geneste, *J. Phys.: Condens. Matter* **23** (2011) 125901.

# Large scale dense hard sphere molecular dynamics simulation in the nonequilibrium phase transition

Masaharu ISOBE

*Nagoya Institute of Technology*

*Gokiso-cho, Showa-ku, Nagoya, 466-8555*

In this project, we investigated nonequilibrium phenomena and phase transition in the hard core model system by using event-driven molecular dynamics (EDMD) [1] and event-chain Monte Carlo (ECMC) [2].

(i) *Dynamic Facilitation in Binary Hard Disk Systems*: Important predictions of dynamic facilitation theory (DynFT) for structural glass forming materials, results like the parabolic law of transport properties, and the non-equilibrium phase transition in the trajectory space with the  $s$  field (i.e., the so-called “s-ensemble”), have been tested with lattice models and continuous force atomistic models [3]. We provide extensions of DynFT to hard disk systems. It is well known that the rapid decreasing temperature (i.e., quenching) such as the soft disk system show the variety of transitions from liquid state to crystallization or supercooled liquid in which kinetic temperature  $T$  is one of the primary control parameter. On the contrary, in the hard disk system, since there is no kinetic temperature (energy) scale, the thermodynamic properties in the system can only be described by the pressure  $p$ . As quenching soft disk system, compressing hard disk system have been expected to show the behavior of glass. In this work, extended dynamic facilitation theory as a function of pressure in the “supercompressed” liquid of additive binary hard disk mixture is numerically investigated. We consider three generalized equations of DynFT, in which the usual dependence on inverse temperature,  $1/T$  is replaced

by dependence on pressure  $p/T$ . We confirmed generalized DynFT equations numerically by extensive systematic simulations with efficient algorithm [1, 2].

(ii) *Hard-sphere melting and crystallization with Event-Chain Monte Carlo*: The crystallization and melting process of three-dimensional hard spheres is simulated in systems with up to one million particle with local and Event-Chain Monte Carlo (MC), as well as with Molecular Dynamics (MD). We concentrate on the nucleation process above the density of the coexistence regime. We find the CPU speed depends on system size, density, and optical chain length of ECMC. We conclude that ECMC with the optimal chain length have a great advantage on the simplicity and complexity of algorithm in case of dense and large particle number, which results in the efficiency and reduction of actual CPU hour.

## References

- [1] M. Isobe: Int. J. Mod. Phys. C **10** (1999) 1281.
- [2] E. P. Bernard, W. Krauth, and D. B. Wilson: Phys. Rev. E **80** (2009) 056704.
- [3] D. Chandler and J. P. Garrahan, Annu. Rev. Phys. Chem. **61** (2010) 191.; L. O. Hedges, R. L. Jack, J. P. Garrahan and D. Chandler, Science **323** (2009) 1309.; A. S. Keys, L. O. Hedges, J. P. Garrahan, S. C. Glotzer, and D. Chandler, Phys. Rev. X, **1** (2011) 021013.



# Molecular Simulation Study of Micellar Shape Change in Amphiphilic Solution

Susumu FUJIWARA

*Graduate School of Science and Technology, Kyoto Institute of Technology*

*Matsugasaki, Sakyo-ku, Kyoto 606-8585*

Amphiphilic molecules such as lipids and surfactants contain both a hydrophilic group and a hydrophobic group. In aqueous solutions, amphiphilic molecules spontaneously self-assemble into various structures such as micelles, vesicles, and bicontinuous structures [1-3]. Self-assembly of amphiphilic molecules is of great importance in many biological and industrial processes. Although several computer simulations have so far been performed on the micelle formation, there have been few simulation studies on the micellar shape change. The purpose of this study is to clarify the effect of molecular rigidity on micellar shape change in amphiphilic solutions. With a view to investigating the micellar shape change in amphiphilic solutions at the molecular level, we perform the molecular dynamics (MD) simulations of coarse-grained semiflexible amphiphilic molecules with explicit solvent molecules and analyze the dynamical processes of micellar shape change.

The computational model is the same as that used in the previous work [4]. An amphiphilic molecule is modeled as a semiflexible chain

which is composed of one hydrophilic head particle and three hydrophobic tail particles. A solvent molecule is modeled as a hydrophilic particle. Particles interact via the non-bonded potentials and the bonded potentials. As for non-bonded potentials, the interaction between a hydrophilic particle and a hydrophobic particle is modeled by a repulsive soft core potential and all other interactions are modeled by a Lennard-Jones potential. As bonded potentials, we consider a bond-stretching potential and a bond-bending potential. The molecular rigidity is controlled by the bending modulus  $k_3^*$  of the bond-bending potential.

The equations of motion for all particles are solved numerically using the velocity Verlet algorithm at constant temperature with a time step of  $\Delta t^* = 0.0005$  and the temperature is controlled at every 10 time steps by ad hoc velocity scaling. We apply the periodic boundary conditions and the number density is set to  $\rho^* = 0.75$ . Initially, we prepare an isolated micelle of 120 flexible amphiphilic molecules with a certain value of the bending modulus  $k_3^*$  in solutions. The number of

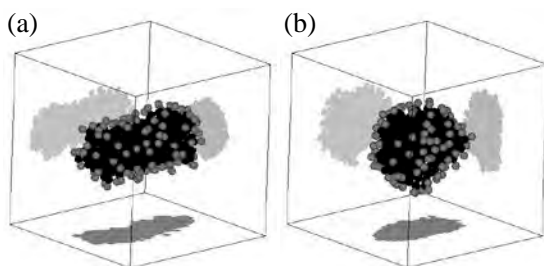


Fig. 1: Snapshots of micelles formed by amphiphilic molecules after sudden increase of  $k_3^*$  from 4.0 to 16.0 (a) at  $t^* = 0$  and (b) at  $t^* = 200$ . Light gray and dark gray particles denote hydrophilic head particles and hydrophobic tail particles, respectively. Solvent molecules are not displayed for clarity.

solvent molecules is 7520, which leads to the amphiphilic concentration of 0.06. The bending modulus  $k_3^*$  is then changed to various values suddenly and MD simulations of  $t^* = 5.0 \times 10^3$  ( $1.0 \times 10^7$  time steps) are carried out for each simulation run.

In our previous paper [4], we found that the dominant micellar shape at  $k_3^* = 4.0$  is a cylinder and that at  $k_3^* = 16.0$  is a disc. Here we examine the micellar shape change between a cylinder and a disc by sudden increase or decrease of the bending modulus  $k_3^*$ . In Fig.1, we show our simulation results in the case of sudden increase of  $k_3^*$  from 4.0 to 16.0. Gray shadows of the amphiphilic molecules projected on three planes are also depicted in this figure to show the micellar shape clearly. This figure tells us that the micellar shape changes from a cylinder to a disc as the intensity of the molecular rigidity,  $k_3^*$ ,

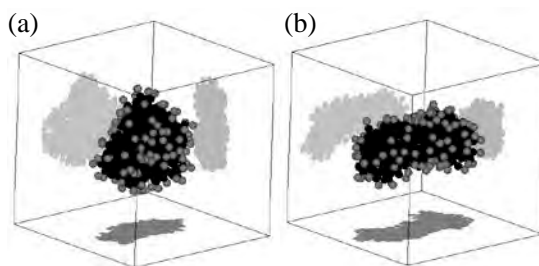


Fig. 2: Snapshots of micelles formed by amphiphilic molecules after sudden decrease of  $k_3^*$  from 16.0 to 4.0 (a) at  $t^* = 300$  and (b) at  $t^* = 500$ . Light gray and dark gray particles denote hydrophilic head particles and hydrophobic tail particles, respectively. Solvent molecules are not displayed for clarity.

increases from 4.0 to 16.0. Simulation results in the case of sudden decrease of  $k_3^*$  from 16.0 to 4.0 are shown in Fig.2. This figure indicates that the micellar shape changes from a disc to a cylinder as the intensity of the molecular rigidity,  $k_3^*$ , decreases from 16.0 to 4.0.

## References

- [1] J. N. Israelachvili: *Intermolecular and Surface Forces*, 2nd ed. (Academic Press, London, 1992).
- [2] *Micelles, Membranes, Microemulsions, and Monolayers*, edited by W. M. Gelbart, A. Ben-Shaul and D. Roux (Springer-Verlag, New York, 1994), pp. 1-104.
- [3] I. W. Hamley: *Introduction to Soft Matter*, Rev. ed. (J. Wiley, Chichester, 2007).
- [4] S. Fujiwara, T. Itoh, M. Hashimoto, H. Nakamura and Y. Tamura: *Plasma Fusion Res.* **5** (2010) S2114.

## Numerical Diagonalization Study of the Spin-1/2 Heisenberg Antiferromagnet on the Cairo-Pentagon Lattice

Makoto ISODA<sup>1</sup>, Hiroki NAKANO<sup>2</sup>, and Tōru SAKAI<sup>2,3</sup>

<sup>1</sup> *Department of Science Education, Faculty of Education, Kagawa University  
Takamatsu 760-8522*

<sup>2</sup> *Graduate School of Material Science, University of Hyogo, 3-2-1 Kouto, Kamigori-cho, Akou-gun,  
Hyogo 678-1297, Japan*

<sup>3</sup> *Japan Atomic Energy Agency, SPring-8, Sayo 679-5148, Japan*

Two-dimensional frustrated spin-1/2 Heisenberg antiferromagnet on the Cairo-pentagon lattice<sup>1,2</sup> has been investigated by the numerical diagonalization method on the finite-size clusters up to 36 sites<sup>3,4</sup> with the periodic boundary condition.

The lattice is constituted with the three-coordinated A-sites and the four-coordinated B-sites in the occupation ratio of 2 to 1. Hence the Heisenberg-type Hamiltonian requires two-types of nearest neighbor interactions, such as  $J = J_{AA}$  and  $J' = J_{AB}$ , at least.

The magnetization under the magnetic field has been calculated. The so-called 1/3-plateau is observed for every value of  $x \equiv J/J'$ , with the exceptional narrow region around  $x \sim 0.8$ , where the plateau may vanish or survive with a narrow width in the thermodynamic limit. The magnetization jumps accompanying the change of the total spin  $\Delta S_t \geq 2$  are observed at the upper-field edge of the 1/3-plateau for  $0 < x < 0.8$  and at the lower-field edge of the 1/3-plateau for  $0.8 < x < 2.0$ . Such jump in the isotropic spin system is peculiar and has been found in some spin frustrated systems<sup>5</sup>. The mechanism is attributed to the spin flop transition under the isotropic spin system<sup>3,5</sup> and is confirmed by the drastic change in the correlation function and the local magnetizations  $m_A$

and  $m_B$  as functions of  $x$ .

From the results of the magnetization process and the nn correlation functions for the longitudinal ( $z$ -axis) and the transverse components, the magnetic phase diagram was derived in the plane of  $x - h/J$ , where  $h$  is the magnetic field applied along the  $z$ -axis.

The specific heat and the magnetic susceptibility have also been calculated by using the Householder algorithm for the 18-site cluster with periodic boundary condition<sup>4</sup>. The obtained characteristic feature is that the specific heat shows the double peak structure. The lower peak gradually approaches to the higher peak, which reveals at the temperature corresponding to  $J$ , with increasing  $x$ .

### References

- 1) E. Ressouche et al.: Phys. Rev. Lett. **103** (2009) 267204.
- 2) I. Rousochatzakis et al.: Phys. Rev. B **85** (2012) 104415.
- 3) H. Nakano, M. Isoda, and T. Sakai: J. Phys. Soc. Jpn. **83** (2014) 053702.
- 4) M. Isoda, H. Nakano, and T. Sakai: J. Phys. Soc. Jpn. **83** (2014) 084710.
- 5) H. Nakano, T. Sakai, and Y. Hasegawa: J. Phys. Soc. Jpn. **83** (2014) 084709.

## 3.5 CMSI projects

# Nonadiabatic electron dynamics and many-body nuclear dynamics in molecules

Satoshi TAKAHASHI and Kazuo TAKATSUKA

*Department of Basic Science, Graduate School of Arts and Sciences, University of Tokyo  
Komaba, Meguro, Tokyo 153-8902*

To understand the quantum effects of heavy particles (nuclei) in chemical reactions, it is necessary to track the wavepacket dynamics during the reactions. However, even with the modern massive parallel computers, it is still prohibitive to perform a primitive fully-quantum wavepacket dynamics simulations, because the required amount of calculation grows exponentially with the number of degrees of freedom. To overcome such a situation, we have been continuing researches based on the action decomposed function (ADF) [1, 2].

In the theoretical framework of ADF, wavepacket dynamics is described in terms of an ensemble of classical trajectories. Starting from the linear fundamental equation of ADF, it is found that dynamics is decomposed into two terms. One is proved to represent geometry of small spatial region around the reference trajectory, and the other is the “diffusion operator” with a pure imaginary diffusion constant.

Our preliminary numerical studies have already shown that the geometrical change around the reference path is described well with the nearby running ones, and also that quantum effects are able to be well incorporated thereby. These facts provide a significant advantage for the calculations of real systems with many dimensions, because a reference trajectory is reused as a nearby for some other nearby paths. Although we have not embarked on practical massive parallel computations based on this theory, we are going to

make a start of many-body nuclear dynamics simulation, further proceeding to the connection to nonadiabatic electron dynamics.

Besides the advantage of describing multidimensional wavepacket dynamics, because of its structure, ADF theory also possesses an ability to reveal the quantum-classical correspondence in detail. Our previous study has made it clear that energy quantization is performed with action integrals and the so-called Maslov phases in the semiclassical regime [3]. However, such semiclassical phase quantization can yield a small deviation in the energy values, which becomes non-negligible when the Planck constant is large. We have performed many trajectory calculations to construct quasi-correlation function, leading to the quantized energies for multidimensional chaotic systems. Analyses of them via the ADF are now underway to lead to both more accurate description of energy quantization and better understanding of the role of the quantum phase in the wavepacket dynamics.

## References

- [1] S. Takahashi and K. Takatsuka: Phys. Rev. A **89** (2014) 012108.
- [2] K. Takatsuka and S. Takahashi: Phys. Rev. A **89** (2014) 012109.
- [3] S. Takahashi and K. Takatsuka: J. Chem. Phys. **127**, (2007) 084112.

# Density-matrix renormalization group study of the extended Kitaev-Heisenberg model

Takami TOHYAMA

*Department of Applied Physics, Tokyo University of Science, Tokyo 125-8585*

The Kitaev-Heisenberg (KH) honeycomb lattice model has recently been proposed to describe magnetic properties in  $A_2\text{IrO}_3$  ( $A = \text{Na, Li}$ ). The model includes an isotropic Heisenberg term and strongly anisotropic Kitaev terms. However, it has turned out that the KH model cannot straightforwardly explain a zigzag-type antiferromagnetic order observed in  $\text{Na}_2\text{IrO}_3$ . This discrepancy has inspired further studies about more suitable effective spin models for  $\text{Na}_2\text{IrO}_3$ . For example, anisotropic interactions due to trigonal distortions [1] have been introduced to the KH model to explain the zigzag order.

Motivated by these previous studies, we examine an extended KH model including such anisotropic interactions by using two-dimensional density-matrix renormalization group method (2D-DMRG) [2]. The 2D-DMRG calculations are carried out under periodic boundary conditions. We mainly use a system with 6 (along the  $y$  axis)  $\times$  8 (along the  $x$  axis) sites, i.e., a 48-site system. To perform 2D-DMRG, we construct a snakelike one-dimensional chain by combining the eight zigzag lines along the  $y$  axis, leading to a spin chain with long-range interactions. We keep 1000 states in the DMRG block and performed more than 10 sweeps, resulting in a typical truncation error  $5 \times 10^{-6}$  or smaller.

We make a phase diagram of the extended KH model around the Kitaev spin-liquid phase from the ground-state energy and spin-spin correlation functions [2]. Furthermore, we investigate entanglement entropy (EE) and the entanglement spectrum (ES). We find that the lowest level of ES at magnetically ordered states is nondegenerate. This is clearly in contrast to the Kitaev spin-liquid state, where all of ES form pairs. Such a degenerate structure in the Kitaev spin liquid is due to its gauge structure coming from its topological nature, and it depends on the boundary conditions. As a result, the Schmidt gap defined as the energy difference between the lowest and first excited ES changes at the phase boundary between the Kitaev spin liquid and other magnetically ordered phases. However, we find that the Schmidt gap cannot be a good measure of the phase transition between magnetically ordered phases.

## 参考文献

- [1] Y. Yamaji, Y. Nomura, M. Kurita, R. Arita, and M. Imada: Phys. Rev. Lett. **113**, 107201 (2014).
- [2] K. Shinjo, S. Sota, and T. Tohyama: Phys. Rev. B **91** 054401 (2015).

# Study of Novel Quantum Phases and Critical Phenomena by Monte Carlo Method and Tensor Network \*

Naoki KAWASHIMA

*Institute for Solid State Physics,*

*The University of Tokyo, Kashiwa-no-ha, Kashiwa, Chiba 277-8581*

The objective of our group --- the QMC-TN collaboration in CMSI --- is to clarify the novel quantum phase transitions and phases using a massively parallel computation. Our list of specific targets includes (1) to clarify the existence/absence of the novel phase transition called deconfined critical point in the  $SU(N)$  Heisenberg model, and (2) to obtain quantitatively accurate phase diagram of spin-orbit Ir-compounds using the new numerical technique based on the tensor network variational wave functions.

As for the first target, in SY2014, we carried out a large-scale quantum Monte Carlo on the system C of ISSP for the  $SU(N)$  J-Q model at finite temperature. Because of the spontaneously broken discrete symmetry in the VBS phase at zero-temperature, in the VBS region, we are allowed to have a phase transition at finite temperature without violating the Mermin-Wagner theorem. Our calculation [1] revealed that this is indeed the case. We also studied the universality class of this finite-temperature phase transition to find

that it is consistent with the Ashkin-Teller type transition for the square lattice and the 3-state Potts model for the honeycomb lattice. This is in consistent with the natural expectation since the  $Z_4$  symmetry and the  $Z_3$  symmetry are broken in these two cases respectively. Particularly interesting was that the critical index  $\nu$  seems to diverge as we approach the quantum critical point of the square lattice model.

As for the phase diagram of the Iridium-based compounds, we developed an original computer program based on the PEPS wave function and the corner-transfer-matrix renormalization technique for the network contraction. Applying this program, we succeeded in obtaining the phase diagram of the effective model obtained through the first-principles calculation. [2]

[1] T.Suzuki, K.Harada, H.Matsuo, S.Todo and N.Kawashima, Phys. Rev. B **91** 094414 (2014).

[2] T. Okubo et al., unpublished.

\* This work is done in collaboration with Tsuyoshi Okubo and other members of the QMC-TN/CMSI collaboration.

## Multi-scale simulation of nano-structured devices from electronic structures to mechanical properties

Shuji OGATA

*Nagoya Institute of Technology*

*Gokiso-cho, Showa-ku, Nagoya 466-8555, Japan*

In the fiscal year of 2014, we have mainly treated two subjects. One is the hybrid quantum-classical (QM-CL) simulation study of the thermal diffusion of correlated Li-ions in graphite. The other is the rigid-body molecular dynamics study of the quasi-liquid layer of sub-micrometer-scale Ice.

Diffusion of Li-ions in graphite is an essential elementary process in the current lithium-ion battery. The C-layers of graphite deform with Li due to relatively large size of Li-ion, which acts to confine the Li-ions and thereby create correlation between them. We address theoretically the thermal diffusivity of such correlated Li-ions in graphite by the hybrid quantum-classical simulation method. In this method, the quantum-region composed of the Li-ions and surrounding C atoms is treated by the density-functional theory, while it is embedded dynamically in the total system described with an empirical inter-atomic interaction potential. We thereby take into account the long-ranged deformation field in graphite in simulating the Li-ion dynamics.

Two kinds of settings of Li-ions are considered for the simulation runs at temperature 443K: (i) seven Li-ions are inserted in the same inter-layer space of the C-layers to study their intra-plane correlation, and (ii) additional seven Li-ions are inserted in the neighboring space (i.e., fourteen Li-ions totally) to study their inter-plane correlation. As for (i) depicted in Fig. 1, the Li-ions, concentrated initially with inter-ion distances of 2.5-4.2 Å, scatter due to their mutual Coulomb repulsion. After about 1ps, the Li-ions and surrounding C atoms thermalize well with deformed C-layers creating a cage for Li-ions, the radius of which is estimated about 13.5Å from present simulation runs. Diffusivity of Li-ions inside the cage is much higher than that of the cage itself. The long-time diffusion constant of the cage is the same order as that of an isolated Li-ion in graphite.

As for (ii), the Li-ions, concentrated initially in the higher and lower inter-layer spaces of the C-layer, firstly form domains, and then the domains repel each other horizontally. The result is in accord with the experimental finding that the Li-rich and Li-poor planes stack in an alternating sequence in graphite [1].

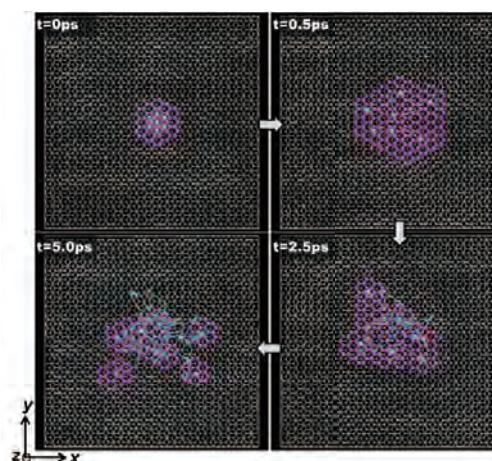


Fig. 1: The snapshots in a hybrid QM-CL simulation run. Cyan and magenta spheres are Li-ions and QM-C atoms, respectively. Gray spheres are CL-C atoms. Cyan curves are the trajectories of Li-ions.

The molecular dynamic simulation of a faceted ice-Ih crystal with the largest dimension of 0.06μm in a vacuum is performed by employing the TIP4P intermolecular potential at temperatures  $T_m - 23$  K,  $T_m - 13$  K, and  $T_m - 1$  K, where  $T_m$  is the melting point of the TIP4P bulk ice. The settings are depicted in Fig. 2. We thereby observe at all the temperatures that the quasi-liquid layers (QLLs) formed on the basal (0001) surfaces are bumpy and that the liquid bumps repeatedly form and break at various places in a random manner. At  $T_m - 1$  K, a liquid sheet appears under the liquid bumps. As explained in Fig. 3, at an





## Materials design for spintronics/multiferroics applications

Mineo SAITO, Tasuki, ODA and Fumiyuki ISHII

*Division of Mathematical and Physical Science, Institute of Science and Technology,  
Kanazawa University, Kakuma, Kanazawa, 920-1192 Japan*

In this project, we have developed codes which enable the study of spintronics and multiferroics materials. We have developed a program code of newly parallelized density functional electronic structure calculations (CPVO). We also make a program that enables drawing spin textures by using numerical results which are calculated by using the OpenMX code. This program is useful to analyze the results of fully-relativistic density functional theory calculations.

We have performed the first-principles density functional calculation for the slab systems; single interface MgO/Fe, magnetic junction Fe/MgO/Fe, the double interface MgO/Fe/MgO, and Fe/TiO<sub>2</sub>/SrO/TiO<sub>2</sub> [1]. To clarify the origin of electric field (EF) effect on the magnetic anisotropy energy from the interface, we discussed the electronic structure of interface Fe atom with using the calculated results. The partial density of states projected to the Fe atom at interface was calculated, for example, as shown in Fig. 1. In these PDOSs, the minority spin states of 3d orbitals are located around the Fermi level ( $E_F$ ). Particularly, the angular orbitals except 3d(3z<sup>2</sup>-r<sup>2</sup>) tends to have a peak on or above  $E_F$ . This is because these

orbitals have no tight covalent bond within plane or to the interface. It was speculated that the important point was a non-linear behavior with respect to in-plane lattice constant. The energy location of Fe 3d (minority spin) states is raised when the lattice constant decreases due to an Fe-Fe orbital hybridization. However, as shown in Fig. 1, the location was lowered at a range of lattice constants. This may be ascribed to an entanglement among the orbital hybridizations of Fe and O atoms and electron exchange-correlations. By solving this entanglement, we could give a plausible explanation to the result about EF effects on MAE. To this end, systematic parallel computation, for example, of a set of many in-plane lattice constants, accelerates or allows us to draw an important insight for magnetic materials in electron junction devises.

We also study the spintronics application of ZnO. Recently, the physical properties induced by spin-orbit coupling (SOC) attract much wide scientific interests because of their applications to the spintronics. Spin textures induced by SOC has been extensively studied because they are crucially important to induce useful physical properties. The spin textures of persistent spin

helix (PSH) has been investigated because it enables long spin life time, and thus new spintronics devices are expected to be achieved. Thus far, PSH has been studied only for zinc-blende semiconductors. We in the first time find that the PSH can be achieved for the wurtzite semiconductors.

We perform fully relativistic first-principles calculation on ZnO (10-10) surface and find the PSH spin textures (Fig. 2). These spin textures are well explained based on a simple spin-orbit Hamiltonian. The calculated values of the spin-orbit strength is comparable with those observed for various zinc-blende quantum well structures. Furthermore, the wavelength of the PSH is much small and thus the miniaturization of device can be achieved. Therefore, this study opens the gateway into the application of wurtzite structure semiconductors to the PSH spintronics.

## References

- [1]D. Yoshikawa et al., JPS Conf. Proc. **5**, (2015) 011012.

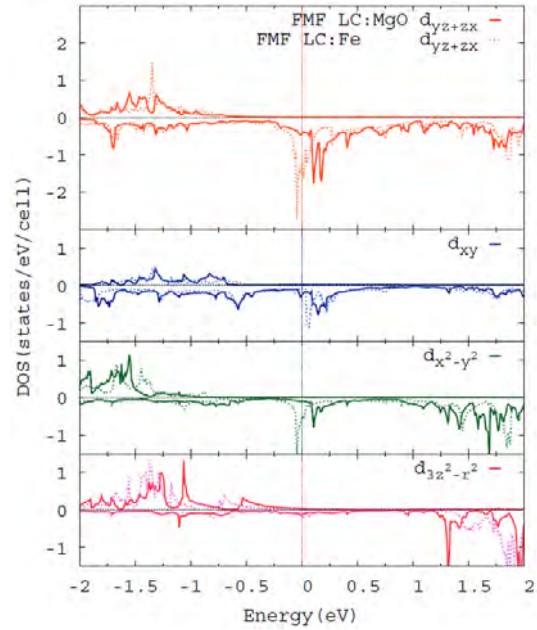


Fig 1. Partial density of states (PDOS) on the Fe atom at interface. The full and dotted curves specify large (bulk MgO) and small (bulk Fe) in-plane lattice constants, respectively.

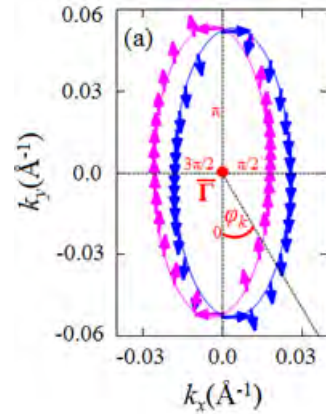


Fig. 2 Spin texture of the ZnO(10-10) slab. The z axis is in the (10-10) axis.

# Large-scale molecular dynamics calculation study of viruses

Susumu Okazaki

*Department Applied Chemistry,*

*Nagoya University, Furo-cho, Chikusa-ku, Nagoya, 464-8603, Japan*

Polio virus capsids are composed of 240 proteins. The diameter is about 30 nm. The system may be constructed in computer by about 6.5-10 million atoms including solvent electrolyte solution. The K-computer is capable of executing MD calculation of this very large system. In a series of this study, calculations have been performed focusing our attention on the stability of the capsids[1]. Then, we extended our calculations to the initial process of infection, i.e. recognition of the capsid by a receptor. In order to investigate the interaction between the poliovirus capsid and the receptor, all-atomistic MD calculations have been performed for the system consisting of a poliovirus capsid and a receptor (CD155-D1) in aqueous electrolyte solution (see Fig. 1).

Last year, we showed attractive interactions found between the virus capsid and the receptor in aqueous electrolyte solution in spite of the same negative sign of the total net charge of each capsid and receptor. This is the first calculation investigating virus infection

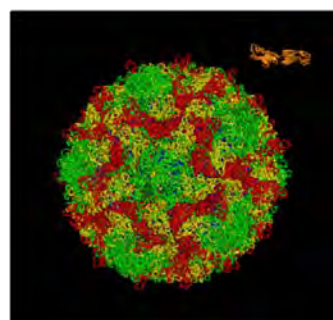


Fig.1 A poliovirus capsid and D1 domain of CD155 receptor in solution. Solvent molecules and ions are not drawn in the figure.

at a molecular level based on the all-atomistic MD calculations. However, statistics was rather small such that we couldn't reach a conclusion that the attraction works between the virus and receptor.

This year, we continued our calculations in order to obtain sufficient statistics to make a conclusion. Statistics of force more than ten times greater than before has been obtained. Based on the calculations, we concluded that the attractive forces do work between the capsid and receptor.

## References

- [1] Y. Andoh et al. *J. Chem. Phys.* **141**, 165101(2014).

# Large scale calculations on the fundamental processes of solar cells and their optimization in conversion efficiency

Koichi YAMASHITA

*Department of Chemical System Engineering,*

*The University of Tokyo, Hongo, Bunkyo-ku, Tokyo 113-8656*

## **1. Density functional based molecular dynamics study on redox potential of $\text{Cu}^{2+/+}$ and $\text{I}^{0/-}$ in non-aqueous solution**

The redox potential calculation using density functional based molecular dynamics simulation (DFT-MD) have been applied and revealed the changes of solvent coordinations of redox reaction in aqueous solution. The method is now applicable to directly compare experimentally observed redox potentials with the help of reference electrode calculation. We establish the calculation method of redox potentials in non-aqueous solution, especially aprotic solvent for understanding and predicting the efficient organic synthesis and devices related electrochemistry because aqueous solution is mere one of solutions.

All the thermodynamic integral methods were performed with CP2K package. The dummy / proton atom,  $\text{I}^{0/-}$  or  $\text{Cu}^{2+/1+}$  were immersed in 44 explicit acetonitrile (AN) molecules under periodic boundary condition. The length of unit cell is set to 15.74 Å to reproduce experimental densities. All quantum chemical calculations were performed with PBE functional, DZVP-MOLOPT-GTH basis set, Goedecker-Teter-Hutter type potential and 280 Ry for cutoff energy of the finest grid level under Gaussian and plane wave mixed basis method (QUICKSTEP). The MD simulations were performed for 6 ps after initial equilibration.

The calculated redox potential of  $\text{I}^{0/-}$  and  $\text{Cu}^{2+/+}$  in AN are in good agreement with experiments. The redox potential estimated with linear response is also good approximation for  $\text{I}^{0/-}$  half reaction in AN because the solvation structure is almost same except for  $r < 4$  Å. On the other hand, the radial distribution functions from Cu atom show that acetonitrile molecules strongly solvate both  $\text{Cu}^{2+/+}$  ions. The solvation numbers of acetonitrile molecule for  $\text{Cu}^{2+}$  and  $\text{Cu}^{+}$  are 5 and 4 in our DFT-MD simulations. This change of coordination number in AN is smaller than that in aqueous solution but affects the redox potential to stray from linear response regime.

## **2. Large scale calculations of electronic excited states of molecular aggregates**

We are, recently, developing software for molecular dynamics, which is based on quantum chemical calculation, on multiple electronic excited states including nonadiabatic effects because photocurrent conversions in organic solar cells take place on the electronic excited states. To do so, we optimized our software to run on the FX10 and K-computer with openMP/MPI hybrid parallelization technique. In detail, load balances between Hartree Fock for the ground state and configurational interaction for excited states are tuned. As a result, our code could obtain strong scalability (more than 10,000 cores) for the calculation of electronic excited states.

# Efficient Implementation of 3D-RISM Theory to the FMO Method, and Its Applications

Norio YOSHIDA

*Department of Chemistry, Graduate School of Sciences  
Kyushu University, Hakozaki, Higashi-ku, Fukuoka 812-8581*

An efficient implementation of the three-dimensional reference interaction site model (3D-RISM) theory to the fragment molecular orbital (FMO) method was proposed.[1] The method is referred to as FMO/3D-RISM method. The method allows us to treat an electronic structure of whole part of macromolecules, such as protein, as well as a solvent distribution around the solute macromolecules. The electrostatic potential should be calculated on grid point in the three-dimensional real space which is used in 3D-RISM theory. Therefore, the reducing the computational cost to calculate the electrostatic potential is most serious concern.

In this article, we propose a procedure to save the computational cost for calculating the electrostatic potential in the framework of FMO method. The strategy of this procedure is to evaluate the electrostatic potential and the solvated Fock matrix in different ways, depending on the distance between solute and solvent. In the vicinity of solute molecule, the electrostatic potential is evaluated directly by integrating the molecular orbitals of monomer

fragments of solute molecule, whereas that is described as the superposition of multipole interactions by using Taylor expansion of the electronic distribution of monomer fragment. The results are compared with those from the other methods. We apply the FMO/3D-RISM method to investigate the selective binding of cellulose by cellulose binding module (CBM).

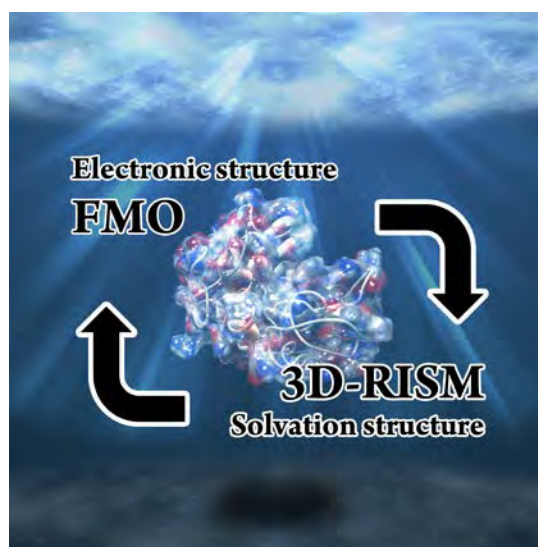


Figure 1: Schematic description of FMO/3D-RISM scheme.

## References

- [1] N. Yoshida, J. Chem. Phys., **140** (2014) 214118

# Fluctuation and surface tension on membrane surface

Hayato SHIBA

*Institute for Solid State Physics, University of Tokyo  
Kashiwa-no-ha, Kashiwa, Chiba 277-8581*

Bilayer membranes can be treated as two-dimensional sheets. They form various forms, for example, vesicles, stomatocytes, and so on owing to its surface elasticity. The energy functional can be written in terms of mean bending curvature  $H = c_1 + c_2$  as

$$\mathcal{H} = \sigma A + \int dA \frac{\kappa}{2} H^2, \quad (1)$$

where  $\sigma$  represents the surface tension,  $A$  is the real area of the membrane. Based on this model, we have recently been performing large-scale simulation of structure formation in surfactant membranes. Recent topic include in my project includes large-scale deformation of multilamellar membranes under shear flow induced by implanted screw dislocations, which is ongoing at present.

This year, as a related problem, we are working on “residual tension” on a fluctuating membrane area. The area can be defined either as a real area or as the area of a projected area, which is two-dimensional area by projecting the membrane area onto an arbitrary plane. The surface tension  $\sigma$  is a quantity that is conjugate to the real area.

If we stretch a membrane surface, the surface area gets extended because of both the stretching of the actual surface and the suppression of fluctuations. The suppressed fluctuation leads to change in the projected area  $A_p$ , and therefore, there can be another definition of surface tension, which is called the “frame tension” in the literature.  $\sigma$  is the other tension which is specifically named “internal tension”. We employ Monte-Carlo simulation on a lattice model of surfactant membrane, in an stress-controlled

extended ensemble. On the membrane surface, we can control both the two tensions *i.e.* frame and internal tensions, and  $A$  and  $A_p$  assumes certain values in accord with these tensions. Whether or not these tensions agrees with each other has been an target issue of discussions for a long time. We have proven using the simulations that the difference between these tension should remain in the thermodynamic limit, and investigated their relation to the effective surface tensions reflecting the cutoff frequency (usually given by the molecular length unit providing the highest cutoff frequency.), on which we are now writing the paper draft[1].

## References

- [1] H. Shiba, H. Noguchi, and J.-B. Fournier, in preparation.

# Computational-Science Study of Frustrated Magnets

Hiroki NAKANO

*Graduate School of Material Science, University of Hyogo  
3-2-1 Kouto, Kamigori-cho, Ako-gun, Hyogo 678-1297, Japan*

Since a quantum spin system is a typical many-body problem, it is difficult to study such systems generally. For the study, computational approaches therefore are quite useful. However, each method has not only merits but also demerits. Quantum Monte Carlo method can treat large systems but faces with a so-called negative sign problem when a system includes frustrations in it. Density matrix renormalization group (DMRG) method can treat systems when they are frustrated but this method is a powerful to a one-dimensional system. The application of this method to systems in dimensions larger than one is now under developing. On the other hand, numerical-diagonalization method is a reliable way irrespective of the point whether or not a system of target magnet is frustrated and irrespective of spational shape of the system. The largest weak point of this method is that this method can treat only very small systems. Under circumstances, we developed an MPI-parallelized code of numerical diagonalizations based on the Lanczos algorithm[1]. This code can treat systems with its sizes that are larger than those determined by computer resources when calculations are carried out in a single node.

The primary study of the present project is to clarify the behavior of the magnetization process of the Heisenberg antiferromagnet on the kagome lattice by means of the Lanczos-diagonalization code mentioned in the above[2]. The magnetization process was originally studied in Ref. 3, in which the existence of the magnetization plateau was pointed out at one-third of the height of the saturation. The plateau was detected in the DMRG calculation with a help of sign-squared deformation in Ref. 4 which reported that a unique and particular quantum state with the nine-

site structure is realized at the plateau. If such a unique state is realized, the critical behavior just outside the plateau is determined by the parabolic dispersion; thus the critical exponent  $\delta$  is supposed to be unity. It was, however, clarified that the critical behavior around the height is different from the conventional one that is widely observed in two-dimensional magnets[5, 6]. Under this controvertial situation, we tackle to obtain a numerical-diagonalization result of the magnetization process of this model with a size that has not been reached before. We successfully calculate the result for a 42-site system by the use of the K computer. This size is the *world record* among all the cases irrespective to lattice structure of the  $S = 1/2$  spin models to the best of our knowledge. The additional and novel result provides us with a more precise estimate of the critical exponents that are different from the conventional  $\delta = 1$ . Our study furthermore the case when the lattice is distorted in the  $\sqrt{3} \times \sqrt{3}$  type. Under controll of the distortion, our result indicates that the undistorted kagome point is just on the boundary between the ferrimagnetic state and the state proposed in Ref. 4. This indication suggests that the state with the nine-site structure as the long-range order is no longer stable at the undistorted kagome point.

Our result of a quantum spin system by large-scale parallelized calculations of Lanczos diagonalization make the true behavior of the system that other methods failed to detect. Our study suggests that large-scale Lanczos diagonalizations continue to contribute much to our understandings of these systems.



## References

- [1] H. Nakano and A. Terai: J. Phys. Soc. Jpn. **78**, 014003 (2009).
- [2] H. Nakano and T. Sakai: J. Phys. Soc. Jpn. **83** (2014) 104710.
- [3] K. Hida: J. Phys. Soc. Jpn. **70** (2001) 3673.
- [4] S. Nishimoto, N. Shibata, and C. Hotta: Nat. Commun. **4** (2013) 2287.
- [5] H. Nakano and T. Sakai: J. Phys. Soc. Jpn. **79** (2010) 053707.
- [6] T. Sakai and H. Nakano: Phys. Rev. B **83** (2011) 100405(R).

# First-principles electronic structure calculation of permanent magnets using the screened KKR Green's function method

Shotaro DOI

*Institute for Solid State Physics, University of Tokyo  
Kashiwa-no-ha, Kashiwa, Chiba 277-8581*

The KKR Green's function method is a method for first-principles electronic structure calculations. In this method, instead of solving eigenvalue problems as in most of band calculation codes, Green's function of the Kohn-Sham equation is directly calculated. By taking the imaginary part of the Green's function, we can obtain the electron density very accurately and efficiently.

The Green's function is calculated from that of an arbitrary reference system by solving the Dyson-type equation. In the process of solving the Dyson equation, inversions of matrices of a dimension proportional to  $N$  ( $N$ : the number of atoms in a unit-cell) is required. In the usual KKR method, the free space is chosen as the reference system. When  $N$  becomes large, the computational cost increases drastically. This is because  $O(N^3)$  operations are required to invert a  $N \times N$  matrix. To overcome this difficulty, the concept of screened KKR was proposed. In the screened KKR method, a system with repulsive muffin-tin potentials of a constant height is chosen as the reference system. In that reference system, the Green's function decays exponentially in real-space if the energy range is sufficiently lower than the repulsive potential height. Then, we can ignore long range propagations without sacrificing the accuracy, which results in the matrix that we should invert being sparse. Therefore, one can expect a substantial improvement of the calculational efficiency through the use of an efficient sparse matrix solver. This technique has been mainly applied to the multi-layered systems which extend to only one dimensional direction assuming two-dimensional periodicity. For such systems, the matrix becomes

block tridiagonal and the computational cost is exactly proportional to the thickness of layer.

It is desirable to apply the screened KKR technique to more general and complex systems which extend to all three dimensional directions. For such general large super-cells, we must treat general non-Hermitian block sparse matrices. As a sparse matrix solver, the iterative method, which is often used to solve linear simultaneous equations with sparse coefficient matrices, is more efficient than the direct method such as the  $LU$ -factorization. This algorithm is also suitable for the parallel computing.

We developed a full-potential based screened KKR code which can treat such large super-cells by combining the iterative method for solving the Dyson equation with parallel computing techniques [1]. Through the test calculations, it has been shown that our code is reliable and well parallelized w.r.t the number of atoms in the super-cell, also confirming that our code runs on the FX10 computer without any trouble. By the use of our code, it is possible to execute the all-electron level first-principles calculations for super-cells which include thousands of atoms within a reasonable time. We also implemented the routines to calculate the effective magnetic exchange interactions *ab-initio*, which is very useful for studying permanent magnetic materials.

## References

- [1] S. Doi *et al.*: J. Phys.: Conf. Ser. **454** (2013) 012019.

# Ordering of topological excitations of the frustrated magnets

Tsuyoshi OKUBO

*Institute for Solid State Physics, University of Tokyo  
Kashiwa-no-ha, Kashiwa, Chiba 277-8581*

In several two-dimensional frustrated Heisenberg spin systems, a topologically stable point defect, a  $Z_2$  vortex, plays an important role for ordering. About 30 years ago, a possible topological phase transition driven by  $Z_2$ -vortex binding-unbinding was proposed [1]. The remarkable feature of the  $Z_2$ -vortex transition is that the spin correlation length keeps finite at the transition temperature  $T = T_v$ . It is a sharp contrast to the Kosterlitz-Thouless transition, where the spin correlation length diverges below the transition temperature.

The nature of the possible  $Z_2$ -vortex transition has been studied mainly on the triangular-lattice Heisenberg antiferromagnet. Indeed, recent Monte Carlo (MC) simulation upto  $L = 1536$  suggested the occurrence of  $Z_2$ -vortex transition at a finite temperature [2]. However, the existence of “true” phase transition has not been resolved because the spin-correlation length at the estimated transition temperature was longer than the system size [2]. In order to clarify the existence of the  $Z_2$ -vortex transition, we need larger systems beyond the spin-correlation length.

In order to perform such larger scale MC simulations, we consider an effective model of two-dimensional frustrated Heisenberg magnets. The Hamiltonian of the model is give by

$$\mathcal{H} = -\frac{J}{4} \sum_{\langle i,j \rangle} \text{Tr} R_i R_j^t \quad (J > 0), \quad (1)$$

where  $R_i$  is a  $SO(3)$  rotation matrix on the site  $i$ , and  $\sum_{\langle i,j \rangle}$  means the sum over the

nearest-neighbor pairs on the square lattice. We have implemented MPI parallelized Wolff-Swendsen-Wang type cluster algorithm and investigated nature of possible  $Z_2$ -vortex transition by extensive MC simulation. In this CMSI project, we performed MC simulation for  $L \leq 4096$ . We also performed calculations for  $L = 8192$  by using another resource.

In order to check the equilibration of the MC simulations, we prepare two types of initial condition: one is the ground state of the model and the other is a random state. By comparing two types of data sets starting from different initial conditions, we confirmed that our MC steps are enough long to remove the effect of initial conditions.

A preliminary extrapolation of the characteristic temperature extracted from the order parameter of the  $Z_2$ -vortex transition leads  $T_v/J \simeq 0.275$ . At this temperature, the spin correlation length is estimated about from 5000 to 10000 lattice spacings. Because the present system is limited  $L \leq 8192$  comparable to the correlation length, we need a careful analysis to conclude the existence of the finite-temperature topological phase transition.

## References

- [1] H. Kawamura and S. Miyashita: J. Phys. Soc. Jpn. **53** (1984) 4138.
- [2] H. Kawamura, A. Yamamoto, and T. Okubo: J. Phys. Soc. Jpn. **79** (2010) 023701.

## Photo-induced electron dynamics in nanostructures and development of quantum devices with optical and electronic functionality

Katsuyuki NOBUSADA

*Institute for Molecular Science,  
Myodaiji, Okazaki, Aichi 444-8585*

A light and matter (LM) interaction in molecules is a fundamental physical phenomenon for understanding their physicochemical properties. We usually assume two conditions in the conventional theoretical approach to optical response of molecules: (i) Wavelength of incident light is considered to be much longer than molecular size, i.e., dipole approximation. Thus, a target molecule is well approximated by a point dipole and the dipole feels an external uniform electromagnetic field. (ii) Electric polarization in a molecule induced by incident-light excitation inevitably generates a new electromagnetic field, referred to as an “optical near field”, according to Maxwell’s equations. However, such a self-consistent light-matter interaction between electron and electromagnetic field dynamics is ignored.

The optical near-field confined in a nanometer-sized region induces characteristic physical and chemical phenomena. To understand such LM interaction in a nanoscale region, we must develop a more general optical response theory, i.e., nano-optical response theory taking account of nonuniform and self-

consistent LM interactions and a corresponding computational code suitable for large nanostructure systems of more than ten-nanometers in size.

In our group, we have developed a generalized theoretical description beyond the conventional optical response theory invoking the dipole approximation. In our theoretical approach, electron dynamics in a nanostructure interacting with an electromagnetic field is described by the time-dependent Kohn-Sham (TDKS) equation based on minimal coupling Hamiltonian with Coulomb gauge. Electromagnetic field dynamics, on the other hand, is represented by the microscopic Maxwell's equations. The nonuniform LM interaction is taken into account in the vector potential and the self-consistent LM interaction is described by solving the electron and electromagnetic field coupled equations self-consistently. The coupled equations are solved numerically by using our developed computational program [1] (GCEED: Grid-based Coupled Electron and Electromagnetic field Dynamics). Our computational approach

is based on a finite-difference method in real-time and real-space. Since the approach employs very simple algorithms, it is very suitable for massively parallelized computations. We have carried out the GCEED program by utilizing the System C, FUJITSU PREMEHPC FX10, in the Supercomputer Center at the Institute for Solid State Physics. Our theory and its computational applications to nanostructures clearly illustrated that the

optical-near-field interaction induced unusual phenomena that are completely absent in the conventional optical response under the dipole approximation.

## Reference

- [1] M. Noda, K. Ishimura, K. Nobusada, K. Yabana, and T. Boku, J. Comp. Phys. **265**, 145 (2014).

# Development of multicomponent quantum chemistry based on stochastic method for material design

Masanori TACHIKAWA and Tsutomu KAWATSU

*Graduate School of NanoBioScience,*

*Yokohama City University, Kanazawa-ku, Yokohama 236-0027, Japan*

In our project we would like to focus on the hydrogen-bonded systems with multicomponent quantum chemistry for material design. It is important to take account of the nuclear quantum effect and thermal effect. For example, in the case of  $\text{H}_3\text{O}_2^-$ , the experimental hydrogen-bonded structure where the proton is located at the center between two oxygen atoms is reproduced by the calculations including nuclear quantum effect [1, 2].

In this year, we have widely explored nuclear quantum effect and thermal effect on deprotonated hydrogen sulfide dimer anion  $\text{H}_3\text{S}_2^-$ , composed of second row elements, by *ab initio* path integral molecular dynamics (PIMD) simulation. At low temperature, the hydrogen-bonded proton tends to be diffusively located at the center between two sulfur atoms, which is the character of the low-barrier hydrogen bond (LBHB). This is the first case of the LBHB composed of the second row elements, although the hydrogen-bonded distance in  $\text{H}_3\text{S}_2^-$  (over 3.4 Å) is much longer

than the previously reported LBHB composed of first row elements (less than 2.5 Å). At high temperature, the distance between two sulfur atoms is longer than that at low temperature, and the hydrogen-bonded proton localizes to each sulfur atom. Similar tendency is obtained in the deuterated  $\text{D}_3\text{S}_2^-$  species at all temperature.

Analyzing the relationship between the position of the hydrogen-bonded proton and the quantum fluctuation effect of the proton, we elucidate that the LBHB is induced by the quantum tunneling at low temperature, while such trend becomes weak and the character of LBHB vanishes at room temperature for  $\text{H}_3\text{S}_2^-$ .

## References

- [1] M. Tachikawa and M. Shiga: J. Am. Chem. Soc., **127** (2005) 11908-11909.
- [2] K. Suzuki, M. Shiga, and M. Tachikawa: J. Chem. Phys., **129** (2008) 144310.
- [3] Y. Ogata, T. Kawatsu, and M. Tachikawa, submitted (2015).

## 4 PUBLICATION LIST

Example:

**LASTNAME, Firstname** [ project class; # points (A), # points (B), # points (C) ]

(Page #)

— *Project title*

1. First paper  
Names of Authors, etc.
2. Second paper
- ...

## □ ISSP Joint Research Projects

**ADACHI, Takahiro** [ C class; 8000 (A), 1000 (B), 300 (C) ] (217)

— *Heat Transfer Characteristics of Condensate Film Flow along Vertical Plates with Microscopic Grooves*

1. Linear stability of flow in rectangular ducts in the vicinity of the critical aspect ratio  
Takahiro ADACHI: European Journal of Mechanics B/Fluids 41 (2013) 163–168
2. Velocity and temperature profiles extending over the liquid and gas phases of two-phase flow falling down vertical plates  
Takahiro ADACHI: Applied Thermal Engineering 51 (2013) 827e832
3. Heat Transfer Enhancement of the Film Flow Falling along Vertical Fluted Plates  
Shouta SATO and Takahiro ADACHI: Proceedings of 4th International Conference on Simulation and Modeling Methodologies, Technologies and Applications(Vienna, Austria,2014)

**AKAI, Hisazumi** [ B class; 0 (A), 800 (B), 500 (C) ] (135)

— *Electronic structure of rare earth magnets*

1. Role of N in a permanent magnet material  $\text{Sm}_2\text{Fe}_{17}\text{N}_x$   
M. Ogura, A. Mashiyama, and H. Akai: submitted to J. Phys. Soc. Jpn. (2015).

**ANDO, Yasunobu** [ C class; 0 (A), 2500 (B), 1700 (C) ] (104)

— *Nano-capacitance analysis based on density functional theory with applied bias*

**AOKI, Hideo** [ C class; 0 (A), 4000 (B), 0 (C) ] (163)

— *Non-equilibrium phase transitions in superconductors and electron-phonon systems*

1. Interaction quench in the Holstein model: Thermalization crossover from electron- to phonon-dominated relaxation  
Yuta Murakami, Philipp Werner, Naoto Tsuji and Hideo Aoki: Phys. Rev. B **91**, 045128 (2015).
2. Supersolid phase accompanied by a quantum critical point in the intermediate coupling regime of the Holstein model  
Yuta Murakami, Philipp Werner, Naoto Tsuji and Hideo Aoki: Phys. Rev. Lett. **113**, 266404 (2014).
3. Nonequilibrium dynamical mean-field theory and its applications  
Hideo Aoki, Naoto Tsuji, Martin Eckstein, Marcus Kollar, Takashi Oka and Philipp Werner: Rev. Mod. Phys. **86**, 779 (2014).
4. Nonequilibrium dynamical cluster theory  
Naoto Tsuji, Peter Barmettler, Hideo Aoki and Philipp Werner: Phys. Rev. B **90**, 075117 (2014).
5. Light-induced collective pseudospin precession resonating with Higgs mode in a superconductor  
Ryusuke Matsunaga, Naoto Tsuji, Hiroyuki Fujita, Arata Sugioka, Kazumasa Makise, Yoshinori Uzawa, Hirotaka Terai, Zhen Wang, Hideo Aoki, and Ryo Shimano: Science **345**, 1145 (2014).



**ARAI, Masaaki** [ C class; 0 (A), 4000 (B), 900 (C) ] (137)

— *First-Principles Modeling on Emerging Memory Devices*

**ARAKAWA, Naoya** [ B class; 0 (A), 600 (B), 0 (C) ] (152)

— *Microscopic theory for transport phenomena of multi-orbital strongly correlated electron systems*

1. Orbital-cooperative spin fluctuation and orbital-dependent transport in Ru oxides  
N. Arakawa: Phys. Rev. B **90** (2014) 245103.
2. Many-body effects on the resistivity of a multiorbital system beyond Landau's Fermi-liquid theory  
N. Arakawa: arXiv:1503.06937; accepted for publication in Modern Physics Letters B as an invited brief review article.
3. Controlling spin Hall effect by using a band anticrossing and nonmagnetic impurity scattering  
T. Mizoguchi and N. Arakawa: arXiv:1411.5432.

**ARAKI, Takeaki** [ B class; 1800 (A), 700 (B), 0 (C) ] (248)

— *Conformations of polymer chains in nematic liquid crystals II*

1. Controlled motion of a Janus particle in periodically phase-separating binary fluids  
T. Araki and S. Fukai: Soft Matter **11** (2015) 3470–3479.
2. Nematic caps on a colloidal particle in a nematogenic liquid under electric field  
T. Uchida, T. Araki and A. Onuki: Soft Matter **11** (2015) 2874

**ARITA, Ryotaro** [ C,D class; 0 (A), 18500 (B), 2300 (C) ] (23)

— *Study of strongly-correlated multiorbital systems with continuous-time quantum Monte Carlo method*

— *Study of multi-orbital correlated electron systems by cluster dynamical mean field theory*

— *Nonempirical study of superconductivity in correlated fullerenes*

1. Effect of Hund's coupling on nonlocal correlations: a cluster DMFT study  
Y. Nomura, S. Sakai and R. Arita: arXiv:1408.4402
2. Unified understanding of superconductivity and the Mott transition in alkali-doped fullerenes from first principles  
Y. Nomura, S. Sakai, M. Capone and R. Arita: submitted

**DEKURA, Haruhiko** [ C class; 0 (A), 1000 (B), 0 (C) ] (140)

— *First-principles calculations of iron solid solution effects on the lattice thermal conductivity of lower mantle minerals*

**EGAMI, Yoshiyuki** [ C class; 0 (A), 1500 (B), 3200 (C) ] (97)

— *Development and application of first-principles simulator for dynamics of electron transport*

1. First-principles calculation method for electron transport based on grid Lippmann-Schwinger equation  
Y. Egami, S. Iwase, S. Tsukamoto, T. Ono and K. Hirose: submitted to Phys. Rev. E.

**FUCHIZAKI, Kazuhiro** [ C class; 17000 (A), 2500 (B), 0 (C) ] (200)

— *Slow Dynamical Processes in Nonequilibrium Metastable States*

1. Melting Behavior of a Model Molecular Crystalline GeI<sub>4</sub>  
K. Fuchizaki and Y. Asano: J. Phys. Soc. Jpn. **84** (2015) in press.

**FUJIMOTO, Yoshitaka** [ C class; 20500 (A), 0 (B), 0 (C) ] (53)

— *Atomic structures, structural stabilities, and electronic properties of impurity-doped carbon-based materials*

1. Hydrogen adsorption and anomalous electronic properties of nitrogen-doped graphene  
Y. Fujimoto and S. Saito: Journal of Applied Physics **115**, 153701 (2014).
2. Electronic structures of hexagonal boron-nitride monolayer: strain-induced effects  
Y. Fujimoto, T. Koretsune, and S. Saito: Journal of the Ceramic Society of Japan **122**, 346 (2014).
3. Adsorption of Molecules on Nitrogen-Doped Graphene: A First-Principles Study  
Y. Fujimoto and S. Saito: JPS Conference Proceedings, **4**, 012002 (2015).

4. Pyridine-Type Defects in Graphene: Stability, Reactivity and Electronic Property  
Y. Fujimoto: *Advances in Materials Science Research* Vol.18 (Nova Science Publishers, USA), pp.91 (2015).
5. Electronic structures and stabilities of bilayer graphene doped with boron and nitrogen  
Y. Fujimoto and S. Saito: *Surface Science*, in press.
6. Atomic geometries and electronic structures of hexagonal boron-nitride bilayers under strain  
Y. Fujimoto and S. Saito: Submitted.

**FUJIWARA, Susumu** [ B class; 0 (A), 600 (B), 0 (C) ] (264)

— *Molecular Simulation Study of Micellar Shape Change in Amphiphilic Solution*

1. Molecular Dynamics Simulation of Micellar Shape Transition in Amphiphilic Solutions  
S. Fujiwara, M. Hashimoto, Y. Tamura, H. Nakamura and R. Horiuchi: *Plasma Fusion Res.* **9** (2014) 3401067.
2. Molecular Dynamics Simulation of Phase Behavior in a Bolaamphiphilic Solution  
S. Fujiwara, T. Miyata, M. Hashimoto, Y. Tamura, H. Nakamura and R. Horiuchi: *Plasma Fusion Res.*, in press.
3. Melt memory of a spherulite nucleus formed through a seeding process in the crystal growth of isotactic polystyrene  
M. Hashimoto, J. Ohishi, S. Moriya and S. Fujiwara: *Polymer J.*, in press.

**FUKUI, Ken-Ichi** [ E class; 0 (A), 5000 (B), 3500 (C) ] (80)

— *Structural and Electronic Properties of Solid / Liquid Interfaces Using First-Principles and Classical Molecular Dynamics*

— *First-Principles and Classical Molecular Dynamics Investigations of Electrolyte Solution / Electrode Interfaces*

**FURUKAWA, Akira** [ C class; 11500 (A), 6500 (B), 0 (C) ] (202)

— *Hydrodynamic effects on the collective dynamics of soft matter systems*

— *Rheology of heterogeneous soft matter systems*

1. Activity-induced clustering in model dumbbell swimmers: The role of hydrodynamic interactions  
a) A. Furukawa, D. Marenduzzo, and M.E. Cates, *Phys. Rev. E*, **90**, 022303 (2014).
2. Probing colloidal gels at multiple lengthscales: the role of hydrodynamics  
C. P. Royall, J. Eggers, A. Furukawa, and H. Tanaka, accepted for publication in *Phys. Rev. Lett.*

**FUSEYA, Yuki** [ B class; 3400 (A), 0 (B), 0 (C) ] (169)

— *Enhancement mechanism of dynamical spin-fluctuation in iron-based superconductors*

— *Effect of spin-orbit interactions in thermoelectric materials*

1. Theoretical study of correlation between spin fluctuations and  $T_c$  in isovalent-doped 1111 iron-based superconductors  
Hayato Arai, Hidetomo Usui, Katsuhiko Suzuki, Yuki Fuseya, and Kazuhiko Kuroki: *Phys. Rev. B* **91**, 134511 (2015).

**GOHDA, Yoshihiro** [ C class; 0 (A), 4000 (B), 2100 (C) ] (94)

— *Interface magnetic anisotropy of NdFeB magnets*

1. Strain effects on the magnetic anisotropy of  $Y_2Fe_{14}B$  examined by first-principles calculations  
Z. Torbatian, T. Ozaki, S. Tsuneyuki, and Y. Gohda: *Appl. Phys. Lett.* **104**, 242403 (2014).

**HAMADA, Ikutaro** [ C class; 6500 (A), 500 (B), 0 (C) ] (87)

— *Density functional theory study of stability and dynamics of metal nanoclusters on a silicon surface*

1. Room-temperature-concerted switch made of a binary atom cluster  
E. Inami, I. Hamada, K. Ueda, M. Abe, S. Morita, Y. Sugimoto: *Nat. Commun.* **6**, 6231 (2015)

**HAMAMOTO, Yuji** [ E class; 0 (A), 2000 (B), 2700 (C) ] (98)

— *First principles calculation of van der Waals interaction in Pt clusters on graphene*

**HARADA, Kenji** [ C class; 4000 (A), 4500 (B), 900 (C) ] (212)

— *Numerical study of non-magnetic phase in quantum spin systems*

1. Thermal phase transition of generalized Heisenberg models for SU(N) spins on square and honeycomb lattices  
T. Suzuki, K. Harada, H. Matsuo, S. Todo, and N. Kawashima: Physical Review B **91** (2015) 094414.

**HASHIMOTO, Tamotsu** [ C class; 0 (A), 1000 (B), 0 (C) ] (262)

— *Molecular dynamics simulation of ferroelectrics using shell models*

1. Dielectric properties of BaTiO<sub>3</sub> by molecular dynamics simulations using a shell model  
T. Hashimoto and H. Moriwake: Molecular Simulation, in press.

**HATSUGAI, Yasuhiro** [ C class; 16000 (A), 5000 (B), 1000 (C) ] (199)

— *Numerical studies of bulk-edge correspondence*

1. Topological Order Parameters of the Spin-1/2 Dimerized Heisenberg Ladder in Magnetic Field  
T. Kariyado and Y. Hatsugai, arXiv:1412.7901
2. Disentangled Topological Numbers by a Purification of Entangled Mixed States for Non-Interacting Fermion Systems  
T. Fukui and Y. Hatsugai, Journal of the Physical Society of Japan, **84**, 043703 (2015).
3. Survival of sharp  $n=0$  Landau levels in massive tilted Dirac fermions: Role of the generalized chiral operator  
Y. Hatsugai, T. Kawarabayashi and Hideo, Aoki, Phys. Rev. B **91** 085112 (2015).
4. Flat bands in the Weaire–Thorpe model and silicene  
Y. Hatsugai, K. Shiraishi and Hideo, Aoki, New J. Phys. **17** 025009 (2015).
5. Entanglement Chern Number for an Extensive Partition of a Topological Ground State  
T. Fukui and Y. Hatsugai, Journal of the Physical Society of Japan, **83**, 113705 (2014).
6. Characterizing weak topological properties: Berry phase point of view  
Y. Yoshimura, K.-I. Imura, T. Fukui and Y. Hatsugai, Phys. Rev. B **90**, 155443 (2014).
7. Fractionally Quantized Berry Phase, Adiabatic Continuation, and Edge States  
T. Kariyado and Y. Hatsugai, Phys. Rev. B **90**, 085132 (2014).
8. Polarization as a topological quantum number in graphene  
H. Aoki and Y. Hatsugai, Phys. Rev. B **90**, 045206 (2014).

**HATTORI, Ken** [ B class; 1500 (A), 0 (B), 0 (C) ] (131)

— *Model calculations in Si surfaces with adsorbates*

1. Surface structure and electronic states of epitaxial  $\beta$ -FeSi<sub>2</sub>(100)/Si(001) thin films: Combined quantitative LEED, *ab initio* DFT, and STM study  
O. Romanyuk, K. Hattori, M. Someta, H. Daimon: Phys. Rev. B **90** (2014) 155305.

**HIDA, Kazuo** [ B class; 800 (A), 600 (B), 0 (C) ] (255)

— *Numerical Study of One Dimensional Frustrated Quantum Spin Systems*

1. Ground-State Phases of Anisotropic Mixed Diamond Chains with Spins 1 and 1/2 :  
K. Hida: J. Phys. Soc. Jpn. **83** (2014) 114711

**HIRAI, Kunitomo** [ B class; 0 (A), 300 (B), 100 (C) ] (143)

— *Electronic State and Proximity Effects around Interface in Layered Superlattices*

**HIROSE, Kenji** [ C class; 2500 (A), 1000 (B), 700 (C) ] ( )

— *Multi-scale Electric and Thermal Transport Calculations*

**HOSHI, Takeo** [ E class; 0 (A), 13500 (B), 2200 (C) ] (58)

— *Parallelized ultra-large-scale electronic-structure theory based on first principle calculation and novel numerical method*

1. Novel linear algebraic theory and one-hundred-million-atom quantum material simulations on the

K computer

- T. Hoshi, T. Sogabe, T. Miyata, D. Lee, S.-L. Zhang, H. Imachi, Y. Kawai, Y. Akiyama, K. Yamazaki, S. Yokoyama, PoS 202, 065, 13 (2014).
- Convergence analysis of the parallel classical block Jacobi method for the symmetric eigenvalue problem  
Y. Yamamoto, L. Zhang and S. Kudo, JSIAM Letters, **6**, 57–60 (2014).
  - A new subtraction-free formula for lower bounds of the minimal singular value of an upper bidiagonal matrix  
T. Yamashita, K. Kimura and Y. Yamamoto, Numerical Algorithms, to appear ( DOI: 10.1007/s11075-014-9931-z )
  - Implementation details of an extended oqds algorithm for singular values  
S. Araki, K. Kimura, Y. Yamamoto and Y. Nakamura, JSIAM Letters, **7**, 9–12 (2015).

**HOSHINO, Shintaro** [ C class; 0 (A), 3000 (B), 0 (C) ] (171)

— *Monte Carlo Approach to Chiral Helimagnets*

- Superconductivity from emerging magnetic moments  
Shintaro Hoshino and Philipp Werner: arXiv:1503.08164 (2015).
- Anisotropic Magnetic Response in Kondo Lattice with Antiferromagnetic Order  
Taku Kikuchi, Shintaro Hoshino and Yoshio Kuramoto: J. Phys. Soc. Jpn. **83**, 114706 (2014).

**HOTTA, Takashi** [ C class; 12000 (A), 0 (B), 0 (C) ] (156)

— *Study of Kondo effect in electron-phonon systems by numerical renormalization group method*

- Relation between electron mass enhancement and potential shape: Numerical analysis of two-site anharmonic Holstein-Hubbard model  
Tomoya Matsuura and Takashi Hotta: J. Phys.: Conf. Ser. **592** (2015) 012144/1-6.
- Chaos in Jahn-Teller Rattling  
Takashi Hotta and Akira Shudo: J. Phys. Soc. Jpn. **83** (2014) 083705/1-5.
- Kondo Effect of a Jahn-Teller Ion Vibrating in a Cubic Anharmonic Potential  
Takashi Hotta: J. Phys. Soc. Jpn. **83** (2014) 104706/1-7.
- Effect of phonon-mediated attraction on the Kondo phenomenon emerging from a vibrating magnetic ion  
Takahiro Fuse and Takashi Hotta: JPS Conf. Proc. **3** (2014) 016024/1-6.

**HUKUSHIMA, Koji** [ C class; 4000 (A), 10500 (B), 2000 (C) ] (203)

— *A possible replica symmetry breaking in finite-dimensional statistical-mechanics models*

- Minimum vertex cover problems on random hypergraphs: Replica symmetric solution and a leaf removal algorithm  
S. Takabe and K. Hukushima: Phys. Rev. E **89** (2014) 043801/1-4
- Evidence of one-step replica symmetry breaking in a three-dimensional Potts glass model  
T. Takahashi and K. Hukushima: Phys. Rev. E **91** (2015) 020102(R)/1-4

**IGARASHI, Ryo** [ C class; 0 (A), 500 (B), 1200 (C) ] ( )

— *Development of ALPS/MPS and its application to 2-dimensional quantum lattice system*

**IKUHARA, Yuichi** [ C class; 0 (A), 2500 (B), 1700 (C) ] (105)

— *Atomic Structure and Electronic Property of Oxide Interfaces*

- A dislocation core in titanium dioxide and its electronic structure  
R. Sun, Z. Wang, N. Shibata, and Y. Ikuhara: RSC Adv. **5** (2015) 18506.
- Misfit accommodation mechanism at the heterointerface between diamond and cubic boron nitride  
C. Chen, Z. Wang, T. Kato, N. Shibata, T. Taniguchi, and Y. Ikuhara: Nat. Commun. **6** (2015) 6327.
- Atomic and electronic structure of the SrNbO<sub>3</sub>/SrNbO<sub>3.4</sub> interface  
C. L. Chen, S. H. Lv, Z. Wang, K. Akagi, F. Lichtenberg, Y. Ikuhara, and J. G. Bednorz: Appl. Phys. Lett. **105** (2014) 221602.
- Full determination of individual reconstructed atomic columns in intermixed heterojunctions

- Z. Wang, M. Saito, C. L. Chen, Y. Matsubara, K. Ueno, M. Kawasaki, and Y. Ikuhara: *Nano Lett.* **14** (2014) 6584.
5. Polymorphism of dislocation core structures at the atomic scale  
Z. Wang, M. Saito, K. P. McKenna, and Y. Ikuhara: *Nat. Commun.* **5** (2014) 3239.
  6. Fluorine in Shark Teeth: Its direct atomic-resolution imaging and strengthening function  
C. L. Chen, Z. Wang, M. Saito, T. Tohei, Y. Takano, and Y. Ikuhara: *Angew. Chem.* **126** (2014) 1569.

**IMADA, Masatoshi** [ E class; 0 (A), 16000 (B), 2300 (C) ] (147)

— *Numerical studies on novel quantum phases induced by cooperative spin-orbit couplings and electron correlations*

1. Quantum Spin Liquid in Spin 1/2 J1-J2 Heisenberg Model on Square Lattice: Many-Variable Variational Monte Carlo Study Combined with Quantum-Number Projections  
S. Morita, R. Kaneko and M. Imada: *J. Phys. Soc. Jpn.* **84** (2015) 024720.
2. Superconductivity and its mechanism in an ab initio model for electron-doped LaFeAsO  
T. Misawa, M. Imada: *J. Phys. Soc. Jpn.* **5** (2014) 5738.
3. Gapless Spin-Liquid Phase in an Extended Spin 1/2 Triangular Heisenberg Model  
R. Kaneko, S. Morita and M. Imada: *J. Phys. Soc. Jpn.* **83** (2014) 093707.
4. First-Principles Study of the Honeycomb-Lattice Iridates Na<sub>2</sub>IrO<sub>3</sub> in the Presence of Strong Spin-Orbit Interaction and Electron Correlations  
Y. Yamaji, Y. Nomura, M. Kurita, R. Arita and M. Imada: *Phys. Rev. Lett.* **113** (2014) 107201.
5. Origin of High-T<sub>c</sub> Superconductivity in Doped Hubbard Models and Their Extensions: Roles of Uniform Charge Fluctuations  
T. Misawa and M. Imada: *Phys. Rev. B* **90** (2014) 115137.
6. Electron Correlation Effects on Topological Phases  
M. Imada, Y. Yamaji and M. Kurita: *J. Phys. Soc. Jpn.* **83** (2014) 061017.
7. Universal departure from Johnson-Nyquist relation caused by limited resolution  
Y. Yamada and M. Imada: *Phys. Rev. B* **89** (2014) 205421.
8. Metallic Interface Emerging at Magnetic Domain Wall of Antiferromagnetic Insulator: Fate of Extinct Weyl Electrons  
Y. Yamaji and M. Imada: **4** (2014) 021035.
9. Variational Monte Carlo Method for Electron-Phonon Coupled Systems  
T. Ohgoe and M. Imada: *Phys. Rev. B* **89** (2014) 195139.

**INAGAKI, Kouji** [ C class; 16000 (A), 4500 (B), 3300 (C) ] (48)

— *First-principles meta-dynamics analysis of Catalytic Referred Etching method (Reaction barrier in etching of GaN, SiC and SiO<sub>2</sub>)*

**INAOKA, Takeshi** [ C class; 1500 (A), 500 (B), 600 (C) ] (246)

— *Physical properties of low-dimensional electron systems created at solid surfaces and their control*

1. Origin of the band dispersion in a metal phthalocyanine crystal  
S. Yanagisawa, K. Yamauchi, T. Inaoka, T. Oguchi, and I. Hamada: *Phys. Rev. B* **90** (2014) 245141 (6 pages).
2. Tensile-strain effect of inducing the indirect-to-direct band-gap transition and reducing the band-gap energy of Ge  
T. Inaoka, T. Furukawa, R. Toma, and S. Yanagisawa: submitted to *J. Appl. Phys.*

**ISHIHARA, Sumio** [ B class; 0 (A), 1400 (B), 0 (C) ] (175)

— *Study of Non-equilibrium States in Correlated Electron Systems with Multi-degrees of Freedom*

— *Dielectric and optical responses and dynamics in correlated electron systems*

1. Transient Carrier Dynamics in a Mott Insulator with Antiferromagnetic Order  
E. Iyoda, and S. Ishihara, *Phys. Rev. B* **89** (2014) 125126.
2. Electronic Ferroelectricity in Molecular Organic Crystals  
S. Ishihara, *J. Phys.: Cond. Matt.* **26** (2014) 493201.
3. Photo-Induced Dynamics in Charge-Frustrated Systems

H. Hashimoto, H. Matsueda, H. Seo and S. Ishihara, J. Phys. Soc. Jpn. **83** (2014) 123703.

4. Optical freezing of charge motion in an organic conductor  
Ishikawa, Y. Sagae, Y. Naitoh, Y. Kawakami, H. Itoh, K. Yamamoto, K. Yakushi, H. Kishida, T. Sasaki, S. Ishihara, Y. Tanaka, K. Yonemitsu and S. Iwai, Nat. Comm. **5** (2014) 5528.
5. Resonating Valence-Bond State in an Orbital Degenerate Quantum Magnet with Dynamical Jahn-Teller Effect  
J. Nasu and S. Ishihara, Phys. Rev. B **91** (2015) 045117.
6. Orbital Dynamics Coupled with Jahn-Teller Phonons in Strongly Correlated Electron Systems  
J. Nasu, and S. Ishihara, JPS Conf. Proc. **3**(2014) 016022.

**ISHII, Fumiya** [ C class; 0 (A), 2500 (B), 3800 (C) ] (92,93)

— *First-Principles Calculation of Oxide Topological Insulators*

— *First-Principles Calculation of Transition Metal Oxides Interfaces*

1. First-Principles Study of Topological Insulators  $A_2B_3$  ( $A=Bi$  and  $Sb$ , and  $B=O, S, Se$  and  $Te$ )  
T. Kato, H. Kotaka, and F. Ishii: JPS Conf. Proc. **5**, 011022 (2015).
2. Thermopower of Doped Quantum Anomalous Hall Insulators: The case of Dirac Hamiltonian  
Y.P. Mizuta and F. Ishii: JPS Conf. Proc. **5**, 011023 (2015).
3. First-Principles Study of Rashba Effect in the  $(LaAlO_3)_2/(SrTiO_3)_2$   
M. Nishida, F. Ishii, H. Kotaka, and M. Saito: Mol. Simul. DOI:10.1080/08927022.2014.987986.
4. Magnetism-Driven Electric Polarization of Multiferroic Quasi-One-Dimensional  $Ca_3CoMnO_6$ : First-Principles Study Using Density Functional Theory  
M. Nishida, F. Ishii, and M. Saito: J. Phys. Soc. Jpn., **83**, 124711 (2014).
5. First-principles study of surface states in topological insulators  $Bi_2Te_3$  and  $Bi_2Se_3$ : Film thickness dependence  
T. Kato, H. Kotaka, and F. Ishii: Mol. Simul. DOI:10.1080/08927022.2014.964476.
6. Spin-Orbit Interaction Effects in the Electronic Structure of B20-type  $CoSi$ : First-Principles Density Functional Study  
F. Ishii, T. Onishi, and H. Kotaka: JPS Conf. Proc. **3**, 016019(2014).
7. Contribution of Berry Curvature to Thermoelectric Effects  
Y. P. Mizuta, and F. Ishii : JPS Conf. Proc. **3** 017035(2014).
8. First-principles study of Exchange Interaction in Ising-type Multiferroic  $Ca_3CoMnO_6$   
M. Nishida, F. Ishii, and M. Saito: JPS Conf. Proc. **3** , 014040 (2014).

**ISOBE, Masaharu** [ B class; 500 (A), 400 (B), 0 (C) ] (263)

— *Nonequilibrium phase transition in the large scale dense hard sphere molecular dynamics simulation*

**ISODA, Makoto** [ B class; 400 (A), 0 (B), 0 (C) ] (266)

— *The phase transition under magnetic field of the quantum spin on the Cairo pentagon lattice*

1. Magnetization Process of the  $S = 1/2$  Heisenberg Antiferromagnet on the Cairo Pentagon Lattice  
H. Nakano, M. Isoda, and T. Sakai, J. Phys..Soc. Jpn. **83** 053702 (2014).
2. Frustration-Induced Magnetic Properties of the Spin-1/2 Heisenberg Antiferromagnet on the Cairo Pentagon Lattice  
M. Isoda, H. Nakano, and T. Sakai, J. Phys..Soc. Jpn. **83** 084710 (2014).

**KAGESHIMA, Hiroyuki** [ C class; 7000 (A), 1500 (B), 0 (C) ] (81)

— *Study on physical and structural properties of defects, surfaces, and interfaces for 2D semiconductors*

**KAKEHASHI, Yoshiro** [ C class; 0 (A), 1000 (B), 0 (C) ] (261)

— *Numerical Study of Long-Range Magnetic Correlations Based on the Nonlocal Dynamical CPA*

1. Momentum-dependent local ansatz approach to correlated electrons  
Y. Kakehashi, S. Chandra, D. Rowlands, and M.A.R. Patoary : Modern Phys. Lett. B **28** (2014) 1430007 1-32.
2. Two-state Weiss model for the anomalous thermal expansion in  $EuNi_2P_2$   
Y. Kakehashi and S. Chandra: Physica B **447** (2014) 19-22.

**KASAI, Hideaki** [ C class; 0 (A), 7000 (B), 4200 (C) ] (71)

— *Analysis of hydrogen and oxygen reactions on solid surface/interface.*

1. Surface magnetism in  $\alpha$ PbO induced by Fe interstitials  
E. Arguelles, S. Amino, S. Aspera, H. Nakanishi, H. Kasai: J. Phys. Soc. Jpn. **84** (2015) 45002/1-2.
2. Effect of oxygen vacancy on the adsorption of O<sub>2</sub> on anatase TiO<sub>2</sub>(001): a DFT-based study  
N.H. Linh, T.Q. Nguyen, W.A. Diño, H. Kasai: Surf. Sci. **633** (2015) 38.
3. Oxygen reduction reaction on neighboring Fe-N4 and quaternary-N sites of pyrolyzed Fe/N/C catalyst  
A.G. Saputro, H. Kasai: Phys. Chem. Chem. Phys. **17** (2015) 3059–3071.
4. A Theoretical Study on the Adsorption of CO<sub>2</sub> on CuO(110) Surface  
J.L.V. Moreno, R.L. Arevalo, M.C.S. Escaño, A.A.B. Padama, H. Kasai: J. Phys. Soc. Jpn. **84** (2015) 015003/1-2.
5. Mechanism of dopachrome tautomerization into 5,6-dihydroxyindole-2-carboxylic acid catalyzed by Cu(II) based on quantum chemical calculations  
R. Kishida, A.G. Saputro, H. Kasai: Biochim. Biophys. Acta **1850** (2015) 281-286.
6. First-Principles Study of Nitric Oxide Oxidation on Pt(111) versus Pt Overlay on 3d Transition Metals  
R.L. Arevalo, M.C.S. Escaño, H. Kasai: J. Vac. Sci. Technol. A **33** (2015) 021402(1)-02401(8).
7. Interstitial impurity-induced in  $\alpha$ -PbO surface  
E. Arguelles, S. Amino, S. Aspera, H. Nakanishi, H. Kasai: J. Phys.: Condens. Matter **27** (2015) 016002/1-7.
8. Towards Optimizing the Performance of Self-Regenerating Pt-Based Perovskite Catalysts  
I. Jarrige, K. Ishii, D. Matsumura, Y. Nishihata, M. Yoshida, H. Kishi, M. Taniguchi, M. Uenishi, H. Tanaka, H. Kasai, J. Mizuki: ACS Catal. **5** (2015) 112-118.
9. First principles study of N and H atoms adsorption and NH formation on Pd(111) and Pd<sub>3</sub>Ag(111) surfaces  
B. Chantaramolee, A.A.B. Padama, H. Kasai, Y.W. Budhi: J. Membr. Sci. **474** (2015) 57-63.
10. Oxidation of NO on Pt/M (M = Pt, Co, Fe, Mn): a first-principles density functional theory study  
R.L. Arevalo, K. Oka, H. Nakanishi, H. Kasai, H. Maekawa, K. Osumi, N. Shimazaki: Catal. Sci. Technol. **5** (2015) 882-886.
11. The effects of alloying and segregation for the reactivity and diffusion of oxygen on Cu<sub>3</sub>Au(111)  
K. Oka, Y. Tsuda, T. Makino, M. Okada, M. Hashinokuchi, A. Yoshigoe, Y. Teraokae, H. Kasai: Phys. Chem. Chem. Phys. **16** (2015) 19702-19711.
12. A DFT+U Study of Strain-Dependent Ionic Migration in Sm-Doped Ceria  
M. Alaydrus, M. Sakaue, S.M. Aspera, T.D.K. Wungu, N.H. Linh, T.L.P. Thuy, H. Kasai, T. Ishihara, T. Mohri: Journal of the Physical Society of Japan, **83**, 094707 (2014).
13. Electrocatalysis of borohydride oxidation: a review of density functional theory approach combined with experimental validation  
M.C.S. Escaño, R.L. Arevalo, E. Gyenge, H. Kasai
14. Atomic oxygen adsorption on core-shell Ni@Pt and pure Pt Nanoparticles  
F. Oemry, H. Nakanishi, H. Kasai, H. Maekawa, K. Osumi, K. Sato: Journal of the Vacuum Society of Japan **57**, 277-283 (2014).
15. First principles investigation of the initial stage of H-induced missing-row reconstruction of Pd(110) surface  
A.A.B. Padama and H. Kasai: The Journal of Chemical Physics **140**, 144707 (2014).
16. Effect of pH on elementary steps of dopachrome conversion from first-principles calculation  
R. Kishida, Y. Ushijima, A.G. Saputro, H. Kasai: Pigment Cell and Melanoma Research **27**, 734-743 (2014).
17. Surface as a Foundation to Realizing Designer Materials  
H. Kasai, W.A. Diño, K. Kojima, Y. Kawahito: e-Journal of Surface Science and Nanotechnology, **12**, 203-216 (2014).
18. First-principles calculation on oxygen ion migration in alkaline-earth doped La<sub>2</sub>GeO<sub>5</sub>  
T.P.T. Linh, M. Sakaue, S.M. Aspera, M. Alaydrus, T.D.K. Wungu, N.H. Linh, H. Kasai, T.

- Mohri, T. Ishihara: J. Phys.: Condens. Matter **26** (2014) 255503.
19. Odd-frequency pairing in topological superconductivity in a one-dimensional magnetic chain  
H. Ebisu, K. Yada, H. Kasai, Y. Tanaka: Phys. Rev. B **91** (2015) 54518.
  20. Majorana edge states and topological properties in 1D/2D Rashba semiconductor proximity coupled to iron-based superconductor  
H. Ebisu, K. Yada, H. Kasai, Y. Tanaka: Supercond. Sci. Technol **28** (2015) 14001.
  21. A molecular dynamics investigation of water migration in a lipid bilayer for microalgae drying  
R. Manrique, A. Ubando, A. Villagracia, J. Corpuz, A.A. Padama, M. David, N. Arboleda Jr., A. Culaba, H. Kasai: Phil. Sci. Letts. **7** (2014) 138-145.
  22. Incident angle dependence of H<sub>2</sub> adsorption on a defective Pt(111) surface: first principles calculation  
M.T. Natividad, N.B. Arboleda Jr., H. Kasai: Phil. Sci. Letts. **7** (2014) 81-87.

**KAWAKAMI, Norio** [ C class; 0 (A), 8000 (B), 0 (C) ] (158,159)

— *Theoretical Analysis of Quantum Properties at Heterostructures and Superlattices of Strongly Correlated Systems*

— *Theoretical Studies of Correlation Effects on Quantum Phase Formation in Inhomogeneous Systems*

1. Destruction of long-range order by quenching the hopping range in one dimension  
Masaki Tezuka, Antonio M. García-García, and Miguel A. Cazalilla: Phys. Rev. A **90** (2014) 053618.
2. Topological Properties of Ultracold Bosons in One-Dimensional Quasiperiodic Optical Lattice  
Fuyuki Matsuda, Masaki Tezuka, and Norio Kawakami: J. Phys. Soc. Jpn. **83** (2014) 083707.
3. Spin density waves in the Hubbard model: A DMFT approach  
Robert Peters and Norio Kawakami: Phys. Rev. B **89** (2014) 155134.
4. Local origin of the pseudogap in the attractive Hubbard model  
Robert Peters and Johannes Bauer: arXiv:1503.03075.
5. Characterization of a topological Mott insulator in one dimension  
Tsuneya Yoshida, Robert Peters, Satoshi Fujimoto, and Norio Kawakami: Phys. Rev. Lett. **112** (2014) 196404.
6. Topological properties of correlated insulators in one dimension  
Tsuneya Yoshida, Robert Peters, Satoshi Fujimoto, and Norio Kawakami: JPS Conference Proceedings **3**, (2014) 016010.
7. Partial Kondo screening in a geometrically frustrated heavy electron system  
Kazuto Noda, Tsuneya Yoshida, Robert Peters, and Norio Kawakami: JPS Conference Proceedings **3**, (2014) 014019.
8. Superfluid-Insulator Transition Caused by Binary Disorder  
Masaru Sakaida, Kazuto Noda, and Norio Kawakami: JPS Conference Proceedings **3**, (2014) 016002.
9. Disorder-induced charge-density-wave superfluid transition in SU(N) Fermi systems  
Masaru Sakaida and Norio Kawakami: Phys. Rev. A **90** (2014) 013632.

**KAWAMURA, Hikaru** [ B,C class; 35900 (A), 8100 (B), 0 (C) ] (184,186)

— *Novel order in frustrated magnets*

— *Numerical simulations on statistical models of earthquakes*

1. Nucleation process in the Burridge-Knopoff model of earthquakes  
Y. Ueda, S. Morimoto, S. Kakui, T. Yamamoto and H. Kawamura: Europhys. Lett. **106**, (2014) 69001.
2. Quantum spin-liquid behavior in the spin-1/2 random-bond Heisenberg antiferromagnet on the triangular lattice  
H. Kawamura, K. Watanabe and H. Kawamura: J. Phys. Soc. Jpn. **83**, (2014) 103704.
3. Low-temperature magnetic properties of the Kondo lattice model in one dimension  
S. Minami and H. Kawamura: J. Phys. Soc. Jpn. **84**, (2015) 044702.

**KAWASHIMA, Naoki** [ E class; 0 (A), 36000 (B), 5000 (C) ] (187)

— *Parallelization of Tensor Network Methods*



1. Thermal phase transitions to valence-bond-solid phase in the two dimensional; generalized SU(N) Heisenberg models  
Takafumi Suzuki, Kenji Harada, Haruhiko Matsuo, Synge Todo and Naoki Kawashima: J. Phys.: Conf. Ser. 592, 012114 (2015).
2. Thermal phase transition of generalized Heisenberg models for SU(N) spins on square and honeycomb lattices  
Takafumi Suzuki, Kenji Harada, Haruhiko Matsuo, Synge Todo and Naoki Kawashima: Phys. Rev. B 91, 094414 (2015).
3. Parallelized Quantum Monte Carlo Algorithm with Nonlocal Worm Updates  
Akiko Masaki-Kato, Takafumi Suzuki, Kenji Harada, Synge Todo, and Naoki Kawashima: Physical Review Letters 112, 140603 (5 pages) (2014).
4. Phase Transitions with Discrete Symmetry Breaking in Antiferromagnetic Heisenberg Models on a Triangular Lattice  
Ryo Tamura, Shu Tanaka, and Naoki Kawashima: JPS Conf. Proc. — Proceedings of the 12th Asia Pacific Physics Conference (APPC12), 012125 (2014)

**KITAO, Akio** [ C class; 0 (A), 5500 (B), 2500 (C) ] (223)

— *Efficient sampling simulation of the soft modes significantly contribute to protein properties*

1. TRPV4 channel activity is modulated by direct interaction of the ankyrin domain to PI(4,5)P2.  
N. Takahashi, S. Hamada-Nakahara, Y. Itoh, K. Takemura, A. Shimada, Y. Ueda, M. Kitamata, R. Matsuoka, K. Hanawa-Suetsugu, Y. Senju, M. X. Mori, S. Kiyonaka, D. Kohda, A. Kitao, Y. Mori and S. Suetsugu: Nature Comm. **5** (2014) 4994.
2. Conformational transition pathway and free energy analyses of proteins by parallel cascade selection molecular dynamics (PaCS-MD).  
R. Harada, Y. Nishihara, N. Wakai, and A. Kitao: AIP Conference Proceedings, **1618** (2014) 86.
3. Ligand-Induced Protein Responses and Mechanical Signal Propagation Described by Linear Response Theories.  
L.-W. Yang, A. Kitao, B.-C. Huang, N. Go: J. Chem. Phys., **139** (2013) 035103.

**KIZAKI, Hidetoshi** [ C class; 0 (A), 1500 (B), 0 (C) ] (133)

— *First-principles Molecular Dynamics Simulations on a Water Dissociation in Water-bi-layer on Stepped Pt(322)*

**KOBAYASHI, Katsuyoshi** [ B class; 1500 (A), 200 (B), 0 (C) ] (130)

— *Search for electronic properties of new nanoscale interfaces*

1. Electronic states of SnTe and PbTe (001) monolayers with supports  
K. Kobayashi: to be published in Surf. Sci.

**KOBAYASHI, Michikazu** [ B class; 700 (A), 500 (B), 0 (C) ] (257)

— *Universality class of thermally equilibrium states for cold atoms with internal degrees of freedom*

1. Non-relativistic Nambu-Goldstone modes associated with spontaneously broken space-time and internal symmetries  
M. Kobayashi and M Nitta: Phys. Rev. Lett. **113** (2014) 120403.
2. Non-relativistic Nambu-Goldstone modes propagating along a skyrmion line  
M. Kobayashi and M Nitta: Phys. Rev. D **90** (2014) 025010.
3. Color Magnetism in Non-Abelian Vortex Matter  
M. Kobayashi, Eiki Nakano, and M Nitta: JHEP **06** (2014) 130.

**KOBAYASHI, Nobuhiko** [ C,E class; 2000 (A), 8000 (B), 1600 (C) ] (69)

— *First-principles study of quantum transport in nanostructures*

1. Atomistic Calculations of Heat Transport in a Silicon Crystal  
N. Kobayashi, K. Yamamoto, H. Ishii, K. Hirose: e-J. Surf. Sci. Nanotechnol. **12** (2014) 154-156.
2. Large-scale conductivity-tensor calculations for Hall effects in time-dependent wave-packet diffusion method  
H. Ishii, H. Tamura, M. Tsukada, N. Kobayashi, K. Hirose: Phys. Rev. B **90** (2014) 155458 (1-5).

3. First-Principles Study of TiN/MgO Interfaces  
K. Kobayashi, N. Kobayashi, K. Hirose: e-J. Surf. Sci. Nanotechnol. 12 (2014) 230-237.
4. Electronic Band Structure of Various TiN/MgO Superlattices,  
K. Kobayashi, H. Takaki, N. Kobayashi, and K. Hirose: JPS Conf. Proc. 5 (2015) 011013.
5. Efficient Ab-Initio Electron Transport Calculations for Heterostructures by the Nonequilibrium Green's Function Method  
H. Takaki, N. Kobayashi, K. Hirose: J. Nanomaterials, 2014 (2014) 172169 (1-5).
6. Correlation between thermal fluctuation effects and phase coherence factor in carrier transport of single-crystal organic semiconductors  
T. Fukami, H. Ishii, N. Kobayashi, T. Uemura, K. Sakai, Y. Okada, J. Takeya, and K. Hirose: Appl. Phys. Lett. 106 (2015) 143302 (1-4).

**KOGA, Akihisa** [ C,D class; 4000 (A), 11500 (B), 2600 (C) ] (149,150)

— *Stability of the superfluid state with internal degree of freedom*

— *Stability of the superfluid state in three-component Fermions with asymmetric repulsive interaction*

— *Inter site electron correlations in two-dimensional Hubbard Penrose Lattice*

1. Superconductivity in the two-band Hubbard model  
A. Koga and P. Werner, Phys. Rev. B 91,085108 (2015).
2. Local Electron Correlations in a Two-dimensional Hubbard Model on the Penrose Lattice  
N. Takemori, A. Koga, J. Phys. Soc. Jpn. 84, 023701 1-5 (2015).
3. DMFT study of the local correlation effects in quasi-periodic system  
N. Takemori and A. Koga, J. Phys.: Conf. Ser. 592, 012038 (2015).
4. Valence Fluctuations and Electric Reconstruction in the Extended Anderson Model on the Two-Dimensional Penrose Lattice  
S. Takemura, N. Takemori, and A. Koga, Phys. Rev. B 91, 165114 (2015).

**KUNISADA, Yuji** [ C class; 0 (A), 4000 (B), 0 (C) ] (107)

— *First principles based analysis of electronic structures and reactions on surfaces/interfaces*

1. Stability of 111<sub>Pd</sub>/0002<sub>ZnO</sub> polar interface formed by internal oxidation of Pd-Zn alloy  
Norihito Sakaguchi, Kei Watanabe, Yuji Kunisada: Microscopy 63 (2014) 463.
2. Two-Dimensional Quantum Dynamics of O<sub>2</sub> Dissociative Adsorption on Ag(111)  
Yuji Kunisada, Norihito Sakaguchi: RSC Adv. 4 (2014) 63508.

**KUROKI, Kazuhiko** [ C,D class; 34000 (A), 2500 (B), 0 (C) ] (145)

— *Study on the pressure effect of iron-based and cuprate superconductors*

— *Study on multiple origins for stripe-type antiferromagnetic spin fluctuations in iron-based superconductors*

— *Study of superconducting mechanisms in carrier doped band insulators*

1. Orbital mixture effect on the Fermi surface-T<sub>c</sub> correlation in the cuprate superconductors – bilayer vs single layer  
H. Sakakibara, K. Suzuki, H. Usui, S. Miyao, I. Maruyama, K. Kusakabe, R. Arita, H. Aoki, K. Kuroki, Phys. Rev. B **89**, 224505 (2014).
2. Model of the Electronic Structure of Electron-Doped Iron-Based Superconductors: Evidence for Enhanced Spin Fluctuations by Diagonal Electron Hopping  
K. Suzuki, H. Usui, S. Iimura, Y. Sato, S. Matsuishi, H. Hosono, K. Kuroki, Phys. Rev. Lett. **113**, 027002 (1-5) (2014).
3. Theoretical Study of the Chemical Pressure Effect on T<sub>c</sub> in the Cuprate Superconductors  
H. Sakakibara, K. Suzuki, H. Usui, K. Kuroki, R. Arita, H. Aoki, Physics Procedia **58**, 34-37 (2014).
4. Theoretical Analysis on the Band Structure Variance of the Electron Doped 1111 Iron-based Superconductors  
K. Suzuki, H. Usui, S. Iimura, Y. Sato, S. Matsuishi, H. Hosono, K. Kuroki, Physics Procedia **58**, 38-41 (2014).

**KUSAKABE, Koichi** [ C class; 0 (A), 2000 (B), 0 (C) ] (251)

— *Theoretical design of graphene quantum devices*

1. Role of edge geometry and chemistry in the electronic properties of graphene nanostructures  
Shintaro Fujii, Maxim Ziatdinov, Misako Ohtsuka, Koichi Kusakabe, Manabu Kiguchi, and Toshiaki Enoki: Faraday Discuss., 2014, 173, 10-1-27

**KUWABARA, Akihide** [ C class; 0 (A), 4500 (B), 0 (C) ] (100,101)

— *First principles calculations of point defects nearby grain boundaries of alpha Al<sub>2</sub>O<sub>3</sub>*

— *First principles calculations of ionic conductivity in solid electrolytes*

**MASAKI-KATO, Akiko** [ C class; 2500 (A), 2000 (B), 1700 (C) ] (228)

— *Quantum Monte Carlo study of the edge state of hardcore bosons on a Kagome lattice*

**MATSUKAWA, Hiroshi** [ C class; 7000 (A), 500 (B), 0 (C) ] ( )

— *Physics of Friction*

**MATSUSHITA, Katsuyoshi** [ C class; 0 (A), 3000 (B), 0 (C) ] (241)

— *Reconstruction of protein folding energy landscape based on a Multicanonical sampling method*

— *Detection of frustration of intra-protein interaction based on energy landscape calculation*

1. Design of Domain Wall Spin Torquemeter  
Katsuyoshi Matsushita and Munetaka Sasaki: J. Phys. Soc. Jpn. **84** (2015) 043801.

**MATSUURA, Hiroyasu** [ C class; 12000 (A), 3000 (B), 1900 (C) ] (151)

— *Theoretical Study of Novel Electronic States in Strongly Correlated Electron Systems*

1. Orbital-cooperative spin fluctuation and orbital-dependent transport in Ru oxides  
N. Arakawa: Phys. Rev. B **90** (2014) 245103.
2. Many-body effects on the resistivity of a multiorbital system beyond Landau's Fermi-liquid theory  
N. Arakawa: arXiv:1503.06937; accepted for publication in Modern Physics Letters B as an invited brief review article.
3. Controlling spin Hall effect by using a band anticrossing and nonmagnetic impurity scattering  
T. Mizoguchi and N. Arakawa: arXiv:1411.5432.
4. Meissner Effect of Dirac Electrons in Superconducting State due to Inter-band Effect  
T. Mizoguchi and M. Ogata: arXiv:1502.05769.
5. Controlling spin Hall effect by using a band anticrossing and nonmagnetic impurity scattering  
S. C. Furuya, H. Matsuura, and M. Ogata: arXiv:1503.02499.

**MINOGUCHI, Tomoki** [ C class; 0 (A), 2500 (B), 0 (C) ] (249)

— *The ground state properties of Boltzmann liquid and its crystallization*

**MISAWA, Takahiro** [ C class; 0 (A), 3000 (B), 1900 (C) ] (162)

— *Ab initio calculations for Mn analog of iron-based superconductors LaMnAsO and LaMnPO*

1. Origin of high-T<sub>c</sub> superconductivity in doped Hubbard models and their extensions: Roles of uniform charge fluctuations  
T. Misawa and M. Imada: Phys. Rev. B **90** (2014) 1115137 .
2. Superconductivity and its mechanism in an ab initio model for electron-doped LaFeAsO  
T. Misawa and M. Imada: Nat. Commun. **5** (2014) 5738.

**MIURA, Yoshio** [ B class; 0 (A), 1300 (B), 0 (C) ] (136)

— *A first-principles study on noncollinear magnetic structures in magnetic films*

— *A first-principles study on exchange stiffness constants in magnetic films*

**MIYAKE, Takashi** [ C class; 0 (A), 2000 (B), 0 (C) ] (126)

— *First-principles approach to magnetic properties and spin-orbit interaction*

1. Ab-initio study of the downfolded self-energy for correlated systems: momentum dependence and effects of dynamical screening  
R. Sakuma, C. Martins, T. Miyake and F. Aryasetiawan, Phys. Rev. B **89**, 235119 (2014).

2. Asymmetric band widening by screened exchange competing with local correlations in  $\text{SrVO}_3$ : new surprises on an old compound from combined GW and dynamical mean field theory GW+DMFT  
J.M. Tomczak, M. Casula, T. Miyake and S. Biermann, Phys. Rev. B **90**, 165138 (2014).
3. First-Principles Study of Structural and Magnetic Properties of  $\text{R}(\text{Fe,Ti})_{12}$  and  $\text{R}(\text{Fe,Ti})_{12}\text{N}$  ( $\text{R}=\text{Nd, Sm, Y}$ )  
Yosuke Harashima, Kiyoyuki Terakura, Hiori Kino, Shoji Ishibashi and Takashi Miyake, JPS Conf. Proc. **5**, 011021 (2015).
4. Dirac Point in Trigonal tellurium and selenium  
Motoaki Hirayama, Ryo Okugawa, Shoji Ishibashi, Shuichi Murakami and T. Miyake, JPS Conf. Proc. **5**, 011024 (2015).

**MIYASHITA, Seiji** [ C class; 7000 (A), 4000 (B), 2100 (C) ] (205)

— *Explore in new aspects of phase transitions*

1. Condition for emergence of the Floquet-Gibbs state in periodically driven open systems  
T. Shirai, T. Mori, S. Miyashita: Phys. Rev. E, **91** (2015) 030101(R).
2. Floquet resonant states and validity of the Floquet-Magnus expansion in the periodically driven Friedrichs models  
T. Mori: Phys. Rev. A **91** (2015), 020101(R).
3. Anisotropy of the molecular magnet V-15 spin Hamiltonian detected by high-field electron spin resonance  
M. Marthens, J. Tol. van, NS Dalal, S. Bertaina, B. Barbara, B. Tsukerblat, A. Muller, S. Garai, S. Miyashita, I. Chiorescu: Phys. Rev. B **89**(2014) 195439.
4. Possible Singlet-triplet Transition of ESR in the Kagome-Lattice Antiferromagnet  
T. Sakai, K. Hijii, S. Okubo, H. Ohta, H. Nakano, and S. Miyashita: Applied Magnetic Resonance, **03** (2015) [DOI 10.1007/s00723-015-0652-9].
5. Electron Transport Dynamics in Redox-Molecule-Terminated Branched Oligomer Wires on Au (111)  
R. Sakamoto, S. Katagiri, H. Maeda, Y. Nishimori, S. Miyashita, H. Nishihara: J. Am. Chem. Soc. **137** (2015), 734.
6. Natural correlation between a system and a thermal reservoir  
T. Mori: Phys. Rev. A **89** (2014) 040101(R).
7. Role of open boundary conditions on the hysteretic behaviour of one-dimensional spin crossover nanoparticles  
D. Chiruta, J. Linares, S. Miyashita, K. Boukheddaden: J. App. Phys. **115** (2014) 194309.
8. Shape effects on the cluster spreading process of spin-crossover compounds analyzed within an elastic model with Eden and Kawasaki dynamics  
C. Enachescu, M. Nishino, S. Miyashita, K. Boukheddaden, F. Varret, P.A. Rikvold: Phys. Rev. B **91** (2015) 104102.
9. Realization of the thermal equilibrium in inhomogeneous magnetic systems by the Landau-Lifshitz-Gilbert equation with stochastic noise, and its dynamical aspects  
M. Nishino and S. Miyashita: Phys. Rev. B **91** (2015), 134411.
10. Doping control of realization of an extended Nagaoka ferromagnetic state from the Mott state  
H. Onishi, S. Miyashita: Phys. Rev. B. **90** (2014) 224426.
11. Two limiting regimes of interacting Bessel processes  
S. Andraus, M. Katori, S. Miyashita: J. Phys. A: Math. Theor. **47** (2014) 235201.
12. Existence of shape-dependent thermodynamic limit in spin systems with short- and long-range interactions  
T. Mori: J. Phys. A: Math. Theor. **48** (2015) 145001.

**MIYATA, Naoyuki** [ C class; 0 (A), 0 (B), 800 (C) ] ( )

— *Study on Effects of Momentum-dependent Perturbation on the Scaling Theory of the Quantum Hall Systems*

**MOMIDA, Hiroyoshi** [ C class; 3000 (A), 2500 (B), 1400 (C) ] (90)

— *First-principles study on charge-discharge reaction mechanism in cathode materials of secondary*

*batteries*

1. *Ab Initio* Study of Electronic, Magnetic, and Spectroscopic Properties in *A*- and *B*-Site-Ordered Perovskite  $\text{CaCu}_3\text{Fe}_2\text{Sb}_2\text{O}_{12}$   
H. Fujii, M. Toyoda, H. Momida, M. Mizumaki, S. Kimura, and T. Oguchi: *Phys. Rev. B* **90** (2014) 014430.
2. First-Principles Study on Structural and Electronic Properties of  $\alpha$ -S and Na-S Crystals  
H. Momida, T. Yamashita, and T. Oguchi: *J. Phys. Soc. Jpn.* **83** (2014) 124713.
3. First-Principles Investigation on a Phase Transition in  $\text{Na}_x\text{C}_6\text{O}_6$  as an Organic Cathode Material for Na-Ion Batteries: Role of Inter-Molecule Bonding of  $\text{C}_6\text{O}_6$   
T. Yamashita, H. Momida, and T. Oguchi: submitted.

**MORIKAWA, Yoshitada** [ E class; 0 (A), 25500 (B), 4800 (C) ] (43)

— *First-principles simulations of atomic geometries, electronic properties, and chemical reactions at interfaces*

1. Search for a Self-Regenerating Perovskite Catalyst with *Ab Initio* Thermodynamics II: Cu-Doped Layered Perovskites with  $\text{K}_2\text{NiF}_4$  Structure  
S. Yanagisawa, A. Takeda, K. Inagaki, I. Hamada, and Y. Morikawa: *Catal. Lett.* **144** (2014) 736.
2. Theoretical investigation of the band structure of picene single crystals within the *GW* approximation  
S. Yanagisawa, Y. Morikawa, and A. Schindlmayr: *Jpn. J. Appl. Phys.*, **53** (2014) 05FY02.
3. Cooperative  $\text{H}_2$  Activation at Ag Cluster/ $\theta$ - $\text{Al}_2\text{O}_3$ (110) Dual Perimeter Sites: A Density Functional Theory Study  
P. Hirunsit, K.-i. Shimizu, R. Fukuda, S. Namuangruk, Y. Morikawa, and M. Ehara: *J. Phys. Chem. C*, **118** (2014) 7996.
4. Dissociative adsorption of  $\text{CO}_2$  on flat, stepped, and kinked Cu surfaces  
F. Muttapien, Y. Hamamoto, K. Inagaki, and Y. Morikawa: *J. Chem. Phys.* **141** (2014) 034702.
5. Electronic structure of the  $4 \times 4$  silicene monolayer on semi-infinite Ag(111)  
H. Ishida, Y. Hamamoto, Y. Morikawa, E. Minamitani, R. Arafune, and N. Takagi: *New Journal of Physics*, **17** (2015) 015013.

**MORITA, Satoshi** [ B class; 0 (A), 700 (B), 500 (C) ] (260)

— *Topological quantum-number projection in variational Monte Carlo method*

1. Gapless Spin-Liquid Phase in an Extended Spin 1/2 Triangular Heisenberg Model  
R. Kaneko, S. Morita, and M. Imada: *J. Phys. Soc. Jpn.* **83**, 093707 (2014).
2. Quantum Spin Liquid in Spin 1/2  $J_1$ – $J_2$  Heisenberg Model on Square Lattice: Many-Variable Variational Monte Carlo Study Combined with Quantum-Number Projections  
S. Morita, R. Kaneko, and M. Imada: *J. Phys. Soc. Jpn.* **84**, 024720 (2015).

**MOTOME, Yukitoshi** [ D class; 0 (A), 15000 (B), 0 (C) ] (204)

— *Finite-temperature phase transitions and their characterization in 3D quantum spin liquids*

— *Numerical study of quantum spin liquid states in a 3D Kitaev model*

1. Low-energy Majorana states in spin liquid transitions in a three-dimensional Kitaev model  
Joji Nasu, Masafumi Udagawa, and Yukitoshi Motome: *Physical Review Letters* **113**, 197205 (2014)
2. Finite-temperature phase transition to a quantum spin liquid in a three-dimensional Kitaev model on a hyperhoneycomb lattice  
J. Nasu, T. Kaji, K. Matsuura, M. Udagawa, and Y. Motome: *Physical Review B* **89**, 115125 (2014)
3. Low-energy Majorana states in spin liquid transitions in a three-dimensional Kitaev model  
Joji Nasu, Masafumi Udagawa, and Yukitoshi Motome: *Journal of Physics: Conference Series* **592** (2015) 012115

**MOTOYAMA, Yuichi** [ B class; 0 (A), 500 (B), 0 (C) ] (180)

— *Numerical simulation of  $^4\text{He}$  adsorbed on substrates*

**MURASHIMA, Takahiro** [ E class; 0 (A), 19500 (B), 2500 (C) ] (197)

— *Multiscale Simulation of Polymer Melts with Element Deformation*

**NADA, Hiroki** [ C class; 0 (A), 3500 (B), 0 (C) ] (240)

— *Molecular Dynamics Simulation Study of Mechanism of Ice Nucleation Promotion by Calcium Oxalate Monohydrate*

1. Difference in the Conformation and Dynamics of Aspartic Acid on the Flat Regions, Step Edges, and Kinks of a Calcite Surface: A Molecular Dynamics Study  
H. Nada: J. Phys. Chem. C, **118** (2014) 14335.
2. Importance of Water in the Control of Calcite Crystal Growth by Organic Molecules  
H. Nada: Polym. J., **47** (2015) 84.

**NAGAI, Yuki** [ B class; 1600 (A), 600 (B), 400 (C) ] (244)

— *Bound states in unconventional superconductors*

1. Impurity Effect on the Local Density of States around a Vortex in Noncentrosymmetric Superconductors  
Y. Higashi, Y. Nagai and N. Hayashi: JPS Conf. Proc. **3** (2014) 015003.
2. Vortex Core Structure in Multilayered Rashba Superconductors  
Y. Higashi, Y. Nagai, T. Yoshida and Y. Yanase: J. Phys.: Conf. Ser. **568** (2014) 022018.
3. Excitation spectra and wave functions of quasiparticle bound states in bilayer Rashba superconductors  
Y. Higashi, Y. Nagai, T. Yoshida, M. Kato and Y. Yanase: Physica C in press.
4. Robust zero-energy bound states around a pair-density-wave vortex core in locally noncentrosymmetric superconductors  
Y. Higashi, Y. Nagai, T. Yoshida, Y. Masaki and Y. Yanase: submitted to Phys. Rev. B.

**NAKAMURA, Kazuma** [ C,D class; 0 (A), 7500 (B), 0 (C) ] (82)

— *Ab initio GW analysis for low-energy plasmaron states of transition-metal oxides*

— *Ab initio GW calculations for SrVO<sub>3</sub> and SrRuO<sub>3</sub>*

— *Ab initio GW analysis for low-energy plasmaron states*

1. GW calculation of plasmon excitations in the quasi-one-dimensional organic compound (TMTSF)<sub>2</sub>PF<sub>6</sub>  
Kazuma Nakamura, Shiro Sakai, Ryotaro Arita, and Kazuhiko Kuroki: Physical Review B **88** (2013) 125128.
2. Effect of Electron-Phonon Interactions on Orbital Fluctuations in Iron-Based Superconductors  
Yusuke Nomura, Kazuma Nakamura, and Ryotaro Arita: Phys. Rev. Lett. **112** (2014) 027002.

**NAKAMURA, Kohji** [ C class; 10000 (A), 0 (B), 0 (C) ] (73)

— *First principles calculations on electronic structures and magnetism in transition-metal films and organic metal complexes*

1. Electric-field-induced modification of the magnon energy, exchange interaction, and Curie temperature of transition-metal thin films  
M. Oba, K. Nakamura, T. Akiyama, T. Ito, M. Weinert, A. J. Freeman: Phys. Rev. Lett. **114**, (2015) 107202.
2. Giant perpendicular magnetocrystalline anisotropy of 3d transition-metal thin films on MgO  
K. Nakamura, Y. Ikeura, T. Akiyama, T. Ito: J. Appl. Phys. **117**, (2015) 17C31.
3. Electronic configurations and magnetic anisotropy in organometallic metallocenes  
K. Nawa, Y. Kitaoka, K. Nakamura, T. Akiyama, T. Ito: J. Appl. Phys. **117**, (2015) 17E131.

**NAKANO, Hiroki** [ E class; 0 (A), 5000 (B), 1700 (C) ] (226)

— *Numerical study on low-energy states of quantum spin systems*

1. The Magnetization Process of the  $S = 1/2$  Heisenberg Antiferromagnet on the Cairo Pentagon Lattice  
H. Nakano, M. Isoda, and T. Sakai: J. Phys. Soc. Jpn. **83** (2014) 053702.

2. Frustration-induced Magnetic Properties of the Spin-1/2 Heisenberg Antiferromagnet on the Cairo Pentagon Lattice  
M. Isoda, H. Nakano, and T. Sakai: J. Phys. Soc. Jpn. **83** (2014) 084710.
3. Spin-Flop Phenomenon of Two-Dimensional Frustrated Antiferromagnets without Anisotropy in Spin Space  
H. Nakano, Y. Hasegawa, and T. Sakai: J. Phys. Soc. Jpn. **83** (2014) 084709.
4. Anomalous Behavior of the Magnetization Process of the  $S = 1/2$  Kagome-Lattice Heisenberg Antiferromagnet at One-Third Height of the Saturation  
H. Nakano and T. Sakai: J. Phys. Soc. Jpn. **83** (2014) 104710.
5. Anomalous Quantum Magnetization Behaviors of the Kagome and Triangular Lattice Antiferromagnets  
H. Nakano and T. Sakai: JPS Conf. Proc. **3** (2014) 014003.
6. Exotic Quantum Phase Transition of the Spin Nanotube  
T. Sakai, H. Nakano, and K. Okunishi: J. Low. Phys. **568** (2014) 042024.
7. Novel Field Induced Quantum Phase Transition of the Kagome Lattice Antiferromagnet  
T. Sakai and H. Nakano: J. Low. Phys. **568** (2014) 042025.
8. Instability of a ferrimagnetic state of a frustrated  $S=1/2$  Heisenberg antiferromagnet in two dimensions  
H. Nakano and T. Sakai: Jpn. J. App. Phys. **54** (2015) 00305.

**NAKAYAMA, Takashi** [ C class; 14500 (A), 0 (B), 0 (C) ] (61)

— *Adsorption and clustering of metal atoms on organic molecular semiconductors*

1. First-principles study of doping properties in  $\text{ZnSnAs}_2$   
M. Ishikawa, T. Nakayama: phys. stat. sol. (c) (2015) in press.
2. Theory of metal-atom diffusion in organic systems  
Y. Tomita, T. Nakayama: Springer Series in Materials Science **209** (2015) 303.

**NISHIDATE, Kazume** [ C class; 8000 (A), 1000 (B), 300 (C) ] (78)

— *Ab-initio study of organic semiconductor thin film growth*

1. Work function of Pentacene on graphene  
K. Nishidate et. al.: submitted to J. Phys. Condens. Matter

**NOGAWA, Tomoaki** [ B class; 0 (A), 1200 (B), 0 (C) ] (259)

— *Search of close packing states of multicomponent hard-sphere systems by the parallelized Wang-Landau sampling*

**NOGUCHI, Hiroshi** [ C class; 0 (A), 9000 (B), 2200 (C) ] (207,208)

— *Protein self-assembly on biomembranes*

— *Shape transformation of lipid membranes induced by protein adsorption and chemical reaction*

1. Shape transformations of toroidal vesicles  
H. Noguchi, A. Sakashita, and M. Imai: aSoft Matter, **11** (2015) 193.
2. Two- or three-step assembly of banana-shaped proteins coupled with shape transformation of lipid membranes  
H. Noguchi: EPL **108** (2014) 48001.
3. Morphological changes of amphiphilic molecular assemblies induced by chemical reaction  
K. M. Nakagawa and H. Noguchi: Soft Matter **11** (2015) 1403.

**NOGUCHI, Yoshifumi** [ C class; 0 (A), 2500 (B), 1800 (C) ] (15)

— *All-electron first-principles GW+Bethe-Salpeter method: development and application*

1. First-principles investigation on Rydberg and resonance excitations: A case study of the firefly luciferin anion  
Y. Noguchi, M. Hiyama, H. Akiyama, and N. Koga, J. Chem. Phys. **141**, 044309 (2014).
2. Symmetry breaking and excitonic effects on optical properties of defective nanographenes  
Y. Noguchi and O. Sugino, J. Chem. Phys. **142**, 064313 (2015).
3. First-Principles Investigation of Strong Excitonic Effects in Oxygen 1s X-ray Absorption Spectra

Y. Noguchi, M. Hiyama, H. Akiyama, Y. Harada, and N. Koga, J. Chem. Theor. Compt. **11**, 1668 (2015).

**OBATA, Shuji** [ C class; 8000 (A), 0 (B), 600 (C) ] (79)

— *Magnetization and electronic structure calculations of Fe compounds*

1. Computer Simulations on Barkhausen Effects and Magnetizations in Fe Nano-Structure Systems  
Shuji Obata: Materials Transactions, **55** (2014) 1591/1-8

**ODA, Tatsuki** [ D,E class; 0 (A), 17000 (B), 3100 (C) ] (49,50,51)

— *Analyses on atomic structure, magnetism, and electronic structure in spintronics materials and molecular magnets*

— *Analyses on atomic structure, magnetism, and electronic structure in spintronics materials*

— *Exploratory study on electric field effect of the magnetic anisotropy in the spintronics material with the oxide layer*

1. An ab initio approach to free-energy reconstruction using logarithmic mean force dynamics  
M. Nakamura, M. Obata, T. Morishita, T. Oda: J. Chem. Phys., **140** (2014) 184110.
2. Phase with pressure-induced shuttlewise deformation in dense solid atomic hydrogen  
T. Ishikawa, H. Nagara, T. Oda, N. Suzuki, and K. Shimizu: Phys. Rev. B, **90** (2014) 104102.
3. Symmetry-induced peculiar Rashba effect on thallium adsorbed Si(111) surfaces  
K. Sakamoto, T. Oda, A. Kimura, Y. Takeichi, J. Fujii, R. I. G. Uhrberg, M. Donath, H. W. Yeom: Journal of Electron Spectroscopy and Related Phenomena, in press.
4. Possible origin of non-linear magnetic anisotropy variation in electric field effect in a double interface system  
D. Yoshikawa, M. Obata, Y. Taguchi, S. Haraguchi, and T. Oda: Appl. Phys. Express, **7** (2014) 113005.
5. Review on distorted face-centered cubic phase in yttrium via genetic algorithm  
T. Ishikawa, T. Oda, N. Suzuki, and K. Shimizu: High Pressure Research (regular article), DOI: 10.1080/08957959.2014.983501.
6. Improving the Description of Nonmagnetic and Magnetic Molecular Crystals via the van der Waals Density Functional  
M. Obata, M. Nakamura, I. Hamada, and T. Oda: J. Phys. Soc. Jpn., **84** (2015) 024715.
7. Molecular Interactions for Modeling of Oxygen System Using van der Waals Density Functional Approach  
M. Obata, I. Hamada, and T. Oda, : JPS Conf. Proc., **5** (2015) 011011.
8. First-principles study on structural and electronic properties in Fe/MgO double interface  
D. Yoshikawa, M. Obata, and T. Oda: JPS Conf. Proc., **5** (2015) 011012.

**OGUCHI, Tamio** [ C class; 1500 (A), 4000 (B), 1700 (C) ] (85)

— *First-Principles Calculation of Transition-Metal Compounds*

1. Ab-initio Prediction of Magnetoelectricity in Infinite-Layer  $\text{CaFeO}_2$  and  $\text{MgFeO}_2$   
K. Yamauchi, T. Oguchi, and S. Picozzi: J. Phys. Soc. Jpn. **83** (2014) 094712.
2. First-Principles Study on Structural and Electronic Properties of  $\alpha$ -S and Na-S Crystals  
H. Momida, T. Yamashita, and T. Oguchi: J. Phys. Soc. Jpn. **83** (2014) 124713.
3. Origin of the band dispersion in a metal phthalocyanine crystal  
S. Yanagisawa, K. Yamauchi, T. Inaoka, T. Oguchi, and I. Hamada: Phys. Rev. B **90** (2014) 245141.
4. Ab Initio Study on Pressure-Induced Phase Transition in  $\text{LaCu}_3\text{Fe}_4\text{O}_{12}$   
K. Isoyama, M. Toyoda, K. Yamauchi, and T. Oguchi: J. Phys. Soc. Jpn. **84** (2015) 034709.
5. *Ab initio* study of electronic, magnetic, and spectroscopic properties in A- and B-site-ordered perovskite  $\text{CaCu}_3\text{Fe}_2\text{Sb}_2\text{O}_{12}$   
H. Fujii, M. Toyoda, H. Momida, M. Mizumaki, S. Kimura, and T. Oguchi: Phys. Rev. B **90** (2014) 014430.
6. Ferromagnetic Half Metallicity in Doped Chalcopyrite Semiconductors  $\text{Cu}(\text{Al}_{1-x}\text{A}_x)\text{Se}_2$  ( $\text{A}=3d$  Transition-Metal Atoms)  
M. Shahjahan, M. Toyoda, and T. Oguchi: J. Phys. Soc. Jpn. **83** (2014) 094702.



7. Quasi-One-Dimensional Nature of the Rashba States of Au Wires on Si(557) Surface  
T. Oguchi: J. Electron Spectrosc. Relat. Phenom. (2014). doi:10.1016/j.elspec.2014.09.004
8. Symmetry-breaking 60°C *efc*-spin order in the A-site-ordered perovskite  $\text{LaMn}_3\text{V}_4\text{O}_{12}$   
T. Saito, M. Toyoda, C. Ritter, S. Zhang, T. Oguchi, J. P. Attfield, and Y. Shimakawa: Phys. Rev. B **90** (2014) 214405.
9. One-dimensional edge states with giant spin splitting in a bismuth thin film  
A. Takayama, T. Sato, S. Souma, T. Oguchi, and T. Takahashi: Phys. Rev. Lett. **114** (2015) 066402.
10. Topological proximity effect in a topological insulator hybrid  
T. Shoman, A. Takayama, T. Sato, S. Souma, T. Takahashi, T. Oguchi, K. Segawa, and Y. Ando: Nature Commun. **6** (2015) 6547.
11. Signature of high  $T_c$  around 25K in higher quality heavily boron-doped diamond  
H. Okazaki, T. Wakita, T. Muro, T. Nakamura, Y. Muraoka, T. Yokoya, S. Kurihara, H. Kawarada, T. Oguchi, and Y. Takano: Appl. Phys. Lett. **106** (2015) 052691.

**OHGOE, Takahiro** [ C class; 0 (A), 2000 (B), 0 (C) ] (174)

— *Multi-variable variational Monte Carlo study of the Holstein-Hubbard model*

**OHMURA, Satoshi** [ C class; 0 (A), 3000 (B), 0 (C) ] (115,116)

— *Ab initio molecular dynamics study of molecular dissociation by irradiation of X-FEL*

— *Ultrahigh-pressure structures of liquid oxygen and nitrogen*

1. Structural Properties of  $\text{Fe}_2\text{O}_3$  at High Temperatures  
M. Misawa, S. Ohmura, and F. Shimojo: Journal of the Physical Society of Japan **83** (2014) 105002/1-2.
2. Reaction of ethylene molecules with a nickel cluster: ab initio molecular dynamics study  
K. Shimamura<sup>1</sup>, R. Arifin, T. Oguri, Y. Shibuta, S. Ohmura, F. Shimojo and S. Yamaguchi: Transactions of the Materials Research Society of Japan
3. Non-equilibrium dynamics in disordered materials: ab initio molecular dynamics simulations  
S. Ohmura, K. Nagaya, F. Shimojo and M. Yao: AIP conference proceeding
4. Charge transfer and nuclear dynamics following deep inner-shell multiphoton ionization of  $\text{CH}_3\text{I}$  molecules by intense x-ray free-electron laser pulses  
K. Motomura, E. Kukk, H. Fukuzawa, S. Wada, K. Nagaya, S. Ohmura, S. Mondal T. Tachibana, Y. Ito, R. Koga, T. Sakai, K. Matsunami, A. Rudenko, C. Nicolas, X.-J. Liu, C. Miron, Y. Zhang, Y. H. Jiang, J. Chen, M. Anand, D. Kim, K. Tono, M. Yabashi, M. Yao, and K. Ueda: Physical Review Lett

**OHNO, Takahisa** [ B,C class; 0 (A), 6700 (B), 0 (C) ] ()

— *Computational Analysis on Ionic Conduction Properties of All Solid-State Lithium Secondary Battery Materials*

— *ab initio analysis on solid/solid interfaces for all-solid-state batteries*

— *Theoretical design of the high ionic conductor*

**OHSAWA, Kazuhito** [ C class; 0 (A), 2000 (B), 0 (C) ] (125)

— *Study of interaction between radiation damage and interstitial atom*

**OHTO, Tatsuhiko** [ B,C class; 0 (A), 6200 (B), 3700 (C) ] (76,77)

— *First-principles molecular dynamics simulation of the water/surfactant interfaces*

— *Ab initio study of thermoelectric properties of molecules between magnetic electrodes*

1. Single molecular resistive switch obtained via sliding multiple anchoring points and varying effective wire length  
Manabu Kiguchi, Tatsuhiko Ohto, Shintaro Fujii, Kazunori Sugiyasu, Shiegeto Nakajima, Masayuki Takeuchi and Hisao Nakamura: JACS **136** (2014) 7327.
2. Thermopower of benzenedithiol and C60 molecular junctions with Ni and Au electrodes  
See Kei Lee, Tatsuhiko Ohto, Ryo Yamada and Hirokazu Tada: Nano Lett. **14** (2014) 5276.

**OHTSUKI, Tomi** [ C class; 2000 (A), 5000 (B), 500 (C) ] (225)

— *Phase diagram and critical properties of disordered topological insulators*

1. Engineering Dirac electrons emergent on the surface of a topological insulator  
Y. Yoshimura, K. Kobayashi, T. Ohtsuki, K.-I. Imura: Science and Technology of Advanced Materials **16** (2015), 014403
2. Modification and Control of Topological Insulator Surface States Using Surface Disorder  
V. Sacksteder, T. Ohtsuki, K. Kobayashi: arXiv:1410.7621
3. Dimensional crossover of transport characteristics in topological insulator nanofilms  
K. Kobayashi, K.-I. Imura, Y. Yoshimura, T. Ohtsuki: arXiv:1409.1707
4. Dimensional Dependence of Critical Exponent of the Anderson Transition in the Orthogonal Universality Class  
Yoshiki Ueoka, and Keith Slevin: J. Phys. Soc. Jpn. **83** (2014) 084711
5. Critical exponent of metal-insulator transition in doped semiconductors: the relevance of the Coulomb interaction  
Y. Harashima, K. Slevin: Phys. Rev. B **89** (2014), 205108
6. Survival of sharp  $n=0$  Landau levels in massive tilted Dirac fermions: Role of the generalized chiral operator  
Yasuhiro Hatsugai, Tohru Kawarabayashi, and Hideo Aoki: Phys. Rev. B **91** (2015), 085112

**OKA, Takashi** [ C class; 6000 (A), 3000 (B), 0 (C) ] (219)

— *Theoretical study of non-equilibrium phase transitions in strongly correlated superconductors*

**OKADA, Susumu** [ C class; 13500 (A), 0 (B), 0 (C) ] (64)

— *Design of nanoscale carbon materials*

1. Energetics and electronic structures of polymerized cyclobutadiene  
Mina Maruyama, Kyoko Nakada, and Susumu Okada: Japanese Journal of Applied Physics, Vol. 53, 035103 (2014)
2. Electrostatic modulation of electron-states in MoS<sub>2</sub>: First-principles Calculations  
Nguyen Thanh Cuong, Minoru Otani, and Susumu Okada: Journal of Physics: Condensed Matter Vol. 26, 135001 (2014)
3. Flexible metallic nanowires with self-adaptive Ohmic contact to semiconducting transition-metal dichalcogenide monolayers  
Junhao Lin, Ovidiu Cretu, Wu Zhou, Kazu Suenaga, Dhiraj Prasai, Kirill I. Bolotin, Nguyen Thanh Cuong, Minoru Otani, Susumu Okada, Andrew R. Lupini, Juan-Carlos Idrobo, Dave Caudel, Arnold Burger, Nirmal J. Ghimire, Jiaqiang Yan, David G. Mandrus, Stephen J. Pennycook, Sokrates T. Pantelides: Nature Nanotechnology Vol. 9, 436 – 442 (2014)
4. Two-dimensional sp<sup>2</sup> Carbon Networks of Fused Pentagons  
Mina Maruyama and Susumu Okada: Japanese Journal of Applied Physics Vol. 53, 06JD02 (2014)
5. Structural Dependence of Electronic Properties of Graphene Nanoribbons on an Electric Field  
Ayaka Yamanaka and Susumu Okada: Japanese Journal of Applied Physics Vol. 53, 06JD05 (2014)
6. Energetics and Electronic Structures of C<sub>60</sub> Included in [*n*]Cyclacene Molecules: Dynamical and Electronic Properties of C<sub>60</sub>  
Shota Kigure and Susumu Okada: Japanese Journal of Applied Physics Vol. 53, 06JD06 (2014)
7. An anomalous dipole-dipole arrangement of water molecules encapsulated into C<sub>60</sub> dimer  
Kazuya Nomura and Susumu Okada: Chemical Physics Letters Vol. 608, pp. 351–354 (2014)
8. Spin-state tuning of decamethyl C<sub>60</sub> by an external electric field  
Kohei Narita and Susumu Okada: Chemical Physics Letters Vol. 614, pp. 10-14 (2014)
9. Coulomb Interaction Effects on Optical Properties of Monolayer Transition Metal Dichalcogenides  
Satoru Konabe and Susumu Okada: Physical Review B Vol. 90, 155304 (2014)
10. Electronic structures of carbon nanotubes with monovacancy under an electric field  
U Ishiyama, Nguyen Thanh Cuong, and Susumu Okada: Japanese Journal of Applied Physics Vol. 53, 115102 (2014)
11. Electronic and Geometric Structures of Carbon Nanotubes Encapsulating Polycyclic Aromatic Hydrocarbon Molecules

Shota Kigure, Yoko Iizumi, Toshiya Okazaki, and Susumu Okada: Journal of the Physical Society of Japan Vol. 83, 124709 (2014)

12. Electron injection into nearly free electron states of graphene nanoribbons under a lateral electric field

Ayaka Yamanaka and Susumu Okada: Applied Physics Express Vol. 7, 125103 (2014)

13. Nanoporous Carbon Tubes from Fullerene Crystals as the  $\pi$ -Electron Carbon Source  
Lok Kumar Shrestha, Rekha Goswami Shrestha, Yusuke Yamauchi, Jonathan P. Hill, Toshiyuki Nishimura, Kun'ichi Miyazawa, Katsunori Wakabayashi, Takazumi Kawai, Susumu Okada, and Katsuhiko Ariga: Angewandte Chemie International Edition, Vol. 53, pp. 951 - 955 (2014).

**OKAMOTO, Yuko** [ E class; 0 (A), 16500 (B), 0 (C) ] (31)

— *Study on complex systems by generalized-ensemble algorithms*

1. Predictions of tertiary structures of  $\alpha$ -helical membrane proteins by replica-exchange method with consideration of helix deformations  
R. Urano, H. Kokubo, and Y. Okamoto: J. Phys. Soc. Jpn., in press.
2. Deterministic replica-exchange method without pseudo random numbers for simulations of complex systems  
R. Urano and Y. Okamoto: submitted for publication; arXiv:1412.6959.
3. Designed-walk replica-exchange method for simulations of complex systems  
R. Urano and Y. Okamoto: submitted for publication; arXiv:1501.00772.

**OKITSU, Kouhei** [ C class; 1000 (A), 3000 (B), 400 (C) ] (237)

— *Study on X-ray n-beam dynamical and kinematical diffraction theories and numerical methods to solve them*

— *Study on X-ray n-beam diffraction and phase problem in protein crystal structure analysis*

**OKUBO, Tsuyoshi** [ C,S class; 5500 (A), 31000 (B), 4000 (C) ] (188,190)

— *Novel phases in frustrated magnets*

— *Topological phase transition in the frustrated magnets*

1. Field-induced incommensurate phase in the strong-rung spin ladder with ferromagnetic legs  
H. Yamaguchi, H. Miyagai, M. Yoshida, M. Takigawa, K. Iwase, T. Ono, N. Kase, K. Araki, S. Kittaka, T. Sakakibara, T. Shimokawa, T. Okubo, K. Okunishi, A. Matsuo, and Y. Hosokoshi: Phys. Rev. B **89** (2014) 220402(R)
2. A Scaling Relation for Dangerously Irrelevant Symmetry-Breaking Fields  
T. Okubo, K. Oshikawa, H. Watanabe, and N. Kawashima: Phys. Rev. B., in press
3.  $SU(N)$  Heisenberg model with multi-column representations  
T. Okubo, K. Harada, J. Lou, and N. Kawashima: Submitted to Phys. Rev. B

**ONISHI, Hiroaki** [ C class; 0 (A), 2000 (B), 0 (C) ] (252)

— *Excitation dynamics of frustrated quantum spin chain*

1. Doping control of realization of an extended Nagaoka ferromagnetic state from the Mott state  
H. Onishi and S. Miyashita, Phys. Rev. B **90**, 224426 (2014).
2. Effects of magnetic anisotropy on spin dynamics of ferromagnetic frustrated chain  
H. Onishi, J. Phys.: Conf. Ser. **592**, 012109 (2015).

**ONO, Tomoya** [ C class; 1000 (A), 7500 (B), 4300 (C) ] (66)

— *Development of first-principles electronic-structure and transport calculation method based on real-space finite-difference approach*

1. Electronic Structures and Magnetic Anisotropy Energies of Graphene with Adsorbed Transition-Metal Adatoms  
H. D. Nguyen and T. Ono: J. Phys. Soc. Jpn. **83** (2014) 094716.
2. Electron-transport properties of ethyne-bridged diphenyl zinc-porphyrin molecules  
H. D. Nguyen and T. Ono: Jpn. J. Appl. Phys. **54** (2015) 055201.
3. First-principles study on the effect of  $\text{SiO}_2$  layers during oxidation of 4H-SiC  
T. Ono and S. Saito: Appl. Phys. Lett. **106** (2015) 081601.

**OSHIKAWA, Masaki** [ B class; 0 (A), 800 (B), 0 (C) ] (177)

— *Numerical study of flux quench in one-dimensional quantum systems*

**OSHIYAMA, Atsushi** [ E class; 0 (A), 31000 (B), 4700 (C) ] (40)

— *Atomic Structures and Electronic Properties of Hard- and Soft-Nanomaterials*

1. Performance evaluation of ultra-largescale first-principles electronic structure calculation code on the K computer  
Y. Hasegawa, J.-I. Iwata, M. Tsuji, D. Takahashi, A. Oshiyama, K. Minami, T. Boku, H. Inoue, Y. Kitazawa, I. Miyoshi, M. Yokokawa: International Journal of High Performance Computing Applications **28** (2014) 335-355
2. Surface energy of Si(110)- and 3C-SiC(111)-terminated surfaces  
E. K. K. Abavare, I.-I. Iwata, A. Yaya and A. Oshiyama: Phys. Status Solidi B **251** (2014) 1408 - 1415
3. Electron Confinement due to Stacking Control of Atomic Layers in SiC Polytypes: Role of Floaing States and Spontaneous Polarization  
Y.-I. Matsushita S. Furuya, and A. Oshiyama: J. Phys. Soc. Jpn. **83** (2014) 094713
4. Atomic corrugation and electron localization due to Moiré patterns in twisted bilayer graphenes  
K. Uchida, S. Furuya, J.-I. Iwata and A. Oshiyama: Phys. Rev. B **90** (2014) 155451
5. Large-Scale Real-Space Density-Functional Calculations: Moiré-Induced Electron Localization in Graphene  
A. Oshiyama, J.-I. Iwata, K. Uchida and Y. Matsushita: J. Appl. Phys **117** (2015) 112811
6. Energetics, Electron States, and Magnetization in Nearly Zigzag-Edged Graphene Nano-Ribbons  
S. Suda and A. Oshiyama: J. Phys. Soc. Jpn. **84** (2015) 024704

**OTANI, Minoru** [ E class; 0 (A), 13000 (B), 2200 (C) ] (60)

— *Simulation of Electrochemical reaction using constant electrode potential method*

**OTOMO, Junichiro** [ B,C class; 0 (A), 3200 (B), 0 (C) ] (111,113)

— *Evaluation of ion conductivity at interfaces in proton conducting composite electrolyte*

— *Numerical simulation of metal oxides redox reaction on various supports*

— *Evaluation of ion conductivity of interfaces in composite-type proton conducting electrolyte*

**OTSUKI, Junya** [ B class; 0 (A), 700 (B), 0 (C) ] (179)

— *Investigation of unconventional superconductivities by extension of the dynamical mean-field theory*

1. Superconductivity, antiferromagnetism, and phase separation in the two-dimensional Hubbard model: A dual-fermion approach  
J. Otsuki, H. Hafermann, A. I. Lichtenstein: Phys. Rev. B **90** (2014) 235132.

**OZEKI, Yukiyasu** [ C class; 0 (A), 6000 (B), 0 (C) ] (231)

— *Improvement of dynamical scaling by the use of kernel method and its applications to nonequilibrium relaxation analyses*

**RAEBIGER, Hannes** [ C class; 0 (A), 2500 (B), 0 (C) ] ()

— *Theory of self-organized nano-interfaces for electronic devices*

**SAITO, Mineo** [ C class; 0 (A), 4500 (B), 0 (C) ] (102)

— *Simulation of electronic properties in materials for spintronics*

1. Spin polarized positron lifetimes in ferromagnetic metals: First-principles study  
J. Lin, T. Yamasaki, and M. Saito: Jpn. J. Appl. Phys. **53**, 05302 (2014).
2. Band gap design of thiophene polymers based on density functional theory  
Patricia Lubis and Mineo Saito: Jpn. J. Appl. Phys. **53**, 071602 (2014).
3. Tunable Rashba effect on strained ZnO: First-principles density-functional study  
Moh Adhib Ulil Absor, Hiroki Kotaka, Fumiyuki Ishii, and Mineo Saito: Appl. Phys. Express **7**, 053002 (2014).

4. Density Functional Theory Calculations of Formation Energies and Vacancy Concentrations of the Silicon Vacancy  
Sholihun, M. Saito, T. Ohno, and T. Yamasaki: Jpn. J. Appl. Phys. **54**, 041301 (2014)

**SAKAI, Toru** [ C class; 25000 (A), 5500 (B), 3800 (C) ] (191)

— *Ring Exchange Induced New Quantum Phases in Quantum Spin Systems*

— *Numerical Study on Novel Phases of the Spin Nanotubes*

1. Quantum Spin-Liquid Behavior in the Spin-1/2 Random Heisenberg Antiferromagnet on the Triangular Lattice  
K. Watanabe, H. Kawamura, H. Nakano and T. Sakai: J. Phys. Soc. Jpn. **83** (2014) 034714.
2. Exotic Quantum Phenomena in the Spin Nanotubes  
T. Sakai, K. Okamoto: JPS Conf. Proc. **1** (2014) 012025.
3. Exotic Magnetism of the Quantum Spin Nanotube  
T. Sakai, K. Okamoto: JPS Conf. Proc. **2** (2014) 010208.
4. Edge Modes in the Intermediate-D and Large-D Phases of the  $S = 2$  Quantum Spin Chain with XXZ and On-Site Anisotropies  
K. Okamoto, T. Tonegawa, T. Sakai, M. Kaburagi: JPS Conf. Proc. **3** (2014) 014002.
5. Magnetization Process of the  $S=1/2$  Heisenberg Antiferromagnet on the Cairo Pentagon Lattice  
H. Nakano, M. Isoda, T. Sakai: J. Phys. Soc. Jpn. **83** (2014) 053702.
6. Anomalous Quantum Magnetization Behaviors of the Kagome and Triangular Lattice Antiferromagnets  
H. Nakano, T. Sakai: JPS Conf. Proc. **3** (2014) 014003.
7. Exotic Quantum Phase Transition of the Spin Nanotube  
T. Sakai, H. Nakano, K. Okunishi: J. Phys.: Conf. Ser. **568** (2014) 042024.
8. Novel Field Induced Quantum Phase Transition of the Kagome Lattice Antiferromagnet  
T. Sakai, H. Nakano: J. Phys.: Conf. Ser. **568** (2014) 042025.
9. Spin-Flop Phenomenon of Two-Dimensional Frustrated Antiferromagnets without Anisotropy in Spin Space  
H. Nakano, T. Sakai, Y. Hasegawa: J. Phys. Soc. Jpn. **83** (2014) 084709.
10. Frustration-Induced Magnetic Properties of the Spin-1/2 Heisenberg Antiferromagnet on the Cairo Pentagon Lattice  
M. Isoda, H. Nakano, T. Sakai: J. Phys. Soc. Jpn. **83** (2014) 084710.
11. Anomalous Behavior of the Magnetization Process of the  $S=1/2$  Kagome-Lattice Heisenberg Antiferromagnet at One-Third Height of the Saturation  
H. Nakano, T. Sakai: J. Phys. Soc. Jpn. **83** (2014) 104710.
12. Instability of a ferromagnetic state of a frustrated  $S=1/2$  Heisenberg antiferromagnet in two dimensions  
H. Nakano, T. Sakai: Jpn. J. Appl. Phys. **54** (2015) 030305.
13. Possible Singlet-Triplet Transition of ESR in the Kagome-Lattice Antiferromagnet  
T. Sakai, K. Hijii, S. Okubo, H. Ohta, H. Nakano, S. Miyashita: Applied Magnetic Resonance, in press.
14. Magnetization Process of the Spin-S Kagome-Lattice Heisenberg Antiferromagnet  
H. Nakano, T. Sakai: J. Phys. Soc. Jpn., in press.
15. Spin nanotubes with the ring exchange interactions  
T. Sakai, T. Kasahara, K. Hijii, H. Ohta, H. Nakano: submitted to Synthetic Metals

**SAKAKIBARA, Hirofumi** [ B class; 2000 (A), 800 (B), 500 (C) ] (109)

— *Theoretical material design of transition metal oxide hetero structure based on the orbital distillation effect*

**SAKASHITA, Tatsuya** [ B class; 0 (A), 900 (B), 0 (C) ] ( )

— *Parallelization and High Precision Computation of Exact Diagonalization Package for Spin Systems*

**SATO, Toshihiro** [ C class; 0 (A), 4000 (B), 0 (C) ] (165,167)

— *Electric transport near the antiferromagnetic transition in a square-lattice Hubbard model*

— *Insulating state of multi-orbital electronic system with strong spin-orbit coupling*

1. Spin-orbit-induced exotic insulators in a three-orbital Hubbard model with  $(t_{2g})^5$  electrons  
Toshihiro Sato, Tomonori Shirakawa, and Seiji Yunoki: Phys. Rev. B **91** (2015) 125122.

**SATO, Yukio** [ B class; 0 (A), 700 (B), 0 (C) ] (142)

— *First-principles calculation of atomic arrangement and electronic structure in ceramic grain boundaries*

1. Grain Boundary Plane Effect on Pr Segregation Site in ZnO S13 [0001] Symmetric Tilt Grain Boundaries  
J.-Y. Roh, Y. Sato, and Y. Ikuhara, Journal of the American Ceramic Society, in press.
2. Role of grain boundaries in ZnO  
Y. Sato and Y. Ikuhara, Oxide-based Materials and Devices V, ed. by Teherani, Look, and Rogers, Proceeding of SPIE, 8987 89871B-1-7, (2014).
3. Grain Boundary Structure Transformation and Reconstruction in Oxide Ceramics  
Y. Ikuhara, Y. Sato, and N. Shibata, AMTC Letters, 4, 4-5 (2014).
4. Structural Multiplicity in Pr-doped ZnO [0001] 27.8° and 30.0° Tilt Grain Boundaries  
J.-Y. Roh, Y. Sato, and Y. Ikuhara, AMTC Letters, 4, 26-27 (2014).
5. Atomic Structure and Energetics of Oxygen Vacancy in CeO<sub>2</sub> Grain Boundaries  
B. Feng, H. Hojo, Y. Sato, H. Ohta, N. Shibata, and Y. Ikuhara, AMTC Letters, 4, 98-99 (2014).

**SHIBA, Hayato** [ B,E class; 1000 (A), 19400 (B), 2100 (C) ] (195,196)

— *Quest for static and dynamical heterogeneities in structural glass by huge-scale molecular simulation*

— *Dynamics of higher-order structure formation in surfactant membranes*

— *Absorbing states and viscoelasticity in low-Re non-Brownian particle dispersions*

1. Rheological evaluation of colloidal dispersions using smoothed profile method - formulation and applications  
J. J. Molina, K. Otomura, H. Shiba, H. Kobayashi, M. Sano, and R. Yamamoto: submitted to J. Fluid Mech.

**SHIGETA, Yasuteru** [ C class; 24500 (A), 6000 (B), 0 (C) ] (42)

— *Theoretical studies on heat resistance of Nyl-C*

— *Theoretical analyses on hydrolysis mechanism of Nyl C*

1. Simple, Yet Powerful Methodologies for Conformational Sampling of Proteins  
H. Harada, Y. Takano, T. Baba, Y. Shigeta: Phys. Chem. Chem. Phys. (invited feature article) 17, 6155-6173 (2015).
2. Hydration Effects on Enzyme-Substrate Complex of Nylon Oligomer Hydrolase: Inter-Fragment Interaction Energy Study by the Fragment Molecular Orbital Method  
H. Ando, Y. Shigeta, T. Baba, C. Watanabe, Y. Okiyama, Y. Mochizuki, M. Nakano: Mol. Phys. 113, 319-326 (2015).
3. Unraveling the degradation of artificial amide bonds in nylon oligomer hydrolase: from induced-fit to acylation processes  
T. Baba, M. Boero, K. Kamiya, H. Ando, S. Negoro, M. Nakano, Y. Shigeta: Phys. Chem. Chem. Phys. 17, 4492-4504(2015).
4. On the induced-fit mechanism of substrate-enzyme binding structures of Nylon-oligomerhydrolase  
T. Baba, R. Harada, M. Nakano, Y. Shigeta: J. Comp. Chem. 35, 1240-47 (2014).
5. A Nylon-oligomer Hydrolase Promoting Cleavage Reactions in Unnatural Amide Compounds  
K. Kamiya, T. Baba, M. Boero, T. Matsui, S. Negoro, Y. Shigeta: J. Phys. Chem. Lett. 5, 1210-1216 (2014).

**SHIMIZU, Akira** [ C class; 0 (A), 3000 (B), 1800 (C) ] ( )

— *Thermal pure quantum state calculus of Fermion systems*

**SHIMOJO, Fuyuki** [ C class; 0 (A), 8000 (B), 4500 (C) ] (68)

— *First-Principles Molecular-Dynamics Study of Structural and Electronic Properties of Covalent Liquids under Pressure*

1. Structural properties of  $\text{Fe}_2\text{O}_3$  at high temperatures  
M. Misawa, S. Ohmura, and F. Shimojo: J. Phys. Soc. Jpn. **83** (2014) 105002.
2. Oxygen 2p partial density of states in a typical oxide glass  $\text{B}_2\text{O}_3$   
S. Hosokawa, H. Sato, K. Mimura, Y. Tezuka, D. Fukunaga, K. Shimamura, and F. Shimojo: J. Phys. Soc. Jpn. **83** (2014) 114601.
3. A divide-conquer-recombine algorithmic paradigm for large spatiotemporal quantum molecular dynamics simulations  
F. Shimojo, S. Hattori, R. K. Kaila, M. Kunaseth, W. Mou, A. Nakano, K. Nomura, S. Ohmura, P. Rajak, K. Shimamura, and P. Vashishta: J. Chem. Phys. **140** (2014) 18A529.
4. Hydrogen-on-Demand Using Metallic Alloy Nanoparticles in Water  
K. Shimamura, F. Shimojo, R. K. Kalia, A. Nakano, K. Nomura, and P. Vashishta: Nano Lett. **14** (2014) 4090.

**SHIMOKAWA, Tokuro** [ B class; 3100 (A), 1100 (B), 600 (C) ] (234)

— *Numerical study of the novel magnetic phenomenon on the honeycomb magnetism*

**SHIOMI, Junichiro** [ C class; 0 (A), 3000 (B), 0 (C) ] (242)

— *Characterization of thermal transport at nanostructure interface*

1. Scaling laws of cumulative thermal conductivity for short and long phonon mean free paths  
Daisuke Aketo, Takuma Shiga, Junichiro Shiomi: Applied Physics Letters **105**, 131901 (2014).
2. Probing and tuning inelastic phonon conductance across finite-thickness interface  
Takuru Murakami, Takuma Hori, Takuma Shiga, and Junichiro Shiomi: Applied Physics Express **7**, 121801 (2014).
3. Effective phonon mean free path in polycrystalline nanostructures  
Takuma Hori, Junichiro Shiomi, Chris Dames: Applied Physics Letters **106**, 171901 (2015).
4. Controllability of thermal conductance across sintered silicon interface by local nanostructures  
Masanori Sakata, Takuma Hori, Takafumi Oyake, Jeremie Maire, Masahiro Nomura, Junichiro Shiomi: Nano energy, Rapid communication, **13**, 601 (2015).
5. Impeded thermal transport in Si multiscale hierarchical architectures with phononic crystal nanostructures  
M. Nomura, Y. Kage, J. Nakagawa, T. Hori, J. Maire, J. Shiomi, D. Moser, O. Paul: Physical Review B (in press), arXiv:1502.02789
6. Anomalous reduction of thermal conductivity in coherent nanocrystal architecture for silicon thermoelectric material  
Yoshiaki Nakamura, Masayuki Isogawa, Tomohiro Ueda, Shuto Yamasaka, Hideki Matsui, Jun Kikkawa, Satoaki Ikeuchi, Takafumi Oyake, Takuma Hori, Junichiro Shiomi, Akira Sakai: Nano Energy, Rapid communication

**SHIRAISHI, Kenji** [ C class; 13500 (A), 4000 (B), 2100 (C) ] ( )

— *First Principles Design of Future SiC-Based Power Devices*

**SHIRO, Masanori** [ B class; 1300 (A), 0 (B), 0 (C) ] (256)

— *High precision computation of Feigenbaum constant, 2nd.*

**SHOJI, Mitsuo** [ C class; 0 (A), 2500 (B), 0 (C) ] (123)

— *Theoretical elucidation on the full reaction mechanism of threonine synthase*

1. An Efficient Initial Guess Formation of Broken-Symmetry Solutions by using Localized Natural Orbitals  
M.Shoji, Y.Yoshioka, K.Yamaguchi: Chem. Phys. Lett. **608** (2014) 50-54.
2. Light absorption and excitation energy transfer calculations in primitive photosynthetic bacteria  
Y.Komatsu, M.Kayanuma, M.Shoji, K.Yabana, K.Shiraishi, M.Umemura: Molecular Physics, accepted 2014.
3. Light absorption efficiencies of photosynthetic pigments: the dependence on spectral types of central stars  
Y.Komatsu, M.Umemura, M.Shoji, M.Kayanuma, K.Yabana, K.Shiraishi: International Journal

of Astrobiology, accepted 2014.

4. Involvement of Propionate Side Chains of the Heme in Circular Dichroism of Myoglobin: Experimental and Theoretical Analyses  
M.Nagai, C.Kobayashi, Y. Nagai, K.Imai, N.Mizusawa, H.Sakurai, S.Neya, M.Kayanuma, M.Shoji, S.Nagatomo: J. Phys. Chem. B **119** (2015) 1275-1287.
5. On the guiding principles for lucid understanding of the damage-free S1 structure of the CaMn4O5 cluster in the oxygen evolving complex of photosystem II  
M.Shoji, H.Isobe, S.Yamanaka, M.Suga, F.Akita, J.-R.Shen, K.Yamaguchi: Chem. Phys. Lett. **627** (2015) 44-52.
6. Theoretical studies of the damage-free S1 structure of the CaMn4O5 cluster in oxygen-evolving complex of photosystem II  
M.Shoji, H.Isobe, S.Yamanaka, M.Suga, F.Akita, J.-R.Shen, K.Yamaguchi: Chem. Phys. Lett. **623** (2015) 1-7.
7. A QM/MM Study of the Initial Steps of Catalytic Mechanism of Nitrile Hydratase  
M.Kayanuma, K.Hanaoka, M.Shoji, Y. Shigeta: Chem. Phys. Lett. **623** (2015) 8-13.

**SHUDO, Ken-Ichi** [ C class; 1000 (A), 500 (B), 0 (C) ] (132)

— *Bonding states of organic molecules adsorbed at defects on metal surface*

**SUGINO, Osamu** [ C class; 0 (A), 2500 (B), 900 (C) ] (108)

— *Oxide electrocatalysts*

1. Exceptionally long-ranged lattice relaxation in oxygen-deficient Ta<sub>2</sub>O<sub>5</sub>  
Y. Yang, O. Sugino and Y. Kawazoe, Solid State Communications 195 (2014) 16.

**SUWA, Hidemaro** [ C class; 0 (A), 1500 (B), 0 (C) ] (254)

— *Efficient Monte Carlo Spectral Analysis and Application to Quantum Spin Systems*

1. Generalized Moment Method for Gap Estimation and Quantum Monte Carlo Level Spectroscopy  
Hidemaro Suwa and Synge Todo: submitted to Phys. Rev. Lett.

**SUZUKI, Takafumi** [ C class; 1500 (A), 4500 (B), 2200 (C) ] (220,222)

— *Successive phase transition and magnetic orders in rare-earth metals*

1. Thermal phase transition of generalized Heisenberg models for SU(N) spins on square and honeycomb lattices  
T. Suzuki, K. Harada, H. Matsuo, S. Todo, and N. Kawashima, Phys. Rev. B **91**, 094414 (2015).
2. Thermal phase transition to valence-bond-solid phase in the two-dimensional generalized SU(N) Heisenberg models  
T. Suzuki, K. Harada, H. Matsuo, S. Todo, and N. Kawashima, J. Phys.: Conf. Ser. **592**, 012114 (2015).

**TACHIKAWA, Masanori** [ C class; 13500 (A), 0 (B), 0 (C) ] (63)

— *Theoretical analysis of deuterated effect on hydrogen-bonded molecular materials*

**TAKAGI, Noriaki** [ B class; 0 (A), 2500 (B), 0 (C) ] (118,120)

— *Exploring low-dimensional honeycomb sheets*

1. Electronic structure of the 4x4 silicene monolayer on semi-infinite Ag(111)  
H. Ishida, Y. Hamamoto, Y. Morikawa, E. Minamitani, R. Arafune, N. Takagi: New J. Phys. **17** (2015) 015013.
2. Silicene on Ag(111): geometric and electronic structures of a new honeycomb material of Si  
N. Takagi, C.-L. Lin, K. Kawahara, E. Minamitani, N. Tsukahara, M. Kawai, and R. Arafune: Prog. Surf. Sci. **90** (2015) 1.
3. Electronic decoupling by h-BN layer between silicene and Cu(111): A DFT based analysis  
M. Kanno, R. Arafune, C. -L. Lin, E. Minamitani, M. Kawai, N. Takagi: New J. Phys. **16** (2014) 105019.
4. Controlling orbital-selective Kondo effects in a single molecule through coordination chemistry  
N. Tsukahara, E. Minamitani, Y. Kim, M. Kawai, N. Takagi: J. Chem. Phys. **141** (2014) 054702.



**TAMARIBUCHI, Tsuguhiro** [ B class; 1800 (A), 700 (B), 500 (C) ] ( )

— *Development of fast algorithms for sparse Pfaffians and their applications to Ising systems*

**TAMURA, Ryo** [ C class; 0 (A), 5500 (B), 3800 (C) ] (213,215)

— *Quest for exotic functional properties under magnetic field in frustrated systems*

— *Study on Relation between Anisotropic Magnetic Structure and Magnetocaloric Effect*

1. Entanglement Properties of a Quantum Lattice-Gas Model on Square and Triangular Ladders  
S. Tanaka, R. Tamura, and H. Katsura: "Physics, Mathematics, And All That Quantum Jazz" (World Scientific) (2014) 71.
2. A Method to Change Phase Transition Nature – Toward Annealing Method –  
R. Tamura and S. Tanaka: "Physics, Mathematics, And All That Quantum Jazz" (World Scientific) (2014) 135.
3. Magnetic ordered structure dependence of magnetic refrigeration efficiency  
R. Tamura, S. Tanaka, T. Ohno, and H. Kitazawa: Journal of Applied Physics **116** (2014) 053908.
4. Sample dependence of giant magnetocaloric effect in a cluster-glass system  $\text{Ho}_5\text{Pd}_2$   
S. Toyozumi, H. Kitazawa, Y. Kawamura, H. Mamiya, N. Terada, R. Tamura, A. Dönni, K. Morita, and A. Tamaki: Journal of Applied Physics, **117** (2015) 17D101.
5. Structural phase transition between  $\gamma\text{-Ti}_3\text{O}_5$  and  $-\text{Ti}_3\text{O}_5$  by breaking of one-dimensionally conducting pathway  
K. Tanaka, T. Nasu, Y. Miyamoto, N. Ozaki, S. Tanaka, T. Nagata, F. Hakoe, M. Yoshikiyo, K. Nakagawa, Y. Umeta, K. Imoto, H. Tokoro, A. Namai, and S.-I. Ohkoshi: Crystal Growth and Design, **15** (2015) 653.
6. Phase diagram and sweep dynamics of a one-dimensional generalized cluster model  
T. Ohta, S. Tanaka, I. Danshita, and K. Totsuka: arXiv:1503.03204 (2015) [to appear in Journal of the Physical Society of Japan].

**TANAKA, Shu** [ C class; 0 (A), 5500 (B), 3900 (C) ] (209,211)

— *Study on Quantum Information Science Based on Statistical Physics*

— *Study on Phase Transition in Frustrated Spin Systems*

1. Entanglement Properties of a Quantum Lattice-Gas Model on Square and Triangular Ladders  
S. Tanaka, R. Tamura, and H. Katsura: "Physics, Mathematics, And All That Quantum Jazz" (World Scientific) (2014) 71.
2. A Method to Change Phase Transition Nature – Toward Annealing Method –  
R. Tamura and S. Tanaka: "Physics, Mathematics, And All That Quantum Jazz" (World Scientific) (2014) 135.
3. Magnetic ordered structure dependence of magnetic refrigeration efficiency  
R. Tamura, S. Tanaka, T. Ohno, and H. Kitazawa: Journal of Applied Physics **116** (2014) 053908.
4. Sample dependence of giant magnetocaloric effect in a cluster-glass system  $\text{Ho}_5\text{Pd}_2$   
S. Toyozumi, H. Kitazawa, Y. Kawamura, H. Mamiya, N. Terada, R. Tamura, A. Dönni, K. Morita, and A. Tamaki: Journal of Applied Physics, **117** (2015) 17D101.
5. Structural phase transition between  $\gamma\text{-Ti}_3\text{O}_5$  and  $-\text{Ti}_3\text{O}_5$  by breaking of one-dimensionally conducting pathway  
K. Tanaka, T. Nasu, Y. Miyamoto, N. Ozaki, S. Tanaka, T. Nagata, F. Hakoe, M. Yoshikiyo, K. Nakagawa, Y. Umeta, K. Imoto, H. Tokoro, A. Namai, and S.-I. Ohkoshi: Crystal Growth and Design, **15** (2015) 653.
6. Phase diagram and sweep dynamics of a one-dimensional generalized cluster model  
T. Ohta, S. Tanaka, I. Danshita, and K. Totsuka: arXiv:1503.03204 (2015) [to appear in Journal of the Physical Society of Japan].

**TANIGAKI, Kenichi** [ B class; 0 (A), 500 (B), 0 (C) ] ( )

— *First principles analysis for suppression of grain boundary embrittlement of aluminum alloys by liquid metals*

**TATENO, Masaru** [ C class; 0 (A), 7000 (B), 0 (C) ] (88)

— *Hybrid ab initio QM/MM calculations of biological macromolecules*

**TATEYAMA, Yoshitaka** [ E class; 0 (A), 23500 (B), 1000 (C) ] (47)

— *DFT free energy analysis of redox reaction mechanism at interfaces in batteries and catalysts*

1. Space-Charge Layer Effect at Interface between Oxide cathode and Sulfide Electrolyte in All-Solid-State Lithium-Ion Battery  
Jun Haruyama, Keitaro Sodeyama, Liyuan Han, Kazunori Takada, Yoshitaka Tateyama: Chem. Mater. **26**, 4248-4255 (2014).
2. Sacrificial anion reduction mechanism for electrochemical stability improvement in highly concentrated Li-salt electrolyte  
Keitaro Sodeyama, Yuki Yamada, Koharu Aikawa, Atsuo Yamada, Yoshitaka Tateyama: J. Phys. Chem. C **118**, 14091-14097 (2014).
3. Acetonitrile Solution Effect on Ru N749 Dye Adsorption and Excitation at TiO<sub>2</sub> Anatase Interface  
Yoshitaka Tateyama, Masato Sumita, Yusuke Ootani, Koharu Aikawa, Ryota Jono, Liyuan Han, Keitaro Sodeyama: J. Phys. Chem. C **118**, 16863-16871 (2014).
4. A double-QM/MM method for investigating donor-acceptor electron-transfer reactions in solution  
Zdenek Futera, Keitaro Sodeyama, Jaroslav V. Burda, Yoshitaka Tateyama: Phys. Chem. Chem. Phys. **16**, 19530-19539 (2014).
5. Termination Dependence of Tetragonal CH<sub>3</sub>NH<sub>3</sub>PbI<sub>3</sub> Surfaces for Perovskite Solar cells  
Jun Haruyama, Keitaro Sodeyama, Liyuan Han, Yoshitaka Tateyama: J. Phys. Chem. Lett. **5**, 2903-2909 (2014).
6. First Principles Calculation Study on Surfaces and Water Interfaces of Boron-Doped Diamond  
Zdenek Futera, Takeshi Watanabe, Yasuaki Einaga, Yoshitaka Tateyama: J. Phys. Chem. C, **118**, 22040-22052 (2014).
7. Possibility of NCS Group Anchor for Ru Dye Adsorption to Anatase TiO<sub>2</sub> (101) Surface: A Density Functional Theory Investigation  
Yusuke Ootani, Keitaro Sodeyama, Liyuan Han, Yoshitaka Tateyama: J. Phys. Chem. C, **119**, 234-241 (2015).
8. Water Adsorption and Dissociation at Metal-Supported Ceria Thin Films: Thickness and Interface-Proximity Effects Studied with DFT+U Calculations  
Lucie Szabova, Yoshitaka Tateyama, Vladimir Matolin, Stefano Fabris: J. Phys. Chem. C **119**, 2537-2544 (2015).

**TERAO, Takamichi** [ B class; 2700 (A), 1000 (B), 800 (C) ] (236)

— *Dynamical properties of Coulomb glass*

1. Vibrational properties of acoustic metamaterial multilayers  
T. Terao and Y. Ohnishi: J. Appl. Phys. **117** (2015) 134305.
2. Numerical study of photonic metamaterial composites  
T. Terao: NEMO2014 conference proceedings, in press.

**TODO, Syngé** [ C class; 0 (A), 4000 (B), 2200 (C) ] (230)

— *Study of quantum correlations and topological order in quantum spin systems*

1. Parallelized Quantum Monte Carlo Algorithm with Nonlocal Worm Updates  
A. Masaki, T. Suzuki, K. Harada, S. Todo, and N. Kawashima, Phys. Rev. Lett. **112**, 140603 (2014).
2. Thermal Phase Transition of Generalized Heisenberg Models for SU(*N*) Spins on Square and Honeycomb Lattices  
T. Suzuki, K. Harada, H. Matsuo, S. Todo, N. Kawashima, Phys. Rev. B **91**, 094414 (2015).
3. Numerical Analysis of Quantum Phase Transitions with Dynamic Control of Anisotropy  
S. Yasuda, S. Todo, JPS Conf. Proc. **1**, 012127 (2014).
4. Path-Integral Monte Carlo for the Gauge-Fixed Berry Connection and the Local Z<sub>2</sub> Berry Phase  
Y. Motoyama, S. Todo, JPS Conf. Proc. **1**, 012130 (2014).
5. MateriApps — a Portal Site of Materials Science Simulation  
Y. Konishi, R. Igarashi, S. Kasamatsu, T. Kato, N. Kawashima, T. Kawatsu, H. Kouta, M. Noda, S. Sasaki, Y. Terada, S. Todo, S. Tsuchida, K. Yoshimi, K. Yoshizawa, JPS Conf. Proc. **5**, 011007

(2015).

**TOHYAMA, Takami** [ C class; 0 (A), 4000 (B), 2200 (C) ] (229)— *DMRG study of a frustrated two-leg spin ladder*

1. Magnetic Raman scattering study of spin frustrated systems,  $\kappa$ -(BEDT-TTF)<sub>2</sub>X  
Y. Nakamura, N. Yoneyama, T. Sasaki, T. Tohyama, A. Nakamura, and H. Kishida: J. Phys. Soc. Jpn. **83**, (2014) 074708.
2. Lifshitz Transition Induced by Magnetic Field in Frustrated Two-Leg Spin-Ladder Systems  
T. Sugimoto, M. Mori, T. Tohyama, and S. Maekawa: JPS Conference Proceedings, in press.
3. Magnetization Plateaux by Reconstructed Quasi-spinons in a Frustrated Two-Leg Spin Ladder under a Magnetic Field  
T. Sugimoto, M. Mori, T. Tohyama, and S. Maekawa: submitted to Phys. Rev. Lett.

**TONEGAWA, Takashi** [ C class; 29500 (A), 0 (B), 0 (C) ] (193)— *Numerical Study of the One-Dimensional Quantum Spin Systems with Spatial Structures*

1. Edge Modes in the Intermediate- $D$  and Large- $D$  Phases of the  $S = 2$  Quantum Spin Chain with  $XXZ$  and On-Site Anisotropies  
K. Okamoto, T. Tonegawa, T. Sakai, and M. Kaburagi: JPS Conf. Proc. **3** (2014) 014022.

**TOYODA, Masayuki** [ C class; 0 (A), 2500 (B), 0 (C) ] (122)— *First-principles study on magnetism and atomic structures of transition-metal oxides*

1. Ab initio study on pressure-induced phase transition in LaCu<sub>3</sub>Fe<sub>4</sub>O<sub>12</sub>  
K. Isoyama, M. Toyoda, K. Yamauchi, and T. Oguchi: J. Phys. Soc. Jpn., **84**, 034709 (2015)
2. Symmetry-breaking 60°-spin order in the A-site-ordered perovskite LaMn<sub>3</sub>V<sub>4</sub>O<sub>12</sub>  
T. Saito, M. Toyoda, C. Ritter, S. Zhang, T. Oguchi, J. P. Attfield, and Yuichi Shimakawa: Phys. Rev. B **90**, 214405 (2014)
3. Ab initio study of electronic, magnetic, and spectroscopic properties in A- and B-site-ordered perovskite CaCu<sub>3</sub>Fe<sub>2</sub>Sb<sub>2</sub>O<sub>12</sub>  
H. Fujii, M. Toyoda, H. Momida, M. Mizumaki, S. Kimura, and T. Oguchi: Phys. Rev. B **90**, 014430 (2014)

**TOYOURA, Kazuaki** [ C class; 0 (A), 2000 (B), 0 (C) ] (128)— *Structures and Catalytic Properties of Supported Metal Nanoclusters***TSUNEYUKI, Shinji** [ E class; 0 (A), 16000 (B), 2300 (C) ] ( )— *Development and Application of New Methods for First-Principles Simulation of Material Structure and Electronic Properties***UCHIDA, Takashi** [ B,C class; 0 (A), 900 (B), 0 (C) ] (141)— *Temperature dependence of magnetic and electronic structure for Mn-based ordered alloys with Cu<sub>3</sub>Au-type crystal structure*— *Theory of magnetic and electronic structure for Mn-based ordered alloys with Cu<sub>3</sub>Au-type crystal structure***UDA, Yutaka** [ B class; 0 (A), 1000 (B), 0 (C) ] (138)— *Wear mechanism of diamond tool***UDAGAWA, Masafumi** [ C class; 8500 (A), 4000 (B), 0 (C) ] (155)— *Study of multipolar ordering composed of magnetic and orbital degrees of freedom in pyrochlore lattice systems*

1. Vaporization of Kitaev spin liquids  
Joji Nasu, Masafumi Udagawa, Yukitoshi Motome: Phys. Rev. Lett. **113**, 197205
2. Entanglement Spectrum in Cluster Dynamical Mean-Field Theory  
Masafumi Udagawa, Yukitoshi Motome: J. Stat. Mech. (2015) P01016
3. Correlations and entanglement in flat band models with variable Chern numbers

- Masafumi Udagawa, Emil J. Bergholtz: J. Stat. Mech. (2014) P10012
4. Topology and Interactions in a Frustrated Slab: Tuning from Weyl Semimetals to  $C_2$  Fractional Chern Insulators  
E.J. Bergholtz, Zhao Liu, M. Trescher, R. Moessner, M. Udagawa: Phys. Rev. Lett. **114**, 016806 (2015)
  5. Spin-orbit Coupling and Multiple Phases in Spin-triplet Superconductor  $Sr_2RuO_4$   
Youichi Yanase, Shuhei Takamatsu, Masafumi Udagawa: J. Phys. Soc. Jpn. **83**, 061019 (2014)
  6. Effect of magnetoelastic coupling on spin-glass behavior in Heisenberg pyrochlore antiferromagnets with bond disorder  
Hiroshi Shinaoka, Yusuke Tomita, and Yukitoshi Motome: Physical Review B **90**, 165119 (2014)
  7. Spin-orbit coupling in octamers in the spinel sulfide  $CuIr_2S_4$ : Competition between spin-singlet and quadrupolar states and its relevance to remnant paramagnetism  
Joji Nasu and Yukitoshi Motome: Physical Review B **90**, 045102 (2014)
  8. Exotic magnetic phases in an Ising-spin Kondo lattice model on a kagome lattice  
Hiroaki Ishizuka and Yukitoshi Motome: Physical Review B **91**, 085110 (2015)
  9. Toroidal order in metals without local inversion symmetry  
S. Hayami, H. Kusunose and Y. Motome: Phys. Rev. B **90**, 024432 (2014)
  10. Multiple- $Q$  instability by ( $d-2$ )-dimensional connections of Fermi surfaces  
S. Hayami and Y. Motome: Phys. Rev. B **90**, 060402 (2014)
  11. Spontaneous parity breaking in spin-orbital coupled systems  
S. Hayami, H. Kusunose and Y. Motome: Phys. Rev. B **90**, 081115 (2014)
  12. Topological semimetal-to-insulator phase transition between noncollinear and noncoplanar multiple- $Q$  states on a square-to-triangular lattice  
S. Hayami and Y. Motome: Phys. Rev. B **91**, 075104 (2014)
  13. Toroidal order in a partially disordered state on a layered triangular lattice: implication to  $UNi_4B$   
S. Hayami, H. Kusunose and Y. Motome: J. Phys.: Conf. Ser. **592**, 012101 (2015)

**UEDA, Akiko** [ C class; 0 (A), 2000 (B), 1900 (C) ] (239)

— *Impurity Scattering in Junctionless transistor*

**WATANABE, Hiroshi** [ C class; 0 (A), 3500 (B), 2000 (C) ] (232)

— *Scaling Analysis for Ostwald-like ripening of bubbles*

1. Ostwald ripening in multiple-bubble nuclei  
H. Watanabe, M. Suzuki, H. Inaoka, and N. Ito: J. Chem. Phys. **141** (2014), 234703

**WATANABE, Hiroshi** [ B class; 0 (A), 300 (B), 0 (C) ] (181)

— *Theoretical study for exciton condensation, CDW, and superconductivity induced by interband interaction*

1. A variational Monte Carlo study of exciton condensation  
H. Watanabe, K. Seki, and S. Yunoki: J. Phys.: Conf. Ser. **592** (2015) 012097.
2. Charge-density wave induced by combined electron-electron and electron-phonon interactions in  $1T$ - $TiSe_2$ : A variational Monte Carlo study  
H. Watanabe, K. Seki, and S. Yunoki: submitted to Phys. Rev. B.

**WATANABE, Kazuyuki** [ C class; 8000 (A), 7000 (B), 800 (C) ] (56)

— *Ab Initio Study of Excited Electronic States and Nonadiabatic Processes of Nanostructures under External Fields*

1. Nanoplasmon Dynamics and Field Enhancement of Graphene Flakes by First-principles Simulations  
N. Yamamoto, C. Hu, S. Hagiwara, and K. Watanabe, Appl. Phys. Express **8**, 045103 (2015).
2. Energetics and Dynamics of Laser-Assisted Field Emission from Silicene Nanoribbons: Time-Dependent First-Principles Study  
T. Higuchi, C. Hu, and K. Watanabe, e-J. Surf. Sci. Nanotech. **13**, 115 (2015).
3. Time-Dependent Density Functional Theory Simulation of Electron Wave-Packet Scattering with Nanoflakes

- K. Tsubonoya, C. Hu, and K. Watanabe, Phys. Rev. **B90**, 035416 (2014).  
 4. Positron states at a lithium-adsorbed Al(100) surface: Two-component density functional theory simulation  
 S. Hagiwara, C. Hu, and K. Watanabe, Phys. Rev. **B91**, 115409 (2015).

**WATANABE, Satoshi** [ C class; 0 (A), 6500 (B), 3500 (C) ] (74)

— *Theoretical Analyses on Electronic and Ionic Transport Properties of Nanostructures*

1. Oxygen vacancy effects on an amorphous-TaO<sub>x</sub>-based resistance switch: a first principles study  
 B. Xiao and S. Watanabe: Nanoscale **6** (2014) 10169.
2. Alternating current response of carbon nanotubes with randomly distributed impurities  
 D. Hirai, T. Yamamoto and S. Watanabe: Appl. Phys. Lett. **105** (2014) 173106.
3. Anomalous satellite inductive peaks in alternating current response of defective carbon nanotubes  
 D. Hirai, T. Yamamoto and S. Watanabe: J. Appl. Phys. **115** (2014) 174312.
4. Spin-polarized Currents through a Quantum Dot: Non-Equilibrium Green's Function Simulations under Hartree Approximation  
 K. Sasaoka, T. Yamamoto and S. Watanabe: Jpn. J. Appl. Phys. **53** (2014) 115203.
5. Controlling orbital-selective Kondo effects in a single molecule through coordination chemistry  
 N. Tsukahara, E. Minamitani, Y. Kim, M. Kawai and N. Takagi: J. Chem. Phys. **141** (2014) 054702.
6. Nonequilibrium Phonon Green's Function Simulation and Its Application to Carbon Nanotubes  
 T. Yamamoto, K. Sasaoka and S. Watanabe: in G. Zhang (Eds.), "Nanoscale Energy Transport and Harvesting: A Computational Study" (Pan Stanford Publishing, 2014), Chapter 2.
7. Interface Structure in Cu/Ta<sub>2</sub>O<sub>5</sub>/Pt Resistance Switch: A First-Principles Study  
 B. Xiao and S. Watanabe: ACS Appl. Mater. Interfaces **7** (2015) 519.
8. Materials Search of Perovskite Cathode in SOFC by Statistical Analysis  
 J. Hwang, Y. Ando and S. Watanabe: ECS Trans., accepted.
9. First-principles calculation of the charged capacitor under open-circuit condition using the orbital-separation approach  
 S. Kasamatsu, S. Watanabe and S. Han: submitted to Phys. Rev. B.
10. Spatially Extended Underscreened Kondo State from Collective Molecular Spin  
 E. Minamitani, Y. Fu, Q.-K. Que, Y. Kim and S. Watanabe: submitted to Phys. Rev. Lett.
11. マテリアルズ・インフォマティクスによる分子電気伝導シミュレーション解析の試み  
 安藤 康伸, 藤掛 壮, 渡邊 聡: 表面科学、投稿中.

**YABANA, Kazuhiro** [ E class; 0 (A), 16000 (B), 0 (C) ] (55)

— *First-principles calculation of interactions between extreme pulse light and matter*

1. Attosecond band-gap dynamics in silicon  
 M. Schultze, K. Ramasesha, C.D. Pemmaraju, S.A. Sato, D. Whitmore, A. Gandman, J.S. Prell, L.J. Borja, D. Prendergast, K. Yabana, D.M. Neumark, S.R. Leone: Science **346** (2014) 1348.
2. Dielectric response of laser-excited silicon at finite electron temperature  
 S.A. Sato, Y. Shinohara, T. Otobe, K. Yabana: Phys. Rev. **B90** (2014) 174303.
3. Ab Initio Simulation of Electrical Currents Induced by Ultrafast Laser Excitation of Dielectric Materials  
 G. Wachter, C. Lemell, J. Burgdoerfer, S.A. Sato, X.-M. Tong, K. Yabana: Phys. Rev. Lett. **113** (2014) 087401.
4. Efficient basis expansion for describing linear and nonlinear electron dynamics in crystalline solids  
 S.A. Sato, K. Yabana: Phys. Rev. **B89** (2014) 224305.
5. Numerical pump-probe experiments of laser-excited silicon in nonequilibrium phase  
 S.A. Sato, K. Yabana, Y. Shinohara, T. Otobe, G.F. Bertsch: Phys. Rev. **B89** (2014) 064304.

**YAMAJI, Youhei** [ C class; 0 (A), 4000 (B), 2400 (C) ] (161)

— *Numerical studies on localization and fractionalization of many-body electrons with strong spin-orbit couplings*

1. First-Principles Study of the Honeycomb-Lattice Iridates Na<sub>2</sub>IrO<sub>3</sub> in the Presence of Strong Spin-Orbit Interaction and Electron Correlations

- Y. Yamaji, Y. Nomura, M. Kurita, R. Arita, and M. Imada: Phys. Rev. Lett. 113 (2014) 107201
2. Variational Monte Carlo Method in the Presence of Spin-Orbit Interaction and Its Application to the Kitaev and Kitaev-Heisenberg Model  
M.Kurita,Y.Yamaji,S.Morita,andM. Imada: arXiv:1411.5198
3. Condensed-Matter Ab initio Approach for Strongly Correlated Electrons: Application to A Quantum Spin Liquid Candidate  
Y. Yamaji: to appear in AIP Conference Proceedings.

**YAMASHITA, Koichi** [ C class; 0 (A), 3500 (B), 2000 (C) ] (95)

— *Large scale ab initio calculations on the fundamental processes of energy convergence devices and on their optimization for high conversion efficiency*

1. The proton conduction mechanism in a material consisting of packed acids  
T. Ogawa, T. Aonuma, T. Tamaki, H. Ohashi, H. Ushiyama, K. Yamashita, and T. Yamaguchi: Chem. Sci. **5** (2014) 4878.
2. Multi-wall effects on the thermal transport properties of nanotube structures  
T. Hata, H. Kawai, R. Jono and K. Yamashita: Nanotechnology **25** (2014) 245703.
3. Electron-electron and electron-phonon correlation effects on the finite-temperature electronic and optical properties of zinc-blende GaN  
H. Kawai, K. Yamashita, E. Cannuccia, and A. Marini: Phys. Rev. B **89** (2014) 085202.
4. Cation Role in Structural and Electronic Properties of 3D Organic-Inorganic Halide Perovskites: A DFT Analysis  
G. Giorgi, J. Fujisawa, H. Segawa, and K. Yamashita: J. Phys. Chem. C **118** (2014) 12176.
5. Organic-Inorganic Hybrid Lead Iodide Perovskite Featuring Zero Dipole Moment Guanidinium Cations: A Theoretical Analysis  
G. Giorgi, J. Fujisawa, H. Segawa, and K. Yamashita: J. Phys. Chem. C **119** (2014) 4694.
6. Reparametrization Approach of DFT Functionals Based on the Equilibrium Temperature of Spin-Crossover Compounds  
A. Slimani, X. Yu, A. Muraoka, K. Boukheddaden, and K. Yamashita: J. Phys. Chem. A **118** (2014) 9005.
7. Theoretical studies on the mechanism of oxygen reduction reaction on clean and O-substituted Ta<sub>3</sub>N<sub>5</sub>(100) surfaces  
E. Watanabe, H. Ushiyama and K. Yamashita: Catal. Sci. Technol. **5** (2015) 2769.
8. Comparative Study of Sodium and Lithium Intercalation and Diffusion Mechanism in Black Phosphorus from First-principles Simulation  
X. Yu, H. Ushiyama, K. Yamashita: Chem. Lett. **43** (2014) 1940.
9. Electronic Schrödinger equation with nonclassical nuclei  
Y. Suzuki, A. Abedi, N. T. Maitra, K. Yamashita and E.K.U. Gross: Physical Review A **89** (2014) 040501(R).
10. A Density Functional Tight Binding Study of Acetic Acid Adsorption on Crystalline and Amorphous Surfaces of Titania  
S. Manzhos, G. Giorgi, K. Yamashita: Molecules **20** (2015) 3371.
11. Semiclassical quantization of nonadiabatic systems with hopping periodic orbits  
M. Fujii and K. Yamashita: J. Chem. Phys. **142** (2015) 074104.
12. Alternative, lead-free, hybrid organic-inorganic perovskites for solar applications: a DFT analysis  
G. Giorgi, K. Yamashita: Chem. Lett., Advance Publications, (2015) 150143.
13. The Mechanism of Slow Hot-Hole Cooling in Lead-Iodide Perovskite: First-Principles Calculation on Carrier Lifetime from Electron-Phonon Interaction  
H. Kawai, G. Giorgi, A. Marini, and K. Yamashita: Nano Lett., in press, (2015)

**YAMAUCHI, Jun** [ B class; 1700 (A), 700 (B), 500 (C) ] (117)

— *First-principles study on the defects in semiconductors*

**YAMAUCHI, Kunihiko** [ C class; 0 (A), 5000 (B), 2300 (C) ] (84)

— *Ab-initio study of magnetism, ferroelectricity, and topological properties in transition-metal oxides*

1. Impact of Ferroelectric Distortion on Thermopower in BaTiO<sub>3</sub>

- H. Saijo, K. Yamauchi, K. Shirai, and T. Oguchi: J. Phys. Soc. Jpn. **84** (2015) 054701.
2. Ab-initio Prediction of Magnetoelectricity in Infinite-Layer  $\text{CaFeO}_2$  and  $\text{MgFeO}_2$   
K. Yamauchi, T. Oguchi, and S. Picozzi: J. Phys. Soc. Jpn. **83** (2014) 094712.
3. Origin of the band dispersion in a metal phthalocyanine crystal  
S. Yanagisawa, K. Yamauchi, T. Inaoka, T. Oguchi, and I. Hamada: Phys. Rev. B **90** (2014) 245141.
4. Giant spin-driven ferroelectric polarization in  $\text{TbMnO}_3$  under high pressure  
T. Aoyama, K. Yamauchi, A. Iyama, S. Picozzi, K. Shimizu, and T. Kimura: Nat. Commun. **5** (2014) 4927.

**YANAGI, Yuki** [ C,D class; 0 (A), 16660 (B), 0 (C) ] (154)

- *Mott Transition in the Hubbard Model on the  $\text{CaV}_4\text{O}_9$  Lattice*
- *Antiferromagnetism in 1/5-Depleted Square Lattice Hubbard Model*
- *Quantum Phase Transition in the Hubbard Model on the  $\text{CaV}_4\text{O}_9$  Lattice*
- 1. Quantum Phase Transition in the 1/5 Depleted Square Lattice Hubbard Model  
Y. Yanagi and K. Ueda: JPS Conf. Proc. **3** (2014) 013005.
- 2. Continuous Mott transition in a two-dimensional Hubbard model  
Y. Yanagi and K. Ueda: Phys. Rev. B **90** (2014) 085113.

**YANAGISAWA, Susumu** [ B,C class; 17800 (A), 7300 (B), 0 (C) ] (45)

- *Theoretical investigation on electronic structures of organic molecular aggregates and solids*
- *Theoretical investigation of spin polarization induced at the organic-metal interfaces*
- 1. Scanning tunneling microscopy/spectroscopy of picene thin films formed on  $\text{Ag}(111)$   
Y. Yoshida, H.-H. Yang, H.-S. Huang, S.-Y. Guan, S. Yanagisawa, T. Yokosuka, M.-T. Lin, W.-B. Su, C.-S. Chang, G. Hoffmann, and Y. Hasegawa: J. Chem. Phys. **141** (2014) 114701.
- 2. Theoretical investigation of the band structure of picene single crystals within the *GW* approximation  
S. Yanagisawa, Y. Morikawa, and A. Schindlmayr: Jpn. J. Appl. Phys. **53** (2014) 05FY02.
- 3. Origin of the band dispersion in a metal phthalocyanine crystal  
S. Yanagisawa, K. Yamauchi, T. Inaoka, T. Oguchi, and I. Hamada: Phys. Rev. B **90** (2014) 245141.

**YANAGISAWA, Takashi** [ B class; 800 (A), 1000 (B), 800 (C) ] (172)

- *Quantum Monte Carlo simulations and electronic state calculations in correlated electron systems*
- *Quantum Monte Carlo simulations and first principles calculations in correlated electron systems*
- 1. Mott transition in cuprate superconductors - Role of  $t'_d$  in the three-band d-p model -  
T. Yanagisawa, M. Miyazaki and K. Yamaji: JPS Conference Proc. **3** (2014) 015046.a
- 2. Electronic structure of  $\text{LaTSb}_2$  (T=Cu, Ag, Au)  
I. Hase and T. Yanagisawa: Physics Procedia **58** (2014) 42.
- 3. Material-parameter dependence of superconductivity in high-temperature cuprates  
T. Yanagisawa, M. Miyazaki and K. Yamaji: Physics Procedia **58** (2014) 26.
- 4. Stripes and superconductivity in the two-dimensional Hubbard model  
M. Miyazaki, K. Yamaji and T. Yanagisawa: Physics Procedia **58** (2014) 30.
- 5. Electron correlation in high temperature superconductors  
T. Yanagisawa, M. Miyazaki and K. Yamaji: J. Appl. Math. Phys. **2** (2014) 72.
- 6. Mott transition in cuprate high temperature superconductors  
T. Yanagisawa and M. Miyazaki: Europhysics Letters **107** (2014) 27004a
- 7. Fluctuation-induced Nambu-Goldstone boson in a Higgs-Josephson model  
T. Yanagisawa and Y. Tanaka: New Journal of Physics **16** (2014) 123014
- 8. Multi-phase physics in multi-condensate superconductivity  
T. Yanagisawa: J. Super. Novel Magnetism **28** (2014) 1285.
- 9. Inhomogeneous Electronic Distribution in High- $T_c$  Cuprates  
S. Koikegami, M. Kato and T. Yanagisawa: J. Phys. Soc. Jpn. **84** (2014) 054704.
- 10. High Temperature Superconductivity from Strong Correlation  
T. Yanagisawa: Physics Procedia (2015) in press.

11. The Absence of CDW order in PbSb, and its unexpected softness  
I. Hase, K. Yasutomi, T. Yanagisawa, K. Odagiri and T. Nishio: Physics Procedia (2015) in press.
12. Dirac fermions and Kondo effect  
T. Yanagisawa: JPS Conference Proc. (2015) in press.

**YASUDA, Chitoshi** [ C class; 500 (A), 1000 (B), 0 (C) ] (253)

— *Phonon Effects and Frustration in Quantum Spin Systems*

1. Quantum Phase Transition Induced by Geometrical Changes in Spin-Phonon Interaction  
C. Yasuda and S. Akiyama: J. Phys. Soc. Jpn., **84** (2015) 014705.

**YASUDA, Shugo** [ C,D class; 0 (A), 4000 (B), 1000 (C) ] (233)

— *Multiscale Simulation for non-isothermal flows of complex fluids*

— *Multiscale simulation of thermohydrodynamic lubrication of polymeric liquid*

1. Synchronized molecular-dynamics simulation via macroscopic heat and momentum transfer: an application to polymer lubrication  
S. Yasuda and R. Yamamoto: Phys. Rev. X **4** (2014) 041011
2. Multiscale simulation for thermo-hydrodynamic lubrication of a polymeric liquid between parallel plates  
S. Yasuda and R. Yamamoto: Mol. Sim. (2014) Proceedings of the 3rd international conference on molecular simulation
3. Synchronized Molecular Dynamic 法による高分子潤滑の解析  
安田修悟、山本量一: アンサンブル **17** (2015) 30
4. Synchronized molecular-dynamics simulation for the thermal lubrication of a polymeric liquid between parallel plates  
S. Yasuda and R. Yamamoto: Comput. Fluids (submitted)

**YASUOKA, Kenji** [ C class; 0 (A), 4500 (B), 0 (C) ] (103)

— *First principles study on lattice thermal conductivity reduction in multinary chalcopyrite semiconductors*

— *Phase stability and defect properties of stannite  $\text{Cu}_2\text{FeSnS}_4$*

1. Four  $\text{Ti}^{3+}$  defects below oxygen vacancy on  $\text{TiO}_2(110)$ : a clear interpretation of STM  
T. Shibuya, K. Yasuoka, S. Mirbt and B. Sanyal: to be submitted
2. Suppressing thermal conductivity in multi-component semiconductors through cation mutation  
T. Shibuya, J. M. Skelton, K. Yasuoka, A. Togo, I. Tanaka and A. Walsh: to be submitted



## □ CMSI Projects

**DOI, Shotaro** [ R class; 0 (A), 0 (B), 4000 (C) ] (281)— *First-principles Electronic Structure Calculation of Permanent Magnets using the Screened KKR Green's Function Method***IMADA, Masatoshi** [ R class; 0 (A), 0 (B), 10000 (C) ] ()— *New mechanisms and controllability of real strongly correlated electron materials*

1. Quantum Spin Liquid in Spin 1/2 J1-J2 Heisenberg Model on Square Lattice: Many-Variable Variational Monte Carlo Study Combined with Quantum-Number Projections  
S. Morita, R. Kaneko and M. Imada: J. Phys. Soc. Jpn. **84** (2015) 024720.
2. Superconductivity and its mechanism in an ab initio model for electron-doped LaFeAsO  
T. Misawa, M. Imada: J. Phys. Soc. Jpn. **5** (2014) 5738.
3. Gapless Spin-Liquid Phase in an Extended Spin 1/2 Triangular Heisenberg Model  
R. Kaneko, S. Morita and M. Imada: J. Phys. Soc. Jpn. **83** (2014) 093707.
4. First-Principles Study of the Honeycomb-Lattice Iridates Na<sub>2</sub>IrO<sub>3</sub> in the Presence of Strong Spin-Orbit Interaction and Electron Correlations  
Y. Yamaji, Y. Nomura, M. Kurita, R. Arita and M. Imada: Phys. Rev. Lett. **113** (2014) 107201.
5. Origin of High-Tc Superconductivity in Doped Hubbard Models and Their Extensions: Roles of Uniform Charge Fluctuations  
T. Misawa and M. Imada: Phys. Rev. B **90** (2014) 115137.
6. Electron Correlation Effects on Topological Phases  
M. Imada, Y. Yamaji and M. Kurita: J. Phys. Soc. Jpn. **83** (2014) 061017.
7. Universal departure from Johnson-Nyquist relation caused by limited resolution  
Y. Yamada and M. Imada: Phys. Rev. B **89** (2014) 205421.
8. Metallic Interface Emerging at Magnetic Domain Wall of Antiferromagnetic Insulator: Fate of Extinct Weyl Electrons  
Y. Yamaji and M. Imada: **4** (2014) 021035.
9. Variational Monte Carlo Method for Electron-Phonon Coupled Systems  
T. Ohgoe and M. Imada: Phys. Rev. B **89** (2014) 195139.

**KAWASHIMA, Naoki** [ R class; 0 (A), 0 (B), 10000 (C) ] (270)— *Monte Carlo Study of Novel Quantum Phases and Critical Phenomena*

1. Thermal phase transitions to valence-bond-solid phase in the two dimensional; generalized SU(N) Heisenberg models  
Takafumi Suzuki, Kenji Harada, Haruhiko Matsuo, Synge Todo and Naoki Kawashima: J. Phys.: Conf. Ser. **592**, 012114 (2015).
2. Thermal phase transition of generalized Heisenberg models for SU(N) spins on square and honeycomb lattices  
Takafumi Suzuki, Kenji Harada, Haruhiko Matsuo, Synge Todo and Naoki Kawashima: Phys. Rev. B **91**, 094414 (2015).
3. Parallelized Quantum Monte Carlo Algorithm with Nonlocal Worm Updates  
Akiko Masaki-Kato, Takafumi Suzuki, Kenji Harada, Synge Todo, and Naoki Kawashima: Physical Review Letters **112**, 140603 (5 pages) (2014).
4. Phase Transitions with Discrete Symmetry Breaking in Antiferromagnetic Heisenberg Models on a Triangular Lattice  
Ryo Tamura, Shu Tanaka, and Naoki Kawashima: JPS Conf. Proc. — Proceedings of the 12th Asia Pacific Physics Conference (APPC12), 012125 (2014)

**NAKANO, Hiroki** [ R class; 0 (A), 0 (B), 4000 (C) ] (279)— *Computational-Science Study of Frustrated Magnets*

1. The Magnetization Process of the  $S = 1/2$  Heisenberg Antiferromagnet on the Cairo Pentagon Lattice

- H. Nakano, M. Isoda, and T. Sakai: J. Phys. Soc. Jpn. **83** (2014) 053702.
2. Frustration-induced Magnetic Properties of the Spin-1/2 Heisenberg Antiferromagnet on the Cairo Pentagon Lattice  
M. Isoda, H. Nakano, and T. Sakai: J. Phys. Soc. Jpn. **83** (2014) 084710.
  3. Spin-Flop Phenomenon of Two-Dimensional Frustrated Antiferromagnets without Anisotropy in Spin Space  
H. Nakano, Y. Hasegawa, and T. Sakai: J. Phys. Soc. Jpn. **83** (2014) 084709.
  4. Anomalous Behavior of the Magnetization Process of the  $S = 1/2$  Kagome-Lattice Heisenberg Antiferromagnet at One-Third Height of the Saturation  
H. Nakano and T. Sakai: J. Phys. Soc. Jpn. **83** (2014) 104710.
  5. Anomalous Quantum Magnetization Behaviors of the Kagome and Triangular Lattice Antiferromagnets  
H. Nakano and T. Sakai: JPS Conf. Proc. **3** (2014) 014003.
  6. Exotic Quantum Phase Transition of the Spin Nanotube  
T. Sakai, H. Nakano, and K. Okunishi: J. Low. Phys. **568** (2014) 042024.
  7. Novel Field Induced Quantum Phase Transition of the Kagome Lattice Antiferromagnet  
T. Sakai and H. Nakano: J. Low. Phys. **568** (2014) 042025.
  8. Instability of a ferrimagnetic state of a frustrated  $S=1/2$  Heisenberg antiferromagnet in two dimensions  
H. Nakano and T. Sakai: Jpn. J. App. Phys. **54** (2015) 00305.

**NOBUSADA, Katsuyuki** [ R class; 0 (A), 0 (B), 10000 (C) ] (283)

— *Photo-induced electron dynamics in nanostructures and development of quantum devices with optical and electronic functionality*

**OGATA, Shuji** [ R class; 0 (A), 0 (B), 10000 (C) ] (271)

— *Multi-scale simulation of nano-structured devices from electronic structures to mechanical properties*

1. Fluctuating Local Recrystallization of Quasi-Liquid Layer of Sub-Micrometer-Scale Ice: A Molecular Dynamics Study  
Y. Kajima, S. Ogata, R. Kobayashi, M. Hiyama, T. Tamura: J. Phys. Soc. Jpn. **83** (2014) 083601.

**OKAZAKI, Susumu** [ R class; 0 (A), 0 (B), 10000 (C) ] (275)

— *Large scale molecular dynamics calculation study of viruses*

**OKUBO, Tsuyoshi** [ R class; 0 (A), 0 (B), 4000 (C) ] (282)

— *Ordering of topological excitations of the frustrated magnets*

1. Field-induced incommensurate phase in the strong-rung spin ladder with ferromagnetic legs  
H. Yamaguchi, H. Miyagai, M. Yoshida, M. Takigawa, K. Iwase, T. Ono, N. Kase, K. Araki, S. Kittaka, T. Sakakibara, T. Shimokawa, T. Okubo, K. Okunishi, A. Matsuo, and Y. Hosokoshi: Phys. Rev. B **89** (2014) 220402(R)
2. A Scaling Relation for Dangerously Irrelevant Symmetry-Breaking Fields  
T. Okubo, K. Oshikawa, H. Watanabe, and N. Kawashima: Phys. Rev. B., in press
3.  $SU(N)$  Heisenberg model with multi-column representations  
T. Okubo, K. Harada, J. Lou, and N. Kawashima: Submitted to Phys. Rev. B

**OSHIYAMA, Atsushi** [ R class; 0 (A), 0 (B), 10000 (C) ] ( )

— *Density Functional Study on Prediction of Electronic Properties of Nanostructures*

**SAITO, Mineo** [ R class; 0 (A), 0 (B), 10000 (C) ] (273)

— *Materials design for spintronics/multiferroics applications*

1. An ab initio approach to free-energy reconstruction using logarithmic mean force dynamics  
M. Nakamura, M. Obata, T. Morishita, T. Oda: J. Chem. Phys., **140** (2014) 184110.
2. Phase with pressure-induced shuttlewise deformation in dense solid atomic hydrogen  
T. Ishikawa, H. Nagara, T. Oda, N. Suzuki, and K. Shimizu: Phys. Rev. B, **90** (2014) 104102.

3. Symmetry-induced peculiar Rashba effect on thallium adsorbed Si(111) surfaces  
K. Sakamoto, T. Oda, A. Kimura, Y. Takeichi, J. Fujii, R. I. G. Uhrberg, M. Donath, H. W. Yeom: Journal of Electron Spectroscopy and Related Phenomena, in press.
4. Possible origin of non-linear magnetic anisotropy variation in electric field effect in a double interface system  
D. Yoshikawa, M. Obata, Y. Taguchi, S. Haraguchi, and T. Oda: Appl. Phys. Express, **7** (2014) 113005.
5. Review on distorted face-centered cubic phase in yttrium via genetic algorithm  
T. Ishikawa, T. Oda, N. Suzuki, and K. Shimizu: High Pressure Research (regular article), DOI: 10.1080/08957959.2014.983501.
6. Improving the Description of Nonmagnetic and Magnetic Molecular Crystals via the van der Waals Density Functional  
M. Obata, M. Nakamura, I. Hamada, and T. Oda: J. Phys. Soc. Jpn., **84** (2015) 024715.
7. Molecular Interactions for Modeling of Oxygen System Using van der Waals Density Functional Approach  
M. Obata, I. Hamada, and T. Oda, : JPS Conf. Proc., **5** (2015) 011011.
8. First-principles study on structural and electronic properties in Fe/MgO double interface  
D. Yoshikawa, M. Obata, and T. Oda: JPS Conf. Proc., **5** (2015) 011012.
9. First-Principles Study of Topological Insulators A<sub>2</sub>B<sub>3</sub>(A=Bi and Sb, and B=O, S, Se and Te)  
T. Kato, H. Kotaka, and F. Ishii: JPS Conf. Proc. **5**, 011022 (2015).
10. Thermopower of Doped Quantum Anomalous Hall Insulators: The case of Dirac Hamiltonian  
Y.P. Mizuta and F. Ishii: JPS Conf. Proc. **5**, 011023 (2015).
11. First-Principles Study of Rashba Effect in the (LaAlO<sub>3</sub>)<sub>2</sub>/(SrTiO<sub>3</sub>)<sub>2</sub>  
M. Nishida, F. Ishii, H. Kotaka, and M. Saito: Mol. Simul. DOI:10.1080/08927022.2014.987986.
12. Magnetism-Driven Electric Polarization of Multiferroic Quasi-One-Dimensional Ca<sub>3</sub>CoMnO<sub>6</sub>: First-Principles Study Using Density Functional Theory  
M. Nishida, F. Ishii, and M. Saito: J. Phys. Soc. Jpn., **83**, 124711 (2014).
13. First-principles study of surface states in topological insulators Bi<sub>2</sub>Te<sub>3</sub> and Bi<sub>2</sub>Se<sub>3</sub>: Film thickness dependence  
T. Kato, H. Kotaka, and F. Ishii: Mol. Simul. DOI:10.1080/08927022.2014.964476.
14. Spin-Orbit Interaction Effects in the Electronic Structure of B20-type CoSi: First-Principles Density Functional Study  
F. Ishii, T. Onishi, and H. Kotaka: JPS Conf. Proc. **3**, 016019(2014).
15. Contribution of Berry Curvature to Thermoelectric Effects  
Y. P. Mizuta, and F. Ishii : JPS Conf. Proc. **3** 017035(2014).
16. First-principles study of Exchange Interaction in Ising-type Multiferroic Ca<sub>3</sub>CoMnO<sub>6</sub>  
M. Nishida, F. Ishii, and M. Saito: JPS Conf. Proc. **3** , 014040 (2014).
17. Spin polarized positron lifetimes in ferromagnetic metals: First-principles study  
J. Lin, T. Yamasaki, and M. Saito: Jpn. J. Appl. Phys. **53** , 05302 (2014).
18. Band gap design of thiophene polymers based on density functional theory  
Patricia Lubis and Mineo Saito: Jpn. J. Appl. Phys. **53** , 071602 (2014).
19. Tunable Rashba effect on strained ZnO: First-principles density-functional study  
Moh Adhib Ulil Absor, Hiroki Kotaka, Fumiyuki Ishii, and Mineo Saito: Appl. Phys. Express **7**, 053002 (2014).
20. Density Functional Theory Calculations of Formation Energies and Vacancy Concentrations of the Silicon Vacancy  
Sholihun, M. Saito, T. Ohno, and T. Yamasaki: Jpn. J. Appl. Phys. **54**, 041301 (2014)

**SHIBA, Hayato** [ R class; 0 (A), 0 (B), 4000 (C) ] (278)

— *Structure Formation of Surfactant Membranes under Shear Flow*

**SUGINO, Osamu** [ R class; 0 (A), 0 (B), 5000 (C) ] ()

— *Basic processes in the electrode catalysis*

**TACHIKAWA, Masanori** [ R class; 0 (A), 0 (B), 5000 (C) ] (285)

— *Development of multicomponent quantum chemistry based on stochastic method for material design*

**TAKATSUKA, Kazuo** [ R class; 0 (A), 0 (B), 5000 (C) ] (268)

— *Nonadiabatic electron dynamics and many-body nuclear dynamics in molecules*

**TOHYAMA, Takami** [ R class; 0 (A), 0 (B), 10000 (C) ] (269)

— *Double-Pulse Deexcitations in a One-Dimensional Strongly Correlated System*

1. Density-Matrix Renormalization Group Study of Extended Kitaev-Heisenberg Model  
K. Shinjo, S. Sota, and T. Tohyama: Phys. Rev. B **91**, (2015) 054401.
2. Density-matrix renormalization group study of third harmonic generation in one-dimensional Mott insulator coupled with phonon  
S. Sota, T. Tohyama, and S. Yunoki: J. Phys. Soc. Jpn. **84**, (2015) 054403.
3. Magnetization Plateaux by Reconstructed Quasi-spinons in a Frustrated Two-Leg Spin Ladder under a Magnetic Field  
T. Sugimoto, M. Mori, T. Tohyama, and S. Maekawa: submitted to Phys. Rev. Lett.

**TSUNEYUKI, Shinji** [ R class; 0 (A), 0 (B), 10000 (C) ] ()

— *Development of first-principles simulation software for exploration of new materials*

**YAMASHITA, Koichi** [ R class; 0 (A), 0 (B), 10000 (C) ] (276)

— *Large scale calculations on the fundamental processes of solar cells and their optimization in conversion efficiency and long lifetime*

1. Cation Role in Structural and Electronic Properties of 3D Organic-Inorganic Halide Perovskites: A DFT Analysis  
G. Giorgi, J. Fujisawa, H. Segawa, and K. Yamashita: J. Phys. Chem. C **118** (2014) 12176.
2. Organic-Inorganic Hybrid Lead Iodide Perovskite Featuring Zero Dipole Moment Guanidinium Cations: A Theoretical Analysis  
G. Giorgi, J. Fujisawa, H. Segawa, and K. Yamashita: J. Phys. Chem. C **119** (2014) 4694.
3. Semiclassical quantization of nonadiabatic systems with hopping periodic orbits  
M. Fujii and K. Yamashita: J. Chem. Phys. **142** (2015) 074104.
4. Alternative, lead-free, hybrid organic-inorganic perovskites for solar applications: a DFT analysis  
G. Giorgi, K. Yamashita: Chem. Lett., Advance Publications, (2015) 150143.
5. A Density Functional Tight Binding Study of Acetic Acid Adsorption on Crystalline and Amorphous Surfaces of Titania  
S. Manzhos, G. Giorgi, K. Yamashita: Molecules **20** (2015) 3371.
6. The Mechanism of Slow Hot-Hole Cooling in Lead-Iodide Perovskite: First-Principles Calculation on Carrier Lifetime from Electron-Phonon Interaction  
H. Kawai, G. Giorgi, A. Marini, and K. Yamashita: Nano Lett., in press, (2015)

**YOSHIDA, Norio** [ R class; 0 (A), 0 (B), 10000 (C) ] (277)

— *Theoretical analysis of hydrolysis of pyrophosphate by 3D-RISM-SCF*

1. Theoretical Studies of Structures and Vibrational Sum Frequency Generation Spectra at Aqueous Interfaces  
T. Ishiyama, T. Imamura, and A. Morita: Chem. Rev. **114** (2014) 8447-8470
2. Computation of the Free Energy due to Electron Density Fluctuation of a Solute in Solution: A QM/MM Method with Perturbation Approach Combined with a Theory of Solutions  
D. Suzuoka, H. Takahashi, and A. Morita: J. Chem. Phys. **140** (2014) 134111 (12 pages)
3. Theory and Efficient Computation of Differential Vibrational Spectra  
S. Sakaguchi, T. Ishiyama, and A. Morita: J. Chem. Phys. **140** (2014) 144109 (13 pages)
4. A Direct Evidence of Vibrationally Delocalized Response at Ice Surface  
T. Ishiyama and A. Morita: J. Chem. Phys. **141** (2014) 18C503 (4 pages)
5. Erratum: 'Theory and Efficient Computation of Differential Vibrational Spectra' [J. Chem. Phys., **140**, 144109 (2014)]  
S. Sakaguchi, T. Ishiyama, and A. Morita: J. Chem. Phys. **141** (2014) 149901
6. Molecular Dynamics Analysis of NaOH Aqueous Solution Surface and the Sum Frequency Gen-

- eration Spectra: Is Surface OH<sup>-</sup> Detected by SFG Spectroscopy?  
 T. Imamura, T. Ishiyama, and A. Morita: J. Phys. Chem. C **118** (2014) 29017-29027
7. Why is Benzene Soluble in Water? Role of OH<sup>-</sup> Interaction in Solvation  
 H. Takahashi, D. Suzuoka, and A. Morita: J. Chem. Theory Comput. **11** (2015) 1181-1194
  8. Molecular Dynamics Study of Two-Dimensional Sum Frequency Generation Spectra at Vapor/Water Interface  
 T. Ishiyama, A. Morita, and T. Tahara: J. Chem. Phys. **142** (2015) 212407 (13 pages)
  9. Theoretical analysis of salt effect on intramolecular proton transfer reaction of glycine in NaCl aqueous solution  
 Y. Kasai, N. Yoshida, and H. Nakano: J. Mol. Liq. **200** (2014) 32-37
  10. Distinct configurations of cations and water in the selectivity filter of the KcsA potassium channel probe by 3D-RISM theory  
 S. Phongphanphanee, N. Yoshida, S. Oiki and F. Hirata: J. Mol. Liq. **200** (2014) 52-58
  11. Efficient implementation of the three-dimensional reference interaction site model method in the fragment molecular orbital method  
 N. Yoshida: J. Chem. Phys. **140** (2014) 214118 (13 pages)

## □ Doctor theses

1. **FUJI, Yohei**  
Symmetries and quantum phases in one-dimensional spin systems  
University of Tokyo, 2015-03
2. **HIGASHI, Yoichi**  
Theoretical study for identifying unconventional superconductivity through vortex core bound states  
Osaka Prefecture University, 2015-03
3. **KITAOKA, Yukie**  
Investigation on Multiplets in Metal-Complexes from Constraint Density Functional Theory  
Mie University, 2014-09
4. **KURITA, Moyuru**  
Numerical Studies on Quantum Phases Emergent from Interplay of Spin-Orbit Interactions and Strong Electron Correlations  
University of Tokyo, 2015-03
5. **NISHIDA, Miho**  
Theoretical studies on spin structures and physical properties of transition metal oxides  
Kanazawa University, 2015-03
6. **NOMURA, Yusuke**  
Ab initio studies on superconductivity in alkali-doped fullerides  
University of Tokyo, 2015-03
7. **YAMAMOTO, Kentaro**  
Coupled proton-electron transfer in excited states of X-MnOH<sub>2</sub>: A nonadiabatic electron wavepacket study  
University of Tokyo, 2015-03

## □ Master Theses

1. **AKIYAMA, Sumito**  
Electronic Properties of Redox Active Molecules Attached on Metal Electrodes Using First-Principles Calculations  
Osaka University, 2015-03
2. **ARAI, Hayato**  
Theoretical studies on the superconducting mechanism of iron-pnictide and the thermoelectricity of black phosphorus by the first-principles calculation and multiband effective model  
University of Electro-Communications, 2015-03
3. **FUTAMI, Futoshi**  
Static and dynamical properties of magnetic order in small world networks  
University of Tokyo, 2015-03
4. **HIYAMA, Masaaki**  
Diffusion and ionization of metal atoms around metal/SiO<sub>2</sub> interfaces: first-principles study  
Chiba University, 2015-03
5. **IDO, Kota**  
Time-Dependent Variational Monte Carlo Method for Quantum Dynamics  
University of Tokyo, 2015-03
6. **ISHIHARA, Takashi**  
Development and tuning of "CALNOS" for nonlinear spectroscopy calculation and its application to gas-liquid interface of water/methanol mixture  
Tohoku University, 2015-03
7. **KASAI, Yukako**  
Theoretical Prediction of pKa Value of Amino Acids using 3D-RISM-SCF Method  
Kyushu University, 2015-03
8. **KAWASHIRI, Yuuki**  
Theoretical study on DC response of single molecular device using first-principles calculations  
University of Tokyo, 2015-03
9. **KIDANI, Naotaka**  
Analysis of etching mechanism in CARE method by means of first-principles calculations -Atom removal mechanism at step edge of alpha-quartz-  
Osaka University, 2015-03
10. **KUBOTA, Dai**  
Extension of Cluster Dynamical Mean Field Theory by Real Space Renormalization  
University of Tokyo, 2015-03
11. **LI, Han**  
Development of Real-Space Car-Parrinello Molecular Dynamics and its Application to SiC Oxidation  
University of Tokyo, 2015-03
12. **MIKI, Yuji**  
Free energy analyses for ATP hydrolysis using massively parallel QM/MM simulations  
Tohoku University, 2015-03

13. **NAKAGAWA, Koh, M.**  
Morphological changes of amphiphilic molecular assemblies induced by chemical reaction  
University of Tokyo, 2015-03
14. **NAKAGAWA, Yuya**  
Flux quench in the  $S=1/2$  XXZ chain  
University of Tokyo, 2015-03
15. **NAKAMURA, Syunya**  
First-principles calculations of surface structures and electronic states on perovskite-type manganese  
University of Tokyo, 2015-03
16. **NISHIKAWA, Yoshihiko**  
Statistical-mechanical study of glass transition in lattice gas models  
University of Tokyo, 2015-03
17. **OKUMA, Koji**  
Theoretical study on the cohesive properties of organic solids with the van der Waals density functional  
University of the Ryukyus, 2015-03
18. **SATO, Shouta**  
Heat Transfer Enhancement of the Film Flow Falling along Vertical Fluted Plates  
Akita University, 2015-03
19. **SHINEI, Chikara**  
Atomic structures and electronic states of Intrinsic defects clusters in silicon carbide studied by density functional theory  
University of Tokyo, 2015-03
20. **SHINOZAKI, Misako**  
Monte Carlo Simulations for Chiral Helimagnets  
University of Tokyo, 2015-03
21. **TAKAHASHI, Takashi**  
Monte-Carlo study of a three dimensional Potts glass model  
University of Tokyo, 2015-03
22. **TSUKUDA, Shingo**  
Impurity state and electronic conductivity of organic semiconductors: first-principles study  
Chiba University, 2015-03
23. **UEHARA, Amane**  
Theoretical Study of Charge-Spin-Orbital Fluctuations of Mixed Valence Spinel  
University of Tokyo, 2015-03
24. **YANAGISAWA, Koichi**  
Tensor network study of two-dimensional frustrated quantum spin model  
University of Tokyo, 2015-03